CE OR PR-DOPED TYPE III KGD(PO3)4 CRYSTALLINE MATERIALS. GROWTH AND CHARACTERIZATION AS SCINTILLATORS

Irina Adell Barbarà

UNIVERSITAT ROVIRA i VIRGILI

Ce or Pr-doped type III $KGd(PO_3)_4$ crystalline materials. Growth and characterization as scintillators

IRINA ADELL BARBARÀ



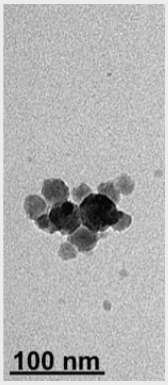

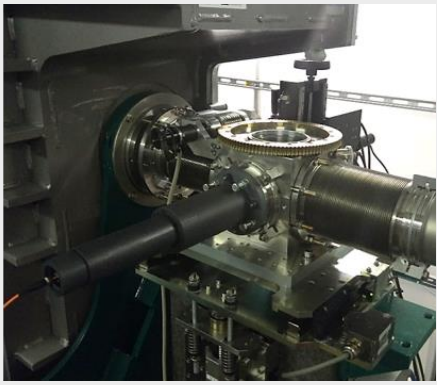

DOCTORAL THESIS
2019

UNIVERSITAT ROVIRA I VIRGILI
CE OR PR-DOPED TYPE III KGD(PO3)4 CRYSTALLINE MATERIALS. GROWTH AND CHARACTERIZATION AS SCINTILLATORS
Irina Adell Barbarà

Ce or Pr-doped type III $KGd(PO_3)_4$ crystalline materials. Growth and characterization as scintillators

Irina Adell Barbarà

Doctoral Thesis

Supervised by:

Dr. Maria Cinta Pujol Baiges

Dr. Rosa Maria Solé Cartañà

Prof. Dr. Francesc Díaz González

Doctoral Programme in Nanoscience, Materials and Chemical Engineering
Departament de Química Física i Inorgànica
Física i Cristal·lografia de Materials i Nanomaterials (FiCMA-FiCNA)

UNIVERSITAT ROVIRA i VIRGILI

Tarragona, 2019

Ce or Pr-doped type III $KGd(PO_3)_4$ crystalline materials. Growth and characterization as scintillators

Irina Adell Barbarà

Física i Cristal·lografia de Materials i Nanomaterials (FiCMA-FiCNA)

Departament de Química Física i Inorgànica

Universitat Rovira i Virgili

c/ Marcel·lí Domingo, 1

E-43007, Tarragona, Spain

UNIVERSITAT ROVIRA I VIRGILI
DEPARTAMENT DE QUÍMICA FÍSICA I INORGÀNICA
Campus Sescelades
Marcel·lí Domingo, s/n
43007 Tarragona
Tel. +34 977 55 81 37
Fax +34 977 55 95 63
www.quimica.urv.es

We STATE that the present study, entitled "**Ce or Pr-doped type III $KGd(PO_3)_4$ crystalline materials. Growth and characterization as scintillators**", presented by Irina Adell Barbarà for the award of the degree of Doctor, has been carried out under our supervision at the Department of Physical and Inorganic Chemistry of this university.

Tarragona, September 2, 2019

Doctoral Thesis Supervisor/s

Prof. Dr. Francesc Díaz González

Dr. Maria Cinta Pujol Baiges

Dr. Rosa Maria Solé Cartañà

UNIVERSITAT ROVIRA I VIRGILI
CE OR PR-DOPED TYPE III KGD(PO3)4 CRYSTALLINE MATERIALS. GROWTH AND CHARACTERIZATION AS SCINTILLATORS
Irina Adell Barbarà

Abstract

Ce or Pr-doped type III $KGd(PO_3)_4$ crystalline materials. Growth and characterization as scintillators

Irina Adell Barbarà

Scintillator materials, or simply scintillators, are extensively used as detectors in the detection systems of a variety of applications, such as medical imaging [planar X-ray imaging, X-ray computed tomography (CT), positron emission tomography (PET), single-photon emission computed tomography (SPECT)], astrophysics, high energy physics (HEP), non-destructive testing (airport security, industrial control, etc.) and homeland security. The search for new inorganic scintillators with better properties than those of the existing scintillators that suit the needs of each application is of great interest. Many efforts are being made to find them, as indicated by the large research activity.

In this Thesis, Ce^{3+}- and Pr^{3+}-doped type III $KGd(PO_3)_4$ bulk single crystals with high crystalline quality and type III $Pr:KGd(PO_3)_4$ nanocrystals are grown and structurally and optically characterized as possible new scintillator materials. These bulk single crystals are grown from high temperature solutions by the Top Seeded Solution Growth-Slow Cooling (TSSG-SC) technique, while the nanocrystals are synthesized by the Pechini method. The structural characterization includes the chemical composition, crystal morphology, changes in the unit cell parameters with doping content, as well as the thermal stability, thermal expansion and particle size distribution. The spectroscopy of the 5*d*–4*f* electronic transitions, on which the scintillation mechanism in inorganic scintillators containing lanthanide ions is based, is studied in detail. These spectroscopic studies are unpolarized and polarized optical absorption measurements at room temperature and 6 K, luminescence and decay time measurements under synchrotron vacuum ultraviolet-ultraviolet (VUV-UV) excitation, decay time measurements under visible excitation, and radioluminescence measurements after synchrotron X-ray irradiation. In addition to this, since Pr^{3+} also arouses great interest as active ion in laser applications, the basic spectroscopic data of the type III $Pr:KGd(PO_3)_4$ crystal for lasing applications in the visible wavelength range based on the 4*f*–4*f* electronic transitions is provided.

The primary crystallization region of type B KYP_4O_{12} and type IV $KY(PO_3)_4$ in the K_2O–Y_2O_3–P_2O_5 ternary system is determined, since these are interesting candidates as hosts for active lanthanide ions in scintillation applications.

Keywords: crystal growth, bulk single crystals, Top Seeded Solution Growth-Slow Cooling technique, nanocrystals, Pechini method, Ce^{3+}- and Pr^{3+}-doped type III $KGd(PO_3)_4$, optical spectroscopy, luminescence, radioluminescence, synchrotron radiation, scintillator materials.

UNIVERSITAT ROVIRA I VIRGILI
CE OR PR-DOPED TYPE III KGD(PO3)4 CRYSTALLINE MATERIALS. GROWTH AND CHARACTERIZATION AS SCINTILLATORS
Irina Adell Barbarà

"*We must have perseverance and above all confidence in ourselves. We must believe that we are gifted for something and that this thing must be attained."*

Marie Curie

UNIVERSITAT ROVIRA I VIRGILI
CE OR PR-DOPED TYPE III KGD(PO3)4 CRYSTALLINE MATERIALS. GROWTH AND CHARACTERIZATION AS SCINTILLATORS
Irina Adell Barbarà

Preface

The Ph.D. investigation contained in this Thesis has been carried out at the research group of *Física i Cristal·lografia de Materials i Nanomaterials* (FiCMA-FiCNA) in the *Departament de Química Física i Inorgànica* of the *Universitat Rovira i Virgili* (URV), in Tarragona, and supervised by Dr. Maria Cinta Pujol Bages, Dr. Rosa Maria Solé Cartañà and Prof. Dr. Francesc Díaz González.

During the development of this Thesis, we have collaborated with Dr. Matthieu Lancry from the *Institut de Chimie Moléculaire et des Matériaux d'Orsay* of the *Université de Paris-Saclay* (Orsay, France) and Dr. Nadège Ollier from the *Laboratoire des Solides Irradiés* of the *Université de Paris-Saclay* (Palaiseau, France).

This research project has been possible thanks to the financial support provided by the Spanish Government under Projects MAT2016-75716-C2-1-R (AEI/FEDER,UE) and TEC 2014-55948-R, and from the Catalan Government under Projects 2014 SGR 1358 and 2017 SGR 755. We would also like to thank SOLEIL Synchrotron (Saint-Aubin, France) and ALBA Synchrotron (Cerdanyola del Vallès, Spain) for provision of synchrotron radiation facilities under the projects with proposal numbers 20151215 (standard) and 20161324 (standard), and the project with proposal number 2016091932, respectively. I am deeply grateful to the Catalan Government for the personal funding under grants 2015 FI_B 00711, 2016 FI_B1 00113 and 2017 FI_B2 00017.

Irina Adell Barbarà

Tarragona, 2019

UNIVERSITAT ROVIRA I VIRGILI
CE OR PR-DOPED TYPE III KGD(PO3)4 CRYSTALLINE MATERIALS. GROWTH AND CHARACTERIZATION AS SCINTILLATORS
Irina Adell Barbarà

Acknowledgments

Primerament, vull agrair a la Prof. Dra. Magdalena Aguiló i Prof. Dr. Francesc Díaz per haver-me donat l'oportunitat de dur a terme la Tesi Doctoral al grup de recerca que lideren, FiCMA-FiCNA. Agraeixo moltíssim a la Magdalena Aguiló que des del principi hagi confiat en mi i que m'hagi animat sempre a seguir. Com a codirectors de tesi, vull agrair a la Dra. Maria Cinta Pujol, Dra. Rosa Maria Solé i, de nou, al Prof. Dr. Francesc Díaz el seu esforç, perseverança, dedicació, temps i paciència en cada una de les etapes de la tesi. Moltes gràcies per tot el coneixement que heu compartit amb mi, no només durant el doctorat sinó també des de la carrera. Magdalena Aguiló, gràcies per endinsar-me al món de la Cristal·lografia i per resoldre els dubtes que alguns cops han sorgit durant la tesi. Rosa Maria Solé, gràcies per ensenyar-me tot el que sé sobre Creixement cristal·lí, i també agraeixo que cada dia de la setmana durant aquests anys hagis trobat temps, ni que fos un moment, per venir a preguntar-me com anava la feina i, si calia, ajudar-me. Cinta Pujol, gràcies per ensenyar-me tant i ser tant propera. He gaudit molt aprenent al teu costat, discutint tots els dubtes que m'han sorgit sobre Espectroscòpia al llarg de la tesi i especialment durant la discussió de resultats. També agraeixo moltíssim tot el que m'has ensenyat pel que fa a la redacció d'un article científic. Francesc Díaz, gràcies per tots els coneixements de Física que has compartit amb mi, i també pel teu entusiasme i la teva empenta per a la realització satisfactòria de la tesi.

M'agradaria agrair a la resta dels membres del grup de recerca del FiCMA-FiCNA la seva contribució. Agraeixo al Dr. Joan Josep Carvajal, Dr. Jaume Massons i Dr. Xavier Mateos l'ajuda que m'han donat a través dels seus comentaris i coneixements en algunes ocasions durant la tesi. Especialment vull agrair la gran ajuda que he rebut per part dels tècnics de suport a la recerca, tant per aquells que estan al grup actualment com pels que ja no hi treballen: Nicolette Bakker, Dr. Josué Mena, Dra. Gemma Marsal, Agustí Montero, Dr. Josep Maria Serres i Laura Escorihuela. Agraeixo profundament a la Nicole Bakker tot el que ha fet per mi durant tots aquests anys, tant professionalment com personalment. Gràcies per trobar sempre temps per resoldre qualsevol dubte o problema que em sorgís al laboratori, per haver dedicat tant de temps al tall i polit dels meus cristalls, cosa que sense ells no hagués estat possible bona part de les mesures realitzades a la tesi, i també per haver-me ajudat tant durant les estades als sincrotrons. Nicole, agraeixo moltíssim els bons moments que hem viscut, que sempre m'hagis escoltat quan ho he necessitat i que sempre m'hagis animat a seguir. Al Josué Mena vull agrair-li tota l'ajuda que m'ha proporcionat, especialment en microscòpia electrònica i espectroscòpia Raman, dedicant-hi temps i compartint els seus coneixements per resoldre'm dubtes i problemes. Josu, gràcies pels bons moments, per animar-me en els moments més durs i per resoldre, sense queixar-te, els infinits dubtes que m'han sorgit en relació a la redacció, el dipòsit i la defensa de la tesi. També vull donar-li gràcies a la Gemma Marsal per la seva ajuda i gran dedicació en la síntesi de nanocristalls i en diverses mesures d'espectroscòpia. Gemma, gràcies pels ànims i per tots els consells que m'has donat, especialment en l'última etapa de la tesi.

It has been a pleasure to work with all the PhD, master and bachelor students with whom I have coincided during these years. Those PhD students with whom I have shared most of these years are Marc Medina, Dr. Josué Mena, Dr. Eric Pedrol, Dr. Esrom Aschenaki Kifle, Dr. Josep Maria Serres, Dr. Dad Nguyen, Dr. Javier Martínez and Albenc Nexha. I appreciate the good times I experienced with them and the help they gave me when I needed it. Entre ells, especialment vull agrair-li al Marc Medina que m'hagi escoltat i ajudat en innumerables ocasions, que haguem compartit tantes converses interessants sobre la vida o sobre qualsevol tema que tinguéssim ganes de parlar mentre fèiem el cafè, i també per ser tant divertit. També ha estat un plaer coincidir amb l'estudiant de grau Paulí Figueras, a qui li agraeixo el recolzament en l'última etapa de la tesi.

Així doncs, agraeixo profundament haver compartit aquests anys especialment amb la Nicole, el Marc i el Josu, que han passat a convertir-se en amics. Vosaltres heu fet molt més fàcil i amè el trajecte gràcies a tots els moments que hem viscut junts, com per exemple totes les escenes súper divertides a l'Office, els *sustos* que m'heu fet i totes les converses de mil temes diferents.

També vull donar-li les gràcies al Dr. Francesc Gispert, responsable de la Unitat de Caracterització de Materials (SRCiT, URV), per la seva grandíssima ajuda durant tots aquests anys, la seva paciència per respondre una i cada una de les meves preguntes, dubtes i inquietuds en el camp de la Difracció de pols de raigs X, i també per compartir tant de coneixement amb mi. També voldria agrair l'ajuda rebuda per part dels membres de l'Àrea de Microscòpia i Tècniques Nanomètriques (SRCiT, URV), especialment per la Dra. Mariana Trifonova. Vull agrair-li al Dr. Xavier Llovet, responsable de la Microsonda electrònica en els Centres Científics i Tecnològics de la Universitat de Barcelona (CCiTUB), que sempre m'hagi ajudat tant amablement en relació a les mesures d'EPMA.

I would like to deeply acknowledge Dr. Matthieu Lancry and Dr. Nadège Ollier for lending us the necessary equipment to carry out the luminescence and decay time measurements under synchrotron vacuum ultraviolet-ultraviolet excitation, and for sharing their knowledge. I would also like to thank SOLEIL Synchrotron for provision of synchrotron radiation facilities under the projects with proposal numbers 20151215 (standard) and 20161324 (standard), Nelson de Oliveira for assistance in using the DESIRS beamline, and the SOLEIL staff for smoothly running the facility. I thank ALBA Synchrotron for allocating beamtime at BL22-CLAESS beamline under the project with proposal number 2016091932, and Carlo Marini for his help and technical support during the radioluminescence measurements. Also, I would like to thank Medcom Advance for provision of its facilities to perform the luminescence and decay time curves measurements under visible excitation.

Ara vull agrair a tots els meus amics, Coia, Judith, Montse, Roger, Nàroa, Sergi, Edu, Sergi, Héctor, Edu, Fran, Claudia i Marta, el fet que m'hagin acompanyat en aquest trajecte donant-me tot el seu suport, interessant-se per la meva feina, animant-me a seguir i sempre preocupant-se per mi. Quiero agradecer a mi amiga del máster, Christhy, todo su apoyo, ayuda, gran comprensión y ánimos.

Vull agrair de tot cor a mons pares, Adrià Adell i Gemma Barbarà, el seu suport incondicional, per ajudar-me sempre en tot el possible, per creure en mi, per animar-me a seguir i per intentar fer més fàcil l'última etapa de la tesi. També vull agrair profundament a mon germà i a la meva cunyada, Adrià i Cori, tot el seu suport, per preocupar-se sempre per mi, per ajudar-me en tot el possible, per animar-me a seguir fent-me veure les coses pel costat bo i per estar sempre al meu costat. Agraeixo que el meu nebot, Jan, estigui de fa uns pocs anys a les nostres vides, perquè ens l'omple d'alegria. També vull agrair tot l'amor i la companyia que m'ha donat el nostre gos, Dexter, durant tot aquest trajecte. Por último, quiero sinceramente agradecer a mi pareja, Nicolás, todo su apoyo desde el día que nos conocimos, por creer en mí, por animarme cada día y por hacerlo todo más fácil.

UNIVERSITAT ROVIRA I VIRGILI
CE OR PR-DOPED TYPE III KGD(PO3)4 CRYSTALLINE MATERIALS. GROWTH AND CHARACTERIZATION AS SCINTILLATORS
Irina Adell Barbarà

To my close family and Nicolás
with great love

UNIVERSITAT ROVIRA I VIRGILI
CE OR PR-DOPED TYPE III KGD(PO3)4 CRYSTALLINE MATERIALS. GROWTH AND CHARACTERIZATION AS SCINTILLATORS
Irina Adell Barbarà

List of publications and conferences

This Ph.D. Thesis is partially based on the work contained in the following papers:

Paper I:

I. Adell, R. M. Solé, M. C. Pujol, M. Lancry, N. Ollier, M. Aguiló and F. Díaz. Single crystal growth, optical absorption and luminescence properties under VUV-UV synchrotron excitation of type III Ce^{3+}:$KGd(PO_3)_4$, a promising scintillator material. *Sci. Rep.* **2018**, *8*, 11002.
https://doi.org/10.1038/s41598-018-29372-z

Paper II:

I. Adell, M. C. Pujol, R. M. Solé, M. Lancry, N. Ollier, M. Aguiló and F. Díaz. Single crystal growth, optical absorption and luminescence properties under VUV-UV synchrotron excitation of type III Pr^{3+}:$KGd(PO_3)_4$. *Submitted to Sci. Rep.*

Paper III:

I. Adell, R. M. Solé, M. C. Pujol, M. Aguiló and F. Díaz. Optimization of the synthesis and physical characterization of praseodymium-doped type III $KGd(PO_3)_4$ nanocrystals. *ACS Omega* **2018**, *3* (9), 11307-11316.
https://doi.org/10.1021/acsomega.8b01321

Paper IV:

I. Adell, M. C. Pujol, R. M. Solé, M. Aguiló and F. Díaz. Radioluminescence properties under X-ray excitation of type III Ce^{3+}- and Pr^{3+}-doped $KGd(PO_3)_4$ single crystals. *Submitted to J. Phys. Chem. C*

The results of this Ph.D. Thesis have been presented at the following international conferences:

I. Adell, R. Solé, A. Ródenas, M. C. Pujol, M. Aguiló and F. Díaz. Synthesis and preliminary characterization of praseodymium-doped type III $KGd(PO_3)_4$ nanocrystals: a promising new scintillator material. 7th International Symposium on Optical Materials (IS-OM7). Lyon, France, **2016**.

I. Adell, R. Solé, M. C. Pujol, M. Aguiló and F. Díaz. Single crystal growth and spectroscopic characterization of cerium and praseodymium single doped type III $KGd(PO_3)_4$. 26th International Conference on Advanced Laser Technologies (ALT'18). Tarragona, Spain, **2018**.

I. Adell, R. M. Solé, M. C. Pujol, M. Aguiló and F. Díaz. Praseodymium-doped type III $KGd(PO_3)_4$ nanocrystals: synthesis and characterization. 8th International Workshop on Photoluminescence in Rare Earths: Photonic Materials and Devices (PRE'19). Nice, France, **2019**.

I. Adell, R. M. Solé, M. C. Pujol, M. Lancry, N. Ollier, M. Aguiló and F. Díaz. Characterization of Ce^{3+} or Pr^{3+}- single doped type III $KGd(PO_3)_4$ bulk crystals as scintillator materials. 8th International Workshop on Photoluminescence in Rare Earths: Photonic Materials and Devices (PRE'19). Nice, France, **2019**.

Table of contents

UNIVERSITAT ROVIRA I VIRGILI
CE OR PR-DOPED TYPE III KGD(PO3)4 CRYSTALLINE MATERIALS. GROWTH AND CHARACTERIZATION AS SCINTILLATORS
Irina Adell Barbarà

Chapter 1.
Introduction

This Chapter is divided into three blocks. The first block consists of an introduction to the compounds known as scintillator materials, along with the history and the state of the art of inorganic scintillators. The second block is dedicated to those inorganic scintillators containing lanthanide ions (Ln), including the corresponding scintillation mechanism and a description of the characteristics of cerium- and praseodymium-doped compounds, with Ce^{3+} and Pr^{3+} being the doping ions used in this Doctoral Thesis. By last, the third block describes the crystalline hosts to be doped used in this Ph.D. Thesis.

1.1. Introduction to scintillators

Scintillator materials, or simply scintillators, are materials able to convert a high-energy photon from the X-ray or γ-ray range (typically from KeV to GeV) into a bunch of photons in the UV-visible range. Alternatively, scintillators can also detect the energy of accelerated charged particles (electrons, protons and heavier ions) or neutrons and convert it into UV-visible radiation. In practice, a scintillation detector consists of two parts: the scintillating material itself, and a photodetector which is responsible for converting the UV-visible photons emitted by the scintillator into an electrical signal via the photoelectric effect. The scintillator material affects both the efficiency and the resolution of the detector, so the characteristics of the scintillator material are important.[1,2,3]

The scintillation property is observed in solids, liquids and gases. Among the solids, there are two big families: inorganic and organic scintillators. Inorganic scintillators are the most used in practical applications and occupy a large part of the research activity. The classification of the inorganic scintillator materials based on the scintillation mechanism divides them into three classes. These classes are *activated scintillators*, based on crystalline compounds doped with activating ions; *self-activated scintillators*, where emitting centres are ions, anionic complexes or various excitonic states from the host itself; and *cross-luminescent scintillators*, which can be crystals with or without impurities[4]. Inorganic scintillators are widely used in the detection systems addressing different fields such as medical imaging[5] [planar X-ray imaging, X-ray computed tomography (CT), single-photon emission computed tomography (SPECT), positron emission tomography (PET)], high energy physics (HEP), non-destructive testing (airport security, industrial control, etc.), astrophysics, homeland security, amongst others.[1,3,6,7,8]

Many efforts are dedicated to find inorganic materials with optimal scintillation properties. The following requirements are important to evaluate favourably the performance of any scintillator, although it is worth mentioning that some requirements are more restrictive for some applications than for others, depending on the specific minimum needs of each application.[9,10,11]

❖ High light yield

Light yield (LY) is defined as the number of UV-visible photons emitted by a scintillator after absorbing the incoming ionizing radiation divided by the energy value of this incoming radiation. It is typically given as the number of photons emitted per MeV of energy of the incoming radiation ($ph \cdot MeV^{-1}$). Logically, the essential feature required of any scintillator is to be an effective energy converter. Thus, LY must be as high as possible. The more UV-visible light is generated, the higher the sensitivity will be. This is especially important in diagnostic techniques because a high sensitivity allows to reduce the exposure of ionizing radiation to the patient[12]. The LY for scintillators used in PET-scanners are typically above 25 000 $ph \cdot MeV^{-1}$.

❖ High total absorption coefficient

It is important that all the energy of the ionizing radiation is absorbed by the scintillator and then converted to UV-visible radiation. A high total absorption coefficient allows

the use of smaller scintillators, which generally results in lower production costs. The absorption coefficient depends on the composition of the scintillator material and the energy of the radiation. For X-rays and γ-rays detection, high-density scintillators are most often used because they permit the absorption of the total energy of the incoming radiation. Thus, the effective atomic number (Z_{eff}) of the scintillator should also be large, since it provides a higher absorption cross-section for X-rays and γ-rays because of higher electron density. Z_{eff} is defined as follows, where w_i is the mass fraction of atom *i* within the specific material and Z_i is its atomic number[3].

$$Z_{eff}^4 = \sum_i w_i Z_i^4 \qquad \text{Eq. 1.1}$$

The density of the material and its Z_{eff} should be large for most applications, although this requirement is not so strong for α-rays and low-energy β-rays detection.

❖ **Efficient energy transfer**

After exciting the inorganic scintillators with ionizing radiation, electronic excitations are created (such as correlated electron−hole pairs, excitons, separated electrons and holes, etc.). The scintillation mechanism continues with the energy transfer from the final electronic excitations to the emitting centres, and ends with the light emission by these centres. Thus, the energy transfer efficiency is closely related to the light output of the scintillator.

❖ **Short emission lifetime**

Lifetime is the time required for scintillation emission to decrease to 1/e of its initial intensity value. A short emission lifetime/fast decay time is especially important in PET-scanners for any improvement in spatial resolution and sensitivity, since PET technique is based on a precise temporal measurement of two simultaneously emitted γ-rays at nearly 180º during a positron−electron annihilation process[5,13,14] (see Figure 1.1). Thus, PET-scanners require emission lifetimes below 100 ns. The acceptable time regime for planar X-ray imaging and CT-scanners is microseconds and even milliseconds.

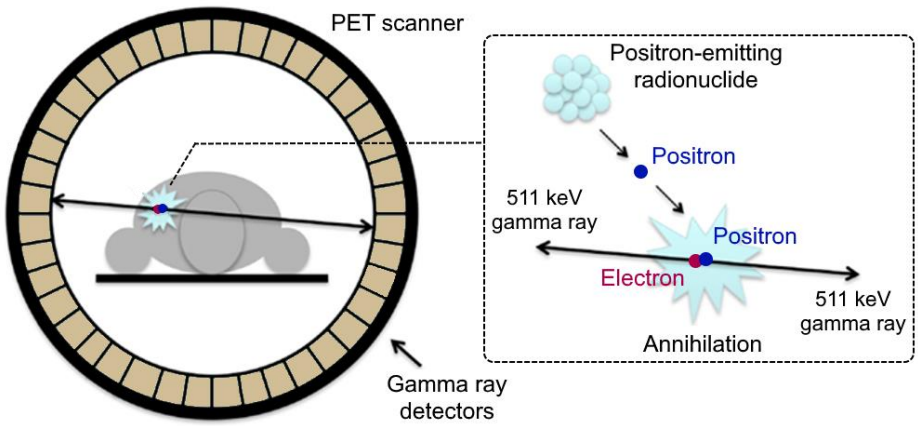

Figure 1.1. Positron Emission Tomography (PET) technology[15].

❖ **Transmission of its own emitted light**

In most applications, the scintillator should transmit its own emitted light.

❖ **No afterglow**

The term “afterglow” refers to the emission that continues for several microseconds, seconds, minutes or even hours after excitation has ended. Afterglow reduces the direct light output. The non-existence or low intensity of afterglow is particularly necessary for CT-scanners[5], otherwise, afterglow would result in ghost images, that is, less reliable images and therefore, worse diagnostics. Afterglow is caused by the thermally activated release of trapped charge carriers (electrons or holes) at defect sites in the crystalline lattice and the recombination of these charge carriers at an emitting centre. These defect sites, or traps, can be inherently present in the material, or can be produced by external means, such as by doping the crystal with impurities or after irradiating the material with ionizing radiation. Therefore, the afterglow properties (intensity, spectral composition and decay time) depend on the purity of raw material, crystal conditions, heat treatment, doses of irradiation, amongst others. Accordingly, afterglow can be reduced by optimizing the crystal growth process, and in addition, some correction is possible by software.

❖ **Radiation hardness**

The interaction of ionizing radiation with a crystalline scintillator invariably creates radiation damage. The term “radiation damage” refers to the formation of radiation-induced defects in the crystalline structure of the scintillator, such as bond breaking or atom/ion displacement. The presence of vacancies in the crystalline structure leads to the creation of colour centres, which can be holes located in cation vacancies (V centre), electrons located in anion vacancies (F centre), or others[16]. Colour centres and defects reduce the efficiency of the scintillation process by competitive trapping of the charge carriers with the emitting centres of interest. In addition, colour centres may absorb the photons emitted by the luminescent centres, also reducing the efficiency of the scintillation process. The radiation damage can be produced during irradiation and after accumulating large doses. Therefore, it is crucial that the scintillator shows radiation hardness for long-term performance. It is worth mentioning that the defect production depends on the concentration of uncontrolled impurities. In oxides, the cause of radiation damage is usually the existence of defects related to stoichiometry, such as oxygen vacancies in the crystalline structure[16].

❖ **Chemical stability**

The chemical composition of a scintillator should not change over time under normal atmospheric conditions and under high-energy irradiation. Examples of undesired chemical changes are the absorption of water from the environment (for hygroscopic scintillators) or the change in valence states of the activator ions in an oxidizing environment. This limits the application of the scintillator, although encapsulation can be used to protect it, which increases production costs.

❖ **Favourable mechanical properties**

In many industrial applications, the scintillator crystals are used in severe environments. Consequently, the scintillators should be resistant to shocks and have large

mechanical ruggedness and hardness. Cleavage of a scintillator crystal causes difficulties during the mechanical treatment to obtain the desired dimensions and shape, and can lead to deterioration of the scintillator performance.

❖ **Detection efficiency**

As previously mentioned, a scintillation detector consists of the scintillating material itself and a photodetector, which is the responsible for converting the UV-visible photons into an electrical signal. Logically, the emission of the scintillator material should peak near the maximum quantum efficiency of the photodetector. That is, the emission has to be detected with the highest possible sensitivity. The choice of the photodetector is determined by the emission wavelength of the scintillator material. In 1997, Rodnyi[10] already reported on the photodetectors used, which cover the spectral range from vacuum ultraviolet (VUV) to visible radiation. When the emission is in the UV-blue spectral range, the photodetector that provides the best signal to noise ratio is a photomultiplier (PMT). More specifically, for emissions at wavelengths from 280 to about 500 nm, a PMT with a bialkali photocathode and a glass window should be used. While a PMT with a bialkali photocathode and a quartz or MgF_2 window is the best choice for emissions in the UV and VUV regions, since the second maximum of the quantum efficiency is at 180 nm. If the emission is in the red spectral region, a charge coupled device (CCD) camera or a silicon photodiode are the suitable photodetectors to obtain the best sensitivity. When the emission is not within the mentioned spectral ranges, a wavelength shifter can be used to increase the sensitivity.[10]

❖ **Temperature stability of the scintillation yield**

The scintillators are used at room temperature in most applications. The temperature of the scintillation detector (scintillating material itself + photodetector) can vary slightly due to irradiation or change of ambient conditions. In space applications, it is particularly difficult to keep a stable regime for detector operation. The change of light output with temperature of the scintillator material results in a change of the output signal of the photodetector. Hence, the thermal stability of the scintillation yield is needed for proper operation of the detector. Apart from this, the “onset temperature of photoluminescence thermal quenching” of a specific scintillator material is usually searched. This term is defined as the temperature at which the decay time obtained from the single exponential fitting has dropped to half the value at the plateau before the initial drop occurs[1]. Thus, scintillators with the onset of thermal quenching at high temperatures can be used in high-temperature applications.

❖ **Proportionality of scintillation response**

The scintillation yield should be proportional to the absorbed energy from the incoming ionizing radiation over the widest possible range of energies.

❖ **Low radioactivity of the constituent elements**

The existence of a radioactive isotope of the constituent elements of a scintillator with relatively high natural abundance results in an intrinsic radioactivity of such scintillator, which disables its use in low-signal-count-rate applications, since the emission of the radioisotope can interfere with the detection process.

- **Availability to grow large and high crystalline quality samples**
- **Homogeneity or uniform distribution of impurities (activator ions)**
- **Low cost**

Low cost raw materials with their required purity and cheap production techniques are desirable for most applications of scintillators.

Since until the time the ideal scintillator that simultaneously meets all of these criteria perfectly does not exist, one must select the most suitable combination of properties for each application from the existing scintillators. The scintillator requirements for each modality of medical imaging are reported in ref.[5], and the requirements for various applications such as high energy physics (HEP), intermediate energy physics, gamma spectroscopy and low energy region are extensively explained in ref.[7].

1.2. History and state of the art of inorganic scintillators

The discovery of X-rays by W. C. Röntgen in November 1895[17] promoted the initiation of research on scintillator materials. It was found that a simple photographic film was inefficient for X-ray registration, so the search for materials capable of converting X-ray radiation into visible light started immediately afterwards. $CaWO_4$ powder was employed in an X-ray screen for this purpose in early 1896, becoming the first scintillator material. Later, ZnS powder was introduced for X-ray detection as well. Subsequently, $CaWO_4$- and ZnS-based powders became scintillators widely used for X-ray detection[18]. In 1949, R. Hofstadter introduced Tl:NaI single crystal and demonstrated the use of PMT tubes to detect the scintillation flashes[19]. This fact initiated the widespread use of inorganic scintillators and the era of scintillation counters. Figure 1.2 summarizes the historical development of inorganic scintillator materials since 1949. In the early years of the 1950s, $CdWO_4$ (CWO) [20], Tl:CsI [21], CsI [22], CsF [23] and Eu:LiI [24] were introduced in this order. The search for new inorganic scintillators was quite inactive during the next twenty years, although Na:CsI [25], Eu:CaF_2 [26] and $Bi_4Ge_4O_{12}$ (BGO)[27] were proposed. Tl:NaI and Tl:CsI halide scintillators were the most used, followed by CWO and BGO for versatile applications in the field of high energy physics. Today, these four scintillators are often used as standard samples to evaluate the performance of the materials under study.[1,2,28] In fact, these materials are commercial scintillators, which are manufactured, along with others, by companies such as Hellma Materials[29] and Saint-Gobain Crystals[30]. BGO is used in several PET/CT systems, which consisted of a CT scanner in tandem with a PET scanner, manufactured by GE Medical Systems[31].

In the 1980s, a renewal of interest in inorganic scintillators was triggered by the demand for high density scintillation materials with fast decay times for applications in medical diagnosis, high energy physics and industrial processes, along with the introduction of integrated electronics and computers. The fast emission in BaF_2 was discovered[32,33] and interpreted[34], initiating the search for new types of fast scintillators with radiative core-to-valence transitions, which are characteristic of materials

known as cross-luminescent scintillation materials. During the period between the 1980s and the 2000s, the Ce-doped and Ce-based crystals became particularly promising as fast scintillators, as can be seen in Figure 1.2. From the 1990s to the present, the investigations have focused mainly on materials doped with Ce^{3+}, Pr^{3+}, Nd^{3+} and Eu^{2+} due to the fast decay and the high quantum efficiency of the electronic transitions responsible of the scintillation emission, which are the $5d \rightarrow 4f$ transitions of the lanthanide ions. The distinctive characteristic of Ce^{3+} and Pr^{3+} is the even faster decay time of the corresponding $5d \rightarrow 4f$ electronic transitions under direct $4f \rightarrow 5d$ excitation, which are typically within 20–60 ns and 8–20 ns, respectively.[1,2,35,36,37,38]

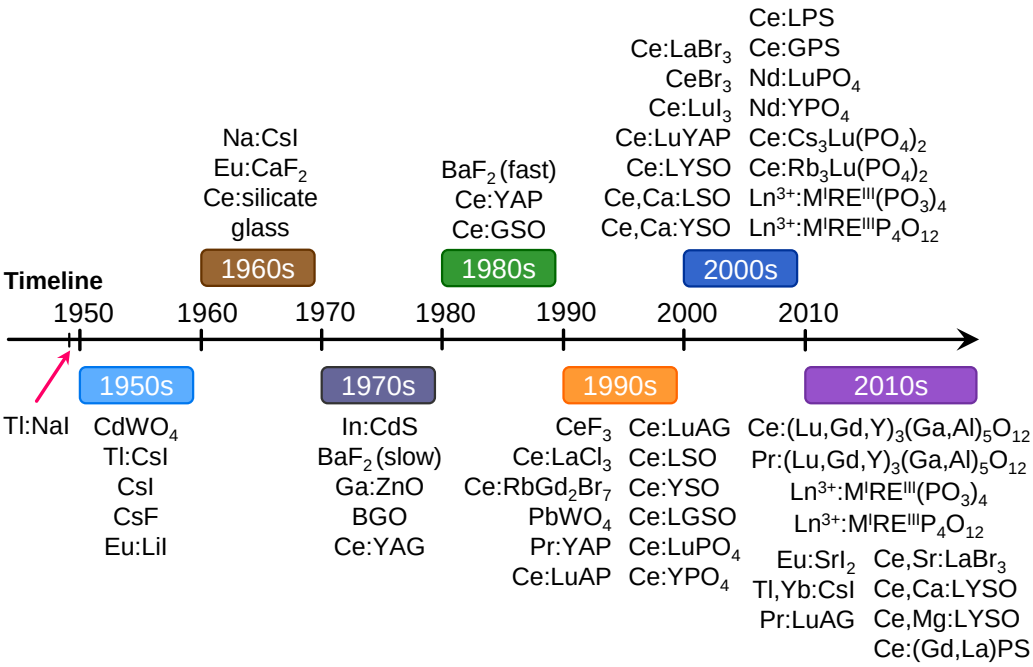

Figure 1.2. Historical development of inorganic scintillator materials since 1949 to 2010s. The chemical compositions corresponding to the acronyms are found in the text below.

Below is a summary of the state of the art of inorganic scintillator materials considering the research works of the last approximately 20 years[1,2], focused on single crystals and crystalline powders. The review of ref.[3] is based on inorganic scintillator materials in the form of thin films or nanoparticles. The optical and scintillation characteristics of the most efficient modern halide scintillators and the characteristics of some selected oxide-based scintillators are summarized in the review of Nikl and Yoshinawa[1]. These are: $Ce:LaCl_3$, $Ce:LaBr_3$, $Ce,Sr:LaBr_3$, $CeBr_3$, $Sr:CeBr_3$, $Ce:LuI_3$, $Eu:SrI_2$, $Eu:CsBa_2I_5$, Ce:YAG, Ce:GGAG, Ce:LuAG, Pr:LuAG, Pr:LuYAG, Ce:YAP, Pr:YAP, Ce,Ca:LYSO and Ce:(Gd,La)PS. The chemical compositions corresponding to the previous acronyms are found in the text below. In ref.[39], the specifications of traditional inorganic scintillators in commercial scintillator catalogues are found, as well as the experimental data of a total of about 75 inorganic scintillators. The scintillation properties of a huge number of inorganic scintillators are also summarized in refs.[4,8,40,41].

❖ Halide scintillators

The well-known Tl:NaI and Tl:CsI single crystals are conventional scintillators due to their widespread use in many different fields. For instance, single-crystal sodium iodide doped with thallium ions, Tl:NaI, is a conventional medical scintillator[42]. However, Tl:NaI is not an ideal scintillator, since it has a comparatively long decay time and a low density. The Tl:CsI single-crystal scintillator shows a high afterglow, which disables its use in CT imaging. Tl:CsI has been co-doped with various aliovalent ions, such as Sm^{2+}, Eu^{2+}, Bi^{3+} and Yb^{2+}, in order to decrease its afterglow. Regarding the first three mentioned co-dopants[43,44,45,46], the authors concluded that these ions are efficient tools to decrease the Tl:CsI afterglow, although the light yield was severely deteriorated in all cases. In contrast, the optimized Tl,Yb:CsI crystal grown by Wu *et al.*[47] largely suppressed afterglow and exhibited an ultra-high LY value of 90 000 ± 6000 ph·MeV^{-1}, as well as a better energy resolution♦[48] compared to that of Tl:CsI. However, Tl,Yb:CsI crystals are slightly hygroscopic.

Ce:$LaCl_3$ and Ce:$LaBr_3$ single crystals were the first scintillators belonging to the family of Ce-doped rare-earth (RE) halides reported[49,50]. Ce^{3+}:$LaCl_3$ shows a high LY and a high energy resolution, although its scintillation decay consists not only of a fast component but also a slow component on a microsecond timescale[51]. Ce^{3+}:$LaBr_3$ has the best scintillation performance in terms of LY, decay time and energy resolution compared to existing scintillators. Ce:$LaBr_3$ exhibits a very high LY of 61 000 ± 5000 ph·MeV^{-1} and the scintillation decay is dominated by a fast approximately single-exponential component with a decay time of about 16 ns[50,52]. Another halide within the same family was introduced later, Ce^{3+}:LuI_3, achieving potentially even higher performances than the previous two scintillators. However, the high percentage of slower components in its scintillation decay and the very high price of the raw materials have hindered its further development[53]. A common drawback in Ce:$LaCl_3$, Ce:$LaBr_3$ and Ce:LuI_3 is the high hygroscopicity, so they must be sealed in appropriate ampoules for handling and characterization[1]. Some compounds belonging to the family of Pr-doped RE halides have also been studied[54,55], which are Pr:$LuCl_3$, Pr:$LuBr_3$, and Pr:$LaBr_3$. None of these compounds shows a fast scintillation response, since the 5*d* level of Pr^{3+} is not populated or is non-radiatively depopulated in the scintillation mechanism. The intrinsic radioactivity of Ce:LaX_3 (X = halogens) scintillators, due to the existence of the lanthanum radioisotope ^{138}La with a natural abundance of 0.09% and half-life $\tau_{1/2} \approx 1.05 \times 10^{11}$ years,

♦ The term “energy resolution” is used in gamma spectroscopy. The standard gamma spectrometer contains a scintillator, a PMT, an electronic amplifier and a multichannel analyser. The last two electronic devices are responsible for amplifying the PMT pulses that result in voltage pulses suitable to count within a channel gate of the analyser. The energy of the incident gamma quanta can be determined by measuring the “pulse height distribution” or “pulse height spectrum”. The excitation source commonly used is ^{137}Cs, whose photopeak (i.e. the peak formed by the full energy of the incident gamma ray) appears centred at 662 keV. The ability to discriminate the gamma quanta with slightly different energies is described by the energy resolution *R* which is defined as $\Delta E/E$ (in %), where $\Delta E/E$ is the full width with a half maximum of a photopeak occurring at pulse-height *E*. The common nomenclature used is: *R*@662 keV. The resolution *R* depends on scintillator material, crystal dimensions, and type of PMT.

is a drawback for low-signal-count-rate applications, e.g. in radioastronomy, because ^{138}La can interfere with the detection process[56]. Because of this, $CeBr_3$ single crystals have been studied [57,58,59] and compared with $Ce:LaBr_3$ [60]. The reported emission maximum for $CeBr_3$ has a decay time of 17 ns, which is very close to that of $Ce:LaBr_3$. Considering the scintillation LY and energy resolution under comparable experimental conditions, these values are about 10% and 25% lower compared to those in $Ce:LaBr_3$, respectively. However, since the intrinsic radioactivity is dramatically reduced using $CeBr_3$, the sensitivity of gamma-ray detection is about an order of magnitude better than that of $5\%Ce:LaBr_3$ at energies within 1–3 MeV[59]. In addition to this, $CeBr_3$ also offers an excellent timing resolution▲[14,61] of 93 ps at 511 keV for 1 cm^3 crystals[62], which is 2-3 times better than that of $Ce:LaBr_3$ or $Ce:Lu_2SiO_5$ (Ce:LSO) under comparable conditions. This excellent feature of $CeBr_3$ makes it a great candidate for time-of-flight positron emission tomography (ToF-PET)[61]. With the aim of increasing the reliability of $CeBr_3$ for application, aliovalent doping by selected divalent (Ca^{2+}, Sr^{2+}, Ba^{2+}, Zn^{2+}, Cd^{2+} and Pb^{2+}) and tetravalent (Zr^{4+} and Hf^{4+}) cations has been attempted at a level of 500–1000 ppm to strengthen the crystal lattice[63]. All the doped crystals clearly showed an increase in the fracture toughness compared to undoped $CeBr_3$, with the exception of Pb^{2+} which appeared to be detrimental to the scintillation properties of $Pb:CeBr_3$[64]. More recently, two studies focused on improving the energy resolution of $CeBr_3$ and $Ce:LaBr_3$, respectively, by doping with strontium were performed[65,66]. The Sr dopant causes a positive effect since clearly improves the energy resolution in both cases. In fact, Sr-co-doped $Ce:LaBr_3$ ($Ce,Sr:LaBr_3$) established the world record in energy resolution for single-crystal inorganic scintillators at 2%@662 keV[66].

Usage of divalent europium in R&D activities for Eu^{2+}-doped scintillators became a hot topic in the last 15 years due to the growing interest in the upcoming security-related applications[67,68]. Since the decay time of the $5d \rightarrow 4f$ luminescence transition of Eu^{2+} is at least one order of magnitude longer than that of the Ce^{3+} emitter, and the critical parameters of such applications are high light yield and excellent energy resolution, while a scintillation response on the order of a few microseconds is still acceptable, Eu^{2+} became a stimulating option. Due to the 2+ charge state of the europium emitter, other hosts, different from those used to introduce Ce^{3+} and Pr^{3+} ions, can be considered and exploited. One of the hosts currently most used for this purpose is SrI_2 single crystals[69], which in fact was patented 51 years ago[70]. $Eu:SrI_2$ exhibits very high LY values between 80 000–120 000 ph·MeV^{-1} and decay time values that vary in the range 0.6–1.6 μs, depending on the Eu^{2+} concentration and other reasons[71,72]. However, reabsorption is one of the disadvantages of this system, together with its high hygroscopicity, which is higher than that of Tl:NaI. Several ternary compounds suitable for incorporating Eu^{2+} emitters have also been recently

▲ The timing (or temporal) resolution of a PET detector (see Figure 1.1) is defined as its ability to record the minimum time difference between two subsequent annihilation events and differentiate between them efficiently. The timing resolution determines the timing performance or accuracy of the detector. The timing resolution of modern conventional PET systems ranges from 2 to 10 ns, while the values achieved in commercial ToF-PET systems usually vary from 500 to 700 ps.

reported in the literature, such as Eu^{2+}-doped $CsBa_2I_5$ and $Cs(Sr,Ba)I_3$ single crystals[73,74,75]. Eu:$CsBa_2I_5$ shows better tolerance to moisture than Eu:SrI_2. For a 1.0×1.0×1.0 cm^3 sample dimension of 2%Eu:$CsBa_2I_5$, a very good energy resolution of 3.9%@662 keV, a high light output of about 80 000 ph·MeV^{-1} and a principal decay time of about 900 ns were reported[74].

❖ Oxide scintillators

Garnet compounds

The potential of Ce^{3+}-doped $Y_3Al_5O_{12}$ (Ce:YAG) single crystals as fast scintillators was reported for the first time in 1978[76], although the first comprehensive description of the scintillation characteristics of Ce:YAG was reported more than 15 years later[77]. At that time, the authors included Ce:YAG among the high figure-of-merit oxide scintillators. Isostructural $Lu_3Al_5O_{12}$ (LuAG) aroused interest as a host for scintillator materials suitable for hard X- and γ-ray detection due to its higher density and effective atomic number Z_{eff} (6.67 g·cm^{-3}, Z_{eff} = 63) in comparison with YAG (4.56 g·cm^{-3}, Z_{eff} = 32). Consequently, Ce^{3+} and Pr^{3+}-doped LuAG single crystals were grown and studied in the 2000s in order to obtain fast scintillators[78,79]. More recently, the onsets of photoluminescence thermal quenching for Ce^{3+} centres[80] and Pr^{3+} centres[81] in LuAG host were determined, which were high temperatures of approximately 790 K and 680 K, respectively. The high resistance of these emission centres indicates the possible use of Ce:LuAG and Pr:LuAG in high-temperature applications. Early in the research of these scintillators, intense slow components in the scintillation response of Ce:LuAG were reported in the 2000s, which the authors attributed to the presence of shallow traps below the conduction band of the host that act as electron traps, resulting in delayed radiative recombination at emission centres[82,83,84]. The strategy used to combat the problem of trapping electrons in shallow traps was the immersion of these traps in the conduction band of the host by decreasing the bottom edge of the conduction band due to the modification of the chemical composition of the garnet. The balanced admixture of Gd and Ga cations in Ce:LuAG efficiently decreases the trapping effects, which results in LY values almost three times higher compared to Ce:LuAG[85,86]. Currently, the multicomponent garnets are the most efficient bulk single-crystal oxide scintillators. The decrease of the bottom edge of the conduction band is mainly due to the Ga admixture[87,88]. However, this modification considerably reduced the onset of photoluminescence thermal quenching, which limits the use of these scintillators to room temperature applications. The main cause of this problem was attributed to the ionization of the Ce^{3+} excited state[89,90]. This family is the so-called Ce^{3+}-doped multicomponent garnets Ce:$(Lu,Gd)_3(Ga,Al)_5O_{12}$, a new ultra-efficient single-crystal family, which was introduced in 2011[91,92] and it is the result of a decade of intense research, extensively explained in the review of Nikl *et al.*[8]. An alternative strategy has been formulated to deal with the problem of trapping electrons in shallow traps in Ce:LuAG and, at the same time, preserving the high-temperature stability of the Ce^{3+} centres. The strategy consists in the creation of an additional fast radiative recombination pathway that would efficiently compete with the shallow traps mentioned for the capture of electrons. This would lead to a positive impact on the light yield, speed of scintillation emission, and afterglow. Such pathway is the presence of tetravalent Ce^{4+} centres, which act as electron traps, in

the garnet lattice due to their stabilization by divalent rare earth ion co-doping[80,93] and/or by air annealing[94] or annealing at other atmospheres[95]. The scintillation properties of Pr^{3+}-doped garnets have also been optimized by the growth of this kind of multicomponent garnets, $(Lu,Gd)_3Ga_3Al_2O_{12}$ [96,97]. The admixture of Y cations in Ce:LuAG ($Ce:(Lu,Y)_3Al_5O_{12}$) shows an increase in the light yield of about 10% compared to Ce:LuAG[98]. More recently, an enormous increase of LY value up to 33 000 ph·MeV^{-1} has been reported for a sample of $Pr:(Lu_{0.75}Y_{0.25})_3Al_5O_{12}$ with 1 mm thickness[99]. The scintillation properties of Ce^{3+}-doped multicomponent garnets without Lu, $Gd_3Al_2Ga_3O_{12}$ (GGAG), have also been studied[100,101]. Ce:GGAG single crystals show a high LY of about 56 000 ph·MeV^{-1} and a scintillation response of about 90 ns. The decay time of the scintillation emission becomes faster when Ce:GGAG is co-doped with low Mg^{2+} concentrations, but the LY value slightly decreases.

Currently, the garnet-based scintillation ceramics appear as serious competitors to the garnet-based scintillation single crystals. Ce^{3+}-doped YAG ceramic for fast scintillator applications was reported for the first time in 1996[102,103]. In those studies, the materials were translucent, which resulted in a scintillation light output of about 50% of the value corresponding to Ce:YAG single crystal. In the early 2000s, Konoshima Chemicals Co. developed a transparent Ce:YAG ceramic with a scintillation light output exceeding the value of the single-crystal counterpart[104]. Due to the same reasons mentioned above for single crystals, LuAG-based ceramics aroused interest compared to YAG-based ceramics. Transparent Ce:LuAG ceramic was reported by several groups from 2005 to 2008[105,106,107,108], showing an absolute light output markedly lower than that of the single crystal. Physical properties of transparent ceramics heavily depend on the fabrication method. Thus, after pioneering studies in the fabrication process, Konoshima Chemicals Co. synthesized a transparent 0.5%Ce:LuAG ceramic in 2011, which showed a superior light yield compared to that of the Czochralski-grown, high-quality Ce:LuAG single crystal[109]. The first transparent Pr^{3+}-doped LuAG ceramic was reported in 2009, and its LY value was approximately half that of its single-crystal counterpart[110]. However, in 2012, Konoshima Chemicals Co. prepared a LuAG ceramic doped with 0.25 mol% of Pr^{3+} that showed a LY value that exceeded the value of a high-quality single crystal by approximately 20%[111]. Besides that, the transparent 0.25%Pr:LuAG ceramic showed a less intense afterglow under X-ray excitation compared to the single-crystal counterpart. The fabrication process used for such ceramic was similar to that of its transparent 0.5%Ce:LuAG ceramic. The authors concluded that the optimized fabrication process could suppress the formation of volume defects in crystals (such as inclusions) and efficiently passivated the surface defects and traps.[111] Regarding the family of multicomponent garnet materials described above for single crystals, analogous R&D activities for ceramics were also carried out. Transparent $Ce:(Gd,Y)_3(Al,Ga)_5O_{12}$ (Ce:GYGAG) ceramics show a high light yield of 50 000 ph·MeV^{-1} and an energy resolution of 4.5–4.8%@662 keV[112]. The Ce:GYGAG scintillators, both single crystals and ceramics, have a dominant decay time of about 250 ns, considerably longer that the value obtained (50–60 ns) from the photoluminescence decay under direct $4f \rightarrow 5d_1$ excitation of Ce^{3+} centres[92]. The authors attributed this phenomenon to an energy migration across the Gd^{3+} ions, followed by an energy transfer to Ce^{3+}[112]. In a work on $Ce:Gd_3(Al,Ga)_5O_{12}$ ceramics[113], it was observed that the afterglow was

reduced for a small excess of Gd cation with respect to a stoichiometric composition. The authors attributed this behaviour to the formation of antisite disorders in the crystalline lattice that give rise to localized energy levels in the lower part of the band gap of the material, being slightly higher than the Ce^{3+} ground state level. So, they would not act as hole trap centres and, consequently, would not compete with Ce.[113]

Apparently, transparent ceramic and single-crystal multicomponent garnets show similar luminescence and scintillation characteristics. Due to their high scintillation efficiency, high density and relatively fast decay time, these compounds are very promising for X- and γ-ray detectors. However, for example, the first performance results of Ce^{3+}-doped $Gd_3Al_2Ga_3O_{12}$ (Ce:GAGG) crystals with silicon photomultipliers showed a poorer timing performance compared to the widely used Ce:$(Lu,Y)_2SiO_5$ (Ce:LYSO) scintillator[114].

Aluminium perovskite compounds

Fast $5d \rightarrow 4f$ luminescence of Ce^{3+} and Pr^{3+} in $YAlO_3$ (YAP) were reported in 1973[115] and 1992[116], respectively. The obtained lifetimes at around 18 ns and 8 ns, respectively, are among the shortest within the wide family of the Ce- and Pr-doped oxide-based scintillators, so this feature makes these materials attractive. In the early 1980s, favourable properties of Ce:YAP for scintillation applications were described [117,118]. In the mid-1990s, several research groups replaced yttrium with lutetium in a YAP crystal in order to increase the density and the effective atomic number Z_{eff} from 5.35 $g \cdot cm^{-3}$ and 33.5, respectively, up to 8.34 $g \cdot cm^{-3}$ and 64.9 for LuAP. However, mixed Ce:$(Lu,Y)AlO_3$ (Ce:LuYAP) scintillators were finally chosen for industrial-scale production due to a severe instability of the LuAP perovskite phase in the process of crystal growth from the melt, resulting in high costs[119]. The Ce:LuYAP crystals were used in the prototype of a high-resolution small animal PET scanner designed by the Crystal Clear Collaboration in 2004[120], but its price and relatively lower light yield compared to Ce:YAP caused that it had a difficult commercialization. Several attempts, e.g. by co-doping, were made to substantially improve the LY of Lu-rich aluminium perovskites, although no successful strategy was found[121,122,123]. In addition, bandgap engineering of YAP by compositional variation was performed in Ce:YAP introducing gadolinium cations, 1%Ce:$(Gd_xY_{1-x})AlO_3$, but no higher LY values were obtained compared to Ce:YAP[124]. Several reviews show the R&D results for the family of Ce-doped aluminium perovskite[125,126]. With respect to Pr:YAP, photoluminescence measurements under VUV-UV excitation as well as radioluminescence, scintillation decay and relative light yield measurements under γ-ray excitation of Czochralski-grown Pr:YAP crystals were already reported by Pedrini *et al.*[127] in 1994. Initial results of studies on X-ray excited radioluminescence of Czochralski-grown Pr:YAP crystals were reported by Wisniewska *et al.*[128] in 2001. In 2010, the scintillation performance of a numerous set of Pr:YAP single crystals prepared by different methods was evaluated[129], showing results that suggested the presence of delayed radiative recombination processes in Pr:YAP, unlike Ce:YAP. However, the existence of the mentioned processes was attributed to a defect instead of being an intrinsic property of Pr:YAP[129]. At the end of that same year, a Czochralski-grown 0.05%Pr:YAP crystal was reported by Yanagida *et al.*[130], with an estimated LY of 20 400 ± 2000 $ph \cdot MeV^{-1}$ under ^{137}Cs 662 keV excitation and a decay

time constant due to the $5d \rightarrow 4f$ electronic transition of Pr^{3+} of 10.9 ns under pulsed X-ray excitation. In addition, Pr:YAP presents a high thermal stability, since the onset of photoluminescence thermal quenching for the Pr^{3+} centres in YAP is 690 K[131,132], which is slightly higher than that in LuAG host (680 K).

Oxyorthosilicate compounds

Scintillation characteristics of the Ce^{3+}-doped rare earth oxyorthosilicates $Ce:Gd_2SiO_5$ (Ce:GSO) and $Ce:Lu_2SiO_5$ (Ce:LSO) were reported for the first time in 1983[133] and 1992[134], respectively. Later, Ce:GSO and Ce:LSO single-crystal scintillators became well known and commercially successful due to the favourable combination of high density, high effective atomic number and fast scintillation response[135], together with mechanical and chemical stability. Ce:GSO was the scintillator material used in one of the first commercial scanners that followed successful clinical imaging with the PET/CT system. Such system was presented by Philips Medical in early 2001[31]. Ce:LSO is used in several PET imaging systems manufactured by Siemens Healthineers since the 1990s[136,137]. The fundamental optical and luminescence characteristics under UV and γ-ray excitations of $Ce:Y_2SiO_5$ (Ce:YSO) were reported together with those of Ce:GSO and Ce:LSO in 1992[135]. Such study revealed that the orthosilicate structure has two different sites for the Ce^{3+} emission centres, called Ce1 and Ce2[135]. Ce:LSO has a number of advantages over Ce:GSO and Ce:YSO, as well as other known scintillators, Tl:NaI and BGO, since Ce:LSO has a fast decay time (40 ns), large effective atomic number (66), high density (7.4 $g \cdot cm^{-3}$) and a relatively high light yield (almost 30 000 $ph \cdot MeV^{-1}$)[138]. However, Ce:LSO presents some drawbacks, such as strong afterglow, high inhomogeneity of the Ce distribution along the ingots obtained by the Czochralski method, and intrinsic background signal due to the existence of the radioactive isotope ^{176}Lu [139]. Since Ce:GSO does not exhibit the disadvantageous intrinsic background signal, it can be used in low-signal-count-rate applications such as hard X(γ)-ray astronomy[140]. Ce:GSO is widely used in the oil well industry and geophysical explorations up to at least 420 K thanks to the high temperature stability of the Ce1 centres in the GSO host[141]. In addition to this, Ce:GSO demonstrates good radiation hardness[142]. The light yield of Ce:GSO at room temperature is less than half of that of Ce:LSO due to thermal quenching of the Ce2 centres in the GSO host above 200 K, which is insufficient to be used Ce:GSO in modern PET scanners[139,141]. Another drawback of this scintillator is the difficulty in producing large GSO crystals because of easy cleavage[139]. In 2000, Cooke *et al.*[143] introduced Ce^{3+}-doped $(Lu,Y)_2SiO_5$ (Ce:LYSO) crystals with the composition $Ce:Lu_{1.8}Y_{0.2}SiO_5$, showing the favourable growth properties of Ce:YSO and the desirable physical and optical scintillator properties of Ce:LSO. The crystal growth of LYSO by the Czochralski method in comparison with that of LSO provides a reduction of melting point, easier incorporation of cerium into the host lattice, less susceptibility for formation of crystalline inclusions, and lower cost of raw materials. Optimized Ce:LSO and especially Ce:LYSO show a LY exceeding 30 000 $ph \cdot MeV^{-1}$ [144]. As in the case of Ce:LSO, Ce:LYSO is used in the latest generation of scintillation detectors in PET imaging. Philips Healthcare manufactures various PET imaging systems using Ce:LYSO as a scintillator material[136]. It is worth mentioning that, due to the early

ionization of the excited state of both Ce centres in Ce:LSO, this scintillator cannot be used in applications above room temperature[145]. However, increasing the yttrium content in Ce:LSO crystals increases the temperature of the onset of the ionization process of the excited state for Ce1 and Ce2 centres in Ce:LYSO. In other words, both Ce centres become more stable against thermally-induced ionization of their 5*d* excited states, so Ce:LYSO can be used in applications above room temperature[144]. In 1996, Loutts *et al.*[146] introduced Ce^{3+}-doped $(Lu_{1-x}Gd_x)_2SiO_5$ (Ce:LGSO) single crystals as a possible alternative to both Ce:LSO and Ce:GSO scintillators. This work, along with other more recent works, showed that Ce:LGSO is an efficient, dense scintillator with high light yield, fast decay and weak afterglow[147,148]. The phenomenon of light-yield improvement for intermediate mixed crystal compositions was demonstrated in a systematic compositional study carried out by Sidletskiy *et al.*[139] in 2012. It is worth mentioning that LGSO may crystallize in the monoclinic system with the space groups $P2_1/c$ or $C2/c$ depending on the Lu/Gd ratio in the host[139]. In 2014, a systematic comparison of the luminescence and scintillation properties of Ce:LGSO, Ce:LSO and Ce:GSO allowed concluding that there is a real advantage of Ce:LGSO for scintillator applications around room temperature[141]. Ce:LGSO is not a suitable option for high-temperature applications due to the evidenced thermal ionization of both Ce1 and Ce2 centres above room temperature. In 2008 and 2009, effects of Ca^{2+} co-doping on the scintillation properties of Ce:LSO and Ce:YSO were studied, showing a positive role in the performance of these scintillators[149,150,151]. The works related to Ce,Ca:LSO reveal that the Ca^{2+} co-doping combined with an optimized crystal growth atmosphere improve the scintillation light output and decay time, which reach values of 38 800 ph·MeV^{-1} and 31 ns with no long components, respectively. The Ca^{2+} co-doping significantly reduces the trapped charge population in the crystal host, resulting in a shortening of the scintillation decay time and strong suppression of the afterglow compared to Ce:LSO[149,150]. In the work related to Ce,Ca:YSO, the Ca^{2+} co-doping results in the reduction or elimination of the population of various shallow traps, which enables faster energy transfers to the luminescence centres, achieving a scintillation decay time of 38 ns at a Ca^{2+} co-dopant concentration of approximately 0.3 at. % replacing Y[151]. Later, in 2013, the presence of a stable Ce^{4+} centre in Ce:LYSO single crystals co-doped with Ca^{2+} or Mg^{2+} (Ce,Ca:LYSO, Ce,Mg:LYSO) was evidenced in a detailed study, in which the role of Ce^{4+} in the scintillation mechanism is explained[152]. The co-doping with divalent ions, as well as annealing in air[153,154], stabilize the Ce^{4+} centres. The Ce^{4+} immediately captures an electron from the conduction band of the host, then the resulting excited Ce^{3+} centre is de-excited radiatively, and finally, the non-excited Ce^{3+} centre captures a hole from the valence band, returning to the Ce^{4+} stable initial state. This mechanism works in parallel with the standard one based on the stable Ce^{3+} centre (see Sections 1.3.1.1 and 1.3.2), so that these two centres do not compete for the capture of charge carriers. However, their relative ratio must be adequately tuned for material optimization[80]. Thus, as mentioned above in the garnet compounds, the stable Ce^{4+} centre creates a new fast radiative recombination pathway, which positively influences the light yield, speed of scintillation response and afterglow. The LY value is increased from 28 000 ph·MeV^{-1} for Ce:LYSO up to 34 000 ph·MeV^{-1} for Ce,Ca:LYSO under ^{137}Cs 662 keV excitation, and the afterglow after X-ray excitation decreased by

one order of magnitude[152]. In the case of Pr^{3+}-doped LSO single crystals, the $5d_1$ level of Pr^{3+} is close to the conduction band of the host, resulting in a degradation of the light yield of this scintillator at room temperature[155]. The Pr^{3+} doping ion was also studied in LGSO host, showing unfavourable results as a scintillator material, since only the narrow emission band at around 312 nm corresponding to Gd^{3+} appeared in the emission spectrum under X-ray excitation[156].

Pyrosilicate compounds

Ce^{3+}-doped lutetium pyrosilicate, $Ce:Lu_2Si_2O_7$ (Ce:LPS), was found to be a potentially interesting scintillator material in 2000[157]. The Ce^{3+} ion in the structure of LPS host replaces Lu^{3+} in its single crystalline site, unlike Ce:LSO whose structure has two different sites for the Ce^{3+} centres. This fact should avoid parasitic energy transfer processes that contribute to reduce scintillation efficiency. Ce:LPS exhibits chemical stability, an average light yield value of 26 300 ± 3000 ph·MeV^{-1} and a fast decay time of 38 ns without afterglow[157,158]. The lack of afterglow in Ce:LPS, in contrast to Ce:LSO, was correlated with the significantly high temperature maxima of the TSL (i.e. thermally stimulated luminescence[159]) glow peaks above room temperature[160]. The luminescence efficiency of Ce:LPS is very high at temperatures up to 450 K, while the efficiency of Ce:LYSO remains high at temperatures up to 330 K[158]. More recently, it was found that annealing in air at elevated temperatures was effective to increase the scintillation efficiency of Ce:LPS[161]. The intrinsic background signal due to the existence of the radioactive isotope ^{176}Lu is a disadvantage of this compound as a scintillator material. Ce^{3+}-doped gadolinium pyrosilicate, $Ce:Gd_2Si_2O_7$ (Ce:GPS), was introduced in 2007 in crystalline powder form, showing a light output 1.2 times greater than that of Ce:GSO single crystals and a fast decay time of 52 ns, which is faster than the Ce:GSO scintillation response[162]. Ce:GPS melts incongruently[163], which disables its preparation by the Czochralski method, being this technique frequently used in the industry due to a favourable combination of dimensions, quality and cost of the crystals obtained[164]. Ce:GPS doped at high Ce^{3+} concentrations of at least 10 mol% enables its congruent growth[165], although this fact results in the reduction of the light output because of self-absorption and concentration quenching. Congruent crystal growth of Ce:GPS at low Ce^{3+} concentrations is achieved by the partial substitution of La^{3+} for Ce^{3+} [166]. In 2012, the optical and scintillation properties of $(Ce_{0.01},Gd_{0.90},La_{0.09})_2Si_2O_7$ (Ce:La-GPS or Ce:(Gd,La)PS) single crystals, grown by the floating zone method in argon atmosphere, were reported for the first time by Suzuki *et al.*[166]. In such work, Ce:La-GPS showed a high LY of 36 000 ph·MeV^{-1}, fast scintillation decay time of 46 ns and a high energy resolution of 5%@662 keV. In 2014, Ce:La-GPS exhibited excellent values of LY and energy resolution using a silicon avalanche photodiode detector, achieving 41 000 ± 1000 ph·MeV^{-1} and 4.4 ± 0.1%@662 keV at 23.0 ± 0.2 ºC, respectively[167]. Also in 2014, the absorption and photoluminescence spectra, photoluminescence decay curves, X-ray excited radio-luminescence spectra and afterglow curves were studied for $1\%Ce:(Gd_{0.7}La_{0.3})_2Si_2O_7$ (Ce:GPSLa30%), $1\%Ce:(Gd_{0.52}La_{0.48})_2Si_2O_7$ (Ce:GPSLa48%) and $0.5\%Ce:Lu_2Si_2O_7$ (Ce:LPS) single crystals grown by the Czochralski technique[168]. After studying how the nanosecond decay time of the Ce^{3+} emission varies depending on temperature, the authors concluded that its shortening began around 380 K for Ce:LPS, and

around 440 K for Ce:GPSLa30% and Ce:GPSLa48%. This shortening with increasing temperature was attributed to thermally-induced ionization of the Ce^{3+} excited state. Since the Ce^{3+} ionization onset occurs well above room temperature, Ce:LPS and particularly Ce:La-GPS can be used in high-temperature applications. In addition, the authors evaluated the scintillation efficiency of the three samples and a BGO reference sample by integrating their X-ray excited radioluminescence spectra. The scintillation efficiency of Ce:LPS, Ce:GPSLa48% and Ce:GPSLa30% reached values of about 250%, 1210%, and 1530% of that of the BGO single crystal standard, respectively. The afterglow in Ce:La-GPS samples is fairly low and tends to decrease with increasing La concentration, becoming comparable to that of BGO, which is known for its negligible afterglow. Conversely, the scintillation efficiency apparently increases as the La concentration in the Ce:GPSLa samples decreases, so future efforts are needed to optimize the crystal composition and scintillation properties. Ce:La-GPS single crystals have a drawback, which is an intrinsic radioactivity due to the existence of the radioactive isotope ^{138}La (0.09% natural abundance and half-life $\tau_{1/2} \approx 1.05 \times 10^{11}$ years). However, their intrinsic radioactivity is two orders of magnitude lower compared to Lu-based scintillators due to the presence of the radioisotope ^{176}Lu with a natural abundance of 2.59% and a half-life of $\tau_{1/2} \approx 3.78 \times 10^{10}$ years. Hence, Ce:La-GPS single crystals show a favourable combination of characteristics for medical imaging, the oil industry and geophysical applications.[168] More recently, in 2016, Murakami *et al.*[169] grown Ce:La-GPS single crystals using the Czochralski technique with the chemical composition $(Gd_{0.75},Ce_{0.015},La_{0.235})_2Si_2O_7$, whose light yield value were estimated to be ~42 000 ph·MeV^{-1}.

Phosphate compounds

Cerium-doped lutetium orthophosphate, Ce:$LuPO_4$ (Ce:LOP), single crystals is among the first phosphates that was considered a new promising scintillator material, which was introduced by Lempicki *et al.*[170] in 1993. LOP aroused interest because of its high density (6.53 g·cm^{-3}), high effective atomic number ($Z_{eff} = 63.7$), its extreme resistance to radiation damage, and its extreme durability since, at normal temperatures, it is not attacked by water, water vapor, organic solvents and most of the common concentrated acids. Under γ-ray excitation and at room temperature, Ce:LOP single crystals showed fast, single-exponential decay of 25 ns and a light output of 17 200 ph·MeV^{-1}. The decay time of Ce:LOP is temperature dependent, increasing up to about 36 ns at 550 K. This material has some inconveniences related to the host, which are the intrinsic radioactivity due to the existence of the ^{176}Lu radioisotope, and the high cost of lutetium. In the same work[170], Ce:YPO_4 (Ce:YOP) was studied preliminary, showing less attractive characteristics, such as a lower density (4.31 g·cm^{-3}) and a rise time in the decay time curve, which means a slow-down of the energy transfer from the lattice to the Ce^{3+} centres. Later, Nd^{3+}-doped $LuPO_4$ and YPO_4 single crystals were studied in the work done by Wisniewski *et al.*[38] in 2002. Nd:LOP and Nd:YOP single crystals showed non-single-exponential decays with a time constant of 10.1−12.5 ns for the fastest component, along with longer scintillation components. Nd:LOP exhibited a limited light yield, attributed to host defects, while Nd:YOP manifested better scintillation properties. However, the authors concluded that both materials could be further improved by eliminating the traps

responsible for the longer scintillation components.[38] Nearly 20 years later, low and high temperature thermoluminescence measurements of Nd^{3+}:XPO_4 (X = Y, Lu, La, Sc) single crystals have been reported by Makowski *et al.*[171], in addition to their photoluminescence and radioluminescence spectra for various temperatures from 10 to 350 K, among other studies. These authors conclude that Nd:YPO_4 is the best candidate as a modern scintillator material due to its highest yield and the best energy resolution, although its density is relatively low (4.28 $g \cdot cm^{-3}$). Since Nd:$LuPO_4$ is denser (6.53 $g \cdot cm^{-3}$), the authors propose the study of mixed Nd:$Lu_zY_{1-z}PO_4$ crystals. In 2003, the alkali lutetium double phosphates Ce:$Cs_3Lu(PO_4)_2$ and Ce:$Rb_3Lu(PO_4)_2$ single crystals were studied under UV, X- and γ-ray excitation[172]. The scintillation light yield, dominant component time and energy resolution for a 1%Ce:$Cs_3Lu(PO_4)_2$ crystal are 13 500 $ph \cdot MeV^{-1}$, 49.0 ns and 16%@662 keV, respectively, while for a 1%Ce:$Rb_3Lu(PO_4)_2$ crystal are 14 800 $ph \cdot MeV^{-1}$, 36.8 ns and 8%@662 keV. The high light yield and relatively fast scintillation decay of these materials indicate that both are promising scintillator materials, in particular, Ce:$Rb_3Lu(PO_4)_2$. However, the main shortcomings of both compounds are their hygroscopic nature and moderate density, which is 4.885 $g \cdot cm^{-3}$ for $Cs_3Lu(PO_4)_2$ and 4.676 $g \cdot cm^{-3}$ for $Rb_3Lu(PO_4)_2$. The photoluminescence of lithium lanthanum phosphate doped with some trivalent rare earths, $LiLa_{1-z}M_zP_4O_{12}$ (M = Ce^{3+}, Eu^{3+}, Tb^{3+}, Bi^{3+}), in crystalline powder form was studied by Blasse and Dirken in 1982[173]. However, the scintillation properties of the cyclophosphate $LiLaP_4O_{12}$ (LiLaPO) doped with Ce^{3+}, Eu^{3+} and Tb^{3+} ions have not been studied until very recently by Suzart *et al.*[174]. The scintillation characteristics of these powders reported in this work are the X-ray excited radioluminescence (RL), time-resolved luminescence under pulsed X-ray radiation and stability of the RL emission after prolonged X-ray exposure. The luminescence decay time curves showed the characteristic decay time constants of Ce, Eu and Tb, which are around 17 ns for the Ce-doped sample and a few milliseconds for the Eu- and Tb-doped samples. In addition, a very slow component was found for the Eu- and Tb-doped LiLaPO samples, which the authors attributed to the existence of shallow traps. After prolonged X-ray exposure, the results showed that the RL efficiency of Ce:LiLaPO increased almost 40% and the efficiencies of Eu:LiLaPO and Tb:LiLaPO almost 25%. The LiLaPO host is considered to be responsible for this behaviour due to the presence of deep trapping centres that capture charge carriers generated during the first minutes of irradiation, increasing the probability of the electron−hole pair recombination in the emitting centres (Ce, Eu and Tb) as a function of the time. In 2007, the optical absorption and luminescence properties under VUV-UV excitation of Ce^{3+}-doped cyclophosphates $LiGdP_4O_{12}$ and $KGdP_4O_{12}$, and polyphosphates $NaGd(PO_3)_4$ and $CsGd(PO_3)_4$ as polycrystalline samples were reported by Zhong *et al.*[175]. Considering the VUV luminescence spectra, the energy level diagram of Gd^{3+} and Ce^{3+} in the four systems and the luminescence decay curves of Ce^{3+} emission, the authors reported on the existence of an efficient energy transfer from the $^6P_{7/2}$ level of Gd^{3+} to the $5d_1$ level of Ce^{3+}. In fact, in Ce^{3+}:$CsGd(PO_3)_4$, the absorption peak of the $5d_1$ level is in the same energy position as the peak of the $^6P_{7/2}$ level, so all the energies absorbed by Gd^{3+} ions are transferred to Ce^{3+} ions, and the emission peak corresponding to the $^6P_{7/2} \rightarrow {}^8S_{7/2}$ transition of Gd^{3+} disappears completely. Under direct $4f \rightarrow 5d_1$ excitation of Ce^{3+} ions, the lifetime of the $5d_1$ level of Ce^{3+} is ranged

from around 11 ns to 23 ns, depending on the system. Then, due to the efficient energy transfer from Gd^{3+} to Ce^{3+} ions and the short lifetime of the Ce^{3+} emission, the authors concluded that this series of compounds doped with Ce^{3+} could be used as promising scintillator materials. In fact, the radioluminescence properties under X-ray radiation of the same condensed phosphates were reported by Zhong *et al.* in 2009[176]. The highest X-ray excited light yield was exhibited by the 1.0 mol% Ce^{3+}:$CsGd(PO_3)_4$ pellet, which reached a value of 24 400 ph·MeV^{-1} with maximal emission peaks at 337 and 358 nm at room temperature. In addition to its suitable emission wavelength range, high LY and fast luminescence decay of Ce^{3+} emission, Ce^{3+}:$CsGd(PO_3)_4$ shows high chemical stability. For these reasons, the 1.0 mol% Ce^{3+}:$CsGd(PO_3)_4$ pellets were considered a prospective scintillator material, so it would be worthwhile to improve the scintillation efficiency by optimizing Ce^{3+} content and to obtain single crystals. The luminescence properties upon VUV and X-ray excitation of Ce^{3+}-doped cyclophosphates $LiGdP_4O_{12}$ and $LiYP_4O_{12}$, and polyphosphate $NaGd(PO_3)_4$ were reported by Shalapska *et al.* in 2009, showing that the presence of Gd^{3+} ions increases substantially the light yield of the investigated compounds in this work[177]. However, the contribution of the fast decay component (18.0 ns) in the scintillation emission was small in Gd^{3+}-containing phosphates, since the predominant component was a slow decay attributed to an energy migration across the Gd^{3+} ions. This slow component was absent in $LiY_{0.9}Ce_{0.1}P_4O_{12}$, where the decay time constant was 24.7 ns. In 2010, Shalapska *et al.* reported on the luminescent properties of $LiY_{0.9}Ce_{0.1}P_4O_{12}$ as a function of temperature[178]. Later, Kang *et al.* studied the luminescence of Ce^{3+}, Pr^{3+} doped and Ce^{3+}–Pr^{3+} co-doped $NaLa(PO_3)_4$ powders under VUV-UV excitation[179]. Primary investigations in the scintillation properties of the Pr^{3+}-containing cyclophosphates $CsPrP_4O_{12}$ and $RbPrP_4O_{12}$, in form of single crystals, were reported by Horchani *et al.*[180]. The main fast component (>85%) of the main emissions observed under pulsed X-ray excitation had decay times of 9 ns and 5 ns for $CsPrP_4O_{12}$ and $RbPrP_4O_{12}$, respectively. The authors estimated that the light yield values of $CsPrP_4O_{12}$ and $RbPrP_4O_{12}$ are around 37% and 16% of the BGO one, respectively.[180]

1.3. Inorganic scintillators containing lanthanide ions

1.3.1. Scintillation mechanism in inorganic scintillators containing lanthanide ions

The scintillation mechanism in inorganic scintillators excited by ionizing radiation can be summarized in **creation of electronic excitations** (such as correlated electron −hole pairs, excitons, separated electrons and holes, etc.), **energy transfer to emitting centres** of interest and **light emission** by these luminescent centres in the ultraviolet and/or visible spectral ranges. As mentioned earlier, the scintillation mechanism is different depending on the type of scintillator. The classification of the inorganic scintillator materials based on the scintillation mechanism divides them into three classes: *activated*, *self-activated* and *cross-luminescent scintillators*.[4,181,182]

In this Ph.D. Thesis, we focus on crystals containing lanthanide ions, i.e. lanthanide-doped or lanthanide-based crystals, which belong to the classes of *activated* and *self-activated scintillators*. Figure 1.3 shows a scheme of the scintillation mechanism in

inorganic scintillator containing lanthanide ions using the electronic band structure of the crystal. This electronic band structure consists of only one core band for simplicity (top energy E_c and bandwidth ΔE_c), the valence band (top energy $E_V = 0$ and bandwidth ΔE_V), the conduction band (bottom energy E_C) separated by the forbidden energy band gap (band gap width E_{VC} or E_g or E_C), and the 4*f* band of the lanthanide ion (top energy E_{4f}), in general, in the band gap. The 4*f* and 5*d* levels of the lanthanide ions play an important role in the scintillation process, since the light emission is produced predominantly through the $5d \rightarrow 4f$ electronic transitions of these ions, which act as luminescent or emitting centres.[181,182]

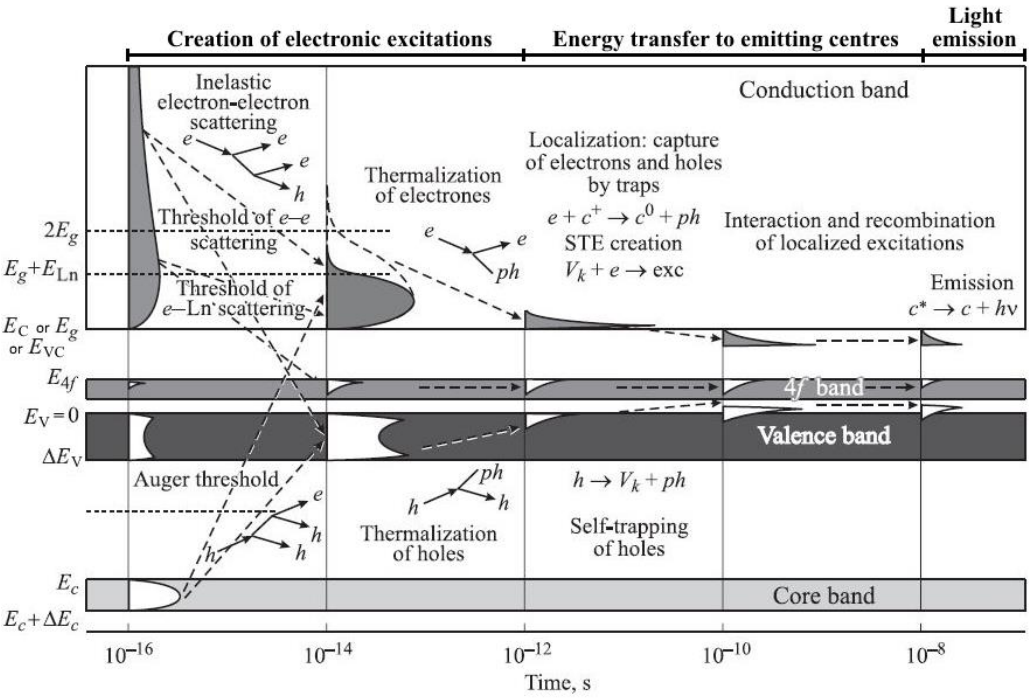

Figure 1.3. Scintillation mechanism in inorganic scintillators containing lanthanide ions. Ln for lanthanide ions, *e* for electrons, *h* for holes, *ph* for phonons, $h\nu$ for photons, V_k for self-trapped holes, STE for self-trapped excitons, c^n for ionic centres with charge *n*, *c** for excited ionic centres, E_c for the top energy of the only core band represented for simplicity, ΔE_c for the bandwidth of this core band, E_V for the top energy of the valence band, ΔE_V for its bandwidth, E_C for the bottom energy of the conduction band, E_{VC} or E_g or E_C for the forbidden energy band gap between the conduction and valence bands, E_{4f} for the top energy of the 4*f* band of the lanthanide ion, $E_g + E_{Ln}$ for the *e*–Ln scattering threshold, $2E_g$ for the *e*–*e* scattering threshold. This figure has been extracted from ref.[182].

The first stage of the scintillation mechanism consists in the creation of electronic excitations due to the interaction of the ionizing radiation with the material. The initial interaction with the scintillator lattice occurs mainly through one of the next processes: 1) the photoelectric effect, when the energy of the incident photon is below a few hundred keV (depending on the density and effective atomic number of the material), 2) Compton scattering, when the photon energy is in the range from a few

hundred keV to 8000 keV, and 3) pair production, when the photon energy is above 8000 keV. Then, in a very short time (time scale is represented on the abscissa axis of Figure 1.3), the electronic excitations are relaxed through inelastic electron−electron (*e*−*e*) scattering and Auger processes, leading to a multiplication of electronic excitations. This multiplication is stopped when the electrons and holes created have an energy below the *e*−*e* scattering threshold and Auger threshold, respectively. Next, hot electrons decrease their kinetic energy by producing phonons that result in low kinetic energy electrons in the bottom of the conduction band, as it happens with deep holes that result in low kinetic energy holes in the top of the valence band and of the 4*f* band. This physical process is called thermalization of electronic excitations, more specifically, thermalization of electrons and thermalization of holes, respectively.[1,181,182]

The next stage, which is titled as energy transfer to emitting centres in Figure 1.3, is characterized by the localization of electronic excitations due to the interaction of these excitations with stable defects of the crystal lattice leading to the formation of self-trapped holes (V_k centres), excitons and self-trapped excitons (STE) and the capture of electrons and holes by the lanthanide ions present in the crystal that act as hole or electron traps. Lanthanide ions act as hole traps or electron traps depending on the $4f \rightarrow 6s$ promotion energy of the lanthanide ion[183] (see Section 1.3.1.1). As shown in the figure, the self-trapping of a hole creates a V_k centre and releases a phonon. An exciton is an electron−hole pair which propagates in non-metallic solids[184]. STE can be formed by trapping electrons in the V_k centres (as mentioned in the figure) or directly from the localization of electron−hole pairs. STE are formed in materials with a strong coupling of the excitons with the lattice vibrations, resulting in excitons that do not move through the crystal lattice[184]. The localization of electronic excitations results in centres that have localized states located in the band gap, as can be seen in Figure 1.3. Thereafter, the luminescent centres (in this case, lanthanide ions) become excited (*c**) by their interaction and recombination with the localized electronic excitations. When the localized excitations are correlated electron−hole pairs, the excitation channel for lanthanide ions is usually a charge transfer process with a sequential capture of charge carriers (electrons and holes). In addition to this, the lanthanide ions can be excited by the recombination of electrons with mobile V_k centres [$V_k + e^-$] close to them, or in other words, by the energy transfer process due to the creation of self-trapped excitons (STE). Apart from that, STE can exhibit luminescence. When it comes to excitons, they can also transfer their energy to lanthanide ions.[181,182]

The energy transfer processes mentioned above can be distinguish by taking into account the time duration of the process. The energy transfer process is very fast when it happens through direct capture of correlated electron−hole pairs, fast when it is through recombination of electrons with mobile V_k centres (known as binary electron–hole recombination) and slower when the energy transfer to the lanthanide ions is through diffusion of STE. It is worth commenting that, in crystals containing lanthanides, not all the localized excitations are useful due to the interaction between excitations themselves. The quenching of scintillation process that may occur when closely spaced electronic excitations interact is called local density-induced quench-

ing. Apart from these energy transfer processes mentioned, the lanthanides ions can be excited through electronic impact. The probability of this excitation is significant when the kinetic energy of the electron is below the threshold of *e*–*e* scattering and above the threshold of *e*–Ln scattering (see to the left of Figure 1.3).[181,182]

The last stage of the scintillation mechanism is the luminescence by the emitting centres after being excited by the final electronic excitations. The interest lies in the 5*d* → 4*f* emission transitions of the lanthanide ions because they are parity-allowed transitions (Laporte selection rule), so they present high oscillator strengths, which is a parameter directly related to the probability of radiative transition, and in addition, because these radiative transitions have fast decay times (from tens to hundreds of nanoseconds). Unlike 4*f* electrons, 5*d* electrons of the lanthanide ions are highly influenced by the crystal field of host, since 5*d* levels are outer orbitals, which gives rise to broad absorption and emission bands. The energy of the 5*d* levels of a same lanthanide ion depends on the host in which this ion is doped, i.e. as an example, the energy difference corresponding to the $5d_1 \rightarrow {}^2F_{5/2}$ electronic transition of Ce^{3+} is different depending on the host in which Ce^{3+} is. The 4*f* electrons of the lanthanide ions are efficiently shielded by the filled *s* and *p* outer orbitals, so they are weakly influenced by the crystal field of host. Because of this, the optical transitions between 4*f* levels are characterized by sharp peaks and, considering a specific lanthanide ion, the energy of its 4*f* levels is approximately the same, regardless of the host.[1,185,186]

1.3.1.1. Lanthanide ions acting as hole or electron traps

As already mentioned above, when the localized electronic excitations are correlated electron−hole pairs, the lanthanide ions are excited through sequential capture of charge carriers (electrons and holes) by the Ln centres. Some lanthanides tend to begin with the capture of an electron, whereas others usually begin with the capture of a hole, among other possibilities. The determining factor for this behaviour is the 6*s*–4*f* energy difference of the lanthanide ion, as explained below. Figure 1.4 displays the energy needed for moving an electron from a 4*f* orbital to a 6*s* orbital for each Ln ion for the 3+ and 2+ oxidation states. The ionization energies belonging to the Ln^{3+} ions increase strongly compared to those energies belonging to the Ln^{2+} ions. When an electron is removed from an ion, there is a reduction in the repulsive forces among the remaining electrons, so the attraction of these electrons with the nucleus is stronger. Therefore, as the number of tightly bound 4*f*-electrons decreases, the energy required to remove an electron is higher. Consequently, the energy levels of a Ln^{3+} ion lie lower in the energy scheme of the electronic band structure of the crystal than the energy levels introduced by the same Ln ion with the 2+ oxidation state, as shown in Figure 1.5. The position of the Fermi level (E_F) determines which of these levels are occupied and which are not. The Fermi level usually is in the middle of the forbidden energy band gap of an undoped and perfect crystal, although it can be intentionally changed by doping and, at the same time, could be compensated by unintentional creation of compensating defects during the crystal growth. Therefore, in most cases, the levels close to the valence band and those belonging to the valence states of dopant ions (that is, the Ln ions) are occupied, whereas the levels close to the conduction band are empty.[183]

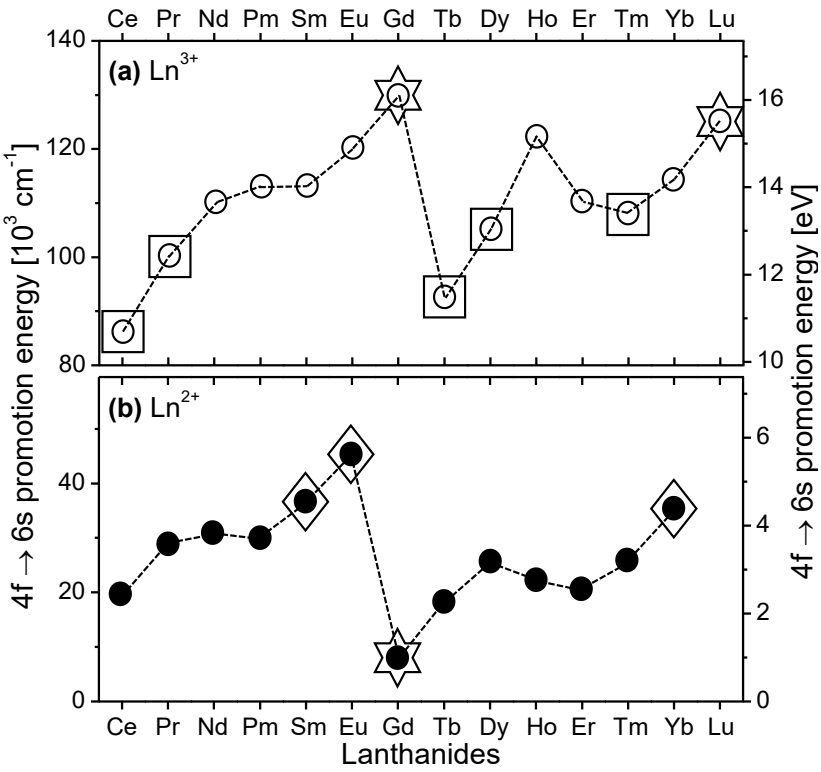

Figure 1.4. Energies of 4*f* → 6*s* promotion for lanthanide ions (Ln) in their (a) 3+ and (b) 2+ states. The dashed lines are guides for the eye. The ions most likely to act as hole traps are indicated by squares, while those most likely to act as electron traps by rhombus, and the best candidates as neutral constituents by stars. This figure is inspired by ref.[183].

Hence, the smaller the 6*s* → 4*f* energy difference in a Ln^{3+} ion, the higher the probability of having a filled 4*f* electronic level of the Ln^{3+} in the forbidden energy band gap, avoiding the combination of this level with the valence band (see Figure 1.5). The filled electronic level in the band gap introduces hole traps, so Ce^{3+}, Pr^{3+}, Tb^{3+}, Dy^{3+} and Tm^{3+} are prime candidates to act as efficient hole traps, as indicated in Figure 1.4.a. In other words, to be considered a good candidate for hole trap, the Ln ion has to have a stable $Ln^{(n+1)+}$ charge state. In contrast, considering that the Fermi level is low enough, whether the 6*s* → 4*f* energy difference in a Ln^{2+} ion is high, the probability of having an empty lower lying 4*f*-level below the conduction band increases (see Figure 1.5). The introduction of an empty 4*f* level in Ln^{2+} makes the Ln^{3+} ion act as an efficient electron trap. Accordingly, the Sm^{3+}, Eu^{3+} and Yb^{3+} ions are prime candidates for electron traps, as indicated in Figure 1.4.b. Analogous to the previous case, the Ln ion has to have a stable $Ln^{(n-1)+}$ charge state to be considered a good candidate for electron trap. It is worth mentioning that it is very unlikely that Gd^{3+}, Ho^{3+} and Lu^{3+} introduce hole traps, while Gd^{3+} and Lu^{3+} are very unlikely to introduce electron traps as well. Consequently, the latter two ions could be considered the best candidates as neutral constituents in Ln-based crystals (see Figure 1.4), since competition for the capture of charge carriers against the activator ions would not be expected.[183,187]

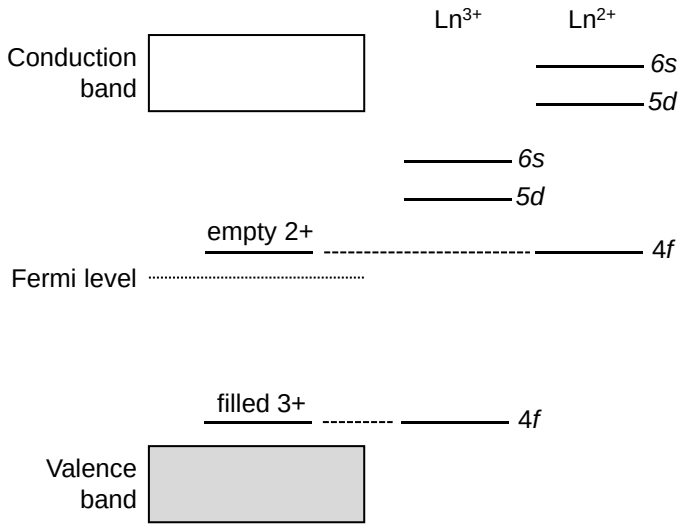

Figure 1.5. A schematic electronic band structure of a crystal doped by Ln^{3+} ions, along with the energy levels of Ln^{2+} and Ln^{3+}. This figure is inspired by ref.[183].

The energy transfer to Ln^{3+} ions based on the sequential capture of charge carriers consists in three consecutive steps. When the sequence of carrier trapping begins with the capture of a hole, a hot band hole moving through the crystal is trapped by a Ln^{3+} ion, which consequently becomes a Ln^{4+} ion (step 1). Because of this, the Ln^{4+} ion has all its corresponding 3+ states empty and available for electrons, so the lower lying 5*d* and 6*s* levels of the Ln^{3+} (located below the conduction band) ensure large capture cross sections for electrons by Ln^{4+}. This binding leads to the formation of an ion-bound exciton (step 2). Then, the exciton decays, thus transferring its energy non-radiatively to the electronic structure of the Ln^{3+} (step 3). The radiative decay of the excited ion finishes the cycle. When the filled 4*f* level of the unexcited Ln^{3+} ion (introducing a hole trap) and the 5*d* and 6*s* levels of the excited Ln^{3+} ion are properly located, an efficient radiative recombination of electron−hole pairs occurs through the Ln^{3+}. On the other hand, as previously mentioned, the sequence of carrier trapping can be reversed by capturing an electron first, which becomes a $Ln^{(n-1)+}$ ion. Since holes usually relax much faster than electrons due to their capture by some killer centres before they have the opportunity to be trapped by the $Ln^{(n-1)+}$ ions, this reversed sequence is likely to produce lower light yields.[183,188]

It is worth mentioning that although the levels of the Ln^{3+} ion can be located in the forbidden energy band gap of the crystal in such a way that they have large capture cross sections, the capture process may be severely impeded by energy barriers due to electron−lattice coupling. Wojtowicz *et al.*[183] introduced a model for Ce-doped lutetium orthophosphate and orthoaluminate (Ce:$LuPO_4$, Ce:$LuAlO_3$), yttrium oxide (Ce:Y_2O_3) and cerium trifluoride (CeF_3) in order to calculate the energy barriers for the processes of hole capture, electron capture terminating with the Ce^{3+} ion in its ground state, and electron capture terminating with the Ce^{3+} ion in its excited state.

1.3.2. Cerium-doped compounds

The free Ce^{3+} ion has a single electron in its 4*f* shell: ^2F_J. The spin−orbit interaction splits the ^2F_J state into two levels, $^2F_{5/2}$ and $^2F_{7/2}$, separated by 2250 cm^{-1}, the first level being the ground state. In cerium-based or cerium-doped compounds, the 4*f* levels of Ce^{3+} fall within the forbidden energy band gap of the host and its 5*d* levels fall partially or totally within.[181,189]

After irradiating cerium-doped scintillation materials with ionizing radiation, most of the energy absorbed is transformed into separated or correlated electron−hole pairs. Accordingly, most of the localized excitations are correlated electron−hole pairs and, therefore, the energy transfer process to Ce^{3+} ions is based on the sequential capture of charge carriers by Ce centres.[183,190] As mentioned in the previous section, Ce^{3+} is a good hole trap. For this reason, in Ce^{3+}-doped or based crystals, the sequential capture begins with the capture of a hole by Ce^{3+} and then of an electron by Ce^{4+}. The probability that Ce^{3+} captures a hole strongly depends on the energy difference between the 4*f* ground state of Ce^{3+} and the top of the valence band of the host, i.e. the smaller the energy difference, the higher the efficiency of the capture of a hole.[181,182,190,191] In Ce^{3+}-doped oxides and halides, the ground state usually lies very low in the forbidden energy band gap close to the top of the valence band, which leads to systems that can have a very efficient scintillation. In Ce^{3+}-doped fluoride crystals, the hole capture probability is low because the 4*f* ground state of Ce^{3+} is far above the valence band, so they cannot exhibit very high light yield[192]. A high scintillation efficiency is connected with a high probability of hole capture[190,191]. It is worth mentioning that Ce^{4+} is an efficient electron trap, so the coexistence of Ce^{4+} and Ce^{3+} ions sometimes can be harmful, since both centres can compete for the capture of charge carriers. This fact would induce severe limitations in scintillation efficiency, so their relative ratio must be adequately tuned.[181,182]

As can be seen in Section 1.2, Ce^{3+} has been used as the dopant ion in the vast majority of the new inorganic scintillator materials reported over the last approximately 20 years. As mentioned previously, this is due to the fast luminescence decay time of the $5d \rightarrow 4f$ radiative transitions under direct $4f \rightarrow 5d$ excitation (typically within 20–60 ns for Ce^{3+}) together with the high quantum efficiency of these transitions at room temperature.[1]

1.3.3. Praseodymium-doped compounds

The free Pr^{3+} ion has two electrons in its 4*f* shell, which give rise to the term symbols (in ascending order of their respective energy): $^3H_{4,5,6}$, $^3F_{2,3,4}$, $^1G_4$, $^1D_2$, $^3P_{0,1}$, $^1I_6$, $^3P_2$ and $^1S_0$. In praseodymium-doped materials, the $5d_1$ level of Pr^{3+} not always fall within the forbidden energy band gap of the host, which is necessary to observe radioluminescence from this level. However, if the $5d_1$ level is within the forbidden energy band gap of the host and close to the conduction band or located just above its 4*f* level of the highest energy ($^1S_0$), the scintillation mechanism will degrade.[193]

In the scintillation materials doped with praseodymium, the energy transfer process based on the sequential capture of charge carriers by Pr centres usually begins with the capture of a hole by Pr^{3+}, since it is a good hole trap, as explained in Section 1.3.1.1. Analogous to the explanation of the cerium-doped compounds, the smaller the energy difference between the top of the valence band of the host and the ground 4*f* state of Pr^{3+} in the forbidden energy band gap, the higher the efficiency of hole capture by Pr^{3+}, and the higher the scintillation efficiency.

As can be seen in Section 1.2, Pr^{3+} is the second most commonly used doping ion in the inorganic scintillators reported in the last 20 years or so due to the fast luminescence decay time of the $5d \rightarrow 4f$ radiative transitions of Pr^{3+} under direct $4f \rightarrow 5d$ excitation of typically within 8–20 ns, and the high quantum efficiency of these transitions at room temperature.[1] In addition to this, Pr^{3+} also arouses great interest as active ion in laser applications[185].

1.4. Double condensed phosphates as hosts for inorganic scintillators

The family of condensed phosphates is formed by ionic compounds containing condensed phosphoric anions, PO_4^{3-}, that, depending on the type of condensation between the PO_4 tetrahedra, is divided into three subfamilies: polyphosphates, cyclophosphates and ultraphosphates. The type of condensation for the first subfamily is a progressive linear linkage of the PO_4 tetrahedra by corner-sharing that results in the formation of finite or infinite chains. When the number of phosphorus atoms in the anionic entity with general formula $[P_nO_{3n+1}]^{(n+2)-}$ is 2 the terminology used is diphosphates, when n=3 the corresponding ionic compounds are called triphosphates, and so on up to n=5. Whereas when n is very large, the P/O ratio tends to be 1/3 and the anion can be described as an infinite chain: $(PO_3)_n$. These compounds are commonly called long-chain polyphosphates or simply polyphosphates. In the subfamily of cyclophosphates, each PO_4 tetrahedron shares two corners in such a way that they form cyclic anions, or rings, with the anionic formula $[P_nO_{3n}]^{n-}$. When the number of phosphorus atoms is 3 the corresponding ionic compounds are called cyclotriphosphates, for n=4 the compounds are called cyclotetraphosphates, and in a homologous manner for the other well-characterized rings (n=5, 6, 8, 9, 10 and 12). Unlike the two types of condensation mentioned above, in the subfamily of ultraphosphates, some PO_4 tetrahedra share three of their corners with the adjacent ones. The anionic formula in this case is given by $n[PO_3]^- + mP_2O_5$ or $[P_{(2m+n)}O_{(5m+3n)}]^{n-}$, so there is an infinite number of possible branches according to the values of m and n. The ultraphosphate anions exist as finite groups, infinite ribbons, layers or three-dimensional networks. It is worth mentioning that, unlike the first two subfamilies, there is no correlation between the chemical formula of an ultraphosphate anion and its geometry.[194,195]

The above-mentioned anionic entities can form neutral compounds with one or more cationic entities, as for example the double condensed phosphates of alkali (M^I) and lanthanide (Ln^{III}) ions. These double condensed phosphates can be found with a long-chain geometry, $M^ILn^{III}(PO_3)_4$, and with a cycling geometry, $M^ILn^{III}P_4O_{12}$. The former

are termed trivalent-monovalent cation long-chain polyphosphates and the other trivalent-monovalent cation cyclotetraphosphates.[196,197] These compounds can be classified on the basis of the ordering of the ions into ten different structure types. In the case of double polyphosphates, into seven structure types denoted by Roman numerals (I-VII), while in cyclotetraphosphates, into three types denoted by Latin letters (A-C). Table 1.3 of the Ph.D. Thesis of I. Parreu[195,198] includes the main structural features of the ten structure types: space group, formula units (Z), geometry of phosphoric anions, coordination number of the alkali ion and that of the lanthanide ion. It should be noted that there is a typographical error in the space group of type I, with *C*2/*c* being the correct one[195,199,200]. Several of these compounds show polymorphism, i.e. they can adopt different structural arrangements with the same chemical composition, such as the double phosphate of potassium and gadolinium that has three polymorphs: type III $KGd(PO_3)_4$ (space group: $P2_1$)[201], type IV $KGd(PO_3)_4$ (space group: $P2_1/n$)[202] and type B $KGdP_4O_{12}$ ($C2/c$)[198,203], as well as the double phosphate of potassium and yttrium that has the following polymorphs: type III $KY(PO_3)_4$ ($P2_1$)[204], type IV $KY(PO_3)_4$ ($P2_1/n$)[205] and type B KYP_4O_{12} ($C2/c$)[206].

1.4.1. Type III $KGd(PO_3)_4$

The potassium gadolinium long-chain polyphosphate, $KGd(PO_3)_4$(henceforth, KGdP), is a monoclinic crystal that belongs to the large family of condensed phosphates. When the crystalline structure is the type III phase, the corresponding space group is $P2_1$. The primary crystallization region of type III KGdP in the K_2O–Gd_2O_3–P_2O_5 ternary system was determined in 2005 by Parreu *et al.*[207] and its crystal structure was solved in 2006 by Parreu *et al.*[201]. Its unit cell parameters are $a = 7.255(4)$ Å, $b = 8.356(5)$ Å, $c = 7.934(5)$ Å, $\beta = 91.68(5)°$ and $Z = 2$. Its crystal cell contains one structural position for gadolinium, also one for potassium, four inequivalent positions for phosphorus, and twelve inequivalent positions for oxygen. All atomic positions are doubled due to the existence of a 2-fold screw axis parallel to [010] direction. Type III KGdP is characterized by the progressive linear linkage of PO_4 tetrahedra by sharing two of their vertexes, resulting in zigzag long chains, which extend along the [100] direction. Each PO_4 tetrahedron is formed by a phosphorus atom that is four-coordinated with the nearest oxygen atoms. The basic unit of the chains consists of four PO_4 tetrahedra, which repeats by periodicity. Each gadolinium atom is coordinated with eight oxygen atoms that are at different distances, so gadolinium forms a distorted dodecahedron. Figure 1.6 shows a projection of the type III KGdP structure parallel to the *b* crystallographic direction, showing the Gd coordination polyhedron. These GdO_8 polyhedra are surrounded by four other GdO_8 polyhedra, although they are isolated from each other, since they share oxygen atoms with the PO_4 tetrahedra, which leads to the joining of the phosphate chains. The potassium ion is also eight-coordinated with oxygen atoms. That is, the other two vertexes of the tetrahedra are shared with the K^+ and Gd^{3+} atoms. These two atoms alternate with a zigzag arrangement parallel to the phosphate chains. The largest distances in the structure are those between the potassium atom and the eight different oxygens atoms, so K^+ is weakly linked to the crystal lattice.[201]

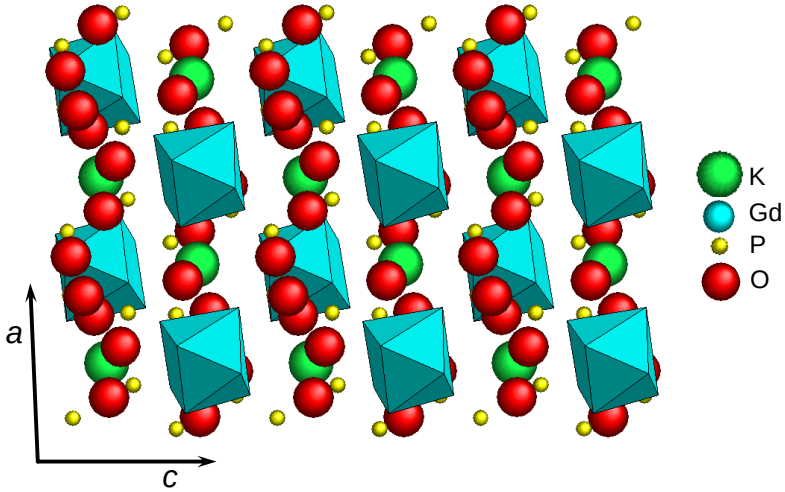

Figure 1.6. Projection of the type III $KGd(PO_3)_4$ structure parallel to the *b* crystallographic direction, showing the Gd coordination polyhedron.

Regarding the crystal habit of type III KGdP, Figure 1.7 shows two schemes of the crystal morphology in different orientations. The commonly observed as-grown faces are {001}, {100}, {011}, {0$\bar{1}$1}, {110}, {1$\bar{1}$0}, {101}, {10$\bar{1}$} and {$\bar{1}\bar{1}$1}. Type III KGdP has cleavage planes perpendicular to the *b* and *c** crystallographic directions, so these crystals can split up along these planes[208].

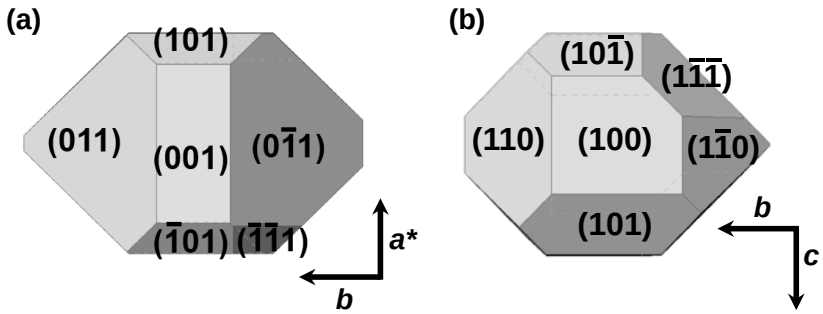

Figure 1.7. Schemes of the crystal morphology of type III $KGd(PO_3)_4$ in different orientations.

When it comes to the orientation of the optical frame in type III KGdP crystal, the principal optical axis N_p coincides with the crystallographic direction *b*, whereas the principal optical axes N_m and N_g do not correspond to other main directions of the crystallographic coordinate system. As the N_p, N_m and N_g are orthogonal by definition, the principal optical axes N_m and N_g lie on the plane perpendicular to N_p//*b*. The *a*-*c* plane contains the N_m and N_g. Considering a plate sample of type III KGdP with *b* positive toward the observer, the principal optical axis N_g is at 37.3º clockwise from the *c* direction, and the principal optical axis N_m is at 39.1º clockwise from the *a* direction, determined for 632.5 nm and at room temperature.[201] Nevertheless, no wavelength dependence has been observed in the position of the N_g–N_m principal

axes in the wavelength range between 532 and 1064 nm[209]. The authors of the ref.[201] first determined the direction of the principal optical axes and then measured the refractive indices along such axes to label each direction with the corresponding principal optical axis.

Type III KGdP is a non-hygroscopic crystal that presents good chemical stability[208] and high hardness (around 7 in Moh's hardness scale[208]), which means that surfaces can be polished to a good optical quality[210]. So, it meets two of the requirements described in Section 1.1 to evaluate favourably the performance of any scintillator, which are chemical stability and favourable mechanical properties. Due to the non-hygroscopicity of type III KGdP, its encapsulation is not necessary to protect it from the environment, so there would be no additional production costs. Moreover, this crystal is suitable for the incorporation of other Ln^{3+} in the structure due to the high substitution capacity of gadolinium (Gd^{3+}) by other lanthanide ions due to the common valence and the proximity of the ionic radii of Gd^{3+} with the other Ln^{3+} ions. This host has a unique crystalline site for the Gd^{3+} ions (point symmetry: C_1) and, consequently, for the doping Ln^{3+} ions introduced into the crystalline lattice that partly replace the Gd^{3+} ions[201]. For this reason, all doping Ln^{3+} ions will have the same crystal field in type III KGdP and, therefore, a single band will appear for each specific electronic transition between the 4*f* and 5*d* levels of the Ln^{3+} ion.

In this Ph.D. Thesis, type III $KGd_{1-x}Ce_x(PO_3)_4$ and $KGd_{1-x}Pr_x(PO_3)_4$ bulk single crystals have been grown by Top Seeded Solution Growth-Slow Cooling (TSSG-SC) technique. The ionic radii of Gd^{3+}, Ce^{3+} and Pr^{3+} ions with coordination VIII are 1.053 Å, 1.143 Å and 1.126 Å, respectively[211]. It was expected that KGdP can be doped with high concentrations of Ce^{3+} and Pr^{3+} due to the existence of type III $KCe(PO_3)_4$ [212] and type III $KPr(PO_3)_4$ [213]. This fact leads to the possibility of obtaining large and high crystalline quality bulk single crystals, which is another requirement to assess favourably the performance of a scintillator (see Section 1.1).

Type III KGdP has a wide transparency window that extends from 160 nm to 4 μm[209], covering a large number of absorption and emission wavelengths belonging to Ln^{3+} ions. The deep ultraviolet cut-off of its transparency window is particularly interesting for scintillation applications, since the light emission in the scintillation process of inorganic scintillators containing lanthanide ions is produced mainly through the $5d \rightarrow 4f$ electronic transitions of the lanthanides (see Section 1.3.1), which correspond to wavelengths that appear basically in the vacuum ultraviolet and ultraviolet spectral regions. Thus, the deep ultraviolet cut-off of the transparency window of type III KGdP host would allow the scintillator material to transmit its own emitted light, which is a requirement to evaluate favourably the performance of a scintillator (see Section 1.1).

Since Gd^{3+} has a large number of high energy 4*f* levels, energy transfer processes between the 4*f* levels of Gd^{3+} and the 5*d* levels of Ce^{3+} and Pr^{3+} are expected, so it could contribute to an increase of the emissions through the $5d \rightarrow 4f$ transitions of Ce^{3+} and Pr^{3+}. Although it should be mentioned that depending on the energy position of such levels, the energy transfer processes could be counterproductive if they are from the 5*d* levels of Ln^{3+} to the 4*f* levels of Gd^{3+}.

By comparing the minor Gd−Gd interatomic distances corresponding to the three polymorphs of KGdP, it can be observed that the type III phase has the longest distance. Since the Ln^{3+} ions that act as emitting centres are located in the atomic position of Gd^{3+}, this means that a priori type III KGdP will provide a minor occurrence of emission quenching due to a high concentration of Ln^{3+} ions. The minor Gd−Gd interatomic distance is 6.59 Å[201], 6.316 Å[202] and 5.269 Å[203] for the type III, type IV and type B phases of KGdP, respectively. It is worth mentioning that the type III phase has a distinctive feature; it is a non-centrosymmetric crystalline phase, so it has nonlinear optical properties, as can be seen in the Ph.D. Thesis of I. Parreu[214].

As mentioned in Section 1.1, one of the important requirements to evaluate favourably the performance of a scintillator material is a high total absorption coefficient. The process of absorbing the energy of incoming ionizing radiation involves the interaction of the radiation with the electrons of the scintillator. Thus, a higher absorption cross-section for X-rays and γ-rays is obtained when the density and the effective atomic number of the scintillator material are high.[11] The density of type III KGdP is 3.538 $g \cdot cm^{-3}$ [201], and its effective atomic number is $Z_{eff} = 47.7$. Considering the scintillation mechanism in a Ln^{3+}-doped KGdP crystal, it is interesting to note that the Gd^{3+} ion does not compete with the doping Ln^{3+} ions for the sequential capture of charge carriers because Gd^{3+} is very unlikely to introduce both hole and electron traps (see Sections 1.3.1 and 1.3.1.1). However, the existence of the radioisotope ^{40}K (0.0117 % natural abundance and half-life $\tau_{1/2} \approx 1.25 \times 10^9$ years) may limit the usefulness of type III KGdP as a host for inorganic scintillators by increasing the background radiation. Nevertheless, this radioisotope, together with others such as ^{176}Lu (2.59% natural abundance and half-life $\tau_{1/2} \approx 3.78 \times 10^{10}$ y), ^{87}Rb (27.8% natural abundance and half-life $\tau_{1/2} \approx 4.75 \times 10^{10}$ y) and ^{138}La (0.09% natural abundance and half-life $\tau_{1/2} \approx 1.05 \times 10^{11}$ y), is present in some scintillator materials that are promising or already in use.[215,216] Therefore, taking into account all the mentioned properties, type III KGdP is considered as a good candidate as a host for inorganic scintillators.

1.4.2. Type B KYP_4O_{12} and type IV $KY(PO_3)_4$

Double phosphate of potassium and yttrium is a polymorphic compound that belongs to the wide and versatile family of condensed phosphates. The primary crystallization region of type B KYP_4O_{12} and type IV $KY(PO_3)_4$ in the $K_2O–Gd_2O_3–P_2O_5$ ternary system has been determined in this Ph.D. Thesis (see Section 3.1). The polymorphs of KYP corresponding to the type B and IV crystalline phases crystallize in the monoclinic system with the space groups *C*2/*c* and $P2_1/c$, respectively. Type B crystalline phase belongs to the subfamily of condensed phosphates called cyclophosphates, in which the PO_4 tetrahedra form rings by sharing two of their vertexes, while type IV phase belongs the subfamily named polyphosphates, in which the PO_4 tetrahedra form zigzag long chains.

Type B and IV KYP are non-hygroscopic crystals that are suitable for the incorporation of Ln^{3+} ions in the structure due to the common valence with yttrium and the proximity of their ionic radii. Comparing, the ionic radii of Y^{3+}, Gd^{3+}, Ce^{3+} and Pr^{3+}

with coordination VIII are 1.019 Å, 1.053 Å, 1.143 Å and 1.126 Å, respectively[211]. As mentioned above, the $5d \rightarrow 4f$ emission transitions of the lanthanide ions are of interest in the scintillation mechanism of inorganic scintillators containing lanthanides (see Section 1.3.1). Then, considering a Ln^{3+}-doped KYP crystal, there is no possibility of energy transfers from the 5*d* levels of Ln^{3+} to the hypothetic 4*f* levels of Y^{3+}, since yttrium does not have 4*f* electrons. Therefore, this means that the possible problem of obtaining a non-radiative decay of the 5*d* levels of Ln^{3+} due to an energy transfer to 4*f* levels of other elements constituent of the crystal is completely eliminated using the KYP host, unlike the KGdP host. In KYP, a lower absorption coefficient (see Section 1.1) of incoming ionizing radiation could be expected because the atomic number of yttrium is lower than that of gadolinium, although the density depends not only on the composition of the crystal but also its crystalline structure[7,11]. As in KGdP, the 0.0117 % natural abundance and half-life $\tau_{1/2} \approx 1.25 \times 10^9$ years of the radioisotope ^{40}K may limit the usefulness of KYP as a host for inorganic scintillators by increasing the background radiation. Nonetheless, some of the scintillator materials that are promising or already in use have ^{40}K or other radioisotopes such as ^{176}Lu (2.59% natural abundance and half-life $\tau_{1/2} \approx 3.78 \times 10^{10}$ y), ^{87}Rb (27.8% natural abundance and half-life $\tau_{1/2} \approx 4.75 \times 10^{10}$ y) and ^{138}La (0.09% natural abundance and half-life $\tau_{1/2} \approx 1.05 \times 10^{11}$ y) in their structure.[215,216] After all, type B and type IV KYP could be good candidates as hosts for inorganic scintillators.

1.5. The aims of this Ph.D. Thesis

Throughout the beginning of this chapter, it has been explained that the compounds known as scintillator materials are currently extensively used in the detection systems addressing different fields, and that there is a large research activity based on the search for new inorganic scintillators with better properties than those of the existing scintillators. Thereafter, the characteristics of Ce^{3+} and Pr^{3+} ions as doping elements for scintillator applications and of type III $KGd(PO_3)_4$ (KGdP) as a host have been provided, concluding that type III Ce:KGdP and type III Pr:KGdP are two promising combinations as scintillator materials.

Hence, the first aim of this Ph.D. Thesis is to grow type III Ce:KGdP and Pr:KGdP bulk single crystals with high crystalline quality from high temperature solutions by the Top Seeded Solution Growth-Slow Cooling (TSSG-SC) technique. The incongruent melting of the KGdP compound[207] is the main reason for using this high temperature solution technique to obtain the bulk single crystals. The solvent/flux used is an excess of K_2O and P_2O_5, which are components that constitute the final desired crystals (self-flux), in order to avoid the possible introduction of foreign ions of the solvent into the crystalline structure. To our knowledge, type III Ce:KGdP and Pr:KGdP single crystals have never been reported in the current literature.

Type B KYP_4O_{12} and type IV $KY(PO_3)_4$ (type B and type IV KYP) are also interesting candidates as hosts for active lanthanide ions in scintillation applications. Because of the incongruent melting of KYP[205], the growth of type B and IV KYP single crystals from solution will be investigated in this Ph.D. Thesis. Thus, the second aim of the

Thesis is to determine the primary crystallization region of the type B KYP and type IV KYP phases in the $K_2O–Y_2O_3–P_2O_5$ ternary system. They will be also grown from self-flux with an excess of K_2O and P_2O_5.

The third aim is to establish and optimize the synthesis conditions of type III Pr:KGdP nanocrystals by the modified Pechini method as a starting point to obtain it as a ceramic scintillator.

The next aim of this Ph.D. Thesis is to find out whether the presence of Ce^{3+} and Pr^{3+} in the crystalline lattice of KGdP implies significant changes in the physical properties of KGdP when it is doped. The structural characterization of the bulk single crystals previously obtained includes the crystal morphology, chemical composition and changes in the unit cell parameters with doping content of both compositions (Ce:KGdP and Pr:KGdP), as well as the discussion on thermal stability and thermal expansion of type III Pr:KGdP single crystals. The structural characterization of the nanocrystals previously obtained covers the same studies mentioned for the single crystals, but with the additional objective of finding the particle size distribution and the predominant particle size, since this has an effect on the sintering process to obtain the ceramic from the nanocrystals.

The last aim of this Ph.D. Thesis consists in an extensive spectroscopic characterization of type III Ce:KGdP and Pr:KGdP bulk single crystals and type III Pr:KGdP nanocrystals to study in detail the spectroscopy of the 4*f*–5*d* electronic transitions, on which the scintillation mechanism in inorganic scintillators containing lanthanide ions is based. In addition to this, since Pr^{3+} also is an active ion in laser applications, the basic spectroscopic data of the type III Pr:KGdP crystal for lasing applications in the visible wavelength range based on the 4*f*–4*f* electronic transitions is of interest. The spectroscopic studies of these materials include unpolarized and polarized optical absorption at room temperature and at 6 K, luminescence and decay time measurements under synchrotron vacuum ultraviolet-ultraviolet (VUV-UV) excitation, decay time measurements under visible excitation and radioluminescence measurements after synchrotron X-ray irradiation.

References

[1] M. Nikl and A. Yoshikawa. Recent R&D trends in inorganic single-crystal scintillator materials for radiation detection. *Adv. Opt. Mater.* **2015**, *3* (4), 463-481.
[2] X. Qin, X. Liu, W. Huang, M. Bettinelli and X. Liu. Lanthanide-activated phosphors based on 4f-5d optical transitions: Theoretical and experimental aspects. *Chem. Rev.* **2017**, *117*, 4488-4527.
[3] J. M. Nedelec. Sol-gel processing of nanostructured inorganic scintillating materials. *J. Nano Mat.* **2007**, *2007*, 1-8.
[4] P. Lecoq, A. Annenkov, A. Gektin, M. Korzhik and C. Pedrini. Classification of inorganic scintillation materials. In *Inorganic scintillators for detector systems: Physical principles and crystal engineering*. Springer Berlin Heidelberg: The Netherlands, **2006**; pp 21-27.
[5] W. W. Moses. Scintillator requirements for medical imaging. Proceedings of the International Conference on Inorganic Scintillators and Their Applications, SCINT (Ed: V. Mikhailin). Moscow, Russia, **1999**.
[6] C. Dujardin, E. Auffray, E. Bourret-Courchesne, P. Dorenbos, P. Lecoq, M. Nikl, A. N. Vasil'ev, A. Yoshikawa and R.-Y. Zhu. Needs, trends, and advances in inorganic scintillators. *IEEE Trans. Nucl. Sci.* **2018**, *65* (8), 1977-1997.
[7] P. A. Rodnyi. Scintillator requirements in various applications. In *Physical processes in inorganic scintillators.* CRC Press: Boca Raton, FL, USA, **1997**; pp 41-51.
[8] M. Nikl. A. Yoshikawa, K. Kamada, K. Nejezchleb, C. R. Stanek, J. A. Mares and K. Blazek. Development of LuAG-based scintillator crystals – A review. *Prog. Cryst. Growth Charact. Mater.* **2013**, *59* (2), 47-72.
[9] C. W. E. van Eijk. New scintillators, new light sensors, new applications. Proceedings of the International Conference on Inorganic Scintillators and Their Applications, SCINT (Eds: Y. Zhiwen, F. Xiqi, L. Peijun and X. Zhilin). Shanghai Branch Press, Shanghai, China, **1997**, pp 3-12.
[10] P. A. Rodnyi. General characteristics of inorganic scintillators. In *Physical processes in inorganic scintillators.* CRC Press: Boca Raton, FL, USA, **1997**; pp 19-40.
[11] A. K. Zych. Luminescence properties of Ce^{3+}, Pr^{3+} and Nd^{3+} activated scintillators for Positron Emission Tomography (PET). Ph.D. Thesis, Utrecht University, **2011**.
[12] L. Yu, X. Liu, S. Leng, J. M. Kofler, J. C. Ramirez-Giraldo, M. Qu, J. Christner, J. G. Fletcher and C. H. McCollough. Radiation dose reduction in computed tomography: techniques and future perspective. *Imaging Med.* **2009**, *1* (1), 65-84.
[13] K. M. Waterstram-Rich and D. Gilmore. PET instrumentation. In *Nuclear Medicine and PET/CT: Technology and Techniques.* Eighth edition. Elsevier: St. Louis, MO, USA, **2017**; pp 326-355.
[14] R. E. Schmitz, A. M. Alessio and P. E. Kinahan. Imaging Research Laboratory, Department of Radiology, University of Washington. The Physics of PET/CT scanners (accessed 06/08/2019). http://depts.washington.edu/imreslab/education/Physics%20of%20PET.pdf
[15] Physics Forums Insights. The Basics of Positron Emission Tomography (PET). https://www.physicsforums.com/insights/basics-positron-emission-tomography-pet/ (accessed 03/07/2019).
[16] R. Y. Zhu. Radiation damage in scintillating crystals. *Nucl. Instr. Meth. Phys. Res. A* **1998**, *413*, 297-311.
[17] W. C. Röntgen. On a new kind of rays. *Science* **1896**, *3*, 227-231.
[18] A. W. Fuchs. *Radiography of 1896*. George Eastman House, **1960**, vol. 9, pp 4-17.
[19] R. Hofstadter. The detection of gamma-rays with thallium-activated sodium iodide crystals. *Phys. Rev.* **1949**, *75*, 796-810.
[20] R. H. Gillette. Calcium and cadmium tungstate as scintillation counter crystals for gamma-ray detection. *Rev. Sci. Instrum.* **1950**, *21* (4), 294-301.
[21] W. van Sciver and R. Hofstadter. Scintillations in thallium-activated CaI_2 and CsI. *Phys. Rev.* **1951**, *84* (5), 1062-1063.
[22] J. Bonanomi and J. Rossel. Scintillations de luminescence dans des iodures d'alcalins. *Helv. Phys. Acta* **1952**, *25* (VII), 725-752.

[23] W. van Sciver and R. Hofstadter. Gamma- and alpha-produced scintillation in cesium fluoride. *Phys. Rev.* **1952**, *87* (3), 522-522.
[24] J. Schenck. Activation of lithium iodide by europium. *Nature* **1953**, *171* (4351), 518-519.
[25] P. Brinkman. CsI(Na) scintillation of crystals. *Phys. Lett.* **1965**, *15* (4), 305-305.
[26] J. Menefee, C. F. Swinehart and E. W. O'Dell. Calcium fluoride as an X-ray and charged particle detector. *IEEE Trans. Nucl. Sci.* **1966**, *13* (1), 720-724.
[27] M. J. Weber and R. R. Monchamp. Luminescence of $Bi_4Ge_3O_{12}$: spectral and decay properties. *J. Appl. Phys.* **1973**, *44* (12), 5495-5499.
[28] P. A. Rodnyi. Introduction. In *Physical processes in inorganic scintillators.* CRC Press: Boca Raton, FL, USA, **1997**.
[29] Hellma. Radiation detection crystals. https://www.hellma.com/en/crystalline-materials/radiation-detection-crystals/ (accessed 25/07/2019).
[30] Saint-Gobain Crystals. Crystal scintillation materials. Physical properties of common inorganic scintillators. https://www.crystals.saint-gobain.com/products/crystal-scintillation-materials (accessed 25/07/2019).
[31] D. W. Townsend and T. Beyer. Anato-molecular imaging: Combining structure and function. State-of-the-art PET/CT systems. In *Positron emission tomography* (Eds: D. L. Bailey, D. W. Townsend, P. E. Valk and M. N. Maisey). Springer: London, UK, **2005**; pp 191-197.
[32] N. N. Ershov, N. G. Zakharov and P. A. Rodnyi. Spectral-kinetic study of the intrinsic-luminescence characteristics of a fluorite-type crystal. *Opt. Spectrosc.* **1982**, *53* (1), 51-54.
[33] M. Laval, M. Moszyński, R. Allemand, E. Cormoreche, P. Guinet, R. Odru and J. Vacher. Barium fluoride — Inorganic scintillator for subnanosecond timing. *Nucl. Instrum. Methods Phys. Res.* **1983**, 206 (1-2), 169-176.
[34] Y. M. Aleksandrov, V. N. Makhov, P. A. Rodnyi, T. I. Syreishchikova and M. N. Yakimenko. Intrinsic luminescence of BaF_2 on the pulse excitation by synchrotron radiation. *Sov. Phys. Solid State* **1984**, *26* (9), 2865-2867.
[35] C. W. E. van Eijk, P. Dorenbos and R. Visser. Nd^{3+} and Pr^{3+} doped inorganic scintillators. *IEEE Trans. Nucl. Sci.* **1994**, *41*, 738-741.
[36] P. Dorenbos, R. Visser, C. W. E. van Eijk, N. M. Khaidukov and M. V. Korzhik. Scintillation properties of some Ce^{3+} and Pr^{3+} doped inorganic crystals. *IEEE Trans. Nucl. Sci.* **1993**, *40*, 388-394.
[37] P. Dorenbos. Fundamental limitations in the performance of Ce^{3+}-, Pr^{3+}-, and Eu^{2+}-activated scintillators. *IEEE Trans. Nucl. Sci.* **2010**, *57*, 1162-1167.
[38] D. Wisniewski, S. Tavernier, A. J. Wojtowicz, M. Wisniewska, P. Bruyndonckx, P. Dorenbos, E. van Loef, C. W. E. van Eijk and L. A. Boatner. $LuPO_4$:Nd and YPO_4:Nd — New promising VUV scintillation materials. *Nucl. Instrum. Methods Phys. Res. Sect. A* **2002**, *486* (1-2), 239-243.
[39] C. W. E. van Eijk. Inorganic-scintillator development. *Nucl. Instr. Meth. Phys. Res. A* **2001**, *460* (1), 1-14.
[40] M. Korzhik, A. Fedorov, A. Annenkov, A. Borissevitch, A. Dossovitski, O. Missevitch and P. Lecoq. Development of scintillation materials for PET scanners. *Nucl. Instr. Meth. Phys. Res. A* **2007**, 571, 122-125.
[41] Lawrence Berkeley National Laboratory with support from the Department of Homeland Security (DHS). Scintillation properties. http://scintillator.lbl.gov/ (accessed 25/07/2019).
[42] B. Liu and C. Shi. Development of medical scintillator. *Chin. Sci. Bull.* **2002**, *47*, 1057-1063.
[43] C. Brecher, A. Lempicki, S. R. Miller, J. Glodo, E. E. Ovechkina, V. Gaysinskiy, V. V. Nagarkar and R. H. Bartram. Suppression of afterglow in CsI:Tl by codoping with Eu^{2+} - I: Experimental. *Nucl. Instrum. Meth. Phys. Res. Sect. A* **2006**, *558* (2), 450-457.
[44] R. H. Bartram, L. A. Kappers, D. S. Hamilton, A. Lempicki, C. Brecher, J. Glodo, V. Gaysinskiy and E. E. Ovechkina. Suppression of afterglow in CsI:Tl by codoping with Eu^{2+} - II: Theoretical model. *Nucl. Instrum. Meth. Phys. Res. Sect. A* **2006**, *558* (2), 458-467.
[45] V. V. Nagarkar, C. Brecher, E. E. Ovechkina, V. Gaysinskiy, S. R. Miller, S. Thacker, A. Lempicki and R. H. Bartram. Scintillation properties of CsI:Tl crystals codoped with Sm^{2+}. *IEEE Trans. Nucl. Sci.* **2008**, *55* (3), 1270-1274.

[46] Y. Wu, G. Ren, F. Meng, X. Chen, D. Ding, H. Li and S. Pan. Effects of Bi^{3+} codoping on the optical and scintillation properties of CsI:Tl single crystals. *Phys. Status Solidi A* **2014**, *211* (11), 2586-2591.

[47] Y. Wu, G. Ren, M. Nikl, X. F. Chen, D. Z. Ding, H. Li, S. Pan and F. Yang. CsI:Tl^{+}, Yb^{2+}: ultra-high light yield scintillator with reduced afterglow. *Cryst. Eng. Comm.* **2014**, *16* (16), 3312-3317.

[48] P. A. Rodnyi. Gamma spectroscopy. In *Physical processes in inorganic scintillators.* CRC Press: Boca Raton, FL, USA, **1997**; pp 44-50.

[49] O. Guillot-Noël, J. T. M. de Haas, P. Dorenbos, C. W. E. van Eijk, K. Krämer and H. U. Güdel. Optical and scintillation properties of cerium-doped $LaCl_3$, $LuBr_3$ and $LuCl_3$. *J. Lumin.* **1999**, *85* (1-3), 21-35.

[50] E. V. D. van Loef, P. Dorenbos and C. W. E. van Eijk. High-energy-resolution scintillator: Ce^{3+} activated $LaBr_3$. *Appl. Phys. Lett.* **2001**, *79* (10), 1573-1575.

[51] E. V. D. van Loef, P. Dorenbos and C. W. E. van Eijk. The scintillation mechanism in $LaCl_3$:Ce^{3+}. *J. Phys.: Condens. Matter* **2003**, *15* (8), 1367-1375.

[52] G. Bizarri, J. de Haas, P. Dorenbos and C. W. E Van Eijk. Scintillation properties of O 1×1 $Inch^3$ $LaBr_3$: 5%Ce^{3+} crystal. *IEEE Trans. Nucl. Sci.* **2006**, *53* (2), 615-619.

[53] M. D. Birowosuto, P. Dorenbos, C. W. E. van Eijk, K. W. Krämer and H. U. Güdel. High-light-output scintillator for photodiode readout: LuI_3:Ce^{3+}. *J. Appl. Phys.* **2006**, *99* (12), 123520.

[54] P. Dorenbos, E. V. D. van Loef, A. P. Vink, E. van der Kolk, C. W. E. van Eijk, K. Krämer, H. U. Güdel, W. M. Higgins and K. S. Shah. Level location and spectroscopy of Ce^{3+}, Pr^{3+}, Er^{3+}, and Eu^{2+} in $LaBr_3$. *J. Lumin.* **2006**, *117* (2), 147-155.

[55] A. M. Srivastava, J. S. Vartuli, S. J. Duclos, P. A. Schmidt, S. B. Chaney and U. Happek. Luminescence of Pr^{3+} doped $LuCl_3$ and $LuBr_3$ under intraconfigurational (4f(2) -> 4f(1)5d(1)) and band gap excitation. *IEEE Trans. Nucl. Sci.* **2009**, *56* (3), 986-988.

[56] F. G. A. Quarati, I. V. Khodyuk, C. W. E. van Eijk, P. Quarati and P. Dorenbos. Study of La-138 radioactive decays using $LaBr_3$ scintillators. *Nucl. Instrum. Methods Phys. Res. Sect. A* **2012**, *683*, 46-52.

[57] K. S. Shah, J. Glodo, W. Higgins, E. V. D. van Loef, W. W. Moses, S. E. Derenzo and M. J. Weber. $CeBr_3$ scintillators for gamma-ray spectroscopy. *IEEE Nucl. Sci. Symp. Conf. Rec.* **2004**, *7*, 4278-4281.

[58] P. Guss, M. Reed, D. Yuan, A. Reed and S. Mukhopadhyay. $CeBr_3$ as a high-resolution gamma-ray detector. *Nucl. Instrum. Methods Phys. Res. Sect. A* **2009**, *608* (2), 297-304.

[59] F. G. A. Quarati, P. Dorenbos, J. van der Biezen, A. Owens, M. Selle, L. Parthier and P. Schotanus. Scintillation and detection characteristics of high-sensitivity $CeBr_3$ gamma-ray spectrometers. *Nucl. Instrum. Methods Phys. Res. Sect. A* **2013**, *729* (21), 596-604.

[60] P. Guss, M. Reed, D. Yuan, M. Cutler, C. Contreras and D. Beller. Comparison of $CeBr_3$ with $LaBr_3$:Ce, $LaCl_3$:Ce, and NaI:Tl detectors. *Proc. SPIE* **2010**, *7805*, 78050L.

[61] M. N. Ullah, E. Pratiwi, J. Cheon, H. Choi and J. Y. Yeom. Instrumentation for Time-of-Flight Positron Emission Tomography. *Nucl. Med. Mol. Imaging* **2016**, *50* (2), 112-122.

[62] N. D'Olympia, S. Lakshmi, P. Chowdhury, E. G. Jackson, J. Glodo and K. Shah. Sub-nanosecond nuclear half-life and time-of-flight measurements with $CeBr_3$. *Nucl. Instrum. Methods Phys. Res. Sect. A* **2013**, *728*, 31-35.

[63] M. J. Harrison, C. Linnick, B. Montag, S. Brinton, M. McCreary, F. P. Doty and D. S. McGregor. Scintillation performance of aliovalently-doped $CeBr_3$. *IEEE Trans. Nucl. Sci.* **2009**, *56* (3), 1661-1665.

[64] M. J. Harrison, P. Ugorowski, C. Linnick, S. Brinton, D. S. McGregor, F. P. Doty, S. Kirpatrcik and D. F. Bahr. Aliovalent doping of $CeBr_3$. *Proc. SPIE* **2010**, *7806*, 78060M.

[65] F. G. A. Quarati, M. S. Alekhin, K. W. Krämer and P. Dorenbos. Co-doping of $CeBr_3$ scintillator detectors for energy resolution enhancement. *Nucl. Instrum. Methods Phys. Res. Sect. A* **2014**, 735, 655-658.

[66] M. S. Alekhin, J. T. M. de Haas, I. V. Khodyuk, K. W. Kramer, P. R. Menge, V. Ouspenski and P. Dorenbos. Improvement of gamma-ray energy resolution of $LaBr_3$:Ce^{3+} scintillation detectors by Sr^{2+} and Ca^{2+} co-doping. *Appl. Phys. Lett.* **2013**, *102* (16), 161915.

[67] R. C. Runkle, A. Bernstein and P. E. Vanier. Securing special nuclear material: Recent advances in neutron detection and their role in nonproliferation. *J. Appl. Phys.* **2010**, *108* (11), 111101.
[68] C. W. E. van Eijk. Inorganic scintillators for thermal neutron detection. *IEEE Trans. Nucl. Sci.* **2012**, *59* (5), 2242-2247.
[69] N. J. Cherepy, G. Hull, A. Drobshoff, S. A. Payne, E. Van Loef, C. Wilson, K. Shah, U. N. Roy, A. Burger, L. A. Boatner, W.-S. Choong and W. W. Moses. Strontium and barium iodide high light yield scintillators. *Appl. Phys. Lett.* **2008**, *92* (8), 083508.
[70] R. Hofstadter. Europium activated strontium iodide scintillators. US Patent No. 3373279, **1968**.
[71] J. Glodo, E. van Loef, N. J. Cherepy, S. A. Payne and K. S. Shah. Concentration effects in Eu doped SrI_2. *IEEE Trans. Nucl. Sci.* **2010**, *57* (3), 1228-1232.
[72] M. S. Alekhin, J. T. M. de Haas, K. W. Kramer and P. Dorenbos. Scintillation properties of and self absorption in $SrI_2:Eu^{2+}$. *IEEE Trans. Nucl. Sci.* **2011**, *58* (5), 2519- 2527.
[73] E. D. Bourret-Courchesne, G. Bizarri, R. Borade, Z. Yan, S. M. Hanrahan, G. Gundiah, A. Chaudhry, A. Canning and S. E. Derenzo. Eu^{2+}-doped Ba(2)Csl(5), a new high-performance scintillator. *Nucl. Instrum. Methods Phys. Res. Sect. A* **2009**, *612* (1), 138-142.
[74] U. Shirwadkar, R. Hawrami, J. Glodo, E. V. D. van Loef and K. S. Shah. Promising alkaline earth halide scintillators for gamma-ray spectroscopy. *IEEE Trans. Nucl. Sci.* **2013**, *60* (2), 1011-1015.
[75] M. S. Alekhin, D. A. Biner, K. W. Kramer and P. Dorenbos. Optical and scintillation properties of $CsBa_2I_5:Eu^{2+}$. *J. Lumin.* **2014**, 145, 723-728.
[76] R. Autrata, P. Schauer, Jo. Kvapil and Ji. Kvapil. A single crystal of YAG - new fast scintillator in SEM. *J. Phys. E Sci. Instrum.* **1978**, *11* (7), 707-708.
[77] M. Moszynski, T. Ludziewski, D. Wolski, W. Klamra and L. O. Norlin. Properties of the YAG-Ce scintillator. *Nucl. Instrum. Methods Phys. Res. Sect. A* **1994**, *345* (3), 461-467.
[78] M. Nikl, E. Mihokova, J. A. Mares, A. Vedda, M. Martini, K. Nejezchleb and K. Blazek. Traps and timing characteristics of LuAG:Ce^{3+} scintillator. *Phys. Status Solidi B* **2000**, *181* (1), R10-R12.
[79] H. Ogino, A. Yoshikawa, M. Nikl, K. Kamada and T. Fukuda. Scintillation characteristics of Pr-doped $Lu_3Al_5O_{12}$ single crystals. *J. Cryst. Growth* **2006**, *292* (2), 239-242.
[80] M. Nikl, K. Kamada, V. Babin, J. Pejchal, K. Pilarova, E. Mihokova, A. Beitlerova, K. Bartosiewicz, S. Kurosawa and A. Yoshikawa. Defect engineering in Ce-doped aluminum garnet single crystal scintillators. *Cryst. Growth Des.* **2014**, *14* (9), 4827-4833.
[81] K. V. Ivanovskikh, J. M. Ogiegło, A. Zych, C. R. Ronda and A. Meijerink. Luminescence temperature quenching for Ce^{3+} and Pr^{3+} d-f emission in YAG and LuAG. *ECS J. Solid State Sci. Technol.* **2013**, *2* (2), R3148-R3152.
[82] M. Nikl, J. A. Mares, N. Solovieva, J. Hybler, A. Voloshinovskii, K. Nejezchleb and K. Blazek. Energy transfer to the Ce^{3+} centers in $Lu^3Al^5O^{12}$:Ce scintillator. *Phys. Status Solidi A* **2004**, *201* (7), R41-R44.
[83] M. Nikl, A. Vedda, M. Fasoli, I. Fontana, V. V. Laguta, E. Mihokova, J. Pejchal, J. Rosa and K. Nejezchleb. Shallow traps and radiative recombination processes in $Lu_3Al_5O_{12}$:Ce single crystal scintillator. *Phys. Rev. B* **2007**, *76* (19), 195121-195128.
[84] W. Chewpraditkul, L. Swiderski, M. Moszynski, T. Szczesniak, A. Syntfeld-Kazuch, C. Wanarak and P. Limsuwan. Scintillation properties of LuAG:Ce, YAG:Ce and LYSO:Ce crystals for gamma-ray detection. *IEEE Trans. Nucl. Sci.* **2009**, *56* (6), 3800-3805.
[85] J. A. Mares, A. Beitlerova, M. Nikl, N. Solovieva, C. D'Ambrosio, K. Blazek, P. Maly, K. Nejezchleb and F. de Notaristefani. Scintillation response of Ce-doped or intrinsic scintillating crystals in the range up to 1 MeV. *Radiat. Meas.* **2004**, *38* (4-6), 353-357.
[86] C. Dujardin, C. Mancini, D. Amans, G. Ledoux, D. Abler, E. Auffray, P. Lecoq, D. Perrodin, A. Petrosyan and K. L. Ovanesyan. LuAG:Ce fibers for high energy calorimetry. *J. Appl. Phys.* **2010**, *108* (1), 013510.
[87] M. Fasoli, A. Vedda, M. Nikl, C. Jiang, B. P. Uberuaga, D. A. Andersson, K. J. McClellan and C. R. Stanek. Band-gap engineering for removing shallow traps in rare-earth $Lu_3Al_5O_{12}$ garnet scintillators using Ga^{3+} doping. *Phys. Rev. B* **2011**, *84* (8), 081102.

[88] A. B. Muñoz-García and L. Seijo. Structural, electronic, and spectroscopic effects of Ga codoping on Ce-doped yttrium aluminum garnet: First-principles study. *Phys. Rev. B* **2010**, *82* (18), 184118.
[89] J. M. Ogiegło, A. Katelnikovas, A. Zych, T. Jüstel, A. Meijerink and C. R. Ronda. Luminescence and luminescence quenching in $Gd_3(Ga,Al)_5O_{12}$ scintillators doped with Ce^{3+}. *J. Phys. Chem. A* **2013**, *117* (12), 2479-2484.
[90] M. Nikl, K. Kamada, S. Kurosawa, Y. Yokota, A. Yoshikawa, J. Pejchal and V. Babin. Luminescence and scintillation mechanism in Ce^{3+} and Pr^{3+} doped $(Lu,Y,Gd)_3(Ga,Al)_5O_{12}$ single crystal scintillators. *Phys. Status Solidi C* **2013**, *10* (2), 172-175.
[91] K. Kamada, T. Yanagida, T. Endo, K. Tsutumi, Y. Fujimoto, A. Fukabori, A. Yoshikawa, J. Pejchal and M. Nikl. Composition engineering in cerium-doped $(Lu,Gd)_3(Ga,Al)_5O_{12}$ single-crystal scintillators. *Cryst. Growth Des.* **2011**, *11* (10), 4484-4490.
[92] K. Kamada, T. Yanagida, J. Pejchal, M. Nikl, T. Endo, K. Tsutumi, Y. Fujimoto, A. Fukabori and A. Yoshikawa. Scintillator-oriented combinatorial search in Ce-doped $(Y,Gd)_3(Ga,Al)_5O_{12}$ multicomponent garnet compounds. *J. Phys. D: Appl. Phys.* **2011**, *44* (50), 505104.
[93] Y. Wu, F. Meng, Q. Li, M. Koschan and C. L. Melcher. Role of Ce^{4+} in the scintillation mechanism of codoped $Gd_3Ga_3Al_2O_{12}$:Ce. *Phys. Rev. Applied* **2014**, *2* (4), 044009.
[94] M. Nikl, V. Babin, J. A. Mares, K. Kamada, S. Kurosawa, A. Yoshikawa, J. Tous, J. Houzvicka and K. Blazek. The role of cerium variable charge state in the luminescence and scintillation mechanism in complex oxide scintillators: The effect of air annealing. *J. Lumin.* **2016**, *169*, 539-543.
[95] C. Wang, D. Ding, Y. Wu, H. Li, X. Chen, J. Shi, Q. Wang, L. Ye and G. Ren. Effect of thermal annealing on scintillation properties of $Ce:Gd_2Y_1Ga_{2.7}Al_{2.3}O_{12}$ under different atmosphere. *Appl. Phys. A* **2017**, *123* (5), 384.
[96] Y. Wu and G. Ren. Energy transfer and radiative recombination processes in $(Gd,Lu)_3Ga_3Al_2O_{12}:Pr^{3+}$ scintillators. *Opt. Mater.* **2013**, *35*, 2146-2154.
[97] Y. Wu and G. Ren. Effects of Gd/Lu ratio on the luminescent properties of Pr^{3+} activated $(Gd,Lu)_3Ga_3Al_2O_{12}$. *ECS J. Solid State Sci. Technol.* **2013**, *2* (3), R49-R55.
[98] J. A. Mares, A. Beitlerova, M. Nikl, A. Vedda, C. D'Ambrosio, K. Blazek and K. Nejezchleb. Time development of scintillating response in Ce- or Pr-doped crystals. *Phys. Status Solidi C* **2007**, *4* (3), 996-999.
[99] W. Drozdowski, K. Brylew, A. J. Wojtowicz, J. Kisielewski, M. Swirkowicz, T. Łukasiewicz, J. T. M. de Haas and P. Dorenbos. 33000 photons per MeV from mixed $(Lu_{0.75}Y_{0.25})_3Al_5O_{12}$:Pr scintillator crystals. *Opt. Mater. Express* **2014**, *4* (6), 1207-1212.
[100] M. Tyagi, F. Meng, M. Koschan, S. B. Donnald, H. Rothfuss and C. L. Melcher. Effect of codoping on scintillation and optical properties of a Ce-doped $Gd_3Ga_3Al_2O_{12}$ scintillator. *J. Phys. D: Appl. Phys.* **2013**, *46*, 475302.
[101] K. Kamada, M. Nikl, S. Kurosawa, A. Beitlerova, A. Nagura, Y. Shoji, J. Pejchal, Y. Ohashi, Y. Yokota and A. Yoshikawa. Alkali earth co-doping effects on luminescence and scintillation properties of Ce doped $Gd_3Al_2Ga_3O_{12}$ scintillator. *Opt. Mater.* **2015**, *41*, 63-66.
[102] E. Zych, C. Brecher and H. Lingertat. Scintillation properties of YAG:Ce optical ceramics. *Mater. Sci. Forum* **1996**, *239*-241, 257-260.
[103] E. Zych, C. Brecher, A. J. Wojtowicz and H. Lingertat. Luminescence properties of Ce-activated YAG optical ceramic scintillator materials. *J. Lumin.* **1997**, *75* (3), 193-203.
[104] T. Yanagida, H. Takahashi, T. Ito, D. Kasama, T. Enoto, M. Sato, S. Hirakuri, M. Kokubun, K. Makishima, T. Yanagitani, H. Yagi and T. Shigeta. Evaluation of properties of YAG (Ce) ceramic scintillators. *IEEE Trans. Nucl. Sci.* **2005**, *52* (5), 1836-1841.
[105] H.-L. Li, X.-J. Liu and L.-P. Huang. Fabrication of transparent cerium-doped lutetium aluminum garnet (LuAG:Ce) ceramics by a solid-state reaction method. *J. Am. Ceram. Soc.* **2005**, *88* (11), 3226-3228.
[106] G. Hull, J. J. Roberts, J. D. Kuntz, S. E. Fisher, R. D. Sanner, T. M. Tillotson, A. D. Drobshoff, S. A. Payne and N. J. Cherepy. Ce-doped single crystal and ceramic garnets for gamma ray detection - art. no. 670617. *Proc. SPIE* **2007**, *6706*, 70617-70617.

[107] M. Nikl, J. A. Mares, N. Solovieva, H.-L. Li, X.-J. Liu, L.-P. Huang, I. Fontana, M. Fasoli, A. Vedda and C. D'Ambrosio. Scintillation characteristics of $Lu_3Al_5O_{12}$:Ce optical ceramics. *J. Appl. Phys.* **2007**, *101* (3), 033515.
[108] H.-L. Li, X.-J. Liu, R.-J. Xie, G.-H. Zhou, N. Hirosaki, X.-P. Pu and L.-P. Huang. Cerium-doped lutetium aluminum garnet phosphors and optically transparent ceramics prepared from powder precursors by a urea homogeneous precipitation method. *Jpn. J. Appl. Phys.* **2008**, *47* (3R), 1657-1661.
[109] T. Yanagida, Y. Fujimoto, Y. Yokota, K. Kamada, S. Yanagida, A. Yoshikawa, H. Yagi and T. Yanagitani. Comparative study of transparent ceramic and single crystal Ce doped LuAG scintillators. *Radiat. Meas.* **2011**, *46* (12), 1503-1505.
[110] S. Yanagida, A. Yoshikawa, A. Ikesue, K. Kamada and Y. Yokota. Basic properties of ceramic Pr:LuAG scintillators. *IEEE Trans. Nucl. Sci.* **2009**, *56* (5), 2955-2959.
[111] T. Yanagida, Y. Fujimoto, K. Kamada, D. Totsuka, H. Yagi, T. Yanagitani, Y. Futami, S. Yanagida, S. Kurosawa, Y. Yokota, A. Yoshikawa and M. Nikl. Scintillation properties of transparent ceramic Pr:LuAG for different Pr concentration. *IEEE Trans. Nucl. Science* **2012**, *59* (5), 2146-2151.
[112] N. J. Cherepy, S. A. Payne, B. W. Sturm, S. P. O'Neal, Z. M. Seeley, O. B. Drury, L. K. Haselhorst, B. L. Rupert, R. D. Sanner, P. A. Thelin, S. E. Fisher, R. Hawrami, K. S. Shah, A. Burger, J. O. Ramey and L. A. Boatner. Performance of europium-doped strontium iodide, transparent ceramics and bismuth-ioaded polymer scintillators. *Proc. SPIE* **2011**, 8142, 81420W.
[113] T. Kanai, M. Satoh and I. Miura. Characteristics of a nonstoichiometric $Gd_3(Al,Ga)_5O_{12}$:Ce garnet scintillator. *J. Am. Ceram. Soc.* **2008**, *91* (2), 456-462.
[114] J. Y. Yeom, S. Yamamoto, S. E. Derenzo, V. Ch. Spanoudaki, K. Kamada, T. Endo and C. S. Levin. First performance results of Ce:GAGG scintillation crystals with silicon photomultipliers. *IEEE Trans. Nucl. Sci.* **2013**, *60* (2), 988-992.
[115] M. J. Weber. Optical spectra of Ce^{3+} and Ce^{3+}-sensitized fluorescence in $YAlO_3$. *J. Appl. Phys.* **1973**, 44 (7), 3205-3208.
[116] E. G. Gumanskaya, M. V. Korzhik, S. A. Smirnova, V. B. Pavlenko and A. A. Fedorov. Interconfiguration luminescence of Pr^{3+} ions in $Y_3Al_5O_{12}$ and $YAlO_3$ single crystals. *Opt. Spectrosc.* **1992**, *72* (1), 155-159.
[117] T. Takeda, T. Miyata, F. Muramatsu and T. Tomiki. Fast decay UV phosphor-$YAlO_3$:Ce. *J. Electrochem. Soc.* **1980**, *127* (2), 438-444.
[118] R. Autrata, P. Schauer, Ji. Kvapil and Jo. Kvapil. A single crystal of $YAlO_3:Ce^{3+}$ as a fast scintillator in SEM. *Scanning* **1983**, *5* (2), 91-96.
[119] J. Trummer, E. Auffray, P. Lecoq, A. Petrosyan and P. Sempere-Roldan. Comparison of LuAP and LuYAP crystal properties from statistically significant batches produced with two different growth methods. *Nucl. Instrum. Methods Phys. Res. Sect. A* **2005**, *551* (2-3), 339-351.
[120] E. Auffray, P. Bruyndonckx, O. Devroede, A. Fedorov, U. Heinrichs, M. Korjik, M. Krieguer, C. Kuntner, C. Lartizien, P. Lecoq, S. Leonard, Ch. Morel, J. B. Mosset, Ch. Pedrini, A. Petrosian, U. Pietrzyk, M. Rey, S. Saladino, D. Sappey-Marinier, L. Simon, M. Streun, S. Tavernier, J. M. Vieira and K. Ziemons. The ClearPET project. *Nucl. Instrum. Methods Phys. Res. Sect. A* **2004**, *527* (1-2), 171-174.
[121] M. Derdzyan, A. Petrosyan, T. Butaeva, K. Ovanesyan, C. Pedrini, C. Dujardin, N. Garnier and I. Kamenskikh. Growth and properties of LuAP co-doped with divalent or tetravalent impurities. *Nucl. Instrum. Methods Phys. Res. Sect. A* **2005**, 537 (1-2), 200-202.
[122] W. Drozdowski, A. J. Wojtowicz, T. Lukasiewicz and J. Kisielewski. Scintillation properties of LuAP and LuYAP crystals activated with cerium and molybdenum. *Nucl. Instrum. Methods Phys. Res. Sect. A* **2006**, *562* (1), 254-261.
[123] A. G. Petrosyan, M. Derdzyan, K. Ovanesyan, P. Lecoq, E. Auffray, J. Trummer, M. Kronberger, C. Pedrini, C. Dujardin and P. Anfre. Properties of LuAP:Ce scintillator containing intentional impurities. *Nucl. Instrum. Methods Phys. Res. Sect. A* **2007**, *571* (1-2), 325-328.

[124] K. Kamada, T. Endo, K. Tsutsumi and A. Yoshikawa. Crystal growth and scintillation properties of Ce doped (Gd,Y)AlO_3 perovskite single crystals. *Phys. Status Solidi C* **2012**, *9* (12), 2263-2266.
[125] P. Lecoq, A. Annenkov, A. Gektin, M. Korzhik and C. Pedrini. Development of Ce^{3+}-doped lutetium-yttrium aluminum perovskite crystals for medical imaging applications. In *Inorganic scintillators for detector systems: Physical principles and crystal engineering*. Springer Berlin Heidelberg: The Netherlands, **2006**; pp 231-243.
[126] M. Nikl, A. Vedda and V. V. Laguta. Aluminum perovskite $XAlO_3$:Ce (X = Y, Lu, Y/Lu)-based scintillators. In *Springer Handbook of Crystal Growth* (Eds: G. Dhanaraj, K. Byrappa, V. Prasad and M. Dudley). Springer: Heidelberg, **2010**; pp 1673-1676.
[127] C. Pedrini, D. Bouttet, C. Dujardin, B. Moine, I. Dafinei, P. Lecoq, M. Koselja and K. Blazek. Fast fluorescence and scintillation of Pr-doped yttrium aluminum perovskite. *Opt. Mater.* **1994**, *3* (2), 81-88.
[128] M. Wisniewska, A. J. Wojtowicz, T. Lukasiewicz, Z. Frukacz, Z. Galazka and M. Malinowski. Radio- and VUV-excited luminescence of YAP:Ce, YAP:Pr and YAG:Pr. Proceedings of the International Conference on Solid State Crystals 2000: Growth, Characterization, and Applications of Single Crystals, ICSSC (Eds: A. Rogalski, K. Adamiec and P. Madejczyk). Zakopane, Poland, **2001**, vol. 4412, pp 351-356.
[129] M. Nikl, J. A. Mares, A. Vedda, M. Fasoli, V. Laguta, E. Mihokova, J. Pejchal, M. Zhuravleva, A. Yoshikawa and K. Nejezchleb. Can Pr-doped YAP scintillator perform better? *IEEE Trans. Nucl. Sci.* **2010**, *57* (3), 1168-1174.
[130] T. Yanagida, K. Kamada, Y. Fujimoto, M. Sugiyama, Y. Furuya, A. Yamaji, Y. Yokota and A. Yoshikawa. Growth and scintillation properties of Pr doped YAP with different Pr concentrations. *Nucl. Instr. Meth. Phys. Res. A* **2010**, *623* (3), 1020-1023.
[131] W. Drozdowski, P. Dorenbos, R. Drozdowska, A. J. J. Bos, N. R. J. Poolton, M. Tonelli and M. Alshourbagy. Effect of electron traps on scintillation of praseodymium activated $Lu_3Al_5O_{12}$. *IEEE Trans. Nucl. Sci.* **2009**, *56* (1), 320-327.
[132] A. J. Wojtowicz, J. Glodo, W. Drozdowski and K. R. Przegietka. Electron traps and scintillation mechanism in $YAlO_3$:Ce and $LuAlO_3$:Ce scintillators. *J. Lumin.* **1998**, *79* (4), 275-291.
[133] K. Takagi and T. Fukazawa. Cerium-activated Gd_2SiO_5 single crystal scintillator. *Appl. Phys. Lett.* **1983**, *42*, 43-45.
[134] C. L. Melcher and J. S. Schweitzer. A promising new scintillator: cerium-doped lutetium oxyorthosilicate. *Nucl. Instrum. Methods Phys. Res. Sect. A* **1992**, *314*, 212-214.
[135] H. Suzuki, T. A. Tombrello, C. L. Melcher and J. S. Schweitzer. UV and gamma-ray excited luminescence of cerium-doped rare-earth oxyorthosilicates. *Nucl. Instrum. Methods Phys. Res. Sect. A* **1992**, *320* (1-2), 263-272.
[136] G. B. Saha. PET scanning systems. Solid scintillation detectors in PET. In *Basics of PET imaging: Physics, chemistry, and regulations*. Springer: New York, NY, USA, **2010**; pp 20-24.
[137] Siemens Healthineers. LSO Crystal Technology. https://www.siemens-healthineers.com/en-us/medical-imaging/low-dose/low-dose-information-by-modality/low-dose-in-molecular-imaging/approaches-to-dose-reduction-in-molecular/pet-ct (accessed 16/07/2019).
[138] C. L. Melcher and J. S. Schweitzer. Cerium-doped lutetium oxyorthosilicate: a fast, efficient new scintillator. *IEEE Trans. Nucl. Sci.* **1992**, *39* (4), 502-505.
[139] O. Sidletskiy, A. Belsky, A. Gektin, S. Neicheva, D. Kurtsev, V. Kononets, C. Dujardin, K. Lebbou, O. Zelenskaya, V. Tarasov, K. Belikov and B. Grinyov. Structure−property correlations in a Ce-doped $(Lu,Gd)_2SiO_5$:Ce scintillator. *Cryst. Growth Des.* **2012**, *12* (9), 4411-4416.
[140] M. Kokubun, K. Abe, Y. Ezoe, Y. Fukazawa, S. Hong, H. Inoue, T. Itoh, T. Kamae, D. Kasama, M. Kawaharada, N. Kawano, K. Kawashima, S. Kawasoe, Y. Kobayaashi, J. Kotoku, M. Kouda, A. Kubota, G. M. Madejski, K. Makishima, T. Mitani, H. Miyasaka, R. Miyawaki, K. Mori, T. Murakami, M. M. Murashima, K. Nakazawa, H. Niko, M. Nomachi, M. Ohno, Y. Okada, K. Oonuki, G. Sato, M. Suzuki, H. Takahashi, I. Takahashi, T. Takahashi, K. Tamura, T. Tanaka, M. Tashiro, Y. Terada, S. Tomonaga, S. Watanabe, K. Yamaoka, T. Yanagida and D.

Yonetoku. Improvements of the Astro-E2 Hard X-ray Detector (HXD-II). *IEEE Trans. Nucl. Sci.* **2004**, *51* (5), 1991-1996.

[141] V. Jarý, E. Mihóková, J. A. Mareš, A. Beitlerová, D. Kurtsev, O. Sidletskiy and M. Nikl. Comparison of the scintillation and luminescence properties of the $(Lu_{1-x}Gd_x)_2SiO_5$:Ce single crystal scintillators. *J. Phys. D* **2014**, *47* (36), 365304.

[142] M. Kobayashi, M. Ieiri, K. Kondo, T. Miura and H. Noumi. Radiation hardness of cerium-doped gadolinium silicate Gd_2SiO_5:Ce against high-energy photons, fast and thermal-neutrons. *Nucl. Instrum. Methods Phys. Res. Sect. A* **1993**, *330* (1-2), 115-120.

[143] D. W. Cooke, K. J. McClellan, B. L. Bennett, J. M. Roper, M. T. Whittaker, R. E. Muenchausen and R. C. Sze. Crystal growth and optical characterization of cerium-doped $Lu_{1.8}Y_{0.2}SiO_5$. *J. Appl. Phys.* **2000**, *88* (12), 7360-7362.

[144] V. Jarý, M. Nikl, E. Mihóková, J. A. Mareš, P. Průša, P. Horodyský, W. Chewpraditkul and A. Beitlerová. Influence of yttrium content on the Ce1 and Ce2 luminescence characteristics in $(Lu_{1-x}Y_x)_2SiO_5$:Ce single crystals. *IEEE Trans. Nucl. Sci*. **2012**, *59* (5), 2079-2084.

[145] E. van der Kolk, S. A. Basun, G. F. Imbush and W. M. Yen. Temperature dependent spectroscopic studies of the electron delocalization dynamics of excited Ce ions in the wide band gap insulator, Lu_2SiO_5. *Appl. Phys. Lett.* **2003**, *83* (9), 1740-1742.

[146] G. B. Loutts, A. I. Zagumenni, S. V. Lavrishichev, Y. D. Zavartsev and P. A. Studenikin. Czochralski growth and characterization of $(Lu_{1-x}Gd_x)_2SiO_5$ single crystals for scintillators. *J. Cryst. Growth* **1997**, *174* (1-4), 331-336.

[147] T. Usui, S. Shimizu, N. Shimura, K. Kurashige, Y. Kurata, H. Ishibashi and H. Yamamoto. Improvement of scintillation properties and weakening of afterglow of $Lu_{2x}Gd_{2(1-x)}SiO_5$:Ce (LGSO, x=0.2) single crystals. *IEEE Nucl. Sci. Symp. Conf. Rec.* **2006**, *2*, 1166-1169.

[148] O. Sidletskiy, V. Bondar, B. Grinyov, D. Kurtsev, V. Baumer, K. Belikov, K. Katrunov, N. Starzhinsky, O. Tarasenko, V. Tarasov and O. Zelenskaya. Impact of Lu/Gd ratio and activator concentration on structure and scintillation properties of LGSO:Ce crystals. *J. Cryst. Growth* **2010**, *312* (4), 601-606.

[149] M. A. Spurrier, P. Szupryczynski, K. Yang, A. A. Carey and C. L. Melcher. Effects of Ca^{2+} co-doping on the scintillation properties of LSO:Ce. *IEEE Trans Nucl. Sci.* **2008**, *55* (3), 1178-1182.

[150] K. Yang, C. L. Melcher, P. D. Rack and L. A. Eriksson. Effects of calcium codoping on charge traps in LSO:Ce crystals. *IEEE Trans Nucl. Sci.* **2009**, *56* (5), 2960-2965.

[151] H. E. Rothfuss, C. L. Melcher, L. A. Eriksson and M. A. Spurrier Koschan. The effect of codoping on shallow traps in YSO:Ce scintillators. *IEEE Trans. Nucl. Sci.* **2009**, *56* (3), 958-961.

[152] S. Blahuta, A. Bessiere, B. Viana, P. Dorenbos and V. Ouspenski. Evidence and consequences of Ce^{4+} in LYSO:Ce,Ca and LYSO:Ce,Mg single crystals for medical imaging applications. *IEEE Trans. Nucl. Sci.* **2013**, *60* (4), 3134-3141.

[153] B. Chai. Method of enhancing performance of cerium doped lutetium orthosilicate crystals and crystals produced thereby. US Patent No. 7151261, **2006**.

[154] D. Ding, H. Feng, G. Ren, M. Nikl, L. Qin, S. Pan and F. Yang. Air atmosphere annealing effects on LSO:Ce crystal. *IEEE Trans. Nucl. Sci.* **2010**, *57* (3), 1272-1277.

[155] M. Nikl, A. Vedda and V. V. Laguta. Single-crystal scintillation materials. In *Springer Handbook of Crystal Growth* (Eds: G. Dhanaraj, K. Byrappa, V. Prasad and M. Dudley). Springer: Heidelberg, **2010**; pp 1663-1700.

[156] Y. Kurata, T. Usui, S. Shimizu, N. Shimura and H. Ishibashi. Emission properties of $Lu_{2x}Gd_{2(1-x)}SiO_5$ (LGSO, x=0.9) with Pr and Ce activators. *IEEE Nucl. Sci. Symp. Conf. Rec.* **2010**, 230-235.

[157] D. Pauwels, N. Le Masson, B. Viana, A. Kahn-Harari, E. V. D. van Loef, P. Dorenbos and C. W. E. van Eijk. A novel inorganic scintillator: $Lu_2Si_2O_7:Ce^{3+}$ (LPS). *IEEE Trans. Nucl. Sci.* **2000**, *47* (6), 1787-1790.

[158] L. Pidol, A. Kahn-Harari, B. Viana, E. Virey, B. Ferrand, P. Dorenbos, J. T. M. De Haas and C. W. E. van Eijk. High efficiency of lutetium silicate scintillators, Ce-doped LPS, and LYSO crystals. *IEEE Trans. Nucl. Sci.* **2004**, *51* (3), 1084-1087.

[159] A. J. J. Bos. Thermoluminescence as a research tool to investigate luminescence mechanisms. *Materials* **2017**, *10* (12), 1357.
[160] L. Pidol, A. Kahn-Harari, B. Viana, B. Ferrand, P. Dorenbos, J. T. M. De Haas, C. W. E. van Eijk and E. Virey. Scintillation properties of $Lu_2Si_2O_7$:Ce^{3+}, a fast and efficient scintillator crystal. *J. Phys. Condens. Matter* **2003**, *15* (12), 2091-2102.
[161] H. Feng, D. Ding, H. Li, S. Lu, S. Pan, X. Chen and G. Ren. Annealing effects on Czochralski grown $Lu_2Si_2O_7$:Ce^{3+} crystals under different atmospheres. *J. Appl. Phys.* **2008**, *103* (8), 083109.
[162] S. Kawamura, J. H. Kaneko, M. Higuchi, F. Fujita, A. Homma, J. Haruna, S. Saeki, K. Kurashige, H. Ishibashi and M. Furusaka. Investigation of Ce-doped $Gd_2Si_2O_7$ as a scintillator material. *Nucl. Instrum. Methods Phys. Res. Sect. A* **2007**, *583* (2-3), 356-359.
[163] N. A. Toropov, F. Ya. Glakhov and S. F. Konovalova. Silicates of the rare earth elements communication 2. Phase diagram of the binary system of gadolinium oxide silica. *Russ. Chem. Bull.* **1961**, *10*, 497-501.
[164] A. Yoshikawa, V. Chani and M. Nikl. Czochralski growth and properties of scintillating crystals. *Acta Phys. Pol. A* **2013**, *124* (2), 250-264.
[165] S. Kawamura, J. H. Kaneko, M. Higuchi, T. Yamaguchi, J. Haruna, Y. Yagi, K. Susa, F. Fujita, A. Homma, S. Nishiyama, H. Ishibashi, K. Kurashige and M. Furusaka. Floating zone growth and luminescence characteristics of cerium-doped gadolinium pyrosilicate single crystals. *IEEE Nucl. Sci. Symp. Conf. Rec.* **2006**, vol. 2, *54* (4), 1160-1163.
[166] A. Suzuki, S. Kurosawa, T. Shishido, J. Pejchal, Y. Yokota, Y. Futami and A. Yoshikawa. Fast and high-energy-resolution oxide scintillator: Ce-doped $(La,Gd)_2Si_2O_7$. *Appl. Phys. Express* **2012**, *5* (10), 102601.
[167] S. Kurosawa, T. Shishido, A. Suzuki, J. Pejchal, Y. Yokota and A. Yoshikawa. Performance of Ce-doped $(La,Gd)_2Si_2O_7$ scintillator with an avalanche photodiode. *Nucl. Instrum. Methods Phys. Res. Sect. A* **2014**, *744*, 30-34.
[168] V. Jarý, M. Nikl, S. Kurosawa, Y. Shoji, E. Mihóková, A. Beitlerová, G. P. Pazzi and A. Yoshikawa. Luminescence characteristics of the Ce^{3+}-doped pyrosilicates: the case of La-admixed $Gd_2Si_2O_7$ single crystals. *J. Phys. Chem. C* **2014**, *118* (46), 26521-26529.
[169] R. Murakami, S. Kurosawa, Y. Shoji, V. Jarý, Y. Ohashi, J. Pejchal, Y. Yokota, K. Kamada, M. Nikl and A. Yoshikawa. Scintillation properties of Zr co-doped Ce:$(Gd, La)_2Si_2O_7$ grown by the Czochralski process. *Radiat. Meas.* **2016**, *90*, 162-165.
[170] A. Lempicki, E. Berman, A. J. Wojtowicz, M. Balecerzyk and L. A. Boatner. Cerium-doped orthophosphates: new promising scintillators. *IEEE Trans. Nucl. Sci.* **1993**, *40* (4), 384-387.
[171] M. Makowski, M. E. Witkowski, W. Drozdowski, A. J. Wojtowicz, K. Wisniewski and L. A. Boatner. Luminescence and scintillation properties of XPO_4:Nd^{3+} (X = Y, Lu, Sc, La) crystals. *Opt. Mater.* **2018**, *79*, 273-278.
[172] D. Wisniewski, A. J. Wojtowicz, W. Drozdowski, J. M. Farmer and L. A. Boatner. $Rb_3Lu(PO_4)_2$:Ce and $Cs_3Lu(PO_4)_2$:Ce – new promising scintillator materials. *Cryst. Res. Technol.* **2003**, *38* (3-5), 275-282.
[173] G. Blasse and G. J. Dirksen. The luminescence of broad-band emitters in $LiLaP_4O_{12}$. *Phys. Status Solidi B* **1982**, *110* (2), 487-494.
[174] K. F. Suzart, A. B. Andrade, Z. S. Macedo and M. E. G. Valerio. Development of high efficient scintillator based on $LiLaP_4O_{12}$. *J. Lumin.* **2018**, *203*, 385-390.
[175] J. Zhong, H. Liang, H. Lin, B. Han, Q. Su and G. Zhang. Effects of crystal structure on the luminescence properties and energy transfer between Gd^{3+} and Ce^{3+} ions in $MGd(PO_3)_4$:Ce^{3+} (M = Li, Na, K, Cs). *J. Mater. Chem.* **2007**, *17*, 4679-4684.
[176] J. Zhong, H. Liang, Q. Su, J. Zhou, I. V. Khodyuk and P. Dorenbos. Radioluminescence properties of Ce^{3+}-activated $MGd(PO_3)_4$ (M = Li, Na, K, Cs). *Opt. Mater.* **2009**, *32* (32), 378-381.
[177] T. Shalapska, G. Stryganyuk, P. Demchenko, A. Voloshinovskii and P. Dorenbos. Luminescence properties of Ce^{3+}-doped $LiGdP_4O_{12}$ upon vacuum-ultraviolet and x-ray excitation. *J. Phys. Condens. Matter* **2009**, *21*, 445901.

[178] T. Shalapska, G. Stryganyuk, A. Gektin, P. Demchenko, A. Voloshinovskii and P. Dorenbos. Crystal structure and luminescence properties of $LiYP_4O_{12}:Ce^{3+}$ phosphor. *J. Phys. Condens. Matter* **2010**, *22* (48), 485503.
[179] Y. Kang, Y. Li, J. Zhang, S. Sun, Y. Huang, Y. Tao, H. Liang and Q. Su. VUV-UV luminescence of Ce^{3+}, Pr^{3+} doped and Ce^{3+}-Pr^{3+} codoped $NaLa(PO_3)_4$. *J. Lumin.* **2013**, *143*, 21-26.
[180] K. Horchani, J.C. Gâcon and C. Dujardin. Scintillation properties of $CsPrP_4O_{12}$ and $RbPrP_4O_{12}$. *Nucl. Instrum. Method. A* **2002**, *486*, 283-287.
[181] P. Lecoq, A. Annenkov, A. Gektin, M. Korzhik and C. Pedrini. Scintillation mechanisms in inorganic scintillators. In *Inorganic scintillators for detector systems: Physical principles and crystal engineering*. Springer Berlin Heidelberg: The Netherlands, **2006**; pp 81-95.
[182] C. Pédrini. Scintillation mechanisms and limiting factors on each step of relaxation of electronic excitations. *Fiz. Tverd. Tela* **2005**, *47* (8), 1359-1363. Also in *Phys. Solid State* **2005**, *47* (8), 1406-1411.
[183] A. J. Wojtowicz. Scintillation mechanism: the significance of variable valence and electron-lattice coupling in R.E.-activated scintillators. Proceedings of the International Conference on Inorganic Scintillators and Their Applications, SCINT (Eds: P. Dorenbos and C. W. E. van Eijk). Delft University Press: The Netherlands, **1995**, pp 95-102.
[184] M. Ueta, H. Kanzaki, K. Kobayashi, Y. Toyozawa and E. Hanamura. *Excitonic processes in solids.* Springer-Verlag Berlin Heidelberg: New York, NY, USA, **1986**.
[185] M. C. Pujol. Obtenció i caracterització de cristalls monoclínics de $KGd(WO_4)_2$ substituïts amb lantànids. Ph.D. Thesis, Rovira i Virgili University, **2001**.
[186] B. Henderson and G. F. Imbusch. Lanthanide rare-earth and actinide ions. In *Optical spectroscopy of inorganic solids.* Oxford University Press: New York, NY, USA, **1989**.
[187] D. J. Robbins and P. J. Dean. The effects of core structure on radiative and non-radiative recombinations at metal ion substituents in semiconductors and phosphors. *Adv. Phys.* **1978**, *27* (4), 499-532.
[188] A. J. Wojtowicz, A. Lempicki, D. Wisniewski and L. A. Boatner. Cerium-doped orthophosphate scintillators. Proceedings of the MRS Symposium P - Scintillator and phosphor materials. San Francisco, CA, USA, **1994**, vol. 348, pp 123-129.
[189] P. A. Rodnyi. Cerium-activated compounds. In *Physical processes in inorganic scintillators.* CRC Press: Boca Raton, FL, USA, **1997**; pp 152-154.
[190] C. Pédrini, D. Bouttet, C. Dujardin, A. Belsky and A. Vasil'ev. Energy transfer and quenching processes in cerium-doped scintillators. Proceedings of the International Conference on Inorganic Scintillators and Their Applications, SCINT (Eds: P. Dorenbos and C. W. E. van Eijk). Delft University Press, The Netherlands, **1995**, pp 103-110.
[191] A. Canning, A. Chaudhry, R. Boutchko and N. Grønbech-Jensen. First-principles study of luminescence in Ce-doped inorganic scintillators. *Phys. Rev. B* **2011**, *83*, 125115.
[192] D. Bouttet, C. Dujardin, C. Pédrini, W. Brunat, D. Tran Minh Duc and J. Y. Gesland. X-ray photoelectron spectroscopy of some scintillating materials. Proceedings of the International Conference on Inorganic Scintillators and Their Applications, SCINT (Eds: P. Dorenbos and C. W. E. van Eijk). Delft University Press, The Netherlands, **1995**, pp 111-113.
[193] P. A. Rodnyi. Nd- and Pr-activated crystals. In *Physical processes in inorganic scintillators.* CRC Press: Boca Raton, FL, USA, **1997**; pp 164.
[194] M.-T. Averbuch-Pouchot and A. Durif. Condensed phosphates. In *Topics in phosphate chemistry*. World Scientific: London, UK, **1996**, pp 31-37.
[195] A. Durif. Trivalent-monovalent cation polyphosphates. In *Crystal chemistry of condensed phosphates*. Plenum Press: New York, NY, USA, **1995**, pp 152-160.
[196] M.-T. Averbuch-Pouchot and A. Durif. *Topics in phosphate chemistry*. World Scientific: London, UK, **1996**.
[197] A. Durif. *Crystal chemistry of condensed phosphates*. Plenum Press: New York, NY, USA, **1995**.
[198] I. Parreu. Crystal growth and characterization of ytterbium or neodymium doped type III-$KGd(PO_3)_4$. A new bifunctional nonlinear and laser crystal. Ph.D. Thesis, Rovira i Virgili University, **2006**, pp 11.

[199] H. Y-P. Hong. Crystal structure of $NdLiP_4O_{12}$. *Mat. Res. Bull.* **1975**, *10*, 635-640.
[200] M. Boujelbene and T. Mhiri. Synthesis and crystal structure of $LiLaP_4O_{12}$. *X-Ray Struct. Anal. Online* **2011**, *27*, 21-22.
[201] I. Parreu, J. J. Carvajal, X. Solans, F. Díaz, and M. Aguiló. Crystal structure and optical characterization of pure and Nd-substituted type III $KGd(PO_3)_4$. *Chem. Mater.* **2006**, *18* (1), 221-228.
[202] W. Rekik, H. Naïli and T. Mhiri. Potassium gadolinium polyphosphate, $KGd(PO_3)_4$. *Acta Cryst.* **2004**, *C60*, i50-i52.
[203] H. Ettis, H. Naïli, and T. Mhiri. Synthesis and crystal structure of a new potassium-gadolinium cyclotetraphosphate, $KGdP_4O_{12}$. *Cryst. Growth Des.* **2003**, *3* (4), 599-602.
[204] K. Horchani-Naifer, A. Jouini and M. Férid. A monoclinic polymorph of $KY(PO_3)_4$. *Acta Crystallogr. Sect. E* **2008**, *E64*, i34.
[205] A. Jouini, M. Férid and M. Trabelsi-Ayadi. Equilibrium diagram of KPO_3–$Y(PO_3)_3$ system, chemical preparation and characterization of $KY(PO_3)_4$. *Thermochim. Acta* **2003**, *400*, 199-204.
[206] A. Hamady, T. Jouini and A. Driss. KYP_4O_{12}. *Acta Crystallogr. Sect. C* **1995**, *C51*, 1970-1972.
[207] I. Parreu, R. Solé, Jna. Gavaldà, J. Massons, F. Díaz and M. Aguiló. Crystal growth, structural characterization, and linear thermal evolution of $KGd(PO_3)_4$. *Chem. Mater.* **2005**, *17*, 822-828.
[208] I. Parreu, R. Solé, J. Massons, F. Díaz, and M. Aguiló. Crystal growth, crystal morphology and surface micromorphology of type III $KGd(PO_3)_4$ and $KNd(PO_3)_4$. *Cryst. Growth Des.* **2007**, *7* (3), 557-563.
[209] R. M. Solé, M. C. Pujol, J. Massons, M. Aguiló, F. Díaz and A. Brenier. Growth, anisotropic spectroscopy and laser operation of the monoclinic Nd:$KGd(PO_3)_4$ crystal. *J. Phys. D Appl. Phys.* **2015**, *48*, 495502-495512.
[210] I. Parreu, R. Solé, J. Massons, F. Díaz and M. Aguiló. Crystal growth and characterization of type III ytterbium-doped $KGd(PO_3)_4$: a new nonlinear laser host. *Chem. Mater.* **2007**, *19* (11), 2868-2876.
[211] R. D. Shannon. Revised effective ionic radii and systematic studies of interatomic distances in halides and chalcogenides. *Acta Cryst.* **1976**, *A32*, 751-767.
[212] M. Rzaigui, M. Dabbabi and N. Kbir-Ariguib. Etude des équilibres solide — Liquide du système pseudo binaire KPO_3 — CeP_3O_9. *J. Chim. Phys.* **1981**, *78* (6), 563-566.
[213] A. Oudahmane, M. Daoud, B. Tanouti, D. Avignant and D. Zambon. $KPr(PO_3)_4$. *Acta Cryst. Sect. E: Struct. Rep. Online* **2010**, *E66*, i59-i60.
[214] I. Parreu. Crystal growth and characterization of ytterbium or neodymium doped type III-$KGd(PO_3)_4$. A new bifunctional nonlinear and laser crystal. Ph.D. Thesis, Rovira i Virgili University, **2006**.
[215] Michael F. L'Annunziata. Appendix A - Table of radioactive isotopes. In *Handbook of radioactivity analysis* (Ed: Michael F. L'Annunziata). Third edition. Elsevier, **2012**; pp 1305-1360.
[216] M. Nikl. Scintillation detectors for x-rays. *Meas. Sci. Technol.* **2006**, *17*, R37-R54.

Chapter 2.

Methodologies and experimental characterization techniques

In this Chapter, the methodologies and all the experimental techniques used for the achievement of this Ph.D. Thesis are summarised. A brief description of each methodology and technique and their theoretical fundamentals are provided together with illustrations, schemes and photographs to help visualize the different methodologies and equipment. The experiments were performed at the laboratories of the FiCMA-FiCNA (*Física i Cristal·lografia de Materials i Nanomaterials)* research group of the *Universitat Rovira i Virgili* (URV, in Tarragona, Spain), at *Servei de Recursos Científics i Tècnics* (SRCiT) of the URV, at *Centres Científics i Tecnològics* of the *Universitat de Barcelona* (CCiTUB, in Barcelona, Spain), at Medcom Advance's laboratories (Tarragona, Spain), at SOLEIL Synchrotron (Saint-Aubin, France) and at ALBA Synchrotron (Cerdanyola del Vallès, Spain).

2.1. Crystal growth

The crystal growth method selected is a flux growth technique, which means that the components of the final desired material are dissolved in a solvent or flux, and the crystals grow below its melting temperature. This technique was chosen because $KGd(PO_3)_4$ (hereinafter, KGdP) melts incongruently (at 1142 K[1]), so that when the melting temperature is achieved these crystals decompose into another solid and a liquid with composition different from the one of the crystals. The selected method is based on preparing a homogeneous solution of the components which form the crystal in an appropriate solvent, afterwards determining the saturation temperature and finally programming a slow decrease of the solution temperature to maintain the solution supersaturated and thus allow the crystal growth. In our case, the solvent/flux used is an excess of K_2O and P_2O_5, which are components that constitute the final desired crystal (self-flux), so that this avoids the possible introduction of foreign ions of the solvent into the crystalline structure.

2.1.1. Determination of a crystallization region in a ternary system

Prior to the crystal growth from high temperature solutions and with the appropriate solvent chosen, it is necessary to determine the region of the phase diagram (binary, ternary, quaternary or high-order systems) where the primary crystallization of the desired phase takes place and the range of temperatures at which this phase is obtained. Moreover, in crystal growth, the knowledge of the physical properties of the solution, such as its density, superficial tension and viscosity, is of great importance.

In general, platinum crucibles of about 25 cm^3 are used to hold the solutions. First, around 15 g of solution are prepared by mixing the desired ratio of the precursor oxides and afterwards, the solution temperature is increased until the homogenization temperature of the solution is achieved. After several hours or days, the solution is homogeneous, and the next step is to decrease the temperature of the solution until observing the appearance of some small crystals on a platinum wire immersed in the solution. The crystals are identified by observing them at the microscope and by X-ray powder diffraction analyses. The saturation temperature of the solution is obtained by decreasing/increasing the temperature of the furnace to obtain neither

growth nor dissolution of the crystals. In solutions with high viscosity, the roughly determination of the saturation temperature can be made by throwing small crystals (millimetre size or lower) of the phase of which one wants to obtain the primary crystallization region, although they have some different element. When the small crystals maintain their size for several hours, a platinum disk is located in contact with the solution surface in a rotating movement around its own axis to mix the solution and contribute to the faster growth of the crystals as well as to act as a surface for the crystal growth. The crystal growth can be produced at constant temperature or by slow cooling by decreasing several degrees the temperature of the solution. When the crystals are relatively large, they are slowly extracted from the furnace.

The crystallization region of the phase to be obtained is determined after studying several tens of solution compositions, where this phase and the boundary phases of its crystallization region are obtained.

In Section 3.1, the growth conditions and cooling programs to determine the crystallization region of type B KYP_4O_{12} (space group: *C*2/*c*) and type IV $KY(PO_3)_4$ (space group: *P*2$_1$/*c*) (hereinafter, type B KYP and type IV KYP) in the K_2O–Y_2O_3–P_2O_5 ternary system are described. The experiments required to determine the KYP crystallization region were performed in vertical tubular furnaces as shown in Figure 2.1 and as explained in the next Section 2.1.2.

2.1.2. Bulk single crystal growth by Top Seeded Solution Growth-Slow Cooling technique

The Top Seeded Solution Growth (TSSG) technique is a flux growth technique commonly used to grow crystals from high temperature solutions. The initial components are melted in a crucible resulting in a homogeneous solution. In the particular case of the TSSG technique, the crystal growth is produced on a crystal seed that is in contact with the solution surface. In order to avoid secondary nucleation, the solution surface is the coldest zone of the solution. The solution temperature gradually increases until reaching the bottom of the crucible, which is the hottest zone. The growing crystal is completely submerged in the solution, which allows the crystal facets to grow freely. In Slow Cooling method, the solution is slowly cooled from its saturation temperature, which is determined by observing the dissolution or the growth of the crystal seed in contact with the solution surface. That is, the crystal growth begins when the solution becomes supersaturated and the crystal seed continues growing while the solution temperature steadily decreases. For the purpose of obtaining inclusion and macroscopic defect-free bulk single crystals of a few millimetres, a good convection flow is required in the solution because this determines the stability and shape of the crystal-solution interface[2,3]. The free convection flow, caused by the axial temperature gradient in the solution, is compensated by the forced convection flow generated by the seed/crystal rotation during the growth process. The direction of the rotation should be periodically reversed to avoid flux inhomogeneity or asymmetrical flow rates, especially in high viscous solutions[4]. Additionally, for viscous solutions, a platinum stirrer submerged in the solution can be used to mix it.

Figure 2.1 shows a scheme of the vertical tubular furnace that it has been used in the laboratories of the FiCMA-FICNA research group to grow the bulk single crystals of type III undoped KGdP, Ce:KGdP (see *Paper I*) and Pr:KGdP (see *Paper II*).

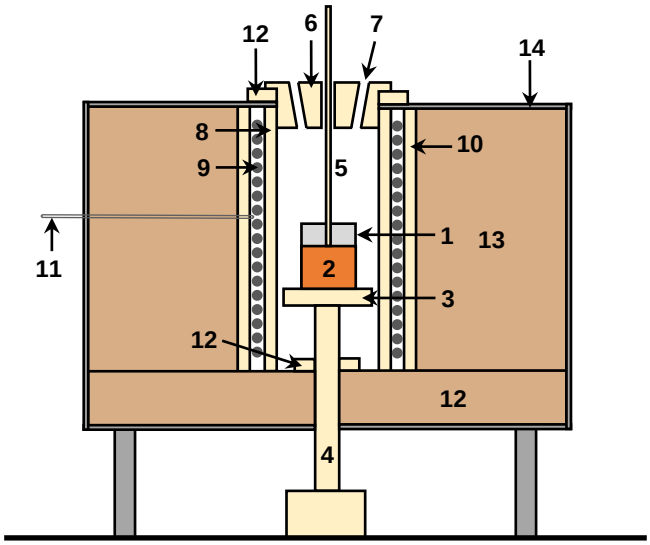

1. Platinum crucible
2. High temperature solution
3. Crucible base
4. Alumina tube
5. Alumina rod
6. Lid of the furnace
7. Holes to observe inside
8. Internal alumina tube
9. Resistance heating coil
10. External alumina tube
11. Thermocouple
12. Insulator bricks
13. Insulator bricks and synthetic glass wool
14. Steel cover

Figure 2.1. Scheme of the vertical section of the vertical tubular furnace used.

The furnace is heated by a Kanthal AF resistance-heating wire with a diameter of 1 mm (No. *9* in Figure 2.1) rolled into an alumina tube (No. *8*) and its power is controlled by a Eurotherm temperature programmer/controller connected to a thyristor. The temperature is measured with an S-type thermocouple Pt/Pt-Rh10% (No. *11*) placed near to the resistances in the central zone to guarantee a reliable and stable measurement. The whole system is thermally insulated using insulator bricks and synthetic glass wool (No. *12* and *13*) and finally covered by a steel cover (No. *14*). The crucible (No. *1*), which in our case is of platinum, is placed on an alumina base (No. *3*) supported by an alumina tube (No. *4*), which can be manually moved to situate the crucible in a suitable position inside the furnace. Before the crystal growth begins, the thermal axial gradient of the furnace as well as the thermal axial gradient of the growth solution must be determined to have proper thermal gradient values and also to ensure that the coldest zone of the solution is found at the top of the solution. The first determination gives an estimation of the best zone for the location of the platinum crucible inside the furnace and the second one allows an accurate measurement of the thermal gradient in the solution for the crystal growth. Given that the growth solution is very viscous[1], we used a rather high axial thermal gradient inside the growth solution as well as a platinum stirrer (Figure 2.2) submerged in the solution to guarantee the convection flow (see *Papers I* and *II*).

To subject, vertically displace and rotate the crystal seed, a mechanical part of the growth device is added above the furnace. This mechanical part is a vertical metal structure extremely rigid and stable from which an alumina rod (No. *5*) is attached. At

the end of this alumina rod, a holder equipped with a platinum stirrer, to increase the mass transport in the solution, and a seed holder are placed (Figure 2.2). To accurately measure the position of the seed crystal, which is crucial to determine the saturation temperature by observing the dissolution or the growth of the crystal seed in contact with the solution surface, a Mitutoyo micrometre is used with an accuracy of 0.01 mm. In our case, the material used for the crucible, stirrer and seed holder is platinum because its melting point is much higher than the crystallization temperature of our crystals, and its reactivity with the oxides used as starting materials is null. Depending on the diameter of the alumina tube of the furnace used to perform the growth experiments, conical or cylindrical platinum crucibles of different volumes were used to hold the solution.

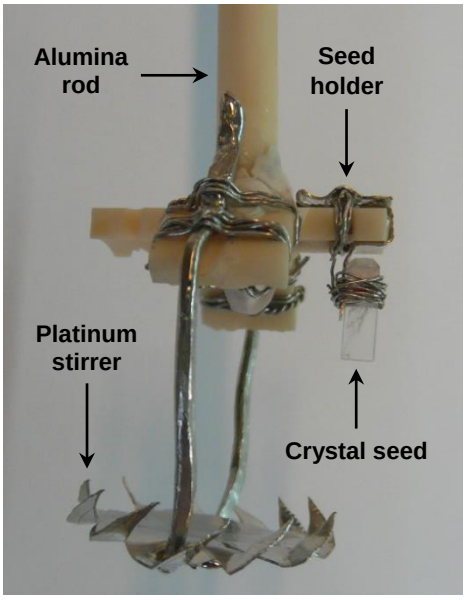

Figure 2.2. Alumina rod with a holder equipped with a platinum stirrer and a seed holder.

In our particular case of KGdP crystal growth, from the saturation temperature, a slow cooling ramp was programmed to a final temperature of 20-35 K below it. During the crystal growth process, the platinum stirrer and the crystal rotate at the same velocity (55 rpm) and with respect to the same axis, changing the sense of rotation every 50 s. The position of the stirrer with respect to the solution surface, the distance between the crystal seed and the central axis of the alumina rod as well as more details regarding the growth conditions and the cooling programs of Ce:KGdP and Pr:KGdP single crystals are described in Sections 3.2.1 and 3.3.1. When it was considered that the growth ramp was over, the crystal was slowly extracted from the solution, and thereafter slowly cooled to room temperature at 15-30 $K \cdot h^{-1}$ to avoid thermal shocks that could cause internal cracks.

2.2. Synthesis of nanocrystals by the Pechini method

Sol-gel methodologies are synthetic routes for preparing inorganic crystalline and amorphous powders, films, fibres as well as hybrid materials incorporating organic molecules at low temperature. The Pechini method is the selected synthetic route. This method yields inorganic powders of well-controlled stoichiometry, excellent phase purity, uniform morphology and fine particle size through the formation of a polymeric organic network between a metallic acid chelate and a polyhydroxide alcohol by polyesterification. Thus, this method allows a homogeneous mixing of the starting materials at the molecular level and the polymeric network maintains the homogeneity on the atomic scale as well as reduces any segregation of the cations.[5,6,7,8]

Pechini method is described in detail and in a generic way below.

1- Stoichiometric amounts of the metal oxide precursors are converted to the lanthanide nitrates by dissolution in concentrated HNO_3 (65 %) and heated at about 423 K under magnetic stirring until the liquid part has evaporated. At the same time, stoichiometric amounts of the other starting materials are dissolved in distilled water into another container and afterwards, the content of this second container is thrown inside the first container.

2- Citric acid, CA, is added as chelating agent in a specific molar ratio (C_M=[CA]/[METAL]) to prepare metal chelated citric acid, or in other words, metal-CA complexes. The metal cations are chelated by the carboxylate groups of CA, therefore, C_M describes the degree of the chelation process of the metal in the organic product[9]. In order to favour a good reaction between the metal cations and CA, the crucible is gently heated for several hours under magnetic stirring and covered with a crystallizer.

3- Ethylene glycol, EG, is added as esterification agent in a specific molar ratio (C_E=[CA]/[EG]) in order to obtain the polymeric resin. C_E describes the degree of esterification between the hydroxyl groups of EG and the carboxylic acid groups of CA[9]. The reagents are heated at about 473 K under magnetic stirring, since the esterification reaction is produced when the solution is heated. During this step, the viscosity of the product resin gradually increases until the resin gels[10], so, after a few hours the stirrer should be removed. This reaction is considered finished when a whitish gel is observed at the bottom of the crucible.

4- When the resin is sufficiently dry, an initial calcination at 573 K for several hours is performed to start its decomposition. Thereafter, a product of spongy texture of shiny black colour is obtained.

5- To end, this product is grinded in an agate mortar and the resulting precursor powder is calcined at higher temperatures and at air atmosphere for several hours to obtain the final product.

The described method has been used, with some differences, to obtain the nanocrystals of type III KGdP and Pr:KGdP included in this Thesis (see *Paper III*). In Section 4.1, the Pechini method is described in a specific way for these nanocrystals and a schematic illustration of the basic chemical reactions of the Pechini process is shown.

2.3. Sample preparation: orientation, cutting and polishing

When it comes to the characterization of anisotropic optical materials as type III KGdP bulk single crystals, the samples must be appropriately oriented and cut in order to evaluate each property as a function of the direction. Plates perpendicular to the crystallographic directions *a**, *b* and *c** have been prepared for structural and spectroscopic studies, and cubes perpendicular to the principal optical axes have also been prepared for spectroscopic studies.

The as-grown faces of the crystals are used as a reference to prepare the plates perpendicular to the *a**, *b* and *c** directions. To appropriately orientate and cut the cubes perpendicular to the principal optical axes N_p, N_m and N_g, it is necessary to find the orientation of the optical frame of the type III Ce:KGdP and Pr:KGdP crystals. As mentioned in Section 1.4.1, in KGdP, the crystallographic direction *b* coincides with the principal optical axis N_p due to its crystalline structure. Then, as the N_p, N_m and N_g are orthogonal by definition, the plane perpendicular to N_p contains the principal optical axes N_m and N_g, which are at the same time at 90º between them. That means that N_m and N_g are in *a*-*c* plane because it is normal to the crystallographic direction *b*. The angle between N_g and *c** was determined by using the setup shown in Figure 2.3, and the experimental value is found in Section 5.1.

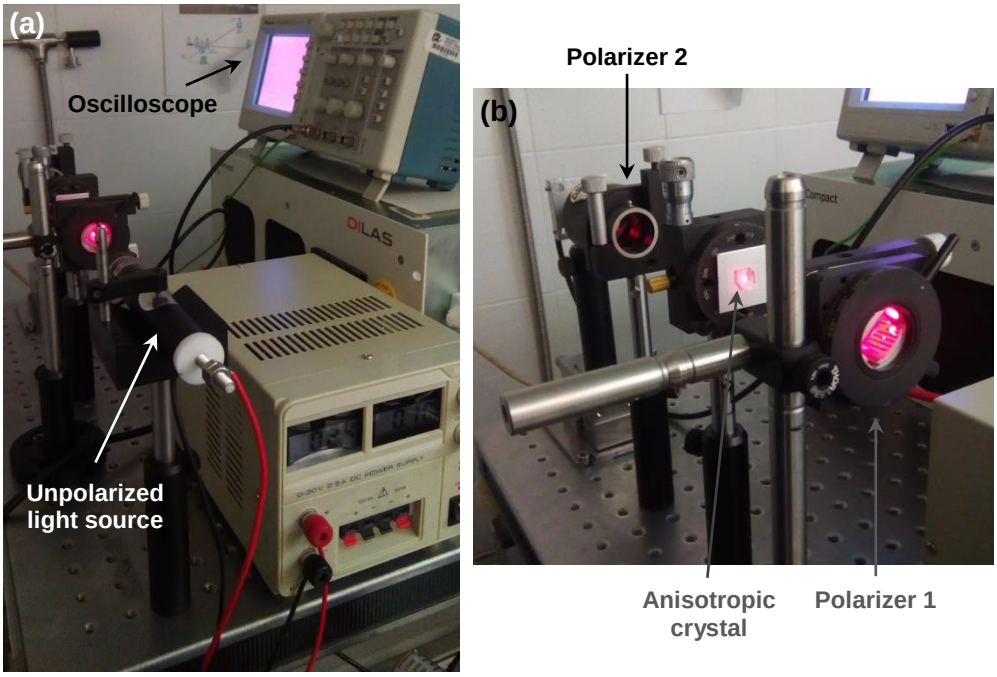

Figure 2.3. (a) General view of the setup used to determine the orientation of the optical frame of Ce:KGdP and Pr:KGdP crystals and (b) detail of the crossed polarizers and the crystal on the rotating support.

This experiment consists in the use of two crossed polarizers. Two polarizers placed one behind the other can eliminate all light which comes from an unpolarized light source if their polarization transmission directions are at 90º. However, in the general case, when an anisotropic crystal is located between the crossed polarizers, light is detected after the second polarizer since the crystal splits the light into two orthogonal components (N_g and N_m, in the case of a KGdP plate perpendicular to the *b* direction), which have different polarization directions than the one of the light which comes out of the first polarizer. This happens unless the incident beam to the crystal is polarized parallel to one of these two orthogonal components, since only this component will be transmitted and the second polarizer will also block the light. This is an extinction position and there will be another one when the crystal is rotated 90º because these components are orthogonal. From Figure 2.3, the unpolarized light source is a diode laser of λ=650 nm, the polarizers are Glan-Taylor and the doped KGdP crystal is a polished plate normal to *b* direction which is stuck to a rotating support with the 360º marked every 0.5º.

The cuts were made with a Model 15 diamond wire saw from Logitech. This saw allows us to avoid cleaving and fractures because it induces less mechanical stress than others like the diamond disk saw[11]. These crystals easily split up perpendicular to the *b* and *c** crystallographic directions because of cleavage planes[12]. Figure 2.4 shows the central zone of the diamond wire saw used while cutting an undoped KGdP crystal parallel to the (001) faces. The crystal is glued with wax on a glass sheet (optional) and a specific T-shaped sample holder for this saw. The holder is stuck in the desired position by turning the base, which is marked with 360º every 1º. The diamond wire is placed on the top of the crystal and then its rotation velocity and the load applied to the crystal during cutting are selected according to the nature of the sample. Since KGdP has cleavage planes perpendicular to the *b* crystallographic direction and parallel to the (001) faces, the selected wire rotation velocity was high and the load applied was as low as just to arch a little the wire, as shown in Figure 2.4, in order to induce as little mechanical stress as possible. To avoid overheating in the cutting area, the saw throws water in this area through a plastic tube.

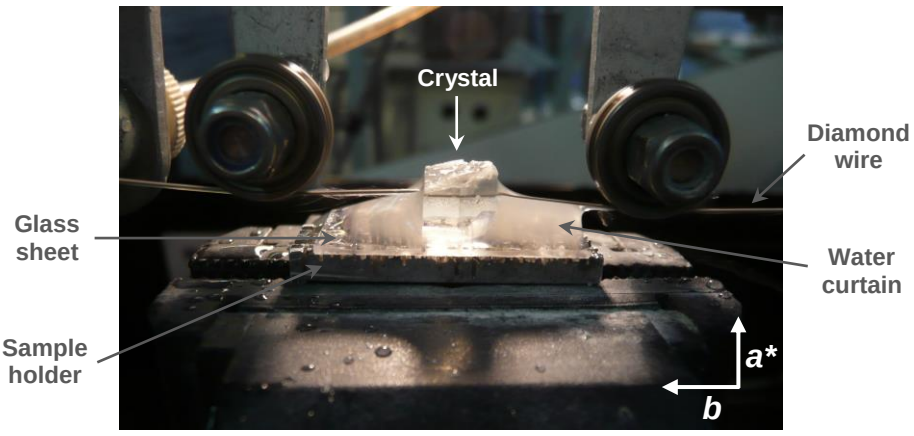

Figure 2.4. Cut parallel to the (001) faces of undoped KGdP using the Model 15 diamond wire saw from Logitech.

Once the slices were obtained by cutting the as-grown crystals, these slices were initially lapped with Al_2O_3 suspension with particle size of 9 μm and then 3 μm in a Logitech PM5 autopolisher machine (Figure 2.5). This equipment has an oscillatory arm that allows us to rotate and pressurise the samples according to their hardness. Later on, these slices were polished with colloidal suspension of amorphous silicon dioxide with a mean particle size of 0.2 μm (called SF1) in a Logitech PM5 polisher. During the lapping and polishing processes, the flatness of the plates was achieved with the flatness of the disk of the polisher, and the parallelism between the two faces of the plate was measured with an autocollimator every time the sample was removed from the polisher and observed in the microscope. The roughness of the sample depends on the particle size of the suspension used in the polishing process and an average roughness value can be obtained by a confocal microscope. Taking into account the considerable hardness of KGdP (around 7 in Moh's hardness scale[208]), the final polishing quality is very high, without any scratch due to polishing and with very low roughness.

The specific procedures carried out to cut, lap and polish each oriented plate and cube are described in Section 5.1.

Figure 2.5. Logitech PM5 autopolisher during the lapping process.

2.4. X-ray powder diffraction (XRPD) technique

X-rays are electromagnetic radiation that their wavelength is characterized by being in the range of 0.5–2.5 Å in the electromagnetic spectrum. The discovery of X-rays took place in 1895 by Wilhelm Conrad Röntgen. Several years later, in 1912, Max von Laue together with his co-workers discovered the property of diffraction when X-rays pass through the crystalline lattice, since the interatomic distance in solids is

of the order of magnitude of the wavelength of X-rays. In 1913, William Lawrence Bragg was the first to use the diffraction of X-rays by crystals to study matter. Since then, X-ray diffraction have allowed to obtain a deep knowledge of the crystalline structure of all crystalline solids in both monocrystalline and powder form and thus to establish detailed features of them, which are called X-ray single crystal diffraction (XRD) and X-ray powder diffraction (XRPD), respectively.[13]

W. L. Bragg showed that scattered radiation from a crystal behaves as if the diffracted beam was "reflected" from a plane passing through each individual atom periodically aligned in a way that resembles a reflecting mirror (Fig. 2.6). From such considerations, W. L. Bragg derived the following equation that receives the name of Bragg's law:

$$n\lambda = 2\, d_{hkl}\, sin(\theta_{hkl}) \qquad \text{Eq. 2.1}$$

where: n = integer number analogous to the order of diffraction from grating within the family of plans, and λ = wavelength of the incident radiation used. This wavelength depends on the X-ray tube that the diffractometer has. $n\lambda$ = path difference between waves scattered by adjacent lattice planes with equivalent indices, d_{hkl} = perpendicular spacing distance between two consecutive lattice planes, within of a family of crystallographic planes (hkl), and θ_{hkl} = angle that the incident X-ray beam forms with the planes (hkl) that diffract.[13]

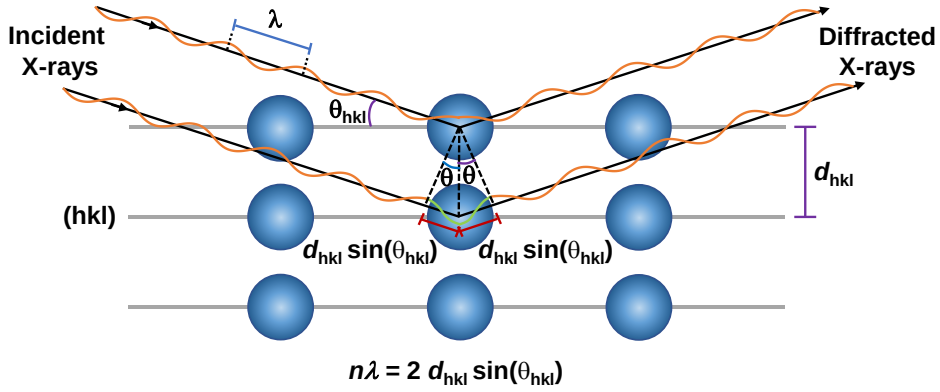

Figure 2.6. Schematic description of the diffraction of crystalline lattice planes according to W. L. Bragg.

Thus, Bragg's law explains the condition in which a monochromatized X-ray beam with an angle of incidence θ_{hkl} with respect to the family of planes (hkl) and a wavelength comparable to the atomic spacing produces constructive interferences.

In XRPD, as the sample is in crystalline powder form, many different orientations of tiny crystals are present simultaneously. Therefore, for any family of planes (hkl), Bragg's law will be fulfilled in some of the crystallites resulting in obtaining the complete diffraction pattern for any orientation of the crystalline powder with respect to

the incident X-ray beam. The diffraction pattern is characteristic for each substance, so that powder diffraction is an extremely powerful non-destructive tool for identifying crystalline phases and analysing mixtures both qualitatively and quantitatively. In addition, the diffraction pattern of a substance can be used to determine the unit cell parameters of the identified crystalline phase and to observe how they evolve as a function of temperature, pressure or dopant concentration by changing these parameters. XRPD is also used to study possible phase transitions with temperature or pressure. The diffraction pattern obtained of a given powder sample is compared with those compiled by the Joint Committee for Powder Diffraction Standards (JCPDS).[13]

We used a D5000 Siemens X-ray powder diffractometer available at SRCiT of the *Universitat Rovira i Virgili* to identify the crystalline phases obtained in the study on the primary crystallization region of type B and IV KYP, as well as those crystalline phases obtained in the experiments carried out to synthesize type III Pr:KGdP nanocrystals by the modified Pechini method. In addition, this diffractometer was used to investigate how the unit cell parameters of Ce:KGdP and Pr:KGdP single crystals evolve as a function of the doping concentration. This diffractometer is in vertical θ-θ configuration with the Bragg-Brentano geometry and is equipped with a Cu source as X-ray target and with a secondary graphite curved monochromator to eliminate the fluorescence from some samples and the Kβ radiation from the Cu source. In vertical θ-θ configuration, the sample is kept fixed in horizontal position in the centre of a vertical imaginary circumference, and the source and the detector are in the periphery of the circumference in an opposite position and rotate synchronously and symmetrically at the same angle θ with respect to the sample plane.

The same D5000 Siemens diffractometer was equipped with an Anton-Paar HTK10 temperature chamber with a platinum ribbon heating stage, which was used to study how the unit cell parameters of a KGdP crystal doped with praseodymium change as a function of temperature and thus determine its linear thermal expansion tensor. The sample is placed in the centre (occupying an area of ~9 × 5 mm^2) on the platinum ribbon that has a thermocouple welded in the opposite site. An electrical current passes through the platinum ribbon and the maximum resistance is located in the centre, where the sample is placed. This setup allows to analyse the sample with a variable temperature and program different heating and cooling rates. In the present experiments, the samples were analysed with the temperature chamber closed without applying vacuum nor inert gas on it.

The crystalline phases obtained were identified using the EVA software[14] and the unit cell parameters were refined using the TOPAS program[15] and the Le Bail method[16]. The crystal data for undoped type III KGdP studied by Parreu *et al.*[17] (171710 ICSD database) was used as powder diffraction standard.

We used a Bruker-AXS D8-Discover diffractometer available at SRCiT of the *Universitat Rovira i Virgili* to study the thermal stability of a KGdP crystal doped with praseodymium. This diffractometer is in vertical θ-θ configuration with the Bragg-Brentano geometry and is equipped with a Cu source, a parallel incident beam (Göbel mirror), a XYZ motorized stage and a HI-STAR GADDS (General Area Detector

Diffraction System). In addition, the diffractometer was equipped with a MRI BTS-Solid temperature chamber with a platinum ribbon heating stage. The sample is placed in the centre (occupying an area of ~1 × 1 mm^2) on the platinum ribbon that has a thermocouple welded in the opposite site. Then, an electrical current passes through the platinum ribbon and the maximum resistance is located in the centre. This stage was covered with a beryllium dome to maintain the temperature.

The measurement parameters used in each case mentioned above, such as the 2θ diffraction range, step size, step time, temperature and others, are detailed in *Papers I*, *II* and *III*.

2.5. Electron probe microanalysis (EPMA)

Electron probe microanalysis (EPMA) is a technique used to non-destructively determine the chemical composition of small regions of solid materials with detection limits of about 100 ppm in routine analyses. EPMA uses a fine and focused electron beam to bombard the sample and produce characteristic X-rays for each element. When an electron from the electron beam impinges on the sample, this one can knock out an electron of an outer state or inner state of the atom, leaving a vacancy. In the case of the vacant state is in an inner state, the amount of energy can be released by the emission of a characteristic X-ray or the ejection of a characteristic Auger electron. In the first case, an outer electron jumps into the inner shell vacancy resulting in the emission of a photon that corresponds to the energy difference between the two excited states, being specific X-rays for each atomic species. The nomenclature used to provide information about the location of the electron that has been knock out is K for 1*s* orbitals, L for 2*s* and 2*p* orbitals, M for 3*s*, 3*p* and 3*d* orbitals, N for 4*s*, 4*p*, 4*d* and 4*f* orbitals, and so on. The letter is complemented with the symbols α, β and γ to inform about the provenance of the electron that has filled the inner shell vacancy. An interesting scheme about some of the more common transitions between K, L, M and N shells of an atom with the corresponding X-ray lines mentioned are shown in ref.[18]. Since the energy required to knock out an electron from the K-shell increases as the atomic number (Z) is higher, it is convenient to use the K lines for elements with an atomic number until Z=49, the L lines for elements heavier than tin (Z=50) and the M lines for very heavy elements.[19,20]

The X-rays generated by the sample can be detected using an energy dispersive spectrometer (EDS) or a wavelength dispersive spectrometer (WDS), which are the main methods used. The detector of the EDS system normally consists of a small piece of a few mm of semiconducting silicon or germanium. Each X-ray coming from the sample excites a number of electrons into the conduction band of the semiconductor leaving exactly the same number of holes in the outer electron shells. The number of electron−hole pairs generated is proportional to the energy of the X-ray photon that is detected, since the energy required for each of these excitations is a known value (3.8 eV in the case of the silicon). Thus, a voltage is applied across the semiconductor and the magnitude of the current generated as each X-ray is absorbed in the detector is exactly proportional to the energy of the X-ray. On the other hand,

the WDS detection system consists of a dispersive/diffracting crystal and an X-ray detector which are located in such way that X-rays that impinge on the dispersive crystal are diffracted according the Bragg's law and therefore only a wavelength reduced range is recorded by the detector. Figure 2.7 shows a schematic diagram of an EPMA operating in WDS mode. The most commonly used dispersive crystals are: lithium fluoride 200 (LIF), pentaerythritol 002 (PET), thallium acid phthalate 1011 (TAP) and W/Si multilayered pseudo-crystal (PC0, PC1, PC2 and PC3).[20]

Comparing these two methods, the EDS detection system is able to collect X-rays of all energies at the same time and very efficiently, while the WDS detection system can determine highly accurately the energy (or wavelength) of a single X-ray line, resolve closely spaced lines and measure the height (intensity) of a peak above the background level. Thus, the EDS is better suited to rapid qualitative analysis and the WDS provides more accurate quantitative results.[20]

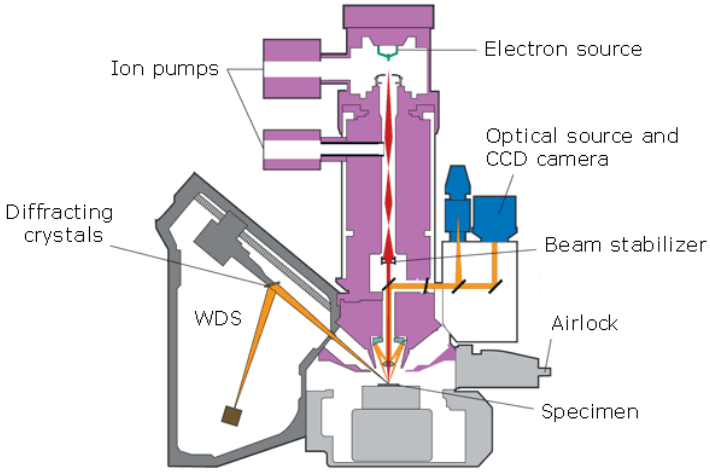

Figure 2.7. Schematic diagram of an EPMA operating in WDS mode[21].

The chemical composition of the samples is determined by comparing the X-ray intensity of standard samples of known concentrations with those of the test sample and by correcting the effects of the atomic number (Z), absorption (A) and fluorescence (F) in the test sample using the ZAF technique. The atomic number effect makes reference to the efficiency with which an element generates X-rays. The second effect refers to the absorption of some of the X-rays generated by the sample due to the considerable distance that these travel through the sample, resulting in a reduction of their intensity. The fluorescence, or also called secondary fluorescence, occurs when the X-ray radiation generated by the sample after being bombarded with the electron beam produces a second generation of X-rays. This happens when the energy of a characteristic X-ray line of an element is higher than the absorption edge energy of another element present in the sample, leading to an increase of the intensity of the characteristic X-ray of the second element. So, the fluorescence effect must be considered in samples containing several elements, not in a pure elemental standard.[20,22]

We used a JEOL JXA-8230 electron microprobe analyzer operating in the wave-length dispersive mode (WDS) to determine the chemical composition of Ce:KGdP single crystals, Pr:KGdP single crystals and Pr:KGdP nanocrystals, especially their dopant concentrations. This equipment is available at *Centres Científics i Tecnològics* of the *Universitat de Barcelona* (CCiTUB). The measurement conditions used in EPMA analysis for the grown single crystals are summarized in Table 2.1. For the nanocrystals, the measurement conditions used were the same as those shown in Table 2.1, less the peak measurement time and the background measurement time for Pr, which were 60 s and 30 s, respectively.

Table 2.1. Measurement conditions used in EPMA analysis for the single crystals.

Element	Line	Dispersive crystal		Standard	Peak meas. time [s]	Background meas. time [s]
K	Kα	PETJ	PETJ	KGdP	10	5
Gd	Lα	LIFH	LIFL	KGdP	10	5
P	Kα	PETL	PETH	KGdP	10	5
Ce	Lα	PETL	-	CeO_2	120	60
Pr	Lα	-	LIFL	REE-1	100	50
O	Kα	LDE1	LDE1	KGdP	10	5

PET: pentaerythritol, J/L/H refers to the sample size (J: normal, L: large, H: huge), LIF: lithium fluoride, LDE1 (layered dispersion element): W/Si multilayer 60 Å thick per layer, REE-1: Si-Al-Ca based glass containing Y, Pr, Dy and Er at 4 wt. % of each lanthanide.

For the single crystals, the accelerating voltage and current intensity were of 20 kV and 20 nA, respectively; and for the nanocrystals were of 15 kV and 15 nA. High accelerating voltages improve the peak/background ratio, although it can introduce a significant secondary fluorescence. It is important to keep the same measurement conditions for all the concentrations of a dopant because the secondary fluorescence varies depending on the amount of the doping element in the sample[22], therefore, it is necessary to keep the other parameters fixed.

The experimental error (ε) for each element analysed can be determined by using the following expression:

$$\varepsilon = \sqrt{\frac{\frac{I_p}{t_p}+\frac{I_b}{t_b}}{(I_p-I_b)^2}+\frac{\frac{I_p^S}{t_p^S}+\frac{I_b^S}{t_b^S}}{(I_p^S-I_b^S)^2}} \times 100 \qquad \text{Eq. 2.2}$$

where: I_p and I_b are the intensities of the peak of the sample and the background in counts per second (c/s), respectively, t_p and t_b are the integration times of the peak of the sample and the background in seconds, and I^s_p, I^s_b, t^s_p and t^s_b are the same as the above terms but for the standard sample.

The detection limit (*DL*) for each element can be calculated using the Equation 2.3, where C^s is the concentration of the element in the standard sample (wt. %).

$$DL = \left[\frac{C^s}{(I_p^s-I_b^s)}\right] 3\sqrt{2}\left(\frac{I_b}{t_b}\right)^{1/2} \qquad \text{Eq. 2.3}$$

To prepare the sample for EPMA measurements, a small piece of macrodefect-free crystal is put in a plastic cylindrical container with the biggest face of the crystal on the bottom of the container and included in a polyester resin with a few drops of its corresponding catalyst. This mixture is completely solidified after about 12 hours and then it is extracted from the plastic container. Initially, the solid sample is planed with a SiC disk and with distilled water as refrigerant. It is then polished with a diamond grinding pad and an abrasive liquid of monocrystalline diamond suspension of 3 μm, and afterwards with an abrasive liquid of 1 μm. Finally, the sample is cleaned with alcohol. This preparation is carried out by using a Struers DAP-7 polisher available at the Growth Laboratory of the FiCMA-FiCNA research group. Before the measurement, the sample is coated with a thin layer of carbon, in the same way as the standards.

2.6. Microscopy techniques

In this Section, we describe the microscopy techniques used to observe the crystal habit of the grown crystals during the determination of the crystallization region of type B and IV KYP in the K_2O–Y_2O_3–P_2O_5 ternary system, as well as to visualize the topography of the Pr:KGdP nanocrystals and determine its particle size distribution.

2.6.1. Reflection optical microscopy

Reflection optical microscopy is a non-destructive technique which is based on the incidence of the visible light of the illumination system on the sample surface and the simultaneous visualization of the sample through the objective. This concrete configuration of the incident and reflected beams allows obtaining the reflected image very illuminated and without any shadows, making easy the observation of the details of the sample surface.

We used an Olympus SZ stereo microscope available at the Growth Laboratory of the FiCMA-FiCNA research group. The power of each eyepiece is 10X and the pancratic magnification (variable magnifying power) is from 0.7 to 4X, so the total magnification of this microscope is from 7 to 40X. It provides the visualization of the crystal habit of the grown crystals during the determination of the crystallization region of type B and IV KYP in an immediate way, since no sample preparation is needed.

2.6.2. Scanning electron microscopy (SEM) and Environmental SEM (ESEM)

The scanning electron microscopy (SEM) is a technique of electron microscopy capable of producing high-resolution images of the surface of a specimen by scanning its surface with a fine focused beam of electrons. A schematic diagram of the SEM equipment is shown in Figure 2.8. The electron beam is first generated and then collimated in a collimator column with an accelerating voltage usually between 1 and 30 kV (typically the maximum value). The electron beam reaches the specimen with a focal spot size very fine due to the use of magnetic lenses and the so-called objective lens above the specimen. This spot size determines the resolution of the image since the electron beam scans the specimen surface. The resolution power of

a modern SEM equipment is typically between 1 nm and 10 nm, therefore close spaced features can be distinguished and examined at a high magnification. This instrument provides magnifications between 20 and 300 000. There must be high vacuum within the column in order to enable a high voltage to be used to accelerate the electrons and thus allow the focusing of electrons without scattering because of the gas molecules that electrons find in their path.[23,24]

When the electron beam impinges on the specimen, the interaction of the electrons with the specimen results in the generation of secondary electrons, backscattered electrons, characteristic X-rays and other phenomena. The secondary electrons and backscattered electrons are used to obtain SEM images. Hence, this technique uses the interaction of the primary electron beam with the specimen to provide information about its nature (its atomic number, chemical and crystallographic characteristics, topography, elemental distribution, etc.). The most commonly used are the secondary electrons generated by the primary electron beam because it carries information about the topography of the specific zone where the beam is impinging. As the secondary electrons have low energy (<50 eV), only the secondary electrons which come from the outer layers of the specimen are detected and collected by a detector located on one side, as shown in Figure 2.8. The backscattered electrons are primary electrons that have been ejected from the specimen by scattering through it at an angle higher than 90º. They are useful for determining the composition of the specimen since provide information about the atomic number of the elements of each specific zone. The backscattered electrons are collected by a detector located above the specimen, as shown in Figure 2.8. Finally, all this information is converted into a signal that is then displayed on a screen as an image where each specific feature of the specimen appears with a concrete colour within the grey scale, from white to black, depending on the nature.[24]

Specimens must be conductive to use this technique. For this reason, the nonconductive specimens are coated with a thin film of a conductor such as carbon or gold.

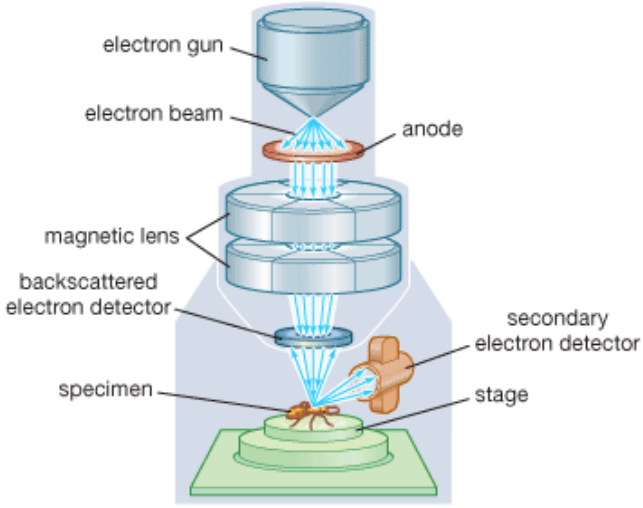

Figure 2.8. Schematic diagram of a SEM equipment[25].

We used a JEOL JSM-6400 electron microscope to visualize the topography of Pr: KGdP nanocrystals. The specimens were coated with gold using a Bal-Tec SCD004 sputter coating. Both apparatus are available at SRCiT of the *Universitat Rovira i Virgili*.

As indicated above, the specimens must be conductive to use the SEM technique. The reason is to prevent that the sample surface is charged because these electrons repel the electrons from the incoming beam, causing drift, blur and low contrast that produce blurry and/or false images[26].

To overcome the specimen-charging problem, the SEM technique uses high vacuum within the column. However, there is an alternative that consists in surrounding the specimen with a gaseous ambient, used in a variant of the technique: environmental scanning electron microscopy (ESEM). The beam electrons ionize the gas molecules before reaching the specimen; then, if the specimen is negatively charged, the positive ions from the gas molecules are attracted toward it, neutralizing the surface charge. The gas surrounding the specimen is often water vapor, so the ESEM equipment allows the wet specimens to be examined without dehydration. Besides, it also allows examining oily, dirty and nonconductive specimens without previous preparation. In the case of nonconductive specimens, ESEM eliminates the constraint to coat them with a conductor, so that the specimens preserve their original characteristics for determining their composition or for further studies. In addition, as ESEM removes the high vacuum constraint on the sample environment, the pressure, temperature and gas composition can be varied.[24]

We used a FEI QUANTA 600 environmental scanning electron microscope combined with an EDX detector system available at SRCiT of the *Universitat Rovira i Virgili*. The EDX detector system (also called EDS, EDXS or XEDS) is explained in Section 2.5. Accordingly, the ESEM-EDX combined system was used to obtain images and visualize the crystal habit of the grown crystals during the determination of the primary crystallization region of type B and IV KYP when this was not possible by reflection optical microscopy due to their small size, and also to carry out an elemental analysis of some grown crystals to determine roughly their chemical composition when this was impossible by X-ray powder diffraction analysis due to the low amount of crystals.

2.6.3. Transmission electron microscopy (TEM)

Transmission electron microscopy (TEM) is an electron microscopy-based technique in which an electron beam with an accelerating voltage between 100 kV and 300 kV is transmitted through an ultrafine specimen to form an image by means of the transmitted electrons. A schematic diagram of the TEM equipment is shown in Figure 2.9. The high voltage results in the increase of the imaging resolution because the electron wavelength decreases. A modern TEM equipment has a resolution power of ~0.2 nm, so it is even possible to image individual atoms.[23]

The electrons emitted from a cathode are accelerated by means of an electric field parallel to the optic axis. This field is generated by applying a potential difference between the cathode and an anode, which is a round metal plate containing a central

hole, as shown in Figure 2.9. The electrons are focused and directed towards the specimen, under high vacuum conditions, by means of magnetic condenser lenses. Then, those electrons that cross the specimen pass through some lenses (in order: objective lens, intermediate lens, and projector lens) and finally impact on a fluorescent screen (of diameter typically 15 cm), which is used to convert the electron image to a visible form. Therefore, the TEM image is formed from the interaction of the primary electrons with the specimen. This image is flat, monochromatic (in grey scale, from white to black) and typically with a magnification in the range 10^3 to 10^6.[27,28]

The requirement for using TEM is that the specimen must always be circular with a diameter of 3 mm and have an ultrathin section of a few nanometres thick, or must be a suspension on a grid.

We used a JEOL JEM-1011 electron microscope with a MegaView III Soft Imaging System from the SRCiT of the *Universitat Rovira i Virgili* to determine the particle size distribution of Pr:KGdP nanocrystals. The software used to evaluate the size of the particles was iTEM 5.1 software package, from Olympus Soft Imaging Solutions GmbH. To prepare the sample, the nanocrystals were dispersed in ethanol solution and then a drop was deposited on a copper grid.

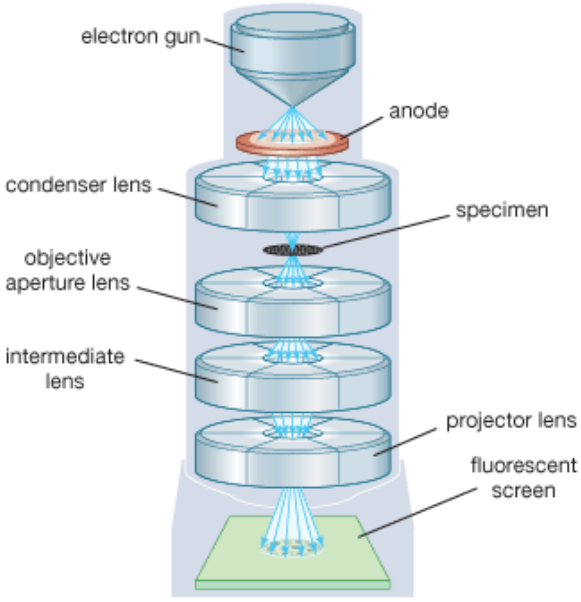

Figure 2.9. Schematic diagram of a TEM equipment[29].

2.7. Differential thermal analysis (DTA) and thermogravimetric analysis (TGA)

Differential thermal analysis (DTA) is a technique in which the substance under study and a reference material are made to undergo identical heating and cooling ramps in a controlled way, while any temperature difference between the substance and the reference is recorded. The reference material must be inert in the studied tempera-

ture range, given that when a substance is heated or cooled, its chemical composition and structure can undergo changes such as melting, crystallization, decomposition, reaction, oxidation and phase transition. Then, when the substance under study absorbs heat (endothermic process), its temperature is lower than that of the reference material. On the contrary, when the substance releases heat (exothermic process), its temperature is higher than that of the reference. Therefore, this can be expressed as peaks of phase changes.

Thermogravimetric analysis (TGA) is a technique used to determine the weight gain or loss of a substance as a function of temperature in a controlled way and under a controlled atmosphere. This technique provides information about the purity of the sample as well as its content of water, carbonate and organic part.

The DTA-TGA system combines the previous two techniques allowing the simultaneous measurement of the heat exchanges and the gain or loss of mass of a sample compared to a reference material. This combined system leads valuable information in recognising the chemical or physical change that the substance has suffered, since it is possible to differentiate between exothermic transitions with weight change (e.g. decomposition with loss of water, carbonate and/or organic part) and without weight change (e.g. crystallization), and the same goes for endothermic transitions.

We used a TA Instruments SDT 2960 simultaneous DSC-TGA available at FiCMA-FiCNA's laboratories in the combined DTA-TGA system to exactly determine the temperatures at which there are temperature exchanges and changes in weight in a grinded Pr:KGdP crystal with the aim to complement the study on thermal stability obtained from XRPD technique. Besides, this equipment was also used to analyse the Pr:KGdP nanocrystals with different doping content. Al_2O_3 was used as the inert reference material, and the heating and cooling rates were at 10 $K \cdot min^{-1}$ with an air flux of 90 $cm^3 \cdot min^{-1}$.

2.8. Spectroscopic techniques

In this Section, we describe the fundamentals of the spectroscopic techniques used to optically characterize the Ce:KGdP and Pr:KGdP bulk single crystals grown by the Top Seeded Solution Growth-Slow Cooling (TSSG-SC) technique, and the Pr:KGdP nanocrystals synthesized by the modified Pechini method.

2.8.1. Optical absorption and transmission

Optical absorption is the fraction of incident electromagnetic radiation in a material which is absorbed by the material depending on the wavelength. The energy of the incident photons is absorbed by the electrons present in atoms or molecules of a material resulting in an electronic transition to a state of higher energy. Transmission is the complementary process to the absorption since it is the fraction of incident radiation that is not absorbed by the material but is transmitted.

The Beer-Lambert law (Eq. 2.4) is a basic law in the process of light absorption that is based on an empirical relationship that relates the absorption of light to the properties of the material through which the light is traveling.

$$I = I_0 e^{-\alpha d} \quad \text{Eq. 2.4}$$

where: I_0 is the intensity of the incident electromagnetic radiation to the sample (counts, c), α is the absorption coefficient of the sample (cm^{-1}), d is the thickness of the sample (cm) and I is the intensity of the radiation at the output of the sample (c).

In order to obtain the absorption coefficient of the sample, we experimentally measure the optical density (*OD*) using a double ray spectrophotometer:

$$OD = -\log(I/I_0) = \log(I_0/I) \quad \text{Eq. 2.5}$$

Afterwards, by combining the Equations 2.4 and 2.5, we can correlate the optical density (*OD*) with the absorption coefficient (α) resulting in the following expression:

$$\alpha = OD\left(\frac{1}{d\ loge}\right) \quad \text{Eq. 2.6}$$

We can correlate α with the absorption cross section (σ) of every absorbing atom or ion present in the sample by the Equation 2.7, where N is the density of absorbent centres, which are Ce^{3+}, Pr^{3+} and Gd^{3+} ions in the framework of this Thesis. Considering that α is given in cm^{-1} and N in atoms·cm^{-3}, the units of σ are atoms·cm^{-2} or simply cm^{-2}.

$$\sigma = \frac{\alpha}{N} \quad \text{Eq. 2.7}$$

The optical absorption and transmission were measured at FiCMA-FiCNA research group using a double ray spectrophotometer, an Agilent Cary 5000 UV-Vis-NIR spectrophotometer. It measures an effective spectral range from 175 to 3300 nm with a limiting spectral resolution of <0.05 nm in the UV-Vis range and of <0.2 nm in the NIR range. The UV light source is a deuterium flash lamp and the Vis-IR light source a quartz halogen lamp. The UV-Vis light is detected by a silicon photodetector and the IR light is detected by a lead sulphide detector called PbSmart.

The unpolarized optical absorption of undoped KGdP, Ce:KGdP and Pr:KGdP polished plates were studied at room temperature to identify the absorption bands of Gd^{3+}, Ce^{3+} and Pr^{3+} in the spectral range from 190 to 2475 nm as well as to observe whether there was a change in their optical absorption after exciting them with X-rays radiation (see Section 2.8.4). The unpolarized transmittance spectrum of Pr:KGdP nanocrystals at room temperature was measured from 200 to 500 nm by using a Hellma Analytics QS UV cell (highly purified synthetic quartz) to contain the nanocrystals suspended in distilled water. To obtain the polarized optical absorption at room temperature, a Glan-Taylor polarizer was situated before the sample. For measurements at 6 K, we used this spectrophotometer with a helium closed circuit by Leybold consisting of a Combivac IT23 vacuum gauge, Turbotronik NT10 turbo

pump controller, RDK 6-320 cryostat, a LTC 60 temperature controller and Coolpak 6000 compressor unit. The polarized optical absorption both at room temperature and at 6 K of Pr:KGdP plates were measured to study the $4f \rightarrow 4f$ electronic transitions of Pr^{3+} as a function of light polarization for possible future lasing applications.

2.8.2. Luminescence and decay time measurements under visible excitation

Luminescence, or optical emission, is the result of a radiative transition of an electron from an excited state or higher energy level to a lower energy level. When the light emission is produced after the excitation of an electron by part of a photon, the process is called photoluminescence. Hence, the luminescence spectra are measured by keeping the excitation wavelength fixed and changing the detection wavelength.

The decay time measurements consist in determining the temporal evolution of the luminescence after excitation by recording the luminescence intensity of a specific emission peak over time. The luminescence intensity usually declines exponentially. An important parameter called lifetime (τ) can be extracted from the decay time curve, which is the time at which the luminescence intensity has decreased to 1/e of its initial value. This parameter characterizes how an electronic level is depopulated and what the thermalisation mechanisms of this excitation are. To determine the lifetime, a pulsed excitation source is needed. In addition, it is also needed that the pulse duration must be shorter and the interpulse duration longer than the mean lifetime of the electronic level of the ion we are studying in a specific material.

The luminescence and decay time curves by exciting in the visible were measured using an Agilent Cary Eclipse fluorescence spectrophotometer, available at Medcom Advance's laboratories (Tarragona, Spain). It incorporates a xenon flash lamp with a pulse frequency of 80 Hz, pulse width at half peak height of ~2 μs and peak power equivalent to 75 kW. It measures an effective emission wavelength range from 190 to 1100 nm due to high performance R928 photomultiplier detectors. Unpolarized and polarized luminescence spectra of Pr:KGdP single crystals were investigated at room temperature and under visible light excitation to study the emission of these samples through the $4f \rightarrow 4f$ electronic transitions of Pr^{3+} and find out whether there is an anisotropic behaviour in the optical emission. The long component of the luminescence decay curves of the $5d \rightarrow 4f$ transitions of Ce^{3+}, as well as the luminescence decay curves of the $4f \rightarrow 4f$ transitions of Pr^{3+} and Gd^{3+}, were studied in the Ce:KGdP and Pr:KGdP single crystals by the same fluorimeter. Unpolarized luminescence spectra of Pr:KGdP nanocrystals were studied at room temperature and under visible light excitation by using a Hellma Analytics QS UV cell (highly purified synthetic quartz) to contain the nanocrystals suspended in ethylene glycol.

2.8.3. Luminescence and decay time measurements under VUV-UV excitation – SOLEIL Synchrotron

The explanation of the theoretical basis about luminescence and decay time measurements is at the beginning of Section 2.8.2. The luminescence and decay time curves of Ce:KGdP and Pr:KGdP polished single crystalline plates under vacuum

ultraviolet-ultraviolet (VUV-UV) excitation were carried out at room temperature in the DESIRS beamline at SOLEIL Synchrotron (Saint-Aubin, France). The aims were to study the luminescence of these samples under direct $4f \rightarrow 5d$ excitation of Ce^{3+} and of Pr^{3+}, and observe the fast component of the decay time curves of their 5*d* levels.

Synchrotron is a particle accelerator with a fixed closed-loop path. More broadly, synchrotron is a facility used to produce, accelerate, confine and maintain a high-energy electron (or positron) beam in a closed orbit at essentially the speed of light for several hours while synchrotron radiation is emitted from all curved parts of this orbit tangentially to the direction of the electrons. The synchrotron radiation is extremely intense over a broad spectral range extending from the infrared to the hard X-rays. In addition, this radiation is also characterized by other properties: polarization, collimation, pulsed-time structure, brightness, coherence and high-vacuum environment. Due to all these characteristics, synchrotron radiation is a powerful tool for basic and applied studies in biology, medicine, chemistry and physics.[30,31]

That is, when electrons (or positrons) pass through a magnetic field that is uniform and perpendicular to the velocity of the particles, they are subjected to an acceleration perpendicular to their velocity (that is, a centripetal acceleration) that force them to change their direction and thus travel in a circular path. When the electron (or positron) velocity is non-relativistic or low compared to the velocity of light, the radiation emitted has a non-directional pattern (called a dipole pattern). In contrast, when charged particles travel at relativistic speeds, the radiation emitted is highly directional and highly polarized in the plane of the orbit. Since the synchrotron radiation is highly directional, highly collimated beams can be used. In the plane of the orbit, the electric field vector of the emitted radiation is in the direction of the instantaneous acceleration. However, those photons emitted out-of-plane can manifest a degree of ellipticity. Thus, every experiment can be affected by contaminations from circularly polarized radiation. Due to the requirements of each experiment, the circular polarization can be desired or not. For that reason, the contributions of circularly polarized radiation can be filtered out, or conversely, various devices can be used to achieve it.[30,32]

The electrons are accumulated and stored in bunches in the storage ring (Figure 2.10). The maximum number of bunches that can be stored (usually on the order of 100 or more) and the minimum spacing (usually a few nanoseconds) are determined by the parameter called RF frequency, which is one of the main parameters that constitute the radio-frequency (RF) system of each synchrotron. Since it is not necessary to fill each bunch, this can result in dark periods between pulses of several hundred nanoseconds to a microsecond or more. Hence, due to the pulsed-time structure of the synchrotron radiation, it allows carrying out time-resolved studies. [30,33,34]

The synchrotron radiation emitted by an electron comes out into a cone with an opening angle. The term used to describe the angular collimation of the radiation is the brightness, which is defined as the spectral flux normalized to a solid angle of 1 $mrad^2$. The spectral flux is the photon flux normalized to a relative spectral bandwidth. Going to the beginning, the transverse size and angular divergence of the electron

beam determine to a large extent the brightness and coherence of the synchrotron radiation. The opening angle of the emitted radiation can be significantly reduced using the so-called insertion devices (wigglers and undulators), which are integrated into the storage ring of the third-generation synchrotrons, and thus increase the brightness of the synchrotron radiation. As a result, those samples that are smaller, thinner and more diluted become accessible to be studied.[30,32]

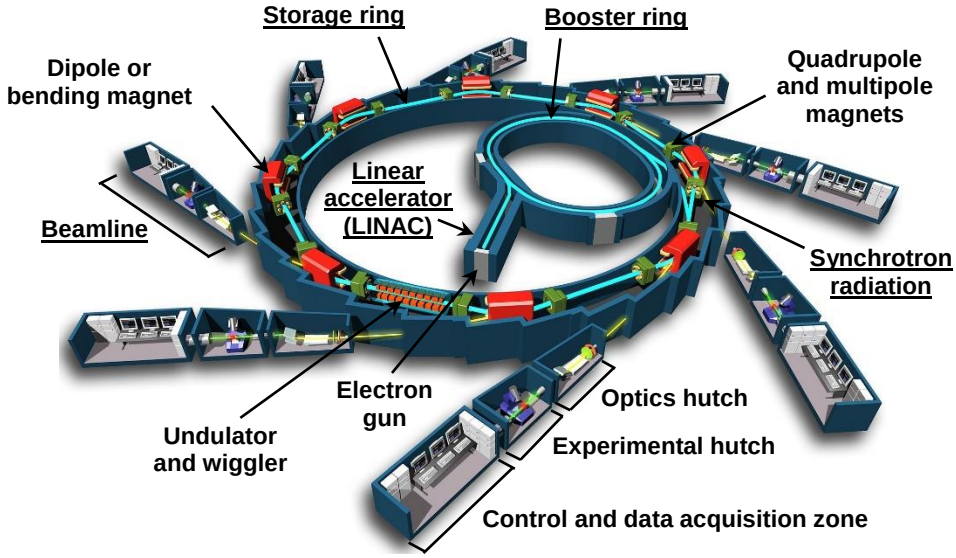

Figure 2.10. Schematic diagram of SOLEIL Synchrotron (Saint-Aubin, France), a third-generation synchrotron[35].

Any third-generation synchrotron consists of the devices and zones showed in Figure 2.10, which is specifically the schematic diagram of SOLEIL Synchrotron. In the linear accelerator (LINAC), first, electrons are produced in a metal after heating it, and then they are subjected to a first acceleration and collected in bunches with a hair size by an electrical field. When the electrons leave the LINAC, they enter the booster ring, in which they are accelerated enormously. In SOLEIL Synchrotron, in just a fraction of a second, their energy become increased from 100 MeV to 2.75 GeV. In ALBA Synchrotron, the energy of the electrons is increased from 100 MeV to 3 GeV. After, the electrons are injected to the storage ring, which is a closed tube with a series of straight and curved segments. In this ring, the electrons circle for periods of several hours very close to the speed of light in a circular path by using dipole or bending magnets. The dipole magnets generate a uniform magnetic field with vertical field lines to make to bend the trajectory of the electrons into an arc in the horizontal plane with the objective that these electrons spontaneously emit synchrotron radiation (explained above) tangentially to the direction of the electrons. In the storage ring, there are also quadrupole and multipole magnets. The first are used to prevent the dispersion of the electron beam to the edges of the tube because the field gradients of said magnets serve to focus (confine) the electron beam. Multipole magnets are

used to provide even more precision in the beam control. In the straight segments of the ring, one can find the so-called insertion devices, which are undulators and wigglers. An insertion device consists of a periodic array of magnets with alternating polarities that is used to force the electrons to follow a sinusoidal trajectory, so that at every bend of this oscillation synchrotron radiation is emitted. Hence, the insertion devices make the light beam more intense than those emitted by the dipoles. Then, as the electrons lose energy in form of electromagnetic radiation in both the dipoles and in the insertion devices, the average energy of the electron beam is maintained by using radio-frequency cavities, since they accelerate the electrons. Lastly, the synchrotron radiation is guided towards outlets known as beamlines, which are divided into, in order: optics hutch, experimental hutch, and control and data acquisition zone. In the optics hutch, the desired wavelength range is selected, and in the experimental hutch, the experimental setup specific for each study is mounted. [32,36,37,38]

The luminescence measurements were performed within the standard proposal with number 20151215. Figure 2.11 shows the DESIRS beamline seen from above, in which the optics hutch is observed, as well as two of the three work zones (experimental hutch + control and data acquisition zone) of this beamline. The emission spectroscopy of Ce^{3+} and of Pr^{3+} doped in KGdP host were studied under VUV-UV excitation in the wavelength spectral range from 120 to 248 nm (10−5 eV). Polished plates of undoped KGdP, Ce:KGdP and Pr:KGdP crystals were placed in a metallic sample holder within a vacuum chamber (Figure 2.12) that can be evacuated to a

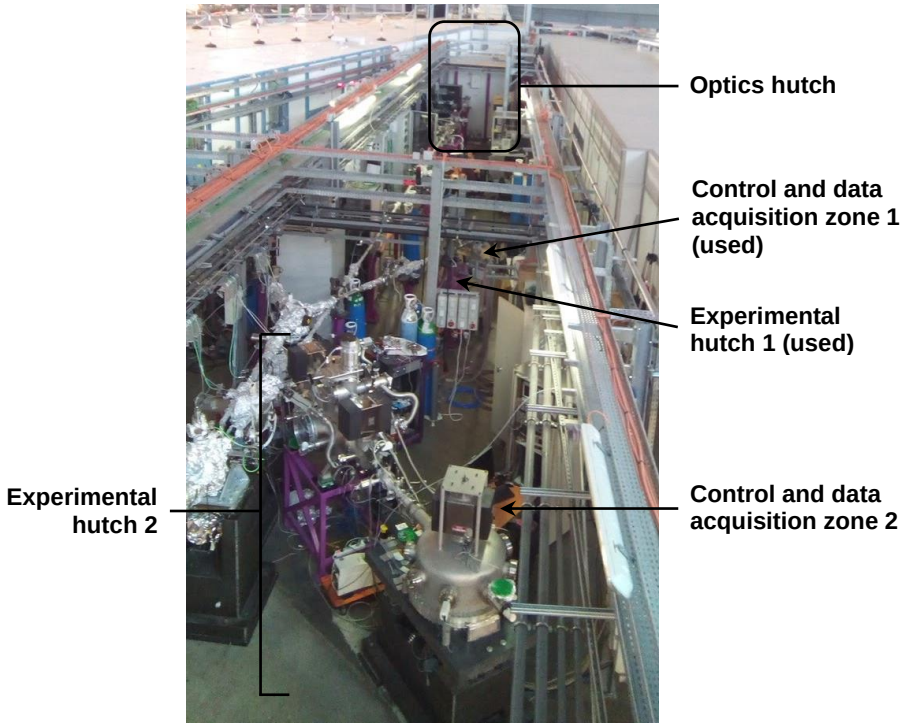

Figure 2.11. Photograph of DESIRS beamline of SOLEIL Synchrotron (Saint-Aubin, France).

pressure less than 2×10^{-5} bars. The air must be removed because it has absorptions when the wavelength of the radiation is below 190 nm. At the entrance of the vacuum chamber, a lithium fluoride (LiF) window separates it from the synchrotron line. The monochromatic synchrotron radiation reached perpendicularly to the sample and the luminescence emitted by the sample was collected at 45º, as shown in Figure 2.12. The luminescence was focused with a silica lens, analysed with an Ocean Optics JAZ spectrometer with a minimum spectral resolution of 0.3 nm and recorded in the electromagnetic range of 192 to 886 nm.

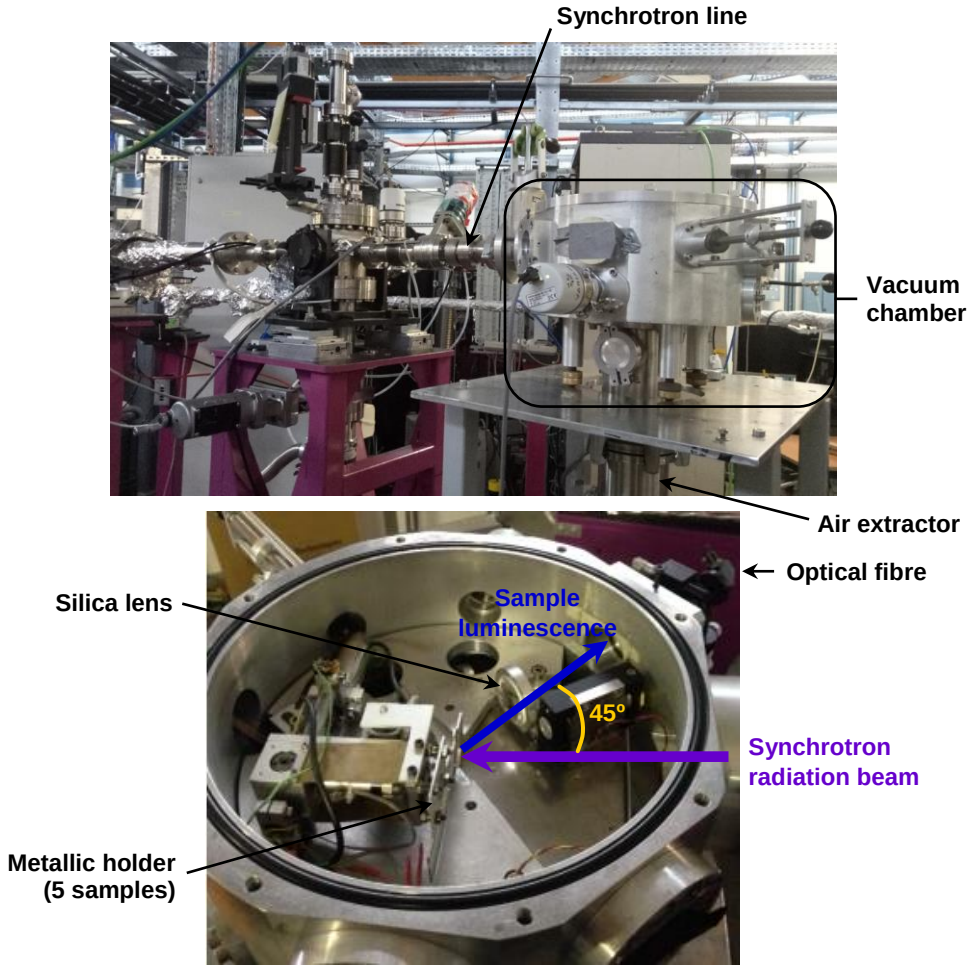

Figure 2.12. Photographs of the vacuum chamber used in the luminescence and decay time measurements in the DESIRS beamline at SOLEIL Synchrotron (Saint-Aubin, France) and of the internal configuration.

The decay time measurements were carried out within the standard proposal with number 20161324. In order to measure the decay time curves and thus determine the lifetime, a pulsed excitation source with the pulse duration shorter and the inter-pulse duration longer than the mean lifetime of the $5d_1$ level of Ce^{3+} (~18 ns)[39,40] and

that of Pr^{3+} (~12 ns)[39,41,42] in hosts similar to the KGdP host is required. Therefore, the single bunch mode of operation of pulsed DESIRS beamline was used, since it provides a full width at half-maximum (FWHM) pulse duration of 50 ps and an inter-pulse duration of 1118 ns. However, photon flux is divided by a factor 30 as compared to the multi-bunch mode that we used for the luminescence measurements. The samples were placed at the same vacuum chamber with the same internal configuration (Figure 2.12) as in the luminescence measurements. The luminescence emitted by the sample was guided with an optical fibre to an ANDOR Shamrock 193i spectrograph (grating 150 lines/mm) coupled to an iStar Intensified Charge Coupled Device (ICCD) camera with fast response (DH734-18F-03 model). To increase the photon flux reaching the sample, once the vacuum in the chamber was enough high (at least 2×10^{-5} bars), the LiF window between the vacuum chamber and the synchrotron line was removed. In addition, with the same objective, the excitation beam had a bandwidth of around 7%, being not purely monochromatic.

2.8.4. Luminescence measurements under X-ray excitation

As mentioned earlier, luminescence or optical emission is the result of a radiative transition of a previously excited electron from a high energy level to a lower energy level. In this Section, the excitation radiation used to perform the luminescence measurements is X-rays.

As X-rays are high-energy electromagnetic radiation, they excite electrons from the inner orbitals of the atoms. Thus, the aim of these measurements was to observe whether the energy transfer from the electron−hole pairs created by X-rays to the 5*d* levels of Ce^{3+} and those of Pr^{3+} in KGdP is efficient or inefficient, and consequently check their suitability as promising new scintillators.

2.8.4.1. ALBA Synchrotron

The luminescence measurements of Ce:KGdP and Pr:KGdP polished single crystalline plates using X-rays as excitation radiation were performed at room temperature in the BL22-CLAESS beamline at ALBA Synchrotron (Cerdanyola del Vallès, Spain) within the proposal number 2016091932. ALBA Synchrotron is a third-generation synchrotron light source. The description of a third-generation synchrotron and a schematic diagram of it are shown in Section 2.8.3.

The available energy range in the BL22-CLAESS beamline is from 2400 to 63000 eV, so it was possible to excite the orbitals $2p_{3/2}$ and 1*s* of Gd^{3+}, 1*s* of Ce^{3+} and 1*s* of Pr^{3+} because their energy are 7243, 50239, 40443 and 41991 eV, respectively[43]. The samples were placed one by one in the central position of a sample holder, which was hung diagonally in the central part of an AISI 304 stainless steel cube, attached to the upper window of the cube. Figure 2.13 shows the experimental setup and Figure 2.14 displays the sample holder used and the position of the sample. The monochromatic synchrotron radiation reached to the sample with a 45º incident angle and the luminescence emitted by the sample was collected at 90º to the excitation radiation. The synchrotron radiation that is not absorbed by the sample, it passes

through it and leaves by the fourth window of the cube. The luminescence emitted from the sample was focused by means of an UV fused silica biconvex lens with a focal length of 75 mm (Eksma Optics, code: 111-1508E), guided with an optical fibre (Thorlabs, code: UM22-600) and detected by an Ocean Optics FLAME-S-UV-VIS-ES spectrometer with a spectral resolution of ~1.5 nm. The biconvex lens was located inside two PVC concentric tubes (at the beginning of the outer tube) and the optical fibre was located at the end of the inner tube. The tubes were not fixed to each other to move them easily until the luminescence was focused. This configuration also provides the opportunity to avoid the ambient light pollution from the experimental hutch. The luminescence spectra were recorded in the spectral range from 180 nm to 870 nm.

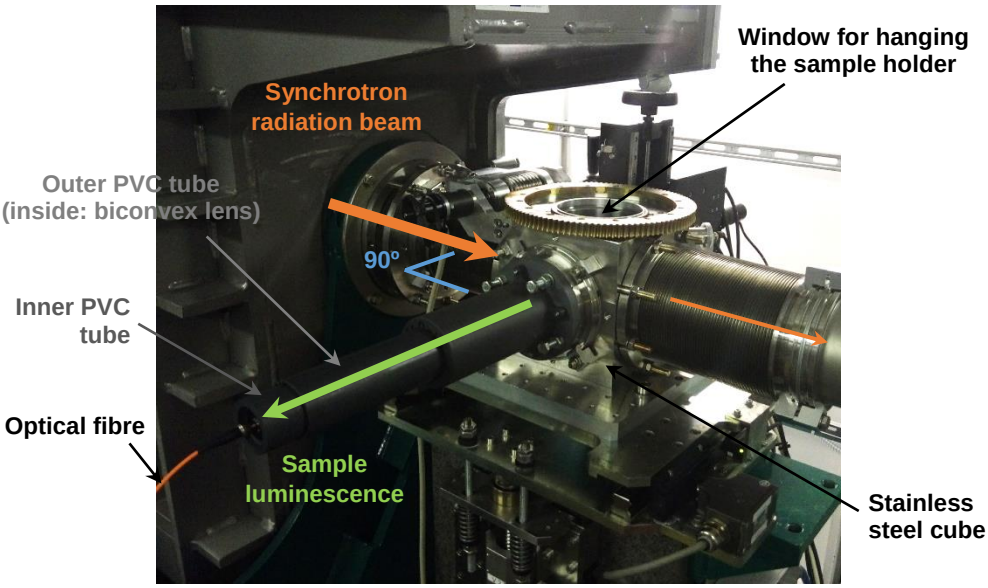

Figure 2.13. Photograph of the setup used for the luminescence measurements in the BL22-CLAESS beamline at ALBA Synchrotron (Cerdanyola del Vallès, Spain).

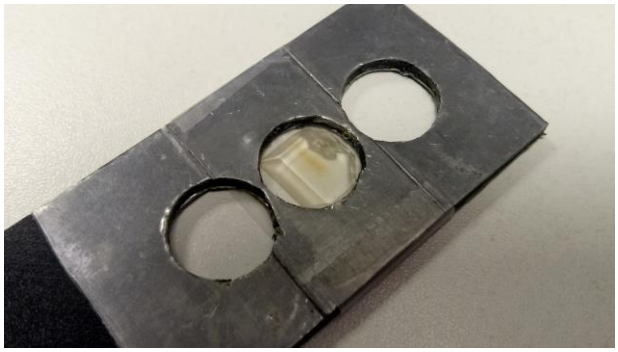

Figure 2.14. Photograph of the sample holder used in the luminescence measurements in the BL22-CLAESS beamline at ALBA Synchrotron (Cerdanyola del Vallès, Spain).

2.8.4.2. Servei de Recursos Científics i Tècnics of the Universitat Rovira i Virgili

The luminescence measurements at room temperature of Pr:KGdP nanocrystals under X-ray excitation were performed using an X-ray tube with a copper target operating at 40 kV and 30 mA, available at *Servei de Recursos Científics i Tècnics* (SRCiT) of the *Universitat Rovira i Virgili*. The nanocrystals were prepared in pellet form and the experimental setup used is shown in Figure 2.15. The incident angle of the X-ray radiation with respect to the pellet sample plane was 63º. The sample luminescence was collected at 90º with respect to the pellet plane, focused with an UV fused silica biconvex lens, guided with an optical fibre and detected by an Ocean Optics FLAME-S-UV-VIS-ES spectrometer with a spectral resolution of ~1.5 nm.

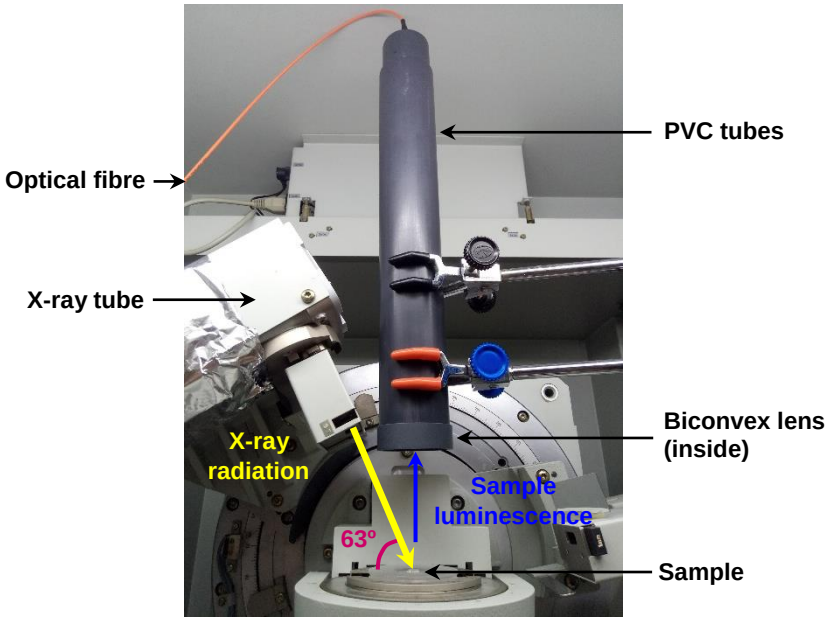

Figure 2.15. Photograph of the setup used for the luminescence measurements at *Servei de Recursos Científics i Tècnics* (SRCiT) of the *Universitat Rovira i Virgili*.

2.8.5. Raman spectroscopy

Raman spectroscopy is a technique that provides useful information about the vibrational energy levels and other low-frequency modes of molecules and condensed matter, such as the lattice vibrations of the crystals. It does not require sample preparation and is a non-contact and non-destructive technique. The Raman spectrum, or the so-called Raman shift, is characteristic of each material, therefore it acts as a fingerprint, allowing a material to be distinguished from others. Infrared spectroscopy is a complementary technique to Raman spectroscopy, making it possible to completely characterize the vibrational energy levels.[44]

When light impinges on a molecular system or condensed matter, it scatters elastically and inelastically. Most of photons are elastically scattered (Rayleigh scat-

tering), so the excited molecules or atoms relax to the ground state by emitting a photon with the same energy as the absorbing photon. To a much lesser extent, the scattered photons have an energy different from that of the absorbing photon, resulting in an inelastic scattering (Raman scattering). Thus, Raman spectroscopy receives that name because it relies on the inelastic scattering of a monochromatic light that impinges on a material to provide useful information about the material. When the excited molecule or atom relaxes to a vibrational energy level of the ground state with higher energy than the initial one, the energy of the scattered photon becomes smaller (Stokes Raman scattering). Whereas if the vibrational energy level has less energy than the initial one, the energy of the scattered photon becomes higher (anti-Stokes Raman scattering). The three possibilities of light scattering are represented in Figure 2.16. The shift in energy is attributed to the vibrational energy spacing at the ground level, so it gives information about the phonon modes in the system. The energy difference of the Stokes Raman scattered photon and the anti-Stokes Raman scattered photon with respect to the Rayleigh scattered photon is the same because the vibrational quantum energy is lost or gained, respectively, as shown in Figure 2.16. However, the anti-Stokes Raman scattering occurs less frequently than the Stokes Raman scattering because there are exponentially fewer molecules or atoms that start in the higher energy vibrational state.[44]

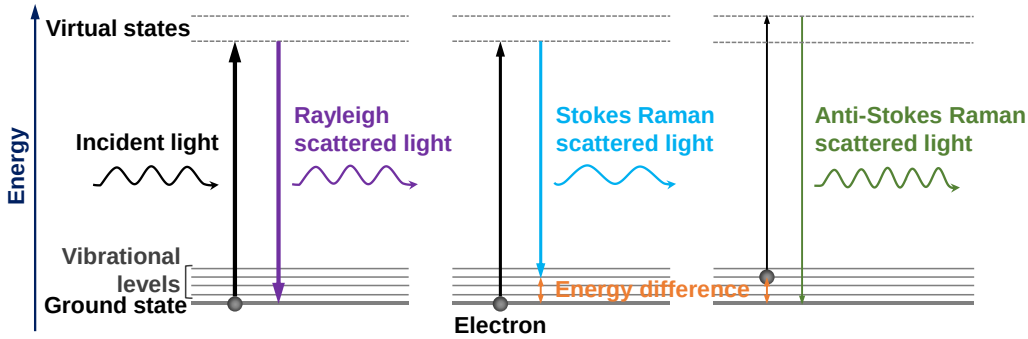

Figure 2.16. Energy diagram of the three possibilities of light scattering.

As the spontaneous Raman scattering is typically very weak compared to the Rayleigh scattering, Raman spectroscopy needs a high power monochromatic excitation source. Usually, the source is a laser in the visible, near infrared or near ultraviolet range. The sample is first illuminated with the excitation light and then the scattered light is collected with a lens and sent through an interference filter or spectrophotometer. Wavelengths close to the laser line (due to the elastic scattering) are filtered out and those wavelengths that are different from the laser line are dispersed into a detector. When the polarization of the incident light and that of the scattered light emerging from the sample are taken into account, the technique is called polarized Raman spectroscopy.[45]

We obtained unpolarized Raman spectra using a Renishaw FT-IR Raman spectrometer connected to a Leica DM 2500 confocal microscope available at SRCiT of

the *Universitat Rovira i Virgili*. The objective was to observe whether the undoped KGdP, Ce:KGdP and Pr:KGdP polished plates had undergone some change in their chemical structure after being excited with X-rays radiation. The excitation source was a visible laser at 514 nm with an output power of 25 mW. Since a part of the excitation radiation is filtered, the laser power incident on the sample was about 1 mW. The laser spot was located on the surface of the crystals. Next, an image of the surface of each sample was acquired using a 5X microscope objective and subsequently the Raman spectrum was obtained from several points of the sample surface using a 50X microscope objective. The Raman spectra were recorded in the Raman shift range from 100 to 1600 cm^{-1} with a spectral resolution of <1.5 cm^{-1}.

References

[1] I. Parreu. Crystal growth and characterization of ytterbium or neodymium doped type III-$KGd(PO_3)_4$. A new bifunctional nonlinear and laser crystal. Ph.D. Thesis, Rovira i Virgili University, **2006**.
[2] V. Nikolov, K. Iliev and P. Peshev. Relationship between the hydrodynamics in the melt and the shape of the crystal/melt interface during Czochralski growth of oxide single crystals. I. Determination of the critical crystal rotation rate from physical simulation on free and forced convections. *J. Cryst. Growth* **1988**, *89* (2-3), 313-323.
[3] V. Nikolov, K. Iliev and P. Peshev. Relationship between the hydrodynamics in the melt and the shape of the crystal/melt interface during Czochralski growth of oxide single crystals. II. Determination of the critical crystal rotation rate from physical simulation on free and forced convections; comparison with experimental data on crystal growth. *J. Cryst. Growth* **1988**, *89* (2-3), 324-330.
[4] W. Tolksdorf. *Handbook of Crystal growth*. Vol. 2, part A. Elsevier Science publishers: Amsterdam, Netherlands, **1994**.
[5] J. M. Nedelec. Sol-gel processing of nanostructured inorganic scintillating materials. *J. Nano Mat.* **2007**, *2007*, 1-8.
[6] W. Liu, C. C. Forrington, F. Chaput and B. Dunn. Synthesis and electrochemical studies of spinel phase $LiMn_2O_4$ cathode materials prepared by the Pechini process. *J. Electrochem. Soc.* **1996**, *143* (3), 879-884.
[7] P. Mendonça, A. Eduardo, D. M. de Araújo, A. M. Garrido, J. Dantas and C. Neco. Pechini synthesis and microstructure of nickel-doped copper chromites. *Mater. Res.* **2005**, *8* (2), 221-224.
[8] E. W. Barrera. Lanthanide-based dielectric nanoparticles for upconversion luminescence. Ph.D. Thesis, Rovira i Virgili University, **2013**.
[9] M. Galceran, M. C. Pujol, M. Aguiló and F. Díaz. Sol-gel modified Pechini method for obtaining nanocrystalline $KRE(WO_4)_2$ (RE = Gd and Yb). *J. Sol-Gel Sci. Techn.* **2007**, *42*, 79-88.
[10] A. L. Morrissey. Preparation of high purity doped oxides for fundamental studies. Ph.D. Thesis, Colorado School of Mines, **2013**.
[11] Logitech. Model 15 diamond & wire disc saw. https://logitech.uk.com/product/model-15-diamond-wire-disc-saw/ (accessed 08/08/2018).
[12] I. Parreu, R. Solé, J. Massons, F. Díaz, and M. Aguiló. Crystal growth, crystal morphology and surface micromorphology of type III $KGd(PO_3)_4$ and $KNd(PO_3)_4$. *Cryst. Growth Des.* **2007**, *7* (3), 557-563.
[13] J. Pickworth Glusker and K. N. Trueblood. *Crystal structure analysis: A primer.* Part 1. Oxford University Press: New York, NY, USA, **1985**.
[14] XRD software – DIFFRAC.SUITE EVA. Bruker.
[15] XRD software – DIFFRAC.SUITE TOPAS V4.2. Bruker.
[16] A. Le Bail. Whole powder pattern decomposition methods and applications: A retrospection. *Powder Diffr.* **2005**, *20* (4), 316-326.
[17] I. Parreu, J. J. Carvajal, X. Solans, F. Díaz, and M. Aguiló. Crystal structure and optical characterization of pure and Nd-substituted type III $KGd(PO_3)_4$. *Chem. Mater.* **2006**, *18* (1), 221-228.
[18] P. J. Goodhew, J. Humphreys and R. Beanland. Chemical analysis in the electron microscope. The generation of X-rays within a specimen. In *Electron microscopy and analysis*. Third Edition. Taylor & Francis: London, UK, **2001**; pp 170.
[19] P. J. Goodhew, J. Humphreys and R. Beanland. Electrons and their interaction with the specimen. In *Electron microscopy and analysis*. Third Edition. Taylor & Francis: London, UK, **2001**.
[20] P. J. Goodhew, J. Humphreys and R. Beanland. Chemical analysis in the electron microscope. In *Electron microscopy and analysis*. Third Edition. Taylor & Francis: London, UK, **2001**.

[21] CAMECA. Introduction to EPMA. https://www.cameca.com/products/epma/technique (accessed 01/02/2018).
[22] S. J. B. Reed. Characteristic fluorescence corrections in electron-probe microanalysis. *Brit. J. Appl. Phys.* **1965**, *16*, 913-926.
[23] R. F. Egerton. An introduction to microscopy. In *Physical principles of electron microscopy. An introduction to TEM, SEM, and AEM.* Springer Science+Business Media: New York, NY, USA, **2005**.
[24] R. F. Egerton. The scanning electron microscope. In *Physical principles of electron microscopy. An introduction to TEM, SEM, and AEM.* Springer Science+Business Media: New York, NY, USA, **2005**.
[25] Encyclopædia Britannica. Scanning electron microscope (accessed 30/01/2018). https://www.britannica.com/technology/scanning-electron-microscope
[26] Pythography. SEM sample charging. http://www.pythography.com/sem/charging.html (accessed 22/08/2018).
[27] R. F. Egerton. The transmission electron microscope. In *Physical principles of electron microscopy. An introduction to TEM, SEM, and AEM.* Springer Science+Business Media: New York, NY, USA, **2005**; pp 57.
[28] R. F. Egerton. The transmission electron microscope. In *Physical principles of electron microscopy. An introduction to TEM, SEM, and AEM.* Springer Science+Business Media: New York, NY, USA, **2005**.
[29] Encyclopædia Britannica. Transmission electron microscope (accessed 30/01/2018). https://www.britannica.com/technology/transmission-electron-microscope
[30] H. Winick. Introduction to synchrotron radiation sources. In *Synchrotron radiation sources: A primer*. World Scientific: London, UK, **1994**.
[31] P. J. Duke. Synchrotron radiation from dipole magnets. In *Synchrotron radiation: Production and properties.* Oxford University Press: New York, NY, USA, **2000**.
[32] R. Röhlsberger. Methods and instrumentation. Properties of synchrotron radiation. In *Nuclear condensed matter physics with synchrotron radiation: Basic principles, methodology and applications.* Springer: Berlin, Germany, **2004**.
[33] J. C. Liu, S. H. Rokni and V. Vylet. Operational radiation protection in synchrotron light and free electron laser facilities. *Radiat. Prot. Dosim.* **2009**, *137* (1-2), 18-34.
[34] SESAME (Synchrotron-light for Experimental Science and Applications in the Middle East). Radiofrequency System. http://old.sesame.org.jo/sesame/images/sesame-publications/RF.pdf (accessed 27/08/2018).
[35] Wikipedia; obtained from SOLEIL Synchrotron. Schéma de principe du synchrotron. https://es.m.wikipedia.org/wiki/Archivo:Sch%C3%A9ma_de_principe_du_synchrotron.jpg (accessed 07/02/2018).
[36] P. J. Duke. Introduction to electron storage rings. In *Synchrotron radiation: Production and properties.* Oxford University Press: New York, NY, USA, **2000**.
[37] SOLEIL Synchrotron. https://www.synchrotron-soleil.fr/en/about-us/what-soleil/soleil-3-questions#3 (accessed 07/02/2018).
[38] ALBA Synchrotron. Accelerators. https://www.cells.es/en/accelerators/rf-systems-1 (accessed 28/08/2018).
[39] T. Shalapska, G. Stryganyuk, A. Gektin, A. Kotlov, P. Demchenko and A. Voloshinovskii. Luminescence properties of Ce^{3+}-doped $NaPrP_4O_{12}$ polyphosphate. *J. Phys. Condens. Matter* **2013**, *25* (10), 105403 (6 pp).
[40] J. Zhong, H. Liang, H. Lin, B. Han, Q. Su and G. Zhang. Effects of crystal structure on the luminescence properties and energy transfer between Gd^{3+} and Ce^{3+} ions in $MGd(PO_3)_4:Ce^{3+}$ (M = Li, Na, K, Cs). *J. Mater. Chem.* **2007**, *17*, 4679-4684.
[41] M. Trevisani, K. V. Ivanovskikh, F. Piccinelli and M. Bettinelli. Fast 5*d*-4*f* luminescence in Pr^{3+}-doped $K_3Lu(PO_4)_2$. *J. Lumin.* **2014**, *152*, 2-6.
[42] A. Jouini, J. C. Gâcon, M. Ferid and M. Trabelsi-Ayadi. Luminescence and scintillation properties of praseodymium poly and diphosphates. *Opt. Mater.* **2003**, *24*, 175-180.
[43] J. A. Bearden and A. F. Burr. Reevaluation of X-ray atomic energy levels. *Rev. Mod. Phys.* **1967**, *39*, 125-142.

[44] University of Cambridge. Raman spectroscopy (accessed 23/08/2018). https://www.doitpoms.ac.uk/tlplib/raman/index.php
[45] Princeton Instruments. Raman. http://web.pdx.edu/~larosaa/Applied_Optics_464-564/Projects_Optics/Raman_Spectrocopy/Raman_Spectroscopy_Basics_PRINCETON-INSTRUMENTS.pdf (accessed 23/08/2018).

Chapter 3.

Crystal growth and structural characterization

This Chapter shows the primary crystallization region of the type B KYP_4O_{12} and type IV $KY(PO_3)_4$, and their boundary phases, in the K_2O–Y_2O_3–P_2O_5 ternary system together with ESEM images of each crystalline phase or compound. The growth conditions and cooling programs of the study on the primary crystallization region mentioned are described, as well as those of the crystal growth of type III Ce:$KGd(PO_3)_4$ and type III Pr:$KGd(PO_3)_4$ bulk single crystals. In addition, the crystal morphology, composition and changes in the unit cell parameters with doping content are shown for the bulk single crystals. Finally, the thermal stability and thermal expansion of type III Pr:$KGd(PO_3)_4$ single crystals are discussed. The crystal growth was carried out at the laboratories of the FiCMA-FiCNA research group of the *Universitat Rovira i Virgili* (URV, in Tarragona, Spain), the EPMA measurements required to obtain the chemical composition of the bulk crystals were made at *Centres Científics i Tecnològics* of the *Universitat de Barcelona* (CCiTUB, in Barcelona, Spain), and the structural characterization was performed at *Servei de Recursos Científics i Tècnics* (SRCiT) of the URV.

3.1. Primary crystallization region of the type B KYP_4O_{12} and type IV $KY(PO_3)_4$ in the $K_2O–Y_2O_3–P_2O_5$ ternary system

The primary crystallization region of the type B KYP_4O_{12} (space group: *C*2/*c*) and type IV $KY(PO_3)_4$ (space group: $P2_1/c$) (hereinafter, type B KYP and type IV KYP) was determined in its self-flux to avoid foreign ions inside the crystals, despite the high viscosity of the growth solution expected taking into account previous works on the crystal growth of type III $KGd(PO_3)_4$ (space group: $P2_1$) (hereinafter, type III KGdP)[1,2]. Hence, the crystals were grown from the corresponding oxides, $K_2O–Y_2O_3–P_2O_5$, and with an excess of K_2O and P_2O_5 as a solvent because of the incongruent melting of KYP[3]. The starting reagents were K_2CO_3 anhydrous (Alfa Aesar A. Johnson Matthey Company, 99%), Y_2O_3 (Sigma-Aldrich, 99.99%) and $NH_4H_2PO_4$ (Fluka Analytical, ≥99.0%). First, K_2CO_3 and $NH_4H_2PO_4$ were mixed, placed inside a platinum crucible and heated to the total release of CO_2 and NH_3. Then, Y_2O_3 was added and heated. Taking into account the study on the $KPO_3–Y(PO_3)_3$ binary system carried out by Jouini *et al.*[3], we chose the initial solution composition to determine the KYP primary crystallization region and crystallization temperatures in the ternary system mentioned above. The total weight of the solutions was approximately 15 g.

Due to the high viscosity of the solution, the saturation temperature of each solution composition studied was usually determined by throwing millimetre size crystals of type III KGdP or type B KYP onto the solution surface and observing visually their size as a function of the solution temperature and time. Once the size of the crystals present on the solution surface was maintained constant for several hours, the temperature of the solution was slowly decreased while a platinum disk of ~10 mm diameter was located in contact with the solution surface in a rotating movement to favour the crystal growth. The temperature of the solution was usually reduced with cooling rates of 0.2-0.5 $K \cdot h^{-1}$ for 10-25 K after determining the saturation temperature, and the disk was rotated at 20 rpm. Afterwards, the disk with relatively large crystals adhered was slowly extracted from the furnace.

Once the crystals that were adhered to the disk reached room temperature, they were observed through a reflection optical microscope (see Section 2.6.1) to draw their crystal habit. Later, the disk was immersed in distilled water to dissolve the solution and acquire the crystals individually. Once the water evaporated totally, the crystals of interest were photographed directly without sample preparation with an environmental scanning electron microscope (ESEM) to obtain high-resolution images of their external shape (see Section 2.6.2). At the same time, some of the crystals obtained were grinded in an agate mortar to be analysed by X-ray powder diffraction (XRPD) technique (see Section 2.4).

Figure 3.1 shows the obtained crystallization region of type B and IV KYP with saturation temperature isotherms in the $K_2O–Y_2O_3–P_2O_5$ system along with ESEM images of the KYP and their neighbouring phases. In the region delimitated, KYP can crystallize in two different monoclinic crystalline phases: type B (space group: *C*2/*c*) and type IV (space group: $P2_1/c$). KYP crystallizes inside the following limit lines: K_2O concentration from 34 to 38 mol %, Y_2O_3 concentration from approximately 2.5 to 8 mol %, and P_2O_5 concentration from 55.5 to 64 mol %. Table 3.1 shows the saturation

temperature experimentally determined in five solution compositions spaced from each other within the KYP crystallization region or at the boundary (indicated in Figure 3.1). The saturation temperature isotherms are roughly parallel to the limit curve of the KYP crystallization region poorer in Y_2O_3 and P_2O_5 (i.e. right limit).

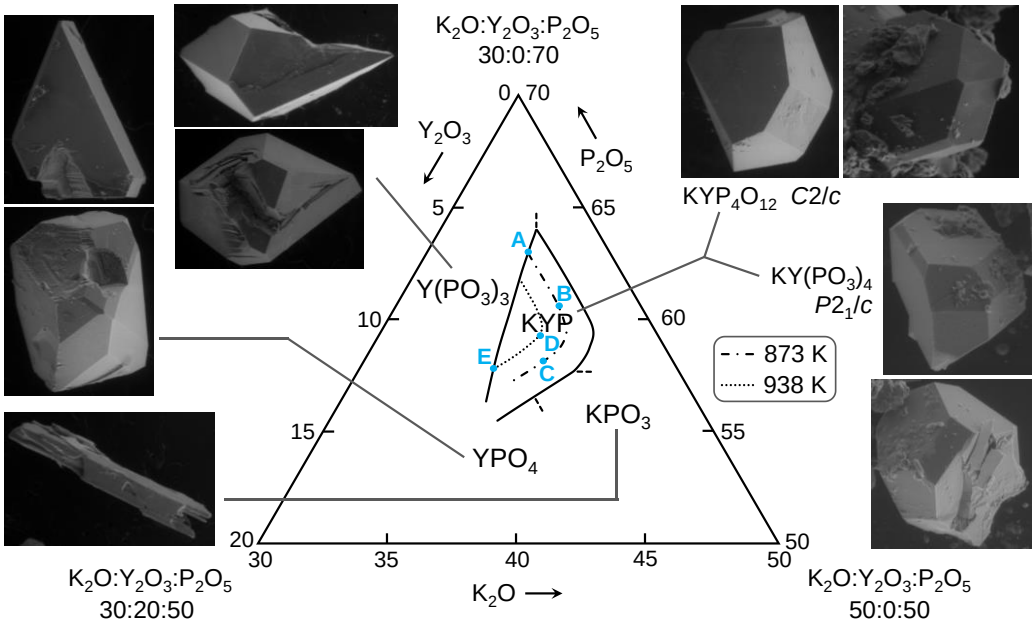

Figure 3.1. Primary crystallization region of the type B KYP (space group: *C*2/*c*) and type IV KYP (space group: *P*2$_1$/*c*) with saturation temperature isotherms in the K_2O–Y_2O_3–P_2O_5 ternary system. The solution compositions shown in Table 3.1 are indicated in this figure as ●A–●E. ESEM images of the KYP and their neighbouring phases.

Table 3.1. The saturation temperature of the solution of some solution compositions within the KYP crystallization region or at the boundary.

Point	Solution composition [mol %]		Saturation temperature [K]
	Molar ratio K_2O/P_2O_5	Y_2O_3	
A*	35/65	3	~875
B	37.5/62.5	3	~863
C	39/61	5	~873
D	38/62	4.5	~943
E*	38/62	7	~933

* Type B KYP crystallizes together with another crystalline phase.

The neighbouring crystalline phases of KYP were identified as: $Y(PO_3)_3$, KPO_3 and YPO_4. Table 3.2 shows some solution compositions that result in the neighbouring crystalline phases determined. $Y(PO_3)_3$ grows using solution compositions that are poorer in K_2O and richer in Y_2O_3 than those required in the KYP crystallization region. In the poorest P_2O_5 zone, below the KYP crystallization region, KPO_3 crystallizes

when the solution is poor in Y_2O_3, and YPO_4 grows when the solution is richer in Y_2O_3 than in the case of KPO_3. When the molar ratio of K_2O/P_2O_5 is 35/65 and the molar percentage of Y_2O_3 is 2 or less, it was not possible to analyse the neighbouring crystalline phase because there were not enough crystals on the solution surface or the compound obtained dissolved in water. We also had difficulties in identifying the neighbouring phase when the molar ratio of K_2O/P_2O_5 is 40/60 and the Y_2O_3 concentration is up to about 3.5 mol % because the compound grew difficultly.

Table 3.2. Solution compositions that result in the neighbouring crystalline phases.

Solution composition [mol %]		Neighbouring phases
Molar ratio K_2O/P_2O_5	Y_2O_3	
35/65	4	$Y(PO_3)_3$
36/64	5	$Y(PO_3)_3$
36/64	7	$Y(PO_3)_3$
45/55	3	KPO_3
41/59	5	KPO_3
40/60	7	YPO_4

The optimal composition zone to perform growth experiments of KYP bulk single crystals is with a K_2O/P_2O_5 molar ratio of around 38/62 and an Y_2O_3 percentage of 4-5 mol %. If the solution is rich in P_2O_5, it becomes more viscous, which causes the crystalline growth units to reach the crystal with more difficulty. Regarding the concentration of Y_2O_3, it is necessary to establish a compromise. The increase in the molar percentage of Y_2O_3 allows the crystal growth of KYP to be faster. However, the homogenization of the solution becomes harder when the concentration of Y_2O_3 is high, which makes it necessary to maintain the solution at high temperatures for long periods of time (Y_2O_3, melting point: 2723 K[4,5]), even using a platinum disk to mix the solution. Some of the X-ray powder diffractograms obtained are shown in *Appendix I* along with the XRD standard patterns of the type B KYP, type IV KYP and neighbouring crystalline phases of KYP.

As mentioned above, KYP can crystallize in two different crystalline phases in the KYP crystallization region determined, as shown in Figure 3.1. Since the stability of the two KYP phases is quite similar, it is expected that a KYP single crystal with the desired phase can be grown by choosing a crystal seed with such phase of interest by the Top Seeded Solution Growth-Slow Cooling (TSSG-SC) technique.

3.2. Type III Ce:$KGd(PO_3)_4$ bulk single crystals

3.2.1. Growth conditions, crystal morphology and composition

Type III Ce:$KGd(PO_3)_4$ (space group: $P2_1$) (hereinafter, Ce:KGdP) bulk single crystals were grown from high temperature solutions composed of Ce_2O_3, K_2O, Gd_2O_3 and P_2O_5 by the TSSG-SC technique. The solvent used was an excess of K_2O and P_2O_5, so that the crystals were grown from their self-flux to avoid impurities inside the

crystalline structure. The compositions of the solutions were K_2O:((1−x) Gd_2O_3 + x Ce_2O_3):P_2O_5 = 36:4:60 (mol %) with x in the range 0-0.02, chosen taking into account the primary crystallization region of type III KGdP in the K_2O–Gd_2O_3–P_2O_5 ternary system, determined in previous works[1,6]. The reagents used were $Ce_2(CO_3)_3$ hydrate (Sigma-Aldrich, 99.9%), K_2CO_3 anhydrous (Alfa Aesar, 99%), Gd_2O_3 (Sigma-Aldrich, 99.9%) and $NH_4H_2PO_4$ (Fluka Analytical, ≥99.0%). First, due to the hygroscopicity of $Ce_2(CO_3)_3$ hydrate[7] and K_2CO_3 anhydrous[8], these two reagents were heated to evaporate the water. Then, $Ce_2(CO_3)_3$, K_2CO_3 and $NH_4H_2PO_4$ were heated up to the total release of CO_2 (coming from the first two reagents mentioned) and NH_3 (from the last reagent) was achieved. By last, Gd_2O_3 was added into the same container and heated. The total weight of the solutions was approximately 100 g and were prepared in a platinum cylindrical crucible with a diameter of 40 mm and 45 mm height.

The expected dynamic viscosity of the growth solution is high[2]. To achieve a good mixing of the solution and favour the approach of the growth units towards the crystal surface, a high axial thermal gradient of 3.0 K·mm^{-1} in depth with the coolest zone at the solution surface was used, together with a platinum stirrer of 20 mm diameter rotating at 55 rpm that was located at ~12 mm below the surface of the solution. The crystal seed used to initiate the crystal growth and the stirrer were joined with the alumina rod as shown in Figure 2.2 (and Figure 3.2.a), so that they were rotating on the same axis[2]. An undoped KGdP seed with *a** orientation and the *b* crystallographic direction tangential to the rotation direction was located in contact with the solution surface at ~10 mm from the central axis of the alumina rod. This orientation was chosen because in previous works it was observed that it provides high quality crystals[9]. Since the morphology of this crystal generally presents an edge perpendicular to the *b* crystallographic direction and natural {100} and {001} faces, the mentioned orientation is appropriate to reduce the resistance of the solution in the crystal during its movement. Besides, this crystal has cleavage planes perpendicular to the *b* and *c** crystallographic directions and with the aim of avoiding the risk of losing the crystals when using seeds oriented along the *c** direction, the most successful orientation was using *a**-oriented seeds[9].

The saturation temperature of the solutions was determined to be at ~950 K. From the saturation temperature determined, cooling rates of 0.1 K·h^{-1} for the first 15 K and 0.05 K·h^{-1} for the next 10-15 K were programmed to maintain the supersaturation of the solution and thus obtain crystal growth. Table 1 of *Paper I* summarizes the growth conditions of the crystal growth experiments carried out and the weight, the dimensions in *a** × *b* × *c** directions and the growth rate of the Ce:KGdP bulk single crystals obtained. The crystals were colourless, transparent and generally free of inclusions and macroscopic defects, as can be seen in Figure 3.2. The crystalline habit corresponds to the type III phase of KGdP (space group: $P2_1$). The visible crystalline faces of the crystal of Figure 3.2.b have been labelled in the morphological scheme of Figure 1.c of *Paper I*. The weights ranged from 0.62 to 1.76 g, the sizes in *a** × *b* × *c** crystallographic directions were 3.1-6.1 mm × 9.9-15.7 mm × 9.9-13.3 mm, and the crystal growth rates were generally higher than 3 × 10^{-3} g·h^{-1}. Comments and discussion about these values are found in *Paper I*.

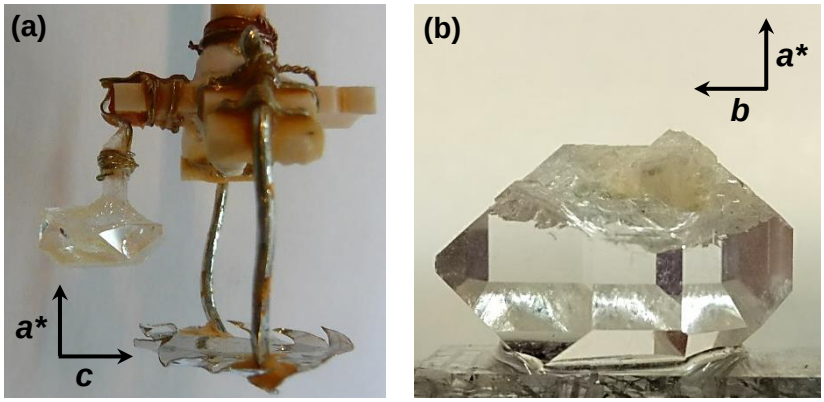

Figure 3.2. (a) As-grown Ce:KGdP single crystal with the platinum stirrer, (b) as-grown Ce:KGdP single crystal.

Using the atomic percentage of each element present in the chemical compound as obtained from the EPMA results, the chemical composition of the crystals was determined and the distribution coefficient of Ce^{3+}, K_{Ce}, in KGdP was calculated according to the formula: $K_{Ce} = ([Ce]/([Ce]+[Gd]))_{crystal} / ([Ce]/([Ce]+[Gd]))_{solution}$, where [Ce] and [Gd] are the Ce^{3+} and Gd^{3+} concentrations, respectively, in atomic % in the crystal and the solution. These values along with their error are shown in Table 3.2, while the corresponding number of Ce^{3+} ions per unit cell volume in the crystals, calculated from the EPMA results as well, is shown in Table 2 of *Paper I*. The K_{Ce} in KGdP is larger than the unit in the doping concentrations studied, up to 2 at. % in the solution. Taking these results into account, the distribution of Ce^{3+} inside the crystals may be not homogeneous. As mentioned in *Paper I*, the distribution coefficient of Nd in KGdP[10] is similar to the observed for Ce^{3+}, and the distribution coefficient of Yb[11] is smaller than for Ce^{3+}. In equal ionic charge of the different lanthanide doping ions and Gd^{3+}, the behaviour mentioned can be related to the difference between the ionic radii of the doping ions.

Table 3.2. EPMA results for Ce:KGdP single crystals. K_{Ce} denotes the distribution coefficient of the Ce^{3+} in the crystal.

[Ce]/([Gd]+[Ce]) atomic % ratio in the solution	[Ce]/([Gd]+[Ce]) atomic ratio in the crystal	Chemical formula	K_{Ce}
0.25	0.004 ± 0.001	$KGd_{0.996}Ce_{0.004}(PO_3)_4$	1.8 ± 0.4
0.50	0.006 ± 0.001	$KGd_{0.994}Ce_{0.006}(PO_3)_4$	1.3 ± 0.2
1.00	0.019 ± 0.002	$KGd_{0.981}Ce_{0.019}(PO_3)_4$	1.9 ± 0.2
2.00	0.026 ± 0.001	$KGd_{0.974}Ce_{0.026}(PO_3)_4$	1.3 ± 0.1

3.2.2. Changes in unit cell parameters with Ce^{3+} doping

For type III $KGd_{0.974}Ce_{0.026}(PO_3)_4$ crystal (2 at. % Ce^{3+} in solution), the unit cell parameters are $a = 7.2520(4)$ Å, $b = 8.3524(2)$ Å, $c = 7.9265(2)$ Å, $\beta = 91.826(3)°$, with

$Z = 2$, and the unit cell volume is 479.88(3) Å^3. For comparison, an undoped type III KGdP crystal was analysed by X-ray powder diffraction technique with the same conditions as the Ce-doped KGdP crystal, and its unit cell parameters were also refined using the TOPAS program[12], the Le Bail method[13] and the crystal data for undoped type III KGdP studied by Parreu *et al.*[14] (171710 ICSD database). Then, for the undoped KGdP, the unit cell parameters are $a = 7.2510(4)$ Å, $b = 8.3498(2)$ Å, $c = 7.9240(2)$ Å, $\beta = 91.823(3)°$, with $Z = 2$, and the unit cell volume is 479.51(3) Å^3. As can be seen, the parameters and volume of the unit cell increase slightly with the Ce^{3+} doping. This behaviour was expected because the ionic radius of Ce^{3+} with coordination VIII (1.143 Å[15]) is higher than the ionic radius of Gd^{3+} with the same coordination (1.053 Å[15]).

3.3. Type III Pr:KGd(PO$_3$)$_4$ bulk single crystals

3.3.1. Growth conditions, crystal morphology and composition

Type III Pr:KGd$(PO_3)_4$ (space group: $P2_1$) (hereinafter, Pr:KGdP) bulk single crystals were grown from high temperature solutions by the TSSG-SC technique. The solutions were composed of Pr_2O_3, K_2O, Gd_2O_3 and P_2O_5 with an excess K_2O and P_2O_5 as solvent, with the ratio K_2O:((1−x) Gd_2O_3 + x Pr_2O_3):P_2O_5 = 36:4:60 mol % with x ranging from 0 to 0.05[1,6]. The initial compounds were Pr_2O_3 (Alfa Aesar, 99.9%), K_2CO_3 anhydrous (Alfa Aesar, 99%), Gd_2O_3 (Sigma-Aldrich, 99.9%) and $NH_4H_2PO_4$ (Fluka Analytical, ≥99.0%). As the internal alumina tube (Figure 2.1) of the vertical tubular furnace used to grow the Pr:KGdP crystals had a larger diameter than the tube of the furnace used for the growth of the Ce:KGdP crystals, the solutions were prepared in a bigger platinum cylindrical crucible (50 mm in diameter and 50 mm in height). The total weight of the growth solutions, after the complete release of CO_2 and NH_3 coming from the starting reagents, was around 130 g.

Due to the high level of dynamic viscosity (~19 Pa·s[2]) of the growth solution, a high thermal gradient of around 1.1 K·mm^{-1} in depth with the hottest zone at the bottom of the crucible was applied to mix the solution and favour the arrival of the growth units to the crystal. In addition to this, a platinum stirrer of 18-22 mm diameter rotating at 55 rpm with a change of sense of rotation every 50 s was situated at 12-14 mm below the solution surface. The crystal seed used in each growth experiment was a small piece of undoped KGdP with the a^* crystallographic axis along the longer direction. The crystal seed was located in contact with the solution surface at 12 mm from the solution centre, with the *b* crystallographic direction tangential to the rotation movement and the *c* crystallographic direction in radial direction. The orientation of the seed described was chosen because it leads to the growth of single crystals with high crystalline quality[1,10]. The angular velocity of the crystal seed was the same as that of the stirrer because they were attached to the alumina rod with the same axis of rotation[2].

The saturation temperature of the solution in all the experiments was around 993 K. To maintain the supersaturation of the solution and thus allow the growth of the

crystal, the temperature of the solution was decreased 15 K from the saturation temperature with a cooling rate of 0.1 $K \cdot h^{-1}$ and for the next 10-15 K with a cooling rate of 0.05 $K \cdot h^{-1}$. The growth conditions of the crystal growth experiments carried out and the features of the Pr:KGdP bulk single crystals obtained are summarized in Table 1 of *Paper II*. The crystals were usually transparent, free of inclusions and cracks, and greenish due to the presence of Pr^{3+}. The green colour is more intense when the Pr^{3+} content is higher. Figure 3.3 shows as-grown type III Pr:KGdP single crystals (space group: $P2_1$) with the platinum stirrer or a centimetre scale. Figure 1 of *Paper II* shows an as-grown Pr:KGdP single crystal seen from the face of the crystal that is resting on the pylon (Figure 3.3.b-c) and a scheme of the crystal morphology with its faces labelled.

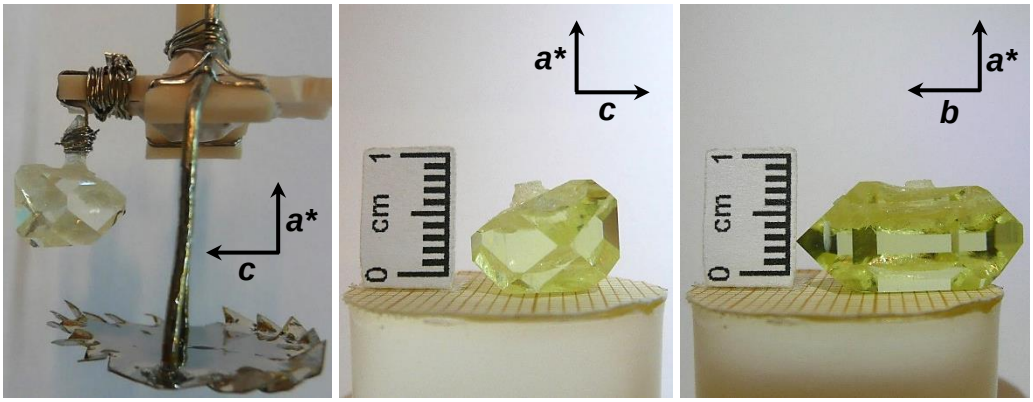

Figure 3.3. (a) As-grown 0.25 at. % Pr:KGdP single crystal with the platinum stirrer, (b) and (c) as-grown 1 at. % Pr:KGdP single crystal with the centimetre scale.

The weight of the Pr:KGdP bulk single crystals obtained ranged from 2.7 to 6.9 g, and their dimensions in $a^* \times b \times c^*$ crystallographic directions were 7.6-13.6 mm × 17.1-24.1 mm × 10.7-13.6 mm. In Figure 3.3, it can be verified that the crystal dimension in *b* direction is the longest and the dimension in *a** direction is the shortest. The growth rate is inversely proportional to the interplanar spacing d_{hkl}, and the sequence in this crystal is $d_{001} > d_{100} > d_{020}$, so this is consistent with the behaviour observed. In addition, the orientation of the seed chosen and the high axial thermal gradient in the solution reinforce the behaviour observed. The faster growth along the *b* crystallographic direction is in agreement with the no presence of the (010) crystalline face, since the faster a crystal grows along a direction, the smaller the face perpendicular to this direction. The faster growth along the crystallographic direction mentioned has been reported for different doping KGdP crystals[6,10,16]. The crystal growth rate varied from 6.1×10^{-3} to 17.4×10^{-3} $g \cdot h^{-1}$.

Using the EPMA results, as in the case of Ce:KGdP single crystals (Section 3.2.1), the chemical composition of the Pr:KGdP bulk single crystals was determined and the distribution coefficient of Pr^{3+}, K_{Pr}, was calculated for each concentration of doping studied according to the formula: $K_{Pr} = ([Pr]/([Pr] + [Gd]))_{crystal} / ([Pr]/([Pr] + [Gd]))_{solution}$. Table 3.3 shows this information along with the error of the values, while the number

of Pr^{3+} ions per unit cell volume in the crystals, calculated from the EPMA results as well, is shown in Table 2 of *Paper II*. Among the five doping levels studied, for the crystals obtained from solutions with 2.00 and 5.00 at. % of Pr^{3+} in the solution, the atomic percentage of each element was measured at various points along the crystallographic directions *a** and *c* in a plate perpendicular to the crystallographic axis *b* in order to study the homogeneity of the doping ion in the crystal. These results are shown in Figure S.1 in Supporting Information of *Paper II*, indicating that the Pr^{3+} atomic concentration of the growing crystals along the crystallographic directions *a** and *c*, up to 5.8 at. % of Pr^{3+} in the crystal, is uniform because the variation of the measured values of Pr^{3+} atomic concentration along the crystallographic directions is of the same order as the error in the measurements. The values of K_{Pr} in KGdP for the five doping levels studied and their error reveal that the Pr^{3+} distribution coefficient is not far from the unit in any case, and that there is no significant tendency to decrease or increase as the Pr^{3+} concentration in the solution increases.

Table 3.3. EPMA results for Pr:KGdP single crystals. K_{Pr} denotes the distribution coefficient of the Pr^{3+} in the crystal.

[Pr]/([Gd]+[Pr]) atomic % ratio in the solution	[Pr]/([Gd]+[Pr]) atomic ratio in the crystal	Chemical formula	K_{Pr}
0.25	0.003 ± 0.001	$KGd_{0.997}Pr_{0.003}(PO_3)_4$	1.2 ± 0.4
0.50	0.005 ± 0.002	$KGd_{0.995}Pr_{0.005}(PO_3)_4$	1.0 ± 0.4
1.00	0.010 ± 0.002	$KGd_{0.990}Pr_{0.010}(PO_3)_4$	1.0 ± 0.2
2.00	0.026 ± 0.001	$KGd_{0.974}Pr_{0.026}(PO_3)_4$	1.30 ± 0.05
5.00	0.058 ± 0.001	$KGd_{0.942}Pr_{0.058}(PO_3)_4$	1.16 ± 0.02

3.3.2. Changes in unit cell parameters with Pr^{3+} doping

Table 3 of *Paper II* shows the unit cell parameters (*a*, *b*, *c*, β) and unit cell volume of the $KGd_{1-x}Pr_x(PO_3)_4$ crystals with the Pr^{3+} doping concentrations studied, up to 5.8 at. % in the crystal. The evolution of these parameters and unit cell volume with the Pr^{3+} content is represented in Figure 2 of *Paper II*. There is an ascending linear behaviour of the five terms as the Pr^{3+} content in the crystals increases, with the unit cell volume being the term that changes most clearly. The *b* and *c* parameters slightly increase, while the *a* and β parameters practically keep the same as the doping content increases. Since the ionic radius of Pr^{3+} with coordination VIII (1.126 Å[15]) is higher than the ionic radius of Gd^{3+} with the same coordination (1.053 Å[15]), the observed increase of the five terms was expected. In the case of $KGd_{1-x}Nd_x(PO_3)_4$, the *a* parameter also is the unit cell parameter that increases with a minor proportion and the *b* and *c* parameters increase in a similar manner to each other when the Nd^{3+} content increases[14]. The same trend is observed in $KGd_{1-x}Yb_x(PO_3)_4$, but the *a*, *b* and *c* parameters decrease when the Yb^{3+} content increases because the ionic radius of Yb^{3+} with coordination VIII (0.985 Å[15]) is smaller than the ionic radius of Gd^{3+} with the same coordination.[6]

3.3.3. Thermal stability

The thermal stability of the $KGd_{0.942}Pr_{0.058}(PO_3)_4$ crystal, which corresponds to 5 at. % Pr^{3+} substituting Gd^{3+} in the solution, was studied by differential thermal and thermogravimetric analyses (DTA-TGA) and X-ray powder diffraction analyses at different temperatures. Figure 3.4 shows the differential thermal analysis (DTA) of the aforementioned crystal together with the DTA of an undoped KGdP crystal under the same measurement conditions. The thermogravimetric analyses (TGA) are not represented because the weight change was not significant in either cases. The endothermic peak of the undoped KGdP (Figure 3.4) is attributed to an incongruent melting process because this was concluded in a previous work after conducting the thermal study of another undoped KGdP crystal[1]. Consequently, the temperature indicated at the beginning of the endothermic peak (1140 K) of the $KGd_{0.942}Pr_{0.058}(PO_3)_4$ crystal corresponds to its incongruent melting point. Hence, as commented in *Paper II*, there is no appreciable difference in the incongruent melting temperature of KGdP with the Pr^{3+} doping up to 5.8 at. % in the crystal. In the cooling process of DTA, no peaks were observed, so no crystalline phase transitions occurred during this process.

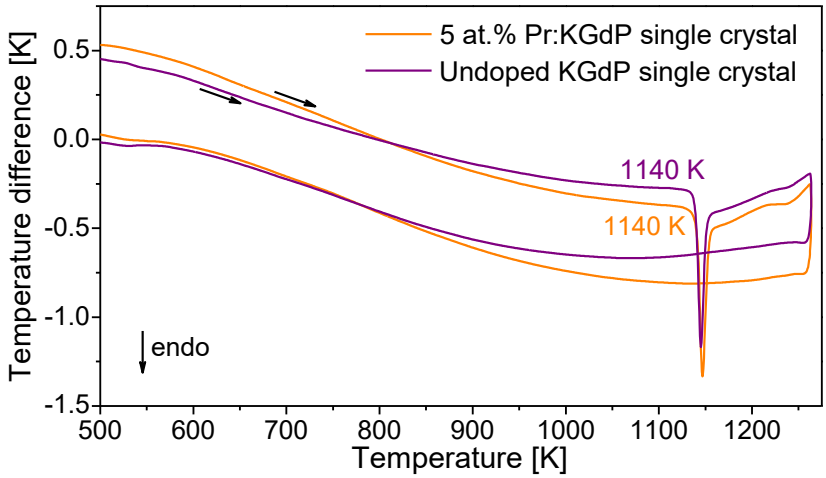

Figure 3.4. DTA of type III undoped KGdP and type III 5 at. % Pr:KGdP bulk single crystals in heating and cooling processes in the 500-1273 K temperature range.

Figure 3.5 shows the X-ray powder diffractogram of $KGd_{0.942}Pr_{0.058}(PO_3)_4$ at room temperature, the key diffractograms that show its evolution with temperature up to 1273 K and the diffractogram at room temperature after the cooling process. The temperature written on the right of each diffractogram are used as labels because it is expected that the temperature distribution in the sample holder was not homogeneous. This could lead to a partial incongruent melting process when the thermocouple of the diffractometer chamber indicated 1093 K. The diffraction standard patterns of type III $KGd(PO_3)_4$ (75-3878 ICDD database[14]), $GdPO_4$ (83-0657 ICDD database[17]) and a diffraction peak of platinum (corresponding to the sample holder used) are also shown. Figure 4 of *Paper II* shows diffractograms recorded at temperatures between those depicted in Figure 3.5.

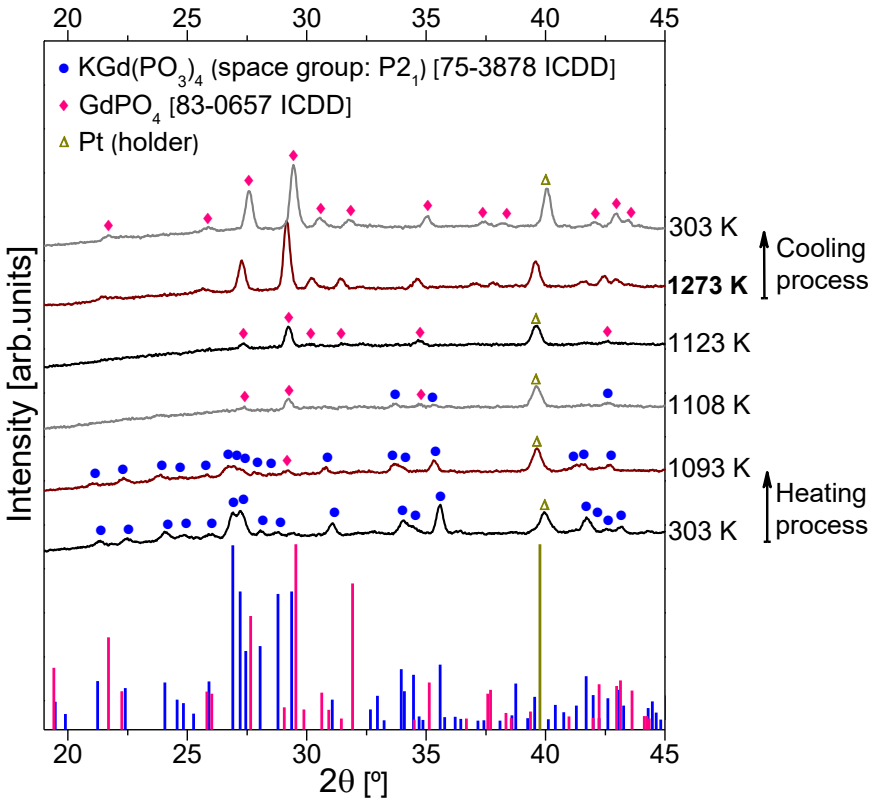

Figure 3.5. X-ray powder diffractogram of $KGd_{0.942}Pr_{0.058}(PO_3)_4$ at room temperature (RT), those selected at several temperatures describing its evolution with temperature in the heating process, the diffractogram at RT after the cooling process and three XRD standard patterns. The labelling of the diffractograms relates to the temperature read in the central part of the sample holder by the thermocouple.

Hence, it can be seen (Figure 3.5) that all diffraction peaks of the diffractogram at room temperature before the heating process correspond to the type III KGdP crystalline phase. The first temperature studied at which it could be seen that a diffraction peak belonged to a crystalline compound different from KGdP was 1093 K. This peak appeared at 29.2º and the new crystalline compound was identified as $GdPO_4$. Besides, the diffraction peaks belonging to KGdP decreased in their sharpness and intensity in the diffractogram at 1093 K. At 1108 K, KGdP and $GdPO_4$ show coexistence and at 1123 K the KGdP crystalline phase decomposed completely. It should be noted that differences in the phase transition temperature of a same compound were also observed in the work carried out by Ponceblanc *et al.*[18] when the authors used different techniques and different heating rates in the same technique. The only crystalline compound that is present from 1123 K to 1273 K is $GdPO_4$, which means that it is stable at this temperature range. In addition, it is necessary to comment that the sharpness and intensity of its diffraction peaks increase as the temperature is higher. During the cooling process, no significant changes were observed in any of the diffractograms studied. Therefore, $GdPO_4$ remains stable until room temperature

and this means that the phase transition of $KGd_{0.942}Pr_{0.058}(PO_3)_4$ is not reversible and the solidification of the liquid phase during the cooling process leads to an amorphous phase.

In summary, according to the differential thermal analysis and X-ray powder diffraction results, $KGd_{0.942}Pr_{0.058}(PO_3)_4$ decomposes irreversibly at 1140 K into $GdPO_4$ and liquid phase, which probably consisted of a mixture of phosphorus and potassium oxides due to the fact that the weight of the sample remained practically constant up to 1273 K. The thermal stability of $KGd_{0.942}Pr_{0.058}(PO_3)_4$ is compared in detail with those of $KGd(PO_3)_4$, $KYb_{0.029}Gd_{0.971}(PO_3)_4$ and $KLa(PO_3)_4$ in *Paper II*.

3.3.4. Evolution of the unit cell parameters with temperature. Thermal expansion tensor

Table 4 of *Paper II* shows the unit cell parameters of $KGd_{0.942}Pr_{0.058}(PO_3)_4$ crystal, which corresponds to 5 at. % Pr^{3+} in solution, at different temperatures (303, 323, 373, 473, 573, 673 and 773 K). The unit cell parameters were refined using the Le Bail method[13] and the crystal data for undoped type III KGdP (space group: $P2_1$) studied by Parreu *et al.*[14] (171710 ICSD database) in the TOPAS program[12]. To consider that a good fit is obtained and, therefore, the values of the unit cell parameters obtained are reliable, the expression that must be fulfilled is $R_{wp} \leq 2 \cdot R_{exp}$. In all cases these values were around $R_{wp} = 21$ and $R_{exp} = 18$.

The evolution of the unit cell parameters as a function of temperature with respect to those at room temperature (303 K) is represented in Figure 5 of *Paper II*. A linear trend was observed in all cases, but with different slope depending on the parameter. As the temperature increases, the *a* and *b* parameters clearly increase, as does the *c* parameter but in a smaller proportion, while β parameter slightly decreases. From these results, the linear thermal expansion coefficients in each crystallographic direction was calculated using the expression: $\alpha=(\Delta L/\Delta T)/L_{RT}$, where $\Delta L/\Delta T$ is the slope of the linear fit of the change of each unit cell parameter with the temperature and L_{RT} is the unit cell parameter at room temperature. The linear thermal expansion coefficients in the crystallophysical system $X_1 \| a$, $X_2 \| b$ and $X_3 \| c^*$ are shown in Table 3.4. Afterwards, by diagonalizing the tensor, the linear thermal expansion coefficients in the principal axes of the tensor X_1', $X_2' \| b$ and X_3' were obtained, and these values are also shown in Table 3.4.

Table 3.4. The linear thermal expansion coefficients of $KGd_{0.942}Pr_{0.058}(PO_3)_4$ at 303 K in (a) the crystallophysical system $X_1 \| a$, $X_2 \| b$ and $X_3 \| c^*$ and in (b) the principal axes of the tensor X_1', $X_2' \| b$ and X_3'.

(a) **Linear thermal expansion coefficients [10^{-6} K^{-1}]**		(b) **Linear thermal expansion coefficients [10^{-6} K^{-1}]**	
α_{11}	12.00	α'_{11}	12.43
α_{22}	12.40	α'_{22}	12.40
α_{33}	7.46	α'_{33}	7.03
α_{13}	1.45	-	-

The X_1' axis is at 16.31º clockwise from the *a* axis, while the X_3' at 14.44º from the *c* axis with the positive *b* axis pointing toward the observer. The linear thermal expansion ellipsoid of $KGd_{0.942}Pr_{0.058}(PO_3)_4$ at 303 K is depicted in Figure 3.6.

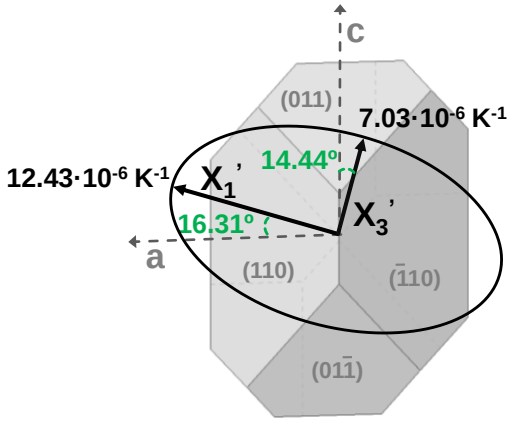

Figure 3.6. Linear thermal expansion ellipsoid of $KGd_{0.942}Pr_{0.058}(PO_3)_4$ at 303 K.

In the case of $KGd(PO_3)_4$, the linear thermal expansion coefficients in the principal axes of the tensor X_1', X_2' || *b* and X_3' are $\alpha'_{11} = 13.55 \times 10^{-6}$ K^{-1}, $\alpha'_{22} = 13.00 \times 10^{-6}$ K^{-1} and $\alpha'_{33} = 5.81 \times 10^{-6}$ K^{-1}, so they have similarity with the values of $KGd_{0.942}Pr_{0.058}(PO_3)_4$. The X_1' principal axis is at 4.76º clockwise from the *a* crystallographic axis, while the X_3' axis at 2.69º clockwise from the *c* axis with the positive *b* axis pointing towards the observer. The linear thermal expansion ellipsoid of $KGd(PO_3)_4$ at room temperature is shown in ref.[1].

References

[1] I. Parreu, R. Solé, Jna. Gavaldà, J. Massons, F. Díaz and M. Aguiló. Crystal growth, structural characterization, and linear thermal evolution of $KGd(PO_3)_4$. *Chem. Mater.* **2005**, *17*, 822-828.
[2] R. Solé, X. Ruiz, M. C. Pujol, X. Mateos, J. J. Carvajal, M. Aguiló and F.Díaz. Physical properties of self-flux and WO_3-containing solutions useful for growing type III $KGd(PO_3)_4$ single crystals. *J. Cryst. Growth* **2009**, *311*, 3656-3660.
[3] A. Jouini, M. Férid and M. Trabelsi-Ayadi. Equilibrium diagram of KPO_3–$Y(PO_3)_3$ system, chemical preparation and characterization of $KY(PO_3)_4$. *Thermochim. Acta* **2003**, 400, 199-204.
[4] Sigma-Aldrich. Yttrium(III) oxide, 99.99% trace metals basis (accessed 24/09/2018). https://www.sigmaaldrich.com/catalog/product/aldrich/205168?lang=es&region=ES
[5] A. Kruk, M. Mrózek, J. Domagała, T. Brylewski and W. Gawlik. Synthesis and physicochemical properties of yttrium oxide doped with neodymium and lanthanum. *J. Electron. Mater.* **2014**, *43* (9), 3611-3617.
[6] I. Parreu, R. Solé, J. Massons, F. Díaz and M. Aguiló. Crystal growth and characterization of type III ytterbium-doped $KGd(PO_3)_4$: A new nonlinear laser host. *Chem. Mater.* **2007**, *19*, 2868-2876.
[7] Sigma-Aldrich. Cerium(III) carbonate hydrate. SDS (Safety Data Sheet). https://www.sigmaaldrich.com/catalog/product/aldrich/325503?lang=es&region=ES (accessed 01/10/2018).
[8] Alfa Aesar. Potassium carbonate, anhydrous. FDS (Ficha de Seguridad de Datos). https://www.alfa.com/es/catalog/A16625/ (accessed 01/10/2018).
[9] I. Parreu, R. Solé, J. Massons, F. Díaz and M. Aguiló. Crystal growth, crystal morphology and surface micromorphology of type III $KGd(PO_3)_4$ and $KNd(PO_3)_4$. *Cryst. Growth Des.* **2007**, *7* (3), 557-563.
[10] R. M. Solé, M. C. Pujol, J. Massons, M. Aguiló, F. Díaz and A. Brenier. Growth, anisotropic spectroscopy and lasing of the monoclinic Nd:$KGd(PO_3)_4$ crystal. *J. Phys. D Appl. Phys.* **2015**, *48*, 495502-495512.
[11] I. Parreu, M. C. Pujol, M. Aguiló, F. Díaz, X. Mateos and V. Petrov. Growth, spectroscopy and laser operation of Yb:$KGd(PO_3)_4$ single crystals. *Opt. Express* **2007**, *15* (5), 2360-2368.
[12] XRD software – DIFFRAC.SUITE TOPAS V4.2. Bruker.
[13] A. Le Bail. Whole powder pattern decomposition methods and applications: A retrospection. *Powder Diffr.* **2005**, *20* (4), 316-326.
[14] I. Parreu, J. J. Carvajal, X. Solans, F. Díaz, and M. Aguiló. Crystal structure and optical characterization of pure and Nd-substituted type III $KGd(PO_3)_4$. *Chem. Mater.* **2006**, *18* (1), 221-228.
[15] R. D. Shannon. Revised effective ionic radii and systematic studies of interatomic distances in halides and chalcogenides. *Acta Cryst.* **1976**, *A32*, 751-767.
[16] I. Adell, R. M. Solé, M. C. Pujol, M. Lancry, N. Ollier, M. Aguiló and F. Díaz. Single crystal growth, optical absorption and luminescence properties under VUV-UV synchrotron excitation of type III Ce^{3+}:$KGd(PO_3)_4$, a promising scintillator material. *Sci. Rep.* **2018**, *8*, 11002. DOI: 10.1038/s41598-018-29372-z.
[17] Y.-X. Ni, J. M. Hughes and A. N. Mariano. Crystal chemistry of the monazite and xenotime structures. *Am. Mineral.* **1995**, *80*, 21-26.
[18] H. Ponceblanc, J. M. M. Millet, G. Thomas, J. M. Herrmann and J. C. Védrine. Comparative study of polymorphic phase transition by differential thermal analysis, high temperature X-ray diffraction, and temperature programmed electrical conductivity measurements. Case study of mixed iron and cobalt molybdate. *J. Phys. Chem.* **1992**, *96*, 9466-9469.

Chapter 4.

Synthesis and structural characterization of type III Pr:KGd(PO_3)$_4$ nanocrystals

4.1. Synthesis parameters of the nanocrystals by the modified Pechini method

4.2. Morphological characterization and particle size distribution

4.3. Changes in unit cell parameters with praseodymium doping

4.4. Thermal behaviour of the nanocrystals

This Chapter describes the details of the synthesis process of type III Pr:KGd(PO_3)$_4$ nanocrystals by modified Pechini method, as well as their morphological characterization and the particle size distribution. The predominant particle size range of the nanocrystals is from 10 to 20 nm. In addition, the effect of doping concentration on the unit cell parameters and the behaviour of these nanocrystals when the temperature increases are discussed. The synthesis of the nanocrystals was performed in the laboratories of the FiCMA-FiCNA research group of the *Universitat Rovira i Virgili* (URV, in Tarragona, Spain), and their characterization was carried out at *Servei de Recursos Científics i Tècnics* (SRCiT) of the URV, at *Centres Científics i Tecnològics* of the *Universitat de Barcelona* (CCiTUB, in Barcelona, Spain) and in the laboratories of Medcom Advance (Tarragona).

4.1. Synthesis parameters of the nanocrystals by the modified Pechini method

Praseodymium-doped KGd(PO$_3$)$_4$ (hereinafter, Pr:KGdP) nanocrystals were synthesized by the modified Pechini method. A schematic diagram of the modified Pechini synthesis process used for the preparation of these nanocrystals is shown in *Paper III* and the corresponding schematic illustration of the basic chemical reactions of the modified Pechini method[1,2,3,4,5,6,7] is shown in Figure 4.1.

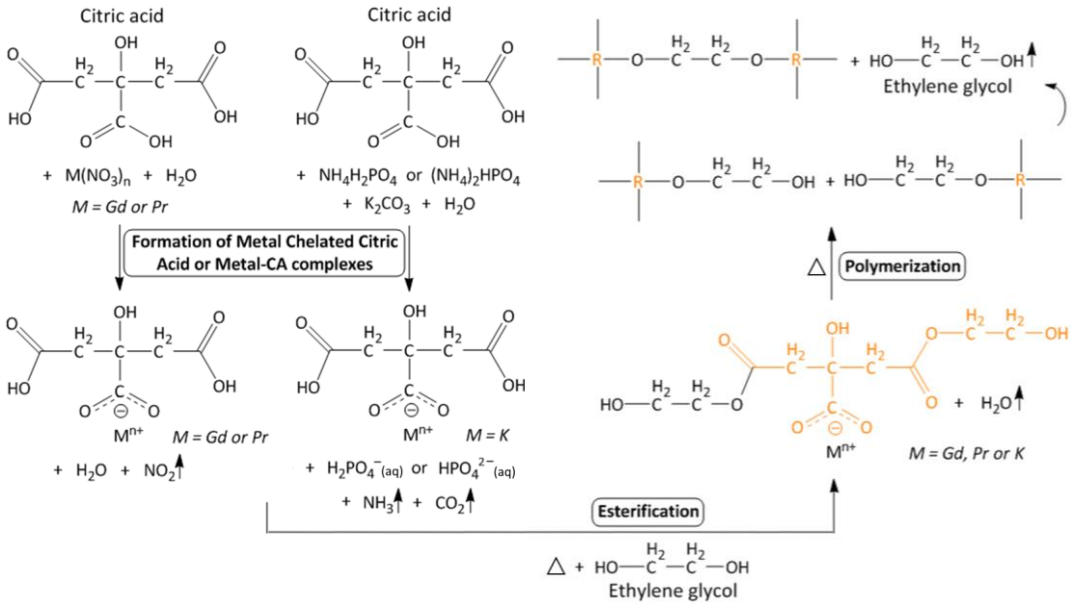

Figure 4.1. Basic chemical reactions involved in the preparation of the organic precursor in the modified Pechini method. Δ = heat is required for the reaction.

Powders of Pr_6O_{11}, K_2CO_3, Gd_2O_3, $NH_4H_2PO_4$ and $(NH_4)_2HPO_4$ anhydrous were used as starting materials. To synthesize 1 g of Pr:KGdP nanocrystals, at first, stoichiometric amounts of Pr_6O_{11} and Gd_2O_3 were mixed with 10 ml of concentrated HNO_3 (65 %) within a quartz crucible to obtain the lanthanide nitrates. To achieve this, the content of the crucible was heated to about 423 K under magnetic stirring until evaporating the liquid part. At the same time, stoichiometric amounts of K_2CO_3 and $NH_4H_2PO_4$ or $(NH_4)_2HPO_4$ were dissolved in distilled water into a glass beaker at 323 K. Unlike the Pechini synthesis process used to obtain nanocrystals of other chemical compounds, in this case, two different containers were used to avoid the precipitation of gadolinium phosphate[8]. Thereafter, citric acid, CA, was added in both containers in a specific molar ratio with the metal cations (C_M=[CA]/[METAL]), acting as chelating agent, to prepare metal-CA complexes. As can be seen in the first chemical reaction of Figure 4.1, the metal cations (M=Gd, Pr and K) are chelated by the carboxylate groups of citric acid. Therefore, C_M describes the degree of the chelation process of the metal cation in the organic chelating product[9]. To give rise to a good reaction between the reagents, the solution of each container was heated up to 348 K for 10-20 h under magnetic stirring and covered with a crystallizer. Just after

the incorporation of the CA, the pH of the solution was measured in order to control the pH of the chelation reaction. The crucible with gadolinium and praseodymium nitrates was named container 1 and the glass beaker with potassium carbonate and the phosphate precursor, $NH_4H_2PO_4$ or $(NH_4)_2HPO_4$, was named container 2. The pH in container 1 was pH_1=1, the pH in container 2 with $NH_4H_2PO_4$ as the phosphate precursor was pH_2=2 and with $(NH_4)_2HPO_4$ as precursor was pH_2=3. In addition, in order to study the effect of pH change in the chelation reaction, in one experiment, NH_4OH was added in the container 2 just after adding CA to vary the pH_2.

Afterwards, the content of the container 2 was added to the container 1 (quartz crucible) with the solution previously prepared in this container, and it was heated up to 373 K for 4 h under stirring and covered with a crystallizer. Then, ethylene glycol, EG, was added as esterification agent in a specific molar ratio, taking into account the previous concentration of citric acid (C_E=[CA]/[EG]), to obtain a polymeric resin[9]. The esterification reaction takes place between the hydroxyl groups of EG and the carboxylic acid groups of CA when enough temperature is applied, as shown the second chemical reaction of Figure 4.1[1,2]. Thus, the reagents were heated up to 473 K in a sand bath without being covered and under magnetic stirring for 3-4 h. During this step, the viscosity of the product gradually increases due to the cross-linking between units of CA until it gels[10], moment in which the magnetic stirrer should be removed. Therefore, the polymerization process occurs (Figure 4.1). Then, the product was maintained at the same temperature of 473 K for about 20 h more to obtain a dry polymeric resin. This stage was considered finished when a whitish gel was observed at the bottom of the quartz crucible, as shown Figure 4.2.a.

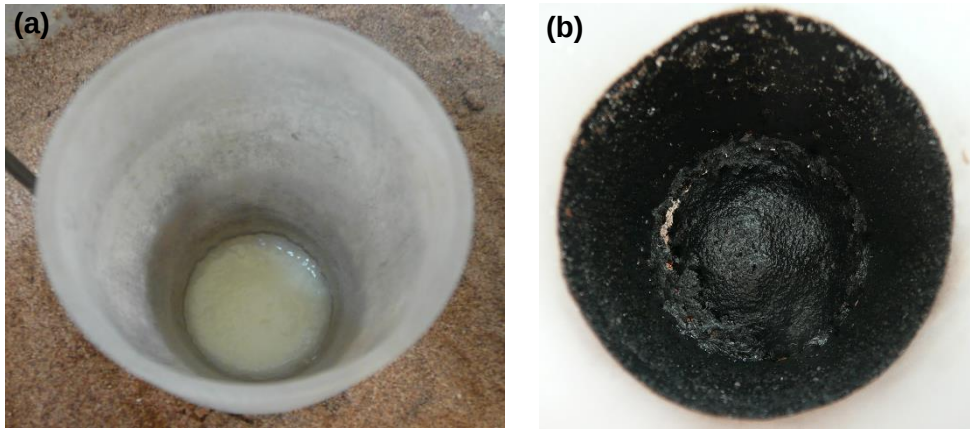

Figure 4.2. Quartz crucible with (a) the whitish gel obtained when the polymerization reaction is considered finished and (b) the shiny black spongy product obtained after the first calcination at 573 K for 10 h.

The following step was a first calcination of the polymeric resin at 573 K for several hours in air atmosphere to start its decomposition. The calcinations were performed in a vertical furnace, similar to the vertical tubular furnace shown in Figure 2.1, controlled by an Eurotherm temperature controller/programmer. After performing the

initial calcination, a product of spongy texture and shiny black colour was obtained, as shown in Figure 4.2.b. This product was grinded in an agate mortar and the resulting precursor powder was calcined at higher temperatures in air atmosphere for several hours in the temperature range from 673 to 1073 K. After each calcination, the resulting powder was grinded to facilitate the mixing of the precursors and the formation of crystalline phases. Tables 4.1 and 4.2 show the experimental parameters studied during the experiments carried out to synthesize $KGd_{1-x}Pr_x(PO_3)_4$ nanocrystals with a unique crystalline phase, type III phase (space group: $P2_1$). The final product of each experiment was analysed by X-ray powder diffraction to identify the obtained crystalline phases. The summary of the crystalline phases obtained in each experiment is shown in Tables 1 and 2 of *Paper III*. Besides, a complete discussion about the results of each experiment that concludes with the optimal experimental parameters required to synthesize these nanocrystals is also in *Paper III*.

Table 4.1. The experimental parameters studied during the experiments carried out to synthesize the type III Pr:KGdP nanocrystals using $NH_4H_2PO_4$ as a source of phosphate groups. In all cases, the atomic percentage of Gd substituted by Pr in KGdP is 1 at. % Pr, the pH in the chelation reaction in the quartz crucible with gadolinium and praseodymium nitrates is 1 (pH_1=1) and the pH in the glass beaker with K_2CO_3 and $NH_4H_2PO_4$ is 2 (pH_2=2).

Exp.	C_M	C_E	Calcination 1 [K-h]	Calcination 2 [K-h]
1	3	2	573-3	1073-3
2a	3	2	573-8	973-10
2b				1073-10
3a	3	1	573-10	973-10
3b				1073-10
4a	6	2	573-10	773-10
4b				873-10
4c				973-10
4d				1073-10
5a	6	1	573-10	773-10
5b				873-10
5c				973-10
5d				1073-10
6a	3	2	573-10	773-10
6b				873-10
6c				973-10
6d				1073-10

Table 4.2. The experimental parameters studied during the experiments carried out to synthesize the type III Pr:KGdP nanocrystals using $(NH_4)_2HPO_4$ as a source of phosphate groups. In all cases, C_M=3, pH_1=1, C_E=2 and a first calcination at 573 K for 10 h.

Exp.	Amount of Pr in KGdP [at. %]	pH_2►	Calcination 2 [K-h]	Calcination 3/4 [K-h]
7a	1	3	773-10	-
7b			673-10	823-10
7c			873-10	-
7d			723-10	873-5
7e			973-10	-
7f			1073-10	-
8a	1	5▼	823-10	-
8b			873-10	-
8c			723-10	873-5
8d			723-10	873-5/873-10
8e			973-10	-
8f			1073-10	-
9a	3	3	723-10	873-5
9b			773-10	873-5
10	5	3	773-10	873-7
11	10	3	773-10	873-7
12	0	3	773-10	873-7

► pH measured at the beginning of the chelation reaction in the glass beaker with $(NH_4)_2HPO_4$ and K_2CO_3 reagents.
▼ This pH was achieved by adding NH_4OH just after the incorporation of the citric acid.

The optimal parameters that make possible the synthesis of type III $KGd_{1-x}Pr_x(PO_3)_4$ nanocrystals by modified Pechini method are: the reaction time between reagents and the experimental conditions previously indicated in this Section, $(NH_4)_2HPO_4$ as the phosphate precursor, C_M=3, pH_2=3, C_E=2, a first calcination at 573 K for 10 h, a second one at 773 K for 10 h, and a third one at 873 K for 7 h.

Figure 4.3 shows the experimental X-ray powder diffractogram of the 5 at. % Pr:KGdP nanocrystals of experiment No. 10 of Table 4.2 and the powder diffraction standard pattern of type III KGd(PO_3)$_4$ (75-3878 ICDD database[11]). It can be clearly seen that the nanocrystals have been synthesized with a unique crystalline phase successfully.

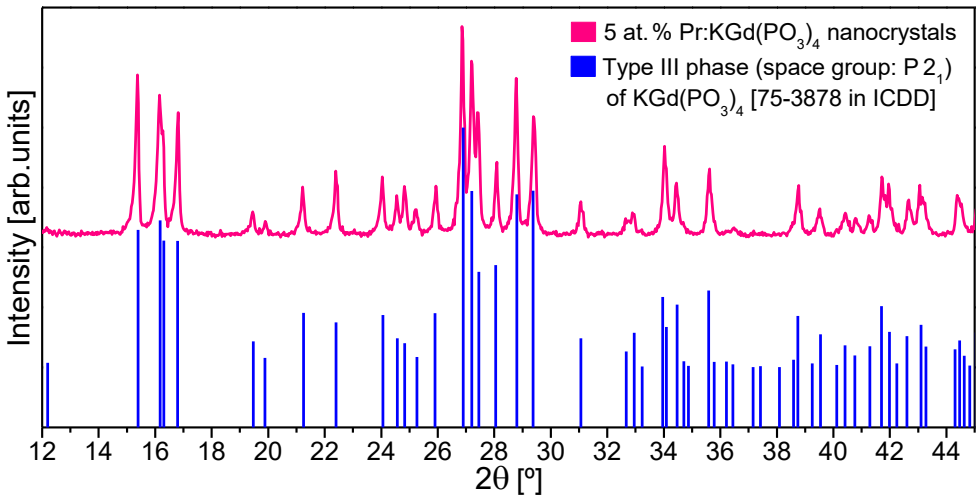

Figure 4.3. X-ray powder diffractogram of 5 at. % Pr:KGdP nanocrystals at room temperature and the powder diffraction standard pattern of type III KGd(PO$_3$)$_4$.

4.2. Morphological characterization and particle size distribution

The morphology of the nanocrystals were observed by scanning electron microscopy (SEM). Figure 4.4 shows representative SEM images of Pr:KGdP nanocrystals, where it can be seen how these nanocrystals form roughened aggregates consisting of several particles of different shapes and sizes.

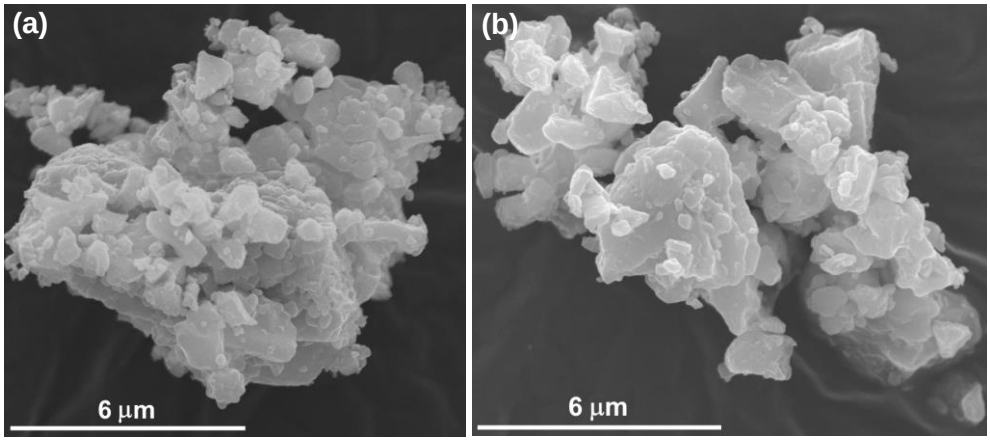

Figure 4.4. SEM images of (a) 3 at. % Pr:KGdP and (b) 5 at. % Pr:KGdP nanocrystals.

The agglomerates of nanocrystals were also seen by transmission electron microscopy (TEM), as can be observed in the irregular shape of some particles of Figure 4.5.a. In addition, this microscopy also allowed us to distinguish single nanocrystals, as it is shown in Figure 4.5.b. The particle size distribution of these nanocrystals was

estimated using multiple TEM images with iTEM 5.1 software, from Olympus Soft Imaging Solutions. To obtain a result statistically significant, around 715 particles of 5 at. % Pr:KGdP nanocrystals were measured. Representative TEM images of these nanocrystals and the histogram of the particle size distribution are shown in Figure 4.5. The particle length (see Figure 4.5.c) refers to the longest dimension of the particle. The distribution of the particle size was fitted by a lognormal function, which is expected in nanocrystals prepared by Pechini method because they follow the steps of nucleation, condensation and crystal particle growth[12,13]. As can be seen, the predominant particle size range is from 10 to 20 nm.

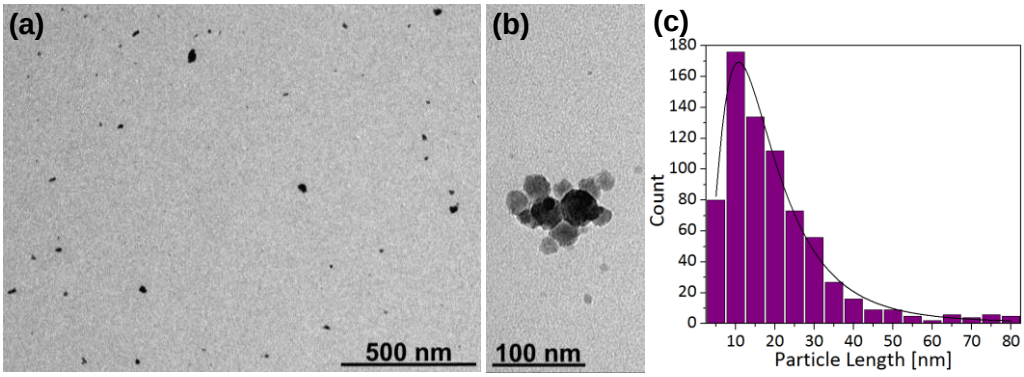

Figure 4.5. (a,b) Representative TEM images of 5 at. % Pr:KGdP nanocrystals and (c) histogram of the particle size distribution fitted by a lognormal function.

4.3. Changes in unit cell parameters with praseodymium doping

Once synthesized the type III $KGd_{1-x}Pr_x(PO_3)_4$ nanocrystals with different concentrations of praseodymium, the real atomic percentage of praseodymium was obtained by EPMA measurements. The first and second columns of Table 4.3 show the theoretical and measured atomic percentages of praseodymium with respect to gadolinium, respectively. The sample with a theoretical atomic percentage of 1 at. % of Pr was not measured by EPMA because the amount of praseodymium was considered too low. However, as the measured at. % of Pr in the other samples was very similar to the theoretical one, it was expected that the real atomic percentage was around 1 at. %.

Table 4.3. The theoretical and measured atomic percentages of Pr with respect to Gd in type III $KGd_{1-x}Pr_x(PO_3)_4$ nanocrystals, and the corresponding *a*, *b*, *c* and β unit cell parameters and unit cell volume.

Theoretical at. % of Pr	Measured at. % of Pr	*a* [Å]	*b* [Å]	*c* [Å]	β [°]	*V* [Å^3]
1	-	7.2486(3)	8.3505(3)	7.9204(3)	91.828(3)	479.17(3)
3	2.8	7.2488(4)	8.3517(4)	7.9215(4)	91.832(3)	479.32(4)
5	4.9	7.2509(4)	8.3553(5)	7.9247(4)	91.827(4)	479.86(5)
10	8.9	7.2512(3)	8.3575(4)	7.9285(4)	91.847(4)	480.23(4)

In order to study how the praseodymium content affects the unit cell parameters and the unit cell volume of these nanocrystals, the parameters of KGdP nanocrystals doped with different praseodymium concentrations and those of undoped KGdP were refined by the Rietveld method[14] using the TOPAS program[15]. The *a*, *b*, *c* and β unit cell parameters and the unit cell volume of undoped nanocrystals and nanocrystals doped with 2.8, 4.9 and 8.9 at. % of Pr with respect to the undoped KGdP are shown in Table 4.3. It can be appreciated that as the praseodymium content increases, the *a*, *b*, *c* and β unit cell parameters and the unit cell volume increase. However, the rate of increase is different depending on the unit cell parameter. This behaviour is graphically observed in Figure 4.6. The least pronounced increase is that of *a* parameter, the steeper one is that of *V*, and *b* and *c* parameters have a similar increase, slightly more pronounced than that of *a* parameter. A very similar trend is observed in the case of type III KGd$_{1-x}$Pr$_x$(PO$_3$)$_4$ single crystals (see Section 3.3.2). The increase of the unit cell volume as a function of praseodymium content within the KGdP structure was expected because the ionic radius of Pr^{3+} is higher than that of Gd^{3+} (ionic radii of Pr^{3+} and Gd^{3+} with coordination VIII are 1.126 Å and 1.053 Å, respectively[16]).

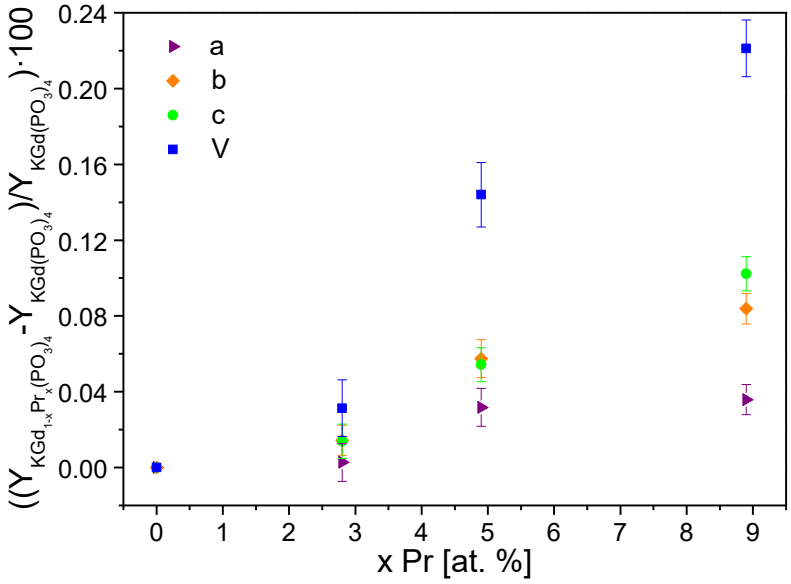

Figure 4.6. Relative evolution of the unit cell parameters and unit cell volume of type III KGd$_{1-x}$Pr$_x$(PO$_3$)$_4$ as a function of the praseodymium content.

4.4. Thermal behaviour of the nanocrystals

Figure 4.7 shows the differential thermal analysis (DTA) of type III 5 at. % Pr:KGdP nanocrystals and the differential thermal and thermogravimetric analyses (DTA-TGA) of type III 10 at. % Pr:KGdP nanocrystals together with the DTA of a type III Pr:KGdP bulk single crystal grown in this Thesis (see Section 3.3). Three endothermic peaks that starts at 1113 K, 1117 K and 1140 K can be observed, as well as a practically

non-existent decrease in the sample weight. Taking into account the study on thermal stability of a type III 5 at. % Pr:KGdP bulk single crystal between room temperature and 1273 K (see Section 3.3.3), the endothermic peaks of Figure 4.7 are attributed to the incongruent melting temperature of each sample. The decrease of the melting temperature of the nanocrystals with respect to that of the bulk single crystal observed was already expected due to a higher surface to volume ratio on the part of the nanocrystals[4,17]. In *Paper III*, it can be observed that the undoped KGdP nanocrystals melts incongruently at 1121 K.

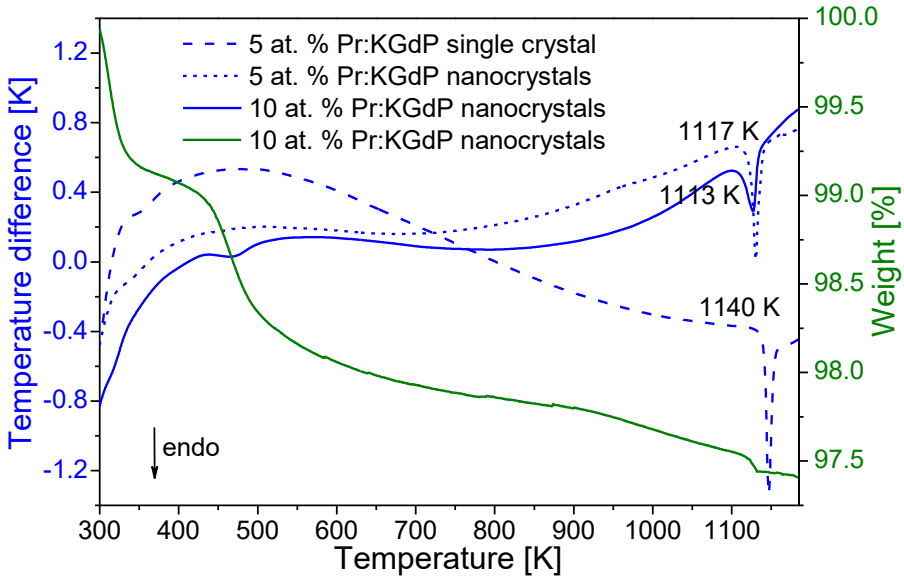

Figure 4.7. DTA of type III 5 at. % Pr:KGdP bulk single crystal, DTA of type III 5 at. % Pr:KGdP nanocrystals and DTA-TGA of type III 10 at. % Pr:KGdP nanocrystals in the 300-1185 K temperature range.

References

[1] W. Liu, C. C. Forrington, F. Chaput and B. Dunn. Synthesis and electrochemical studies of spinel phase $LiMn_2O_4$ cathode materials prepared by the Pechini process. *J. Electrochem. Soc.* **1996**, *143* (3), 879-884.
[2] S. W. Kwon, S. B. Park, G. Seo and S. T. Hwang. Preparation of lithium aluminate via polymeric precursor routes. *J. Nucl. Mater.* **1998**, *257*, 172-179.
[3] R. C. Lindsay. Food Additives. Chelating Agents (Sequestrants). In *Food Chemistry*. Edited by O. R. Fennema. Third Edition. Marcel Dekker Inc.: New York, NY, USA, **1996**; pp 778−780.
[4] M. Galceran, M. C. Pujol, J. J. Carvajal, S. Tkaczyk, I. V. Kityk, F. Díaz and M. Aguiló. Synthesis and characterization of $KTiOPO_4$ nanocrystals and their PMMA nanocomposites. *Nanotechnology* **2009**, *20*, 035705 (10 pp).
[5] D. Thangaraju, P. Samuel and S. Moorthy Babu. Growth of two-dimensional $KGd(WO_4)_2$ nanorods by modified sol–gel Pechini method. *Opt. Mater.* **2010**, *32*, 1321-1324.
[6] A. E. Danks, S. R. Hall and Z. Schnepp. The evolution of 'sol–gel' chemistry as a technique for materials synthesis. *Mater. Horiz.* **2016**, *3*, 91-112.
[7] Jiao Wang and Zhi-Jun Zhang. Luminescence properties and energy transfer studies of color tunable Tb^{3+}-doped $RE_{1/3}Zr_2(PO_4)_3$ (RE = Y, La, Gd and Lu). *J. Alloys Compd.* **2016**, *685*, 841-847.
[8] P. A. Lessing and A. W. Erickson. Synthesis and characterization of gadolinium phosphate neutron absorber. *J. Eur. Ceram. Soc.* **2003**, *23*, 3049-3057.
[9] M. Galceran, M. C. Pujol, M. Aguiló and F. Díaz. Sol-gel modified Pechini method for obtaining nanocrystalline $KRE(WO_4)_2$ (RE = Gd and Yb). *J. Sol-Gel Sci. Techn.* **2007**, *42*, 79-88.
[10] A. L. Morrissey. Preparation of high purity doped oxides for fundamental studies. Ph.D. Thesis, Colorado School of Mines, **2013**.
[11] I. Parreu, J. J. Carvajal, X. Solans, F. Díaz and M. Aguiló. Crystal structure and optical characterization of pure and Nd-substituted type III $KGd(PO_3)_4$. *Chem. Mater.* **2006**, *18* (1), 221-228.
[12] C. G. Granqvist and R. A. Buhrman. Ultrafine metal particles. *J. Appl. Phys.* **1976**, *47*, 2200-2219.
[13] J. Söderlund, L. B. Kiss, G. A. Niklasson and C. G. Granqvist. Lognormal size distributions in particle growth processes without coagulation. *Phys. Rev. Lett.* **1998**, *80* (11), 2386-2388.
[14] H. M. Rietveld. A profile refinement method for nuclear and magnetic structures. *J. Appl. Cryst.* **1969**, *2* (2), 65-71.
[15] XRD software – DIFFRAC.SUITE TOPAS V4.2. Bruker.
[16] R. D. Shannon. Revised effective ionic radii and systematic studies of interatomic distances in halides and chalcogenides. *Acta Cryst.* **1976**, *A32*, 751-767.
[17] S. Bhatt and M. Kumar. Effect of size and shape on melting and superheating of free standing and embedded nanoparticles. *J. Phys. Chem. Solids* **2017**, *106*, 112-117.

Chapter 5.
Spectroscopic characterization

This Chapter reports on the sample preparation of Ce:$KGd(PO_3)_4$ and Pr:$KGd(PO_3)_4$ (henceforth, Ce:KGdP and Pr:KGdP) bulk single crystals with type III crystalline structure (space group: $P2_1$) for spectroscopic studies, and the results of such studies of the resulting samples. The main spectroscopic studies are: optical absorption, luminescence and decay time measurements under VUV-UV excitation, decay time measurements under visible excitation, and radioluminescence measurements after X-ray irradiation. Furthermore, the optical absorption and Raman spectroscopy of these samples were studied before and after being excited with X-ray radiation to find out if there was radiation damage. Lastly, this Chapter describes the transmittance measurements of type III Pr:KGdP nanocrystals and luminescence measurements under visible and X-ray excitations. The main purpose of this exhaustive spectroscopic characterization of type III Ce:KGdP and Pr:KGdP is to find out and discuss the potential of these materials as possible new scintillator materials. These measurements allow us to know valuable information for scintillation applications, such as the determination of the position in energy of the 5*d* levels of Ce^{3+} and Pr^{3+} ions with respect to their corresponding ground states in type III KGdP, the lifetime of the $5d_1$ level of Ce^{3+} and that of Pr^{3+} in this host, the emission mechanisms under VUV-UV excitation and ionizing radiation, among others. On the other hand, some preliminary measurements have been made for possible future lasing applications.

The sample preparation and the optical absorption and transmittance studies were carried out at the laboratories of the FiCMA-FiCNA research group of the *Universitat Rovira i Virgili* (URV, in Tarragona, Spain). The luminescence and decay time measurements under VUV-UV excitation were performed in the DESIRS beamline at SOLEIL Synchrotron (Saint-Aubin, France) under the projects with proposal numbers 20151215 and 20161324. The decay time measurements under visible excitation were carried out at Medcom Advance's laboratories (Tarragona, Spain) and the radioluminescence measurements under X-ray excitation of the bulk single crystals were performed in the BL22-CLAESS beamline at ALBA Synchrotron (Cerdanyola del Vallès, Spain) under the project 2016091932. Finally, the Raman spectroscopy studies of the single crystals and the X-ray excited radioluminescence measurements of the nanocrystals were made at *Servei de Recursos Científics i Tècnics* (SRCiT) of the URV.

5.1. Sample preparation: orientation, cutting and polishing

The undoped, Ce- and Pr-doped KGdP bulk single crystals have been cut, lapped and polished in order to perform structural and spectroscopic studies (see Sections 5.2, 5.3 and 5.4) as a function of the crystallographic directions due to their optical anisotropy.

The faces that appear on the as-grown crystals were used as a reference to prepare plates perpendicular to the crystallographic directions *a**, *b* and *c**. To begin, *c**-oriented plates were prepared by cutting slices of the desired thickness parallel to the (001) faces using a Model 15 diamond wire saw from Logitech, as shown in Figure 2.4. *b*-oriented plates were prepared by cutting slices perpendicular to the (001) faces and with the cut direction parallel to *c** crystallographic direction using the same saw.

On the other hand, *a**-oriented plates were not prepared by cutting slices parallel to the (100) faces using the diamond wire saw, since the cleavage planes parallel to the {001} faces appeared when one performs a cut in this direction. *a**-oriented plates were prepared directly by lapping and polishing the (100) face of the as-grown crystal where the crystal seed zone is by sticking the opposite natural (100) face using a Logitech PM5 autopolisher machine (Figure 2.5) and a Logitech PM5 polisher. The details of the mentioned diamond wire saw for cutting as well as the equipment and procedure used for the lapping and polishing processes are described in Section 2.3. These *a**-, *b*- and *c**-oriented plates will be used in structural and spectroscopic studies to evaluate them as possible new scintillator materials.

In order to appropriately orientate and cut cubes perpendicular to the principal optical axes N_p, N_m and N_g, the angle between the optical axis N_g and the crystallographic axis *c** of the Ce:KGdP and Pr:KGdP crystals was determined. That is, the orientation of the optical frame of these crystals has been ascertained. As mentioned in Section 1.4.1, in KGdP, the principal optical axis N_p coincides with the crystallographic direction *b*. The procedure performed and the setup used to obtain the orientation of the optical frame are found in Section 2.3. Thus, considering a *b*-cut thick slice placed with the [010] direction pointing toward the observer, the principal optical axis N_g in Ce:KGdP and Pr:KGdP crystals is at 37º clockwise from the *c** direction, determined for 650 nm and at room temperature. This means that the principal optical axis N_g is at 53º anticlockwise from a natural edge in the (001) face, which is parallel to the crystallographic direction *a* (see Figure 5.1). The plane normal to N_g is cut with the diamond wire saw and afterwards, the sample is lapped and then polished by checking their parallelism, flatness and roughness (see Section 2.3). Finally, the plane normal to N_m is prepared at 90º of the plane normal to N_g directly by lapping and polishing. The parallelism, flatness and roughness of these two planes is also controlled. These cube-shape cut samples will be used in spectroscopic studies to evaluate them as possible future laser materials.

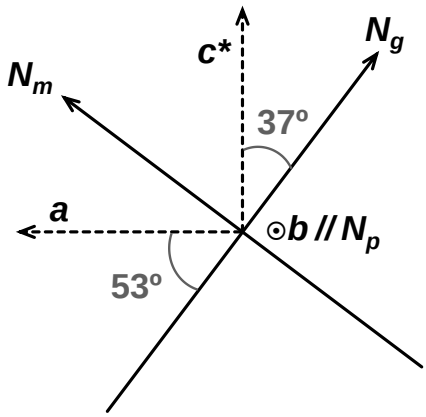

Figure 5.1. Orientation of the optical frame of Ce:KGdP and Pr:KGdP crystals, determined for $\lambda = 650$ nm and at room temperature. Projection parallel to [010] direction.

5.2. Spectroscopic characterization of type III Ce:KGd(PO$_3$)$_4$ bulk single crystals

The reasons for considering type III Ce:KGd(PO$_3$)$_4$ as a promising combination as a scintillator material, with type III KGdP being the host and Ce^{3+} the doping element, have been extensively discussed in Sections 1.3.2 and 1.4.1. The following spectroscopic studies are reported in *Papers I* and *IV*, although most of the figures presented here provide complementary information.

5.2.1. Unpolarized optical absorption at room temperature

Figure 5.2.a shows the unpolarized optical absorption coefficient at room temperature of $KGd_{0.996}Ce_{0.004}(PO_3)_4$ with non-centrosymmetric crystalline structure (type III phase, space group: $P2_1$) in the spectral range from 193 to 330 nm. The sharp peaks have been labelled as $4f \rightarrow 4f$ transitions of Gd^{3+} by using the Dieke's diagram[1], the extended Dieke's diagram[2] and the refs.[3,4], while the broad bands that are centred at 194, 215, 226, 243.5 and 302.5 nm have been assigned to the $4f \rightarrow 5d$ transitions of Ce^{3+} in type III KGdP, more specifically to the $^2F_{5/2} \rightarrow 5d_5$, $^2F_{5/2} \rightarrow 5d_4$, $^2F_{5/2} \rightarrow 5d_3$, $^2F_{5/2} \rightarrow 5d_2$, $^2F_{5/2} \rightarrow 5d_1$ transitions, respectively. As it is known, unlike the $4f$ energy levels of the lanthanide ions, the position of the $5d$ energy levels of a particular lanthanide ion varies depending on the crystal host in which this ion is doped, since the $5d$ electrons present a strong interaction with the crystal field[5,6,7]. The bands corresponding to these electronic transitions are also wide because the $5d$ electrons interact with the lattice phonons. In type III KGdP, Gd^{3+} is in a C_1 position inside a GdO_8 distorted dodecahedra, so the Ce^{3+} is in the same crystalline environment when it is introduced into the crystal when replacing partly the Gd^{3+} ions, which leads to a splitting of the $5d$ levels of Ce^{3+} in five non-degenerated crystal-field levels. As can be seen in Table 5.1, the central value of the broad bands assigned to the five $^2F_{5/2} \rightarrow 5d_x$ transitions of Ce^{3+} in the non-centrosymmetric KGdP crystal are very close to the reported values for the centrosymmetric KGdP (space group: $C2/c$)[8], respectively. The wavelength central values of the absorption bands of the $5d$ levels of Ce^{3+} in other similar crystalline phosphates are also shown in the same table.

Figure 5.2.b displays the optical absorption cross section of four of the five $^2F_{5/2} \rightarrow 5d_x$ transitions of Ce^{3+} in type III KGdP crystal. Subtracting the absorbance background, the observed values are from highest to lowest 350×10^{-20} cm^2 at 302.5 nm, 215×10^{-20} cm^2 at 243.5 nm, 97×10^{-20} cm^2 at 226 nm and 53×10^{-20} cm^2 at 215 nm. As $5d \rightarrow 4f$ transitions are parity-allowed transitions, high values of optical absorption cross section were expected. It is worth mentioning that the photons at 195, 246 and 305 nm excite Gd^{3+} ions, as well as clearly excite Ce^{3+} ions; whereas those at 215 and 226 nm excite only Ce^{3+} ions.

Table 5.1 summarizes the spectroscopic properties and crystallographic space groups of $KGd_{0.996}Ce_{0.004}(PO_3)_4$ and other Ce^{3+}-doped phosphates. The spectroscopic redshift, D(A), the crystal field splitting, ε_{cfs}, and the centroid shift, ε_c, of $KGd_{0.996}Ce_{0.004}(PO_3)_4$ with the non-centrosymmetric crystalline phase (space group: $P2_1$) have been calculated by using the optical absorption spectrum in Figure 5.2.a.

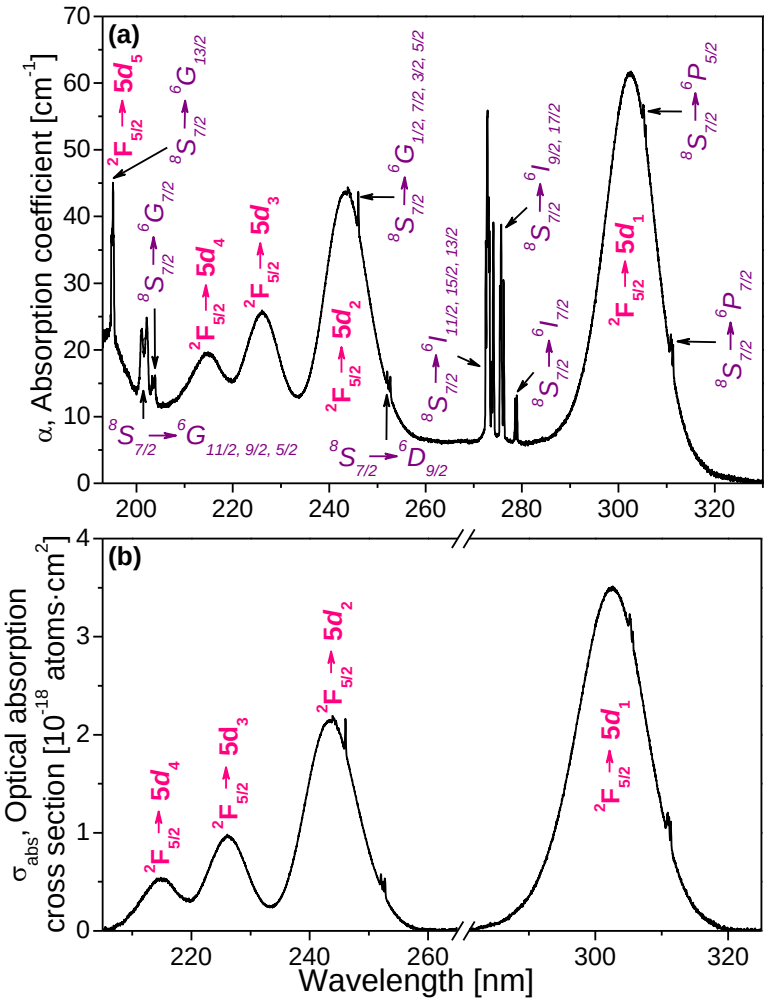

Figure 5.2. (a) Unpolarized optical absorption coefficient of $KGd_{0.996}Ce_{0.004}(PO_3)_4$ at room temperature. Propagation direction is along *b* crystallographic axis. Labels in purple and italics indicate the electronic transitions of Gd^{3+} assigned to each observed peak, and labels in pink and bold those of Ce^{3+}. (b) Unpolarized optical absorption cross section of the $^2F_{5/2} \rightarrow 5d_1$, $5d_2$, $5d_3$, $5d_4$ transitions of Ce^{3+} in KGdP using the same sample at room temperature.

The spectroscopic redshift of a host A, *D*(A), is defined as the decrease in energy of the first $4f \rightarrow 5d$ dipole allowed transition of the lanthanide ion (Ln^{3+}) as free ion with respect to that value when this Ln^{3+} ion is inside the crystalline lattice, due to its strong interaction with the crystal field of the host A[6,9]. Therefore, this shift is expected to be the same for any Ln^{3+} ion used as scintillator centre in the type III KGdP host[10]. As the energy of the $4f \rightarrow 5d_1$ transition of Ce^{3+} as free gaseous ion is 49340 cm^{-1} [10] and that of the Ce^{3+} ion inside the crystal of the type III KGdP host is 33058 cm^{-1} (302.5 nm), the spectroscopic redshift is *D*(type III KGdP) = 16282 cm^{-1}. The tendency observed in the table with regards to the value of the *D*(A) of the different hosts, which

is its decrease as the alkaline ion is smaller (K > Na > Li), was already observed in the phosphates by Dorenbos *et al.*[10]. The polyphosphate compounds have a large fraction of strongly bonded phosphate groups, a fact that causes that their *D*(A) are amongst the smallest of all oxide compounds[11]. As mentioned in Section 1.4.1, PO_4 tetrahedra share one of their four oxygen atoms with a gadolinium atom, so the distance of Gd−O bond is extended due to the strong P−O bonds. For this reason, Gd^{3+} (consequently, Ln^{3+} as well) is less affected by the crystal field of the host, and therefore, there is a minor splitting of the 5*d* levels of the Ln^{3+}.

Table 5.1. Spectroscopic properties and crystallographic space groups of Ce^{3+}-doped phosphates. λ_5, λ_4, λ_3, λ_2, λ_1 = absorption bands of the 5*d* levels, *D*(A) = spectroscopic redshift of host A, ε_c = centroid shift, ε_{cfs} = crystal field splitting, R_{eff} = effective distance of Gd−O, and α_{sp} = spectroscopic polarizability.

Compound [Ref.]	Space group	λ_5, λ_4, λ_3, λ_2, λ_1 [nm]	*D*(A) [cm^{-1}]	ε_{cfs} [cm^{-1}]	ε_c [cm^{-1}]	R_{eff} [Å]	α_{sp} [10^{-30} m^3]
$KGd_{0.996}Ce_{0.004}(PO_3)_4$ [12]	$P2_1$	194, 215, 226, 243.5, 302.5	16282	18489	7944	2.447	1.479
$KGd_{0.99}Ce_{0.01}P_4O_{12}$ [8]	$C2/c$	193, 209, 221, 245, 307	16767	19240	7570	2.453	1.431
$NaGd_{0.99}Ce_{0.01}(PO_3)_4$ [8]	$P2_1/n$	196, 207, 218, 254, 297	15670	17350	7582	2.443	1.398
$NaPr_{0.9}Ce_{0.1}P_4O_{12}$ [13]	$P2_1/n$	195, 230, 252, 268, 295	15442	17300	7332	—	—
$LiLa_{0.95}Ce_{0.05}P_4O_{12}$ [14]	$C2/c$	—, —, —, —, 278	13369	—	—	—	—

The crystal field splitting, ε_{cfs}, is the energy difference between the $5d_1$ and the $5d_5$ levels[9]. This is determined by the strength of the crystal field, which is related to the shape and the size of the coordination polyhedron of the Ln^{3+} ion. That is, for example, considering the same polyhedral shape, a smaller bond length and larger distortion will result in a higher value of the crystal field splitting[6]. Both in the non-centrosymmetric KGdP (space group: $P2_1$)[12] and the centrosymmetric KGdP (space group: $C2/c$)[8], the coordination figure of the Ce^{3+} ion is a dodecahedron. Then, since the average distance between the O and Gd ions in such hosts is 2.4065 Å and 2.408 Å, respectively, and they have similar distortion in the cation site, a higher value of the ε_{cfs} would be expected for the non-centrosymmetric KGdP. Despite all this, the observed behaviour (Table 5.1) is the opposite, so this different crystal field that the Ce^{3+} ions are subject to may be related to effects in the second coordination sphere. Among all oxide compounds, polyphosphates are those that have their ε_{cfs} amongst the largest due to the large fraction of strongly bonding phosphate atoms[11].

The centroid shift, ε_c, is defined as the energy difference between the centroid value of the 5*d* levels of the free ion and the one inside the crystalline structure. The centroid position of the 5*d* energy levels corresponds to the average energy of the five levels, 43286 cm^{-1} being its value for Ce^{3+} ion in the non-centrosymmetric KGdP crystal. The centroid position of the 5*d* energy levels of Ce^{3+} in a free ion is 51230 cm^{-1} [6]. Once

ε_c is obtained, this value along with the crystallographic data of the undoped non-centrosymmetric KGdP[15] are used to calculate the effective distance of Gd−O bond (Å), R_{eff}, and the spectroscopic polarizability (10^{-30} m^3 or Å^3), α_{sp}, as in the ref.[8] using the expressions shown in Eqs. 5.1 and 5.2. Here, *N* is the coordination number of Gd^{3+}, R_i are the distances of each different Gd−O bond in the unperturbed lattice (pm), and Δr is the difference in ionic radii of Ce^{3+} and Gd^{3+} with coord. VIII (Å, tabulated by Shannon[16]). Thus, the centroid shift, ε_c, has no dependence on the crystal field splitting value and may be related to the ligand polarization[7]. The fact that the ε_c for the non-centrosymmetric KGdP is higher than the value for the centrosymmetric KGdP should be attributed, taking into account the ligand polarization model[7], to the major contribution of the effective distances, R_{eff}, in the value of centroid shift.

$$\frac{\varepsilon_c}{N} = \frac{1.44 \times 10^{17}\, \alpha_{sp}}{R_{eff}^6} \qquad \text{Eq. 5.1}$$

$$\frac{1}{R_{eff}^6} = \frac{1}{N} \sum_{i=1}^{N} \frac{1}{\left(R_i - \frac{1}{2}\Delta r\right)^6} \qquad \text{Eq. 5.2}$$

It should be noted that all the spectroscopic parameters discussed previously depend on the crystalline host, so they are affected by the Ce^{3+} concentration in the crystal and temperature.

5.2.2. Luminescence measurements under VUV-UV excitation

Figure 5.3 shows the optical emission spectra of $KGd_{0.981}Ce_{0.019}(PO_3)_4$ and those of $KGd_{0.974}Ce_{0.026}(PO_3)_4$ at room temperature under direct $^2F_{5/2} \rightarrow 5d_x$ excitation of Ce^{3+} in this host. The absorption bands of the 5*d* levels of Ce^{3+} in type III KGdP are centred at 194 nm ($^2F_{5/2} \rightarrow 5d_5$), 215 nm ($^2F_{5/2} \rightarrow 5d_4$), 226 nm ($^2F_{5/2} \rightarrow 5d_3$), 243.5 nm ($^2F_{5/2} \rightarrow 5d_2$) and 302.5 nm ($^2F_{5/2} \rightarrow 5d_1$), as can be seen in Section 5.2.1. The optical emission spectra of $KGd_{0.996}Ce_{0.004}(PO_3)_4$ crystal under 244, 226, 214 and 194 nm excitation are shown in Figure 3 of *Paper I*. In all cases, the intensities have been corrected by the excitation photon flux values. The most intense band in all emission spectra, for each sample studied and under the four different excitation wavelengths, is a doublet peak centred at 322 and 342 nm, which have been ascribed to the $5d_1 \rightarrow {}^2F_{5/2}$ and $5d_1 \rightarrow {}^2F_{7/2}$ transitions, respectively, of Ce^{3+} in KGdP. As can be seen in the Dieke's diagram[1], the energy difference between the $^2F_{5/2}$ and $^2F_{7/2}$ levels of Ce^{3+} is consistent with the energy difference between the central position of the two mentioned bands. Both in Figure 5.3 and in Figure 3 of *Paper I*, differences in emission intensity of the doublet band can be seen depending on the excitation wavelength. This behaviour is in accordance with the values of absorption coefficient for each excitation wavelength (see Figure 5.2.a), except when the samples are excited at 194 nm since an emission intensity similar to that obtained after exciting the samples at ~215 nm would be expected due to their similar absorption coefficient values. This might be attributed to a depopulation of the $5d_5$ level of Ce^{3+} due to an energy transfer to the 4*f* levels of Gd^{3+}.

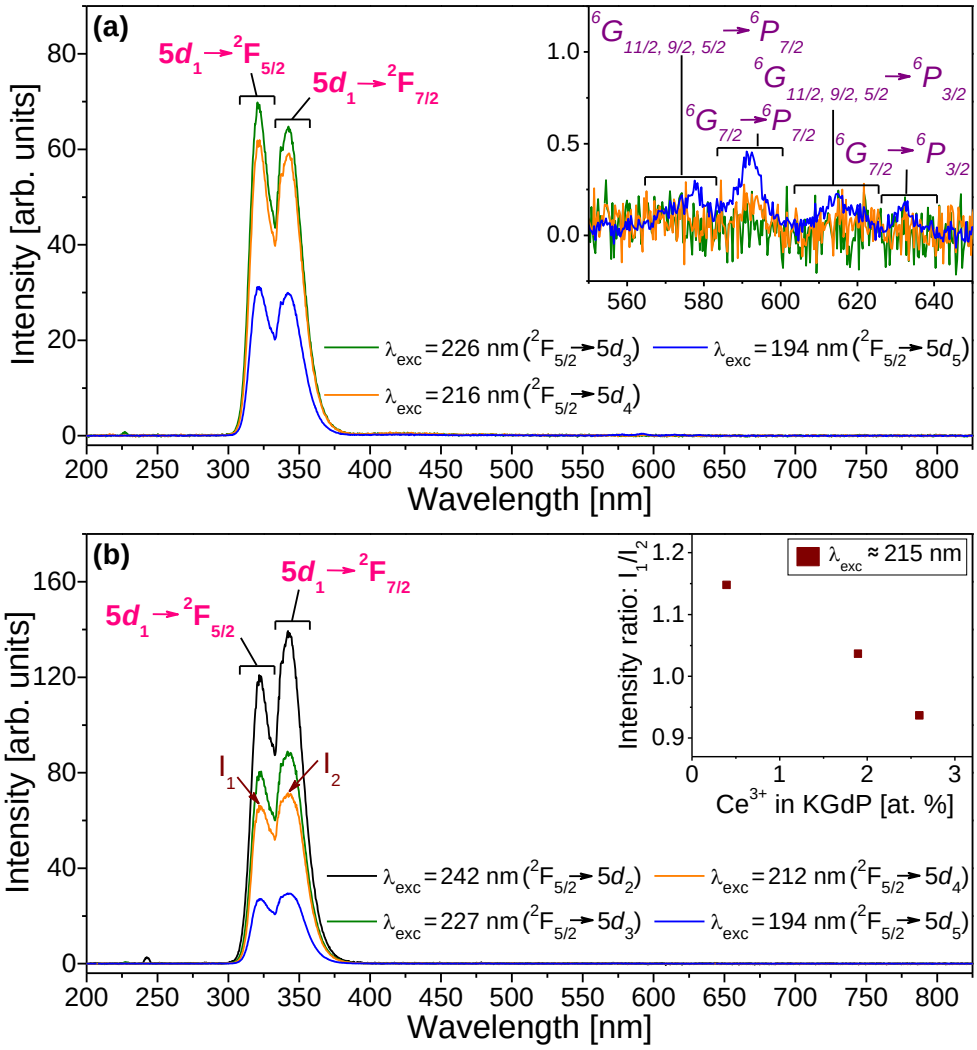

Figure 5.3. (a) Optical emission spectra of $KGd_{0.981}Ce_{0.019}(PO_3)_4$ under 226, 216 and 194 nm excitation at room temperature. Inset: close detail of the wavelength range from 550 to 650 nm. Labels in pink and bold indicate the electronic transitions of Ce^{3+}, and labels in purple and italics those of Gd^{3+}. (b) Optical emission spectra of $KGd_{0.974}Ce_{0.026}(PO_3)_4$ under 242, 227, 212 and 194 nm excitation at room temperature. Inset: intensity ratio of the emission peaks belonging to the $5d_1 \rightarrow {}^2F_{5/2}$ transition (I_1) and the $5d_1 \rightarrow {}^2F_{7/2}$ transition (I_2) of Ce^{3+} under around 215 nm excitation ($^2F_{5/2} \rightarrow 5d_4$) versus the Ce^{3+} content in the crystal. In both cases, propagation direction is along the *c** crystallographic axis, with the *b* crystallographic axis pointing upwards.

The inset of Figure 5.3.b displays the intensity ratio of the emission peaks corresponding to the $5d_1 \rightarrow {}^2F_{5/2}$ transition (I_1) and the $5d_1 \rightarrow {}^2F_{7/2}$ transition (I_2) of Ce^{3+} in the KGdP samples studied under around 215 nm excitation ($^2F_{5/2} \rightarrow 5d_4$) versus the Ce^{3+} content in the crystal. A decrease in intensity of the emission peak belonging to the $5d_1 \rightarrow {}^2F_{5/2}$ transition (I_1) can be clearly observed as the Ce^{3+} content increases.

This behaviour may be due to the existence of reabsorption of the emission corresponding to the $5d_1 \rightarrow {}^2F_{5/2}$ transition by the neighbouring Ce^{3+} atoms due to the increase in Ce^{3+} concentration and, therefore, to a shorter distance between them.

The Stokes shift of a host A, ΔS(A), is a parameter defined as the energy difference between the energy value corresponding to a specific absorption electronic transition of a Ln^{3+} ion in this host and that belonging to the emission between the same levels of the same Ln^{3+} ion. That is, since the energy value corresponding to the ${}^2F_{5/2} \rightarrow 5d_1$ transition of Ce^{3+} in type III KGdP crystal is 33058 cm^{-1} (302.5 nm) and the emission band belonging to the $5d_1 \rightarrow {}^2F_{5/2}$ transition appears centred at 322 nm (31056 cm^{-1}), the Stokes shift of this host is ΔS(type III KGdP) = 2002 cm^{-1}. The ΔS(A) does not depend on the lanthanide ion, but only on the host. Consequently, this value can be extrapolated for future doping ions in type III KGdP crystals[10]. The Stokes shift is induced by lattice relaxation at the excited states. Thus, as the Stokes shift value increases, the relaxation of the electrons at the excited state before emitting electromagnetic radiation also increases, leading to higher non-radiative losses[9,17]. The ΔS(A) of three phosphates similar to our compound has been calculated in *Paper I* taking into account the energy values corresponding to the same electronic transitions of Ce^{3+} in these hosts, the type III KGdP being the host with the highest Stokes shift. However, the most frequent Stokes shift measured in 240 different compounds is 2200 cm^{-1} [5], so the Stokes shift of type III KGdP is slightly below.

It is important to note that the ${}^6P_{7/2} \rightarrow {}^8S_{7/2}$ electronic transition of Gd^{3+}, which is common in many hosts[3,4,18,19] and appears as a sharp emission peak centred around 311 nm, is not present in type III $KGd_{0.996}Ce_{0.004}(PO_3)_4$, $KGd_{0.981}Ce_{0.019}(PO_3)_4$ and $KGd_{0.974}Ce_{0.026}(PO_3)_4$ crystals (space group: $P2_1$) under any wavelength excitation studied, as observed in Figure 3 of *Paper I* and Figure 5.3. In the work on the luminescence properties of the Ce^{3+}-doped $KGdP_4O_{12}$ host with type B phase (space group: $C2/c$) done by Zhong *et al.*[8], similar results were observed under direct ${}^2F_{5/2} \rightarrow 5d_1$ excitation since the emission doublet band corresponding to the $5d_1 \rightarrow {}^2F_{5/2}$ and $5d_1 \rightarrow {}^2F_{7/2}$ transitions of Ce^{3+} appears centred at 323 and 343 nm, respectively, and the emission of Gd^{3+} at 311 nm is not present either. However, when Ce:$KGdP_4O_{12}$ is excited at 193 nm (${}^2F_{5/2} \rightarrow 5d_5$), the aforementioned emission of Gd^{3+} looks very weak as a hump in the band corresponding to the emission from the $5d_1$ level to the ${}^2F_{5/2}$ ground state. This Gd^{3+} emission appears even more intensely than the Ce^{3+} emission peaks corresponding to the $5d_1 \rightarrow {}^2F_{5/2,7/2}$ transitions in Ce:$LiGdP_4O_{12}$ (space group: $C2/c$) and Ce:$NaGdP_4O_{12}$ (space group: $P2_1/n$) crystals[8]. Therefore, in the type III KGdP crystal, this Gd^{3+} emission is extremely rare compared to the emissions of Ce^{3+}.

The inset of Figure 5.3.a is a close detail of the wavelength range from 550 to 650 nm of the spectra. There, it can be seen the existence of four weak peaks centred at 578, 592, 613 and 633 nm when the $KGd_{0.981}Ce_{0.019}(PO_3)_4$ crystal is excited at 194 nm. These emission peaks have been labelled as the ${}^6G_{11/2,9/2,5/2} \rightarrow {}^6P_{7/2}$, ${}^6G_{7/2} \rightarrow {}^6P_{7/2}$, ${}^6G_{11/2,9/2,5/2} \rightarrow {}^6P_{3/2}$ and ${}^6G_{7/2} \rightarrow {}^6P_{3/2}$ transitions of Gd^{3+}, respectively, using the Dieke's diagram[1], the extended Dieke's diagram[2] and the refs.[3,4]. The same behaviour has been observed in the $KGd_{0.996}Ce_{0.004}(PO_3)_4$ sample (see *Paper I*).

The $^8S_{7/2} \rightarrow {}^6G_{13/2}$ absorption transition of Gd^{3+} is about 194 nm, so it overlaps with the $^2F_{5/2} \rightarrow 5d_5$ transition of Ce^{3+}, as can be seen in Figure 5.2.a. Therefore, this may be the reason for the appearance of the emission peaks of Gd^{3+} in the spectral range from 560 to 640 nm. The energy levels of Gd^{3+} and Ce^{3+} ions in $KGd_{0.996}Ce_{0.004}(PO_3)_4$ and $KGd_{0.981}Ce_{0.019}(PO_3)_4$ and the possible energy transfer mechanism are shown in Figure 5.4.

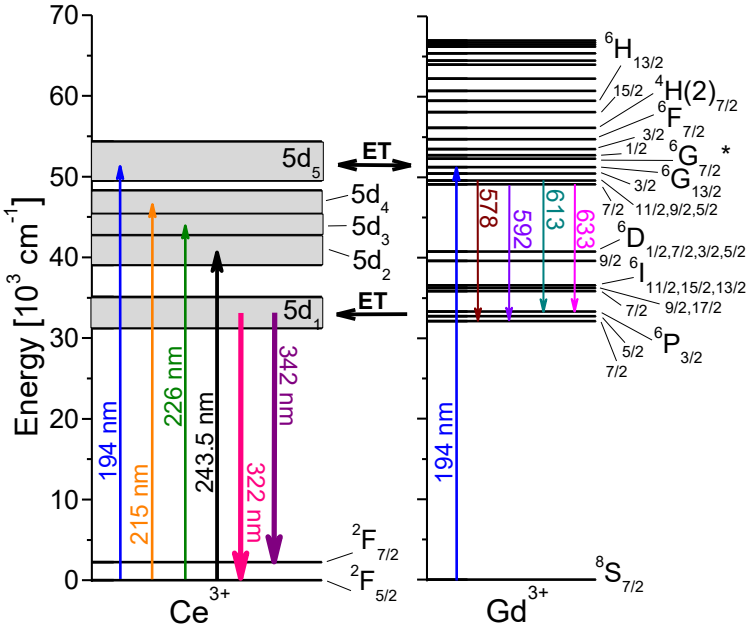

Figure 5.4. Energy levels diagram of Ce^{3+} and Gd^{3+} ions in $KGd_{0.996}Ce_{0.004}(PO_3)_4$ and $KGd_{0.981}Ce_{0.019}(PO_3)_4$ and the emission mechanism. ET = Energy Transfer. The thickness of the arrows is related to the intensity of the optical absorptions and emissions represented.

Figure 5.5 shows the excitation spectra of $KGd_{0.996}Ce_{0.004}(PO_3)_4$ for the emission wavelengths $\lambda_{emi} = 322$ nm ($5d_1 \rightarrow {}^2F_{5/2}$ of Ce^{3+}) and $\lambda_{emi} = 613$ nm ($^6G_{11/2,9/2,5/2} \rightarrow {}^6P_{3/2}$ of Gd^{3+}) at room temperature. The intensities have been corrected by the excitation photon flux values. The excitation spectrum for the emission of Ce^{3+} (Figure 5.5.a) allows us to reaffirm that there is an energy transfer from Gd^{3+} to Ce^{3+} because the $5d_1 \rightarrow {}^2F_{5/2}$ emission of Ce^{3+} takes place not only when Ce^{3+} is excited, but also when Gd^{3+} is excited. In addition to this, the band corresponding to the $5d_5$ level of Ce^{3+} can be seen completely in such figure, which complements the assignment of the 5*d* levels made in the absorption measurements. The excitation spectrum for the emission of Gd^{3+} (Figure 5.5.b) shows that this emission is produced mainly when Gd^{3+} ions are directly excited. Similar behaviours have been observed for the other $4f \rightarrow 4f$ emissions of Gd^{3+}, centred at 578, 592 and 633 nm. Figure 5.5 is similar to the excitation spectra of $KGd_{0.981}Ce_{0.019}(PO_3)_4$ for the emission wavelengths $\lambda_{emi} = 342$ nm ($5d_1 \rightarrow {}^2F_{7/2}$ of Ce^{3+}) and $\lambda_{emi} = 592$ nm ($^6G_{7/2} \rightarrow {}^6P_{3/2}$ of Gd^{3+}), which are shown in Figure 6 of *Paper I*.

After performing the calculations explained in *Paper I*, it was predicted that the energy of the exciton creation, E_{ex}, in type III KGdP is 7.57 eV (164 nm). Therefore, the band corresponding to E_{ex} could appear centred at 164 nm in the excitation spectra, although it would not be appreciated in the excitation spectrum for the emission of Ce^{3+} (Figure 5.5.a) due to an overlapping with the $^8S_{7/2} \rightarrow {}^4F_{9/2}$ transition of Gd^{3+}. In the case of the excitation spectrum for the emission of Gd^{3+} (Figure 5.5.b), it would be possible to see the band corresponding to the exciton creation, so this result tells us that it is unlikely that Gd^{3+} ions are excited by excitons.

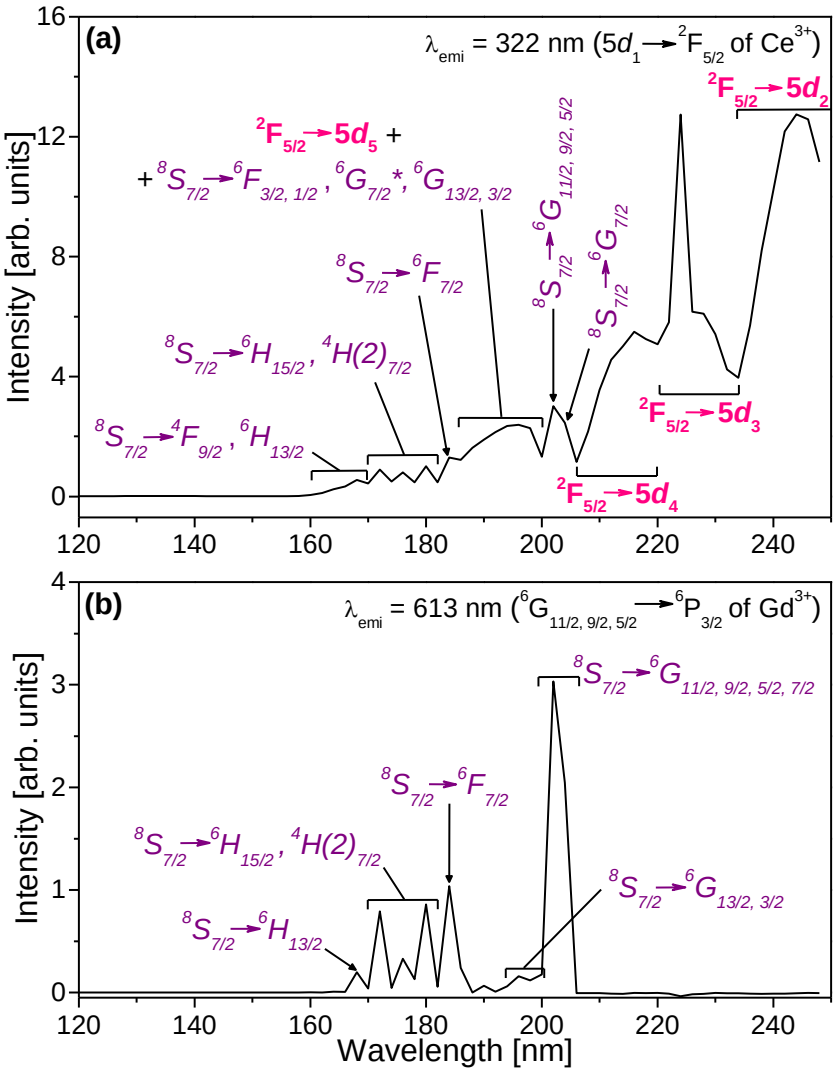

Figure 5.5. Excitation spectra of $KGd_{0.996}Ce_{0.004}(PO_3)_4$ for the emission wavelengths of (a) 322 nm ($5d_1 \rightarrow {}^2F_{5/2}$ of Ce^{3+}) and (b) 613 nm ($^6G_{11/2,9/2,5/2} \rightarrow {}^6P_{3/2}$ of Gd^{3+}) at room temperature. Propagation direction of the excitation radiation is along the *c** crystallographic axis, with the *b* crystallographic axis pointing upwards. Labels in purple and italics indicate the electronic transitions of Gd^{3+} and labels in pink and bold those of Ce^{3+}.

The value of E_{ex} has been used to calculate the approximate energy difference between the bottom of the conduction band (E_C) and the top of the valence band (E_V), E_{VC}, of this host taking into account that this value is approximately 1.08 times the energy of the exciton creation[20]. Therefore, the estimated value for type III KGdP is E_{VC} = 8.17 eV (152 nm).

5.2.3. Decay time measurements

5.2.3.1. Decay time measurements under VUV-UV excitation

Figure 5.6 shows the luminescence decay curves for λ_{emi} = 342 nm ($5d_1 \rightarrow {}^2F_{7/2}$ of Ce^{3+}) of Ce^{3+}-doped type III KGdP crystals with different doping concentrations and at different excitation wavelengths. The samples were excited at 302.5 nm ($^2F_{5/2} \rightarrow 5d_1$ of Ce^{3+}), 195 nm ($^8S_{7/2} \rightarrow {}^6G_{13/2}$ of Gd^{3+} and $^2F_{5/2} \rightarrow 5d_5$ of Ce^{3+}) and 174 nm ($^8S_{7/2} \rightarrow {}^6H_{15/2}$ of Gd^{3+}). However, to gain in photon flux reaching the sample, the excitation beam had a bandwidth of around 7%, being not purely monochromatic. The luminescence decay curves shown in the figure below can be fitted by a single exponential decay, as do the luminescence decay curves for λ_{emi} = 322 nm ($5d_1 \rightarrow {}^2F_{5/2}$ of Ce^{3+}) shown in Figure 7.a of *Paper I*. The time constants obtained from the exponential fittings shown below for λ_{emi} = 342 nm vary from 17 to 19 ns, and those obtained for λ_{emi} = 322 nm vary from 15 to 19 ns, although in most cases it is 16 ns.

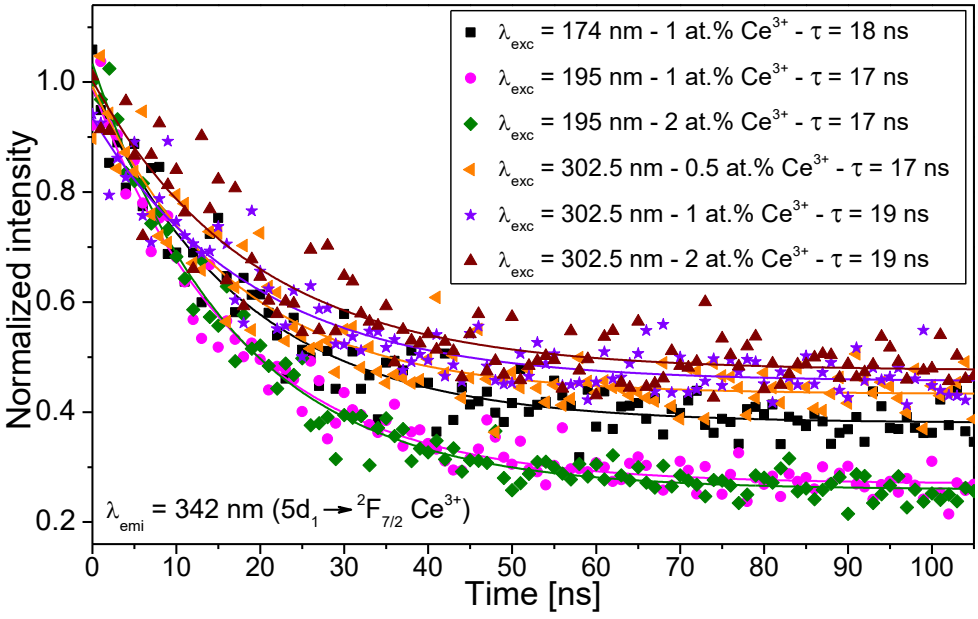

Figure 5.6. Fast component of the luminescence decay curves of Ce:KGdP crystals with different doping concentrations and at different excitation wavelengths for λ_{emi} = 342 nm ($5d_1 \rightarrow {}^2F_{7/2}$ of Ce^{3+}) at room temperature. In all cases, propagation direction of the excitation radiation is along the *c** crystallographic axis, with the *b* crystallographic axis pointing upwards.

Therefore, the lifetime obtained of the $5d_1$ level of Ce^{3+} in type III KGdP (space group: $P2_1$) is around 16−19 ns. No meaningful changes in the lifetime value, τ, were obtained either due to the change of the Ce^{3+} concentration in the crystals or of the excitation wavelength. This value is similar or even shorter than the measured ones in other scintillator materials[8,13,21,22]. The measured lifetime of the $5d_1$ level of Ce^{3+} in type B KGdP (space group: $C2/c$) is 21.1 ns[8], so the lifetime of this level in our compound is lower.

The intensity of the emission bands corresponding to the $5d_1 \rightarrow {}^2F_{5/2,7/2}$ transitions of Ce^{3+} does not reach zero, as observed in Figure 5.6 for λ_{emi} = 342 nm, due to the short interpulse time in the synchrotron measurements. Thus, it was concluded that the luminescence decay curves are composed by a fast component and a slow component. The measurement of its slow component is explained in the next Section.

5.2.3.2. Decay time measurements under visible excitation

Figure 5.7.a shows the slow component of the luminescence decay curve for the emission wavelength λ_{emi} = 342 nm of $KGd_{0.974}Ce_{0.026}(PO_3)_4$ under excitation at 302.5 nm ($^2F_{5/2} \rightarrow 5d_1$ of Ce^{3+}) at room temperature. The data fits an exponential function that results in a decay time of 8 ms. This slow component has already reported in other Ce^{3+}-doped phosphates, as in $Ce:NaPrP_4O_{12}$ [13] and $Ce:CsGd(PO_3)_4$ [8]. The origin of the slow component of the $5d_1$ level of Ce^{3+} in the Ce^{3+}-doped non-centrosymmetric KGdP crystal (8 ms) could be attributed to the energy transfer from the $^6P_{7/2}$ level of Gd^{3+} to this $5d_1$ emitting level (Figure 5.4), since the lifetime of this level is of the same order in the $KGd(PO_3)_4$ itself and in other hosts (4.9 ms in $NaY_{0.80}Gd_{0.20}PO_4$ and 6.36 ms in $NaGd(PO_3)_4$)[19,23]. The emission bands corresponding to the $^6P_J \rightarrow {}^8S_{7/2}$ transitions of Gd^{3+} do not appear in the luminescence spectra of Ce:KGdP samples, but only in the case of Pr:KGdP crystals (Figure 5.16). Hence, Figure 5.7.b shows the luminescence decay curve for λ_{emi} = 312 nm ($^6P_J \rightarrow {}^8S_{7/2}$ of Gd^{3+}) of $KGd_{0.942}Pr_{0.058}(PO_3)_4$ under excitation at 300 nm ($^8S_{7/2} \rightarrow {}^6P_{3/2}$ of Gd^{3+}) at room temperature, showing an exponential fitting with a lifetime value of 9 ms.

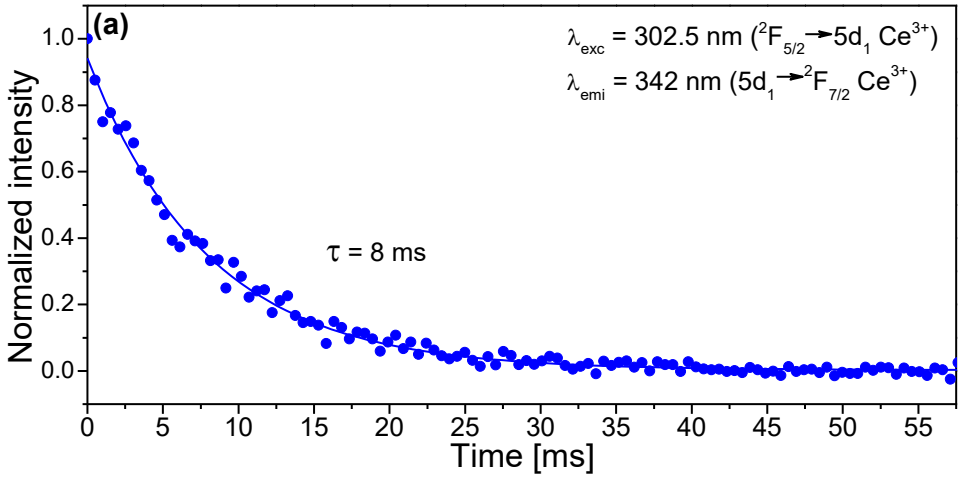

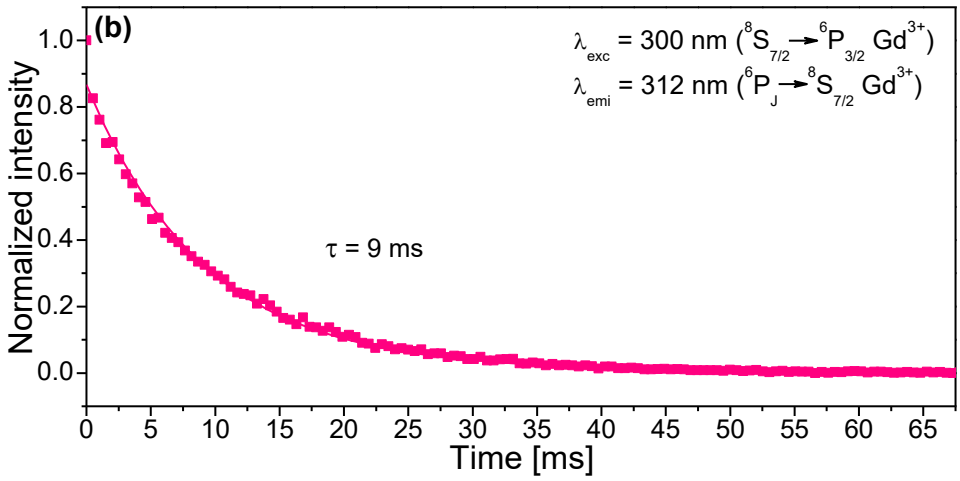

Figure 5.7. (a) Slow component of the luminescence decay curve of $KGd_{0.974}Ce_{0.026}(PO_3)_4$ under excitation at 302.5 nm ($^2F_{5/2} \rightarrow 5d_1$ of Ce^{3+}) for λ_{emi} = 342 nm ($5d_1 \rightarrow {}^2F_{7/2}$ of Ce^{3+}) at room temperature. (b) Luminescence decay curve of $KGd_{0.942}Pr_{0.058}(PO_3)_4$ under excitation at 300 nm ($^8S_{7/2} \rightarrow {}^6P_{3/2}$ of Gd^{3+}) for λ_{emi} = 312 nm ($^6P_J \rightarrow {}^8S_{7/2}$ of Gd^{3+}) at room temperature. In both cases, propagation direction is along the *c** crystallographic axis, with the *a** axis pointing upwards.

5.2.4. Radioluminescence measurements under X-ray excitation

Figure 5.8 shows the X-ray excited radioluminescence (RL) spectra of undoped KGdP and Ce:KGdP at different Ce^{3+} concentrations under 12000 eV, 31000 eV and 46000 eV excitation at room temperature. The RL spectra of the same samples under 16500 eV, 24800 eV, 35500 eV and 40443 eV excitation are shown in Figure 2 of *Paper IV*. The RL spectra of the undoped sample have been used to properly label the emission bands observed in the RL spectra of Ce^{3+}-doped KGdP samples. The labeling process has been carried out using the Dieke's diagram[1], the extended Dieke's diagram[2] and the refs.[3,4,12].

All the emission bands observed in the RL spectra of the undoped KGdP crystal belong to $4f \rightarrow 4f$ transitions of Gd^{3+}, with the band centred at around 312 nm being the most intense, corresponding to the $^6P_{3/2,5/2,7/2} \rightarrow {}^8S_{7/2}$ transitions. The most intense emission band observed in the RL spectra of the Ce^{3+}-doped type III KGdP samples (space group: $P2_1$) extends from 300 to 385 nm and that is formed by the overlapping of two bands corresponding to the $5d_1 \rightarrow {}^2F_{5/2}$ and $5d_1 \rightarrow {}^2F_{7/2}$ transitions of Ce^{3+} in KGdP, respectively. These two electronic transitions are the same observed as a doublet band centred at 322 and 342 nm in the emission spectra of the same samples under direct $4f \rightarrow 5d$ excitation (VUV-UV excitation) in Figure 5.3. In the radioluminescence spectra under X-ray irradiation of Ce:$KGdP_4O_{12}$ (space group: $C2/c$, type B phase)[24], the doublet band corresponding to the $5d_1 \rightarrow {}^2F_{5/2}$ and $5d_1 \rightarrow {}^2F_{7/2}$ transitions of Ce^{3+} has been observed centred at 325 and 345 nm, respectively. So, the polymorphism of the two crystalline phases of $KGd(PO_3)_4$ mentioned does not significantly affect the energy values of these $4f$ and $5d$ levels of Ce^{3+}. A higher

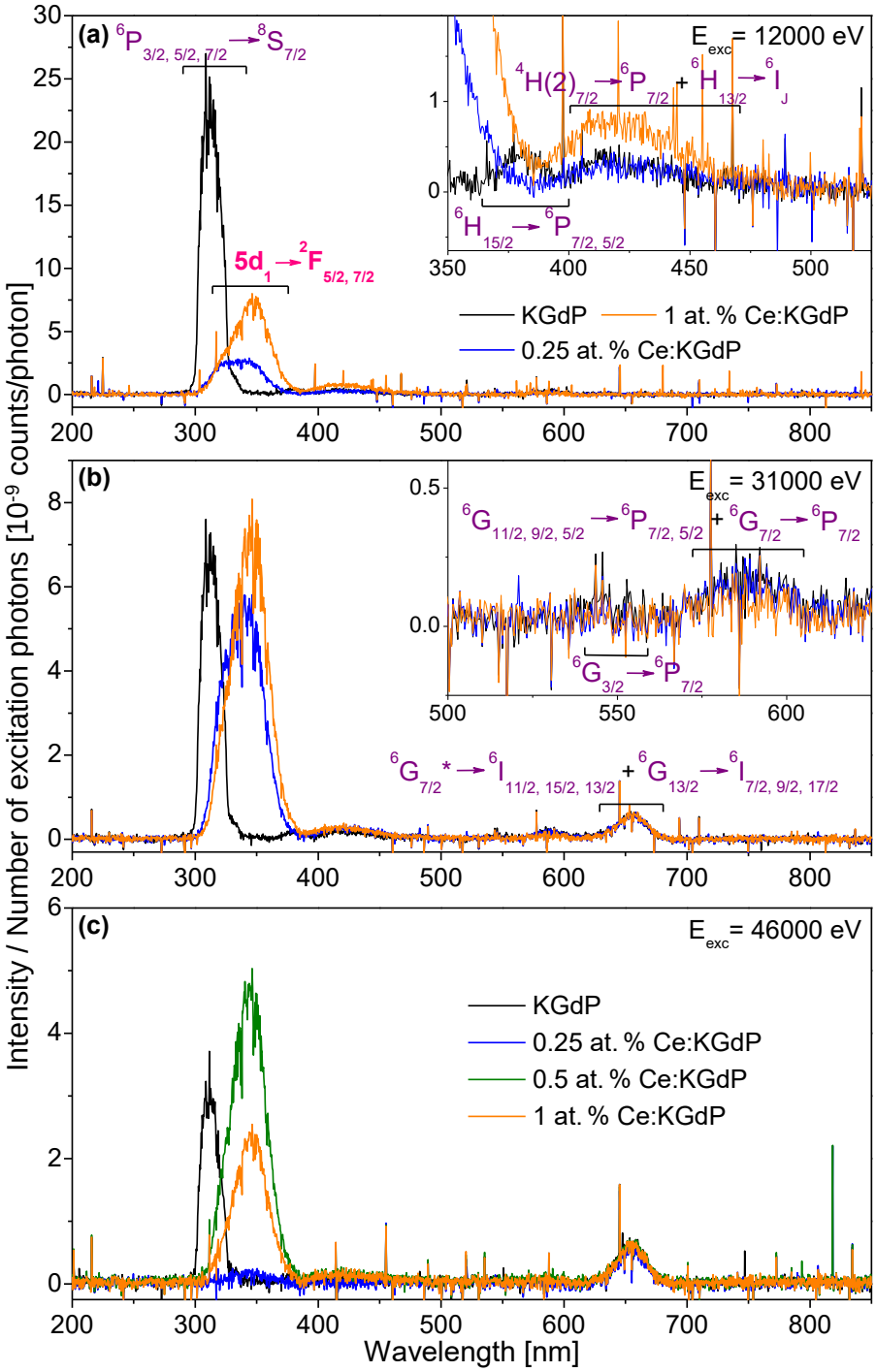

Figure 5.8. X-ray excited radioluminescence (RL) spectra of KGdP and Ce:KGdP at different Ce^{3+} contents under excitation at (a) 12000 eV, (b) 31000 eV, and (c) 46000 eV at RT. Propagation direction is along the *c** axis, with the *b* axis pointing upwards. Labels in purple indicate the electronic transitions of Gd^{3+}, and labels in pink and bold those of Ce^{3+}.

displacement of the doublet band corresponding to the $5d_1 \rightarrow {}^2F_{5/2,7/2}$ transitions of Ce^{3+} is observed in other compounds of the same family: 310 and 329 nm for Ce:$LiGdP_4O_{12}$ (space group: *C*2/*c*), 314 and 333 nm for Ce:$NaGdP_4O_{12}$ (space group: $P2_1/n$), and 336 and 358 nm for Ce:$CsGdP_4O_{12}$ (space group: $P2_1/n$)[24].

It is worth mentioning that the band corresponding to the ${}^6P_{3/2,5/2,7/2} \rightarrow {}^8S_{7/2}$ transitions of Gd^{3+} (around 312 nm) is not present in the RL spectra when Ce^{3+} is present in the crystal, even at concentrations as low as 0.25 at. % Ce^{3+} in KGdP. However, other $4f \rightarrow 4f$ transitions of Gd^{3+} can be observed, which appear in the visible region from 375 to 700 nm with a lower intensity compared to the Ce^{3+} emissions.

The X-ray excited radioluminescence has been studied for different doping levels in order to observe the effect of Ce^{3+} concentration. Figure 5.8 manifests that there is a variation in the intensity of the Ce^{3+} emission depending on the Ce^{3+} content. The reason why the Ce^{3+} emission decreases in the case of 1 at. % Ce:KGdP crystal compared to the crystal of 0.5 at. % Ce:KGdP could be the reabsorption of the emission of a Ce^{3+} ion by its neighbouring Ce^{3+} ions. The 0.25 at. % Ce:KGdP sample exhibits a higher dependence depending on the excitation energy.

Figure 5.9.a shows the energy levels scheme for Ce^{3+} and Gd^{3+} ions with respect to the conduction and valence bands of type III $KGd(PO_3)_4$, together with the schematic illustration of the energy transfer process to Ce^{3+} ions based on the sequential capture of charge carriers by Ce centres, which is the type of energy transfer process that occurs mainly in cerium-doped scintillation materials[25,26,27,28,29]. The refs.[11,12,30] have been used to place the 5*d* and 4*f* energy levels of Ce^{3+} and Gd^{3+} with respect to the conduction and valence bands of this host, as explained in *Paper IV*, and the refs.[9,31] have been used as well. The scintillation mechanism in inorganic scintillators containing lanthanide ions and the details regarding with the cerium-doped compounds are explained in Sections 1.3.1, 1.3.1.1 and 1.3.2. In Ce^{3+}-doped crystals, the energy transfer process usually begins with the capture of a hole by Ce^{3+} and then of an electron by Ce^{4+} because Ce^{3+} is a good hole trap[27,32,33]. By contrast, Ce^{4+} is an efficient electron trap, so the initial coexistence of Ce^{4+} and Ce^{3+} ions in the scintillation crystal is harmful because Ce^{4+} can compete with Ce^{3+} for the capture of charge carriers and induce severe limitations in scintillation efficiency[26,32]. In Ce^{3+}-doped type III KGdP crystals, the presence of Ce^{4+} is not expected because this ion is not present in the initial reagents and, in addition, the crystalline network resulting from the partial replacement of Gd^{3+} by Ce^{3+} is electrically neutral, with a higher stability with Ce^{3+} doping in the structure than the resulting from the partial replacement by Ce^{4+}.

Regarding the Gd^{3+} ion, it is interesting to mention that this ion is one of the two best candidates, together with Lu, to act as a neutral constituent in scintillation materials because it is very unlikely to introduce both hole and electron traps in materials[27]. Thus, the energy transfer process based on the sequential capture of charge carriers is expected to be more effective for Ce^{3+} ions than for Gd^{3+} ions, although it should be noted that the concentration of Gd^{3+} is significantly higher than that of Ce^{3+}. As shown in Figure 5.8, once the emitting centres (in our case, Ce^{3+} and Gd^{3+} ions) are

excited, these centres emit light. Probably because of the above-mentioned explanation, as discussed in *Paper IV*, the emission band corresponding to the $5d_1 \rightarrow {}^2F_{5/2,7/2}$ transitions of Ce^{3+} is very intense, and at the same time, weak emission bands corresponding to some transitions between the *4f* high energy levels of Gd^{3+} can be observed.

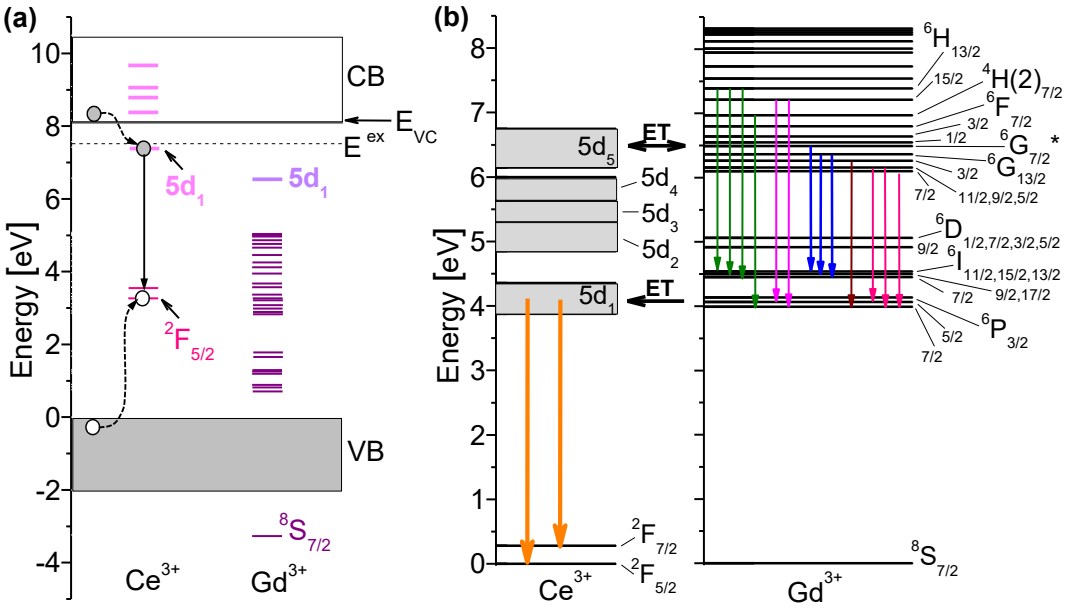

Figure 5.9. (a) Energy levels scheme for Ce^{3+} and Gd^{3+} with respect to the conduction and valence bands of type III $KGd(PO_3)_4$, which schematically illustrates the energy transfer process to Ce^{3+} ions based on the sequential capture of charge carriers by Ce centres. Electrons are symbolized by filled circles and holes by empty circles. The refs.[11,12] have been used to place the energy levels in this host. (b) Energy level diagram of Ce^{3+} and Gd^{3+} in $Ce:KGd(PO_3)_4$ and emissions observed after X-ray irradiation. The thickness of the arrows is related to the intensity of the emissions represented in the radioluminescence spectra, and the arrows with the same colour appear as a single band.

Figure 5.9.b shows the energy level diagram of Ce^{3+} and Gd^{3+} in type III Ce:KGdP, considering the ground states of the Ln^{3+} ions as the zero value of energy. In the same figure, the emissions observed in the RL spectra are also represented, as well as the different energy transfer processes between Ce^{3+} and Gd^{3+} ions, which are explained below. The fact that the band corresponding to the ${}^6P_J \rightarrow {}^8S_{7/2}$ transitions of Gd^{3+} (~312 nm) is not present, it has been attributed to a very efficient non-radiative energy transfer process from the ${}^6P_J$ levels of Gd^{3+} to the $5d_1$ level of Ce^{3+}, as observed in several works related to radioluminescence studies of other Gd^{3+}-containing hosts doped with Ce^{3+} [24,34,35,36]. The results of the mentioned works are summarized in *Paper IV*. Besides, a bidirectional energy transfer between the $5d_5$ level of Ce^{3+} and the ${}^6F_J$ and ${}^6G_J$ levels of Gd^{3+} might take place, since some emission bands corresponding to the electronic transitions from the ${}^6G_J$ levels to the ${}^6I_J$ and ${}^6P_J$ levels of Gd^{3+} have been observed. The bidirectional energy transfer mentioned has

also been observed in the photoluminescence studies of these samples (see Section 5.2.2). Although, it is worth mentioning that the Gd^{3+} ions also receive energy directly from the localized excitations because the Gd^{3+} emissions bands that are in the spectral range from 350 to 475 nm correspond to electronic transitions starting from the ^6H_J and $^4H(2)_{7/2}$ levels of Gd^{3+}, which have higher energy than the $5d_5$ level of Ce^{3+} in type III KGdP.

Figure 5.10 presents the energy conversion efficiency of the $KGd_{0.981}Ce_{0.019}(PO_3)_4$ crystal for the emission bands centred at λ_{emi} = 325 and 345 nm (Ce^{3+}), and λ_{emi} = 656 nm (Gd^{3+}) at various excitation energies up to 62500 eV. In this graph, the X-ray photon energy is represented on the abscissa axis, and the integrated intensity of the emission band divided by the total excitation energy per second (number of X-rays photons per second of the specific excitation energy multiplied by the corresponding excitation energy) is on the ordinate axis. The maximum intensity value of the Ce^{3+} emission bands has been used to normalize all intensity values. Due to the low intensity values of the Gd^{3+} emission bands, the data was multiplied by 10 and the resulting values are those represented in the figure. This graph shows how the conversion efficiency from high energy values into visible or near visible radiation (scintillation properties) depends on the excitation energy. As explained in Section 1.3, since the compound studied is a crystal containing lanthanide ions, for scintillation applications, the interest lies in the $5d \rightarrow 4f$ transitions of Ce^{3+}. The maximum conversion efficiency through the $5d_1 \rightarrow {}^2F_{5/2,7/2}$ transitions of Ce^{3+} is produced by exciting the crystal at 16500 eV. For energies above 31000 eV, the Ce^{3+} emission seems to be almost quenched, as does the Gd^{3+} emission. This behaviour could be

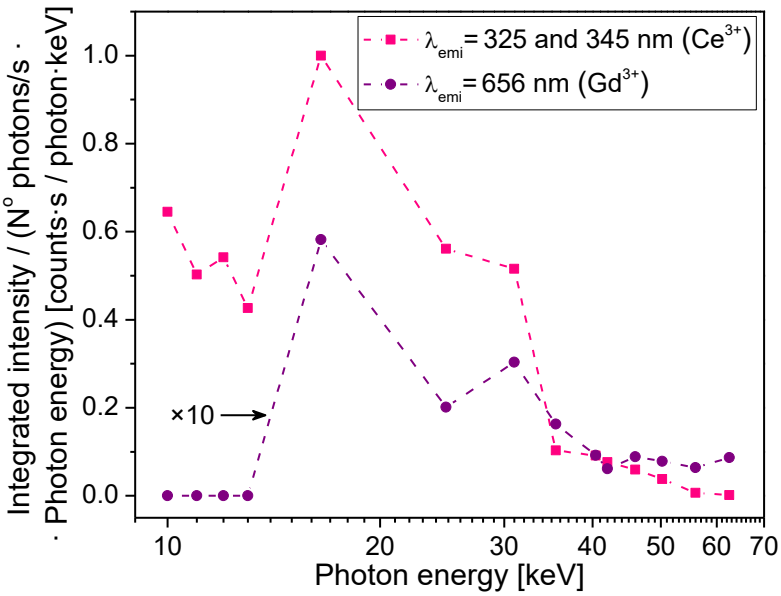

Figure 5.10. Normalized integrated intensity of two emission bands of the X-ray excited radioluminescence spectra of $KGd_{0.981}Ce_{0.019}(PO_3)_4$ as a function of the X-ray photon energy. The dashed lines are guides for the eye.

due to the existence of competition between two processes: (1) the sequential capture of charge carriers by the Ce^{3+} and Gd^{3+} ions, and (2) the capture of electrons by the oxygen vacancies present in the crystal (see Section 5.4.1).

5.3. Spectroscopic characterization of type III Pr:$KGd(PO_3)_4$ bulk single crystals

Sections 1.3.3 and 1.4.1 show the arguments given for considering type III $KGd(PO_3)_4$ as a host and Pr^{3+} as a doping element as a promising combination as a scintillator material. A large part of the following spectroscopic studies are reported in *Papers II* and *IV*, although most of the figures presented here provide complementary information.

5.3.1. Optical absorption

5.3.1.1. Unpolarized optical absorption at room temperature

Figure 5.11.a shows the unpolarized absorption coefficient of $KGd_{0.997}Pr_{0.003}(PO_3)_4$ at room temperature in the spectral range from 193 to 320 nm. To distinguish the absorption bands belonging to Pr^{3+} from those corresponding to Gd^{3+} in Pr:KGdP, the optical absorption of a sample of KGdP without doping was measured (Figure S.2 of *Paper II*, in Supporting Information). The broad, intense band centred at 218 nm (45872 cm^{-1}, 5.69 eV) corresponds to Pr^{3+} and it has been attributed to its $^3H_4 \rightarrow 5d_1$ electronic transition in type III KGdP (space group: $P2_1$). From the crystallographic point of view, in this host, there is only one site expected for the Gd^{3+} ions, with C_1 point symmetry[37]. Since the Pr^{3+} ions replace the Gd^{3+} ions in Pr:KGdP, all Pr^{3+} ions have the same crystal field and, consequently, only one band is expected for the $^3H_4 \rightarrow 5d_1$ transition. This transition of Pr^{3+} has been systematically studied in many other hosts[10], including several phosphates. The value of the $^3H_4 \rightarrow 5d_1$ transition of Pr^{3+} is 212 nm in LaP_3O_9 [38], 222 nm in YPO_4 [38,39] and 224 nm in YP_3O_9 [38], being highly similar to the value in KGdP. The energy value corresponding to the first spin-allowed $4f \rightarrow 5d$ transition of Pr^{3+} ($^3H_4 \rightarrow 5d_1$) can be predicted in a specific host by adding 12240 ± 750 cm^{-1} to the energy value corresponding to the first spin-allowed $4f \rightarrow 5d$ transition of Ce^{3+} ($^2F_{5/2} \rightarrow 5d_1$) in the same host, as shown in the study carried out by Dorenbos[10]. Therefore, since the $^2F_{5/2} \rightarrow 5d_1$ transition of Ce^{3+} in type III KGdP is centred at 302.5 nm (33058 cm^{-1}, 4.10 eV)[12], the predicted energy value of the $^3H_4 \rightarrow 5d_1$ transition of Pr^{3+} in type III KGdP is in the range 217.2−224.5 nm (46048−44548 cm^{-1}, 5.71−5.52 eV), which is consistent with the experimental value (218 nm).

As can be seen in Figure 5.11.a, only the $5d_1$ absorption band was clearly identified out of all the $5d_x$ levels of Pr^{3+} in KGdP. These optical absorption measurements were performed in air atmosphere, so, as the air absorbs below 192 nm, its absorption bands hid the other $5d_x$ levels. Nevertheless, the $5d_2$ and $5d_3$ energy levels of Pr^{3+} in KGdP, together with the $5d_1$ level already identified, were determined in the luminescence measurements under VUV-UV excitation (see Section 5.3.2.1) by studying the excitation spectra for several emission wavelengths. The unpolarized optical

absorption cross section of the $^3H_4 \rightarrow 5d_1$ transition of Pr^{3+} in KGdP at room temperature is depicted in Figure 5.11.b. After subtracting the absorbance background, its value is 780×10^{-20} cm^2 at 218 nm. Since $4f \rightarrow 5d$ electronic transitions are parity-allowed transitions, this high value is expected.

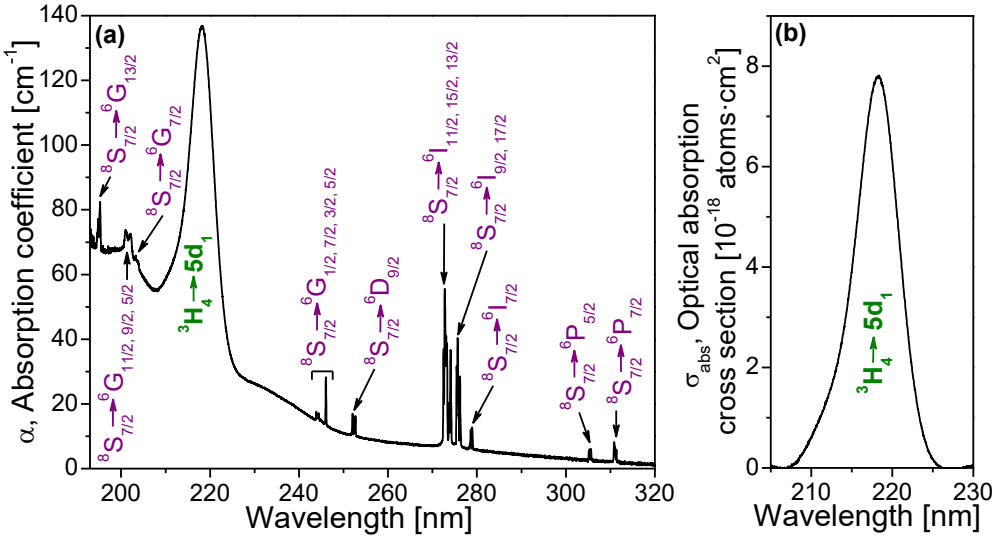

Figure 5.11. (a) Unpolarized optical absorption coefficient of $KGd_{0.997}Pr_{0.003}(PO_3)_4$ at room temperature. Propagation direction is along *b* crystallographic axis. Labels in purple indicate the electronic transitions of Gd^{3+} and the label in green and bold that of Pr^{3+}. (b) Unpolarized optical absorption cross section of the $^3H_4 \rightarrow 5d_1$ transition of Pr^{3+} in KGdP using the same sample at room temperature.

Figure 5.12 shows the unpolarized optical absorption cross sections of the $^3H_4 \rightarrow 4f$ electronic transitions of Pr^{3+} ions in KGdP in the spectral range from 430 to 2475 nm at room temperature. More specifically, the absorption peaks centred at 445, 469.4, 470.4 and 482 nm have been labelled as the $^3H_4 \rightarrow {}^3P_2$, $^3H_4 \rightarrow {}^1I_6$, $^3H_4 \rightarrow {}^3P_1$ and $^3H_4 \rightarrow {}^3P_0$ transitions, respectively, while the absorption bands that appear within the energy ranges 570−620, 925−1125, 1375−1720 and 1850−2475 nm correspond to the $^3H_4 \rightarrow {}^1D_2$, $^3H_4 \rightarrow {}^1G_4$, $^3H_4 \rightarrow {}^3F_4 + {}^3F_3$ and $^3H_4 \rightarrow {}^3F_2 + {}^3H_6$ transitions, respectively. The Dieke's diagram[1] has been used to label such absorption bands. Regarding the optical absorption cross sections, the $^3H_4 \rightarrow {}^3P_0$ transition has the highest with a value of 5.1×10^{-20} cm^2, despite being the $^3H_4 \rightarrow {}^3P_2$ transition the one that is pseudo-hypersensitive. Its value is slightly below the first number, 4.4×10^{-20} cm^2, which is in the suitable range to be used for exciting $4f \rightarrow 4f$ transitions for optical amplification applications. In order to generate visible laser radiation using the Pr^{3+} ion, being very attractive for this purpose[40], this ion is usually excited through its $^3H_4 \rightarrow {}^3P_2$ transition, as can be observed in the works on Pr^{3+}:$YAlO_3$ (Pr:YAP)[41], Pr^{3+},Mg^{2+}:$SrAl_{12}O_{19}$[42] and Pr^{3+}:$LiYF_4$ (Pr:YLF)[43], whose cross sections values are ~2.9×10^{-20} cm^2, 1.3×10^{-20} cm^2 and 8.9×10^{-20} cm^2 in specific polarizations, respectively.

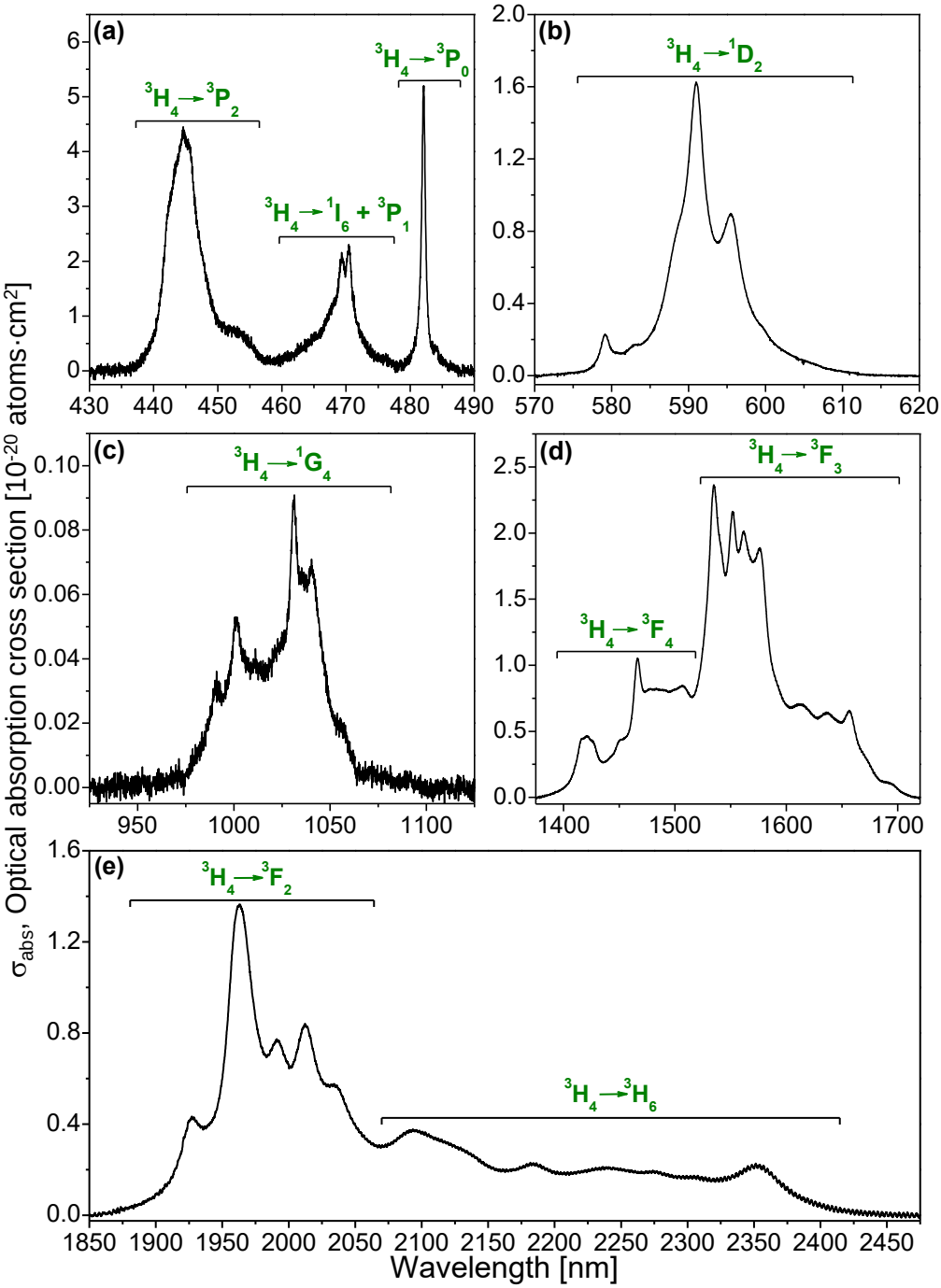

Figure 5.12. Unpolarized optical absorption cross sections of the $^3H_4 \rightarrow 4f$ electronic transitions of Pr^{3+} in Pr:KGdP at room temperature. In all cases, propagation direction is along the *a** crystallographic axis.

5.3.1.2. Polarized optical absorption at room temperature and at 6 K

Figure 5.13 presents the polarized optical absorption cross sections of the $^3H_4 \rightarrow 4f$ electronic transitions of Pr^{3+} in type III Pr:KGdP in the wavelength range from 430 to 2475 nm at room temperature with the electric field of incident light parallel to the crystallographic axes *a**, *b* and *c**, while Figure 5.14 shows those parallel to the principal optical axes N_g, N_m and N_p. The absorption bands have been labelled in the same manner as in the unpolarized optical absorption measurements (Section 5.3.1.1).

In Figure 5.13, the peak with the highest value of optical absorption cross section corresponds to the $^3H_4 \rightarrow {}^3P_0$ transition, although it is interesting to note that its value is considerably reduced when the electric field of incident light is parallel to the crystallographic axis *a**. The peak centred at 445 nm, which corresponds to the $^3H_4 \rightarrow {}^3P_2$ transition, is just below in terms of cross section value. In this case, there is no important difference between the value obtained with the electric field parallel to the *a** axis and those with the field parallel to the *b* and *c** axes, although parallel to *c** acquires the highest value. As for the bands corresponding to the $^3H_4 \rightarrow {}^1D_2$, $^1G_4$, $^3F_{4,3,2}$ transitions, there is a high variety referring to the position of the peaks that appear and their intensity as a function of the polarization of the incident light. Since the symmetry point group for the Pr^{3+} ions in this host is C_1[37], polarization-dependent selection rules are not expected[44]. Hence, the anisotropic behaviour observed in this figure may be related to the behaviour described in the work on anisotropic spectroscopy of type III Nd:KGd$(PO_3)_4$ carried out by Solé *et al.*[45], so that the mentioned behaviour may be caused by this host itself. In Figure 5.14, it can be seen that all the data obtained with the electric field parallel to the principal optical axis N_p have the same profile to those shown in Figure 5.13 for the electric field parallel to the *b* axis. This is because the *b* and N_p axes are parallel in type III KGdP host, as explained in Section 1.4.1. For the $^3H_4 \rightarrow {}^3P_J$, $^1I_6$ transitions, the absorption cross section reaches its maximum value when the electric field is parallel to the principal optical axis N_p. The other transitions exhibit a high variety depending on the polarization, as observed for the measurements with light polarized along the other crystallographic axes.

Figure 5.15 shows the polarized optical absorption of the $^3H_4 \rightarrow {}^3F_{3,4}$ transitions of Pr^{3+} in Pr:KGdP at 6 K depending on the polarization of the incident light and the Pr^{3+} content. The optical absorption measurements at low temperature allow us to determine the energy position of the Stark sublevels of the excited states, since the most populated Stark sublevel of the ground state at low temperature is the lowest in energy. The splitting of a level into sublevels is due to its interaction with an electric field, in this case, the host crystal field.[46] Taking into account that the maximum number of Stark sublevels is 2J+1 when the symmetry point group is C_1, the maxima Stark sublevels of the ^3F_J levels for J=3 and J=4 are 7 and 9, respectively.[44] In Figure 5.15.a, seven peaks can be seen in the lower energy area and nine peaks in the higher energy area, so these peaks may be attributed to the Stark sublevels of the $^3F_3$ and $^3F_4$ levels of Pr^{3+} in type III KGdP crystal, respectively, since this host has a unique crystalline site for the Pr^{3+} ions, which has C_1 point symmetry[37]. The Stark sublevels of the $^3F_3$ level are centred at 6411, 6433, 6479, 6495, 6508, 6515 and 6545 cm^{-1}, while those of the $^3F_4$ level are centred at 6812, 6843, 6862, 6959, 7000, 7024, 7037, 7059 and 7085 cm^{-1}. These results reaffirm that there is a unique site for

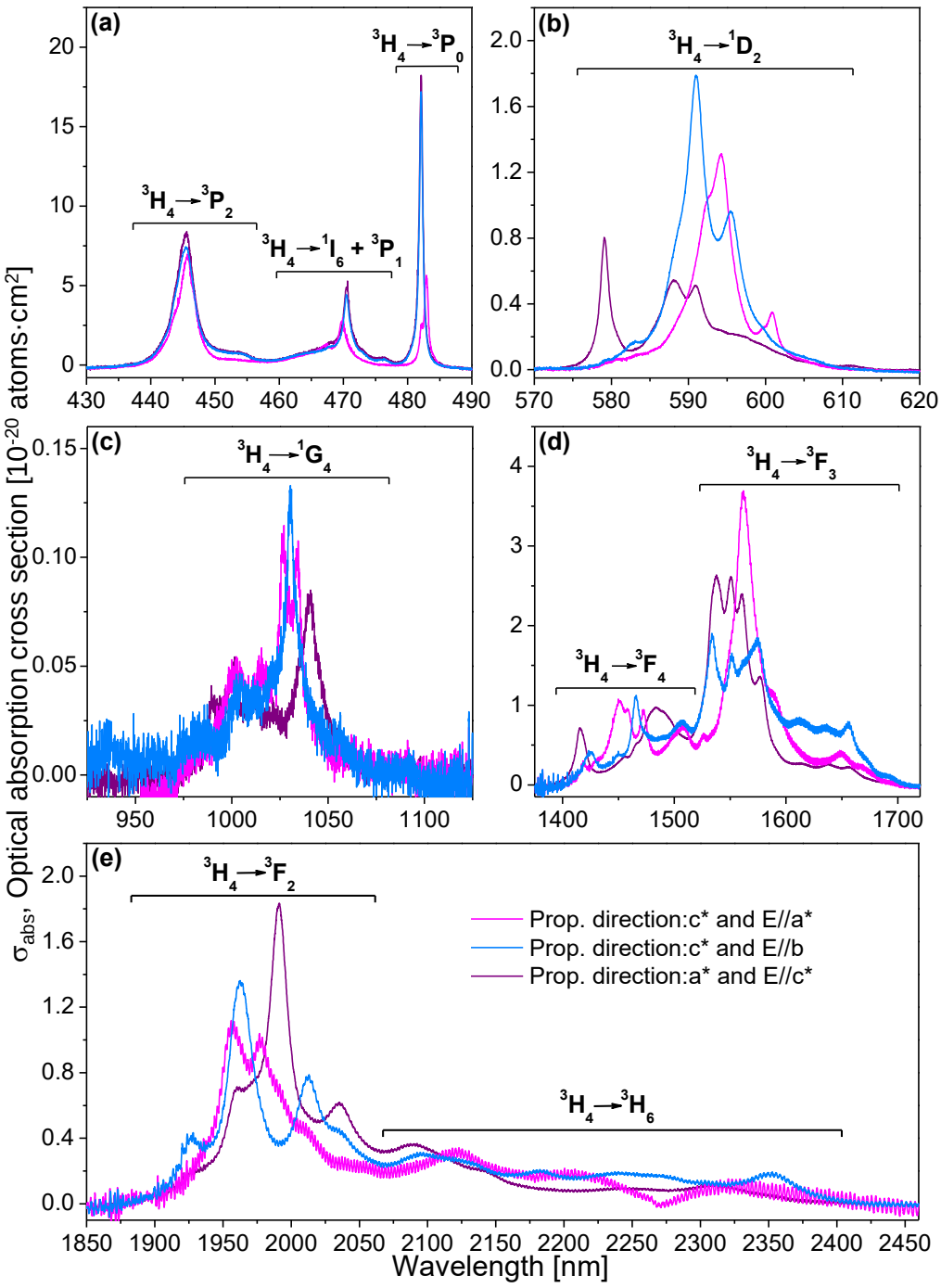

Figure 5.13. Polarized optical absorption cross sections of the $^3H_4 \rightarrow 4f$ electronic transitions of Pr^{3+} in Pr:KGdP with the electric field of incident light parallel to the crystallographic axes *a**, *b* and *c** at room temperature.

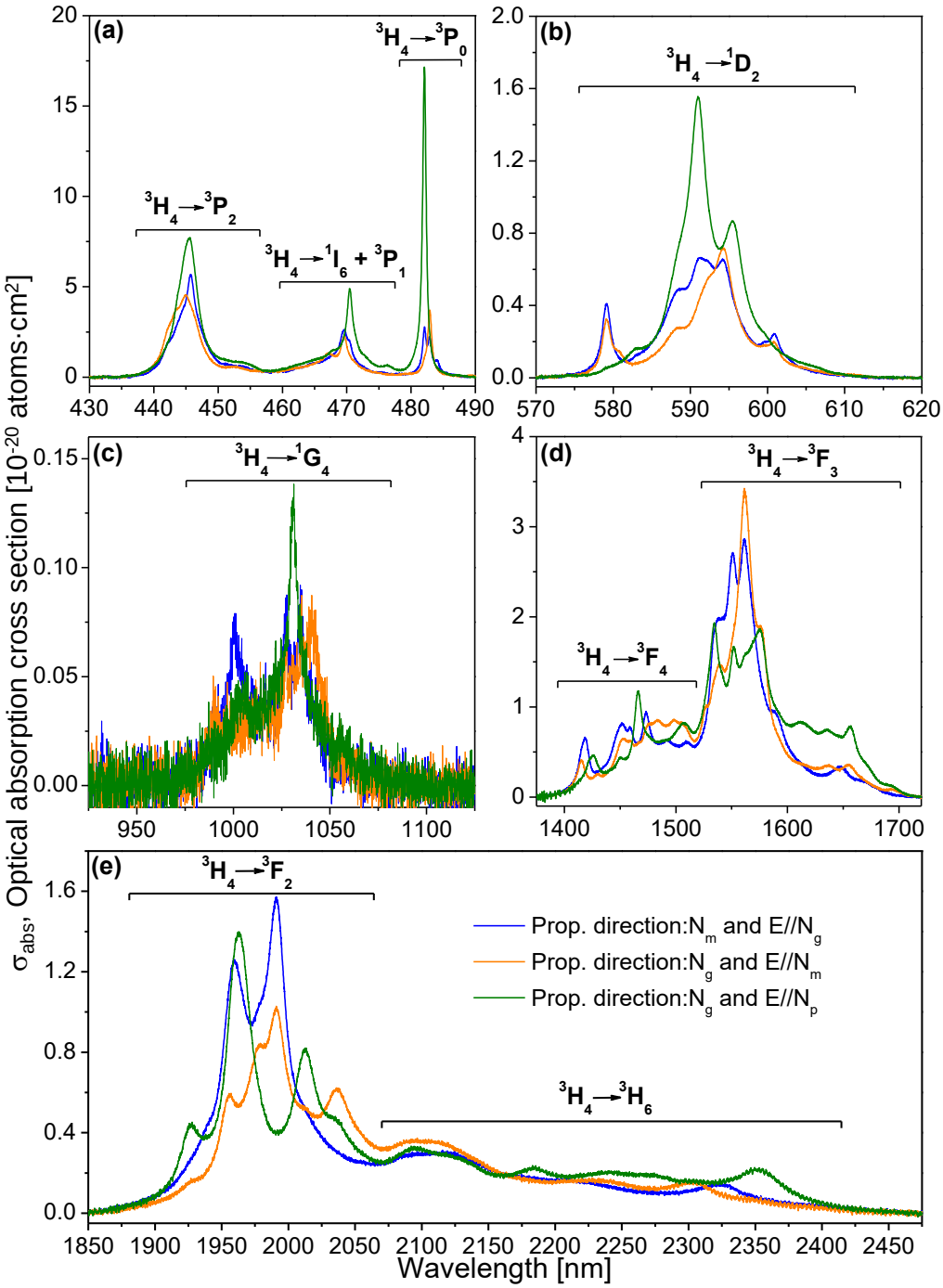

Figure 5.14. Polarized optical absorption cross sections of the $^3H_4 \rightarrow 4f$ electronic transitions of Pr^{3+} in Pr:KGdP with the electric field of incident light parallel to the principal optical axes N_g, N_m and N_p at room temperature.

the Pr^{3+} ions in this host[37]. In Figure 5.15.b, two peaks, in addition to the previous ones, can be seen in the spectrum of the highest doped sample. These peaks, which are centred at 6395 and 6852 cm^{-1}, could correspond to the electronic transitions due to the electronic population of the first Stark sublevels of the $^3H_4$ ground state of Pr^{3+}. Polarized optical absorption measurements at low temperature is a standard study in our research group, which help us to confirm the number of crystalline sites in a specific host for the active ions. Although the type III KGdP host has a unique site for the Pr^{3+} ions with C_1 symmetry, a high anisotropy can be clearly seen in Figure 5.15. This behaviour may be related to the behaviour described in ref.[45], as mentioned earlier in this Section, although further analysis would be necessary.

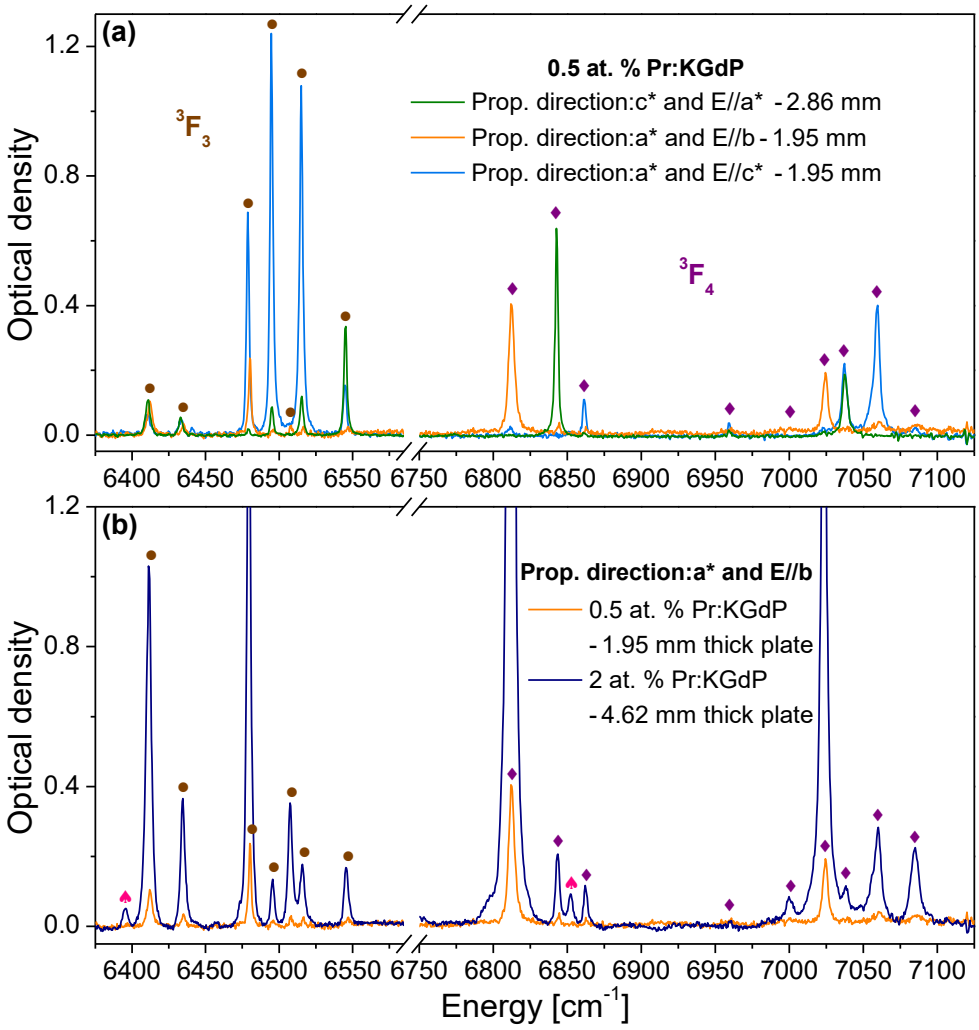

Figure 5.15. Polarized optical absorption of the $^3H_4 \rightarrow {}^3F_{3,4}$ transitions of Pr^{3+} in Pr:KGdP at low temperature, 6 K, depending on (a) the polarization of the incident light, and (b) the Pr^{3+} content. The Stark sublevels of the $^3F_3$ and $^3F_4$ levels of Pr^{3+} in type III KGdP are indicated by ● and ♦, respectively, while two electronic transitions from the first Stark sublevels of the $^3H_4$ ground state by ♠.

5.3.2. Luminescence measurements

5.3.2.1. Luminescence measurements under VUV-UV excitation

Figure 5.16 shows the emission spectra of Pr:KGdP crystals with three different Pr^{3+} concentrations under excitation at λ_{exc} = 218 nm ($^3H_4 \rightarrow 5d_1$ of Pr^{3+}), 196 nm ($^3H_4 \rightarrow 5d_2$ of Pr^{3+} and $^8S_{7/2} \rightarrow {}^6G_{13/2}$ of Gd^{3+}) and 166 nm ($^3H_4 \rightarrow 5d_3$ of Pr^{3+} and $^8S_{7/2} \rightarrow {}^6H_{13/2}$ of Gd^{3+}) at room temperature. The absorption band corresponding to the $5d_1$ level of Pr^{3+} in type III KGdP has been identified in the unpolarized optical absorption measurements (see Section 5.3.1.1) and the $5d_2$ and $5d_3$ energy levels of Pr^{3+} in this host have been determined after studying the excitation spectra for different emission wavelengths (see Figure 5.18.a). The emission spectra were compared with those obtained after exciting an undoped sample of KGdP with the same excitation wavelengths (Figure S.3 of *Paper II*, in Supporting Information) in order to correctly assign the emission bands to the different electronic transitions of Gd^{3+} or Pr^{3+}. For the assignation process, the Dieke's diagram[1], the extended Dieke's diagram[2], and the work carried out by Wegh *et al.*[3] and by Yang *et al*.[4] were taken into account.

After exciting the three samples under direct excitation of the $5d_1$ level of Pr^{3+} in type III KGdP from its $^3H_4$ ground state (Figure 5.16.a), the spectra show that the most intense emission bands are centred at 305, 312 and 323 nm. Such bands correspond to the $^6P_{3/2} \rightarrow {}^8S_{7/2}$, $^6P_{5/2} \rightarrow {}^8S_{7/2}$ and $^6P_{7/2} \rightarrow {}^8S_{7/2}$ transitions of Gd^{3+}, respectively, so this means that there is an energy transfer from Pr^{3+} to Gd^{3+}. Energy transfers from 5*d* levels of Pr^{3+} to 4*f* levels of Gd^{3+} were also observed in other hosts, as for example in the Gd-based multicomponent aluminate garnet $Pr:(Gd,Lu)_3Ga_3Al_2O_{12}$ [47]. In the same Figure 5.16.a, several emission bands have been attributed to $5d \rightarrow 4f$ transitions of Pr^{3+} in type III KGdP. These bands are centred at 229, 239, 256, 265, 358 and 435 nm, and correspond to the $5d_1 \rightarrow {}^3H_5$, $5d_1 \rightarrow {}^3H_6$,$^3F_2$ $5d_1 \rightarrow {}^3F_{3,4}$, $5d_1 \rightarrow {}^1G_4$, $5d_1 \rightarrow {}^1D_2$ and $5d_1 \rightarrow {}^3P_2$ transitions, respectively. The most intense band originating in a 5*d* level is the broad band located around 256−265 nm, while the significantly weaker broad bands are those centred at 358 and 435 nm. It is worth commenting that the emission band corresponding to the electronic transition from the $5d_1$ level to the $^3H_4$ ground state of Pr^{3+} does not appear. This fact is probably due to the self-absorption effect, as observed in $AREP_2O_7$ hosts (A = Na, K, Rb, Cs; RE = Y, Lu)[48].

Also in Figure 5.16.a, in the visible spectral region above 550 nm, three weak emission bands can be observed, being non-existent in some samples. These bands appear centred at 592, 617, 651 and 700 nm, and have been labelled as the $^6G_{7/2} \rightarrow {}^6P_{7/2}$, $^6G_{11/2,9/2,5/2} \rightarrow {}^6P_{3/2}$, $^6G_{13/2} \rightarrow {}^6I_{7/2}$ and $^6G_{3/2} \rightarrow {}^6I_{7/2}$ transitions of Gd^{3+}, respectively. In addition to this, it is interesting to mention the existence of a new emission band in the spectrum of $KGd_{0.995}Pr_{0.005}(PO_3)_4$ in comparison with the other two samples, which is centred at 341 nm and has been attributed to the $^1S_0 \rightarrow {}^1D_2$ transition of Pr^{3+}. By comparing the emission spectra obtained at different Pr^{3+} concentrations, it can be observed that all emission bands observed in the sample with 1 at. % of Pr^{3+} are much more intense than those observed in the least doped sample (0.5 at. %). However, the intensity of all bands belonging to the sample with 2 at. % of Pr^{3+} is even lower than that of the bands of the sample with 0.5 at. %, so there is a visible quenching due to the concentration effect in concentrations equal or larger than 2 at. %.

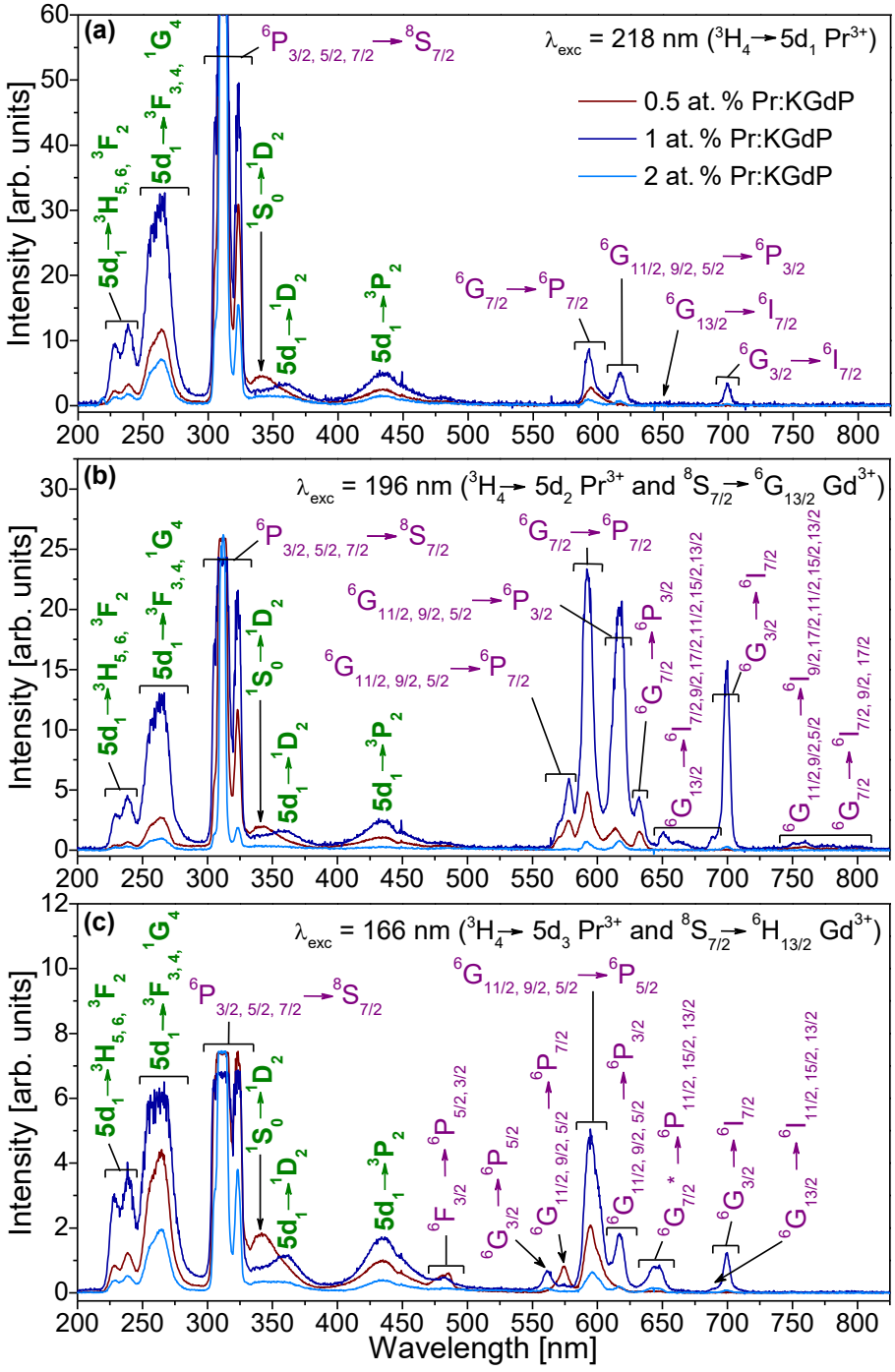

Figure 5.16. Optical emission spectra of $KGd_{0.995}Pr_{0.005}(PO_3)_4$, $KGd_{0.990}Pr_{0.010}(PO_3)_4$ and $KGd_{0.974}Pr_{0.026}(PO_3)_4$ under (a) 218 nm, (b) 196 nm, and (c) 166 nm excitation at RT. In all cases, the incident excitation beam was parallel to the *c** axis of the sample. The samples were plates parallel to the (001) plane, oriented with the *b* axis pointing upwards. Labels in green and bold indicate the transitions of Pr^{3+}, and labels in purple those of Gd^{3+}.

The intensity of each emission band corresponding to transitions of Pr^{3+} or even its existence or not depends on the host, as can be seen in the following selected compounds from the literature. In the case of the work done by Srivastava *et al*. on the phosphate $La_{0.999}Pr_{0.001}PO_4$ [49], its emission spectrum under $^3H_4 \rightarrow 5d_1$ excitation of Pr^{3+} (193 nm) at 300 K shows the emission bands corresponding to the $5d_1 \rightarrow {}^3H_4$ and $5d_1 \rightarrow {}^3H_5$ transitions as the most intense, which are centred at about 230 and 240 nm, respectively. The bands that correspond to the $5d_1 \rightarrow {}^3H_6, {}^3F_2$, $5d_1 \rightarrow {}^1D_2$ and $5d_1 \rightarrow {}^1I_6, {}^3P_J$ transitions appear centred around 255, 375 and 440 nm, respectively, with the 375 nm band being the least intense of those corresponding to the $5d_1 \rightarrow 4f$ transitions. Besides, an emission peak centred at approximately 610 nm can also be observed, with an intensity similar to the 375 and 440 nm bands, which the authors attributes to the $^1D_2 \rightarrow {}^3H_4$ electronic transition of Pr^{3+}. In the same work, the emission of the sample $La_{0.999}Pr_{0.001}PO_4$ under $^3H_4 \rightarrow 5d_1$ excitation was also studied at 1.6 K. This spectrum clearly shows the existence of other bands corresponding to $5d_1 \rightarrow 4f$ and $4f \rightarrow 4f$ transitions of Pr^{3+}, among them, a band centred at approximately 340 nm labelled as the $^1S_0 \rightarrow {}^1D_2$ transition. In the work carried out by Katelnikovas *et al.* on the photoluminescence properties of Pr^{3+}-doped garnets[50], the emission spectra of $Pr:Lu_3Al_5O_{12}$, $Pr:Lu_3Al_4GaO_{12}$ and $Pr:Lu_3Al_3Ga_2O_{12}$ under direct $4f \rightarrow 5d_1$ excitation of Pr^{3+} (280 nm) show the emission bands corresponding to the $5d_1 \rightarrow {}^3H_J$ and $5d_1 \rightarrow {}^3F_J$ transitions, which are centred at 310 and 360 nm, whereas the bands corresponding to the $5d_1 \rightarrow {}^1G_4$, $5d_1 \rightarrow {}^1D_2$ and $5d_1 \rightarrow {}^3P_J$ electronic transitions do not appear. The 310 nm band is clearly the most intense in the three garnets. On the contrary, several almost imperceptible emission peaks appear in the visible spectral range from 480 to 760 nm, which correspond to some of the $4f \rightarrow 4f$ transitions of Pr^{3+}. By last, in the emission spectrum of $Pr:LiYF_4$ obtained by van Pieterson *et al.* after exciting the $5d_1$ level of Pr^{3+} (210 nm) at 10 K[51], it can be observed that emission bands centred at 220, 230, 245, 255 and 272 nm have been labelled as $5d_1 \rightarrow {}^3H_4$, $5d_1 \rightarrow {}^3H_5$, $5d_1 \rightarrow {}^3H_6$, $5d_1 \rightarrow {}^3F_{3,4}$ and $5d_1 \rightarrow {}^1G_4$ transitions of Pr^{3+}, respectively. The intensity of the band corresponding to the $5d_1 \rightarrow {}^3H_5$ transition is the highest, while the band that corresponds to the $5d_1 \rightarrow {}^1G_4$ transition is the least intense. The bands belonging to the $5d_1 \rightarrow {}^1D_2$ and $5d_1 \rightarrow {}^3P_2$ transitions do not appear.

In Figure 5.16.b, it can be seen that the emission spectra obtained after exciting the three samples at 196 nm are very similar to those obtained under 218 nm excitation (Figure 5.16.a) in the spectral range of 200−500 nm, in terms of the intensity of the emission bands depending on the Pr^{3+} content and the intensity ratio of the emission bands of a specific spectrum. The main differences observed are in the 500−825 nm visible range, since the four Gd^{3+} emission bands mentioned in the spectra obtained under 218 nm excitation are considerably intensified and, in addition, several new peaks appear. These new peaks are located at 570−578, 632, 662, 689, 751, 759, 777 and 800 nm and correspond to the $^6G_{11/2,9/2,5/2} \rightarrow {}^6P_{7/2}$, $^6G_{7/2} \rightarrow {}^6P_{3/2}$, $^6G_{13/2} \rightarrow {}^6I_{9/2,17/2}$, $^6G_{13/2} \rightarrow {}^6I_{11/2,15/2,13/2}$, $^6G_{11/2,9/2,5/2} \rightarrow {}^6I_{9/2,17/2}$, $^6G_{7/2} \rightarrow {}^6I_{7/2}$, $^6G_{11/2,9/2,5/2} \rightarrow {}^6I_{11/2,15/2,13/2}$ and $^6G_{7/2} \rightarrow {}^6I_{9/2,17/2}$ transitions of Gd^{3+}, respectively. Besides, except for the sample with 2 at. % of Pr^{3+}, the emission bands corresponding to the $4f \rightarrow 4f$ electronic transitions of Gd^{3+} are more intense than the UV bands corresponding to the $5d \rightarrow 4f$ electronic transitions of Pr^{3+}. This behaviour could be related to the direct Gd^{3+} excitation

($^8S_{7/2} \rightarrow {}^6G_{13/2}$) leading to a larger electronic population in the 4*f* levels of Gd^{3+} and to a simultaneous energy transfer process from Pr^{3+} to Gd^{3+}. Photon cascade emissions of Gd^{3+} in the UV-Visible-near IR range were also observed in $GdBaB_9O_{16}$ under $^8S_{7/2} \rightarrow {}^6G_J$ excitation (202 nm)[4], and in $NaGdFPO_4$ and $NaY_{0.8}Gd_{0.2}FPO_4$ under 195 nm excitation ($^8S_{7/2} \rightarrow {}^6G_J$)[18].

Figure 5.16.c shows some differences in the emission spectra obtained under 166 nm excitation compared with those obtained under 218 and 196 nm excitation. In the spectral range of 500−825 nm, the Gd^{3+} bands centred at 617 nm ($^6G_{11/2,9/2,5/2} \rightarrow {}^6P_{3/2}$) and 700 nm ($^6G_{3/2} \rightarrow {}^6I_{7/2}$) clearly decrease in intensity compared to the emission spectra obtained by exciting the samples at 196 nm and slightly decrease in comparison with the emission spectra under 218 nm excitation. The last difference is the appearance of three new emission bands, which are located at 561, 595 and 645 nm. These bands have been labelled as the $^6G_{3/2} \rightarrow {}^6P_{5/2}$, $^6G_{11/2,9/2,5/2} \rightarrow {}^6P_{5/2}$ and $^6G_{7/2}{}^* \rightarrow {}^6I_{11/2,15/2,13/2}$ transitions of Gd^{3+}, respectively.

Figure 5.17 displays the energy levels diagram of Pr^{3+} and Gd^{3+} ions in Pr^{3+}-doped type III KGdP, the electronic transitions assigned to the observed bands in the emission spectra under 218, 196 and 166 nm excitation, and the energy transfer processes mentioned above.

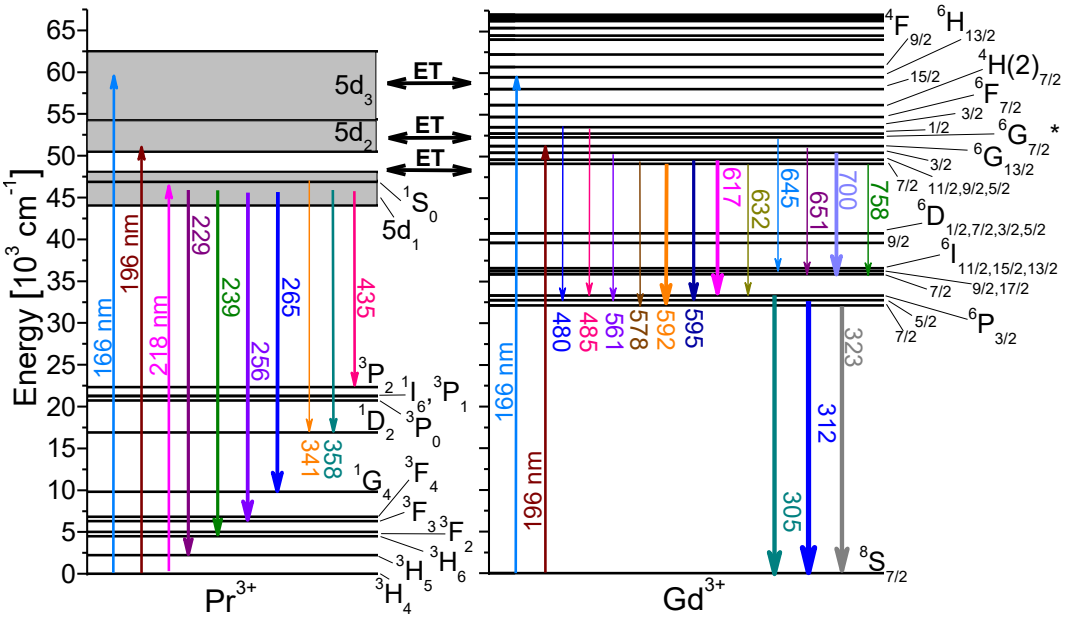

Figure 5.17. Energy levels diagram of Pr^{3+} and Gd^{3+} ions in Pr:KGdP and the emission mechanisms. ET = Energy Transfer. The thickness of the emission arrows is related to the intensity of the corresponding bands observed in the emission spectra under VUV-UV excitation.

As mentioned at the beginning of this Section, the 5*d*$_2$ and 5*d*$_3$ energy levels of Pr^{3+} in type III KGdP have been identified for the first time after studying excitation spectra from 120 to 248 nm for several emission wavelengths. Figure 5.18 shows, as exam-

ples, the excitation spectra of $KGd_{0.990}Pr_{0.010}(PO_3)_4$ for the emission wavelengths λ_{emi} = 435 nm ($5d_1 \rightarrow {}^3P_2$ of Pr^{3+}) and 700 nm (${}^6G_{3/2} \rightarrow {}^6I_{7/2}$ of Gd^{3+}). In the excitation spectrum for the Pr^{3+} emission (Figure 5.18.a), three broad bands centred around 166, 196 and 218 nm can be observed, which have been ascribed to the ${}^3H_4 \rightarrow 5d_3$, ${}^3H_4 \rightarrow 5d_2$ and ${}^3H_4 \rightarrow 5d_1$ electronic transitions of Pr^{3+} in type III KGdP, respectively. The pointed peaks that protrude from these rounded bands have been attributed to $4f \rightarrow 4f$ transitions of Gd^{3+}. Since, apart from the $5d$ levels of Pr^{3+}, some $4f$ levels

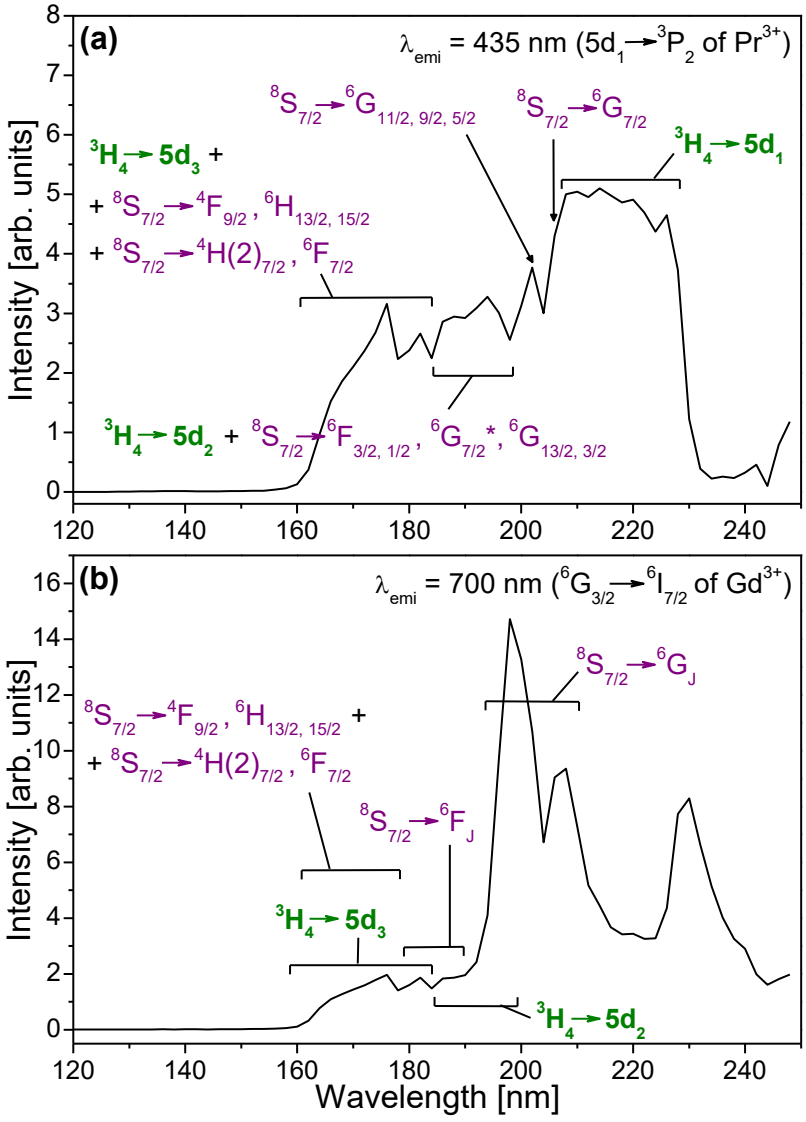

Figure 5.18. Excitation spectra of $KGd_{0.990}Pr_{0.010}(PO_3)_4$ for the emission wavelengths of (a) 435 nm ($5d_1 \rightarrow {}^3P_2$ of Ce^{3+}) and (b) 700 nm (${}^6G_{3/2} \rightarrow {}^6I_{7/2}$ of Gd^{3+}) at room temperature. Propagation direction of the excitation radiation is along the *c** crystallographic axis, with the *b* axis pointing upwards. Labels in purple indicate the electronic transitions of Gd^{3+} and labels in green and bold those of Pr^{3+}.

of Gd^{3+} are also excited, this may be due to an energy transfer process from Gd^{3+} to Pr^{3+}. In the excitation spectrum for the Gd^{3+} emission (Figure 5.18.b), the bands attributed to both the $^3H_4 \rightarrow 5d_x$ transitions of Pr^{3+} and the $4f \rightarrow 4f$ transitions of Gd^{3+} can also be observed, although it seems that the Gd^{3+} emission is more favoured when the ^6G_J levels of Gd^{3+} are excited. The Gd^{3+} emission can be explained by the excitation of the $5d_3$, $5d_2$ and $5d_1$ levels of Pr^{3+} and the subsequent energy transfer to Gd^{3+}. Figure 5.18 resembles in parallel to the excitation spectra of the same sample for the emission wavelengths $\lambda_{emi} = 265$ nm ($5d_1 \rightarrow {}^1G_4$ of Pr^{3+}) and $\lambda_{emi} = 592$ nm ($^6G_{7/2} \rightarrow {}^6P_{3/2}$ of Gd^{3+}), which can be found in Figure 10 of *Paper II*.

Taking into account the calculations explained in *Paper I* to predict the energy of the exciton creation, E^{ex}, and the approximate energy difference between the bottom of the conduction band (E_C) and the top of the valence band (E_V), E_{VC}, of the type III KGdP host, these values are $E^{ex} = 7.57$ eV (164 nm) and $E_{VC} = 8.17$ eV (152 nm). Hence, the band corresponding to E^{ex} could appear in the excitation spectra, although it would not be appreciated due to an overlapping with the $^8S_{7/2} \rightarrow {}^4F_{9/2}$ transition of Gd^{3+}.

5.3.2.2. Luminescence measurements under visible excitation

Figure 5.19 shows the optical emission spectra of four KGdP samples with different Pr^{3+} content under 445 nm excitation ($^3H_4 \rightarrow {}^3P_2$ of Pr^{3+}) at room temperature. All emission peaks belong to $4f \rightarrow 4f$ electronic transitions of Pr^{3+}, so the labelling process has basically been done using the Dieke's diagram[1]. These emission bands have also been observed in the emission spectra of other Pr^{3+}-doped compounds after being excited with visible radiation[50,52,53,54,55].

It can be clearly observed that the most intense band in all spectra is centred at 600 nm and corresponds to the $^1D_2 \rightarrow {}^3H_4$ transition. This band is formed by three peaks centred at 600, 595 and 609.5 nm, but this is only clear in the spectrum of $KGd_{0.974}Pr_{0.026}(PO_3)_4$ and $KGd_{0.995}Pr_{0.005}(PO_3)_4$. The anisotropic behaviour observed could be due to which are the optical axes present in the output plane of the emission. The emission spectra of the cube-shape cut samples $KGd_{0.995}Pr_{0.005}(PO_3)_4$ and $KGd_{0.974}Pr_{0.026}(PO_3)_4$ are highly similar, and it can be verified (see figure caption) that N_m-N_g is the output plane of the emission in both measurements. On the other hand, the emission spectra of the cubes $KGd_{0.990}Pr_{0.010}(PO_3)_4$ and $KGd_{0.997}Pr_{0.003}(PO_3)_4$ are similar, and the output plane of the emission contains the N_p axis in both measurements.

Figure 5.20 displays the polarized optical emission spectra at room temperature of the $^3P_1 \rightarrow {}^3H_6$, $^1D_2 \rightarrow {}^3H_4$ and $^3P_0 \rightarrow {}^3H_6$,$^3F_2$ transitions of Pr^{3+} in $KGd_{0.974}Pr_{0.026}(PO_3)_4$ under 445 nm excitation with the electric field of incident light parallel to the principal optical axes N_g, N_m and N_p. By joining the blue (E//N_m) and pink (E//N_g) spectra, it can be seen that the band corresponding to the $^1D_2 \rightarrow {}^3H_4$ transition would have the same profile as the band of the wine colour spectrum of Figure 5.19.a (output plane of emission: N_m-N_g). The purple spectrum (E//N_p) shows a clearly different behaviour, since the emission bands corresponding to the $^3P_{0,1} \rightarrow {}^3H_6$ transitions are not present

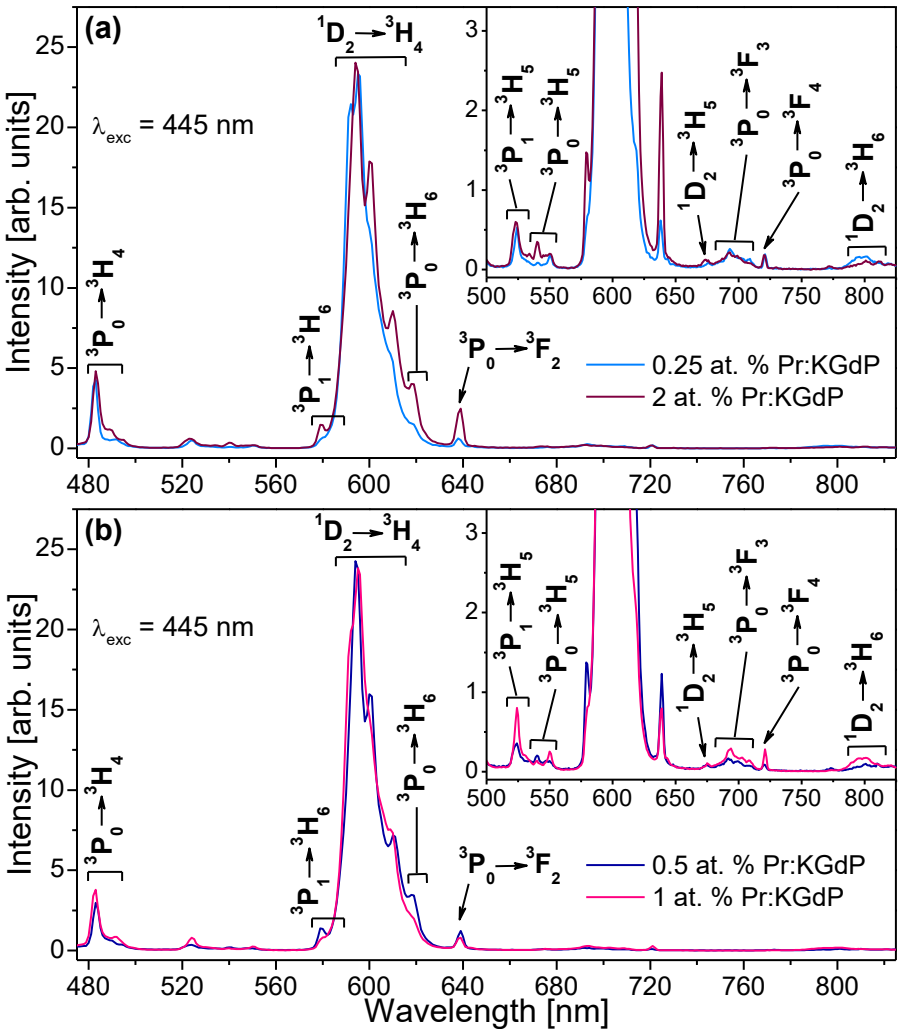

Figure 5.19. (a) Optical emission spectra of cube-shape cut samples of $KGd_{0.997}Pr_{0.003}(PO_3)_4$ and $KGd_{0.974}Pr_{0.026}(PO_3)_4$ under 445 nm excitation ($^3H_4 \rightarrow {}^3P_2$ of Pr^{3+}) at room temperature. The incident excitation beam was parallel to the N_m optical axis in both cubes, and the output plane of the emission was the N_m-N_p for the first sample and the N_m-N_g for the second one. (b) Optical emission spectra of cube-shape cut samples of $KGd_{0.995}Pr_{0.005}(PO_3)_4$ and $KGd_{0.990}Pr_{0.010}(PO_3)_4$ under 445 nm excitation at room temperature. The incident excitation beam was parallel to the N_g optical axis in both cubes, and the output plane of the emission was the N_m-N_g for the first sample and the N_g-N_p for the second one. All labels correspond to electronic transitions of Pr^{3+}.

and, in addition, there is a new band centred around 592 nm. The same happens in the light blue spectrum of Figure 5.19.a (output plane of emission: N_m-N_p). As also observed in the polarized optical absorption measurements of the same samples (Section 5.3.1.2), an important anisotropic behaviour can be seen in the polarized optical emission based on the $4f \rightarrow 4f$ electronic transitions of Pr^{3+}. This anisotropy

cannot be related to the polarization selection rules because the Pr^{3+} ions are located in a single C_1 site in the crystalline structure of this host.[37] The same behaviour was observed in the polarized optical emission based on the $4f \rightarrow 4f$ electronic transitions of the Nd^{3+} doping ion in type III KGdP, so the mentioned anisotropic behaviour may be caused by this host itself.[45]

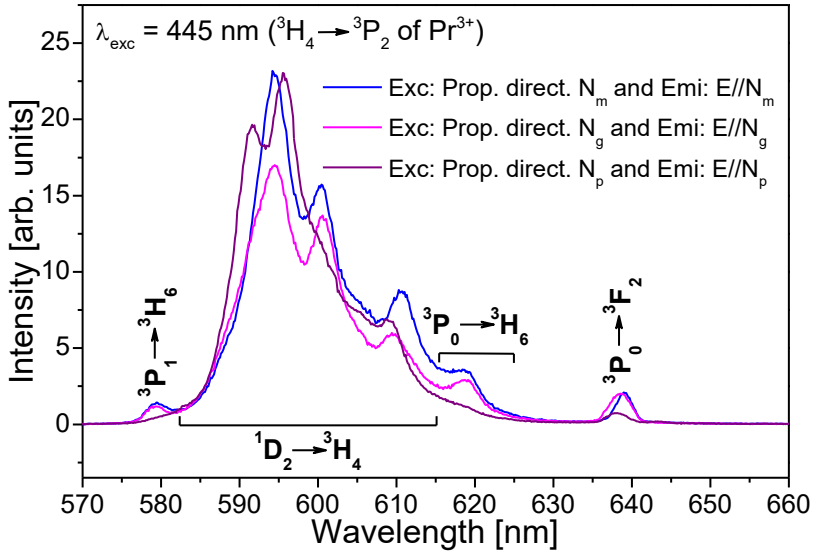

Figure 5.20. Polarized optical emission spectra of the $^3P_1 \rightarrow {}^3H_6$, $^1D_2 \rightarrow {}^3H_4$ and $^3P_0 \rightarrow {}^3H_6, {}^3F_2$ transitions of Pr^{3+} in $KGd_{0.974}Pr_{0.026}(PO_3)_4$ under 445 nm excitation at room temperature.

5.3.3. Decay time measurements

5.3.3.1. Decay time measurements under VUV-UV excitation

Figure 5.21 shows the luminescence decay curves for the central wavelength of the emission band corresponding to the $5d_1 \rightarrow {}^3F_{3,4}$ transitions of Pr^{3+} in type III KGdP host ($\lambda_{emi} = 256$ nm) of Pr:KGdP crystals with different doping concentrations and at different excitation wavelengths at room temperature. The Pr^{3+} concentrations studied were 1, 2 and 5 at. % in solution, corresponding to crystals with stoichiometry $KGd_{0.990}Pr_{0.010}(PO_3)_4$, $KGd_{0.974}Pr_{0.026}(PO_3)_4$ and $KGd_{0.942}Pr_{0.058}(PO_3)_4$, respectively. The excitation wavelengths used were 218 nm ($^3H_4 \rightarrow 5d_1$ of Pr^{3+}) and 166 nm ($^3H_4 \rightarrow 5d_3$ of Pr^{3+} and $^8S_{7/2} \rightarrow {}^6H_{13/2}$ of Gd^{3+}) under pulsed synchrotron radiation a full width at half-maximum pulse duration of 50 ps and an interpulse duration of 1118 ns. In order to increase the photon flux reaching the sample, the excitation beam was not purely monochromatic but had a bandwidth of about 7%. As can be seen in the figure, all the decay curves can be fitted to single exponential decays with practically the same time constant, which means that the lifetime of the $5d_1$ level of Pr^{3+} in type III KGdP is of around 6 ns. In addition to this, it can also be said that the lifetime of this level is not influenced by the excitation wavelengths nor by the Pr^{3+} doping concentration, at least up to 5.8 at. % of Pr^{3+} in the crystal.

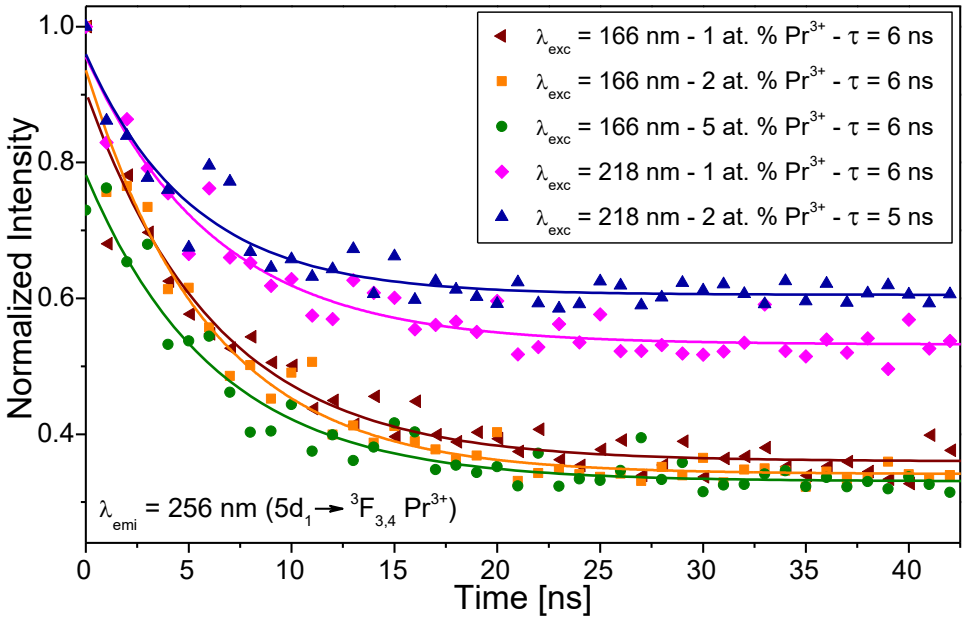

Figure 5.21. Fast component of the luminescence decay curves of Pr:KGdP crystals with different doping concentrations and at different excitation wavelengths for λ_{emi} = 256 nm ($5d_1 \rightarrow {}^3F_{3,4}$ of Pr^{3+}) at room temperature. In all cases, the incident excitation beam was parallel to the *c** crystallographic axis of the sample. The samples were plates parallel to the (001) plane, oriented with the *b* crystallographic axis pointing upwards.

The lifetime of the $5d_1$ level of Pr^{3+} in type III $KGd(PO_3)_4$ ($\tau = 6$ ns) is usually shorter than the lifetimes obtained in other hosts. The lifetime of this level in hosts where the Pr^{3+} is also a doping element is significantly higher, such as 19.9−20.3 ns in $Pr:K_3Lu(PO_4)_2$ [56], 20.1 ns in $Pr:Lu_3Al_5O_{12}$ [57], and 16−19 ns in $Pr:LiYF_4$ [51]. In contrast, the values obtained in compounds where the Pr^{3+} is a host element are more similar to our case, although they seem higher anyway. The lifetime of the $5d_1$ level of Pr^{3+} is 10.5 ns in $LiPrP_4O_{12}$ [58], 10.5 ns in $NaPr_{0.998}Ce_{0.002}P_4O_{12}$ [13], and 6 ns in $Pr(PO_3)_3$ [59]. Hence, the shortening of the lifetime of the $5d_1$ level of Pr^{3+} in the type III KGdP host may be due to an additional depopulation channel, besides the radiative decay. This could be explained by an energy transfer from Pr^{3+} to Gd^{3+}, already mentioned in Section 5.3.2.1 and represented in Figure 5.17. Also in Figure 5.21, it can be seen that the intensity does not reach zero, so the luminescence decay curves are composed by a fast component and a slow component. The short interpulse time of 1118 ns of the synchrotron radiation allows us to determine the fast component of the luminescence decay curves, but not the slow component. The origin of this slow component could be due to an energy transfer from 4*f* levels of Gd^{3+} to 5*d* levels of Pr^{3+}.

5.3.3.2. Decay time measurements under visible excitation

Figure 5.22 shows the luminescence decay curves for λ_{emi} = 600 nm ($^1D_2 \rightarrow {}^3H_4$ of Pr^{3+}) of Pr^{3+}-doped type III KGdP cube-shape cut samples with different doping concentrations under 445 nm excitation ($^3H_4 \rightarrow {}^3P_2$ of Pr^{3+}) at room temperature. As can be seen, each decay curve can be fitted to a single exponential decay with a time constant of the order of a few hundred microseconds, which has been attributed to the lifetime of the $^1D_2$ level of Pr^{3+}. Since the emission band corresponding to the $^1D_2 \rightarrow {}^3H_4$ electronic transition of Pr^{3+} has other intensity maxima (see Figure 5.19), luminescence decay curves have also been performed for the emission wavelengths λ_{emi} = 595 and 609.5 nm for each sample studied in Figure 5.19. The time constant obtained from each single exponential fitting of the decay curves for λ_{emi} = 595 and 609.5 nm is the same (±1 μs) as the value obtained for λ_{emi} = 600 nm for each sample, respectively. Therefore, the lifetime of $^1D_2$ level of Pr^{3+} is 215, 187, 150 and 108 μs for the samples $KGd_{0.997}Pr_{0.003}(PO_3)_4$, $KGd_{0.995}Pr_{0.005}(PO_3)_4$, $KGd_{0.990}Pr_{0.010}(PO_3)_4$ and $KGd_{0.974}Pr_{0.026}(PO_3)_4$, respectively. As can be clearly seen, the value of the $^1D_2$ lifetime decreases as the Pr^{3+} concentration increases in the type III KGdP crystal. This behaviour has also been observed in other hosts doped with Pr^{3+}, such as in the Pr:YPO_4 crystals by Collins *et al.*[52] and in several glasses[54,60,61]. As examples, the $^1D_2$ lifetime in the case of the Pr:YPO_4 crystals[52] is 187 μs for 0.1% of Pr^{3+},104 μs for 1% and 61 μs for 2%, while the $^1D_2$ lifetime in the Pr^{3+}-doped phosphate glasses by Zhang *et al.*[60] is 173, 153, 104, 69, 18 and 6 μs for the concentration values of 0.05, 0.1, 0.25, 0.5, 1.5 and 3.00 mol% of Pr^{3+}, respectively. In all cases[52,54,60,61], the authors attribute this behaviour mainly to cross-relaxation processes derived from the

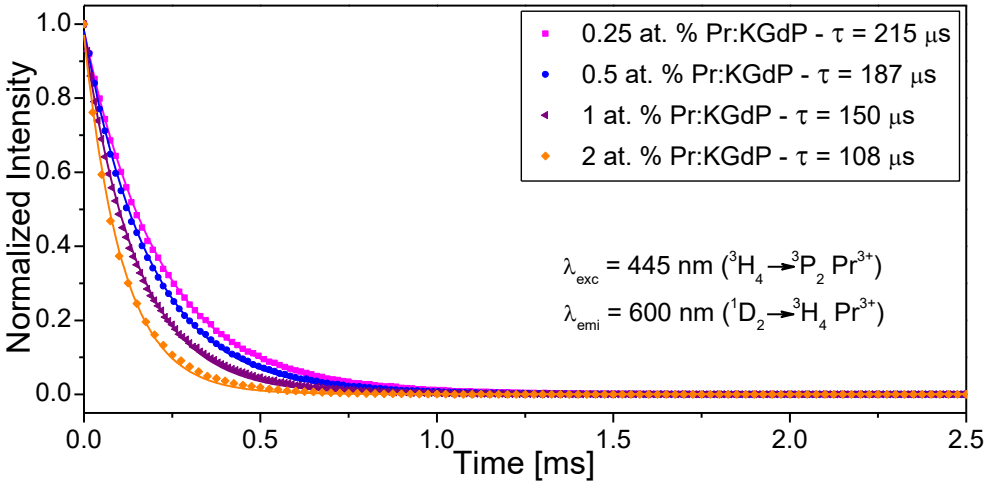

Figure 5.22. Luminescence decay curves of cube-shape cut samples of Pr:KGdP with different doping concentrations for λ_{emi} = 600 nm ($^1D_2 \rightarrow {}^3H_4$ of Pr^{3+}) under 445 nm excitation ($^3H_4 \rightarrow {}^3P_2$ of Pr^{3+}) at room temperature. The incident excitation beam was parallel to the N_m optical axis for $KGd_{0.997}Pr_{0.003}(PO_3)_4$ and $KGd_{0.974}Pr_{0.026}(PO_3)_4$ cubes, and the output planes of the emission were the N_m-N_p and N_m-N_g, respectively. The incident excitation beam was parallel to the N_g optical axis for $KGd_{0.995}Pr_{0.005}(PO_3)_4$ and $KGd_{0.990}Pr_{0.010}(PO_3)_4$ cubes, and the output planes of the emission were the N_m-N_g and N_g-N_p, respectively.

neighbouring Pr^{3+} ions, schematized in their works, which is favoured as the distance between the Pr^{3+} ions decreases. In addition, they also attribute it to energy transfer processes and multi-phonon relaxation. Therefore, the three mentioned processes are detrimental to the quantum efficiency of the $^1D_2$ level of Pr^{3+}, which leads to a reduction of its lifetime. Consequently, the value of the $^1D_2$ lifetime obtained from a compound with a low concentration of Pr^{3+} is closer to the radiative lifetime, so the value of the $^1D_2$ lifetime used to compare it with other compounds will be 215 μs in $KGd_{0.997}Pr_{0.003}(PO_3)_4$. Considering the compounds mentioned previously[52,54,61,60], this value for the least doped samples varies from 108.2 to 187 μs. However, faster lifetimes of the $^1D_2$ level have been observed in other compounds, such as 24.0 μs in $Na_3Y_{0.98}Pr_{0.02}(PO_4)_2$[62] and 5.4 μs in $Pr^{3+}_{0.003}$,$Li^+_{0.003}$:$Zn_{0.994}WO_4$[53] crystalline powders. In the second case, the authors mention that the cause of obtaining this low value is the existence of radiation relaxation channels. In conclusion, the lifetime of $^1D_2$ level of Pr^{3+} in type III KGdP host seems to be less affected by the aforementioned processes: cross-relaxation, energy transfer and multi-phonon relaxation, and it is probably among the longest lifetimes. This long lifetime (in other words, this reduction of depopulating channels) could be related to the large Pr−Pr interatomic distances in type III KGdP host, as mentioned in Section 1.4.1.

5.3.4. Radioluminescence measurements under X-ray excitation

Figure 5.23 shows the X-ray excited radioluminescence (RL) spectra of undoped KGdP and Pr:KGdP at different Pr^{3+} concentrations under 13000 eV, 26700 eV and 56000 eV excitation at room temperature. The RL spectra under 12000 eV, 16500 eV, 31000 eV and 46000 eV excitation of the same samples are shown in Figure 4 of *Paper IV*. In order to label correctly the emission bands observed in the RL spectra of Pr^{3+}-doped KGdP samples, the RL spectra of the undoped sample have been used. The labeling process has been carried out using the Dieke's diagram[1], the extended Dieke's diagram[2] and the refs.[3,4,30].

For each of the X-ray excitation energies studied, both the RL spectra of the undoped sample and those of the Pr^{3+}-doped KGdP samples show an emission band centred at 312 nm as the most intense, corresponding to the $^6P_{3/2,5/2,7/2} \rightarrow {}^8S_{7/2}$ transitions of Gd^{3+}. Two bands centred around 236 and 259 nm can be observed only in the RL spectra of Pr:KGdP, so they have been attributed to electronic transitions of Pr^{3+}. More specifically, these two emission bands correspond to the $5d_1 \rightarrow {}^3H_{4,5,6}$, $^3F_2$ and $5d_1 \rightarrow {}^3F_{3,4}$,$^1G_4$ transitions of Pr^{3+} in type III KGdP (space group: $P2_1$), respectively. Since these and other emission bands corresponding to $5d \rightarrow 4f$ transitions of Pr^{3+} have been observed in the emission spectra of the same samples under direct $4f \rightarrow 5d$ excitation (Figure 5.16), it is reaffirmed that the emissions of 236 and 259 nm originate at the $5d_1$ level of Pr^{3+}. It is worth noting that the bands corresponding to the $5d_1 \rightarrow 4f$ transitions of Pr^{3+} and to the $^6P_{3/2,5/2,7/2} \rightarrow {}^8S_{7/2}$ transitions of Gd^{3+} coexist, so the presence of this Gd^{3+} emission may be attributed to an inefficient energy transfer from the ^6D_J, ^6I_J and ^6P_J levels of Gd^{3+} to the $5d_1$ level of Pr^{3+}. The cause of this inefficiency lies in the fact that the energy difference between the mentioned levels of the two ions in this compound is relatively high and, in addition, the $5d_1$ is slightly

higher in energy than the ^6D_J, ^6I_J and ^6P_J levels, as can be checked in Figure 5.24.b. Such coexistence has also been observed in the RL spectra of some Gd-based multicomponent aluminate garnets: 0.3 at. % Pr:$(Gd,Lu)_3Ga_3Al_2O_{12}$ [47] and 0.2 and 1 at. % Pr:$(Gd,Lu)_3(Ga,Al)_5O_{12}$ [63]. In the first work[47], the authors obtained the spectra of 0.3 at. % Pr:$(Gd,Lu)_3Ga_3Al_2O_{12}$ for six different Gd/Lu ratios. The emission bands corresponding to the $5d_1 \rightarrow {}^3H_4$, $5d_1 \rightarrow {}^3H_5$, $5d_1 \rightarrow {}^3H_6$,$^3F_2$ and $5d_1 \rightarrow {}^3F_{3,4}$ transitions of Pr^{3+} in this host appear centred around 295, 305, 320 and 330 nm, respectively, for the samples with the Gd/Lu ratios: $Gd_{0.025}Lu_{2.975}$, $Gd_{0.05}Lu_{2.95}$ and $Gd_{0.1}Lu_{2.9}$. By contrast, the Gd^{3+} band corresponding to the $^6P_{7/2} \rightarrow {}^8S_{7/2}$ transition, which appears centred at 311 nm, is present in the spectra of all samples studied, i.e. the three samples presented previously, $Gd_{0.2}Lu_{2.8}$, $Gd_{0.4}Lu_{2.6}$ and $Gd_{0.6}Lu_{2.4}$. As the Gd^{3+} content increases, a gradual increment of the intensity of this Gd^{3+} band can be observed along with a decrease of the $5d_1 \rightarrow 4f$ bands of Pr^{3+} until they become irrelevant. The authors conclude that there is an energy transfer process from the Pr^{3+} 5*d* levels to the Gd^{3+} 4*f* levels. In the second work[63], the spectrum of 0.2 at. % Pr:$Gd_{0.5}Lu_{2.5}Ga_2Al_3O_{12}$ shows that the emission belonging to the $5d_1 \rightarrow 4f$ transitions of Pr^{3+} in this host appears as a broad band, which extends from 290 to 420 nm, and the Gd^{3+} band corresponding to the $^6P_{7/2} \rightarrow {}^8S_{7/2}$ transition as a hump, with the maximum centred at 312 nm. On the contrary, the spectrum of a sample with a higher concentration of Gd^{3+} than the previous one, 0.2 at. % Pr:$GdLu_2Ga_2Al_3O_{12}$, shows that the $5d_1 \rightarrow 4f$ bands of Pr^{3+} become practically non-existent and that the Gd^{3+} emission appears as a narrow and intense band. After that, it is interesting to mention that the bands corresponding to the $5d_1 \rightarrow 4f$ transitions of Pr^{3+} in type III KGdP host are present despite the high atomic concentration of Gd^{3+} in all the crystals studied.

Unlike the RL spectra of Ce^{3+}-doped KGdP samples (Figure 5.8), not all emission bands that appear in the spectral range 350−850 nm in the RL spectra of Pr^{3+}-doped KGdP samples have been attributed to $4f \rightarrow 4f$ electronic transitions of Gd^{3+}. The broad band that appears from 560 to 700 nm in the RL spectra obtained by exciting the samples at 13000 eV (Figure 5.23.a) has been labelled as the $^1D_2 \rightarrow {}^3H_4$ and $^3P_0 \rightarrow {}^3H_6$ transitions of Pr^{3+}, since this band does not appear in the RL spectrum of the undoped sample nor in that of the crystal with low concentration of Pr^{3+}. This emission band has also been observed in the RL spectra of Pr:KGdP after excitation at 10000, 11000 and 12000 eV, as well as in the X-ray excited radioluminescence spectra of Pr:$Lu_2Si_2O_7$ [64], 0.3 at. % Pr:$(Gd,Lu)_3Ga_3Al_2O_{12}$ [47], 1 at. % Pr:$K_3(Lu,Y)(PO_4)_2$ [65], 0.2 at. % Pr:$Lu_3Al_5O_{12}$ [66], 0.2 and 2 at. % Pr:$Ca_3Sc_2Si_3O_{12}$ [67]. For the excitation energies from 16500 to 62500 eV (Figures 5.23.b and 5.23.c), all emission bands that appear in the spectral range of 350−850 nm belong to $4f \rightarrow 4f$ electronic transitions of Gd^{3+}, since these bands also are present in the RL spectra of the undoped sample. Among them, the most intense band corresponds to the $^6G_{7/2}{}^* \rightarrow {}^6I_{11/2,15/2,13/2}$ and $^6G_{13/2} \rightarrow {}^6I_{7/2,9/2,17/2}$ transitions of Gd^{3+}, and it extends from 615 to 690 nm. By exciting at 26700 eV, it can also be seen a band extending from 565 to 615 nm, which corresponds to the $^6G_{11/2,9/2,5/2} \rightarrow {}^6P_{7/2,5/2}$ and $^6G_{7/2} \rightarrow {}^6P_{7/2}$ transitions. The intensity of this band is higher for low Pr^{3+} concentrations (0.25 at. % in solution) and, in this case, its intensity is of the order of the band corresponding to the $^6G_{7/2}{}^* \rightarrow {}^6I_{11/2,15/2,13/2}$ and $^6G_{13/2} \rightarrow {}^6I_{7/2,9/2,17/2}$ transitions of Gd^{3+}. With a lower intensity, three weak emission

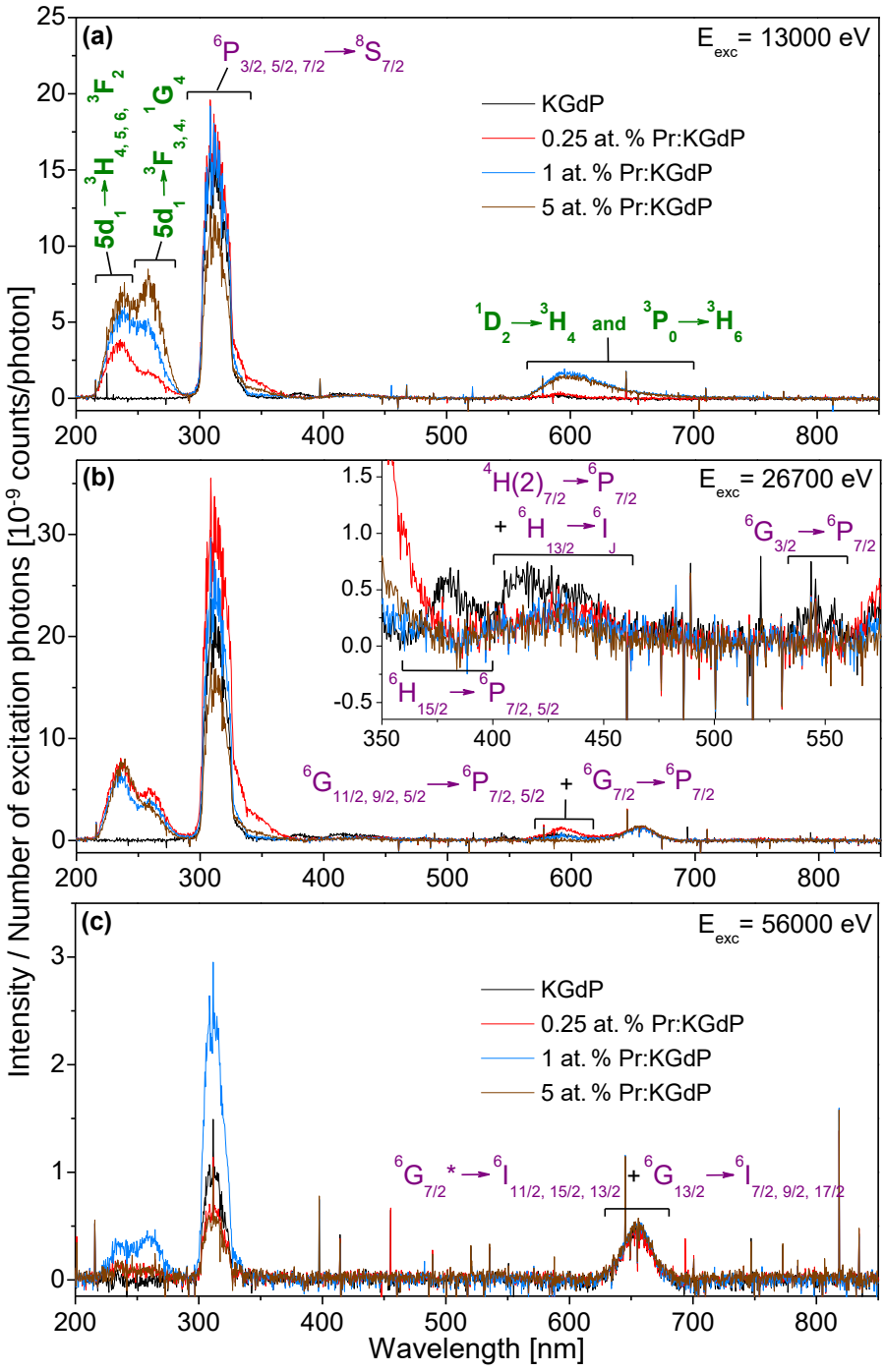

Figure 5.23. X-ray excited radioluminescence (RL) spectra of KGdP and Pr:KGdP at different Pr^{3+} concentrations under excitation at (a) 13000 eV, (b) 26700 eV, and (c) 56000 eV at RT. Propagation direction is along the *c** crystallographic axis, with the *b* axis pointing upwards. Labels in purple indicate the electronic transitions of Gd^{3+}, and labels in green and bold those of Pr^{3+}.

bands can be observed in the inset of Figure 5.23.b. The bands centred at 380 and 547 nm correspond to the $^6H_{15/2} \rightarrow {}^6P_{7/2,5/2}$ and $^6G_{3/2} \rightarrow {}^6P_{7/2}$ transitions, respectively, and finally, the band from 400 to 460 nm corresponds to the $^4H(2)_{7/2} \rightarrow {}^6P_{7/2}$ and $^6H_{13/2} \rightarrow {}^6I_J$ transitions.

To study the effect of the Pr^{3+} concentration on this host, RL spectra were obtained for three different doping levels at each excitation energy. In the spectra obtained by exciting the samples at excitation energies from 10000 to 31000 eV, an increase in the overall emission in the range from 200 to 350 nm can be observed when Pr^{3+} is present in the crystal compared to the undoped sample. Under 13000 eV excitation (Figure 5.23.a), it can be seen that the bands corresponding to the $5d_1 \rightarrow 4f$ transitions of Pr^{3+} increase as the Pr^{3+} content in the crystal increases, even when the crystal is doped with 5 at. % of Pr^{3+}. This indicates that there is no significant emission quenching due to the concentration effect by the Pr^{3+} concentration up to the value studied. As regards the Gd^{3+} band centred at 312 nm in the RL spectra of Pr:KGdP, its intensity gradually decreases as the Pr^{3+} content increases. Therefore, since the $5d_1 \rightarrow 4f$ bands of Pr^{3+} increase and the Gd^{3+} band decreases in intensity as the Pr^{3+} concentration in the crystal is higher, it seems that there is an energy transfer from Gd^{3+} to Pr^{3+} which becomes more efficient when the doping content is higher. Probably, what happens is an energy transfer from the 4*f* levels of higher energy of Gd^{3+} to the $5d_{2,3}$ levels of Pr^{3+}, followed by a non-radiative relaxation to the $5d_1$ level and, finally, a radiative decay from this $5d_1$ level to 4*f* levels of Pr^{3+}.

The behaviour under 26700 eV excitation (Figure 5.23.b) is different compared to that observed after excitation at 13000 eV. The intensity of the bands corresponding to the $5d_1 \rightarrow 4f$ transitions of Pr^{3+} practically remains with the same value, independently of the Pr^{3+} concentration, and the Gd^{3+} band centred at 312 nm corresponding to the crystals doped with 0.25 and 1 at. % of Pr^{3+} clearly exceeds the intensity of the same band of the undoped crystal. This could mean that there is an energy transfer from Pr^{3+} to Gd^{3+}, more specifically, from the $5d_{2,3}$ levels of Pr^{3+} to the ^6G_J levels and other 4*f* levels of higher energy of Gd^{3+}. This would be followed by radiative decay through the $^6G_J \rightarrow {}^6I_J$, ^6P_J transitions of Gd^{3+}, as can be seen in the visible region from 525 to 700 nm, and finally through the $^6P_J \rightarrow {}^8S_{7/2}$ transitions. Since the direction of the energy transfer mentioned above is inverse to that explained now, the energy transfer between the Pr^{3+} and Gd^{3+} ions is not unidirectional, but bidirectional. These energy transfer processes are represented in the energy level diagram of Pr^{3+} and Gd^{3+} shown in Figure 5.24.b, together with the emissions observed in the RL spectra.

A clearly different behaviour can be observed after excitation at 56000 eV (Figure 5.23.c) in function of the Pr^{3+} concentration in the crystal compared to the behaviours explained previously. The crystal doped with 1 at. % of Pr^{3+} shows a higher emission intensity in the spectral range between 200 and 350 nm than the other Pr^{3+}-doped KGdP crystals. This has also been observed by exciting these samples with other excitation energies within the energy range of 35500−62500 eV.

Figure 5.24.a shows the energy levels scheme for Pr^{3+} and Gd^{3+} ions with respect to the conduction (E_C) and valence (E_V) bands of type III $KGd(PO_3)_4$, along with a schematic illustration of the energy transfer process to Pr^{3+} ions based on the sequential

capture of charge carriers by Pr centres, which is one of the possible channels of excitation of the lanthanides in inorganic scintillator materials containing lanthanide ions[25,26,27]. The scintillation mechanism in this type of scintillators and the details regarding the praseodymium-doped compounds are explained in Sections 1.3.1 and 1.3.3. Returning to the figure, the refs.[11,12,30] have been used to locate the 5*d* and 4*f* energy levels of Pr^{3+} and Gd^{3+} with respect to the conduction and valence bands of this host, as explained in *Paper IV*, and the refs.[9,31] have been used as well.

In praseodymium-doped scintillation materials, the sequential capture of charge carriers by Pr centres usually begins with the capture of a hole by Pr^{3+}, since Pr^{3+} is a good hole trap, giving rise to Pr^{4+}, and continues with the capture of an electron by the Pr^{4+} [27,33]. In contrast, Gd^{3+} is very unlikely to introduce both hole and electron traps in scintillation materials, so this ion is one of the two best candidates, along with Lu, to act as a neutral constituent element[27]. Consequently, in the crystal lattice of Pr^{3+}-doped type III KGdP, the energy transfer process based on the sequential capture of charge carriers is expected to be more effective for Pr^{3+} ions than for Gd^{3+} ions, although it should be reminded that the concentration of Pr^{3+} is significantly lower than that of Gd^{3+}. Once Pr^{3+} and Gd^{3+} are excited, these centres emit light, as shown in Figure 5.23, following the emission mechanism depicted in Figure 5.24.b.

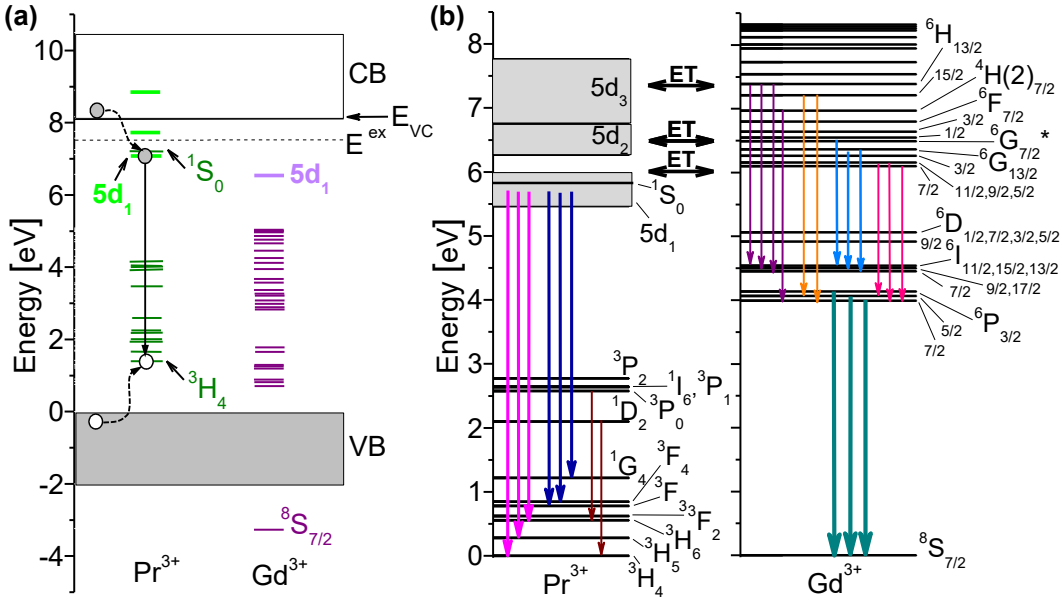

Figure 5.24. (a) Energy levels scheme for Pr^{3+} and Gd^{3+} with respect to the conduction and valence bands of type III $KGd(PO_3)_4$, which schematically illustrates the energy transfer process to Pr^{3+} ions based on the sequential capture of charge carriers by Pr centres. Electrons are symbolized by filled circles and holes by empty circles. The refs.[11,12,30] have been used to place the energy levels in this host. (b) Energy level diagram of Pr^{3+} and Gd^{3+} in $Pr:KGd(PO_3)_4$ and emissions observed after X-ray irradiation. The thickness of the arrows is related to the intensity of the emissions represented in the radioluminescence spectra, and the arrows with the same colour appear as a single band.

Figure 5.25 shows the energy conversion efficiency from several excitation energies of X-ray radiation to visible or near visible radiation for the emission bands centred at λ_{emi} = 236 and 259 nm (Pr^{3+}), λ_{emi} = 312 nm (Gd^{3+}), λ_{emi} = 598 (Pr^{3+}) and λ_{emi} = 656 nm (Gd^{3+}) for the $KGd_{0.997}Pr_{0.003}(PO_3)_4$ and $KGd_{0.990}Pr_{0.010}(PO_3)_4$ crystals. The X-ray photon energy is represented on the abscissa axis, and the integrated intensity of the emission band divided by the total excitation energy per second (number of X-rays photons per second of the specific excitation energy multiplied by the corresponding excitation energy) is on the ordinate axis. The maximum intensity value of the Gd^{3+}

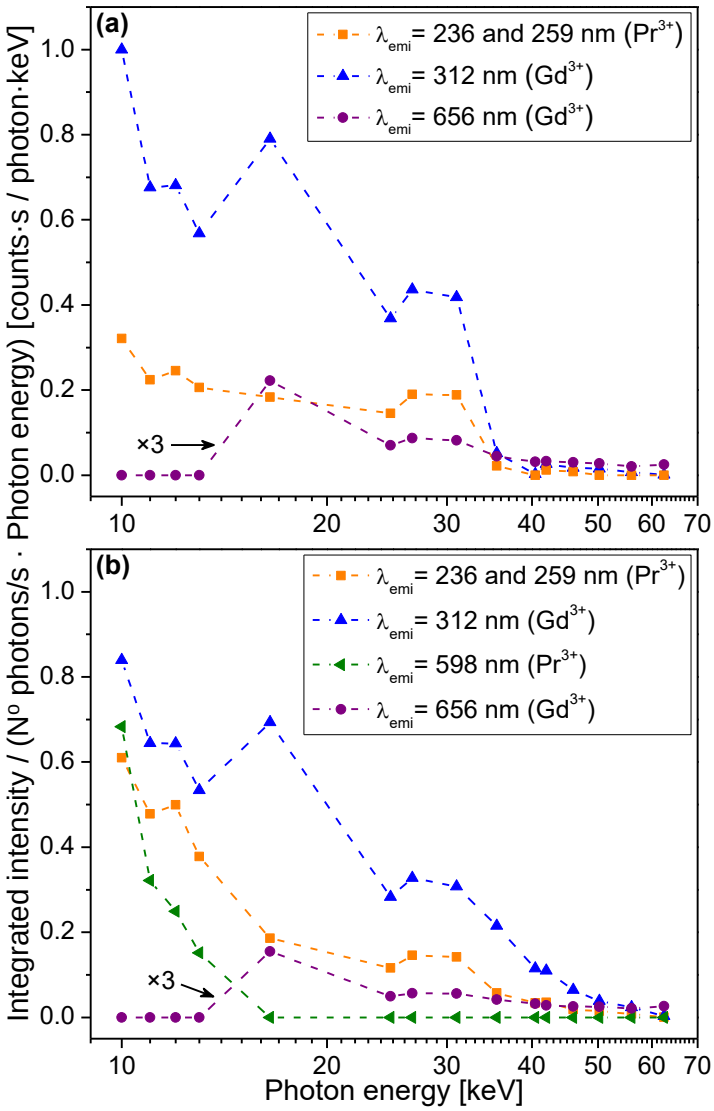

Figure 5.25. Normalized integrated intensity of several emission bands of the X-ray excited radioluminescence spectra of (a) $KGd_{0.997}Pr_{0.003}(PO_3)_4$ and (b) $KGd_{0.990}Pr_{0.010}(PO_3)_4$ as a function of the X-ray photon energy. The dashed lines are guides for the eye.

emission band centred at 312 nm for $KGd_{0.997}Pr_{0.003}(PO_3)_4$ has been used to normalize all intensity values for both samples. Due to the lower intensity values of some emission bands compared to those of the band centred at 312 nm, the data was multiplied by 3, and the resulting values are those represented in the figure. The energy conversion from X-ray radiation to visible or near visible radiation is more effective when the excitation energy is within the range of 10000 to 31000 eV for all the emission bands studied. For energies above 31000 eV, all emissions, both those belonging to Pr^{3+} and Gd^{3+} and regardless of the Pr^{3+} content, seem to be almost quenched. As in the Ce^{3+}-doped KGdP crystals, this behaviour could be due to the existence of competition between two processes: (1) the sequential capture of charge carriers by the Pr^{3+} and Gd^{3+} ions, and (2) the capture of electrons by the oxygen vacancies present in the crystal (see Section 5.4.1).

As a scintillator material of the type known as lanthanide-containing crystal, the focus is on those emissions that correspond to $5d \rightarrow 4f$ transitions. Thus, for scintillation applications, the optima conversion efficiencies are clearly produced when the excitation energies are within the range of 10000−16500 eV for the $KGd_{0.990}Pr_{0.010}(PO_3)_4$ crystal. When it comes to the Ce^{3+}-doped KGdP crystals, the optima conversion efficiencies through the $5d \rightarrow 4f$ transitions are produced by exciting the crystals at higher energies, more specifically up to 31000 eV (Figure 5.10). This different behaviour between the crystals doped with Ce^{3+} or Pr^{3+} could be explained by a larger creation of oxygen vacancies during the crystal growth process of the Pr^{3+}-doped KGdP crystals, so there would be more electron traps after X-ray irradiation and, therefore, more competition between the two processes mentioned above.

5.4.Radiation damage in type III undoped, Ce- and Pr-doped $KGd(PO_3)_4$ samples

Crystalline scintillators suffer from radiation damage under continued X-ray and γ-ray irradiation[68], so some of the samples used to carry out the X-ray excited radioluminescence measurements (Sections 5.2.4 and 5.3.4) have been subjected to two different studies to evaluate the level of radiation damage.

5.4.1. Analysis of radiation-induced visible optical absorption

The appearance of radiation-induced absorption bands is the most common damage and its origin is due to the formation of colour centres. The colour centres may be holes located in cation vacancies (V centre) of the crystalline lattice, electrons located in anion vacancies (F centre), or others. These centres can recover at room temperature, but the depth of the traps determines the speed of recovery. In oxides, defects related to stoichiometry, such as oxygen vacancies, are usually the cause of the radiation damage. The missing of oxygen in the crystalline lattice is an anionic vacancy that acts as an electron trap.[68]

During the X-ray excited radioluminescence measurements, change in coloration was observed in the undoped and Pr-doped KGdP samples, in the regions irradiated. In contrast, the Ce-doped KGdP samples did not change their colour. The undoped

sample showed a dark region, while the Pr-doped KGdP samples showed a brown-yellowish region, as can be seen in Figure 5 of Paper *IV*. The colour disappeared after a few hours, indicating an apparent recovery of the samples. The change in coloration has also been reported for other crystalline materials after being excited with ionizing radiation, such as $Mn:Bi_4Ge_3O_{12}$ under γ-ray excitation[68,69], $Gd:PbWO_4$ irradiated with neutrons[70] and $Pr:Ca_3Sc_2Si_3O_{12}$ under X-ray excitation[67]. A summary of the results of these works is in *Paper IV*.

Figure 5.26 shows the optical absorption spectra before and 5-7 days after continued X-ray irradiation (left) and the spectra resulting from the subtraction of the first data from the second one (right) for three different samples: undoped KGdP, 1 at. % Ce:KGdP and 1 at. % Pr:KGdP plates. All sharp absorption peaks and broad absorption bands present in the spectra obtained before and after irradiation are labelled in the figure itself in a general way. The absorption peaks and bands corresponding to the electronic transitions of Gd^{3+}, Ce^{3+} and Pr^{3+} can clearly be seen in Figures 5.2, 5.11 and 5.12, along with more specific labelling. Also in Figure 5.26, about the subtraction spectra, a broad radiation-induced absorption band from 190 to 600 nm can be observed for the cases of the undoped and Pr-doped KGdP samples, whereas this band is not present for the Ce-doped KGdP sample. The radiation-induced absorption band belonging to the undoped sample has a uniform intensity value, which results in the dark coloration mentioned above, while that belonging to the Pr-doped KGdP sample has a maximum intensity in the blue region, which agrees with the brown-yellowish coloration.

It is worth mentioning that the absorbance just after irradiating the samples was higher than that observed in the absorption spectra 5-7 days after continued X-ray irradiation. Thus, in the Ce-doped KGdP samples, the non-existence of radiation-induced absorption bands after a few days of recovery and the no colour change visible to the naked eye could indicate that these samples might not suffer from radiation damage.

Due to the high similarity between the radiation-induced absorption bands observed in the subtraction spectra of the undoped and Pr-doped KGdP samples, they are expected to have the same origin. Quite possibly, the cause is the formation of colour centres related to defects in the crystalline lattice, in particular due to the presence of oxygen vacancies that probably appeared in the crystal growth process. Consequently, and in accordance with the change in coloration, the undoped and Pr-doped KGdP samples should have more oxygen vacancies after the crystal growth than the Ce-doped KGdP samples.

It is important to mention that due to the capture of electrons by the oxygen vacancies and the sequential capture of charge carriers by the Ce^{3+}, Pr^{3+} and Gd^{3+} ions (see Section 1.3), there could be competition between these two processes and this would affect to the scintillation mechanism. In addition to this, the fact that the emission bands corresponding to the $5d_1 \rightarrow 4f$ transitions of Pr^{3+} overlap with the radiation-induced absorption band could also affect.

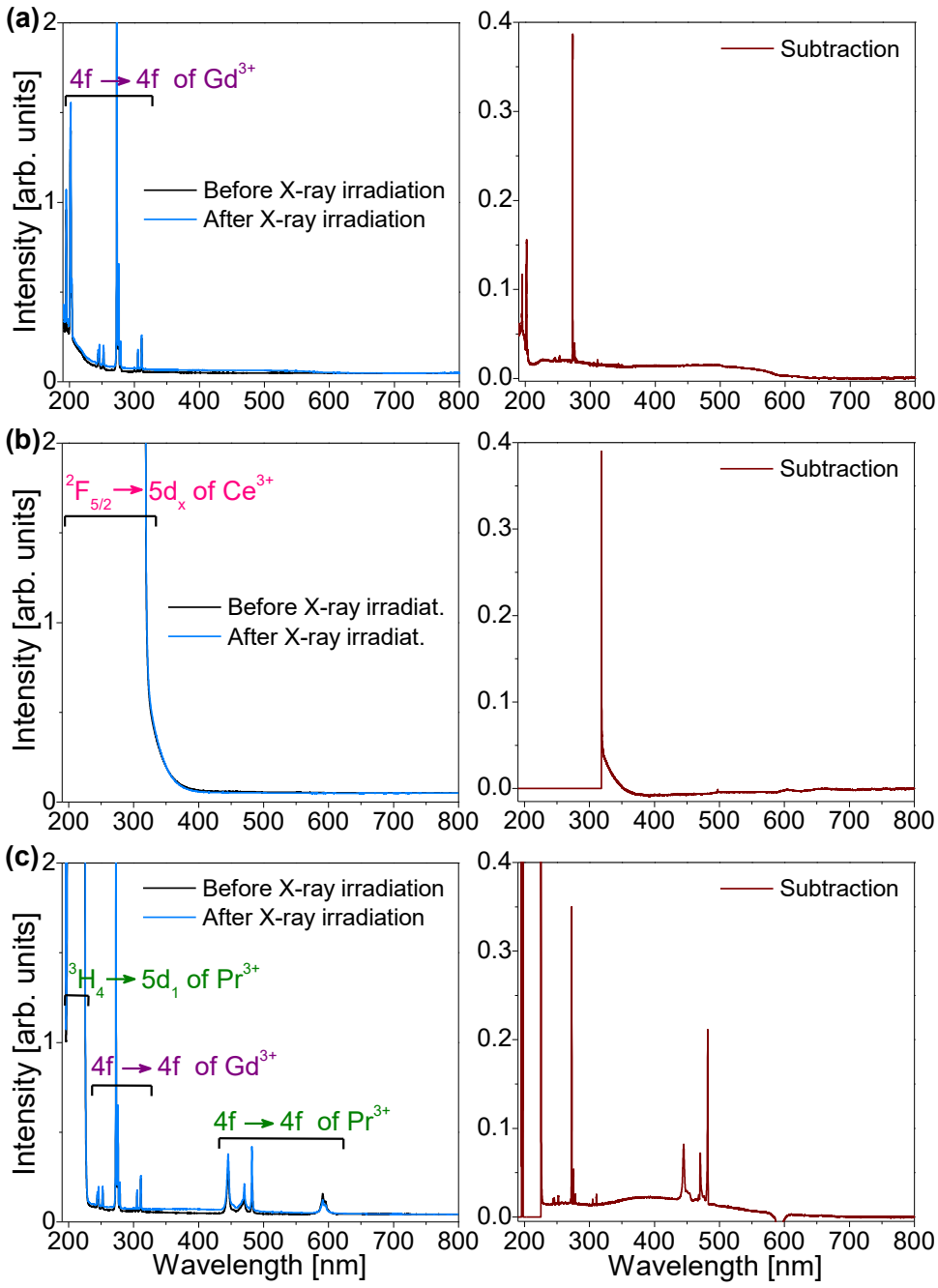

Figure 5.26. Optical absorption spectra before and 5-7 days after continued X-ray irradiation (left) and the spectra resulting from the subtraction of the first data from the second one (right) for (a) undoped KGdP, (b) 1 at. % Ce:KGdP and (c) 1 at. % Pr:KGdP plates.

5.4.2. Analysis of effects of radiation exposure on Raman spectra

In order to assess the degree of radiation damage suffered in some KGdP samples, the Raman spectra of three plates were obtained at several points per sample. The samples studied were $KGd_{0.981}Ce_{0.019}(PO_3)_4$ and $KGd_{0.990}Pr_{0.010}(PO_3)_4$ 10 days after continued X-ray irradiation and an undoped $KGd(PO_3)_4$ plate without being irradiated with synchrotron X-ray radiation. In example mode, Figure 5.27 shows the Raman spectra of the first two samples at a specific point on each plate, corresponding to areas that the synchrotron X-ray radiation irradiated directly. The strongest peak in both cases is centred around 1182 cm^{-1}, which is one of the characteristic peaks present in the Raman spectra of all polyphosphates[71]. This peak is usually attributed to the symmetric stretching vibration, ν_s, of the PO_2 fragment corresponding to the motion of the non-bridging oxygen[72]. Given its importance, this peak has been used to evaluate the possible structural changes of the samples due to prolonged X-ray

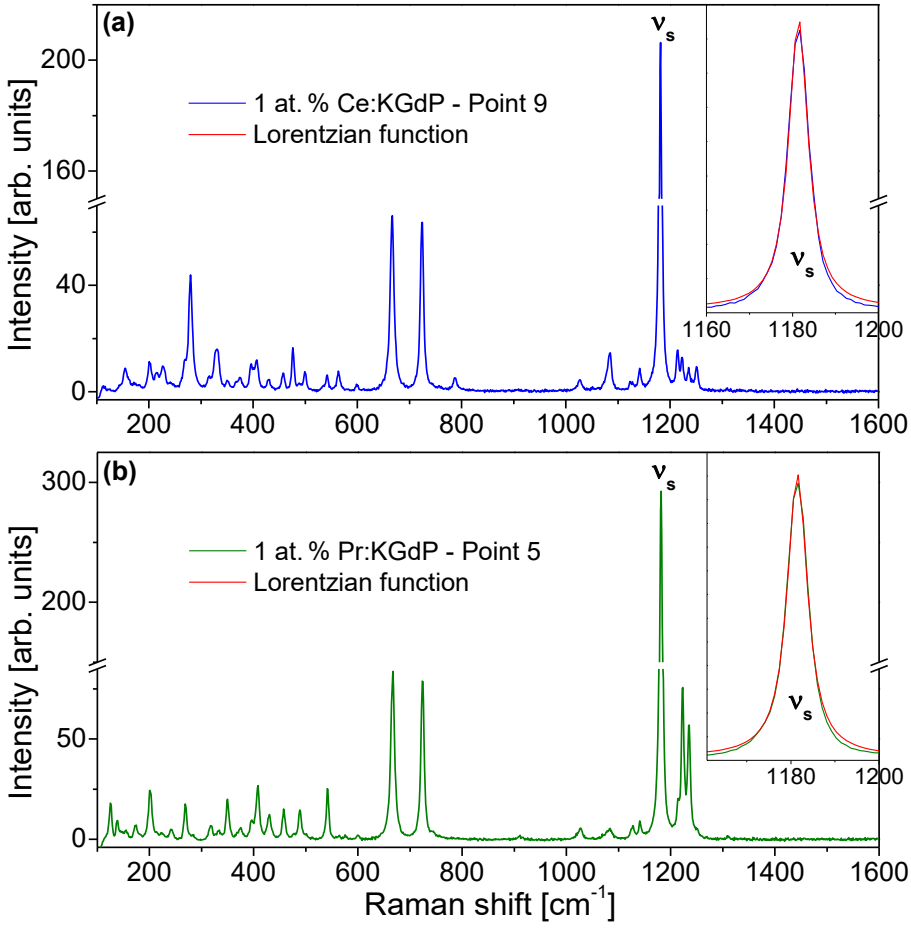

Figure 5.27. Raman spectra of (a) $KGd_{0.981}Ce_{0.019}(PO_3)_4$ and (b) $KGd_{0.990}Pr_{0.010}(PO_3)_4$ 10 days after continued X-ray irradiation at RT. Insets: the peak attributed to the symmetric stretching vibration ν_s of the PO_2 fragment, together with the fitting using Lorentzian function.

irradiation by comparing the values of Raman shift and line width obtained for each case. In all cases, this peak has been fitted using Lorentzian function, as can be seen by way of example in the insets of Figure 5.27, in order to obtain such values. For the undoped KGdP sample, each of the 8 points studied throughout the entire plate has the same values of Raman shift and line width, these being 1181 cm^{-1} and 6 cm^{-1}, respectively. The fact that there are no changes in the values among the different points of the sample is fully expected, since this undoped KGdP sample was not irradiated. Considering the 10 points studied in the $KGd_{0.981}Ce_{0.019}(PO_3)_4$ plate, the Raman shift and line width values are 1181 or 1182 cm^{-1} and 5 or 6 cm^{-1}, respectively, without distinction between the irradiated and non-irradiated areas of the sample. In the case of the $KGd_{0.990}Pr_{0.010}(PO_3)_4$ plate, the Raman shift and line width values are 1182 cm^{-1} and 6 cm^{-1}, respectively, for each of the 9 different points studied, without distinction between irradiated and non-irradiated areas. Thus, there are no significant changes between the values belonging to the irradiated and non-irradiated areas, neither in one sample nor in the other. Consequently, these results could corroborate that the Ce-doped KGdP samples might not suffer from radiation damage, which is one of the conclusions extracted from the section on radiation-induced absorption (Section 5.4.1). However, since the undoped and Pr-doped KGdP samples do suffer from radiation damage, taking into account the conclusions presented in the previous section, these results could allow us to conclude that these samples had already recovered after 10 days.

5.5. Spectroscopic characterization of type III Pr:KGd$(PO_3)_4$ nanocrystals

As mentioned for the Pr:KGd$(PO_3)_4$ single crystals, Sections 1.3.3 and 1.4.1 show the reasons given for considering type III KGdP as a host and Pr^{3+} as a doping element as a promising combination as a scintillator material. The synthesis of this compound in a nanocrystalline form offers the possibility of preparing it in ceramic form because of the almost isometric nature of the type III KGdP structure, which is interesting due to the larger activity in sintering from the nanoscale size[73,74,75]. The following spectroscopic studies are reported in *Paper III*.

5.5.1. Transmittance measurements

Figure 5.28 shows the transmittance spectrum of type III 5 at. % Pr:KGdP nanocrystals suspended in distilled water in the spectral ranges 200−300 nm and 440−485 nm at room temperature. The broad, intense band that extends from 208 to 227 nm, being centred at 218 nm, corresponds to the $^3H_4 \rightarrow 5d_1$ electronic transition of Pr^{3+} in type III KGdP (space group: $P2_1$), as observed in the bulk single crystals (see Figure 5.11.a and related text). The weak bands centred at 445 and 482 nm correspond to the $4f \rightarrow 4f$ electronic transitions of Pr^{3+} labelled as $^3H_4 \rightarrow {}^3P_2$ and $^3H_4 \rightarrow {}^3P_0$, as observed in the bulk single crystals (see Figure 5.12.a and related text).

Given that the praseodymium source of the final product is the initial reagent Pr_6O_{11}, one could think a priori that both the Pr^{4+} ion and the Pr^{3+} ion could be present in the

Pr:KGdP nanocrystals. However, by observing the transmittance spectrum of Figure 5.28.a and taking into account the deep explanation presented in *Paper III*, it is reasonable to say that praseodymium ions are basically in Pr^{3+} form in the final product.

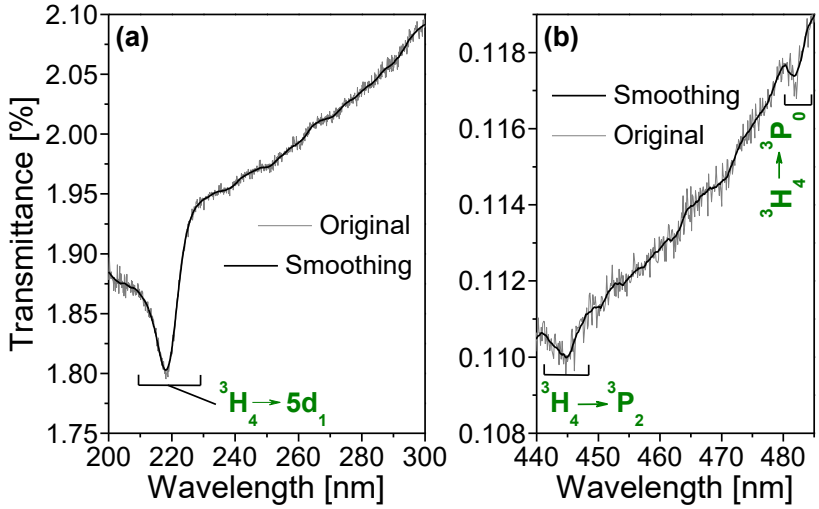

Figure 5.28. Transmittance spectrum of type III 5 at. % Pr:KGdP nanocrystals suspended in distilled water at room temperature. All labels correspond to electronic transitions of Pr^{3+}.

5.5.2. Luminescence measurements under visible excitation

Figure 8 of *Paper III* shows the emission spectrum from 590 to 850 nm of type III 5 at. % Pr:KGdP nanocrystals suspended in ethylene glycol under 445 nm excitation ($^3H_4 \rightarrow {}^3P_2$ of Pr^{3+}) at room temperature. The emission bands appear centred at 594−607, 702, 722 and 838 nm, and have been labelled as the $^1D_2 \rightarrow {}^3H_4 + {}^3P_0 \rightarrow {}^3H_6$, $^3P_0 \rightarrow {}^3F_3$, $^3P_0 \rightarrow {}^3F_4$ and $^1D_2 \rightarrow {}^3F_2$ transitions of Pr^{3+} in type III KGdP, respectively, as observed in the bulk samples (Figure 5.19). These emission bands have also been seen in the emission spectra of several Pr^{3+}-doped hosts under Pr^{3+} $4f \rightarrow 4f$ excitation, such as in $LaAlO_3$ [76], $NaGd(WO_4)_2$ [77] and $La_{1/2}Na_{1/2}TiO_3$ [78], as well as in Bi^{3+} and Pr^{3+} co-doped lead silicate glasses[79].

5.5.3. Radioluminescence measurements under X-ray excitation

Figure 5.29 shows the X-ray excited radioluminescence (RL) spectrum from 180 to 475 nm of type III 5 at. % Pr:KGdP nanocrystals pressed as pellet at room temperature. The most intense band, centred at 313 nm, corresponds to the $^6P_{3/2,5/2,7/2} \rightarrow {}^8S_{7/2}$ transitions of Gd^{3+}, while the two broad bands that partially overlap and are centred around 239 and 261 nm have been labelled as the $5d_1 \rightarrow {}^3H_{4,5,6}$, $^3F_2$ and $5d_1 \rightarrow {}^3F_{3,4}$, $^1G_4$ transitions of Pr^{3+} in type III KGdP, respectively, as observed in the bulk single crystals (see Figure 5.23 and related text).

The RL spectra of type III 1 and 3 at. % Pr:KGdP nanocrystals under the same conditions are shown in Figure 9 of *Paper III*. For 1 at. % Pr:KGdP nanocrystals, the Pr^{3+}

bands have an intensity similar to that observed in Figure 5.29, while the Gd^{3+} band increases considerably. On the contrary, the spectrum of 3 at. % Pr:KGdP nanocrystals shows a lower intensity of the three bands with respect to that observed for 5 at. % Pr:KGdP nanocrystals. Hence, a different behavior is observed depending on the praseodymium concentration. For scintillation applications, the composition that seems to be the most interesting is 5 at. % Pr:KGdP nanocrystals because the intensity of the emission bands corresponding to the $5d_1 \rightarrow 4f$ electronic transitions of Pr^{3+} is the highest, while the band corresponding to the $^6P_J \rightarrow {}^8S_{7/2}$ transitions of Gd^{3+} is not so intense.

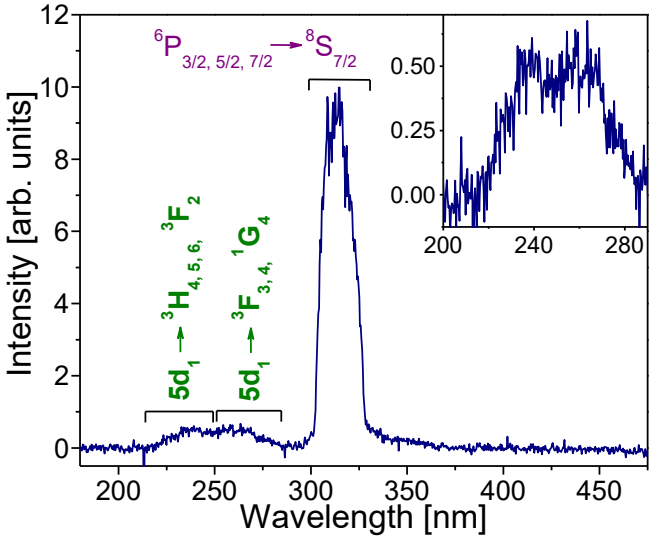

Figure 5.29. X-ray excited radioluminescence (RL) spectrum of type III 5 at. % Pr:KGdP nanocrystals as pellet at room temperature (copper source, operating at 40 kV and 30 mA). Labels in purple indicate the electronic transitions of Gd^{3+} and the label in green and bold that of Pr^{3+}.

References

[1] G. H. Dieke and H. M. Crosswhite. The spectra of the doubly and triply ionized rare earths. *Appl. Opt.* **1963**, *2*, 675-686.
[2] R. T. Wegh, A. Meijerink, R. J. Lamminmaki and J. Holsa. Extending Dieke's Diagram. *J. Lumin*. **2000**, *87-9*, 1002-1004.
[3] R. T. Wegh, H. Donker, A. Meijerink, R. J. Lamminmäki and J. Hölsä. Vacuum-ultraviolet spectroscopy and quantum cutting for Gd^{3+} in $LiYF_4$. *Phys. Rev. B* **1997**, *56* (21), 13841-13848.
[4] Z. Yang, J. H. Lin, M. Z. Su, Y. Tao and W. Wang. Photon cascade luminescence of Gd^{3+} in $GdBaB_9O_{16}$. *J. Alloys Compd.* **2000**, *308*, 94-97.
[5] P. Dorenbos. The 5d level positions of the trivalent lanthanides in inorganic compounds. *J. Lumin.* **2000**, *91*, 155-176.
[6] P. Dorenbos. 5*d*-level energies of Ce^{3+} and the crystalline environment. III. Oxides containing ionic complexes. *Phys. Rev. B* **2001**, *64*, 125117.
[7] P. Dorenbos. 5*d*-level energies of Ce^{3+} and the crystalline environment. I. Fluoride compounds. *Phys. Rev. B* **2000**, *62*, 15640.
[8] J. Zhong, H. Liang, H. Lin, B. Han, Q. Su and G. Zhang. Effects of crystal structure on the luminescence properties and energy transfer between Gd^{3+} and Ce^{3+} ions in $MGd(PO_3)_4$:Ce^{3+} (M = Li, Na, K, Cs). *J. Mater. Chem.* **2007**, *17*, 4679-4684.
[9] X. Qin, X. Liu, W. Huang, M. Bettinelli and X. Liu. Lanthanide-activated phosphors based on 4f-5d optical transitions: theoretical and experimental aspects. *Chem. Rev.* **2017**, *117* (5), 4488-4527.
[10] P. Dorenbos. The $4f^n \leftrightarrow 4f^{n-1}$ 5*d* transitions of the trivalent lanthanides in halogenides and chalcogenides. *J. Lumin.* **2000**, *91* (1-2), 91-106.
[11] P. Dorenbos, T. Shalapska, G. Stryganyuk, A. Gektin and A. Voloshinovskii. Spectroscopy and energy level location of the trivalent lanthanides in $LiYP_4O_{12}$. *J. Lumin.* **2011**, *131* (4), 633-639.
[12] I. Adell, R. M. Solé, M. C. Pujol, M. Lancry, N. Ollier, M. Aguiló and F. Díaz. Single crystal growth, optical absorption and luminescence properties under VUV-UV synchrotron excitation of type III Ce^{3+}:$KGd(PO_3)_4$, a promising scintillator material. *Sci. Rep.* **2018**, *8*, 11002. DOI: 10.1038/s41598-018-29372-z.
[13] T. Shalapska, G. Stryganyuk, A. Gektin, A. Kotlov, P. Demchenko and A. Voloshinovskii. Luminescence properties of Ce^{3+}-doped $NaPrP_4O_{12}$ polyphosphate. *J. Phys. Condens. Matter* **2013**, *25* (10), 105403.
[14] G. Blasse and G. J. Dirksen. The luminescence of broad-band emitters in $LiLaP_4O_{12}$. *Phys. Status Solidi B* **1982**, *110*, 487-494.
[15] I. Parreu, R. Solé, Jna. Gavaldà, J. Massons, F. Díaz and M. Aguiló. Crystal growth, structural characterization, and linear thermal evolution of $KGd(PO_3)_4$. *Chem. Mater.* **2005**, *17* (4), 822-828.
[16] R. D. Shannon. Revised effective ionic radii and systematic studies of interatomic distances in halides and chalcogenides. *Acta Cryst.* **1976**, *A32*, 751-767.
[17] G. Blasse, J. P. M. van Vliet, J. W. M. Verwey, R. Hoogendam and M. Wiegel. Luminescence of Pr^{3+} in scandium borate ($ScBO_3$) and the host lattice dependence of the Stokes shift. *J. Phys. Chem. Solids* **1989**, *50* (6), 583-585.
[18] Z. Tian, H. Liang, B. Han, Q. Su, Y. Tao, G. Zhang and Y. Fu. Photon cascade emission of Gd^{3+} in $Na(Y,Gd)FPO_4$. *J. Phys. Chem. C* **2008**, *112* (32), 12524-12529.
[19] S. P. Feofilov, Y. Zhou, H. J. Seo, J. Y. Jeong, D. A. Keszler and R. S. Meltzer. Host sensitization of Gd^{3+} ions in yttrium and scandium borates and phosphates: Application to quantum cutting. *Phys. Rev. B* **2006**, *74*, 085101.
[20] P. Dorenbos. The Eu^{3+} charge transfer energy and the relation with the band gap of compounds. *J. Lumin.* **2005**, *111*, 89-104.
[21] M. Nikl, A. Yoshikawa, K. Kamada, K. Nejezchleb, C. R. Stanek, J. A. Mares and K. Blazek. Development of LuAG-based scintillator crystals – A review. *Prog. Cryst. Growth Charact. Mater.* **2013**, *59*, 47-72.

[22] D. Ding, J. Yang, G. Ren, M. Nikl, S. Wang, Y. Wu and Z. Mao. Effects of anisotropy on structural and optical characteristics of LYSO:Ce crystal. *Phys. Status Solidi B* **2014**, *251* (6), 1202-1211.
[23] J. Zhong, H. Liang, Q. Su, J. Zhou, Y. Huang, Z. Gao, Y. Tao and J. Wang. Luminescence properties of $NaGd(PO_3)_4:Eu^{3+}$ and energy transfer from Gd^{3+} to Eu^{3+}. *Appl. Phys. B* **2010**, *98* (1), 139-147.
[24] J. Zhong, H. Liang, Q. Su, J. Zhou, I. V. Khodyuk and P. Dorenbos. Radioluminescence properties of Ce^{3+}-activated $MGd(PO_3)_4$ (M = Li, Na, K, Cs). *Opt. Mater.* **2009**, *32*, 378-381.
[25] P. Lecoq, A. Annenkov, A. Gektin, M. Korzhik and C. Pedrini. Scintillation mechanisms in inorganic scintillators. In *Inorganic scintillators for detector systems: Physical principles and crystal engineering*. Springer Berlin Heidelberg: The Netherlands, **2006**; pp 81-95.
[26] C. Pédrini. Scintillation mechanisms and limiting factors on each step of relaxation of electronic excitations. *Fiz. Tverd. Tela* **2005**, *47* (8), 1359-1363. Also in *Phys. Solid State* **2005**, *47* (8), 1406-1411.
[27] A. J. Wojtowicz. Scintillation mechanism: the significance of variable valence and electron-lattice coupling in R.E.-activated scintillators. Proceedings of the International Conference on Inorganic Scintillators and Their Applications, SCINT (Eds: P. Dorenbos and C. W. E. van Eijk). Delft University Press: The Netherlands, **1995**, pp 95-102.
[28] C. Pédrini, D. Bouttet, C. Dujardin, A. Belsky and A. Vasil'ev. Energy transfer and quenching processes in cerium-doped scintillators. Proceedings of the International Conference on Inorganic Scintillators and Their Applications, SCINT (Eds: P. Dorenbos and C. W. E. van Eijk). Delft University Press, The Netherlands, **1995**, pp 103-110.
[29] P. A. Rodnyi. Cerium-activated compounds. In *Physical processes in Inorganic scintillators* (Ed: M. J. Weber). CRC Press LLC: Boca Raton, FL, **1997**; pp 152-154.
[30] I. Adell, M. C. Pujol, R. M. Solé, M. Lancry, N. Ollier, M. Aguiló and F. Díaz. Single crystal growth, optical absorption and luminescence properties under VUV-UV synchrotron excitation of type III Pr^{3+}:$KGd(PO_3)_4$. *Submitted to Sci. Rep.*
[31] M. Nikl and A. Yoshikawa. Recent R&D trends in inorganic single-crystal scintillator materials for radiation detection. *Adv. Opt. Mater.* **2015**, *3* (4), 463-481.
[32] P. Lecoq, A. Annenkov, A. Gektin, M. Korzhik and C. Pedrini. Specific killer ions. In *Inorganic scintillators for detector systems: Physical principles and crystal engineering*. Springer Berlin Heidelberg: The Netherlands, **2006**; pp 88-89.
[33] C. Dujardin, C. Pedrini, J. C. Gâcon, A. G. Petrosyan, A. N. Belsky and A. N. Vasil'ev. Luminescence properties and scintillation mechanisms of cerium- and praseodymium-doped lutetium orthoaluminate. *J. Phys.: Condens. Matter* **1997**, *9*, 5229-5243.
[34] H. Liang, Z. Tian, H. Lin, M. Xie, G. Zhang, P. Dorenbos and Q. Su. Photoluminescence and radioluminescence of pure and Ce^{3+} activated $Na_3Gd(PO_4)_2$. *Opt. Mater.* **2011**, *33*, 618-622.
[35] M. Kucera, M. Hanus, Z. Onderisinova, P. Prusa, A. Beitlerova and M. Nikl. Energy transfer and scintillation properties of Ce^{3+} doped $(LuYGd)_3(AlGa)_5O_{12}$ multicomponent garnets. *IEEE Trans. Nucl. Sci.* **2014**, *61* (1), 282-289.
[36] M. Rathaiah, M. Kucera, J. Pejchal, A. Beitlerova, R. Kucerkova and M. Nikl. Epitaxial growth, photoluminescence and scintillation properties of Gd^{3+} co-doped $YAlO_3:Ce^{3+}$ films. *Radiat. Meas.* **2019**, *121*, 86-90.
[37] I. Parreu, J. J. Carvajal, X. Solans, F. Díaz and M. Aguiló. Crystal structure and optical characterization of pure and Nd-substituted type III $KGd(PO_3)_4$. *Chem. Mater.* **2006**, *18* (1), 221-228.
[38] A. Mayolet. Etude des processus d'absorption et de transfert d'energie au sein de materiaux inorganiques luminescents dans le domaine UV et VUV. Ph.D. Thesis, Université de Paris XI, **1995**.
[39] R. C. Naik, N. P. Karanjikar and N. A. Narasimham. X-ray excited optical luminescence spectrum of Pr-doped YPO_4. *Solid State Commun.* **1981***, 38***,** 389-391.
[40] K. Petermann. Laser-active ions. Rare earth ions. In *Handbook of Solid-State Lasers: Materials, systems and applications* (Eds: B. Denker and E. Shklovsky). Woodhead Publishing Limited: Cambridge, UK, **2013**; pp 6-9.

[41] M. Fibrich, H. Jelínková, J. Šulc, K. Nejezchleb and V. Škoda. Pr:$YAlO_3$ microchip laser at 662 nm. *Laser Phys. Lett.* **2011**, *8* (2), 116-119.
[42] M. Fechner, F. Reichert, N.-O. Hansen, K. Petermann and G. Huber. Crystal growth, spectroscopy, and diode pumped laser performance of Pr, Mg:$SrAl_{12}O_{19}$. *Appl. Phys. B* **2011**, *102* (4), 731-735.
[43] T. Gün, P. Metz and G. Huber. Power scaling of laser diode pumped Pr^{3+}:$LiYF_4$ cw lasers: efficient laser operation at 522.6 nm, 545.9 nm, 607.2 nm, and 639.5nm. *Opt. Lett.* **2011**, *36* (6), 1002-1004.
[44] C. Görller-Walrand and K. Binnemans. Rationalization of crystal-field parametrization. In *Handbook on the Physics and Chemistry of Rare Earths* (Eds: K. A. Gschneidner, Jr. and L. Eyring), vol. 23. Elsevier Science B.V.: Amsterdam, The Netherlands, **1996**; pp 267.
[45] R. M. Solé, M. C. Pujol, J. Massons, M. Aguiló, F. Díaz and A. Brenier. Growth, anisotropic spectroscopy and laser operation of the monoclinic Nd:$KGd(PO_3)_4$ crystal. *J. Phys. D Appl. Phys.* **2015**, *48*, 495502-495512.
[46] M. C. Pujol. Obtenció i caracterització de cristalls monoclínics de $KGd(WO_4)_2$ substituïts amb lantànids. Ph.D. Thesis, Rovira i Virgili University, **2001**.
[47] Y. Wu and G. Ren. Energy transfer and radiative recombination processes in $(Gd,Lu)_3Ga_3Al_2O_{12}$:Pr^{3+} scintillators. *Opt. Mater.* **2013**, *35*, 2146-2154.
[48] J. L. Yuan, X. J. Wang, D. B. Xiong, C. J. Duan, J. T. Zhao, Y. B. Fu, G. B. Zhang and C. S. Shi. VUV spectroscopic properties of Ce^{3+} and Pr^{3+}-doped $AREP_2O_7$-type alkali rare earth diphosphates (A = Na, K, Rb, Cs; RE = Y, Lu). *J. Lumin.* **2007**, *126*, 130-134.
[49] A. M. Srivastava, A. A. Setlur, H. A. Comanzo, W. W. Beers, U. Happek, P. Schmidt. The influence of the Pr^{3+} $4f^15d^1$ configuration on the $^1S_0$ emission efficiency and lifetime in $LaPO_4$. *Opt. Mater.* **2011**, *33*, 292-298.
[50] A. Katelnikovas, H. Bettentrup, D. Dutczak, A. Kareiva and T. Jüstel. On the correlation between the composition of Pr^{3+} doped garnet type materials and their photoluminescence properties. *J. Lumin.* **2011**, *131*, 2754-2761.
[51] L. van Pieterson, R. T. Wegh, A. Meijerink and M. F. Reid. Emission spectra and trends for $4f^{n-1}5d \leftrightarrow 4f^n$ transitions of lanthanide ions: Experiment and theory. *J. Chem. Phys.* **2001**, *115* (20), 9382-9392.
[52] J. Collins, M. Geen. M. Bettinelli and B. Di Bartolo. Dependence of cross-relaxation on temperature and concentration from the $^1D_2$ level of Pr^{3+} in YPO_4. *J. Lumin.* **2012**, *132*, 2626-2633.
[53] K. Wang, W. Feng, X. Feng, Y. Li, P. Mi and S. Shi. Synthesis and photoluminescence of novel red-emitting $ZnWO_4$:Pr^{3+},Li^+ phosphors. *Spectrochim. Acta A* **2016**, *154*, 72-75.
[54] G. A. S. Flizikowski, V. S. Zanuto, A. Novatski, L. A. O. Nunes, L. C. Malacarne, M. L. Baesso and N. G. C. Astrath. Upconversion luminescence and hypersensitive transitions of Pr^{3+}–doped calcium aluminosilicate glasses. *J. Lumin.* **2018**, *202*, 27-31.
[55] M. V. Vijaya Kumar, K. Rama Gopal, R. R. Reddy, G. V. Lokeswara Reddy, N. Sooraj Hussain and B. C. Jamalaiah. Application of modified Judd–Ofelt theory and the evaluation of radiative properties of Pr^{3+}-doped lead telluroborate glasses for laser applications. *J. Non-Cryst. Solids* **2013**, *364*, 20-27.
[56] M. Trevisani, K. V. Ivanovskikh, F. Piccinelli and M. Bettinelli. Fast 5d-4f luminescence in Pr^{3+}-doped $K_3Lu(PO_4)_2$. *J. Lumin.* **2014**, *152*, 2-6.
[57] W. Drozdowski, P. Dorenbos, J. T. M. de Haas, R. Drozdowska, A. Owens, K. Kamada, K. Tsutsumi, Y. Usuki, T. Yanagida and A. Yoshikawa. Scintillation properties of praseodymium activated $Lu_3Al_5O_{12}$ single crystals. *IEEE Trans. Nucl. Sci.* **2008**, *55* (4), 2420-2424.
[58] T. Shalapska, G. Stryganyuk, Y. Romanyshyn, D. Trots, P. Demchenko, A. Gektin, A. Voloshinovskii and P. Dorenbos. Photon cascade luminescence from Pr^{3+} ions in $LiPrP_4O_{12}$ polyphosphate. *J. Phys. D: Appl. Phys.* **2010**, *43*, 405404.
[59] A. Jouini, J. C. Gâcon, M. Ferid and M. Trabelsi-Ayadi. Luminescence and scintillation properties of praseodymium poly and diphosphates. *Opt. Mater.* **2003**, *24*, 175-180.
[60] L. Zhang, Y. Xia, X. Shen and W. Wei. Concentration dependence of visible luminescence from Pr^{3+}-doped
phosphate glasses. *Spectrochim. Acta A* **2019**, *206*, 454-459.

[61] V. Naresh and B. S. Ham. Influence of multiphonon and cross relaxations on $^3P_0$ and $^1D_2$ emission levels of Pr^{3+} doped borosilicate glasses for broad band signal amplification. *J. Alloys Compd.* **2016**, *664*, 321-330.
[62] M. Guzik, T. Aitasalo, W. Szuszkiewicz, J. Hölsä, B. Keller and J. Legendziewicz. Optical spectroscopy of yttrium double phosphates doped by cerium and praseodymium ions. *J. Alloys Compd.* **2004**, *380*, 368-375.
[63] K. Kamada, M. Nikl, S. Kurosawa, Y. Shoji, J. Pejchal, Y. Ohashi, Y. Yokota and A. Yoshikawa. Growth and scintillation properties of praseodymium doped $(Lu,Gd)_3(Ga,Al)_5O_{12}$ single crystals. *J. Lumin.* **2016**, *169*, 811-815.
[64] M. Nikl, A. M. Begnamini, V. Jary, D. Niznansky, and E. Mihokova. Pr^{3+} luminescence center in $Lu_2Si_2O_7$ host. *Phys. Status Solidi RRL* **2009**, *3* (9), 293-295.
[65] I. Carrasco, K. Bartosiewicz, F. Piccinelli, M. Nikl and M. Bettinelli. Structural effects and 5d→4f emission transition shifts induced by Y co-doping in Pr-doped $K_3Lu_{1-x}Y_x(PO_4)_2$. *J. Lumin.* **2017**, *189*, 113-119.
[66] J. Pejchal, M. Buryi, V. Babin, P. Prusa, A. Beitlerova, J. Barta, L. Havlak, K. Kamada, A. Yoshikawa, V. Laguta and M. Nikl. Luminescence and scintillation properties of Mg-codoped LuAG:Pr single crystals annealed in air. *J. Lumin.* **2017**, *181*, 277-285.
[67] K. V. Ivanovskikh, A. Meijerink, F. Piccinelli, A. Speghini, E. I. Zinin, C. Ronda and M. Bettinelli. Optical spectroscopy of $Ca_3Sc_2Si_3O_{12}$, $Ca_3Y_2Si_3O_{12}$ and $Ca_3Lu_2Si_3O_{12}$ doped with Pr^{3+}. *J. Lumin.* **2010**, *130*, 893-901.
[68] R. Y. Zhu. Radiation damage in scintillating crystals. *Nucl. Instr. Meth. Phys. Res. A* **1998**, *413*, 297-311.
[69] R. Y. Zhu, H. Stone, H. Newman, T. Q. Zhou, H. R. Tan and C. F. He. A study on radiation damage in doped BGO crystals. *Nucl. Instr. Meth. Phys. Res. A* **1991**, *302*, 69-75.
[70] S. Burachas, Yu. Saveliev, M. Ippolitov, V. Manko, V. Lomonosov, A. Vasiliev, A. Apanasenko, A. Vasiliev, A. Uzunian, G. Tamulaitis. Physical origin of coloration and radiation hardness of lead tungstate scintillation crystals. *J. Cryst. Growth* **2006**, *293*, 62-67.
[71] I. Parreu. Crystal growth and characterization of ytterbium or neodymium doped type III-$KGd(PO_3)_4$. A new bifunctional nonlinear and laser crystal. Ph.D. Thesis, Rovira i Virgili University, **2006**.
[72] I. Parreu, R. Solé, J. Massons, F. Díaz and M. Aguiló. Crystal growth and characterization of type III ytterbium-doped $KGd(PO_3)_4$: a new nonlinear laser host. *Chem. Mater.* **2007**, *19*, 2868-2876.
[73] A. Podhorodecki, P. Gluchowski, G. Zatryb, M. Syperek, J. Misiewicz, W. Lojkowski and W. Strek. Influence of pressure-induced transition from nanocrystals to nanoceramic form on optical properties of Ce-doped $Y_3Al_5O_{12}$. *J. Am. Ceram. Soc.* **2011**, *94* (7), 2135-2140.
[74] J. Trojan-Piegza, S. Gierlotka, E. Zych and W. Lojkowski. Spectroscopic studies of nanopowder and nanoceramics $La_2Hf_2O_7$:Pr scintillator. *J. Am. Ceram. Soc.* **2014**, *97* (5), 1595-1601.
[75] V. Pankratov, L. Grigorjeva, S. Chernov, T. Chudoba and W. Lojkowski. Luminescence properties and energy transfer processes in nanosized cerium doped YAG. *IEEE Trans. Nucl. Sci.* **2008**, *55* (3), 1509-1513.
[76] M. Dudek, A. Jusza, K. Anders, L. Lipińska, M. Baran and R. Piramidowicz. Luminescent properties of praseodymium doped Y_2O_3 and $LaAlO_3$ nanocrystallites and polymer composites. *J. Rare Earth.* **2011**, *29* (12), 1123-1129.
[77] A. Durairajan, D. Thangaraju, S. Moorthy Babu and M. A. Valente. Luminescence characterization of sol-gel derived Pr^{3+} doped $NaGd(WO_4)_2$ phosphors for solid state lighting applications. *Mater. Chem. Phys.* **2016**, *179*, 195-303.
[78] P. Boutinaud, L. Sarakha, R. Mahiou, P. Dorenbos and Y. Inaguma. Intervalence charge transfer in perovskite titanates $R_{1/2}Na_{1/2}TiO_3$:Pr^{3+} (R=La, Gd, Y, Lu). *J. Lumin.* **2010**, *130*, 1725-1729.
[79] B. Suresh, N. Purnachand, Ya. Zhydachevskii, M. G. Brik, M. Srinivasa Reddy, A. Suchocki, M. Piasecki and N. Veeraiah. Influence of Bi^{3+} ions on the amplification of 1.3 μm emission of Pr^{3+} ions in lead silicate glasses for the applications in second telecom window communications. *J. Lumin.* **2017**, *182*, 312-322.

Conclusions

The most relevant conclusions extracted from this Ph.D. Thesis are the following:

- Type III Ce^{3+}-doped $KGd(PO_3)_4$ bulk single crystals of up to 2.6 atomic % of Ce^{3+} and type III Pr^{3+}-doped $KGd(PO_3)_4$ bulk single crystals of up to 5.8 atomic % of Pr^{3+} substituting Gd^{3+} can be grown with high crystalline quality by the Top Seeded Solution Growth-Slow Cooling (TSSG-SC) technique from self-flux solutions.

- Through the determination of the primary crystallization region of the type B KYP_4O_{12} and type IV $KY(PO_3)_4$ in the K_2O–Y_2O_3–P_2O_5 ternary system, it has been found that the optimal composition range to grow type B and IV KYP bulk single crystals is with a K_2O/P_2O_5 molar ratio of around 38/62 and an Y_2O_3 percentage in the range 4-5 mol %.

- The modified Pechini method allows to synthesize type III $Pr:KGd(PO_3)_4$ nano-crystals with a single crystalline phase.

- $KGd_{0.942}Pr_{0.058}(PO_3)_4$ crystal is thermally stable up to 1140 K, where it suffers an irreversible decomposition into a unique crystalline compound, $GdPO_4$, and a liquid phase. The thermal expansion coefficients of this crystal in the principal axes of the tensor X_1', $X_2'//b$ and X_3' are $\alpha'_{11} = 12.43 \times 10^{-6}\ K^{-1}$, $\alpha'_{22} = 12.40 \times 10^{-6}\ K^{-1}$ and $\alpha'_{33} = 7.03 \times 10^{-6}\ K^{-1}$. When the positive *b* crystallographic axis is pointing toward the observer, the principal axis X_1' is at 16.31º clockwise from the crystallographic direction *a*, while the principal axis X_3' is at 14.44º clockwise from the crystallographic axis *c*.

- The exhaustive spectroscopic characterization of type III Ce:KGdP and Pr:KGdP bulk single crystals allowed to find out the energy position of the 5*d* levels of Ce^{3+} and Pr^{3+} ions with respect to their corresponding ground states in type III KGdP, the lifetime of the $5d_1$ level of Ce^{3+} and that of Pr^{3+} in this host, the emission mechanisms under VUV-UV excitation and ionizing radiation, among others.

  The absorption bands assigned to the $^2F_{5/2} \rightarrow 5d_1$, $5d_2$, $5d_3$, $5d_4$ and $5d_5$ electronic transitions of Ce^{3+} in type III KGdP host are centred at 302.5, 243.5, 226, 215 and 194 nm, respectively. The maximum optical absorption cross section from the $^2F_{5/2}$ ground state to the $5d_1$ level is around 370 x 10^{-20} cm^2. The emission spectra under VUV-UV excitation (i.e. direct $^2F_{5/2} \rightarrow 5d$ excitation) of the Ce:KGdP single crystals show a doublet emission peak centred at 322 and 342 nm attributed to the $5d_1 \rightarrow {}^2F_{7/2}$ and $5d_1 \rightarrow {}^2F_{5/2}$ transitions of Ce^{3+}, respectively, in this host. In these same emission spectra, the $^6P_J \rightarrow {}^8S_{7/2}$ electronic transitions of Gd^{3+} (around 312 nm), which are common in many hosts, are not present. The luminescence decay curves for the emission wavelengths corresponding to the $5d_1 \rightarrow {}^2F_{7/2,5/2}$ transitions of Ce^{3+} under direct $^2F_{5/2} \rightarrow 5d$ excitation are composed by a fast component and a slow component. The fast component has been attributed to the lifetime of the $5d_1$ level of Ce^{3+} in this host, which is around 16−19 ns. The slow component, with a decay time of 8 ms, could be ascribed to an energy transfer from the $^6P_{7/2}$ level of Gd^{3+} to the $5d_1$ level of Ce^{3+}, since the lifetime of the $^6P_{7/2}$

level of Gd^{3+} in type III KGdP host is of the same order, 9 ms. The radioluminescence spectra of the Ce:KGdP samples obtained after exciting them with different X-ray energies show an intense band also attributed to the $5d_1 \rightarrow {}^2F_{7/2,5/2}$ transitions of Ce^{3+} in type III KGdP, while the band corresponding to the ${}^6P_J \rightarrow {}^8S_{7/2}$ transitions of Gd^{3+} does not appear. This behaviour is ascribed to a very efficient energy transfer from the ${}^6P_J$ levels of Gd^{3+} to the $5d_1$ level of Ce^{3+}. In addition, it has been concluded that bidirectional energy transfer processes between the $5d_5$ level of Ce^{3+} and the ${}^6F_J$ and ${}^6G_J$ levels of Gd^{3+} might take place.

The absorption bands corresponding to the ${}^3H_4 \rightarrow 5d_1$, ${}^3H_4 \rightarrow 5d_2$ and ${}^3H_4 \rightarrow 5d_3$ electronic transitions of Pr^{3+} in type III KGdP are centred at 218, 196 and 166 nm, respectively. The maximum optical absorption cross section from the ${}^3H_4$ ground state to the $5d_1$ level of Pr^{3+} in this host is about 780×10^{-20} cm^2. In this host, the ${}^1S_0$ and $5d_1$ levels of Pr^{3+} overlap, which prevents the non-radiative relaxation from the $5d_1$ level to the ${}^1S_0$ level and the subsequent radiative decay to other $4f$ levels that would deteriorate the scintillation efficiency of Pr:KGdP crystals. In the optical emission spectra under VUV-UV excitation (i.e. direct ${}^3H_4 \rightarrow 5d$ excitation) of the Pr:KGdP single crystals appear the bands corresponding to the $5d_1 \rightarrow 4f$ electronic transitions of Pr^{3+} in this host centred at 229, 239, 256, 265, 358 and 435 nm, which specifically correspond to the $5d_1 \rightarrow {}^3H_5$, $5d_1 \rightarrow {}^3H_6, {}^3F_2$, $5d_1 \rightarrow {}^3F_{3,4}$, $5d_1 \rightarrow {}^1G_4$, $5d_1 \rightarrow {}^1D_2$ and $5d_1 \rightarrow {}^3P_2$ electronic transitions, respectively. These spectra also show the presence of intense bands corresponding to the ${}^6P_{3/2,5/2,7/2} \rightarrow {}^8S_{7/2}$ electronic transitions of Gd^{3+}, whose maximum intensity values are centred at 305, 312 and 323 nm, respectively. The luminescence decay curves for the emission wavelengths corresponding to the $5d_1 \rightarrow {}^3F_{3,4}$ electronic transitions of Pr^{3+} under direct ${}^3H_4 \rightarrow 5d$ excitation are composed by a fast component and a slow component. The fast component has been attributed to the lifetime of the $5d_1$ level of Pr^{3+} in type III KGdP host, which is around 6 ns. The radioluminescence spectra of the Pr:KGdP samples obtained after exciting them with different X-ray energies reveal the presence of the Gd^{3+} emission band belonging to the ${}^6P_{3/2,5/2,7/2} \rightarrow {}^8S_{7/2}$ transitions as the most intense band. Two bands corresponding to the $5d_1 \rightarrow {}^3H_{4,5,6}, {}^3F_2$ and $5d_1 \rightarrow {}^3F_{3,4}, {}^1G_4$ transitions of Pr^{3+} in KGdP appear centred around 236 and 259 nm, respectively. After all, it has been concluded that bidirectional energy transfer processes between the $5d_{2,3}$ levels of Pr^{3+} and the Gd^{3+} $4f$ levels of higher energy in this host might take place.

- The polarized optical absorption cross sections of the ${}^3H_4 \rightarrow 4f$ electronic transitions of Pr^{3+} in type III Pr:KGdP, the optical emission spectra of these samples under 445 nm excitation (${}^3H_4 \rightarrow {}^3P_2$ of Pr^{3+}) and the lifetime of the ${}^1D_2$ level of Pr^{3+} in this host determined throughout the Thesis are the basic spectroscopic data of the type III Pr:KGdP crystal for lasing applications in the visible wavelength range based on $4f \rightarrow 4f$ electronic transitions.

- Radiation damage of the type III undoped, Ce^{3+}- and Pr^{3+}-doped KGdP single crystals after prolonged synchrotron X-ray irradiation was observed. The results indicate that the Ce^{3+}-doped KGdP samples might not suffer from radiation damage and, in addition, could allow us to conclude that the Pr^{3+}-doped KGdP samples had already recovered 10 days after synchrotron X-ray irradiation.

- The type III Pr:KGd$(PO_3)_4$ nanocrystals allow the conversion from X-ray radiation to near-visible light.
- For the near future, the following interesting studies are planned: 1) measurement of the so-called gamma ray pulse height spectra of the type III Ce:KGdP and Pr:KGdP bulk single crystals to obtain the energy resolution and the absolute light yield in number of photons emitted per MeV absorbed energy, 2) measurement of their gamma ray pulse height spectra as function of gamma ray energy to provide the so-called non-proportionality curve, 3) study of properties as function of temperature, 4) evaluation of the scintillation decay time to determine the lifetime of the $5d_1$ level of Ce^{3+} and that of Pr^{3+} in KGdP host under ionizing radiation, and 5) study of the beta decay of ^{40}K radioisotopes in these crystals and its influence on scintillator properties.
- As further work, it would be interesting to carry out X-ray photoelectron spectroscopy (XPS) measurements of type III KCe$(PO_3)_4$ and KPr$(PO_3)_4$ single crystals in order to estimate the energy differences between the top of the valence band and the 4*f* ground state of Ce^{3+} and of Pr^{3+}, respectively.

UNIVERSITAT ROVIRA I VIRGILI
CE OR PR-DOPED TYPE III KGD(PO3)4 CRYSTALLINE MATERIALS. GROWTH AND CHARACTERIZATION AS SCINTILLATORS
Irina Adell Barbarà

Appendix I.

X-ray powder diffractograms with the XRD standard patterns of type B KYP_4O_{12}, type IV $KY(PO_3)_4$ and their neighbouring crystalline phases

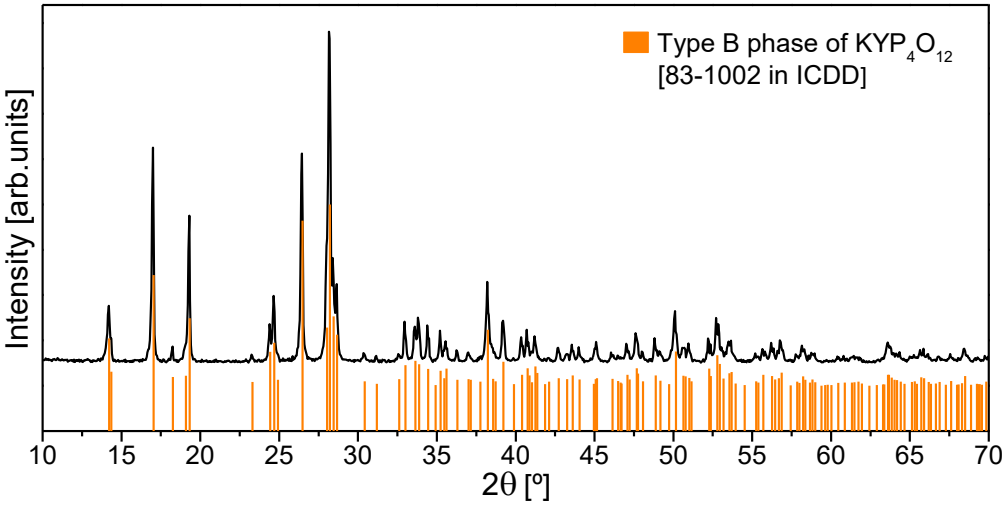

Lattice: Base-centered monoclinic – Space group: *C*2/*c* (15) – Z = 4 – *a* = 7.80670 Å – *b* = 12.32210 Å – *c* = 10.40780 Å – β = 111.17º.

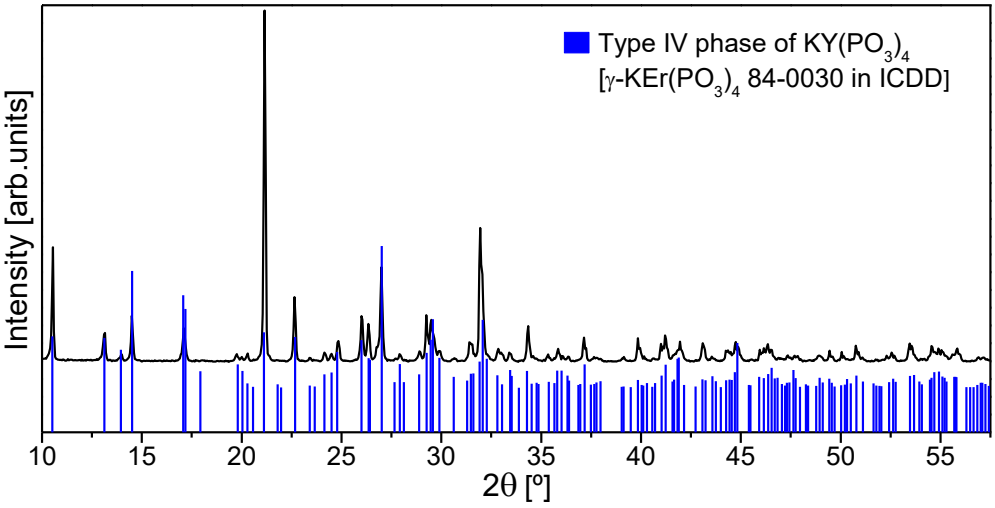

Lattice: Monoclinic – Space group: $P2_1/c$ (14) – Z = 4 – *a* = 10.80000 Å – *b* = 8.85900 Å – *c* = 12.70000 Å – β = 128.89º.

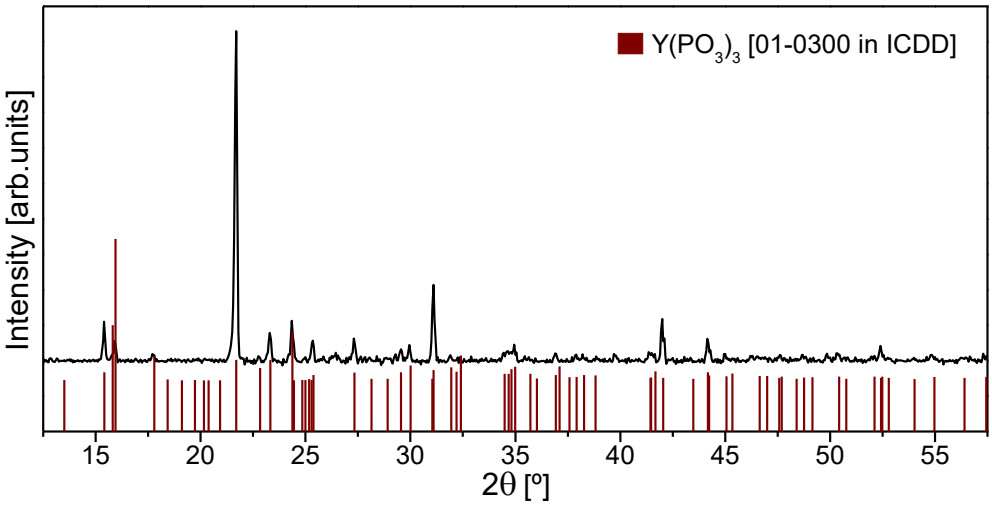

Lattice: Monoclinic – Z = 4 – *a* = 14.12500 Å – *b* = 6.69310 Å – *c* = 10.04530 Å – β = 127.557º.

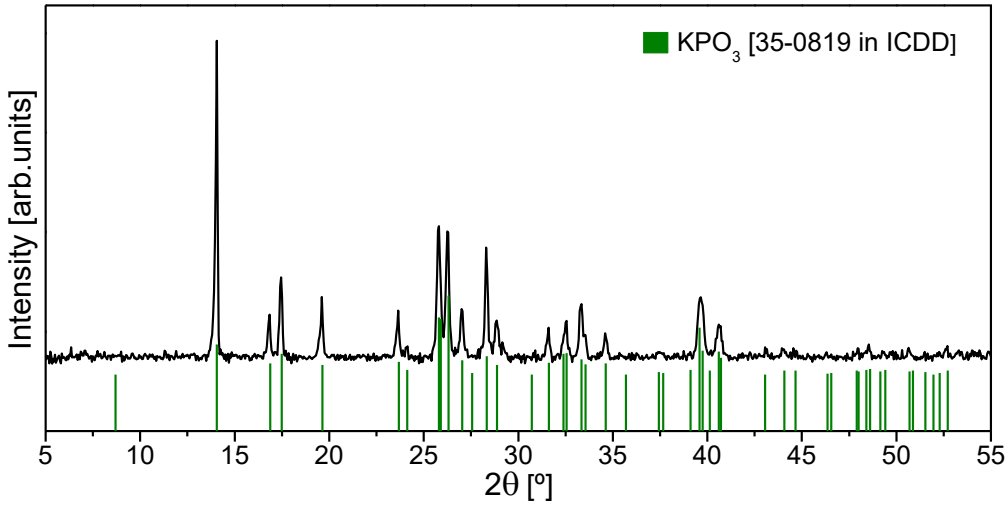

Lattice: Monoclinic – Space group: $P2_1/a$ (14) – Z = 8 – *a* = 14.06700 Å – *b* = 4.54640 Å – *c* = 10.32720 Å – β = 101.09º.

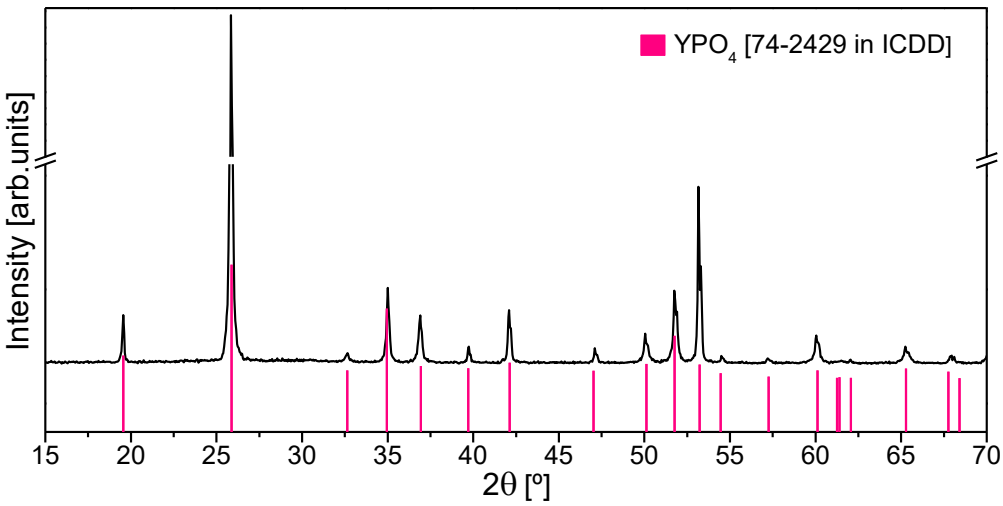

Lattice: Body-centered tetragonal – Space group: $I4_1/amd$ (141) – Z = 4 – a = 6.87800 Å – c = 6.03600 Å.

UNIVERSITAT ROVIRA I VIRGILI
CE OR PR-DOPED TYPE III KGD(PO3)4 CRYSTALLINE MATERIALS. GROWTH AND CHARACTERIZATION AS SCINTILLATORS
Irina Adell Barbarà

Paper I

Single crystal growth, optical absorption and luminescence properties under VUV-UV synchrotron excitation of type III Ce^{3+}:$KGd(PO_3)_4$, a promising scintillator material

I. Adell, R. M. Solé, M. C. Pujol, M. Lancry, N. Ollier, M. Aguiló and F. Díaz

Scientific Reports **2018**, 8, 11002

DOI: *10.1038/s41598-018-29372-z*

UNIVERSITAT ROVIRA I VIRGILI
CE OR PR-DOPED TYPE III KGD(PO3)4 CRYSTALLINE MATERIALS. GROWTH AND CHARACTERIZATION AS SCINTILLATORS
Irina Adell Barbarà

www.nature.com/scientificreports

SCIENTIFIC REPORTS

OPEN

Received: 8 December 2017
Accepted: 5 July 2018
Published online: 20 July 2018

Single crystal growth, optical absorption and luminescence properties under VUV-UV synchrotron excitation of type III Ce^{3+}:$KGd(PO_3)_4$, a promising scintillator material

Irina Adell[1], Rosa Maria Solé[1], Maria Cinta Pujol[1], Matthieu Lancry[2], Nadège Ollier[3], Magdalena Aguiló[1] & Francesc Díaz[1]

Scintillator materials have gained great interest for many applications, among which the medical applications stand out. Nowadays, the research is focused on finding new scintillator materials with properties that suit the needs of each application. In particular, for medical diagnosis a fast and intense response under high-energy radiation excitation is of great importance. Here, type III Ce^{3+}-doped $KGd(PO_3)_4$ single crystals with high crystalline quality are grown and optically characterized as a new promising scintillator material. The $4f \rightarrow 5d$ electronic transitions of Ce^{3+} are identified by optical absorption. The optical absorption cross section of Ce^{3+} for the electronic transition from the $^2F_{5/2}$ to the $5d_1$ level is 370×10^{-20} cm^2. The luminescence of $KGd_{0.996}Ce_{0.004}(PO_3)_4$ crystal by exciting the $5d$ levels of Ce^{3+} with VUV-UV synchrotron radiation shows down-shifting properties with strong emissions at 322 and 342 nm from the $5d_1$ to $^2F_{5/2}$ and $^2F_{7/2}$ levels of Ce^{3+} with a short decay time of ~16 ns, which is very suitable for scintillator applications. Moreover, these intense emissions are also observed when Gd^{3+} is excited since an energy transfer from Gd^{3+} to Ce^{3+} exists.

Scintillator materials have gained great interest for a large number of applications, such as in medical imaging techniques (X-ray computed tomography, positron emission tomography), high energy and nuclear physics, non-destructive testing, amongst others[1–4]. An ideal scintillator material should satisfy different properties, mainly high density, fast emission and a high light yield[5]. Many efforts are dedicated to find novel scintillator materials with the best properties for different applications, especially in the case of medical applications with the aim to reduce the ionizing radiation exposure to the patient in diagnostic techniques[6].

In scintillator materials which contain lanthanide ions, the emissions in the ultraviolet and visible regions suitable for scintillation applications are produced mainly by the $5d \rightarrow 4f$ electronic transitions of these ions, which act as scintillator centres. Typical scintillator materials are Ce^{3+}-doped crystals, such as Ce^{3+}:Lu_2SiO_5 and Ce^{3+}:$LaBr_3$. Both crystals present some drawbacks, such as difficulty for crystal growth and hygroscopicity, respectively[7,8]. Multicomponent garnet crystals doped with Ce^{3+} are also used in medical imaging and gamma spectroscopy due to high light yield and high density, but with poorer timing performance compared with lutetium-yttrium oxyorthosilicate crystals[9]. Ce^{3+} emission bands are based on the $5d$ to $4f$ electronic level transitions, usually as a doublet since the arrival states, $^2F_{5/2}$ and $^2F_{7/2}$, are separated by around 2000 cm^{-1}[10]. These

[1]Universitat Rovira i Virgili, Departament Química Física i Inorgànica, Física i Cristal·lografia de Materials i Nanomaterials (FiCMA-FiCNA) - EMaS, Campus Sescelades, c/Marcel·lí Domingo, 1, E-43007, Tarragona, Spain. [2]Institut de Chimie Moléculaire et des Matériaux d'Orsay, CNRS-Université Paris Sud, Université de Paris Saclay, Bât.410, 91405, Orsay, France. [3]Laboratoire des Solides Irradiés, CEA-CNRS-Ecole Polytechnique, Université Paris-Saclay, Palaiseau, France. Correspondence and requests for materials should be addressed to R.M.S. (email: rosam.sole@urv.cat) or M.C.P. (email: mariacinta.pujol@urv.cat)

Exp. number	$[Ce_2O_3]/([Gd_2O_3]+[Ce_2O_3])$ in the solution [at.%]	Growth interval [K]	Crystal weight [g]	Crystal dimensions along $a^*\times b\times c^*$ directions [mm]	Growth rate [$\times 10^{-3}$ g·h^{-1}]
1	0.25	27.4	0.62	3.1 × 9.9 × 9.9	1.55
2	0.50	30	1.62	6.1 × 15.1 × 10.9	3.61
3	0.50	29	1.65	5.4 × 14.9 × 11.4	3.84
4	1.00	31	1.31	3.9 × 13.2 × 12.2	2.78
5	1.00	32	1.76	6.0 × 15.7 × 11.5	3.58
6	2.00	34.3	1.68	4.9 × 15.5 × 13.3	3.25

Table 1. Crystal growth conditions and crystals obtained from about 100 g of solution.

electronic transitions are allowed and have a very short decay time in the order of nanoseconds[11], which could be suitable for scintillator applications.

Crystalline alkali and rare earth polyphosphates, $MRE(PO_3)_4$ (where M is an alkali cation, M = Li, Na and K; RE is a *r*are *e*arth cation), have been recently studied as candidates for scintillator applications[2] due to their broad transparency range in the ultraviolet region, its relatively high density and the possibility to incorporate Ce^{3+} and Pr^{3+} ions which are characterized by fast emissions in many hosts. They have been also intensively studied for other optical applications due to the low concentration quenching of the luminescence at high concentration of the active Ln^{3+} ions[12]. Ce^{3+} luminescence in phosphate compounds have been deeply studied, by Blasse and Dirken[13] in $LiLaP_4O_{12}$, by Shalapska *et al.*[12] in $LiYP_4O_{12}$, Zhong *et al.*[14] in 2007 in $AGdP_4O_{12}$ (being A = Cs, K, Na and Li) and Novais *et al.*[15] in 2014 in the non-centrosymmetric monoclinic phase $NaYP_2O_7$.

Among them, $KGd(PO_3)_4$ is a suitable crystal to incorporate different Ln^{3+} ions substituting the Gd^{3+} ions of the structure, is not hygroscopic, presents a good chemical stability[16] and its density is 3.538 mg·m^{-3} [17]. Besides, it is a deep-ultraviolet crystal closing at 160 nm[18] indicating a large band gap, which potentially could allow that the 5*d* energy levels of some Ln^{3+} ions be located between the conduction band and the valence band.

The existence of the radioisotope ^{40}K (0.0117% natural abundance) may limit its usefulness for some applications by increasing the background radiation. However, as mentioned in the review of Nikl[19], other radioactive isotopes are also present in several used scintillator crystals such as ^{176}Lu, ^{87}Rb, and ^{138}La contributing in a background signal. Besides, other promising scintillator materials identified in the literature also contain K as ion, such as: $K_2LaI_5:Ce^{3+}$, being attractive by its fast decay time of 24 ns, together with a relative high density[20]; and $KSr_2I_5:Eu^{2+}$ with a very high yield[21].

Finally, we have already reported the feasibility of growing these crystals within the non-centrosymmetric monoclinic crystalline phase with high crystalline quality[18,22]. This compound presents a polymorphism related to the degree of condensation of the phosphoric anions: the PO_4 forms chains in the type III phase (space group: $P2_1$) and type IV phase (space group: $P2_1/n$), belonging to the group of polyphosphates, and the PO_4 forms rings in the type B phase (space group: $C2/c$) belonging to the group of cyclophosphates[22]. High quality bulk single crystals of Ln^{3+}-doped non-centrosymmetric $KGd(PO_3)_4$ (space group: $P2_1$) have been already grown by us by the Top Seeded Solution Growth technique. The unit cell parameters for undoped $KGd(PO_3)_4$ are $a = 7.255(4)$ Å, $b = 8.356(5)$ Å, $c = 7.934(5)$ Å, $\beta = 91.68(5)°$ and $Z = 2$ refined by single crystal X-ray diffraction[17].

Potassium and Ce^{3+} stoichiometric phosphate, $KCe(PO_3)_4$, also presents polymorphism; in this compound, the phosphoric anions can form chains in the type III phase (space group: $P2_1$)[23]. Since $KCe(PO_3)_4$ also presents the type III crystalline phase, it is expected that the non-centrosymmetric phase (type III) $KGd(PO_3)_4$ can be doped with high concentration of Ce^{3+}.

Thus, $KGd(PO_3)_4$ as a host and Ce^{3+} as doping element (hereafter Ce^{3+}:KGdP) is a promising combination to obtain a new scintillator material. The aim of our research is to growth non-centrosymmetric Ce:KGdP single crystals from high temperature solutions with different Ce^{3+} doping concentrations in order to carry out a study of the luminescence properties of these crystals under synchrotron VUV excitation and discuss the potential of this crystalline phase of KGdP for scintillator applications.

Results and Discussion

Bulk single crystal growth. Table 1 summarizes the growth conditions of the different single crystal growth experiments carried out in this work and some features of the crystals obtained.

The saturation temperature of the solutions was determined to be at around 950 K. As expected this saturation temperature is similar to the one reported for the crystal growth of Yb-doped KGdP crystals, grown in similar experimental conditions[24] and lower than reported for undoped KGdP[16]. Lower crystallization temperature would mean higher viscosity in the solution, which can affect negatively to the crystal quality and the growth rate of the crystals.

These crystals were colourless, transparent, and generally free from inclusions and cracks. The size of the crystals obtained along $a^*\times b\times c^*$ directions were 3.1–6.1 × 9.9–15.7 × 9.9–13.3 mm and the weight of the crystals ranged from 0.62 to 1.76 g. In all cases, the crystal dimension along the *b* crystallographic axis was higher than the dimensions in a^* and c^* directions. Comparing the a^* dimension with previous reported grown crystals, in this case the dimensions are smaller. One of the reasons of these smaller crystal dimensions is the lower amount of growth solution in the crucible due to the smaller crucible diameter. In addition, changes in the thermal vertical gradient, especially in the first centimetre of the solution, and different position of the stirrer in relation to the crystal growing can also contribute to produce changes in the crystal dimensions.

Ce^{3+} at.% in solution	K_{Ce}	Ce^{3+} concentration [cm^{-3}]	Chemical formula
0.25	1.77	1.667×10^{19}	$KGd_{0.996}Ce_{0.004}(PO_3)_4$
0.5	1.30	2.501×10^{19}	$KGd_{0.994}Ce_{0.006}(PO_3)_4$
1	1.88	7.919×10^{19}	$KGd_{0.981}Ce_{0.019}(PO_3)_4$
2	1.28	1.084×10^{20}	$KGd_{0.974}Ce_{0.026}(PO_3)_4$

Table 2. EPMA results for Ce:KGdP. K_{Ce} denotes the distribution coefficient of the Ce^{3+} in the crystal.

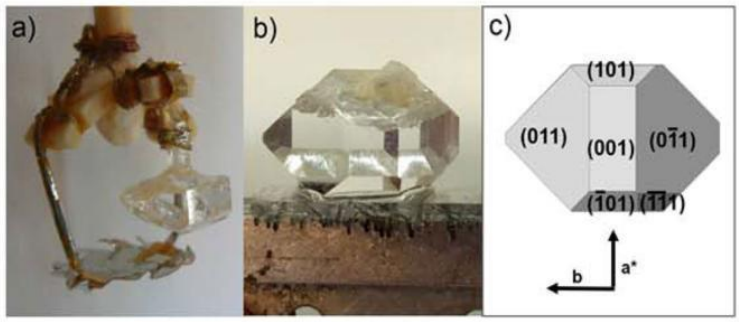

Figure 1. (**a**) As-grown single crystal of Ce^{3+}:KGdP and platinum stirrer, (**b**) As-grown single crystal of Ce^{3+}:KGdP and (**c**) Crystal scheme with the faces observed.

The crystal growth rates were generally higher than 3×10^{-3} g·h^{-1}. In previous reports, the crystal growth rate was around 8-9 $\times 10^{-3}$ g·h^{-1} for undoped KGdP[25] and around 7×10^{-3} g·h^{-1} for Nd-doped KGdP[18]. Several reasons can induce this slower crystal growth, which are the different composition of the solution with a reduced amount of solute in it, the total mass of the solution which in the present work is lower, and finally, the presence of cerium in the solution. However, it is significant to point out the difficulty of the growing high quality crystals due to the high viscosity of the solution, around 19 Pa·s at 950 K, and how by choosing and designing accurate crystal growth conditions, such as appropriate stirring of the solution by the use of stirrer and cooling ramps, high crystalline quality crystals have been obtained. Crystal growth is very difficult in highly viscous solutions, since due to the low molecular mobility inside them, the growth units find difficulties to reach the crystal surface.

As an example, Fig. 1 shows an as-grown Ce^{3+}:KGdP single crystal with the platinum stirrer and a morphological scheme with the crystalline faces observed in this crystal. The crystal scheme corresponds to the crystalline habit of type III phase of KGdP.

The distribution coefficient of Ce^{3+} in KGdP was calculated using the EPMA results according to the formula: $K_{Ce} = ([Ce]/([Ce] + [Gd]))_{crystal}/([Ce]/([Ce] + [Gd]))_{solution}$. The stoichiometry of the crystals and the Ce^{3+} distribution coefficients are shown in Table 2. The cerium distribution coefficient is larger than one; this means that the Ce^{3+} distribution inside the crystal may be not homogeneous. Besides, the distribution coefficient of Ce^{3+} is larger than the observed one for Yb and similar to the one reported for Nd[18,24]. This last fact can be related to the different ionic radii of the lanthanide doping ions.

In addition, X-ray powder diffraction analysis was made to study the effect on the unit cell parameters of KGdP when it is doped with Ce^{3+} ions. For undoped KGdP, with non-centrosymmetric crystalline structure, the unit cell parameters are $a = 7.2510(4)$ Å, $b = 8.3498(2)$ Å, $c = 7.9240(2)$ Å, $\beta = 91.823(3)°$, with $Z = 2$ and the unit cell volume is 479.51(3) Å^3. In the case of $KCe_{0.026}Gd_{0.974}(PO_3)_4$ crystals, the unit cell parameters are $a = 7.2520(4)$ Å, $b = 8.3524(2)$ Å, $c = 7.9265(2)$ Å, $\beta = 91.826(3)°$, with $Z = 2$ and the unit cell volume is 479.88(3) Å^3. As can be seen, the unit cell parameters and the unit cell volume slightly increase when KGdP is doped with Ce^{3+} ions. This is expected since the ionic radius of Ce^{3+} with coordination VIII is higher than the ionic radius of Gd^{3+} with the same coordination (1.143 Å and 1.053 Å, respectively)[26]. Moreover, by acquiring the X-ray diffraction pattern for obtaining the unit cell parameters of the Ce^{3+}-doped crystals, it is proved that the crystalline phase of the crystals is the type III one (space group: $P2_1$).

Ce^{3+} spectroscopy in $KGd(PO_3)_4$ single crystals. *Optical absorption.* As it is known, the 5*d* electrons present a strong interaction with the crystal field, which determines the position of the 5*d* energy levels and its high dependence with the crystal host[27–29]. These bands are also wide due to the 5*d* electron interaction with the lattice phonons. In the non-centrosymmetric KGdP crystalline phase, Ce^{3+} substitutes the Gd^{3+} ions in a C_1 position inside a GdO_8 distorted dodecahedra. The 5*d* level splits in five non-degenerated crystal-field levels.

Compound	Space group	R_{av} (Gd-O) [Å]	CF	$\lambda_5, \lambda_4, \lambda_3, \lambda_2, \lambda_1$ [nm]	D(A) [cm^{-1}]	ε_{cfs} [cm^{-1}]	ε_c [cm^{-1}]	R_{eff} [Å]	α_{sp} [10^{-30} m^3]	Ref.
$KGd_{0.996}Ce_{0.004}(PO_3)_4$	$P2_1$	2.4065	ddh	194, 215, 226, 243.5, 302.5	16282	18489	7944	2.447	1.479	This work
$KGd_{0.99}Ce_{0.01}P_4O_{12}$	$C2/c$	2.408	ddh	193, 209, 221, 245, 307	16767	19240	7570	2.453	1.431	14
$NaGd_{0.99}Ce_{0.01}(PO_3)_4$	$P2_1/n$	— 2.401	— ddh	—, —, 223, 256, 297 196, 207, 218, 254, 297	— 15670	— 17350	— 7582	— 2.443	— 1.398	2, 14
$NaPr_{0.9}Ce_{0.1}P_4O_{12}$	$P2_1/n$	—	ddh	195, 230, 252, 268, 295	15442	17300	7332	—	—	12
$LiLa_{0.95}Ce_{0.05}P_4O_{12}$	$C2/c$	—	ddh	—, —, —, —, 278	13369	—	—	—	—	13

Table 3. Spectroscopic properties and crystallographic space groups of Ce^{3+} doped phosphates. Note: R_{av} = average distance, CF = coordination figure, ddh = dodecahedron, λ_5, λ_4, λ_3, λ_2, λ_1 = absorption bands of the 5*d* levels, D(A) = spectroscopic redshift, ε_c = centroid shift, ε_{cfs} = crystal field splitting, R_{eff} = effective distance of Gd-O, and α_{sp} = spectroscopic polarizability.

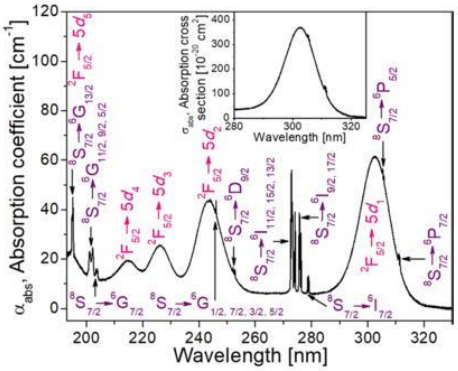

Figure 2. Unpolarised optical absorption coefficient of $KGd_{0.996}Ce_{0.004}(PO_3)_4$ at room temperature. Propagation direction is along *b* axis. Labels in purple indicate the absorption transitions of Gd^{3+} and labels in pink those of Ce^{3+}. Inset: Unpolarised optical absorption cross section of $^2F_{5/2} \rightarrow 5d_1$ transition of Ce^{3+} in $KGd_{0.996}Ce_{0.004}(PO_3)_4$ at room temperature.

Figure 2 shows the unpolarised optical absorption coefficient of $KGd_{0.996}Ce_{0.004}(PO_3)_4$ at room temperature and the inset displays the unpolarised optical absorption cross section of $^2F_{5/2} \rightarrow 5d_1$ transition of Ce^{3+} in the same crystal at room temperature. As can be seen in this Figure, the strongest bands are assigned to the $4f \rightarrow 5d$ vibronic transitions. The wavelengths assigned to each $4f \rightarrow 5d_1$, $5d_2$, $5d_3$, $5d_4$ and $5d_5$ absorptions are resumed in Table 3. The wavelength values for the $4f \rightarrow 5d$ electronic transitions in other hosts are also summarised in Table 3.

The broad band centred at 302.5 nm (33058 cm^{-1}, 4.10 eV) (see Fig. 2) corresponds to the first spin-allowed $4f \rightarrow 5d$ transition from ground state to the first 5*d* level ($5d_1$) of Ce^{3+} in the KGdP host. This value is very close to the reported values in other crystalline phosphates, such as 310 nm for $K_3La(PO_4)_2$[30], and 307 nm for the centrosymmetric KGdP (space group: $C2/c$)[14]. It is worth to point out that the photons at 194, 244 and 302.5 nm excite both Ce^{3+} and Gd^{3+} ions; whereas the other identified wavelengths, 214 and 226 nm, excite predominantly only Ce^{3+} ions.

The centroid position of the 5*d* energy levels of Ce^{3+} in a free ion is 51230 cm^{-1} [28]. Due to the large interaction of the 5*d* electron with the crystal field of the host A, the first dipole allowed $4f \rightarrow 5d$ transition is shifted in relation with the free ion value; this shift is defined as the spectroscopic redshift, D(A)[28]. The spectroscopic redshift of Ce^{3+} due to the type III KGdP host is D(KGdP) = 16282 cm^{-1}. As mentioned by Dorenbos *et al.*, this depression is expected to be the same for each Ln^{3+} ion used as scintillator centre in the same KGdP host[31].

As described by Dorenbos *et al.*[32], the polyphosphate compounds have a large fraction of strongly bonding phosphate atoms, which cause that the D(A) is amongst the smallest, and the crystal field splitting, ε_{cfs}, and the bandgap amongst the largest of all oxide compounds. By comparing the values of the D(A) of Table 3, it can be observed how this value decreases as smaller is the alkaline ion (K > Na > Li); this tendency in the phosphates was already observed by Dorenbos[31].

Table 3 shows the spectroscopic redshift, D(A), as well as the centroid shift, ε_c, crystal field splitting, ε_{cfs}, effective distance of Gd-O bond, R_{eff}, and spectroscopic polarizability, α_{sp}, for the type III KGdP host and others. D(A), ε_c and ε_{cfs} were calculated by using the optical absorption spectrum in Fig. 2; R_{eff} and α_{sp} were calculated considering the ε_c, as in the reference[14], and the crystallographic data of the undoped non-centrosymmetric KGdP[22].

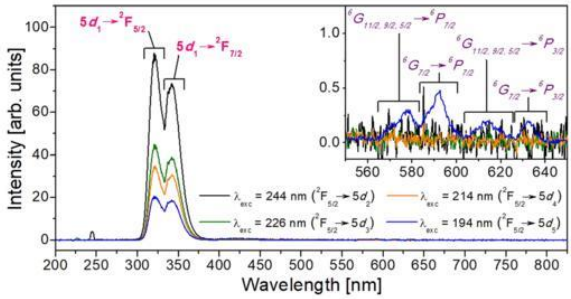

Figure 3. Optical emission spectra of $KGd_{0.996}Ce_{0.004}(PO_3)_4$ under 244, 226, 214 and 194 nm excitation. Labels in purple (inset) indicate the transitions of Gd^{3+} and labels in pink those of Ce^{3+}.

The crystal field splitting, ε_{cfs} (the energy difference between the $5d_1$ and the $5d_5$) for the non-centrosymmetric KGdP is smaller than in the centrosymmetric one. This fact does not follow the expected behaviour since ε_{cfs} is determined by the strength of the crystal field, related to the shape and the size of the coordination polyhedron, and considering the same polyhedral shape, the smaller the bond length and larger distortion, the higher the crystal field splitting[28]. Comparing the two hosts, the non-centrosymmetric KGdP crystal presents shorter bond length than the centrosymmetric one, and they have similar distortion in the cation site. This different crystal field suffered by the Ce^{3+} ions may be related to effects in the second coordination sphere.

The centroid shift, ε_c (energy difference between the centroid value of the 5*d* of the free electron and the one inside the crystal) may be related to the ligand polarization and has no dependence on the crystal field splitting value. As it can be seen in the same table, the ε_c for the non-centrosymmetric KGdP in comparison with the centrosymmetric one is higher. Taking into account the ligand polarization model[29], the fact that the non-centrosymmetric KGdP has a ε_c value larger than the centrosymmetric one, should be attributed to the major contribution of the effective distances, R_{eff}, in the value of centroid shift ($\varepsilon_c \propto R_{eff}^{-6}$).

All discussed parameters until now are dependent of the crystalline host, so they are also related to the Ce^{3+} concentration in the crystal and temperature. The spectroscopic values for non-centrosymmetric KGdP have been calculated for $KGd_{0.996}Ce_{0.004}(PO_3)_4$ and at room temperature.

Moreover, as 4*f*→5*d* transitions are parity allowed transitions, it was also expected a high value of optical absorption cross section. The observed value is 370×10^{-20} cm² at 302.5 nm for Ce^{3+} in the type III KGdP crystal. The 4*f*→4*f* transitions in lanthanide ions are very weakly influenced by the crystal field and for this reason the position of such absorption transitions of Gd^{3+} are the expected ones and have been labelled by using the Dieke's diagram[10].

Optical emission. Figure 3 shows the emission spectra of $KCe_{0.004}Gd_{0.996}(PO_3)_4$ under $\lambda_{exc} = 244$ nm (5.09 eV), 226 nm (5.49 eV), 214 nm (5.80 eV) and 194 nm (6.40 eV), which correspond to the excitation to the $5d_2$, $5d_3$, $5d_4$ and $5d_5$ energy levels, respectively, of Ce^{3+} in the KGdP host. The intensities have been corrected by the excitation photon flux values. From this Figure, it can be seen an intense doublet peak centred at 322 and 342 nm corresponding to the $5d_1 \rightarrow {}^2F_{5/2}$ and $5d_1 \rightarrow {}^2F_{7/2}$ transitions, respectively, of Ce^{3+} in KGdP. The energy difference between these two emission peaks is consistent with the energy difference between the 4*f* levels of Ce^{3+}, $^2F_{5/2}$ and $^2F_{7/2}$ levels, as can be seen in the Dieke's diagram[10]. This emission appears by exciting the sample under all these four different excitation wavelengths, in which the emission intensities are in accordance with the values of absorption coefficient for each excitation wavelength. The intensity of emission when the sample is excited at 194 nm is lower than when it is excited at 214 nm, despite their similar absorption coefficient values. This behaviour might be attributed to a depopulation of the $5d_5$ level of Ce^{3+} due to energy transfer to the 4*f* levels of Gd^{3+}.

It is worth saying that the ${}^6P_{7/2} \rightarrow {}^8S_{7/2}$ transition of Gd^{3+} which should appear as a sharp emission around 311 nm, being common in many hosts[33–36], is not present in the non-centrosymmetric $KGd_{1-x}Ce_x(PO_3)_4$ crystals, as observed in Fig. 3. The same behaviour is observed in the $KGd_{0.981}Ce_{0.019}(PO_3)_4$ and $KGd_{0.974}Ce_{0.026}(PO_3)_4$ crystals, referring to the emissions of Ce^{3+} and Gd^{3+} under the wavelength excitation 244, 226, 214 and 194 nm. By comparing the emission spectrum obtained under VUV excitation and that obtained under X-ray excitation of four highly similar hosts[2,14,37] to our compound, it has been observed that the ${}^6P_{7/2} \rightarrow {}^8S_{7/2}$ transition of Gd^{3+} is not present under VUV excitation, and it does not appear by exciting the compound with X-rays, either. Thus, in type III Ce:KGdP, since the above mentioned 4*f*→4*f* transition of Gd^{3+} is not observed (Fig. 3), it is expected that it will not appear under X-ray excitation. This is a favourable feature for scintillator use because the emissions which are of interest in this application are based on 5*d*→4*f* transitions, instead of the 4*f*→4*f* transitions, since the 5*d* levels have very short decay times, in the order of nanoseconds. However, it should be noted that similar spectra are not always obtained when the compound is excited with VUV radiation and with X-rays.

From the work done by Zhong *et al.*[14] similar results were observed in $KGdP_4O_{12}$ host with type B phase (space group: *C*2/*c*). The $5d_1 \rightarrow {}^2F_{5/2}$ and $5d_1 \rightarrow {}^2F_{7/2}$ transitions appear at 323 and 343 nm, respectively. When Ce:$KGdP_4O_{12}$ is excited at 193 nm ($^2F_{5/2} \rightarrow 5d_5$), the emission of Gd^{3+} at 311 nm looks very weak as a hump in

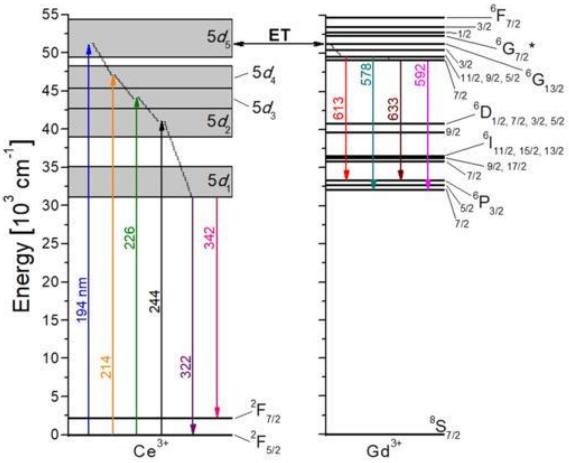

Figure 4. Energy levels diagram of Ce^{3+} and Gd^{3+} in $KGd_{0.996}Ce_{0.004}(PO_3)_4$ and the emission mechanism. ET = Energy Transfer.

the band corresponding to the $5d_1 \rightarrow {}^2F_{5/2}$ emission. Therefore, this emission of Gd^{3+} is extraordinarily rare in comparison with the emissions of Ce^{3+} in the type III KGdP. In a similar phosphates, this Gd^{3+} emission appears more intense than the emission peaks corresponding to $5d_1 \rightarrow {}^2F_{5/2}$, ${}^2F_{7/2}$ transitions of Ce^{3+} in Ce:$LiGdP_4O_{12}$ (space group: *C*2/*c*) under 292 nm ($^2F_{5/2} \rightarrow 5d_1$), 273 nm ($^8S_{7/2} \rightarrow {}^6I_J$ Gd^{3+}) and 188 nm ($^2F_{5/2} \rightarrow 5d_5$) excitation, and in Ce:$NaGdP_4O_{12}$ (space group: $P2_1/n$) under 298 nm ($^2F_{5/2} \rightarrow 5d_1$) and 273 nm ($^8S_{7/2} \rightarrow {}^6I_J$ Gd^{3+}) excitation[14].

In the inset of Fig. 3, it can be seen how several weak peaks appeared in the spectral range from 560 to 640 nm when the $KCe_{0.004}Gd_{0.996}(PO_3)_4$ sample is excited at 194 nm. These four weak peaks centred at 578, 592, 613 and 633 nm correspond to $4f \rightarrow 4f$ transitions of Gd^{3+}, being the $^6G_{11/2,9/2,5/2} \rightarrow {}^6P_{7/2}$, $^6G_{7/2} \rightarrow {}^6P_{7/2}$, $^6G_{11/2,9/2,5/2} \rightarrow {}^6P_{3/2}$ and $^6G_{7/2} \rightarrow {}^6P_{3/2}$ transitions, respectively. This may occur since the $^8S_{7/2} \rightarrow {}^6G_{13/2}$ absorption transition of Gd^{3+} about 194 nm is overlapped with the $^2F_{5/2} \rightarrow 5d_5$ of Ce^{3+}, as can be seen in Fig. 2. The energy levels of Gd^{3+} and Ce^{3+} in KGdP and the possible energy transfer mechanism are shown in Fig. 4. Returning to Figs 2 and 3, since the absorption from $^2F_{5/2}$ ground state of Ce^{3+} to its $5d_1$ level appears at 302.5 nm and the emission corresponding to the $5d_1 \rightarrow {}^2F_{5/2}$ transition appears at 322 nm, the Stokes shift in the type III KGdP host is $\Delta S = 2002\ cm^{-1}$. By observing the work done by Shalapska *et al.*[12], the absorption peak corresponding to $^2F_{5/2} \rightarrow 5d_1$ transition of Ce^{3+} in Ce:$NaPrP_4O_{12}$ (space group: $P2_1/n$) appear at 295 nm, and the $5d_1 \rightarrow {}^2F_{5/2}$ and $5d_1 \rightarrow {}^2F_{7/2}$ transitions appear as emissions at 310 and 328 nm. The characteristics of Ce^{3+}-luminescence in $LiYP_4O_{12}$ host have also been studied by Shalapska *et al.*[38]. In this host, the absorption peaks corresponding to $^2F_{5/2} \rightarrow 5d_1$ transition of Ce^{3+} appear at 295 and the $5d_1 \rightarrow {}^2F_{5/2}$ and $5d_1 \rightarrow {}^2F_{7/2}$ transitions appear at 312 and 333 nm. From the experimental data mentioned, the Stokes shifts are $\Delta S(KGdP_4O_{12}) = 1614\ cm^{-1}$, $\Delta S(NaPrP_4O_{12}) = 1640\ cm^{-1}$ and $\Delta S(LiYP_4O_{12}) = 1847\ cm^{-1}$. Thus, the Stokes shift of type III $KGd(PO_3)_4$ host is higher [$\Delta S = 2002\ cm^{-1}$] than the calculated in the three hosts mentioned above, but still slightly below the most frequent Stokes shift measured in 240 different compounds, being $2200\ cm^{-1}$ [27]. The Stokes shift is induced by lattice relaxation at the excited states. Hence, the higher the value of Stokes shift is, the larger the relaxation of the electron at the excited state is before emitting electromagnetic radiation, resulting in higher non-radiative losses[39,40]. The Stokes shift is not dependent of the lanthanide ion, but only depends on the host. So, it can be extrapolated for future doping ions in the KGdP crystal[31].

Moreover, it is also interesting to observe the intensity ratios of the peaks corresponding to $5d_1 \rightarrow {}^2F_{5/2}$ and $5d_1 \rightarrow {}^2F_{7/2}$ transitions of Ce^{3+}, since it varies with the doping level. As the Ce^{3+} doping is higher, the peak corresponding to the transition from $5d_1$ to $^2F_{5/2}$ becomes less intense compared to the transition to $^2F_{7/2}$. The evolution of this ratio of intensities versus Ce^{3+} concentration can be seen in Fig. 5. This behaviour may be due to the presence of reabsorption of the emission corresponding to the $5d_1 \rightarrow {}^2F_{5/2}$ transition by the neighbouring Ce^{3+} atoms.

Figure 6 shows the excitation spectrum of $KGd_{0.981}Ce_{0.019}(PO_3)_4$ at room temperature for the emission wavelengths $\lambda_{emi} = 342$ nm ($5d_1 \rightarrow {}^2F_{7/2}$ of Ce^{3+}) and $\lambda_{emi} = 592$ nm ($^6G_{7/2} \rightarrow {}^6P_{7/2}$ of Gd^{3+}) with the electronic transitions labelled. In the case of the excitation spectrum for the emission of Ce^{3+}, it can be observed that these emissions take place when Ce^{3+} is excited and also when Gd^{3+} is excited. Therefore, this reaffirms that an energy transfer from Gd^{3+} to Ce^{3+} occurs. In addition, from the same spectrum (Fig. 6a), the complete band of the $5d_5$ level of Ce^{3+} has been observed complementing the assignment of 5*d* levels energy values in the absorption measurements.

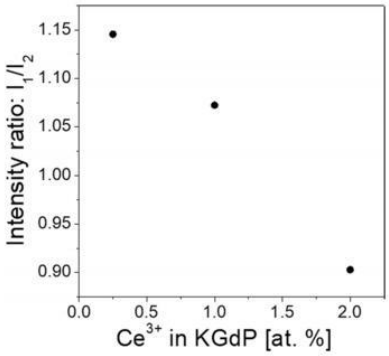

Figure 5. Intensity ratio of the emission peaks belonging to the $5d_1 \rightarrow {}^2F_{5/2}$ transition (I_1) versus the emission peaks belonging to $5d_1 \rightarrow {}^2F_{7/2}$ transition (I_2) of Ce^{3+} under 226 nm excitation ($^2F_{5/2} \rightarrow 5d_3$).

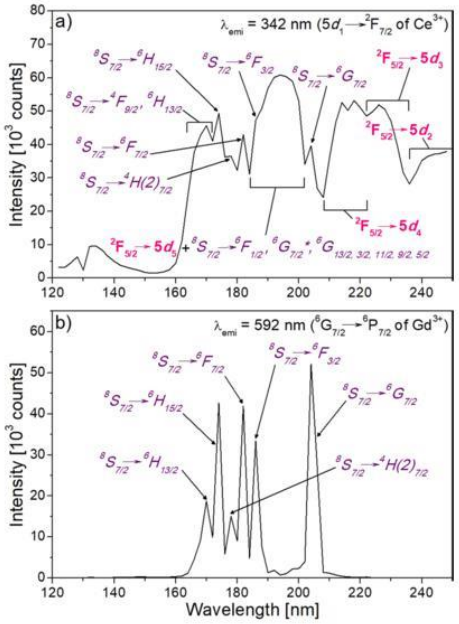

Figure 6. Excitation spectra of $KCe_{0.019}Gd_{0.981}(PO_3)_4$ for the emission wavelengths of (**a**) 342 nm ($5d_1 \rightarrow {}^2F_{7/2}$ of Ce^{3+}) and (**b**) 592 nm ($^6G_{7/2} \rightarrow {}^6P_{7/2}$ of Gd^{3+}). Labels in purple indicate the transitions of Gd^{3+} and labels in pink those of Ce^{3+}.

From Fig. 6b, it can be seen how the emission at 592 nm is produced mainly when Gd^{3+} cations are directly excited. Similar behaviours have been observed for the emissions centred at 578, 613 and 633 nm, all corresponding to $4f \rightarrow 4f$ electronic Gd^{3+} transitions.

The energy of the exciton creation (E^{ex}), that is, bound electron and hole pairs, in type III KGdP has been predicted that appears at 164 nm (7.57 eV) by the calculations explained below. First, the energy of the onset of the

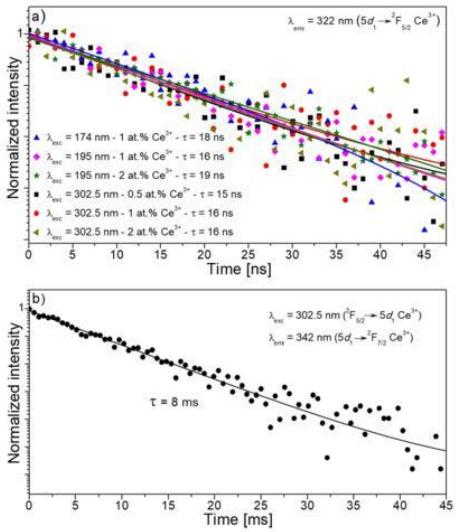

Figure 7. (**a**) Fast component of the luminescence decay curves of Ce^{3+}-doped KGdP crystals with different doping concentrations and at different excitation wavelengths for $\lambda_{emi} = 322$ nm. (**b**) Slow component of the decay curve of $KGd_{0.974}Ce_{0.026}(PO_3)_4$ under excitation at 302.5 nm for $\lambda_{emi} = 342$ nm.

fundamental absorption (E^{fa}) of type III KGdP has been established at 172 nm (7.22 eV) by overlapping a straight line along the ultraviolet absorption edge observed in the transmission spectrum of Nd:$KGd(PO_3)_4$ crystal[18]. This same procedure was used in the work done by Ueda *et al.*[41]. Then, the estimated value of E^{ex} has been obtained by adding 0.35 eV to E^{fa} since these measurements have been performed at room temperature[42]. Hence, the band corresponding to E^{ex} could appear centred at 164 nm in the excitation spectra (Fig. 6), although it would not be appreciated due to an overlapping with the ${}^8S_{7/2} \rightarrow {}^4F_{9/2}$ transition of Gd^{3+}.

From the value of E^{ex}, it can be calculated the approximate energy difference from the bottom of the conduction band to the top of the valence band (E_{VC}); being approximately 1.08 times the energy of the exciton creation[42]. Therefore, the estimated value for type III KGdP is $E_{VC} = 8.17$ eV (152 nm).

Decay time measurements. Ce^{3+}-doped crystals were excited at 302.5 nm ($^2F_{5/2} \rightarrow 5d_1$ of Ce^{3+}), 194 nm (${}^8S_{7/2} \rightarrow {}^6G_{13/2}$ of Gd^{3+} and $^2F_{5/2} \rightarrow 5d_5$ of Ce^{3+}) and 174 nm (${}^8S_{7/2} \rightarrow {}^6H_{15/2}$ of Gd^{3+}). It should be noted that in order to gain in photon flux reaching to the sample, the excitation beam had a bandwidth of around 7%, being not purely monochromatic. Figure 7a shows the luminescence decay curves for the emission at $\lambda_{emi} = 322$ nm of Ce^{3+}-doped KGdP crystals with different doping concentrations and at different excitation wavelengths. As can be seen in the Figure, the decay curves can be fitted by a single exponential decay. The lifetime obtained for $5d_1$ level of Ce^{3+} in this host is around 16 ns. No significant changes in the lifetime value were obtained either due to the change of the wavelength of excitation or the different Ce^{3+} concentration in the crystals.

This measured lifetime of the $5d_1$ level of Ce^{3+} in the KGdP crystal is similar or even shorter than the measured ones in other scintillator materials[3,12,14,43]. By comparing this value with the obtained in the centrosymmetric KGdP (space group: $C2/c$, 21.1 ns), the lifetime of the $5d_1$ level of Ce^{3+} in type III KGdP (space group: $P2_1$) is significantly lower[14].

It has been also observed that in type III Ce^{3+}:KGdP crystals, the $5d_1 \rightarrow {}^2F_{5/2}, {}^2F_{7/2}$ decay is not only composed by a fast component, but also by a slow component. This fact was observed when the intensity of the emission does not reach zero value because of the short interpulse time in the synchrotron measurements. To measure in the appropriate magnitude this slow component, the lifetime was measured in a conventional fluorimeter. Figure 7b shows the slow component of this decay curve in the $KGd_{0.974}Ce_{0.026}(PO_3)_4$ crystal under excitation at $\lambda_{exc} = 302.5$ nm for the emission at $\lambda_{emi} = 342$ nm. In this Figure, it can be seen the exponential fit of the slow component resulting in a decay time around 8 ms. This slow component has been already observed in other Ce^{3+}-doped phosphates, as in $Ce:NaPrP_4O_{12}$[12], and $Ce:CsGd(PO_3)_4$[14]. In the first case, it was only observed at high energy excitations and it was attributed to trapping effect which makes the host-cerium energy transfer process more difficult, but in the case of $Ce:CsGd(PO_3)_4$, the slow component was observed when solely the Gd^{3+} ion was excited and not the Ce^{3+} ions. The long component in the Ce^{3+}-doped non-centrosymmetric KGdP crystal has been observed when exciting at short wavelength values (Fig. 7a) and also when exciting directly to the $5d_1$ level

(Fig. 7b). Therefore, the origin of this slow component could be attributed to some contribution of the trapping effect, but the contribution of the Gd^{3+} emission corresponding to the electronic transition $^6P_{7/2} \rightarrow {}^8S_{7/2}$ cannot be disregarded since the lifetime of this emitting $^6P_{7/2}$ level of Gd^{3+} is of the same order (4.9 ms in $NaY_{0.80}Gd_{0.20}PO_4$[34] and 6.36 ms in $NaGd(PO_3)_4$[44].

Conclusions

Type III Ce^{3+}-doped bulk single crystals have been grown by Top Seeded Solution Growth-Slow cooling technique from self-fluxes in high crystalline quality. Till a Ce^{3+} doping level of 2 at% substituting Gd^{3+} in solution, no effect of the cerium doping has been observed in the crystalline quality of the single crystals. The maximum optical absorption cross section has been measured for the electronic transition from the ground state of Ce^{3+} until the $5d_1$ level, being the value at 302.5 nm around 370×10^{-20} cm^2. The spectroscopic redshift of the 5*d* energy levels of Ce^{3+} in the type III KGdP host is 16282 cm^{-1}. Under ultraviolet excitation, a doublet emission peak centred at 322 and 342 nm has been observed in all grown crystals, corresponding to the $5d_1 \rightarrow {}^2F_{7/2}$ and $5d_1 \rightarrow {}^2F_{5/2}$ transitions of Ce^{3+}, respectively. No important Gd^{3+} $4f \rightarrow 4f$ emissions have been clearly observed by exciting at this range. By last, the lifetime of the $5d_1$ level of Ce^{3+} in type III KGdP has been measured by setting the doublet emission peak and a lifetime around 16 ns has been obtained, which is similar or even shorter than the lifetime of the same level of Ce^{3+} in other hosts. In addition, the presence of a slow component has been observed by setting the same emission peak. The reported results confirm the potentiality of the Ce^{3+}-doped type III $KGd(PO_3)_4$ crystals for scintillation applications.

Experimental

Single crystal growth. Ce^{3+}:KGdP single crystals with non-centrosymmetric monoclinic structure (space group: $P2_1$) have been grown from high temperature solutions. The solvent used was an excess of K_2O and P_2O_5 (self-flux), so that it does not contain foreign ions that could be introduced as impurities in the crystalline structure. The compositions of the growth solutions, chosen on the basis of the primary crystallization region of KGdP in the K_2O-Gd_2O_3-P_2O_5 ternary system, previously determined[22,45], were K_2O:$((1-x)Gd_2O_3 + x\,Ce_2O_3)$:$P_2O_5 = 36{:}4{:}60$ (mol%) with x in the range 0–0.02. The solutions, with a weight of about 100 g, were prepared in a platinum cylindrical crucible of 40 mm in diameter. The reagents used were K_2CO_3 anhydrous (Alfa Aesar A. Johnson Matthey Company, 99%), $NH_4H_2PO_4$ (Fluka Analytical, ≥99.0%) and both Gd_2O_3 and $Ce_2(CO_3)_3$ from Aldrich with a purity of 99.9%.

Due to the relatively high level of dynamic viscosity of the solutions[25], the mixing of the solution was produced by using high axial thermal gradient (3.0 K·mm^{-1} in depth), with the coolest point at the center of the solution surface (the solution density decreases with increasing the temperature), accompanied by the use of a platinum stirrer (20 mm in diameter) located at about 12 mm below the surface of the solution, rotating at 55 rpm. The growth was carried out on an undoped KGdP seed with a^* orientation with the *b* crystallographic direction tangential to the rotation direction, because in previous works it has been proved that this crystalline orientation gives excellent results in terms of crystal quality[16]. The seed, located in contact with the solution surface at about 10 mm from the rotation axis, was joined with the stirrer and rotated together[25].

The saturation temperature of the solution was accurately determined by measuring the growth and dissolution rates of the KGdP seed as a function of the temperature. Beginning at the determined saturation temperature, cooling rates of 0.1 K·h^{-1} for the firsts 15 K and 0.05 K·h^{-1} for the next 10–15 K were applied to achieve the required supersaturation of the solution for crystal growth. After finishing the cooling ramps or when the crystal was big enough, it was slowly removed from the solution. To avoid thermal shocks in the crystal, it was cooled to room temperature inside the furnace at a rate of 20–25 K·h^{-1}.

The composition of the crystals was determined by Electron Probe Microanalysis with Wavelength Dispersive Spectroscopy (EPMA-WDS) using a JEOL JXA-8230. The standard used to measure K, Gd, P and O was a KGdP single crystal, while the Ce content in the crystals was measured using CeO_2 as standard. The measures were made with an accelerating voltage of 20 kV and a current of 20 nA. The measuring time for K, Gd, P and O was 10 s for peak and 5 s for background, while in the case of Ce the measuring time was 120 s for peak and 60 s for background, because of its low concentration in the crystals. K_α X-ray lines of K, P and O and L_α X-ray lines of Gd and Ce were used for the composition measurements. The dispersive crystals were PETJ for K, LIFH for Gd, PETL for P and Ce and LDE1 for O measurements. Under these conditions, the detection limit of Ce was 195 ppm.

X-ray powder diffraction. The unit cell parameters of KGdP with Ce^{3+} doping up to 2 at.% in solution were determined by X-ray powder diffraction. The equipment used was a D5000 Siemens X-ray powder diffractometer in a θ-θ configuration with the Bragg-Brentano geometry. The measurements were carried out with step size of 0.03° and a step time of 7 s and recorded in the range $2\theta = 10$–70°. The unit cell parameters were refined using the TOPAS program[46].

Optical characterization. The grown crystals were cut in plates perpendicular to the crystallographic a^*, *b* and c^* directions with a diamond saw, lapped with Al_2O_3 suspension with particle size of 9 and 3 μm, successively, and polished with colloidal suspension of amorphous silicon dioxide with a mean particle size of 0.2 μm. These plates were used for optical absorption and emission studies. The optical absorption of Ce^{3+} in KGdP has been studied at room temperature using a 0.25 at.% Ce:KGdP plate parallel to the (001) crystallographic plane with a thickness of 0.11 mm and the equipment used was a CARY 5000 UV-Vis-NIR Spectrophotometer.

The emission spectroscopy of Ce^{3+}-doped KGdP single crystals under vacuum ultraviolet excitation was carried out in the wavelength range from 120 to 248 nm (10–5 eV). Experiments were performed in the DESIRS beamline at SOLEIL Synchrotron (France, proposal num. 20151215, Standard). The samples were placed in a

vacuum chamber which can be evacuated to around 10^{-5} bar. A Lithium Fluoride window at the entrance of the vacuum chamber separates it from the synchrotron line. The monochromatic synchrotron light reached perpendicularly to the KGdP plate. The emitted light from the sample was collected at 45° by a silica lens, focused at the entrance of an optical fibre connected to a Jaz spectrometer, Ocean Optics with a minimum spectral resolution of 0.3 nm. The emission spectra were recorded from 192 to 886 nm.

Lifetime measurements were also made in the DESIRS beamline at SOLEIL Synchrotron in a single bunch mode of operation to obtain pulsed radiation with full width at half-maximum pulse duration of 50 ps and interpulse time duration of 1.12 ms (proposal number 20161324, Standard). The crystals were placed at the same vacuum chamber, with the same configuration that in the emission measurements. The output emission of the crystal, focused with the same silica lens, was guided with an optical fibre to an ANDOR Shamrock 193i spectrograph (grating 150 lines/mm) coupled to an iStar Intensified Charge Coupled Device camera with fast response (DH734–18F-03 model). To increase the photon flux reaching the sample, once the vacuum in the chamber was enough high (at least 2×10^{-5} bars), the optical window between the vacuum chamber and the synchrotron line was removed. Long components of the time decays have been checked and measured by a conventional fluorimeter Cary Eclipse Fluorescence Spectrophotometer.

References

1. Rodnyi, P. A. Scintillators requirements in various applications in *Physical Processes in Inorganic Scintillators* 41–51 (CRC Press, 1997).
2. Zhong, J. *et al.* Luminescence of $NaGd(PO_3)_4$:Ce^{3+} and its potential application as a scintillator material. *Chem. Phys. Lett.* **445**(1–3), 32–36 (2007).
3. Nikl, M. *et al.* Development of LuAG-based scintillator crystals – A review. *Prog. Cryst. Growth Charact. Mater.* **59**, 47–72 (2013).
4. Nikl, M. & Yoshikawa, A. Recent R&D trends in inorganic single-crystal scintillator materials for radiation detection. *Adv. Opt. Mater.* **3**(4), 463–481 (2015).
5. van Eijk, C. W. E. Inorganic-scintillator development. *Nucl. Instrum. Methods Phys. Res., Sect. A* **460**, 1–14 (2001).
6. Yu, L. *et al.* Radiation dose reduction in computed tomography: techniques and future perspective. *Imaging Med.* **1**, 65–84 (2009).
7. Sidletskiy, O. *et al.* Structure–property correlations in a Ce-doped $(Lu,Gd)_2SiO_5$:Ce scintillator. *Cryst. Growth Des.* **12**(9), 4411–4416 (2012).
8. Tavernier, S., Gektin, A., Grinyov, B. & Moses, W. W. Inorganic scintillators in *Radiation Detectors for Medical Applications* (ed. Tavernier, S., Gektin, A., Grinyov, B. & Moses, W. W.) 262–265 (Springer, 2005).
9. Yeom, J. Y. *et al.* First performance results of Ce: GAGG scintillation crystals with silicon photomultipliers. *IEEE Trans. Nucl. Sci.* **60**, 988–992 (2013).
10. Dieke, G. H. & Crosswhite, H. M. The spectra of the doubly and triply ionized rare earths. *Appl. Opt.* **2**(7), 675–686 (1963).
11. Duan, C. K. & Reid, M. F. Local field effects on the radiative lifetimes of Ce^{3+} in different hosts. *Curr. Appl. Phys.* **6**, 348–350 (2006).
12. Shalapska, T. *et al.* Luminescence properties of Ce^{3+}-doped $NaPrP_4O_{12}$ polyphosphate. *J. Phys. Condens. Matter* **25**(10), 105403 (2013).
13. Blasse, G. & Dirksen, G. J. The luminescence of broad-band emitters in $LiLaP_4O_{12}$. *Phys. Status Solidi B* **110**, 487–494 (1982).
14. Zhong, J. *et al.* Effects of crystal structure on the luminescence properties and energy transfer between Gd^{3+} and Ce^{3+} ions in $MGd(PO_3)_4$:Ce^{3+} (M = Li, Na, K, Cs). *J. Mater. Chem.* **17**, 4679–4684 (2007).
15. Novais, S. M. V., Dobrowolska, A. P., Bos, A. J. J., Dorenbos, P. & Macedo, Z. S. Optical characterization and the energy level scheme for $NaYP_2O_7$:Ln^{3+} (Ln = Ce, Sm, Eu, Tb, Yb). *J. Lumin.* **148**, 353–358 (2014).
16. Parreu, I., Solé, R., Massons, J., Díaz, F. & Aguiló, M. Crystal growth, crystal morphology and surface micromorphology of type III $KGd(PO_3)_4$ and $KNd(PO_3)_4$. *Cryst. Growth Des.* **7**(3), 557–563 (2007).
17. Parreu, I., Carvajal, J. J., Solans, X., Díaz, F. & Aguiló, M. Crystal structure and optical characterization of pure and Nd-substituted type III $KGd(PO_3)_4$. *Chem. Mater.* **18**(1), 221–228 (2006).
18. Solé, R. M. *et al.* Growth, anisotropic spectroscopy and lasing of the monoclinic Nd:$KGd(PO_3)_4$ crystal. *J. Phys. D Appl. Phys.* **48**, 495502–495512 (2015).
19. Nikl, M. Scintillation detectors for x-rays. *Meas. Sci. Technol.* **17**, R37–R54 (2006).
20. van Loef, E. V. D., Dorenbos, P., van Eijk, C. W. E., Kramer, K. W. & Gudel, H. U. Scintillation properties of K_2LaX_5:Ce^{3+} (X = Cl, Br, I). *Nucl. Instrum. Methods Phys. Res. A* **537**, 232–236 (2005).
21. Stand, L., Zhuravleva, M., Lindsey, A. & Melcher, C. L. Growth and characterization of potassium strontium iodide: A new high light yield scintillator with 2.4% energy resolution. *Nucl. Instrum. Methods Phys Res. A* **780**, 40–44 (2015).
22. Parreu, I. *et al.* Crystal growth, structural characterization, and linear thermal evolution of $KGd(PO_3)_4$. *Chem. Mater.* **17**(4), 822–828 (2005).
23. Rzaigui, M., Dabbabi, M. & Kbir-Ariguib, N. Etude des équilibres solide — Liquide du système pseudo binaire KPO_3 — CeP_3O_9. *J. Chim. Phys.* **78**(6), 563–566 (1981).
24. Parreu, I. *et al.* Growth, spectroscopy and laser operation of Yb:$KGd(PO_3)_4$ single crystals. *Opt. Express* **15**(5), 2360–2368 (2007).
25. Solé, R. *et al.* Physical properties of self-flux and WO_3-containing solutions useful for growing type III $KGd(PO_3)_4$ single crystals. *J. Cryst. Growth* **311**, 3656–3660 (2009).
26. Shannon, R. D. Revised effective ionic radii and systematic studies of interatomic distances in halides and chalcogenides. *Acta Cryst.* **A32**, 751–767 (1976).
27. Dorenbos, P. The 5d level positions of the trivalent lanthanides in inorganic compounds. *J. Lumin.* **91**, 155–176 (2000).
28. Dorenbos, P. 5*d*-level energies of Ce^{3+} and the crystalline environment. III. Oxides containing ionic complexes. *Phys. Rev. B* **64**, 125117 (2001).
29. Dorenbos, P. 5*d*-level energies of Ce^{3+} and the crystalline environment. I. Fluoride compounds. *Phys. Rev. B* **62**, 15640 (2000).
30. Srivastava, A. M., Sobieraj, M. T., Valossis, A., Ruan, S. K. & Banks, E. Luminescence and energy transfer phenomena in Ce^{3+}, Tb^{3+} doped $K_3La(PO_4)_2$. *J. Electrochem. Soc.* **137**, 2959–2962 (1990).
31. Dorenbos, P. The $4f^n \leftrightarrow 4f^{n-1}$ 5*d* transitions of the trivalent lanthanides in halogenises and chalcogenides. *J. Lumin.* **91**, 91–106 (2000).
32. Dorenbos, P., Shalapska, T., Stryganyuk, G., Gektin, A. & Voloshinovskii, A. Spectroscopy and energy level location of the trivalent lanthanides in $LiYP_4O_{12}$. *J. Lumin.* **131**(4), 633–639 (2011).
33. Tian, Z. *et al.* Photon cascade emission of Gd^{3+} in Na(Y,Gd)FPO_4. *J. Phys. Chem. C* **112**(32), 12524–12529 (2008).
34. Feofilov, S. P. *et al.* Host sensitization of Gd^{3+} ions in yttrium and scandium borates and phosphates: Application to quantum cutting. *Phys. Rev. B* **74**, 085101 (2006).
35. Yang, Z., Lin, J. H., Su, M. Z., Tao, Y. & Wang, W. Photon cascade luminescence of Gd^{3+} in $GdBaB_9O_{16}$. *J. Alloys Compd.* **308**, 94–97 (2000).
36. Wegh, R. T., Donker, H., Meijerink, A., Lamminmäki, R. J. & Hölsä, J. Vacuum-ultraviolet spectroscopy and quantum cutting for Gd^{3+} in $LiYF_4$. *Phys. Rev. B* **56**, 13841–13848 (1997).

37. Zhong, J. *et al.* Radioluminescence properties of Ce^{3+}-activated $MGd(PO_3)_4$ (M = Li, Na, K, Cs). *Opt. Mater.* **32**, 378–381 (2009).
38. Shalapska, T. *et al.* Crystal structure and luminescence properties of $LiYP_4O_{12}:Ce^{3+}$ phosphor. *J. Phys. Condens. Matter* **22**, 485503 (2010).
39. Qin, X., Liu, X., Huang, W., Bettinelli, M. & Liu, X. Lanthanide-activated phosphors based on 4f-5d optical transitions: theoretical and experimental aspects. *Chem. Rev.* **117**(5), 4488–4527 (2017).
40. Blasse, G., van Vliet, J. P. M., Verwey, J. W. M., Hoogendam, R. & Wiegel, M. Luminescence of Pr^{3+} in scandium borate ($ScBO_3$) and the host lattice dependence of the Stokes shift. *J. Phys. Chem. Solids* **50**(6), 583–585 (1989).
41. Ueda, J., Meijerink, A., Dorenbos, P., Bos, A. J. J. & Tanabe, S. Thermal ionization and thermally activated crossover quenching processes for 5*d*-4*f* luminescence in $Y_3Al_{5-x}Ga_xO_{12}:Pr^{3+}$. *Phys. Rev. B* **95**, 014303 (2017).
42. Dorenbos, P. The Eu^{3+} charge transfer energy and the relation with the band gap of compounds. *J. Lumin.* **111**, 89–104 (2005).
43. Ding, D. *et al.* Effects of anisotropy on structural and optical characteristics of LYSO:Ce crystal. *Phys. Status Solidi B* **251**, 1202–41211 (2014).
44. Zhong, J. *et al.* Luminescence properties of $NaGd(PO_3)_4:Eu^{3+}$ and energy transfer from Gd^{3+} to Eu^{3+}. *Appl. Phys. B* **98**, 139–147 (2010).
45. Parreu, I., Solé, R., Massons, J., Díaz, F. & Aguiló, M. Crystal growth and characterization of type III Ytterbium-doped $KGd(PO_3)_4$: A new nonlinear laser host. *Chem. Mater.* **19**, 2868–2876 (2007).
46. XRD software –diffract suit TOPAS V4.X. Brukker.

Acknowledgements
The authors acknowledge the financial support from Spanish Government under Project Spanish Government MAT2016-75716-C2-1-R (AEI/FEDER,UE) and TEC 2014-55948-R, and from Catalan Government under Project 2017 SGR 755. I. Adell thanks the Catalan Government for the financial support under grants 2015 FI_B 00711, 2016 FI_B1 00113 and 2017 FI_B2 00017 as well. We are grateful to Nelson de Oliveira for assistance and to the SOLEIL staff for smoothly running the facility under the projects with proposal numbers 20151215 (Standard) and 20161324 (Standard).

Author Contributions
I.A., R.M.S., M.C.P. and F.D. designed the study; I.A. and R.M.S. performed the crystal growth; I.A. measured the optical absorption; I.A., R.M.S., M.C.P. M.L., M.A. and F.D. conducted the proposals 20151215 and 20161324 at SOLEIL Synchrotron; N.O. conducted the proposal 20161324 at SOLEIL Synchrotron; I.A., R.M.S. and M.C.P. wrote the manuscript. All authors discussed results and reviewed the manuscript.

Additional Information
Competing Interests: The authors declare no competing interests.

Publisher's note: Springer Nature remains neutral with regard to jurisdictional claims in published maps and institutional affiliations.

UNIVERSITAT ROVIRA I VIRGILI
CE OR PR-DOPED TYPE III KGD(PO3)4 CRYSTALLINE MATERIALS. GROWTH AND CHARACTERIZATION AS SCINTILLATORS
Irina Adell Barbarà

Paper II

Single crystal growth, optical absorption and luminescence properties under VUV-UV synchrotron excitation of type III Pr^{3+}:$KGd(PO_3)_4$

I. Adell, M. C. Pujol, R. M. Solé, M. Lancry, N. Ollier, M. Aguiló and F. Díaz

submitted to Scientific Reports

UNIVERSITAT ROVIRA I VIRGILI
CE OR PR-DOPED TYPE III KGD(PO3)4 CRYSTALLINE MATERIALS. GROWTH AND CHARACTERIZATION AS SCINTILLATORS
Irina Adell Barbarà

Single crystal growth, optical absorption and luminescence properties under VUV-UV synchrotron excitation of type III Pr^{3+}:$KGd(PO_3)_4$

Irina Adell[1], Maria Cinta Pujol[1,*], Rosa Maria Solé[1,*], Matthieu Lancry[2], Nadège Ollier[3], Magdalena Aguiló[1] and Francesc Díaz[1]

[1] Universitat Rovira i Virgili, Departament Química Física i Inorgànica, Física i Cristal·lografia de Materials i Nanomaterials (FiCMA-FiCNA)-EMaS, Campus Sescelades, E-43007 Tarragona, Spain.

[2] Institut de Chimie Moléculaire et des Matériaux d'Orsay, CNRS-Université Paris Sud, Université de Paris Saclay, Bât.410, 91405 Orsay, France.

[3] Laboratoire des Solides Irradiés, CEA-CNRS-Ecole Polytechnique, Université Paris-Saclay, Palaiseau, France.

* mariacinta.pujol@urv.cat; rosam.sole@urv.cat

Scintillator materials are widely used for a variety of applications such as high energy physics, astrophysics and medical imaging. Since the ideal scintillator does not exist, the search for scintillators with suitable properties for each application is of great interest. Here, Pr^{3+}-doped $KGd(PO_3)_4$ bulk single crystals with monoclinic structure (space group: $P2_1$) are grown from high temperature solutions and their structural, thermal and optical properties are studied as possible candidates for scintillation material. The change in the unit cell parameters as a function of the Pr^{3+} level of doping and temperature is studied. Differential thermal analysis reveals that $KGd_{0.942}Pr_{0.058}(PO_3)_4$ is stable until 1140 K. The $5d_3$, $5d_2$ and $5d_1$ levels of Pr^{3+} with respect to the $^3H_4$ ground state are centred at 166, 196 and 218 nm, respectively, in this host. The luminescence of $KGd_{0.990}Pr_{0.010}(PO_3)_4$, by exciting these $5d$ levels, shows intense emissions centred at 256 and 265 nm from the $5d_1$ to $^3F_{3,4}$ and $^1G_4$ levels of Pr^{3+} with a short decay time of 6 ns. The $^6P_{3/2,5/2,7/2} \rightarrow {}^8S_{7/2}$ transitions of Gd^{3+} appear after exciting the $5d$ levels of Pr^{3+} and the $4f$ levels of Gd^{3+}, showing an energy transfer between Pr^{3+} and Gd^{3+}.

Introduction

Inorganic scintillation materials are widely used in a variety of applications in the field of particles and ionizing radiation detection such us medical imaging, dosimetry, nuclear physics and astrophysics[1]. Current research is focused on the search for new materials with improved scintillation properties[2].

Ray imaging techniques for medical imaging include planar X-ray photography, computed tomography (CT) and positron emission tomography (PET). In the first of these, the number of UV-vis photons emitted by the scintillator material per energy unit of the incoming X-ray photons (light yield) should be high in order to decrease the X-ray dose to the patient. In CT, the stability of the light output should be as high as possible to achieve reliable images and therefore better diagnostics. In PET, a fast decay time of the UV-vis photons emitted by the scintillator is required for any improvement in spatial resolution and sensitivity, since this technique is based on a precise temporal measurement of two simultaneously emitted gamma photons at nearly 180º during a positron-electron annihilation process[3,4].

Ce^{3+} and Pr^{3+} have been used as doping ions in the vast majority of the new single crystal scintillators reported over the last approximately 20 years because of the fast decay time of the $5d \rightarrow 4f$ radiative transitions (usually from 10 to 60 ns), together with the high quantum efficiency of these transitions at room temperature[2]. The scintillation properties of Ce^{3+}- and Pr^{3+}-doped garnets have been optimized by the growth

of multicomponent doped hosts like $(Gd,Lu)_3Ga_3Al_2O_{12}$ [5,6,7,8]. As regards aluminium perovskite crystals, fast lifetimes corresponding to the $5d \rightarrow 4f$ transitions of Ce^{3+} and Pr^{3+} ions doped in $YAlO_3$ host have been obtained at around 18 and 8 ns, respectively[2]. Oxyorthosilicates have also been investigated because they have good scintillation properties, especially $(Lu/Y)_2SiO_5$ (LYSO) doped with Ce^{3+}, which is used in PET imaging[2]. The Ce^{3+}-doped LYSO compound was introduced in 2000 with the composition $Ce:Lu_{1.8}Y_{0.2}SiO_5$ by Cooke *et al.*[9]. Lu_2SiO_5 (LSO) doped with Pr^{3+} has also been studied and the photoluminescence of the $5d \rightarrow 4f$ electronic transition at 273 nm shows a fast decay time of 6-7 ns. However, since the $5d_1$ level of Pr^{3+} in LSO is close to the conduction band, there is a degradation of the light yield of this scintillator at room temperature[10].

In polyphosphate compounds, the photoluminescence of rare earth ions in $LiLaP_4O_{12}$ was studied by Blasse and Dirken[11], with a Ce^{3+} concentration quenching being observed. The luminescence of $LiY_{0.9}Ce_{0.1}P_4O_{12}$ as a function of temperature was reported by Shalapska *et al.*[12] with a decay time for the Ce^{3+} $5d_1 \rightarrow 4f$ transition of 18.6 ns at room temperature. In the research carried out by Zhong *et al.* into Ce^{3+}-doped $MGdP_4O_{12}$ (M=Li, Na, K, Cs)[13], the energy transfer between Gd^{3+} and Ce^{3+} ions and its luminescence was studied and the energy level diagrams of the Gd^{3+} and Ce^{3+} in these compounds were put forward. Ce^{3+}- and Pr^{3+}-doped $NaLa(PO_3)_4$ were studied under VUV-UV excitation by Kang *et al.*[14], showing decay times for the $5d \rightarrow 4f$ transitions of Ce^{3+} of 22.7-23.8 ns and of Pr^{3+} of 9.9-12.9 ns.

Type III $KGd(PO_3)_4$ is a monoclinic crystal with a non-centrosymmetric crystalline structure (space group: $P2_1$) that has nonlinear optical properties similar to KH_2PO_4 (KDP)[15] and a deep UV cut-off of its transparency window at 160 nm[16]. It is non-hygroscopic and chemically stable and its high hardness (close to quartz in the Mohs scale) means the surfaces can be polished to a good optical quality[17]. Considering the literature mentioned above, the $5d \rightarrow 4f$ transitions of Pr^{3+} in $KGd(PO_3)_4$ host is expected to have decay times faster than Ce^{3+} in the same host. Ce^{3+}-doped $KGd(PO_3)_4$ single crystals have already been studied and show interesting luminescence characteristics for scintillator applications[18]. The aim of this paper is therefore to grow $Pr:KGd(PO_3)_4$ single crystals from high temperature solutions with different Pr^{3+} concentrations in order to characterize their thermal stability, study their optical absorption and luminescence properties under UV-VUV synchrotron excitation, and discuss their usefulness as a new scintillator material. However, it should first be mentioned that, a priori, the functionality of $Pr:KGd(PO_3)_4$ single crystals for some scintillator applications could be limited due to the 0.0117% natural abundance of the ^{40}K radioisotope, which means an increase in the background counts is expected. Nevertheless, the ^{40}K radioactive isotope together with others such as ^{176}Lu, ^{87}Rb, and ^{138}La is present in some scintillator materials that are promising or already in use[19].

Results and discussion

Bulk single crystal growth. Table 1 shows the crystal growth experiments carried out for different levels of Pr^{3+} doping and the crystals obtained.

The saturation temperature of all solutions was around 993 K and no significant changes were observed with Pr^{3+} doping at the levels studied in this work. The saturation temperature is slightly higher than that previously reported for the crystal growth of $Ce:KGd(PO_3)_4$ crystals[18] grown in similar experimental conditions. The crystals obtained were generally transparent, free of inclusions and cracks, and slightly greenish due to Pr^{3+} doping. The sizes obtained were $a^* \times b \times c^* = 7.6\text{-}13.6$ mm × 17.1-24.1 mm × 10.7-13.6 mm and the weights ranged from 2.7 to 6.9 g. As can be seen in Table 1, the crystal dimension in b direction was always higher than in a^* and c^* directions. This faster growth in the b crystallographic direction has already been reported by us for different doping $KGd(PO_3)_4$ crystals[16,17,18] and is in agreement with the non-presence of the (010) crystalline face. The growth rate of the {hkl} form is inversely proportional to interplanar spacing d_{hkl} and the sequence in this crystal is $d_{001} > d_{100} > d_{020}$. The chosen orientation of the seed also reinforces this behaviour, together with the thermal gradients in the solution. The crystal growth rate varies from 6.1 × 10^{-3} to 17.4 × 10^{-3} g·h^{-1}.

As an example, Figure 1 shows an as-grown Pr:$KGd(PO_3)_4$ single crystal and a scheme of the crystal morphology in which the main faces of the crystal can be observed. These are generally {001}, {100}, {011}, {0-11}, {110}, {1-10}, {10-1}, {101} and {-1-11}.

Using the atomic percentage of each element present in the chemical compound as obtained from the EPMA (electron probe microanalysis) results, the chemical formula of each crystal was determined and the distribution coefficient of Pr^{3+} in $KGd(PO_3)_4$ calculated according to the formula $K_{Pr}=([Pr]/([Pr]+[Gd]))_{crystal}/([Pr]/([Pr]+[Gd]))_{solution}$, where [Pr] and [Gd] are the Pr^{3+} and Gd^{3+} concentrations, respectively, in atomic % in the crystal and the solution. Table 2 shows, for the five doping levels studied, the Pr^{3+} atomic ratio with respect to Gd^{3+} in the crystal, the chemical formula, the number of Pr^{3+} ions per unit cell volume in the crystal and the distribution coefficient of Pr^{3+} (K_{Pr}). For the crystals obtained from solutions with 2.00 and 5.00 atomic % of Pr^{3+} in the solution, the atomic percentage of each element was measured at several points along the *a** and *c* crystallographic directions in a plate perpendicular to *b* crystallographic axis, obtaining up to about 85 results per sample. These results (see Figure S.1 in Supporting Information) showed that the variation of the measured values of Pr^{3+} atomic concentration along the crystallographic directions is of the same order as the error in the measurements. Therefore, the results indicate the uniformity of Pr^{3+} atomic concentration of the growing crystals along the *a** and *c* crystallographic directions, up to 5.8 atomic % of Pr^{3+} in the crystal. In the samples obtained from solutions with 0.25, 0.50 and 1.00 atomic % of Pr^{3+} in the solution, the EPMA measurements were carried out far from the undoped $KGd(PO_3)_4$ seed, i.e. in the last stages of the crystal growth. Taking into account the values of the Pr^{3+} distribution coefficient in $KGd(PO_3)_4$ and their error, it can be observed that the Pr^{3+} distribution coefficient is not far from the unit in any of the concentrations studied. Besides, the results do not show any significant tendency for its value (K_{Pr}) to decrease or increase as the level of Pr^{3+} doping in the solution increases.

Structural characterization. X-ray powder diffraction analysis was carried out to study the evolution of the unit cell parameters of $KGd_{1-x}Pr_x(PO_3)_4$ depending on the Pr^{3+} doping concentration. The refinement of the unit cell parameters was carried out using the TOPAS program[20]. Table 3 shows the unit cell parameters of the crystals studied, while Figure 2 shows the evolution of these parameters as a function of the praseodymium content in $KGd(PO_3)_4$. It can be seen that there is an ascending linear behaviour of the unit cell parameters on increasing the Pr^{3+} content in the crystals.

As Table 3 and Figure 2 show, the *a* and β parameters remain practically the same, the *b* and *c* parameters increase slightly and the unit cell volume clearly increases when the Pr^{3+} concentration in the crystal increases. This behaviour is expected because the ionic radius of Pr^{3+} with coordination VIII is higher than the ionic radius of Gd^{3+} with the same coordination (1.126 Å and 1.053 Å, respectively[21]).

Thermal stability. Figure 3 shows the thermogram obtained for $KGd_{0.942}Pr_{0.058}(PO_3)_4$ in both the heating and cooling processes in the range 500-1273 K. The weight change during the experiment was not significant.

An endothermic peak beginning at 1140 K can be observed in the heating process, which is attributed to the incongruent melting process of $KGd_{0.942}Pr_{0.058}(PO_3)_4$. This temperature is so similar to the 1142 K obtained for undoped $KGd(PO_3)_4$ [22] that it can be said that there is no appreciable difference in the incongruent melting temperature of $KGd(PO_3)_4$ with the Pr^{3+} doping, at least up to 5.8 atomic % of Pr^{3+} in the crystal. Meanwhile, no heat exchange in the cooling process of the sample was observed, which means that no crystalline phase transitions were produced during the process.

Figure 4 shows the X-ray powder diffractogram of $KGd_{0.942}Pr_{0.058}(PO_3)_4$ at room temperature, its evolution with the temperature up to 1273 K and the cooling process up to room temperature. The temperatures written to the right of the graph are used as labels, since it is expected that the temperature distribution in the sample support during these measurements was not homogeneous.

This could lead to a partial incongruent melting when the thermocouple of the diffractometer chamber indicated 1093 K.

The diffraction standard patterns of $KTb(PO_3)_4$ (89-1424 ICDD database[23]) and $GdPO_4$ (83-0657 ICDD database[24]), together with a Pt diffraction peak (the sample holder was of Pt), are also shown in Figure 4. The diffraction standard pattern of type III $KTb(PO_3)_4$ (space group: $P2_1$) was used due to the non-existence of the type III $KGd(PO_3)_4$ powder diffraction standard pattern in the version of the ICDD database used. Hence at room temperature all diffraction peaks correspond to the monoclinic crystalline phase of type III $KGd(PO_3)_4$ together with a diffraction peak belonging to the Pt crystalline phase of the sample holder. Till 1078 K, there are no extra peaks of any other crystalline phase, and the diffraction peaks belonging to $KGd(PO_3)_4$ present a decrease in their sharpness and intensity, related to the loss of crystallinity. At 1093 K a small peak appeared at 29.2° and was identified as $GdPO_4$. At 1108 K, the two crystalline phases ($KGd(PO_3)_4$ and $GdPO_4$) are coexistent, and at 1123 K the $KGd(PO_3)_4$ crystalline phase has totally decomposed. In Ponceblanc *et al.*[25], differences in the phase transition temperature of the same compound were also observed depending on both the heating rates and technique used. From 1093 to 1108 K, as the intensity of the type III $KGd(PO_3)_4$ peaks decreased, the intensity of the $GdPO_4$ peaks increased. From 1123 K to 1273 K only the diffraction peaks of $GdPO_4$ can be observed, meaning that this crystalline compound is stable at this range of temperatures. Throughout the cooling process from 1273 K until room temperature (see the last four diffractograms) there are no significant changes, so the $GdPO_4$ remains stable. This means that the phase transition is not reversible, as expected for an incongruent melting, and in our case the solidification of the liquid phase leads to an amorphous phase.

Therefore, according to the differential thermal analysis and X-ray powder diffraction results, $KGd_{0.942}Pr_{0.058}(PO_3)_4$ decomposes at 1140 K into $GdPO_4$ and liquid phase, which probably consisted of a mixture of phosphorus and potassium oxides, since the sample weight remained practically constant.

The studies on $KGd(PO_3)_4$ [22] and $KYb_{0.029}Gd_{0.971}(PO_3)_4$ [17] are comparable to that presented in our work. The results for the first compound show that $KGd(PO_3)_4$ decomposes irreversibly at 1142 K into $Gd(PO_3)_3$, $GdPO_4$, $Gd_2P_4O_{13}$ and an amorphous phase, and that at room temperature after the cooling process only $GdPO_4$ remains. Regarding the second case, $KYb_{0.029}Gd_{0.971}(PO_3)_4$ decomposes irreversibly at 1130 K into $Gd(PO_3)_3$, at 1223 K $Gd(PO_3)_3$, $GdPO_4$, $Gd_2P_4O_{13}$, GdP_5O_{14} and an amorphous phase coexist, and at room temperature after the cooling process the $GdPO_4$ and $Gd_2P_4O_{13}$ crystalline phases remain. Thus the difference in the thermal evolution observed for the $KGd_{0.942}Pr_{0.058}(PO_3)_4$ is that this crystal is decomposed into a unique crystalline compound, $GdPO_4$, and a liquid phase. The intermediate $Gd(PO_3)_3$ crystalline compound observed in the previous studies is not observed in our case, and neither are the crystalline phases $Gd_2P_4O_{13}$ and GdP_5O_{14} from the previous works present in our case. Only the $GdPO_4$ crystalline phase is observed to be stable till room temperature in all three studies[17,22].

Another compound whose thermal decomposition has been studied in the literature is $KLa(PO_3)_4$ [26], which decomposes into $La(PO_3)_3$, $LaPO_4$ and an amorphous phase containing phosphorus and potassium oxides. Thus, the thermal decomposition products of $KLa(PO_3)_4$ correlate with those of $KGd(PO_3)_4$ except for the fact that $La_2P_4O_{13}$ is not present.

Linear thermal expansion tensor. Bearing in mind the X-ray powder diffractograms measured in the range from room temperature up to 773 K and using the Le Bail method[27], the unit cell parameters at different temperatures in the $P2_1$ space group were refined. The parameters relating to goodness of fit are R_{wp} and R_{exp}, whose values must fulfil the expression $R_{wp} \leq 2 \cdot R_{exp}$ for it to be considered that a good fit is obtained. In all cases these parameters are around R_{wp}=21.06 and R_{exp}=18.08. Table 4 shows the unit cell parameters of $KGd_{0.942}Pr_{0.058}(PO_3)_4$ at different temperatures, while Figure 5 shows the relative thermal evolution of these parameters with respect to those at room temperature as a function of temperature. It can be seen that the unit cell parameters follow a linear trend. The *a* and *b* parameters clearly increase with temperature, as does

the *c* parameter but in minor proportion, while the β parameter decreases slightly. From these results, the linear thermal expansion coefficients in each crystallographic direction can be calculated using the expression $\alpha=(\Delta L/\Delta T)/L_{RT}$, where $\Delta L/\Delta T$ is the slope of the linear fit of the change of each unit cell parameter with the temperature, and L_{RT} is the unit cell parameter at room temperature, 303 K. The linear thermal expansion coefficients in the crystallophysical system $X_1 \| a$, $X_2 \| b$ and $X_3 \| c^*$ are α_{11}=12.00 × 10^{-6} K^{-1}, α_{22}=12.40 × 10^{-6} K^{-1}, α_{33}=7.46 × 10^{-6} K^{-1} and α_{13}=1.45 × 10^{-6} K^{-1}.

By diagonalizing the tensor, the thermal expansion values in the principal axes of the tensor X_1', $X_2' \| b$ and X_3' are obtained, these being α'_{11}=12.43 × 10^{-6} K^{-1}, α'_{22}=12.40 × 10^{-6} K^{-1} and α'_{33}=7.03 × 10^{-6} K^{-1}. The X_1' axis is at 16.31º clockwise from the *a* axis, while X_3' is at 14.44º from the *c* axis with the positive *b* axis pointing toward the observer (see Figure 6).

Pr^{3+} spectroscopy in $KGd(PO_3)_4$ single crystals. *Optical absorption.* To identify the Pr^{3+} absorption bands and distinguish them from the Gd^{3+} bands in Pr:$KGd(PO_3)_4$, the optical absorption of an undoped sample of $KGd(PO_3)_4$ was measured (see Figure S.2 in Supporting Information). Figure 7 shows the unpolarized optical absorption cross sections of the $^3H_4 \rightarrow 5d_1$ electronic transition and the $4f \rightarrow 4f$ electronic transitions of Pr^{3+} ions in $KGd(PO_3)_4$ in the range 205 to 2475 nm at room temperature.

In Figure 7.a, a broad band centred at 218 nm (45872 cm^{-1}, 5.69 eV) is observed, which corresponds to the electronic transition from the $^3H_4$ ground state of Pr^{3+} to its lowest 5*d* level ($5d_1$) in $KGd(PO_3)_4$. From the crystallographic point of view, there is only one site expected, with C_1 point symmetry, for the Pr^{3+} and Gd^{3+} ions in the $KGd(PO_3)_4$ crystal[28]. Therefore all Pr^{3+} ions have the same crystal field, and consequently only one band for the $^3H_4 \rightarrow 5d_1$ transition is expected. This transition of Pr^{3+} has been systematically studied in many hosts and it can be predicted by considering the study carried out by Dorenbos [29]. In this work, the value of the $^3H_4 \rightarrow 5d_1$ transition of Pr^{3+} in phosphate hosts varies from 212 nm for LaP_3O_9 [29], through 222 nm for YPO_4 [29,30], to 224 nm for YP_3O_9 [29]. In addition, since the average energy difference of the first spin-allowed $4f \rightarrow 5d$ transition of Pr^{3+} ($^3H_4 \rightarrow 5d_1$) with respect to the transition of Ce^{3+} ($^2F_{5/2} \rightarrow 5d_1$) in the same host[Error! Marcador no definido.] is 12240 ± 750 cm^{-1} and because the $^2F_{5/2} \rightarrow 5d_1$ transition of Ce^{3+} in $KGd(PO_3)_4$ is centred at 302.5 nm (33058 cm^{-1}, 4.10 eV)[18], the expected position of the $^3H_4 \rightarrow 5d_1$ transition of Pr^{3+} in $KGd(PO_3)_4$ is in the range 217.2-224.5 nm (46048-44548 cm^{-1}, 5.71-5.52 eV). Therefore the experimental position of the $^3H_4 \rightarrow 5d_1$ transition of Pr^{3+} in $KGd(PO_3)_4$ (218 nm) is consistent with the values found in other phosphates and within the calculated range.

The value of the optical absorption cross section of Pr^{3+} in $KGd(PO_3)_4$ for the $^3H_4 \rightarrow 5d_1$ transition (at 218 nm) is about 780 × 10^{-20} cm^2. This high value is expected since $4f \rightarrow 5d$ transitions are parity-allowed transitions.

It should be noted that, of the optical absorption measurements, only the $5d_1$ absorption band was identified out of all the $5d_x$ levels of Pr^{3+} in $KGd(PO_3)_4$. The reason for this is that, although the UV limit of the equipment used is 175 nm, the measurements were carried out in air atmosphere, and below 190 nm the air absorption hid the other $5d_x$ levels. The $5d_2$ and $5d_3$ energy levels, together with the $5d_1$ energy level already determined, of Pr^{3+} in $KGd(PO_3)_4$ were quantified in the UV-VUV synchrotron measurements (see next section) by studying the excitation spectra for several emission wavelengths.

Figures 7.b-f show the optical absorption cross section of the Pr^{3+} $4f \rightarrow 4f$ transitions in $KGd(PO_3)_4$ in the energy ranges 430-490, 570-620, 925-1125, 1375-1720 and 1850-2475 nm, in which the $^3H_4 \rightarrow {}^1I_6 + {}^3P_J$, $^3H_4 \rightarrow {}^1D_2$, $^3H_4 \rightarrow {}^1G_4$, $^3H_4 \rightarrow {}^3F_4 + {}^3F_3$ and $^3H_4 \rightarrow {}^3F_2 + {}^3H_6$ electronic transitions of Pr^{3+}, respectively, were observed. Although the $^3H_4 \rightarrow {}^3P_2$ pseudo-hypersensitive transition does not have the highest optical absorption cross section, its value of 4.4 × 10^{-20} cm^2 is in the suitable range to be used for exciting $4f \rightarrow 4f$ transitions for optical amplification applications.

Optical emission. Figure 8 shows the emission spectra of Pr:$KGd(PO_3)_4$ under λ_{exc}=218 nm (45872 cm^{-1}, 5.69 eV), 196 nm (51020 cm^{-1}, 6.33 eV) and 166 nm (60241 cm^{-1}, 7.47 eV) at room temperature.

In Figure 8.a, the most intense emissions centred at 305, 312 and 323 nm correspond to the $^6P_{3/2} \rightarrow {}^8S_{7/2}$, $^6P_{5/2} \rightarrow {}^8S_{7/2}$ and $^6P_{7/2} \rightarrow {}^8S_{7/2}$ transitions of Gd^{3+}, respectively, obtained by exciting the $5d_1$ level of Pr^{3+} in

$KGd(PO_3)_4$. This means that an energy transfer (ET) between Pr^{3+} and Gd^{3+} occurs. In other hosts such as $(Gd,Lu)_3Ga_3Al_2O_{12}$:Pr, energy transfers from 5*d* levels of Pr^{3+} to 4*f* levels of Gd^{3+} were also observed[5].

Also in Figure 8.a, parity-allowed transitions from the *d* to *f* levels of Pr^{3+}, which are of great interest for scintillation applications, are also observed. These broad, intense bands correspond to the $5d_1 \rightarrow {}^3H_5$, $5d_1 \rightarrow {}^3H_6$, $5d_1 \rightarrow {}^3F_{3,4}$ and $5d_1 \rightarrow {}^1G_4$ electronic transitions of Pr^{3+}, centred at 229, 239, 256 and 265 nm, respectively. The emission band corresponding to the electronic transition from the $5d_1$ level to the ${}^3H_4$ ground state of Pr^{3+} does not appear, probably due to the self-absorption effect, as occurs in $AREP_2O_7$ hosts (A = Na, K, Rb, Cs; RE = Y, Lu)[31]. We should also note that the significantly weaker broad bands centred at 358 and 435 nm correspond to the $5d_1 \rightarrow {}^1D_2$ and $5d_1 \rightarrow {}^3P_2$ transitions. The most intense band originating in a 5*d* level is the broad band located around 256-265 nm, which corresponds to the overlapping of three electronic transitions, $5d_1 \rightarrow {}^3F_{3,4}$ and $5d_1 \rightarrow {}^1G_4$. By exciting the $5d_1$ level of Pr^{3+} at 210 nm in $LiYF_4$ at 10 K, it can be observed how $5d_1 \rightarrow {}^3H_4$, $5d_1 \rightarrow {}^3H_5$, $5d_1 \rightarrow {}^3H_6$, $5d_1 \rightarrow {}^3F_{3,4}$ and $5d_1 \rightarrow {}^1G_4$ transitions appear at 220, 230, 245, 255 and 272 nm, respectively, while $5d_1 \rightarrow {}^1D_2$ and $5d_1 \rightarrow {}^3P_2$ transitions do not appear. It should also be noted that the band that corresponds to the $5d_1 \rightarrow {}^3H_5$ transition is the most intense, while that corresponding to the $5d_1 \rightarrow {}^1G_4$ transition is the least[32]. Under direct $4f \rightarrow 5d_1$ excitation (280 nm) of Pr^{3+} in $Lu_3Al_5O_{12}$, $Lu_3Al_4GaO_{12}$ and $Lu_3Al_3Ga_2O_{12}$ hosts, the emission bands corresponding to the $5d_1 \rightarrow {}^3H_J$ and $5d_1 \rightarrow {}^3F_J$ electronic transitions appear centred at 310 and 360 nm, respectively, with the first band being the most intense. The bands corresponding to the $5d_1 \rightarrow {}^1G_4$, $5d_1 \rightarrow {}^1D_2$ and $5d_1 \rightarrow {}^3P_J$ transitions do not appear. The emission peaks corresponding to some of the $4f \rightarrow 4f$ electronic transitions of Pr^{3+} are insinuated in the visible range from 480 to 760 nm[33]. The emission spectrum of $La_{0.999}Pr_{0.001}PO_4$ at 300 K under the direct $4f \rightarrow 5d_1$ excitation (193 nm) of Pr^{3+} shows intense emission bands centred at about 230, 240 and 255 nm corresponding to the $5d_1 \rightarrow {}^3H_4$, $5d_1 \rightarrow {}^3H_5$ and $5d_1 \rightarrow {}^3H_6$, ${}^3F_2$ electronic transitions, respectively. Two very weak, broad emission bands appear centred around 375 and 440 nm corresponding to the $5d_1 \rightarrow {}^1D_2$ and $5d_1 \rightarrow {}^1I_6, {}^3P_J$ transitions. It should be noted that an emission peak centred at approximately 610 nm, with an intensity similar to the two previous bands, corresponds to the ${}^1D_2 \rightarrow {}^3H_4$ electronic transition. The most intense emission bands correspond to the $5d_1 \rightarrow {}^3H_4$ and $5d_1 \rightarrow {}^3H_5$ transitions, and the least intense to the $5d_1 \rightarrow {}^1D_2$ transition[34].

The weaker bands observed in the visible region of Figure 8.a are $4f \rightarrow 4f$ transitions corresponding to Gd^{3+}, which belong to the ${}^6G_{7/2} \rightarrow {}^6P_{7/2}$, ${}^6G_{11/2,9/2,5/2} \rightarrow {}^6P_{3/2}$, ${}^6G_{13/2} \rightarrow {}^6I_{7/2}$ and ${}^6G_{3/2} \rightarrow {}^6I_{7/2}$ transitions.

Information on the energy value of the $5d_2$ and $5d_3$ levels of Pr^{3+} in this host was obtained by studying the excitation spectra of Pr:$KGd(PO_3)_4$ for different emission wavelengths (see below in Figure 10). In Figure 8.b, it can be seen that the emission spectrum of Pr:$KGd(PO_3)_4$ under λ_{exc}=196 nm ($5d_2$ level of Pr^{3+} and ${}^6G_{13/2}$ level of Gd^{3+} excitation) is very similar to that obtained by exciting the $5d_1$ level as regards the intensity ratio of the emission bands in the range from 200 to 500 nm. The main difference obtained by exciting at 196 nm is in the 500-825 nm visible range, where the ${}^6G_{7/2} \rightarrow {}^6P_{7/2}$, ${}^6G_{11/2,9/2,5/2} \rightarrow {}^6P_{3/2}$, ${}^6G_{13/2} \rightarrow {}^6I_{7/2}$ and ${}^6G_{3/2} \rightarrow {}^6I_{7/2}$ transitions of Gd^{3+} are significantly intensified. Other new peaks appeared at 570-578, 632, 662, 689, 751, 759, 777 and 800 nm and correspond to the ${}^6G_{11/2,9/2,5/2} \rightarrow {}^6P_{7/2}$, ${}^6G_{7/2} \rightarrow {}^6P_{3/2}$, ${}^6G_{13/2} \rightarrow {}^6I_{9/2,17/2}$, ${}^6G_{13/2} \rightarrow {}^6I_{11/2,15/2,13/2}$, ${}^6G_{11/2,9/2,5/2} \rightarrow {}^6I_{9/2,17/2}$, ${}^6G_{7/2} \rightarrow {}^6I_{7/2}$, ${}^6G_{11/2,9/2,5/2} \rightarrow {}^6I_{11/2,15/2,13/2}$ and ${}^6G_{7/2} \rightarrow {}^6I_{9/2,17/2}$ transitions of Gd^{3+}. Under excitation at 196 nm, the visible bands corresponding to the $4f \rightarrow 4f$ electronic transitions of Gd^{3+} are more intense than the UV band corresponding to the $5d \rightarrow 4f$ electronic transitions of Pr^{3+}. This could be related to a simultaneous energy transfer process from Pr^{3+} to Gd^{3+} and also direct Gd^{3+} excitation leading to a larger electronic population in the Gd^{3+} emitting levels. As in our work, photon cascade emissions of Gd^{3+} in the UV-Visible-near IR range were observed in $GdBaB_9O_{16}$ under ${}^8S_{7/2} \rightarrow {}^6G_J$ excitation (202 nm)[35], and also under 195 nm excitation (${}^8S_{7/2} \rightarrow {}^6G_J$) in $NaY_{0.8}Gd_{0.2}FPO_4$ and $NaGdFPO_4$ [36].

Figure 8.c shows the emission spectrum of Pr:$KGd(PO_3)_4$ under λ_{exc}=166 nm ($5d_3$ level of Pr^{3+} and ${}^6H_{13/2}$ level of Gd^{3+} excitation). In this spectrum it is important to note that the main ${}^6P_{3/2,5/2,7/2} \rightarrow {}^8S_{7/2}$ electronic transitions of Gd^{3+} and the $5d_1 \rightarrow {}^3F_{3,4}$ and $5d_1 \rightarrow {}^1G_4$ emission bands of Pr^{3+} have a similar intensity. In the 500-825 nm range, the Gd^{3+} emissions located at 617 nm (${}^6G_{11/2,9/2,5/2} \rightarrow {}^6P_{3/2}$) and 700 nm (${}^6G_{3/2} \rightarrow {}^6I_{7/2}$) greatly decreased in intensity compared to the emission spectrum obtained by exciting at 196 nm and slightly decreased compared to the emission spectrum obtained by exciting at 218 nm. It should also be

noted that three new emission peaks belonging to Gd^{3+} appear. These are centred at 561 nm ($^6G_{3/2} \rightarrow {}^6P_{5/2}$), 595 nm ($^6G_{11/2,9/2,5/2} \rightarrow {}^6P_{5/2}$) and 645 nm ($^6G_{7/2}{}^* \rightarrow {}^6I_{11/2,15/2,13/2}$).

Finally, it is important to note that in Pr:$KGd(PO_3)_4$, no $4f \rightarrow 4f$ transitions of Pr^{3+} were observed under excitations in the 120-248 nm range. The assignation of the Gd^{3+} and Pr^{3+} transitions was checked by comparing the Pr:$KGd(PO_3)_4$ emission spectra with those of the undoped $KGd(PO_3)_4$ excited at λ_{exc}=218, 196 and 166 nm (see Figure S.3 in Supporting Information) and by consulting the Dieke's diagram[37], the extended Dieke's diagram[38], and the work carried out by Wegh *et al.*[39] and by Yang *et al.*[35].

Figure 9 shows the energy levels scheme for Pr^{3+} and Gd^{3+} and the electronic transitions assigned to the observed emissions by excitation at 218, 196 and 166 nm in a $KGd_{0.990}Pr_{0.010}(PO_3)_4$ single crystal.

In the excitation spectrum of Pr:$KGd(PO_3)_4$ crystal under VUV-UV radiation from 120 to 248 nm for λ_{emi}=265 nm corresponding to the $5d_1 \rightarrow {}^1G_4$ electronic transition (see Figure 10.a), the excitation of the $5d_3$, $5d_2$ and $5d_1$ levels of Pr^{3+} in $KGd(PO_3)_4$ is produced at wavelengths around 166, 196 and 218 nm, respectively. Some $4f$ levels of Gd^{3+} were also excited giving rise to this Pr^{3+} emission, which could be explained by an energy transfer from Gd^{3+} to Pr^{3+}.

As for the excitation spectrum for the Gd^{3+} emission at λ_{emi}=592 nm (see Figure 10.b), although this emission could also be observed by excitation of the $5d$ energy levels of Pr^{3+} and the consequent energy transfer to Gd^{3+}, it seems that it is more favoured when the ^6G_J levels of Gd^{3+} are excited.

Given the calculations explained in our previous work on type III Ce:$KGd(PO_3)_4$ single crystals[18], the energy of the exciton creation (E^{ex}) and the approximate energy difference from the bottom of the conduction band to the top of the valence band (E_{VC}) of the type III $KGd(PO_3)_4$ host were predicted at 7.57 eV (164 nm) and at 8.17 eV (152 nm), respectively. Therefore, as already mentioned in the previous work, the E^{ex} band could appear in the excitation spectra (Figure 10), but it would not be appreciated due to an overlapping with the $^8S_{7/2} \rightarrow {}^4F_{9/2}$ transition of Gd^{3+}.

Decay time measurements. Time profiles were recorded in two time regimes to measure the fast and slow components of the decay curves of the emission at 256 nm and 312 nm, respectively. These curves are shown in Figure 11. Pr:$KGd(PO_3)_4$ crystals were excited at 218 nm ($^3H_4 \rightarrow 5d_1$ of Pr^{3+}) and 166 nm ($^3H_4 \rightarrow 5d_3$ of Pr^{3+} and $^8S_{7/2} \rightarrow {}^6H_{13/2}$ of Gd^{3+}) under pulsed synchrotron radiation. In order to improve the photon flux reaching the sample, the excitation radiation was not exactly monochromatic but had a bandwidth of around 7 %.

As can be seen in Figure 11.a, for the fast component all the decay curves can be fitted to single exponential decays with a time constant of around 6 ns. This value can be attributed to the lifetime of the $5d_1$ level of Pr^{3+} in $KGd(PO_3)_4$, which is significantly shorter than the lifetimes obtained in Ce:$KGd(PO_3)_4$ [18]. The lifetimes obtained for the $5d_1$ emitting electronic state of Pr^{3+} in different hosts are usually longer than 6 ns, as observed in Table 5. The shortening of this lifetime in the $KGd(PO_3)_4$ host could be related to the energy transfer from Pr^{3+} to Gd^{3+}, this being an additional depopulation channel through a non-radiative decay of the $5d_1$ emitting state of praseodymium.

It can also be seen that no significant changes in lifetime with the Pr^{3+} doping content of $KGd(PO_3)_4$ came about, at least up to 5.8 atomic % Pr:$KGd(PO_3)_4$. And no important quenching of the emission is expected due to the concentration effect, so no shortening of the lifetime. This can be seen in the long lifetime of the $LiPrP_4O_{12}$ phosphate (Table 5), where Pr^{3+} is not a doping element but a host element.

As previously stated, the emission at around 312 nm observed in Figure 8 corresponds to some of the $4f \rightarrow 4f$ electronic transitions of Gd^{3+}. The decay time of these electronic transitions (lifetime could be in µs or ms) is significantly slower than those from the $5d$ energy levels and could not be measured at the DESIRS beamline (DESIRS-6.65 m Monochromator) due to the interpulse duration of 1118 ns of the synchrotron radiation. Figure 11.b shows its slow decay time. By fitting to a single exponential decay, the lifetime obtained is 9 ms. As reported previously in the literature, the origin of this slow component could be attributed to the Gd^{3+} emission corresponding to the electronic transition $^6P_J \rightarrow {}^8S_{7/2}$ along with some contribution from the trapping effect, since the lifetime of the emitting $^6P_{7/2}$ level of Gd^{3+} is of the same order (4.9 ms in $NaY_{0.80}Gd_{0.20}PO_4$ and 6.36 ms in $NaGd(PO_3)_4$)[40,41] as the 9 ms.

Conclusions

Type III Pr^{3+}-doped $KGd(PO_3)_4$ single crystals of up to 5.8 atomic % of Pr^{3+} substituting Gd^{3+} with high crystalline quality have been grown by the top seeded solution growth-slow cooling technique from self-flux solutions. It has been demonstrated that $KGd_{0.942}Pr_{0.058}(PO_3)_4$ is thermally stable up to 1140 K, where it suffers an irreversible decomposition into a unique crystalline compound, $GdPO_4$, and a liquid phase. The X_1' principal axis of the thermal tensor of this crystal is at 16.31º clockwise from the *a* crystallographic direction when the positive *b* axis (parallel to the X_2' principal axis) is pointing toward the observer and the X_3' principal axis is at 14.44º clockwise from the *c* axis. The absorption bands corresponding to the $^3H_4 \rightarrow 5d_1$, $^3H_4 \rightarrow 5d_2$ and $^3H_4 \rightarrow 5d_3$ electronic transitions of Pr^{3+} in $KGd(PO_3)_4$ are centred at 218, 196 and 166 nm, respectively. The $^1S_0$ energy level of Pr^{3+} overlaps with the $5d_1$ level of the same ion in this host, preventing the non-radiative relaxation from the $5d_1$ level to the $^1S_0$ energy level and the radiative relaxation between 4*f* levels that would deteriorate the scintillation efficiency of these crystals. Under ultraviolet excitation, an intense, broad emission band located around 256-265 nm was observed in all grown crystals, corresponding to the $5d_1 \rightarrow {}^3F_{3,4}$ and $5d_1 \rightarrow {}^1G_4$ electronic transitions of Pr^{3+}. The lifetime of the $5d_1$ level of the Pr^{3+} in type III $KGd(PO_3)_4$ was measured for the emission band centred at 256 nm and a lifetime of around 6 ns was obtained, which is of great interest for scintillator applications. In most cases this lifetime is shorter than the lifetime obtained for the same level of Pr^{3+} in other hosts. Moreover, the emission spectra show a broad band in the visible range corresponding to the $5d_1 \rightarrow {}^3P_2$ transition of Pr^{3+} with enough intensity under 218 nm excitation, which could be an appropriate transition for use in scintillator applications. It should also be noted that the $^6P_{3/2,5/2,7/2} \rightarrow {}^8S_{7/2}$ electronic transitions of Gd^{3+} were observed centred at 305, 312 and 323 nm by exciting the 5*d* levels of Pr^{3+}, although it would be interesting to study whether the same behaviour occurs under X-ray excitation.

Experimental

Single crystal growth. Type III praseodymium-doped $KGd(PO_3)_4$ single crystals, with doping levels ranging up to 5 atomic % of Pr^{3+} substituting Gd^{3+} in the solution, were grown from self-flux solutions using the top seeded solution growth-slow cooling (TSSG-SC) technique. The growth solutions, with a weight of around 130 g, were placed in a platinum cylindrical crucible 50 mm in diameter and 50 mm in height. The initial reagents used were K_2CO_3 (99%), Gd_2O_3 (99.9 %), Pr_2O_3 (99.9 %) and $NH_4H_2PO_4$ (≥99.0%). The compositions of the solutions, chosen according to the $KGd(PO_3)_4$ primary crystallization region in the K_2O – Gd_2O_3 – P_2O_5 ternary system[22], were K_2O : ((1-x) Gd_2O_3 + x Pr_2O_3) : P_2O_5 = 36 : 4 : 60, mol %, with x ranging from 0 to 0.05.

A platinum stirrer with a diameter of 18 mm, located at 12-14 mm below the solution surface and rotating at 55 rpm with a change of rotation direction every 50 s, was used to mix the solution. This stirring was needed because of the high level of dynamic viscosity of the growth solution, around 19 Pa·s[42]. An *a** oriented $KGd(PO_3)_4$ seed was placed in contact with the surface of the solution at 12 mm from the solution centre, rotating with the same angular velocity as the stirrer. The use of this crystallographic direction in the $KGd(PO_3)_4$ seeds leads to the growth of high crystalline quality crystals[16,22]. The crystallographic *c* direction of the seed was oriented in radial direction, while its *b* direction was tangential to the rotation movement in order to achieve a good aerodynamic orientation of the crystal during its movement. Note that the morphology of this crystal usually presents an edge perpendicular to the *b* crystallographic direction, while it has natural {001} faces. With the aim of further improving the mixing of the solution, high thermal gradients (around 11 K·cm^{-1} in depth, with the hottest point at the bottom) were applied.

Once the solution was homogeneous, its saturation temperature was determined by accurately measuring the growth/dissolution rate of the $KGd(PO_3)_4$ seed depending on the temperature, which will then be used to start the growth of the single crystal. Beginning at the saturation temperature of the solution, cooling rates of 0.1 K·h^{-1} for the first 15 K and 0.05 K·h^{-1} for the next 10-15 K were applied to create supersaturation and grow the single crystal. At the beginning of the crystal growth experiments, the cooling rate was higher in order to initiate growth and not lose contact between the crystal seed and the solution. During this initial cooling rate regime, the supersaturation of the solution increases gradually because of the difficulty in mixing the solution due to its high viscosity. After decreasing the temperature of the furnace 15 K, a second cooling

rate was applied that was slower than the first to avoid an additional increase in the supersaturation of the solution, since this could induce nucleation in different points of the solution and also inclusions of solution inside the crystals. The growth rate can be maintained even with a slower cooling rate due to the accumulated supersaturation of the solution and the larger crystal surface.

After finishing the thermal cooling ramps, the crystal was removed from the solution and maintained at a few mm above the surface of the solution while the furnace was cooled to room temperature at a rate of 20-25 $K \cdot h^{-1}$.

Electron probe microanalysis (EPMA) with wavelength dispersive spectrometry (WDS) was used to determine the Pr content of the crystals. In this non-destructive technique, an electron beam is focused on the sample and the characteristic X-rays emitted (specific to each element of the sample) are dispersed by crystals (WDS) before being recorded and compared with the emission of standard compounds containing the elements to be analysed. The X-rays of the sample and the standards are obtained under the same measurement conditions. The equipment used was a JEOL JXA-8230. The standards used were an undoped $KGd(PO_3)_4$ single crystal for K, Gd, P and O measurements and an REE-1 for determining the Pr concentration. An accelerating voltage of 20 kV and a current of 20 nA were applied, with measuring time of 10 s for K, P, Gd and O and 100 s for Pr peaks and 5 s and 50 s for background measuring, respectively. Kα lines of K, P and O and Lα lines of Gd and Pr were used. The dispersive crystals were PETJ for K, PETH for P, LDE1 for O, and LIFL for Gd and Pr measurements. The detection limit of Pr^{3+} was around 105 ppm.

Structural characterization and thermal stability. The evolution of the unit cell parameters of $Pr:KGd(PO_3)_4$ with the Pr^{3+} content was studied by X-ray powder diffraction measurements, using a D5000 Siemens X-ray powder diffractometer in vertical θ-θ configuration with the Bragg-Brentano geometry. The X-ray diffraction patterns of undoped $KGd(PO_3)_4$ and 1, 2 and 5 atomic % $Pr:KGd(PO_3)_4$ in solution were obtained using Cu Kα radiation and recorded in the 2θ range from 10 to 70º. The measurements were made with a step size of 0.03º and a step time of 7 s. The unit cell parameters were refined using the TOPAS program[20], the Le Bail method[27] and the crystal data for undoped type III $KGd(PO_3)_4$ studied by Parreu *et al.*[28] (171710 ICSD database).

The thermal stability of the $KGd(PO_3)_4$ doped with praseodymium was studied by X-ray powder diffraction. The equipment used was a Bruker-AXS D8-Discover diffractometer equipped with a Cu source, a parallel incident beam (Göbel mirror), a HI-STAR GADDS (general area detector diffraction system) and a MRI BTS-Solid temperature chamber with a platinum ribbon heating stage. The powder samples were placed in the centre (occupying an area of ~1 × 1 mm^2) on the platinum ribbon. This stage was covered with a beryllium dome to maintain temperature. The sample was heated and cooled at a rate of 10 $K \cdot min^{-1}$. Diffraction patterns in the heating and cooling cycles were recorded every 15 K between 1048 and 1273 K and twice at room temperature, one diffraction pattern before the heating process and the other after the cooling process. The measurements were made in the 2θ range from 18 to 52º (one frame) with a detector-sample distance of 15 cm, an exposition time of 300 s per frame and a delay time of 60 s before each frame.

To complement the study of the thermal stability of the $KGd(PO_3)_4$ doped with praseodymium, differential thermal and thermogravimetric analyses (DTA-TGA) were performed using a TA Instruments SDT 2960 Simultaneous DSC-TGA. Al_2O_3 was used as the reference material, and the heating and cooling rates were at 10 $K \cdot min^{-1}$ with an air flux of 90 $cm^3 \cdot min^{-1}$.

The evolution of the unit cell parameters of the crystals grown from a 5 atomic % $Pr:KGd(PO_3)_4$ in solution with temperature was also studied by X-ray powder diffraction. The equipment was the same D5000 Siemens X-ray powder diffractometer previously used to study the $Pr:KGd(PO_3)_4$ unit cell parameters, but with an Anton-Paar HTK10 temperature chamber with a platinum ribbon heating stage. The sample was placed in the centre (occupying an area of ~9 × 5 mm^2) on the platinum ribbon. The diffraction patterns were recorded at temperatures of 298, 323, 373, 473, 573, 673 and 773 K (in which the monoclinic $P2_1$ crystalline phase of $KGd(PO_3)_4$ is stable), in the 2θ range from 10 to 70º with a step size of 0.03º, a step time of 5 s and a delay time of 300 s before each measurement. As before, the unit cell parameters were refined using the TOPAS program[20], the Le Bail method[27] and the crystal data for undoped type III $KGd(PO_3)_4$ studied by Parreu *et al.*[28] (171710 ICSD database).

Optical characterization. The bulk single crystals obtained were cut in plates perpendicular to the crystallographic *a**, *b* and *c** directions with a diamond saw. The plates were initially lapped and then polished with Al_2O_3 particle solutions to a size of 0.1 μm using a Logitech polishing machine. These plates were used for the optical absorption and emission studies. The unpolarized optical absorption of Pr^{3+} in $KGd(PO_3)_4$ was studied using a CARY 5000 UV-Vis-NIR spectrophotometer at room temperature in the wavelength range from 205 to 2475 nm, while the unpolarized optical absorption of undoped $KGd(PO_3)_4$ was studied in the wavelength range from 190 to 315 nm.

The emission spectroscopy was studied under vacuum ultraviolet-ultraviolet (VUV-UV) excitation in the wavelength range from 120 to 248 nm (10-5 eV). Experiments were performed in the DESIRS beamline at SOLEIL Synchrotron, France (proposal number 20151215, standard). The samples were placed in a vacuum chamber which can be evacuated to a pressure below 2×10^{-5} bars. A lithium fluoride window at the entrance of the vacuum chamber separates it from the synchrotron line. The monochromatized synchrotron light reached the sample at an angle of 90º. The emitted light from the sample was collected at 45º, focused with a silica lens and analysed with an Ocean Optics Jaz spectrometer (minimum spectral resolution 0.3 nm). The emission spectra were recorded in the range from 192 to 886 nm. To obtain the excitation spectra, the intensity obtained for a particular emission wavelength was plotted in front of the excitation wavelength in the excitation wavelength range from 120 to 248 nm.

Lifetime measurements were also carried out in the DESIRS beamline of SOLEIL Synchrotron, France (proposal number 20161324, standard) in a single bunch mode operation for pulsed radiation. The same configuration in the vacuum chamber as in previous measurements was used. The light was guided with an optical fibre to an ANDOR spectrograph (Shamrock 193i) with a grating of 150 lines·mm^{-1}, coupled to an iStar Intensified Charge Coupled Device (ICCD) (model DH734-18F-03). When the level of vacuum in the chamber was lower than 2×10^{-5} bars, the window between this chamber and the synchrotron was removed in order to increase the photon flux reaching the sample.

The decay time of the $4f \rightarrow 4f$ electronic transitions, which was significantly slower than those of the 5*d* energy levels, was measured with a Cary Eclipse fluorescence spectrophotometer.

References

1. Rodnyi, P. A. Scintillators requirements in various applications in *Physical Processes in Inorganic Scintillators* 41-51 (CRC Press, 1997).
2. Nikl, M. & Yoshikawa, A. Recent R&D trends in inorganic single-crystal scintillator materials for radiation detection. *Adv. Opt. Mater.* **3 (4),** 463-481 (2015).
3. Zyck, A. K. Luminescence properties of Ce^{3+}, Pr^{3+} and Nd^{3+} activated scintillators for positron emission tomography (PET). Ph.D. Thesis. Utrecht University, Utrecht, Netherlands (2011).
4. Waterstram-Rich, K. M. & Gilmore, D. PET instrumentation in *Nuclear Medicine and PET/CT: Technology and Techniques* 326-355 (Elsevier, 2017).
5. Wu, Y. & Ren, G. Energy transfer and radiative recombination processes in $(Gd,Lu)_3Ga_3Al_2O_{12}:Pr^{3+}$ scintillators. *Opt. Mater.* **35,** 2146-2154 (2013).
6. Tyagi, M. *et al.* Effect of codoping on scintillation and optical properties of a Ce-doped $Gd_3Ga_3Al_2O_{12}$ scintillator. *J. Phys. D: Appl. Phys.* **46,** 475302 (2013).
7. Kamada, K. *et al.* Alkali earth co-doping effects on luminescence and scintillation properties of Ce doped $Gd_3Al_2Ga_3O_{12}$ scintillator. *Opt. Mater.* **41,** 63-66 (2015).
8. Wu, Y. & Ren, G. Effects of Gd/Lu ratio on the luminescent properties of Pr^{3+} activated $(Gd,Lu)_3Ga_3Al_2O_{12}$. *ECS J. Solid State Sci. Technol.* **2 (3),** R49-R55 (2013).
9. Cooke, D. W. *et al.* Crystal growth and optical characterization of cerium-doped $Lu_{1.8}Y_{0.2}SiO_5$. *J. Appl. Phys.* **88,** 7360-7362 (2000).
10. Nikl, M., Vedda, A. & Laguta, V. V. Single-crystal scintillation materials in *Springer Handbook of Crystal Growth* (eds. Dhanaraj, G., Byrappa, K., Prasad, V. & Dudley, M.) 1663-1700 (Springer, 2010).
11. Blasse, G. & Dirksen, G. J. The luminescence of broad-band emitters in $LiLaP_4O_{12}$. *Phys. Status Solidi B* **110,** 487-494 (1982).
12. Shalapska, T. *et al.* Crystal structure and luminescence properties of $LiYP_4O_{12}:Ce^{3+}$ phosphor. *J. Phys. Condens. Matter* **22,** 485503 (2010).
13. Zhong, J. *et al.* Effects of crystal structure on the luminescence properties and energy transfer between Gd^{3+} and Ce^{3+} ions in $MGd(PO_3)_4:Ce^{3+}$ (M = Li, Na, K, Cs). *J. Mater. Chem.* **17,** 4679-4684 (2007).
14. Kang, Y. *et al.* VUV-UV luminescence of Ce^{3+}, Pr^{3+} doped and Ce^{3+}-Pr^{3+} codoped $NaLa(PO_3)_4$. *J. Lumin.* **143,** 21-26 (2013).

15. Parreu, I. Crystal growth and characterization of ytterbium or neodymium doped type III-$KGd(PO_3)_4$. A new bifunctional nonlinear and laser crystal. Ph.D. Thesis. Universitat Rovira i Virgili, Tarragona, Spain (2006).
16. Solé, R. M. *et al.* Growth, anisotropic spectroscopy and laser operation of the monoclinic Nd:$KGd(PO_3)_4$ crystal. *J. Phys. D Appl. Phys.* **48,** 495502-495512 (2015).
17. Parreu, I. *et al.* Crystal growth and characterization of type III ytterbium-doped $KGd(PO_3)_4$: a new nonlinear laser host. *Chem. Mater.* **19 (11),** 2868-2876 (2007).
18. Adell, I. *et al.* Single crystal growth, optical absorption and luminescence properties under VUV-UV synchrotron excitation of type III Ce^{3+}:$KGd(PO_3)_4$, a promising scintillator material. *Sci. Rep.* **8,** 11002; 10.1038/s41598-018-29372-z (2018).
19. Nikl, M. Scintillation detectors for x-rays. *Meas. Sci. Technol.* **17,** R37-R54 (2006).
20. XRD software –diffract suit TOPAS V4.2. Bruker, 2007.
21. Shannon, R. D. Revised effective ionic radii and systematic studies of interatomic distances in halides and chalcogenides. *Acta Cryst.* **A32,** 751-767 (1976).
22. Parreu, I. *et al.* Crystal growth, structural characterization, and linear thermal evolution of $KGd(PO_3)_4$. *Chem. Mater.* **17 (4),** 822-828 (2005).
23. Xing, Y., Hu, N. H., Zhou, Q. L., Hong, G. Y. & Yue, S. Y. *Wuli Huaxue Xuebao* **3,** 218-221 (1987).
24. Ni, Y.-X., Hughes, J. M. & Mariano A. N. Crystal chemistry of the monazite and xenotime structures. *Am. Mineral.* **80,** 21-26 (1995).
25. Ponceblanc, H., Millet, J. M. M., Thomas, G., Herrmann, J. M. & Védrine, J. C. Comparative study of polymorphic phase transition by differential thermal analysis, high temperature X-ray diffraction, and temperature programmed electrical conductivity measurements. Case study of mixed iron and cobalt molybdate. *J. Phys. Chem.* **96,** 9466-9469 (1992).
26. Shan, P. *et al.* Crystal growth and optical characteristics of beryllium-free polyphosphate, $KLa(PO_3)_4$, a possible deep-ultraviolet nonlinear optical crystal. *Sci. Rep.* **6,** 25201; 10.1038/srep25201 (2016).
27. Le Bail, A. Whole powder pattern decomposition methods and applications: a retrospection. *Powder Diffr.* **20 (4),** 316-326 (2005).
28. Parreu, I., Carvajal, J. J., Solans, X., Díaz, F. & Aguiló, M. Crystal structure and optical characterization of pure and Nd-substituted type III $KGd(PO_3)_4$. *Chem. Mater.* **18 (1),** 221-228 (2006).
29. Mayolet, A. Etude des processus d'absorption et de transfert d'energie au sein de materiaux inorganiques luminescents dans le domaine UV et VUV. Ph.D. Thesis. Université de Paris XI, Paris, France (1995).
30. Naik, R. C., Karanjikar, N. P. & Narasimham, N. A. X-ray excited optical luminescence spectrum of Pr-doped YPO_4. *Solid State Commun.* **38,** 389-391 (1981).
31. Yuan, J. L. *et al.* VUV spectroscopic properties of Ce^{3+} and Pr^{3+}-doped $AREP_2O_7$-type alkali rare earth diphosphates (A = Na, K, Rb, Cs; RE = Y, Lu). *J. Lumin.* **126,** 130-134 (2007).
32. van Pieterson, L., Wegh, R. T., Meijerink, A. & Reid, M. F. Emission spectra and trends for $4f^{n-1}5d \leftrightarrow 4f^n$ transitions of lanthanide ions: Experiment and theory. *J. Chem. Phys.* **115 (20),** 9382-9392 (2001).
33. Katelnikovas, A., Bettentrup, H., Dutczak, D., Kareiva, A. & Jüstel, T. On the correlation between the composition of Pr^{3+} doped garnet type materials and their photoluminescence properties. *J. Lumin.* **131,** 2754-2761 (2011).
34. Srivastava, A. M. *et al.* The influence of the Pr^{3+} $4f^15d^1$ configuration on the $^1S_0$ emission efficiency and lifetime in $LaPO_4$. *Opt. Mater.* **33,** 292-298 (2011).
35. Yang, Z., Lin, J. H., Su, M. Z., Tao, Y. & Wang, W. Photon cascade luminescence of Gd^{3+} in $GdBaB_9O_{16}$. *J. Alloys Compd.* **308,** 94-97 (2000).
36. Tian, Z. *et al.* Photon cascade emission of Gd^{3+} in Na(Y,Gd)FPO_4. *J. Phys. Chem. C* **112,** 12524-12529 (2008).
37. Dieke, G. H. & Crosswhite, H. M. The spectra of the doubly and triply ionized rare earths. *Appl. Opt.* **2 (7),** 675-686 (1963).
38. Wegh, R. T., Meijerink, A., Lamminmaki, R. J. & Holsa, J. Extending Dieke's diagram. *J. Lumin.* **87-9,** 1002-1004 (2000).
39. Wegh, R. T., Donker, H., Meijerink, A., Lamminmäki, R. J. & Hölsä, J. Vacuum-ultraviolet spectroscopy and quantum cutting for Gd^{3+} in $LiYF_4$. *Phys. Rev. B* **56 (21),** 13841-13848 (1997).
40. Feofilov, S. P., Seo, H. J., Zhou, Y. & Meltzer, R. S. Host sensitization of Gd^{3+} ions in yttrium and scandium borates and phosphates: Application to quantum cutting. *Phys. Rev. B* **74 (8),** 085101 (2006).
41. Zhong, J. *et al.* Luminescence properties of $NaGd(PO_3)_4$:Eu^{3+} and energy transfer from Gd^{3+} to Eu^{3+}. *Appl. Phys. B* **98,** 139-147 (2010).
42. Solé, R. *et al.* Physical properties of self-flux and WO_3-containing solutions useful for growing type III $KGd(PO_3)_4$ single crystals. *J. Cryst. Growth* **311,** 3656-3660 (2009).
44. Shalapska, T. *et al.* Photon cascade luminescence from Pr^{3+} ions in $LiPrP_4O_{12}$ polyphosphate. *J. Phys. D: Appl. Phys.* **43,** 405404 (2010).
45. Drozdowski, W. *et al.* Scintillation properties of praseodymium activated $Lu_3Al_5O_{12}$ single crystals. *IEEE Trans. Nucl. Sci.* **55 (4),** 2420-2424 (2008).
46. Trevisani, M., Ivanovskikh, K. V., Piccinelli, F. & Bettinelli, M. Fast 5d-4f luminescence in Pr^{3+}-doped $K_3Lu(PO_4)_2$. *J. Lumin.* **152,** 2-6 (2014).
47. Jouini, A., Gâcon, J. C., Ferid, M. & Trabelsi-Ayadi, M. Luminescence and scintillation properties of praseodymium poly and diphosphates. *Opt. Mater.* **24,** 175-180 (2003).
48. Shalapska, T. *et al.* Luminescence properties of Ce^{3+}-doped $NaPrP_4O_{12}$ polyphosphate. *J. Phys.: Condens. Matter* **25,** 105403 (2013).

Acknowledgements

The authors are grateful for the financial support from the Spanish Government under Projects MAT2016-75716-C2-1-R (AEI/ FEDER,UE) and TEC 2014-55948-R, and from the Catalan Government under Project 2017 SGR 755. I. Adell thanks the Catalan Government for financial support under grants 2015 FI_B 00711, 2016 FI_B1 00113 and 2017 FI_B2 00017. In addition, we acknowledge SOLEIL for provision of synchrotron radiation facilities under the projects with proposal numbers 20151215 (standard) and 20161324 (standard) and we would like to thank Nelson de Oliveira for assistance in using the DESIRS beamline, and the SOLEIL staff for smoothly running the facility.

Author contributions

I.A., M.C.P., R.M.S. and F.D. designed the study; I.A. and R.M.S. performed the crystal growth and the studies relating to the structural characterization, thermal stability and linear thermal expansion tensor; I.A. measured the optical absorption; I.A., M.C.P., R.M.S., M.L., M.A. and F.D. conducted proposals 20151215 and 20161324 at SOLEIL Synchrotron; N.O. conducted proposal 20161324 at SOLEIL Synchrotron; I.A., M.C.P. and R.M.S. wrote the manuscript. All the authors discussed the results and reviewed the manuscript.

Additional information

Supplementary information accompanies this paper at http://www.nature.com/srep.

Competing interests. The authors declare no competing interests.

Figure Legends

Figure 1. (**a**) As-grown single crystal of Pr:KGd$(PO_3)_4$, and (**b**) crystal scheme with the faces observed.

Figure 2. Evolution of the *a*, *b*, *c* and β unit cell parameters and unit cell volume of Pr:KGd$(PO_3)_4$ single crystals as a function of the praseodymium content in KGd$(PO_3)_4$.

Figure 3. Thermogram of $KGd_{0.942}Pr_{0.058}(PO_3)_4$ in heating and cooling processes in the range 500-1273 K.

Figure 4. X-ray powder experimental diffractogram of $KGd_{0.942}Pr_{0.058}(PO_3)_4$ at room temperature, those selected at several temperatures describing its evolution with temperature in both the heating and cooling processes and three X-ray powder diffraction standard patterns. The labelling of the patterns is related to the temperature read in the central part of the sample support by the thermocouple.

Figure 5. Evolution of the unit cell parameters of $KGd_{0.942}Pr_{0.058}(PO_3)_4$ from room temperature up to 773 K.

Figure 6. Linear thermal expansion ellipsoid of $KGd_{0.942}Pr_{0.058}(PO_3)_4$ at 303 K.

Figure 7. Unpolarized optical absorption cross sections of Pr:KGd$(PO_3)_4$ at room temperature. Light propagation direction is along the *b* axis in figure (**a**) and along the *a** axis in figures (**b-f**). All labels indicate the electronic transitions of Pr^{3+}.

Figure 8. Optical emission spectra of $KGd_{0.990}Pr_{0.010}(PO_3)_4$ under (**a**) 218 nm, (**b**) 196 nm, and (**c**) 166 nm excitation. Labels in purple and italics indicate the electronic transitions of Gd^{3+} and labels in green and bold those of Pr^{3+}.

Figure 9. Energy level diagram of Pr^{3+} and Gd^{3+} in Pr:KGd$(PO_3)_4$ and emissions observed under excitation at (**a**) 218 nm, (**b**) 196 nm, and (**c**) 166 nm. The thickness of the arrows is related to the intensity of the emissions represented.

Figure 10. Excitation spectra of Pr:KGd$(PO_3)_4$ crystal under VUV radiation for (**a**) λ_{emi}=265 nm and (**b**) λ_{emi}=592 nm. Labels in purple and italics indicate the electronic transitions of Gd^{3+} and labels in green and bold those of Pr^{3+}.

Figure 11. (**a**) Fast component of the decay curves of Pr:$KGd(PO_3)_4$ at different concentrations of praseodymium under excitations at 166 and 218 nm for λ_{emi}=256 nm. (**b**) Slow component of the decay curve of $KGd_{0.942}Pr_{0.058}(PO_3)_4$ under excitation at 300 nm for λ_{emi}=312 nm.

Display Items

Tables

[Pr_2O_3] / ([Gd_2O_3] + [Pr_2O_3]) in the solution [at. %]	Growth interval [K]	Crystal weight [g]	Crystal dimensions in *a** × *b* × *c** directions [mm]	Growth rate [× 10^{-3} g·h^{-1}]
0.25	28.5	2.86	7.6 × 17.7 × 12.0	6.80
0.25	29.9	2.73	8.2 × 17.1 × 11.2	6.09
0.50	27.3	6.88	13.6 × 21.5 × 12.3	17.37
1.00	30	3.16	8.4 × 19.1 × 11.6	7.02
1.00	30	5.87	9.2 × 24.1 × 13.2	13.04
2.00	27.3	3.73	8.4 × 18.8 × 12.7	9.42
2.00	30	6.38	13.2 × 23.8 × 13.6	14.18
2.00	23.9	3.26	9.4 × 17.4 × 10.7	9.93
5.00	27.3	5.13	11.5 × 21.2 × 13.1	12.95
5.00	24.1	4.08	8.9 × 19.6 × 11.8	12.29
5.00	28.6	4.32	10.2 × 18.8 × 11.2	10.24

Table 1. Crystal growth experiments for different Pr^{3+} doping levels and the crystals obtained.

[Pr] / ([Gd]+[Pr]) atomic % ratio in the solution	[Pr] / ([Gd]+[Pr]) atomic ratio in the crystal	Chemical formula	Pr^{3+} concentration [cm^{-3}]	K_{Pr}
0.25	0.003 ± 0.001	$KGd_{0.997}Pr_{0.003}(PO_3)_4$	1.248×10^{19}	1.2 ± 0.4
0.50	0.005 ± 0.002	$KGd_{0.995}Pr_{0.005}(PO_3)_4$	2.080×10^{19}	1.0 ± 0.4
1.00	0.010 ± 0.002	$KGd_{0.990}Pr_{0.010}(PO_3)_4$	4.160×10^{19}	1.0 ± 0.2
2.00	0.026 ± 0.001	$KGd_{0.974}Pr_{0.026}(PO_3)_4$	1.082×10^{20}	1.30 ± 0.05
5.00	0.058 ± 0.001	$KGd_{0.942}Pr_{0.058}(PO_3)_4$	2.413×10^{20}	1.16 ± 0.02

Table 2. Compositional results for Pr:$KGd(PO_3)_4$. K_{Pr} denotes the distribution coefficient of the Pr^{3+} in the crystal.

Pr^{3+} at. % with respect to Gd^{3+} in $KGd(PO_3)_4$ crystal	*a* [Å]	*b* [Å]	*c* [Å]	β [°]	*V* [$Å^3$]
0	7.2493(3)	8.3466(1)	7.9216(1)	91.825(2)	479.07(2)
1.0	7.2491(3)	8.3492(1)	7.9234(1)	91.825(2)	479.31(2)
2.6	7.2492(3)	8.3503(1)	7.9242(1)	91.830(2)	479.43(2)
5.8	7.2501(3)	8.3535(1)	7.9277(1)	91.832(2)	479.89(2)

Table 3. The unit cell parameters and unit cell volume of Pr:$KGd(PO_3)_4$ single crystals at different Pr^{3+} doping concentrations.

T [K]	*a* [Å]	*b* [Å]	*c* [Å]	*β* [°]	*V* [Å^3]
303	7.2486(9)	8.3565(8)	7.9306(8)	91.871(8)	480.12(9)
323	7.2515(9)	8.3584(7)	7.9336(6)	91.840(7)	480.61(8)
373	7.2576(8)	8.3655(7)	7.9382(7)	91.838(7)	481.71(8)
473	7.2651(8)	8.3742(7)	7.9433(7)	91.824(7)	483.02(8)
573	7.2712(10)	8.3835(9)	7.9476(8)	91.827(9)	484.22(10)
673	7.2827(11)	8.3939(10)	7.9535(10)	91.816(10)	485.96(11)
773	7.2909(10)	8.4068(9)	7.9600(8)	91.764(9)	487.66(10)

Table 4. Unit cell parameters and unit cell volume of $KGd_{0.942}Pr_{0.058}(PO_3)_4$ at different temperatures.

Compound	[Pr^{3+}]	Lifetime [ns]	Ref.
$LiPrP_4O_{12}$	100 at. %	10.5	[44]
$Pr:Lu_3Al_5O_{12}$	0.22-0.24 mol %	20.1	[45]
$Pr:K_3Lu(PO_4)_2$	1 at. %	19.9-20.3	[46]
$Pr(PO_3)_3$	100 at. %	6	[47]
$NaPr_{0.998}Ce_{0.002}P_4O_{12}$	99.8 at. %	10.5	[48]
$Pr:LiYF_4$	2 %	16-19	[32]

Table 5. Values for the lifetime of the $5d_1$ level of Pr^{3+} in several hosts.

Figures

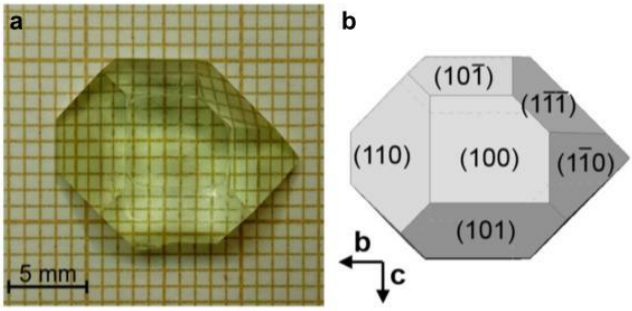

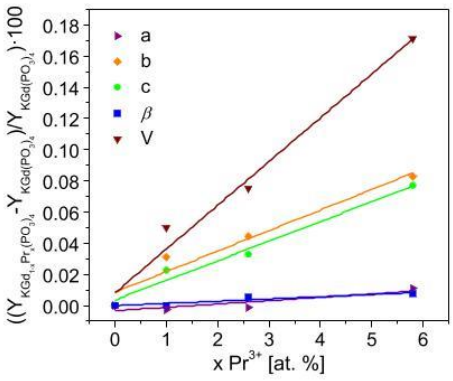
a
b
c
β
V
x Pr3+ [at. %]

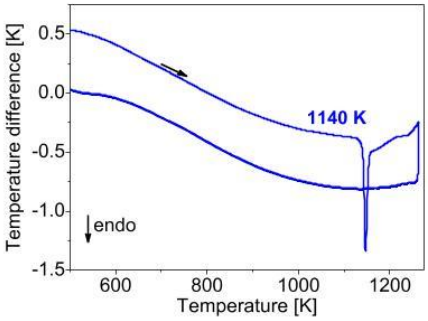
1140 K
endo
Temperature difference [K]
Temperature [K]

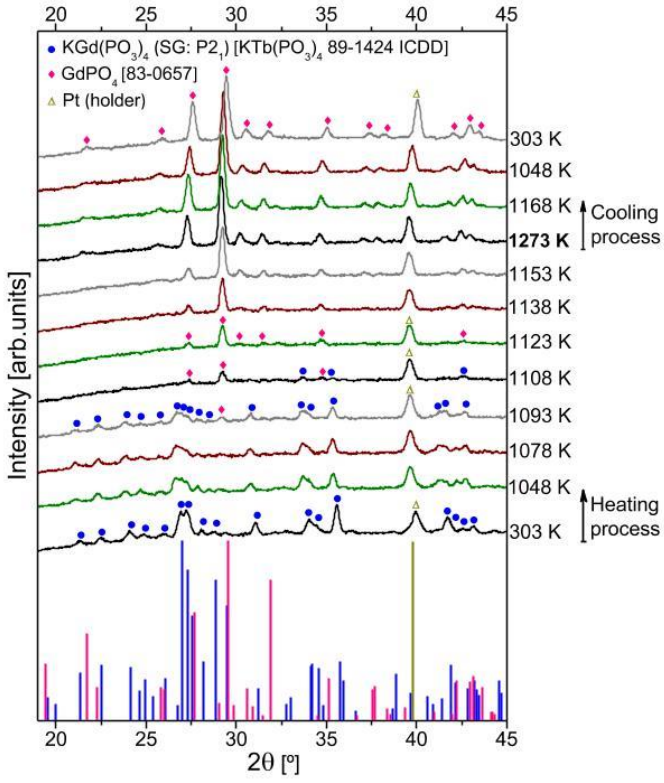
KGd(PO3)4 (SG: P21) [KTb(PO3)4 89-1424 ICDD]
GdPO4 [83-0657]
Pt (holder)
303 K
1048 K
1168 K
1273 K
1153 K
1138 K
1123 K
1108 K
1093 K
1078 K
1048 K
303 K
Cooling process
Heating process
Intensity [arb.units]
2θ [º]

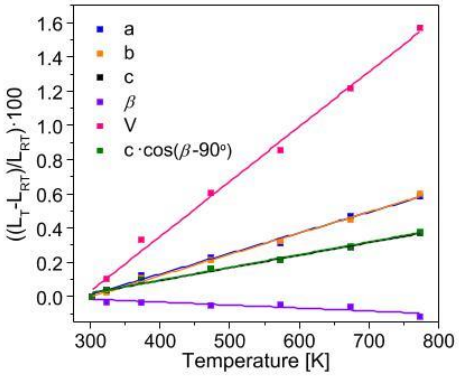
a
b
c
β
V
c·cos(β-90º)
((LT-LRT)/LRT)·100
Temperature [K]

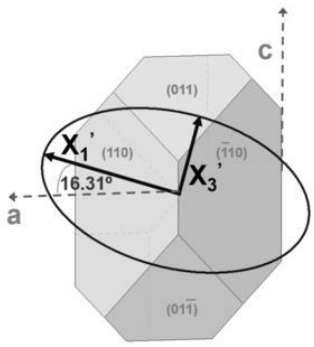
c
(011)
X1'
(110)
(1̄10)
X3'
16.31°
a
(011̄)

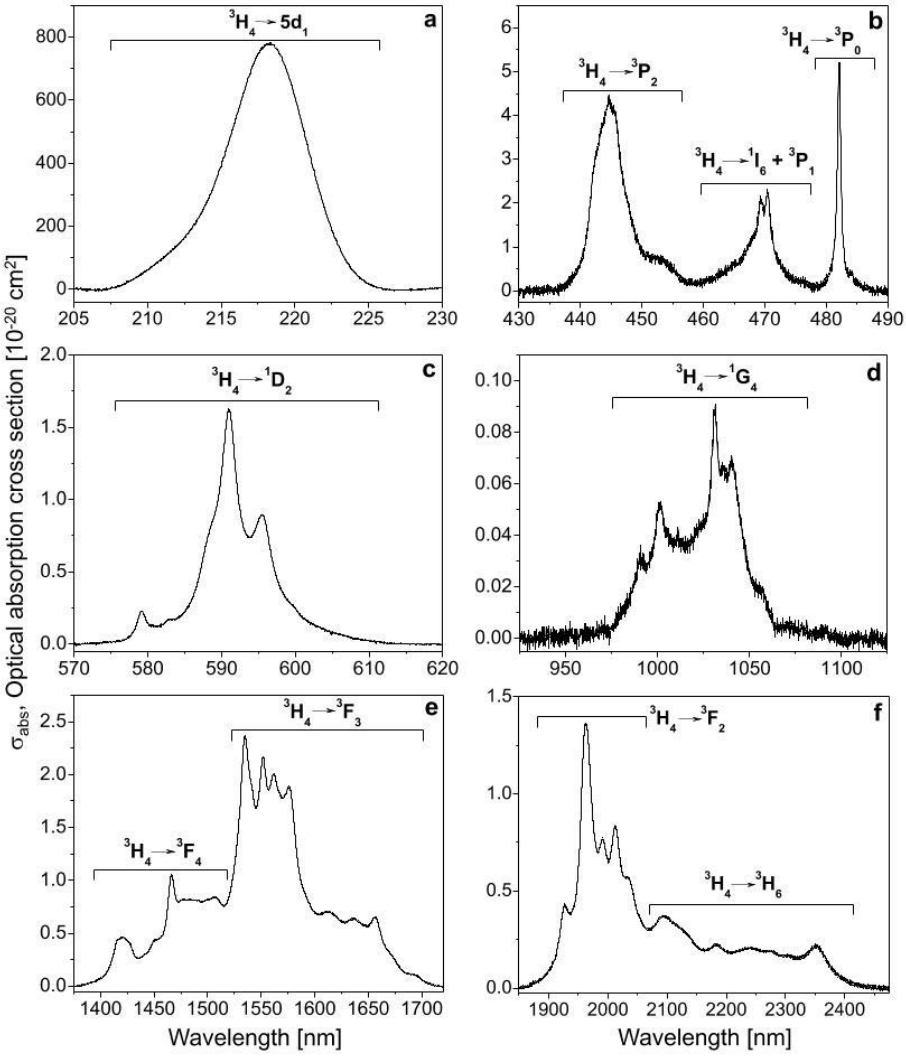
a
$^3H_4 \rightarrow 5d_1$
b
$^3H_4 \rightarrow {}^3P_2$
$^3H_4 \rightarrow {}^3P_0$
$^3H_4 \rightarrow {}^1I_6 + {}^3P_1$
c
$^3H_4 \rightarrow {}^1D_2$
d
$^3H_4 \rightarrow {}^1G_4$
e
$^3H_4 \rightarrow {}^3F_3$
$^3H_4 \rightarrow {}^3F_4$
f
$^3H_4 \rightarrow {}^3F_2$
$^3H_4 \rightarrow {}^3H_6$
Optical absorption cross section [10^{-20} cm^2]
σ_{abs},
Wavelength [nm]
Wavelength [nm]

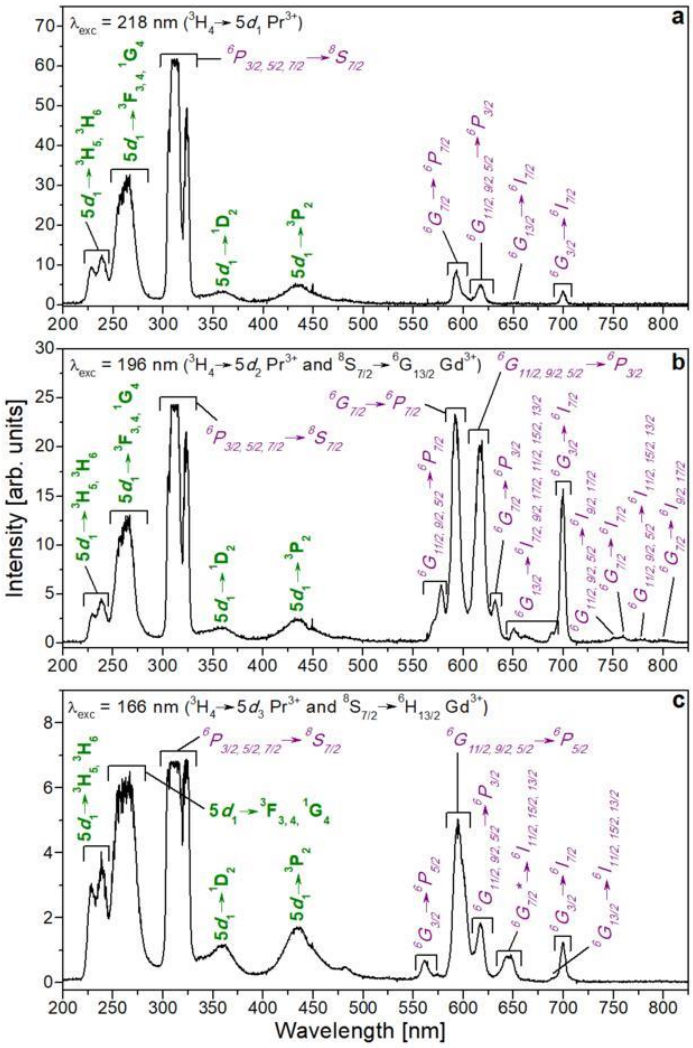
a
λexc = 218 nm (3H4→5d1 Pr3+)
b
λexc = 196 nm (3H4→5d2 Pr3+ and 8S7/2→6G13/2 Gd3+)
c
λexc = 166 nm (3H4→5d3 Pr3+ and 8S7/2→6H13/2 Gd3+)
Intensity [arb. units]
Wavelength [nm]

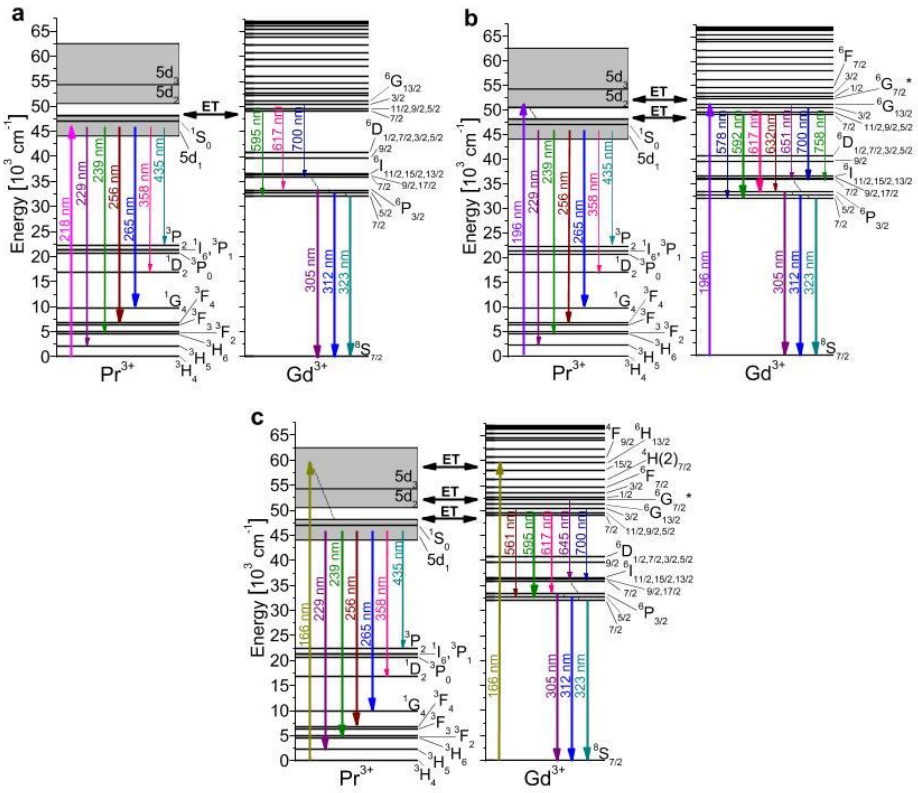
a
b
c
Energy [10^3 cm^-1]
Pr3+
Gd3+
ET
5d3
5d2
5d1
1S0
3P2
1I6
3P1
1D2
3P0
1G4
3F4
3F3
3F2
3H6
3H5
3H4
8S7/2
6G13/2
6D1/2,7/2,3/2,5/2
6P3/2
6F7/2
6G7/2*
4F9/2
6H13/2
4H(2)7/2
218 nm
229 nm
239 nm
256 nm
265 nm
358 nm
435 nm
595 nm
617 nm
700 nm
305 nm
312 nm
323 nm
196 nm
578 nm
592 nm
632nm
651 nm
758 nm
166 nm
561 nm
645 nm

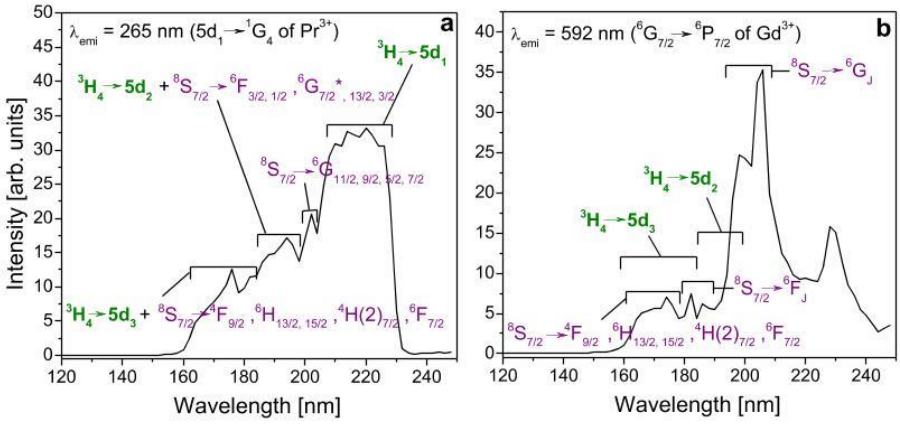
a
λemi = 265 nm (5d1→1G4 of Pr3+)
3H4→5d1
3H4→5d2 + 8S7/2→6F3/2, 1/2, 6G7/2*, 13/2, 3/2
8S7/2→6G11/2, 9/2, 5/2, 7/2
3H4→5d3 + 8S7/2→4F9/2, 6H13/2, 15/2, 4H(2)7/2, 6F7/2
Intensity [arb. units]
Wavelength [nm]
b
λemi = 592 nm (6G7/2→6P7/2 of Gd3+)
8S7/2→6GJ
3H4→5d2
3H4→5d3
8S7/2→6FJ
8S7/2→4F9/2, 6H13/2, 15/2, 4H(2)7/2, 6F7/2
Wavelength [nm]

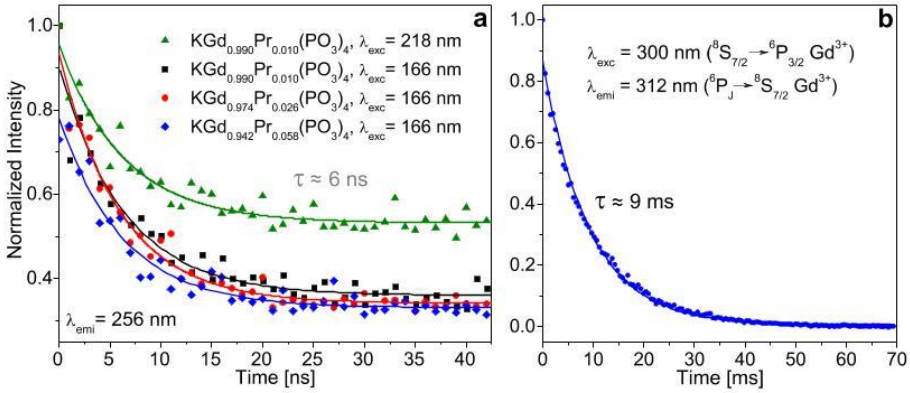
a
b
Normalized Intensity
Time [ns]
Time [ms]
KGd0.990Pr0.010(PO3)4, λexc= 218 nm
KGd0.990Pr0.010(PO3)4, λexc= 166 nm
KGd0.974Pr0.026(PO3)4, λexc= 166 nm
KGd0.942Pr0.058(PO3)4, λexc= 166 nm
τ ≈ 6 ns
λemi = 256 nm
λexc = 300 nm (8S7/2 → 6P3/2 Gd3+)
λemi = 312 nm (6PJ → 8S7/2 Gd3+)
τ ≈ 9 ms

Supporting Information

Single crystal growth, optical absorption and luminescence properties under VUV-UV synchrotron excitation of type III Pr^{3+}:$KGd(PO_3)_4$

Irina Adell[1], Maria Cinta Pujol[1,*], Rosa Maria Solé[1,*], Matthieu Lancry[2], Nadège Ollier[3], Magdalena Aguiló[1] and Francesc Díaz[1]

[1] Física i Cristal·lografia de Materials i Nanomaterials (FiCMA-FiCNA) - EMaS, Dept. Química Física i Inorgànica, Universitat Rovira i Virgili (URV), Campus Sescelades, c/ Marcel·lí Domingo, 1, E-43007, Tarragona, Spain.

[2] Institut de Chimie Moléculaire et des Matériaux d'Orsay, CNRS-Université Paris Sud, Université de Paris Saclay, Bât.410, 91405 Orsay, France.

[3] Laboratoire des Solides Irradiés, CEA-CNRS-Ecole Polytechnique, Université Paris-Saclay, Palaiseau, France.

* mariacinta.pujol@urv.cat; rosam.sole@urv.cat

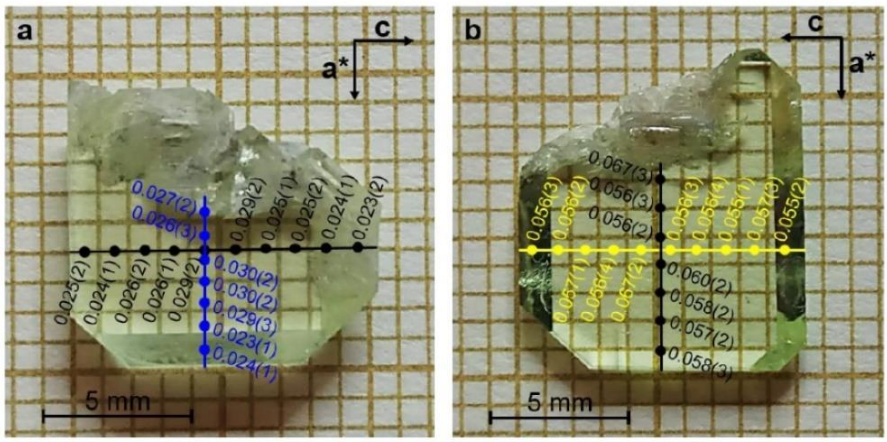

Figure S.1. The [Pr]/([Gd]+[Pr]) atomic ratio in the crystal at several points along the *a** and *c* crystallographic directions in a plate perpendicular to *b* crystallographic axis for (**a**) $KGd_{0.974}Pr_{0.026}(PO_3)_4$ and (**b**) $KGd_{0.942}Pr_{0.058}(PO_3)_4$. The value shown for each dot is the mean Pr^{3+} atomic concentration value of five measurements along with the error of the third decimal in parentheses.

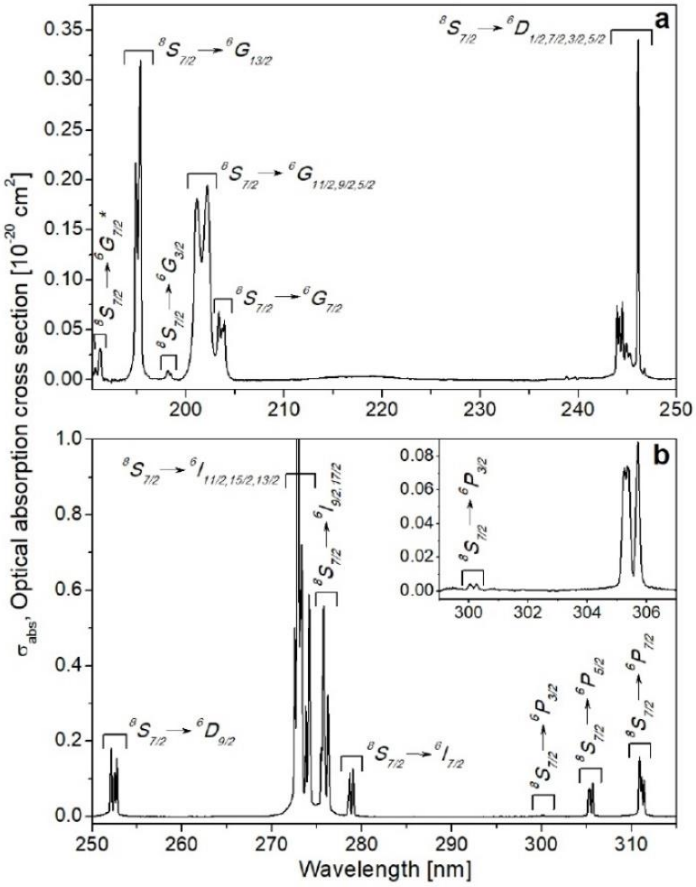

Figure S.2. Unpolarized optical absorption cross section of undoped KGdP at room temperature. Propagation direction is the *b* axis in figures **a** and **b**. All labels indicate the absorption transitions of Gd^{3+}.

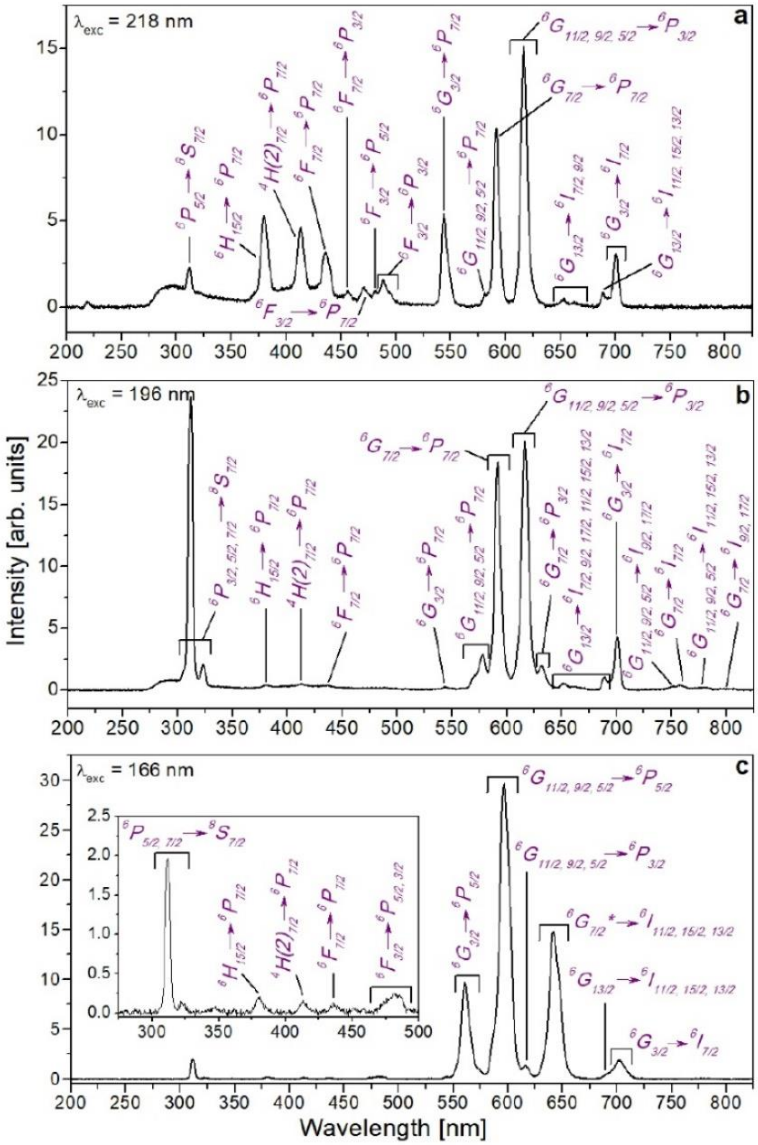

Figure S.3. Optical emission spectra of undoped KGdP under (**a**) 218 nm, (**b**) 196 nm and (**c**) 166 nm excitation. All labels indicate the absorption transitions of Gd^{3+}.

Paper III

Optimization of the synthesis and physical characterization of praseodymium-doped type III $KGd(PO_3)_4$ nanocrystals

I. Adell, R. M. Solé, M. C. Pujol, M. Aguiló and F. Díaz

ACS Omega **2018**, 3 (9), 11307-11316

DOI: *10.1021/acsomega.8b01321*

UNIVERSITAT ROVIRA I VIRGILI
CE OR PR-DOPED TYPE III KGD(PO3)4 CRYSTALLINE MATERIALS. GROWTH AND CHARACTERIZATION AS SCINTILLATORS
Irina Adell Barbarà

ACS OMEGA
Cite This: *ACS Omega* 2018, 3, 11307−11316
Article
http://pubs.acs.org/journal/acsodf

Optimization of the Synthesis and Physical Characterization of Praseodymium-Doped Type III $KGd(PO_3)_4$ Nanocrystals

Irina Adell, Rosa Maria Solé,* Maria Cinta Pujol, Magdalena Aguiló, and Francesc Díaz

Universitat Rovira i Virgili, Departament Química Física i Inorgànica, Física i Cristal·lografia de Materials i Nanomaterials (FiCMA-FiCNA)-EMaS, Campus Sescelades, E-43007 Tarragona, Spain

ABSTRACT: Scintillator materials are used as detectors in the ray imaging techniques for medical diagnosis. Because the ideal medical scintillator material does not exist, many efforts are being made to find new materials that satisfy a greater number of properties. Here, the synthesis conditions of $Pr:KGd(PO_3)_4$ nanocrystals by the modified Pechini method are optimized to obtain a single crystalline phase of those that form the polymorphism of $KGd(PO_3)_4$. The interest lies in the type III phase because less quenching by Pr^{3+} concentration is expected. By performing transmittance measurements and because of the wide transparency window of the type III $KGd(PO_3)_4$ host, the $^3H_4 \rightarrow 5d_1$ absorption transition of Pr^{3+} has been observed in the vacuum ultraviolet spectral range. After creating electron−hole pairs in the host due to the excitation of the material by X-ray radiation, the bands corresponding to the $5d_1 \rightarrow {}^3H_4$, $^3H_5$, $^3H_6$ and $5d_1 \rightarrow {}^3F_3$, $^3F_4$, $^1G_4$ transitions of Pr^{3+} have been observed in the near-visible spectral range, being these 5d → 4f transitions interesting for scintillation applications. Therefore, the type III $Pr:KGd(PO_3)_4$ nanocrystals allow the conversion from high-energy radiation to visible or near-visible light.

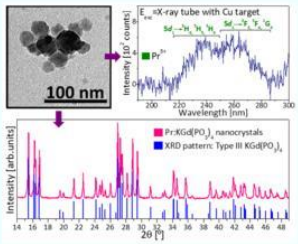

1. INTRODUCTION

Potassium gadolinium phosphate, $KGd(PO_3)_4$, hereafter KGdP, is a monoclinic crystal that belongs to the wide family of condensed phosphates of double phosphates of alkali (M) and lanthanide (Ln) ions with the general formula $M^{I}Ln^{III}(PO_3)_4$. These condensed phosphates are constituted by corner-sharing PO_4 tetrahedra with variable O/P ratio (from 2.5 to 4) building phosphoric anions. Because of the different possibilities of condensation of the phosphoric anions (long chains, rings, and also three-dimensional networks), the condensed phosphates present multiple crystalline structures; so, KGdP can crystallize in three different crystalline structures: type III phase (space group: $P2_1$), type IV (space group: $P2_1/n$), and type B phase (space group: $C2/c$).[1] The first two crystalline structures present long chains of polyphosphates, while the third crystalline structure belongs to the group of cyclophosphates, in which the PO_4 forms rings. Besides this structural feature, the coordination of the cations presents differences among these three different crystalline phases.

KGdP can be easily doped with other lanthanide ions, such as praseodymium (Pr^{3+}), because gadolinium (Gd^{3+}) has a high capacity for substitution with lanthanides ions due to the proximity of the ionic radii and the common valence with the other lanthanides ions[1] (ionic radii of Gd^{3+} and Pr^{3+} with coordination VIII are 1.053 and 1.126 Å, respectively[2]). Besides, $KPr(PO_3)_4$ and KGdP crystals are isostructural (in the polyphosphate form, with type III phase,[3] and in the cyclophosphate form, with the type B phase[4]). To our knowledge, there is no evidence of the existence of the $KPr(PO_3)_4$ with the type IV crystalline structure.

The transparency window of KGdP extends from 160 nm to 4 μm,[5] which covers the main absorption and emission wavelengths of praseodymium. This UV transparency is a great advantage of this compound to be used as a scintillator material based on the d−f electronic transitions of Pr^{3+} as the doping ion. Scintillator materials are extensively used in technological, industrial, and medical applications.[6] One of its main applications is as a detector in the ray imaging techniques for medical diagnosis.[7−9] In general, an ideal medical scintillator should satisfy the following eight properties to be considered a good scintillator: short decay time, high luminous efficacy, no afterglow, short radiation length, high density, low cost, good spectral match to photodetectors, and high light yield.[10,11] However, until the time, the ideal scintillator does not exist, so each modality of medical imaging systems must select the most suitable combination of properties from the existing scintillators. For this reason, many efforts are being made to find the ideal one. Scintillators can be synthesized in different forms, such as single crystals, powder, thin films, and nanoparticles. Single-crystal sodium iodide doped with thallium ions (NaI (Tl)) is a conventional medical scintillator; however, it does not satisfy with some of the requirements. NaI (Tl) has a comparatively long decay time and a low density.[10] Because the parity allowed f−d transitions in lanthanide ion-

Received: June 12, 2018
Accepted: August 10, 2018
Published: September 18, 2018

doped materials present high oscillator strengths and the 5d levels have short lifetimes (typically ns), the lanthanide ion-doped materials are an interesting alternative for scintillator materials.[6] García-Murillo et al.[12] proposed europium-doped Gd_2O_3 thin films as a possible good scintillator because of its middle light yield; nevertheless, later this type of films were not considered good as a scintillator for medical imaging because of its comparatively high afterglow. Pedrini et al.[13] studied praseodymium-doped $YAlO_3$, and they found that this material has fast UV fluorescence because of the allowed d−f transitions of Pr^{3+} but relatively low scintillation efficiency. Thus, praseodymium-doped KGdP crystals could be a novel alternative as a scintillator material because the photoluminescence generated by Pr^{3+} ions, after absorbing high-energetic photons by the crystal, in the visible and UV spectral regions through the $5d_1 \rightarrow {}^3H_4$ transition can be observed because of the low UV transparency cut-off of this material.

Moreover, nanocrystalline form allows the possibility to further prepare ceramic materials because of the larger activity in sintering from the nanoscale size[14−16] and also the almost isometric nature of the KGdP structure. In this work, the Pechini method has been used to synthesize KGdP nanocrystals, which previously was successfully used to prepare KNP nanocrystals.[17] This method yields inorganic oxides of excellent phase purity and well-controlled stoichiometry. It also allows obtaining ceramic powders with fine grain size at relatively low temperature through the formation of a polymeric organic net between a metallic acid chelate and a polyhydroxide alcohol by polyesterification. The polymeric network retains homogeneity on the atomic scale and reduces any segregation of the cations. Furthermore, the Pechini method allows to reach various compositions and to vary the nature and the concentration of the doping ion easily.[18−22]

Thus, the first aim of this work is the optimization of the synthesis conditions of type III KGdP nanocrystals doped with praseodymium by the modified Pechini method in order to obtain the nanocrystals in a single crystalline phase. The next goals are to achieve its physical characterization and then its optical spectroscopy to determine whether this material could be a new scintillator material.

2. EXPERIMENTAL SECTION

2.1. Synthesis of the Nanocrystals. A schematic diagram of the modified Pechini synthesis process used for the preparation of Pr:KGdP nanocrystals is shown in Scheme 1, and an illustration of the basic chemical reactions of the Pechini process[19,23] is shown in Scheme 2.

Powders of Pr_6O_{11} (Aldrich Chemical Company Inc., 99.9%), Gd_2O_3 (Aldrich, 99.9%), $NH_4H_2PO_4$ (Fluka Analytical, ≥99.0%), $(NH_4)_2HPO_4$ (Sigma-Aldrich, ≥98%), and K_2CO_3 anhydrous (Alfa Aesar, A Johnson Matthey Company, 99%) were used as starting materials. At first, stoichiometric amounts of Pr_6O_{11} and Gd_2O_3 are converted to the lanthanide nitrate into a quartz crucible by dissolution in concentrated HNO_3 (Merck, 65%) and heated at about 423 K under stirring to evaporate the liquid part. At the same time, stoichiometric amounts of K_2CO_3 and $NH_4H_2PO_4$ or $(NH_4)_2HPO_4$ are dissolved in distilled water into a glass beaker at 323 K.

After that, citric acid, CA, is added as a chelating agent to each container in a specific molar ratio (C_M = [CA]/[METAL]) to prepare metal-chelated CA. C_M describes the degree of the chelation process of the metal in the organic product.[21] To give rise to good reaction between the metal cations and CA, each container is heated at 348 K for 10−20 h under stirring and covered with a crystallizer. On the contrary to other modified Pechini methods used, in this case, we had to use two different containers to avoid the precipitation of gadolinium phosphate.[24] The quartz crucible with gadolinium and praseodymium nitrates is named container 1 and the glass beaker with K_2CO_3 and the phosphate precursor, $NH_4H_2PO_4$ or $(NH_4)_2PO_4$, is named container 2. Just after the incorporation of the CA, the pH in the chelation reaction in container 1 is 1 (pH_1 = 1); it is 2 in container 2 with $NH_4H_2PO_4$ as the phosphate precursor (pH_2 = 2); and the pH in container 2 with $(NH_4)_2PO_4$ as precursor is 3 (pH_2 = 3). Then, in order to study the effect of pH change in the chelation reaction in container 2, the pH_2 was varied by adding NH_4OH just after the incorporation of the CA in Exp. 8, and afterward, the result from this experiment was compared with others.

Scheme 1. Diagram of the Synthesis Process of Pr:KGdP Nanocrystals by the Modified Pechini Method

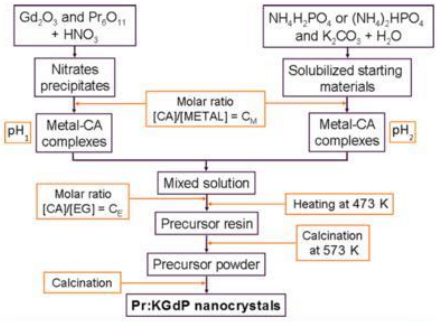

Then, the content of the two containers are joined in the quartz crucible and they are mixed at 373 K for 4 h under stirring and covered with a crystallizer.

Afterward, ethylene glycol, EG, is added as an esterification agent in a specific molar ratio (C_E = [CA]/[EG]) in order to obtain the polymeric resin. C_E describes the degree of esterification between the hydroxyl groups of EG and the carboxylic acid groups of CA.[21] For this purpose, the reagents are heated at 473 K in a sand bath without being covered and under stirring for 3−4 h. During this step, the viscosity of the product resin gradually increases until the resin gels;[22] at this time, the stirrer is removed. To obtain a drier resin, it is heated at the same temperature of 473 K for a 20 h. This reaction is considered finished when a whitish gel is observed at the bottom of the crucible.

The following step is an initial calcination at 573 K for several hours to start the decomposition of the resin. Thereafter, a product of spongy texture of shiny black color is obtained. To end, this product is grinded in an agate mortar and the resulting precursor powder is calcined at different temperatures in the range from 673 to 1073 K and at air atmosphere for several hours. After each calcination, the resulting powder is grinded in an agate mortar to promote easier removal of the organic parts. These calcinations were performed in a vertical muffle controlled by an Eurotherm temperature controller/programmer.

DOI: 10.1021/acsomega.8b01321
ACS Omega 2018, 3, 11307−11316

Scheme 2. Illustration of the Basic Chemical Reactions Involved in the Preparation of the Organic Precursor in the Modified Pechini Method

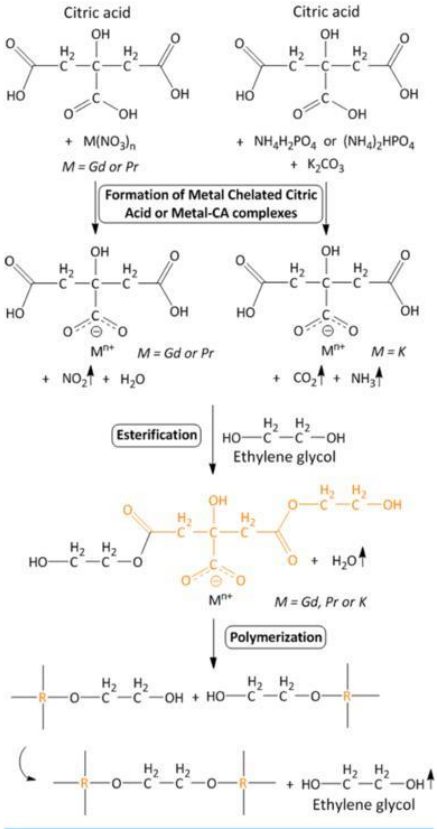

2.2. Characterization Techniques. The crystalline phases of the nanocrystals were identified by X-ray powder diffraction using a Siemens D5000 diffractometer with a Bragg−Brentano parafocusing geometry and vertical $\theta-\theta$ goniometer, fitted with a curved graphite diffracted-beam monochromator, incident and diffracted-beam Soller slits, a 0.06° receiving slit, and a scintillation counter as a detector. Cu Kα radiation was obtained from a copper X-ray tube operated at 40 kV and 30 mA. For conventional analysis, the X-ray powder diffraction patterns were collected from 5 to 70° of 2θ diffraction range with a step size (ss) of 0.05°, a step time (st) equal to 3 s, and sample rotation. For obtaining diffractograms with lower background noise and thus to be able to identify better the presence of undesirable phases or compounds, the data were collected in a 2θ diffraction range from 10 to 60° with a ss of 0.03°, a st equal to 7 s, and sample rotation. The unit cell parameters of the non-centrosymmetric phase were calculated using the Rietveld method.[25]

The chemical composition of the nanocrystals was measured quantitatively by electron probe microanalysis (EPMA) using a JEOL JXA-8230 electron microprobe. Before taking the measurements, the samples were prepared in tablet form and one of the two flat faces was sputtered with carbon, which acts as a conductor media to avoid the overcharge of the samples. The electron beam was generated at an intensity of 15 nA and an accelerating voltage of 15 kV. The concentrations of K, P, and O were determined using the Kα X-ray lines of K, P, and O, respectively, and the concentrations of Pr and Gd using the Lα X-ray lines of these elements. The measurement time for Pr was 60 s, while for the other elements was 10 s. In the case of Pr, the measurement time was higher because of its low atomic concentration in the KGdP host.

Differential thermal analysis (DTA) was used to study the thermal evolution of the nanocrystals with the temperature by using a TA Instruments SDT 2960 simultaneous differential scanning calorimetry−thermogravimetric analysis system. The heating rate was at 10 K/min with an air flux of 90 cm^3/min and the Al_2O_3 was used as a reference.

The morphology, size distribution, and homogeneity of the nanocrystals were observed using a transmission electron microscopy (TEM) JEOL JEM-1011 system with a MegaView III (Soft Imaging System). Previous to the observation of the nanocrystals by TEM, the samples were mixed with ethanol and subsequently were placed in an ultrasound bath for 50 min to reduce and disperse the agglomerates. The TEM images were observed using an accelerating voltage of 80 and 100 kV.

The optical absorption of the praseodymium ion in KGdP nanocrystals was studied by transmittance measurements at room temperature using a Cary 5000 UV−vis−NIR spectrophotometer. The optical absorption spectrum at room temperature of a plate of undoped KGdP single crystal was also obtained in order to help us to label the electronic transitions belonging to praseodymium, using the same apparatus. The undoped KGdP single crystal was grown by the top seeded solution growth—slow cooling technique as reported in Parreu et al.[26]

The emission spectra at room temperature of the Pr:KGdP nanocrystals under 445 nm excitation were obtained using a Cary Eclipse fluorescence spectrophotometer with a xenon lamp as the excitation source. The emission spectra at room temperature under X-ray excitation were performed using an X-ray tube with a copper target operating at 40 kV and 30 mA, available at Servei de Recursos Científics i Tècnics of the Universitat Rovira i Virgili. The X-ray radiation reached the pellet sample with an incident angle of 63° with respect to the pellet sample plane. The luminescence emitted from the sample was collected at 90° with respect to the pellet plane, focused with an UV fused silica biconvex lens, guided with an optical fiber, and detected by an Ocean Optics FLAME-S-UV-VIS-ES spectrometer with a spectral resolution of ∼1.5 nm.

3. RESULTS AND DISCUSSION

3.1. Synthesis of KGdP Nanocrystals. Tables 1 and 2 show a summary of the experimental parameters used in the synthesis experiments and the phases obtained. The column entitled as "proportion of phases" refers to the ratio qualitatively estimated between the following two crystalline phases of KGdP: type III (monoclinic, space group: $P2_1$) and type B phase (monoclinic, space group: $C2/c$). The number of

DOI: 10.1021/acsomega.8b01321
ACS Omega 2018, 3, 11307−11316

Table 1. Summary of the Experimental Parameters and the Observed Results in the Diffractogram Using $NH_4H_2PO_4$ as a Source of Phosphate Groups[b]

Exp.	C_M	C_E	calcination 1 [K-h]	calcination 2 [K-h]	phase $P2_1$	phase $C2/c$	proportion of phases	presence of other compounds
1	3	2	573-3	1073-3	×			yes
2a	3	2	573-8	973-10	×	×	$P2_1 \ll C2/c$	yes↑
2b				1073-10	×	×	$P2_1 \ll C2/c$	yes↑
3a	3	1	573-10	973-10	×	×	$P2_1 \ll C2/c$	no
3b				1073-10	×	×	$P2_1 \lll C2/c$	no
4a[a]	6	2	573-10	773-10	×	×	$P2_1 \lll C2/c$	no
4b[a]				873-10	×	×	$P2_1 \lll C2/c$	no
4c				973-10	×	×	$P2_1 \lll C2/c$	no
4d				1073-10	×	×	$P2_1 \lll\ll C2/c$	no
5a[a]	6	1	573-10	773-10	×	×	$P2_1 \ll C2/c$	no
5b[a]				873-10	×	×	$P2_1 \ll C2/c$	no
5c				973-10	×	×	$P2_1 \ll C2/c$	no
5d				1073-10	×	×	$P2_1 \lll C2/c$	no
6a[a]	3	2	573-10	773-10	×	×	$P2_1 \gg C2/c$	no
6b				873-10	×	×	$P2_1 \ggg C2/c$	yes
6c				973-10	×	×	$P2_1 \ggg C2/c$	yes↑
6d				1073-10	×	×	$P2_1 \gg C2/c$	yes↓

[a]Experiment whose diffractogram has a high background noise due to incomplete calcination. [b]In all cases, the atomic percentage of Gd substituted by Pr in KGdP is 1 at. % Pr, the pH in the chelation reaction in the quartz crucible with gadolinium and praseodymium nitrates is 1 ($pH_1 = 1$), and the pH in the glass beaker with K_2CO_3 and $NH_4H_2PO_4$ is 2 ($pH_2 = 2$).

Table 2. Summary of the Experimental Parameters and the Observed Results in the Diffractogram Using $(NH_4)_2HPO_4$ as a Source of Phosphate Groups[d]

Exp.	amount of Pr in KGdP [at. %]	pH_2[a]	calcination 2 [K-h]	calcination 3/4 [K-h]	phase $P2_1$	phase $C2/c$	proportion of phases	presence of other compounds
7a	1	3	773-10		×			yes
7b			673-10	823-10	×	×	$P2_1 \ggg C2/c$	yes↓
7c			873-10		×			yes
7d			723-10	873-5	×			yes↓
7e			973-10		×			yes↑
7f			1073-10		×	×	$P2_1 \gg C2/c$	yes
8a[b]	1	5[c]	823-10		×	×	$P2_1 \gg C2/c$	yes↑
8b			873-10		×	×	$P2_1 \gg C2/c$	no
8c			723-10	873-5	×	×	$P2_1 \gg C2/c$	yes↓
8d			723-10	873-5/873-10	×	×	$P2_1 \ggg C2/c$	yes
8e			973-10		×	×	$P2_1 \gg C2/c$	yes↑
8f			1073-10		×	×	$P2_1 \gg C2/c$	yes↑
9a	3	3	723-10	873-5	×	×	$P2_1 \ggg C2/c$	no
9b			773-10	873-5	×	×	$P2_1 \ggg C2/c$	no
10	5	3	773-10	873-7	×			no
11	10	3	773-10	873-7	×			no
12	0	3	773-10	873-7	×			no

[a]The pH was measured at the beginning of the chelation reaction in the glass beaker with $(NH_4)_2HPO_4$ and K_2CO_3 reagents. [b]Experiment whose diffractogram has a high background noise due to incomplete calcination. [c]This pH was achieved by adding NH_4OH just after the incorporation of the CA. [d]In all cases, $C_M = 3$, $pH_1 = 1$, $C_E = 2$, and a first calcination at 573 K for 10 h.

> or < symbols is related to the proportion between these two phases. Thus, $P2_1 > C2/c$ means that the intensity of the X-ray diffraction peaks of the $P2_1$ phase is only slightly higher than the corresponding to the $C2/c$ phase, while $P2_1 \ggg C2/c$ means that the $P2_1$ is clearly the majority phase and the $C2/c$ is a very minority phase. The column called "presence of other compounds" indicates the presence in the sample of compounds different from the KGdP type III and type B phases. Our interest lies in obtaining solely the type III phase (space group: $P2_1$) because the minor Gd−Gd interatomic distance in this crystalline phase is the longest one in comparison to the other two phases of KGdP (type IV and type B phases), resulting in a priori minor occurrence of the quenching by Ln^{3+} concentration in the process of emitting light by the optically active lanthanide ions (Ln^{3+}). The minor Gd−Gd interatomic distance is 6.59,[27] 6.316,[28] and 5.269 Å[29] for the type III, type IV and type B phases of KGdP, respectively. Besides, given that the average Gd−O interatomic distance into the Gd coordination polyhedron and its distortion are similar in the three crystalline phases,[27] the Ln^{3+} ions will experience similar interactions with the crystal field.[30] In addition, a distinctive feature of the type III phase is that it is a non-centrosymmetric crystalline phase, which allows it to have nonlinear optical properties. Figure 1 shows a projection of the type III KGdP crystalline structure parallel to the *b* crystallographic direction, in which the Gd coordination

DOI: 10.1021/acsomega.8b01321
ACS Omega 2018, 3, 11307−11316

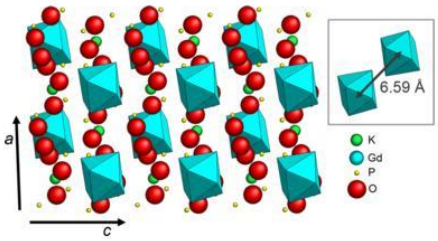

Figure 1. Projection of the type III $KGd(PO_3)_4$ structure parallel to the *b* crystallographic direction, showing the Gd coordination polyhedron and the shortest Gd−Gd interatomic distance.

polyhedron and the shortest Gd−Gd interatomic distance can be observed.

The experimental parameters of the first experiment were as follows: an atomic percentage of praseodymium doping ions of 1 at. %, $C_M = 3$, $C_E = 2$, a first calcination at 573 K for 3 h, and a second one at 1073 K for 3 h. As it can be observed in Figure 2, the obtained product in Exp. 1 corresponds to a mixture of

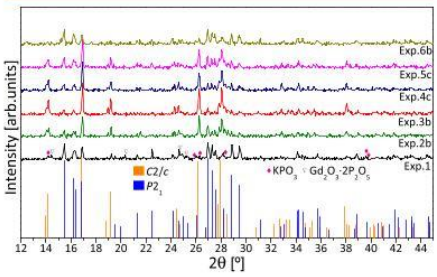

Figure 2. X-ray powder diffractogram pattern for two crystalline phases of KGdP and one experimental diffractogram of Pr:KGdP nanocrystals for each experiment from Exp. 1 to Exp. 6.

$Gd_2O_3{\cdot}2P_2O_5$ (JCPDS 35-0078), KPO_3 (JCPDS 35-0819), which have been identified as intermediate products, and KGdP ($P2_1$ phase). To provoke the complete synthesis of KGdP as a product and eliminate the presence of other compounds in the final product, the reaction times between the reactants in the chelating, esterification, and polymerization reactions (Scheme 2) under stirring were longer than in Exp. 1 and the time in the two calcinations was also elongated (Exp. 2, 3). The effect of the molar ratios C_M and C_E was also studied (Exp. 3−6). Almost in all these experiments, only KGdP product was obtained and its $C2/c$ phase was in a higher proportion than the $P2_1$ phase, as can be seen in Figure 2. Because there is an overlap of many peaks of the type IV phase pattern with the patterns of the type III and B phases, it is difficult to affirm or discard the presence of a low amount of the type IV phase (monoclinic, space group: $P2_1/n$) in these experiments. The ratio of the two majoritarian crystalline phases of KGdP is reverted in Exp. 6 when $C_M = 3$ and $C_E = 2$ are used. Thus, $C_M = 3$ and $C_E = 2$ seem to be the most suitable molar ratios for obtaining mainly the non-centrosymmetric crystalline phase of KGdP (space group: $P2_1$). From now on, all synthesis experiments were performed using these two molar ratios and a first calcination at 573 K for 10 h.

By comparing Exp. 6, 7, and 8, the effect of the pH change in the chelation reaction can be observed. As explained in the Experimental Section, when $NH_4H_2PO_4$ was used as the phosphate precursor (Exp. 6), the pH in this reaction was about $pH_2 = 2$. In order to have the reaction in a less acid medium, ammonium phosphate dibasic, $(NH_4)_2HPO_4$, was used as a source of phosphate groups, leading to an at least $pH_2 = 3$ during this reaction in Exp. 7. Finally, in Exp. 8, ammonium hydroxide, NH_4OH, was added just after the incorporation of CA in order to obtain a $pH_2 = 5$. First, it should be noted that the carboxylate ion functions effectively to form metal chelates, whereas the non-ionized carboxylic acid group is not an efficient donor group.[31] The concentration of the carboxylate ion is higher than the one of non-ionized carboxylic acid group when pH > pK_a.[32] Thus, because the logarithmic acid dissociation constant of the first proton of CA is $pK_{a1} = 3.13$ and of the second one is $pK_{a2} = 4.76$, CA is found with one carboxylate ion when pH is in the range 3.13−4.75 and with two carboxylate ions when pH is between 4.76 and 6.39.[33] Besides, it should also be noted that the esterification reaction needs to be catalyzed by acid and the non-ionized carboxylic acid group is required in order to have the carbonyl activated toward nucleophilic attack. Thus, a pH_2 of at least 3 seems to be the most suitable pH because pH_2 = 3.13−4.75 results in a molecule of CA with one carboxylate ion to prepare one metal−CA chelate and with two non-ionized carboxylic acid groups to give rise to the esterification reaction in order to obtain the polymeric organic network. This homogeneous formation of the polymeric network could contribute to obtain a single crystalline phase of KGdP, as it can be observed in Figure 3. Then, the conditions of Exp. 7 are more appropriate to form type III KGdP than the ones for Exp. 6 and 8.

By changing the calcination time, calcination temperature, and number of calcinations, the product obtained presents different ratios of the $P2_1$ and $C2/c$ crystalline phases and different quantity of subproducts. In the Exp. 7, it is observed by these changes in the calcination procedure than a lower temperature in the calcination 2, and the addition of a third

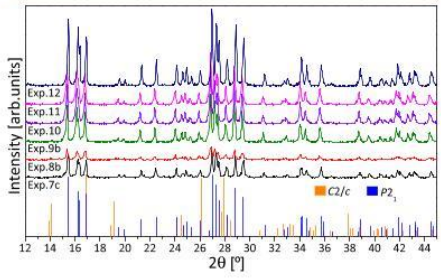

Figure 3. X-ray powder diffractogram pattern for two crystalline phases of KGdP and one experimental diffractogram of Pr:KGdP nanocrystals for each experiment from Exp. 7 to Exp. 12. The diffractograms 9b, 10, 11, and 12 belong to X-ray powder diffraction analysis with ss = 0.03° and st = 7 s.

DOI: 10.1021/acsomega.8b01321
ACS Omega 2018, 3, 11307−11316

calcination favors the obtaining of the $P2_1$ crystalline phase and the reduction of the presence of other phases in the final product. In the Exp. 9, 10, 11, and 12, besides change in the concentration of praseodymium of the obtained product, the temperatures and times of calcination 2 and calcination 3 were optimized till obtaining no presence of other compounds and only obtaining the $P2_1$ crystalline KGdP phase in the product. Thus, summarizing, the optimal conditions of calcination are a first calcination at 573 K for 10 h, a second calcination at 773 K for 10 h, and a third calcination at 873 K for 7 h.

Thus summarizing, the optimal parameters to synthesize $KGd_{1-x}Pr_x(PO_3)_4$ nanocrystals with a unique crystalline $P2_1$ phase by the modified Pechini method are $C_M = 1$ with a $pH_2 = 3$, $C_E = 2$, a reaction time between metal cations and CA of 10−20 h at 348 K under stirring (when the reagents are in two separate containers) followed by 4 h more at 373 K after mixing the content of the containers, a reaction time between metal−CA complexes and EG of around 4 h at 473 K in a sand bath under stirring followed by about 20 h more at the same temperature without stirring, a first calcination at 573 K for 10 h, a second one at 773 K for 10 h, and a third one at 873 K for 7 h.

3.2. Morphological Characterization and Particle Size Distribution. The morphology, size distribution, and homogeneity of the nanocrystals were observed by TEM. The particle size distribution was estimated using multiple TEM images as the pictures shown in Figure 4. In the same

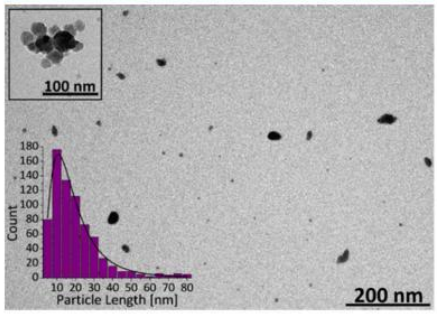

Figure 4. Representative TEM images of 5 at. % Pr:KGdP nanocrystals from Exp. 10 and the total particle size distribution.

figure, the histogram of the particle size distribution of 5 at. % Pr:KGdP nanocrystals is also shown. From the histogram, a predominance of small particles with sizes ranging from 10 to 20 nm can be observed. The distribution of the particle size can be fitted by a lognormal function, as expected in particles prepared by the Pechini method, in which their constitution follows the steps of nucleation, condensation, and crystal particle growth.[34,35]

3.3. Effects of Doping: Changes in Unit Cell Parameters with Praseodymium Doping. The unit cell parameters and unit cell volume of Pr:KGdP nanocrystals were refined by the Rietveld method.[25] Figure 5 shows the observed, calculated and differential X-ray powder diffraction profile obtained after Rietveld refinement of the 10 at. % Pr:KGdP nanocrystals, as an example. In Table 3, it can be seen how as the praseodymium content increases, the *a*, *b*, and *c* unit cell

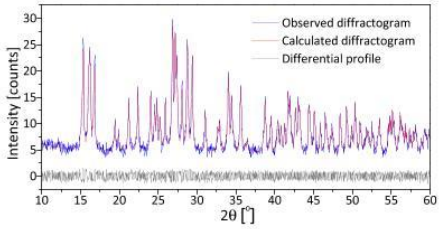

Figure 5. Observed, calculated and differential X-ray powder diffraction profile obtained after Rietveld refinement at room temperature of 10 at. % Pr:KGdP nanocrystals.

parameters and the unit cell volume *V* increase. However, the increase of the *a* unit cell parameter is very slight. This increase in the unit cell volume when Pr^{3+} is introduced as the doping ion in the KGdP structure was expected because the ionic radius of Pr^{3+} is higher than that of Gd^{3+} (ionic radii of Gd^{3+} and Pr^{3+} with coordination VIII are 1.053 and 1.126 Å, respectively[2]).

The atomic percentage of praseodymium with respect to gadolinium obtained by EPMA for the sample labeled as 3 at. % Pr:KGdP was 2.8 at. %, for 5 at. % Pr:KGdP was 4.9 at. %, and 8.9 at. % for the sample labeled as 10 at. % Pr:KGdP. The sample labeled as 1 at. % Pr:KGdP was not measured by EPMA because the amount of praseodymium is quite low; however, its atomic percentage with respect to gadolinium is expected to be similar to 1 at. %.

3.4. Thermal Analysis of the Nanocrystals. Figure 6 shows the DTA thermogram of type III 0, 5, and 10 at. % Pr:KGdP nanocrystals. By DTA of type III KGdP nanocrystals and considering a previous study[26] about how type III KGdP single crystal evolves with temperature between room temperature and 1273 K using DTA and X-ray powder diffraction, it was determined that type III KGdP nanocrystals melt incongruently at 1121 K. The incongruent melting point of type III KGdP single crystal is 1142 K, as reported in ref 26. Because the first ones are nanocrystals, a decrease of its incongruent melting point in relation to the bulk material was already expected, given that a higher surface to volume ratio results in a lower melting temperature.[36,37] From the same Figure 6, it could be observed that as praseodymium content in the nanocrystals increases, the incongruent melting point slightly decreases.

3.5. Optical Spectroscopy of Pr^{3+} in Pr:KGdP Nanocrystals. Figure 7a shows the transmittance spectra at room temperature of type III 5 at. % Pr:KGdP nanocrystals suspended in distilled water. In order to help us identify the absorption peaks observed in the transmittance spectra, the information obtained from the optical absorption spectrum at room temperature of a plate of undoped KGdP single crystal from 190 to 320 nm (Figure 7b) was used. In Figure 7b, by using the Dieke's diagram,[38,39] all the 4f → 4f electronic transitions of Gd^{3+} at wavelengths higher than 190 nm have been labeled. No other absorption belonging to Gd^{3+} can be observed at longer wavelengths than at 320 nm.

In Figure 7a, a broad and intense band centered at 218 nm and two small peaks centered at 445 and 482 nm can be seen. With regard to the intense broad band, it has been proposed that it belongs to the $^3H_4 \rightarrow 5d_1$ transition of Pr^{3+} because an

DOI: 10.1021/acsomega.8b01321
ACS Omega 2018, 3, 11307−11316

Table 3. Unit Cell Parameters and Unit Cell Volume *V* of Undoped KGdP and Pr-Doped KGdP Nanocrystals

real at. % Pr in KGdP	*a* [Å]	*b* [Å]	*c* [Å]	*β* [deg]	*V* [Å^3]
0	7.2486(3)	8.3505(3)	7.9204(3)	91.828(3)	479.17(3)
2.8	7.2488(4)	8.3517(4)	7.9215(4)	91.832(3)	479.32(4)
4.9	7.2509(4)	8.3553(5)	7.9247(4)	91.827(4)	479.86(5)
8.9	7.2512(3)	8.3575(4)	7.9285(4)	91.847(4)	480.23(4)

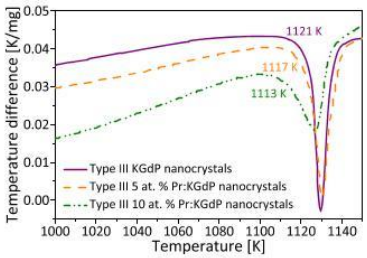

Figure 6. DTA thermogram of type III undoped, 5 and 10 at. % Pr:KGdP nanocrystals.

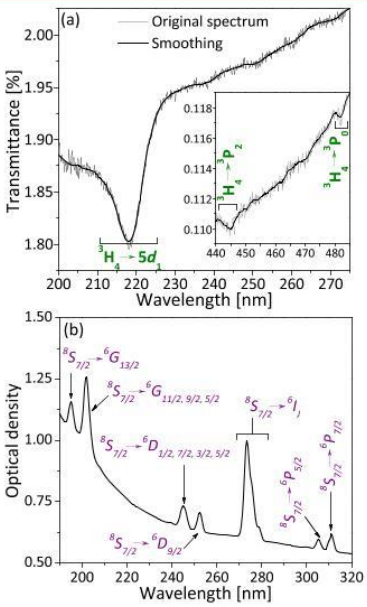

Figure 7. (a) Transmittance spectra of type III 5 at. % Pr:KGdP nanocrystals suspended in distilled water at room temperature. (b) Optical absorption spectrum of a plate of undoped KGdP single crystal at room temperature. In green, the labels corresponding to the electronic transitions of Pr^{3+} assigned to each observed band, and in purple, those corresponding to the electronic transitions of Gd^{3+}.

absorption transition of Gd^{3+} is not expected in this wavelength, as seen in Figure 7b. These 4f → 5d absorption transitions are electric dipole allowed transitions exhibiting very intense and broad bands, and besides, they appear in the spectral range of the vacuum ultraviolet and ultraviolet.[40,41] Thus, the wide transparency window of type III KGdP host allows us to observe the $^3H_4 \rightarrow 5d_1$ transition of Pr^{3+}. By using the Dieke's diagram,[38] the peaks which appear at 445 and 482 nm have been labeled as $^3H_4 \rightarrow {}^3P_2$ and $^3H_4 \rightarrow {}^3P_0$ electronic transitions of Pr^{3+}, respectively. The 4f → 4f absorption peak centered at 445 nm has the highest intensity of these two absorption transitions because of its quite large electric dipole oscillator strength because of its pseudo-hypersensitive nature.[41]

On the other hand, it is worth commenting that the 4f → 5d absorption transitions of Pr^{4+} in KGdP host are not observed in the spectral range of 180−325 nm. That is, because Pr^{4+} is isoelectronic with Ce^{3+}, similar results can be expected in the case of having the same host doped with Pr^{4+} or Ce^{3+}.[42] Hence, taking into account the work made by Zhong et al.,[43] the 4f → 5d absorption transitions of Ce^{3+} in KGdP host are found at 193, 209, 221, 245, and 307 nm for 4f → $5d_5$, 4f → $5d_4$, 4f → $5d_3$, 4f → $5d_2$, and 4f → $5d_1$ transitions of Ce^{3+}, respectively, so that it can be concluded that the 4f → 5d absorption transitions of Pr^{4+} are not observed in Figure 7. During the calcination process, the polymeric network is decomposed, leading to the formation of carbon oxides in addition to other calcination products, among them Pr:KGdP. The formation of CO as a calcinations product is expected.[44] According to the literature, CO can act as a reducing agent resulting in its oxidation by forming CO_2,[45] and in this case, its oxidation could promote the reduction of praseodymium from Pr^{4+} to Pr^{3+} because Pr^{4+} is a very powerful oxidizing agent.[46,47] Therefore, it is reasonable to assume that praseodymium ions are, in the final product, basically in Pr^{3+} form. Thus, the partial substitution of Gd^{3+} by Pr^{3+} in the crystalline network of KGdP will result in an electrically neutral structure, with higher stability than if Pr^{4+} was present.

Figure 8 shows the emission spectrum at room temperature of type III 5 at. % Pr:KGdP nanocrystals suspended in EG under 445 nm excitation. After exciting them at 445 nm ($^3H_4 \rightarrow {}^3P_2$ of Pr^{3+}), five emission peaks can be observed in the wavelength range from 590 to 850 nm. Such emission transitions belong to 4f → 4f transitions of Pr^{3+}. By comparing the obtained emission spectrum with the emission spectra of Pr^{3+} doped in $LaAlO_3$,[48] $NaGd(WO_4)_2$,[49] and $La_{1/2}Na_{1/2}TiO_3$[50] hosts as well as Bi^{3+} and Pr^{3+} co-doped lead silicate glasses[51] under Pr^{3+} 4f → 4f excitation and by using the Dieke's diagram,[38] the emission peaks have been labeled as $^1D_2 \rightarrow {}^3H_4$, $^3P_0 \rightarrow {}^3H_6$, $^3P_0 \rightarrow {}^3F_3$, $^3P_0 \rightarrow {}^3F_4$, and $^1D_2 \rightarrow {}^3F_2$. Because its photoluminescence under Pr^{3+} 4f → 4f excitation occurs from both $^3P_0$ and $^1D_2$ levels of Pr^{3+}, this means that the emission from the $^3P_0$ level is not quenched because of the presence of an intervalence charge transfer state between these two levels, as happens in perovskite titanates

DOI: 10.1021/acsomega.8b01321
ACS Omega 2018, 3, 11307−11316

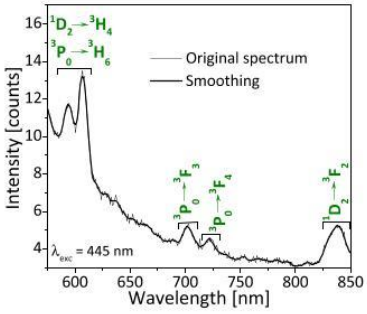

Figure 8. Emission spectrum of type III 5 at. % Pr:KGdP nanocrystals suspended in EG at room temperature under 445 nm excitation ($^3H_4 \rightarrow {}^3P_2$ of Pr^{3+}). In green, the labels corresponding to the electronic transitions of Pr^{3+} assigned to each observed band.

$R_{1/2}Na_{1/2}TiO_3:Pr^{3+}$ (R = La, Gd, Y, Lu)[50] and in Pr^{3+}- and Tb^{3+}-doped double tungstate crystals $KRE(WO_4)_2$ (RE = Y, Gd, Yb, Lu).[52]

Figure 9 shows the emission spectra at room temperature under X-ray excitation of type III Pr:KGdP nanocrystals

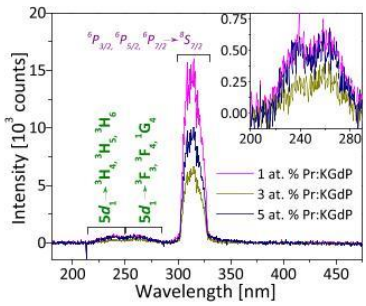

Figure 9. Emission spectra under X-ray excitation of type III 1, 3, and 5 at. % Pr:KGdP nanocrystals as a pellet at room temperature. In purple, the labels corresponding to the electronic transitions of Gd^{3+} assigned to the observed band, and in green, the labels corresponding to the electronic transitions of Pr^{3+} assigned to each observed band.

pressed in a pellet. The most intense band centered at 313 nm corresponds to the $^6P_{3/2}$, $^6P_{5/2}$, $^6P_{7/2} \rightarrow {}^8S_{7/2}$ transitions of Gd^{3+}. The low intensity bands centered at around 239 and 261 nm belong to the $5d_1 \rightarrow {}^3H_4$, $^3H_5$, $^3H_6$ and $5d_1 \rightarrow {}^3F_3$, $^3F_4$, $^1G_4$ transitions of Pr^{3+}, respectively, and as mentioned earlier, the 5d → 4f transitions of lanthanide ions are of special interest for scintillation applications. The level transition assignation has been done using the Dieke's diagram[38] and taking into account that the energy difference from the $5d_1$ level of Pr^{3+} in type III KGdP host to the $^3H_4$ level is about 45 872 cm^{-1} (5.69 eV, 218 nm). As can be seen in the same figure, there is a different behavior depending on the praseodymium content. Hence, the composition that seems to be the most interesting for scintillation applications is type III KGdP nanocrystals doped with 5 at. % of Pr because the intensity of the bands corresponding to the $5d_1 \rightarrow$ 4f transitions of Pr^{3+} is the highest and at the same time that the band corresponding to the 4f → 4f transitions of Gd^{3+} is not so intense.

4. CONCLUSIONS

The present paper reports on obtaining type III Pr:$KGd(PO_3)_4$ nanocrystals by the modified Pechini method for first time up to now. As previously stated, the optimal parameters to synthesize Pr:$KGd(PO_3)_4$ nanocrystals with a unique crystalline phase, type III phase (space group: $P2_1$), by the modified Pechini method are $C_M = 3$ with a $pH_2 = 3$, $C_E = 2$, a reaction time between metal cations and CA of 10−20 h at 348 K under stirring followed by 4 h more at 373 K after mixing the content of the two containers, a reaction time between metal−CA complexes and EG of around 4 h at 473 K in a sand bath under stirring followed by about 20 h more at the same temperature without stirring, a first calcination at 573 K for 10 h, a second one at 773 K for 10 h, and a third one at 873 K for 7 h. By using TEM, a predominance of the nanocrystals with sizes ranging from 10 to 20 nm has been observed.

From the transmittance measurements, it has been found that the $^3H_4 \rightarrow 5d_1$ transition of Pr^{3+} in type III Pr:$KGd(PO_3)_4$ nanocrystals appears as a broad and intense absorption band centered at 218 nm. In the emission spectra of these nanocrystals under X-ray excitation, several $5d_1 \rightarrow$ 4f transitions of Pr^{3+} and the $^6P_{3/2}$, $^6P_{5/2}$, $^6P_{7/2} \rightarrow {}^8S_{7/2}$ transitions of Gd^{3+} have been observed. Therefore, the $5d_1$ level of Pr^{3+} is located within the forbidden band gap of type III $KGd(PO_3)_4$, a fact that was expected due to the wide transparency window of the host.

Despite the lower intensity of the bands corresponding to the $5d_1 \rightarrow$ 4f transitions of Pr^{3+} in comparison with the band corresponding to the 4f → 4f transitions of Gd^{3+}, it would be interesting to excite the nanocrystals under direct f−d excitation to obtain the decay time curves from the $5d_1$ level as well as to excite once again with high-energy radiation to widely study their scintillation properties.

AUTHOR INFORMATION

Corresponding Author

*E-mail: rosam.sole@urv.cat. Phone: +34 977558787.

ORCID

Rosa Maria Solé: 0000-0002-5769-4141

Author Contributions

The manuscript was written through contributions of all authors. All authors have given approval to the final version of the manuscript.

Notes

The authors declare no competing financial interest.

ACKNOWLEDGMENTS

The authors acknowledge the financial support from the Spanish Government under Projects MAT2016-75716-C2-1-R (AEI/FEDER, UE) and TEC 2014-55948-R and from the Catalan Government under Projects 2014 SGR 1358 and 2017 SGR 755. I.A. thanks the Catalan Government for the financial support under grants 2015 FI_B 00711, 2016 FI_B1 00113, and 2017 FI_B2 00017 as well.

DOI: 10.1021/acsomega.8b01321
ACS Omega 2018, 3, 11307−11316

REFERENCES

(1) Parreu, I. Crystal Growth and Characterization of Ytterbium or Neodymium Doped Type III-KGd$(PO_3)_4$. A New Bifunctional Nonlinear and Laser Crystal. Ph.D. Thesis, Rovira i Virgili University, 2006.
(2) Shannon, R. D. Revised Effective Ionic Radii and Systematic Studies of Interatomic Distances in Halides and Chalcogenides. *Acta Crystallogr., Sect. A: Cryst. Phys., Diffr., Theor. Gen. Crystallogr.* **1976**, *32*, 751−767.
(3) Oudahmane, A.; Daoud, M.; Tanouti, B.; Avignant, D.; Zambon, D. KPr(PO3)4. *Acta Crystallogr., Sect. E: Struct. Rep. Online* **2010**, *66*, i59−i60.
(4) Wickleder, M. S. Inorganic Lanthanide Compounds with Complex Anions. *Chem. Rev.* **2002**, *102*, 2011−2088.
(5) Solé, R. M.; Pujol, M. C.; Massons, J.; Aguiló, M.; Díaz, F.; Brenier, A. Growth, anisotropic spectroscopy and laser operation of the monoclinic Nd:KGd(PO3)4crystal. *J. Phys. D: Appl. Phys.* **2015**, *48*, 495502.
(6) Nedelec, J. M. Sol-Gel Processing of Nanostructured Inorganic Scintillating Materials. *J. Nanomater.* **2007**, *2007*, 1−8.
(7) Moses, W. W. Scintillator Requirements for Medical Imaging. Presented at the *5th International Conference on Inorganic Scintillators and Their Applications (SCINT99)*, Moscow, Russian Federation, Aug 16−20, 1999; LBNL-4580.
(8) Conti, M. State of the Art and Challenges of Time-of-flight PET. *Phys. Med.* **2009**, *25*, 1−11.
(9) Cherry, S. R. The 2006 Henry N. Wagner Lecture: Of Mice and Men (and Positrons)—Advances in PET Imaging Technology. *J. Nucl. Med.* **2006**, *47*, 1735−1745.
(10) Liu, B.; Shi, C. Development of Medical Scintillator. *Chin. Sci. Bull.* **2002**, *47*, 1057−1063.
(11) Ogiegło, J. M.; Zych, A.; Jüstel, T.; Meijerink, A.; Ronda, C. R. Luminescence and Energy Transfer in $Lu_3Al_5O_{12}$ Scintillators Co-doped with Ce^{3+} and Pr^{3+}. *Opt. Mater.* **2013**, *35*, 322−331.
(12) García-Murillo, A.; Le Luyer, C.; Garapon, C.; Dujardin, C.; Bernstein, E.; Pedrini, C.; Mugnier, J. Optical Properties of Europium-Doped Gd_2O_3 Waveguiding Thin Films Prepared by the Sol-Gel Method. *Opt. Mater.* **2002**, *19*, 161−168.
(13) Pedrini, C.; Bouttet, D.; Dujardin, C.; Moine, B.; Dafinei, I.; Lecoq, P.; Koselja, M.; Blazek, K. Fast Fluorescence and Scintillation of Pr-Doped Yttrium Aluminum Perovskite. *Opt. Mater.* **1994**, *3*, 81−88.
(14) Podhorodecki, A.; Gluchowski, P.; Zatryb, G.; Syperek, M.; Misiewicz, J.; Lojkowski, W.; Strek, W. Influence of Pressure-Induced Transition from Nanocrystals to Nanoceramic Form on Optical Properties of Ce-Doped Y3Al5O12. *J. Am. Ceram. Soc.* **2011**, *94*, 2135−2140.
(15) Trojan-Piegza, J.; Gierlotka, S.; Zych, E.; Lojkowski, W. Spectroscopic Studies of Nanopowder and Nanoceramics La2Hf2O7:Pr Scintillator. *J. Am. Ceram. Soc.* **2014**, *97*, 1595−1601.
(16) Pankratov, V.; Grigorjeva, L.; Chernov, S.; Chudoba, T.; Lojkowski, W. Luminescence Properties and Energy Transfer Processes in Nanosized Cerium Doped YAG. *IEEE Trans. Nucl. Sci.* **2008**, *55*, 1509−1513.
(17) Tkaczyk, S.; Galceran, M.; Kret, S.; Pujol, M. C.; Aguiló, M.; Díaz, F.; Reshak, A. H.; Kityk, I. V. UV-Excited Piezo-Optical Effects in Oxide Nanocrystals Incorporated into PMMA Matrices. *Acta Mater.* **2008**, *56*, 5677−5684.
(18) Pechini, M. P. Method of Preparing Lead and Alkaline Earth Titanates and Niobates and Coating Method using the Same to Form a Capacitor. U.S. Patent 3,330,697, North Adams, Massachusetts, 1967.
(19) Liu, W.; Forrington, C. C.; Chaput, F.; Dunn, B. Synthesis and Electrochemical Studies of Spinel Phase LiMn[sub 2]O[sub 4] Cathode Materials Prepared by the Pechini Process. *J. Electrochem. Soc.* **1996**, *143*, 879−884.
(20) Pimentel, P. M.; Martinelli, A. E.; de Araújo Melo, D. M.; Pedrosa, A. M. G.; Cunha, J. D.; da Silva Júnior, C. N. Pechini Synthesis and Microstructure of Nickel-Doped Copper Chromites. *Mater. Res.* **2005**, *8*, 221−224.
(21) Galceran, M.; Pujol, M. C.; Aguiló, M.; Díaz, F. Sol-gel modified Pechini method for obtaining nanocrystalline KRE(WO4)2 (RE = Gd and Yb). *J. Sol-Gel Sci. Technol.* **2007**, *42*, 79−88.
(22) Morrissey, A. L. Preparation of High Purity Doped Oxides for Fundamental Studies. Ph.D. Thesis, Colorado School of Mines, 2013.
(23) Kwon, S. W.; Park, S. B.; Seo, G.; Hwang, S. T. Preparation of Lithium Aluminate Via Polymeric Precursor Routes. *J. Nucl. Mater.* **1998**, *257*, 172−179.
(24) Lessing, P. A.; Erickson, A. W. Synthesis and Characterization of Gadolinium Phosphate Neutron Absorber. *J. Eur. Ceram. Soc.* **2003**, *23*, 3049−3057.
(25) Rietveld, H. M. A Profile Refinement Method for Nuclear and Magnetic Structures. *J. Appl. Crystallogr.* **1969**, *2*, 65−71.
(26) Parreu, I.; Solé, R.; Gavaldà, J.; Massons, J.; Díaz, F.; Aguiló, M. Crystal Growth, Structural Characterization, and Linear Thermal Evolution of KGd(PO3)4. *Chem. Mater.* **2005**, *17*, 822−828.
(27) Parreu, I.; Carvajal, J. J.; Solans, X.; Díaz, F.; Aguiló, M. Crystal Structure and Optical Characterization of Pure and Nd-Substituted Type III KGd(PO3)4. *Chem. Mater.* **2006**, *18*, 221−228.
(28) Rekik, W.; Naïli, H.; Mhiri, T. Potassium gadolinium polyphosphate, KGd(PO3)4. *Acta Crystallogr., Sect. C: Struct. Chem.* **2004**, *60*, i50−i52.
(29) Ettis, H.; Naïli, H.; Mhiri, T. Synthesis and Crystal Structure of a New Potassium−Gadolinium Cyclotetraphosphate, KGdP4O12. *Cryst. Growth Des.* **2003**, *3*, 599−602.
(30) Rodnyi, P. A. Gadolinium-Containing Crystals. *Physical Processes in Inorganic Scintillators*; CRC Press LLC: Boca Raton, FL, 1997; pp 162−163.
(31) Lindsay, R. C. Food Additives: Chelating Agents (Sequestrants). In *Food Chemistry*, 3rd ed.; Fennema, O. R., Ed.; Marcel Dekker Inc.: New York, 1996; pp 778−780.
(32) Aguilar Sanjuán, M. Desplazamiento de una Reacción Ácido-Base en Función del pH. *Introducción a los Equilibrios Iónicos*, 2nd ed.; Reverté: Barcelona, Spain, 1999; pp 15−16.
(33) Ionization Constants of Organic Acids in Aqueous Solution. In *CRC Handbook of Chemistry and Physics*, 95th ed.; Haynes, W. M., Ed.; CRC Press Taylor & Francis Group: Boca Raton, FL, 2014; pp 5−98.
(34) Granqvist, C. G.; Buhrman, R. A. Ultrafine Metal Particles. *J. Appl. Phys.* **1976**, *47*, 2200−2219.
(35) Söderlund, J.; Kiss, L. B.; Niklasson, G. A.; Granqvist, C. G. Lognormal Size Distributions in Particle Growth Processes without Coagulation. *Phys. Rev. Lett.* **1998**, *80*, 2386−2388.
(36) Galceran, M.; Pujol, M. C.; Carvajal, J. J.; Tkaczyk, S.; Kityk, I. V.; Díaz, F.; Aguiló, M. Synthesis and characterization of KTiOPO4nanocrystals and their PMMA nanocomposites. *Nanotechnology* **2009**, *20*, 035705.
(37) Bhatt, S.; Kumar, M. Effect of Size and Shape on Melting and Superheating of Free Standing and Embedded Nanoparticles. *J. Phys. Chem. Solids* **2017**, *106*, 112−117.
(38) Dieke, G. H.; Crosswhite, H. M. The Spectra of the Doubly and Triply Ionized Rare Earths. *Appl. Opt.* **1963**, *2*, 675−686.
(39) Wegh, R. T.; Donker, H.; Meijerink, A.; Lamminmäki, R. J.; Hölsä, J. Vacuum-ultraviolet spectroscopy and quantum cutting forGd3+inLiYF4. *Phys. Rev. B: Condens. Matter Mater. Phys.* **1997**, *56*, 13841−13848.
(40) Dorenbos, P. The 5d Level Positions of the Trivalent Lanthanides in Inorganic Compounds. *J. Lumin.* **2000**, *91*, 155−176.
(41) Pujol, M. C. Obtenció i Caracterització de Cristalls Monoclínics de $KGd(WO_4)_2$ Substituïts amb Lantànids. Ph.D. Thesis, Rovira i Virgili University, 2000.
(42) Pawlak, D.; Frukacz, Z.; Mierczyk, Z.; Suchocki, A.; Zachara, J. Spectroscopic and crystallographic studies of YAG:Pr4+ single crystals. *J. Alloys Compd.* **1998**, *275*−*277*, 361−364.
(43) Zhong, J.; Liang, H.; Lin, H.; Han, B.; Su, Q.; Zhang, G. Effects of crystal structure on the luminescence properties and energy transfer

DOI: 10.1021/acsomega.8b01321
ACS Omega 2018, 3, 11307−11316

between Gd3+ and Ce3+ ions in MGd(PO3)4:Ce3+ (M = Li, Na, K, Cs). *J. Mater. Chem.* **2007**, *17*, 4679−4684.
(44) Braun, E.; Levin, B. C. Polyesters: A review of the literature on products of combustion and toxicity. *Fire Mater.* **1986**, *10*, 107−123.
(45) Brackmann, R.; Toniolo, F. S.; Schmal, M. Synthesis and Characterization of Fe-Doped CeO2 for Application in the NO Selective Catalytic Reduction by CO. *Top. Catal.* **2016**, *59*, 1772−1786.
(46) Cotton, F. A.; Wilkinson, G. Other Tetravalent Compounds. *Advanced Inorganic Chemistry*, 3rd ed.; John Wiley & Sons: New York, 1972; p 1073.
(47) Kiebach, W.-R.; Chatzichristodoulou, C.; Larsen Werchmeister, R. M.; Hagen, A. Determination of Redox-Active Centers in Praseodymium Doped Ceria by In Situ-XANES Spectroscopy. *Chem. Phys. Lett.* **2012**, *537*, 80−83.
(48) Dudek, M.; Jusza, A.; Anders, K.; Lipińska, L.; Baran, M.; Piramidowicz, R. Luminescent properties of praseodymium doped Y2O3 and LaAlO3 nanocrystallites and polymer composites. *J. Rare Earths* **2011**, *29*, 1123−1129.
(49) Durairajan, A.; Thangaraju, D.; Moorthy Babu, S.; Valente, M. A. Luminescence Characterization of Sol-Gel Derived Pr^{3+} Doped $NaGd(WO_4)_2$ Phosphors for Solid State Lighting Applications. *Mater. Chem. Phys.* **2016**, *179*, 295−303.
(50) Boutinaud, P.; Sarakha, L.; Mahiou, R.; Dorenbos, P.; Inaguma, Y. Intervalence charge transfer in perovskite titanates R1/2Na1/2TiO3:Pr3+ (R=La, Gd, Y, Lu). *J. Lumin.* **2010**, *130*, 1725−1729.
(51) Suresh, B.; Purnachand, N.; Zhydachevskii, Y.; Brik, M. G.; Reddy, M. S.; Suchocki, A.; Piasecki, M.; Veeraiah, N. Influence of Bi3+ ions on the amplification of 1.3μm emission of Pr3+ ions in lead silicate glasses for the applications in second telecom window communications. *J. Lumin.* **2017**, *182*, 312−322.
(52) Boutinaud, P.; Bettinelli, M.; Diaz, F. Intervalence charge transfer in Pr3+- and Tb3+-doped double tungstate crystals KRE(WO4)2 (RE=Y, Gd, Yb, Lu). *Opt. Mater.* **2010**, *32*, 1659−1663.

DOI: 10.1021/acsomega.8b01321
ACS Omega 2018, 3, 11307−11316

Paper IV

Radioluminescence properties under X-ray excitation of type III Ce^{3+}- and Pr^{3+}-doped $KGd(PO_3)_4$ single crystals

I. Adell, M. C. Pujol, R. M. Solé, M. Aguiló and F. Díaz

submitted to The Journal of Physical Chemistry C

UNIVERSITAT ROVIRA I VIRGILI
CE OR PR-DOPED TYPE III KGD(PO3)4 CRYSTALLINE MATERIALS. GROWTH AND CHARACTERIZATION AS SCINTILLATORS
Irina Adell Barbarà

Radioluminescence Properties under X-ray Excitation of Type III Ce^{3+}- and Pr^{3+}-Doped $KGd(PO_3)_4$ Single Crystals

Irina Adell, Maria Cinta Pujol, Rosa Maria Solé*, Magdalena Aguiló, and Francesc Díaz*

Universitat Rovira i Virgili, Departament Química Física i Inorgànica, Física i Cristal·lografia de Materials i Nanomaterials (FiCMA-FiCNA) - EMaS, Campus Sescelades, c/Marcel·lí Domingo, 1, E-43007 Tarragona, Spain.

ABSTRACT: Currently, the research for new scintillator materials with improved properties is gaining growing interest due to their great variety of applications (including medical diagnosis). Here, bulk single crystals of type III Ce:$KGd(PO_3)_4$ and Pr:$KGd(PO_3)_4$ (Ce:KGdP and Pr:KGdP) have been successfully grown with high crystalline quality. Radioluminescence studies of these crystals under synchrotron X-ray excitation have been carried out showing down-conversion processes, being of great interest for scintillation applications. Concretely, in Ce:KGdP crystals, an intense band between 300 and 385 nm, corresponding to the $5d_1 \rightarrow {}^2F_{5/2},{}^2F_{7/2}$ transitions of Ce^{3+} in type III KGdP, is observed. The absence of the ${}^6P_J \rightarrow {}^8S_{7/2}$ transitions of Gd^{3+} (~312 nm) can be ascribed to an efficient energy transfer from Gd^{3+} to Ce^{3+}. In Pr:KGdP crystals, the emission bands corresponding to the $5d_1 \rightarrow {}^3H_{4,5,6},{}^3F_2$ and $5d_1 \rightarrow {}^3F_{3,4},{}^1G_4$ transitions of Pr^{3+} in type III KGdP

appear centred at 236 and 259 nm, respectively. In undoped and Pr^{3+}-doped KGdP crystals, a change in coloration in the irradiated regions was observed after prolonged X-ray irradiation, which could be related to the presence of colour centres. On the contrary, there is evidence to conclude that the Ce^{3+}-doped KGdP crystals do not suffer from radiation damage.

1. INTRODUCTION

Lanthanide-doped crystals, especially doped with Ce^{3+} and Pr^{3+} ions, are interesting materials for extrinsic luminescence scintillator materials. Already commercial cerium and praseodymium-doped crystals are applied as basis for many radiation detection systems. The scintillation properties required for the detectors depend on the specific application.[1] Bulk inorganic scintillators are a key component of nuclear imaging detectors,[2] surgical gamma probes,[3] X-ray imaging arrays,[4] among others. The operation of a scintillator detector is characterized by the conversion of incident high-energy photons into flashes of ultraviolet-visible light by the action of a solid inorganic scintillator material. The scintillation light, which is desirable to be proportional to the absorbed photon energy, is converted to an electrical output signal by UV-visible detectors as silicon photomultipliers.[1] Typical inorganic scintillators which could be used are: Tl:NaI, Tl:CsI, $Bi_4Ge_3O_{12}$ (BGO), lutetium and gadolinium oxyorthosilicates Lu_2SiO_5 and Gd_2SiO_5 (LSO, GSO), cadmium tungstate $CdWO_4$ (CWO), yttrium and lutetium aluminium perovskite Ce:YAP and Ce:LuAP, and cerium-doped $LaCl_3$ and $LaBr_3$. Already commercial cerium and praseodymium-doped dielectric crystals can be potentially applied for many radiation devices. However, several shortcomings in these crystals could be improved and for this reason the search for cerium and praseodymium doped novel wide band gap materials is still currently done.

The interest of scintillator lanthanide-doped crystals is focused on those emissions that correspond to $5d \rightarrow 4f$ transitions, and not the $4f \rightarrow 4f$ transitions. In the $5d \rightarrow 4f$ transitions of Ce^{3+}, there is a fast luminescence decay time in the order of a few nanoseconds.[5] Also, there is interest in scintillator applications for the Pr^{3+} transitions from its $5d_1$ level because it has even a shorter lifetime than Ce^{3+}, as for example of about 6 ns in the crystal of the present study, the type III $KGd(PO_3)_4$.[6]

Among the oxide crystalline scintillator materials that are being investigated recently, the polyphosphates are interesting due to their large optical transparency window, the relatively large Ln^{3+}-Ln^{3+} distance allowing high doping levels with reduced concentration quenching effect, and the possibility of being prepared in both bulk single crystal and micro and nanopowder. As pointed out by Shalapska *et al.*,[7] Gd stoichiometric scintillator materials when doped with Ce^{3+} are promising due to the existence of the possibility of energy transfer from the Gd^{3+} ions constituting the host to the Ce^{3+} doping ions. Previous results about the potential of Ce-doped condensed phosphates as scintillator materials are found in the same paper of Shalapska *et al.* studying the compounds $LiREP_4O_{12}$ (RE= Gd and Y) and $NaGdP_4O_{12}$, and Zhong *et al.* for $NaGd(PO_3)_4$.[8] Fewer reports can be found in these hosts when they are doped with Pr^{3+}.[9,10,11]

In this work, we report on the study of X-ray excited radioluminescence of single-doped Ce:$KGd(PO_3)_4$ (hereafter Ce.KGdP) and Pr:$KGd(PO_3)_4$ (hereafter Pr: KGdP) bulk single crystals with the non-centrosymmetric (type III phase) crystalline structure. The present spectroscopic study will contribute to the knowledge of the potential of this family of polyphosphate crystals for scintillator applications. The crystal growth technique applied leads to centimetre crystals whose size can be compatible with mid and small sized scintillators detectors.

2. EXPERIMENTAL SECTION

2.1. Bulk single crystal growth

Ce:KGdP and Pr:KGdP single crystals with type III non-centrosymmetric crystalline structure (space group: $P2_1$) and doping levels up to 1 at. % in the case of Ce^{3+} and 5 at. % in the case of Pr^{3+} substituting Gd^{3+} in the solution have been grown from high temperature solutions.

The initial reagents used were K_2CO_3 anhydrous (Alfa Aesar, 99%), Gd_2O_3 (Aldrich, 99.9%), $Ce_2(CO_3)_3$ (Aldrich, 99.9%), Pr_2O_3 (Alfa Aesar, 99.9 %) and $NH_4H_2PO_4$ (Fluka Analytical, ≥99.0%). The solution compositions were 36 mol % of K_2O, 4 mol % of the sum of Gd_2O_3 plus the doping element (Ce_2O_3 or Pr_2O_3) and 60 mol % of P_2O_5. These compositions were chosen taking into account the primary crystallization region of KGdP in the K_2O–Gd_2O_3–P_2O_5 system.[12] The weight of the solutions was around 100 g for Ce:KGdP and 130 g for Pr:KGdP, and they were prepared in platinum cylindrical crucibles of 40 and 50 mm in diameter, respectively. The high level of dynamic viscosity of the solutions (around 19 Pa·s)[13] makes difficult the solution mixing and homogenization. Thus, to improve the mixing of the solution, high thermal gradients were used, around 1.1-3.0 $K \cdot mm^{-1}$ in depth with the coolest point at the central part of the surface of the solution. Simultaneously, a Pt stirrer (18-20 mm in diameter), immersed 12-14 mm in the solution and rotating with a common axis and the same angular velocity than the crystal, was used. The crystal seed was located at 10-12 mm from the centre of the solution. The seeds were cut with a^* orientation from KGdP single crystals and were placed in contact with the solution surface with the b crystallographic direction tangent to the rotation movement and c^* in radial direction. The stirrer-crystal system rotated at 55 rpm with changing the rotation direction every 50 s.

After homogenizing the solution, its saturation temperature was accurately measured by studying the growth/dissolution rates at different temperatures near the saturation one. After that, starting from this temperature, the solution was slowly cooled at rates of 0.05-0.1 $K \cdot h^{-1}$ for 25-30 K to grow the crystal. Finally, the grown crystal was slowly pulled out from the liquid and cooled to room temperature at a rate of 20-25 $K \cdot h^{-1}$.

The Ce and Pr content of the crystals was determined by Electron Probe Microanalysis (EPMA) with Wavelength Dispersive Spectroscopy (WDS) using a JEOL JXA-8230. In these measurements, the accelerating voltage was 20 kV and the current 20 nA. Table 1 shows the measurement conditions used in EPMA-WDS. Using these conditions, the detection limit of Ce was 195 ppm and that of Pr was 105 ppm.

Table 1. Measurement Conditions Used in EPMA-WDS Analysis

Element	Standard	X-ray line	Dispersive crystal*	Measuring time peak / background (s)
K	KGdP	Kα	PETJ / PETJ	10 / 5
Gd	KGdP	Lα	LIFH / LIFL	10 / 5
P	KGdP	Kα	PETL / PETH	10 / 5
O	KGdP	Kα	LDE1 / LDE1	10 / 5
Ce	CeO_2	Lα	PETL / -	120 / 60
Pr	REE-1	Lα	- / LIFL	100 / 50

* On the left, the dispersive crystals used to measure the Ce:KGdP samples, and on the right, those used for the Pr:KGdP samples.

The distribution coefficient of Ce^{3+} and Pr^{3+} substituting Gd^{3+} in KGdP was obtained from the EPMA results and applying the formula: $K_{Ln}=([Ln]/([Ln]+[Gd]))_{crystal}/([Ln]/([Ln]+[Gd]))_{solution}$, where Ln=$Ce^{3+}$ or Pr^{3+}, and [ ] means the concentration of the element in atomic per cent.

2.2. Optical characterization

2.2.1. X-ray excited radioluminescence (RL)

The samples for optical characterization were obtained by cutting and polishing slices from the bulk single crystals obtained in this work. The slices were cut perpendicular to the c^* crystallographic direction. Ce:KGdP and Pr:KGdP with different doping levels as well as undoped KGdP single crystals were excited under several X-ray energies provided by BL22-CLAESS beamline of ALBA Synchrotron. The synchrotron radiation reached to the sample with a 45º incident angle and the radiation emitted by the sample was collected at 90º from the excitation radiation. The emitted radiation was focused using an UV fused silica biconvex lens, guided with an optical fibre and detected by an Ocean Optics FLAME-S-UV-VIS-ES spectrometer with a spectral resolution of ~1.5 nm. The emission was recorded in the range from 180 to 870 nm.

The range of energies available at BL22-CLAESS beamline of ALBA Synchrotron is from 2400 to 63000 eV. Up to 18 different excitation energies were chosen to observe whether there are differences among the RL spectra. These excitation energies are 10000, 11000, 12000, 13000, 15200, 16500, 20000, 24800, 26700, 31000, 34500, 35500, 40443, 41991, 46000, 50239, 56000 and 62500 eV. The values 40443, 41991 and 50239 eV correspond to the electron binding energies of the K label (orbital: 1s) of cerium, praseodymium and gadolinium, respectively.[14] The value 26700 eV corresponds to the band belonging to the X-ray continuum radiation (Bremsstrahlung) from a Cu source operating at 39 kV.[15] The energy value of 24800 eV

corresponds to the band belonging to the X-ray continuum radiation emitted by a Mo anode of an X-ray tube operating at 35 kV.[16] The other excitation energies have been chosen to cover the whole range of energies available and thus obtain a more complete study. The emission intensities of the RL spectra have been corrected by dividing them by the number of photons coming from the synchrotron radiation per second, which depend on the excitation energy.

2.2.2. Optical absorption

The optical absorption at room temperature was studied before and after exciting the samples by X-ray radiation in order to study the possible effects of X-rays on the samples. The measurements were carried out in the range from 190 to 800 nm. The equipment used was an Agilent Cary 5000 UV-Vis-NIR spectrophotometer.

3. RESULTS AND DISCUSSION

3.1. Bulk single crystal growth

The Ce:KGdP and Pr:KGdP single crystals obtained, with doping levels up to 1 at. % of Ce^{3+} and 5 at. % of Pr^{3+} substituting Gd^{3+} in the KGdP host, generally were transparent and without inclusions or other macroscopic defects. The dimensions of the Ce:KGdP crystals along $a^* \times b \times c^*$ directions were 3.1-6.1 mm × 9.9-15.7 mm × 9.9-13.3 mm, their weights ranged from 0.62 to 1.76 g and the crystal growth rates were generally higher than 3×10^{-3} g·h^{-1}. The sizes of the Pr:KGdP crystals along $a^* \times b \times c^*$ directions were 7.6-13.6 mm × 17.1-24.1 mm × 10.7-13.6 mm, their weights ranged from 2.73 to 6.88 g and the crystal growth rates varied from 6.1×10^{-3} to 17.4×10^{-3} g·h^{-1}. The details of these crystal growth experiments as well as the comments on the results obtained can be read in references[6,17]. Figure 1.a shows a photograph of an as-grown

Ce:KGdP single crystal with the platinum stirrer, while Figure 1.b shows a photograph of an as-grown Pr:KGdP single crystal with a centimetre scale.

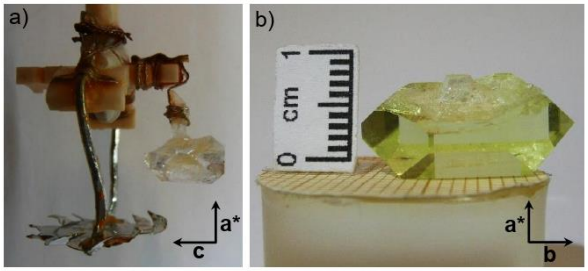

Figure 1. a) As-grown single crystal of Ce:KGdP and platinum stirrer, b) As-grown single crystal of Pr:KGdP with a centimetre scale.

Table 2 shows the stoichiometry of the single crystals grown that have been used in the radioluminescence study. The distribution coefficients of Ce^{3+} (K_{Ce}) in KGdP calculated from the EPMA results of all the concentrations studied are higher than unity. The K_{Ce} is in the range 1.3-1.9, which means that as the crystal is growing, the concentration ratio of $Ce^{3+}/(Ce^{3+} + Gd^{3+})$ in the solution decreases.[12] In the case of Pr^{3+}-doped KGdP crystals, the distribution coefficients of Pr^{3+} (K_{Pr}) are not far from the unit.[6] In neither of the two cases, there is a significant tendency of the distribution coefficient (K_{Ce} and K_{Pr}) to decrease or increase as the level of doping in the solution increases.

Table 2. Chemical Formula of the Single Crystals Grown Used in the Radioluminescence Measurements

Doping element (Ln^{3+})	Atomic % of Ln^{3+} substituting Gd^{3+} in solution	Chemical formula
Ce^{3+}	0.25	$KGd_{0.996}Ce_{0.004}(PO_3)_4$
Ce^{3+}	0.50	$KGd_{0.994}Ce_{0.006}(PO_3)_4$
Ce^{3+}	1.00	$KGd_{0.981}Ce_{0.019}(PO_3)_4$
Pr^{3+}	0.25	$KGd_{0.997}Pr_{0.003}(PO_3)_4$
Pr^{3+}	1.00	$KGd_{0.990}Pr_{0.010}(PO_3)_4$
Pr^{3+}	5.00	$KGd_{0.942}Pr_{0.058}(PO_3)_4$

3.2. X-ray excited radioluminescence (RL)

3.2.1. Ce^{3+}:$KGd(PO_3)_4$ single crystals: Emission labelling

Figure 2 shows the X-ray excited radioluminescence (RL) spectra of undoped and Ce^{3+}-doped KGdP with different doping concentrations under 16500 eV, 24800 eV, 35500 eV and 40443 eV excitation. The RL spectra of Ce:KGdP have been compared with the RL of undoped KGdP under the same excitation energies to properly label the observed emission bands. All the emission bands have been labelled by using the Dieke's diagram[18], the extended Dieke's diagram[19] and the references[17,20,21].

The emission bands in the RL spectra of the undoped KGdP sample (Figure 2.a-d) belong to $4f \rightarrow 4f$ electronic transitions of Gd^{3+}. The band centred at around 312 nm corresponds to the $^6P_{3/2,\ 5/2,\ 7/2} \rightarrow {}^8S_{7/2}$ transitions. It can also be seen a band that extends from 615 to 690 nm, corresponding to the $^6G_{7/2}{}^* \rightarrow {}^6I_{11/2,\ 15/2,\ 13/2}$ and $^6G_{13/2} \rightarrow {}^6I_{7/2,\ 9/2,\ 17/2}$ transitions. In Figure 2.a-b, some weak emission bands can be observed in the visible region that also belong to $4f \rightarrow 4f$ electronic

transitions of Gd^{3+}, as shown the inset. The bands with their maximum intensity value centred at 380 and 547 nm correspond to the $^6H_{15/2} \rightarrow {}^6P_{7/2,\,5/2}$ and $^6G_{3/2} \rightarrow {}^6P_{7/2}$ transitions, respectively. The band that starts at 400 nm and ends at 460 nm corresponds to the $^4H(2)_{7/2} \rightarrow {}^6P_{7/2}$ and $^6H_{13/2} \rightarrow {}^6I_J$ transitions, and finally, the band extending from 565 to 615 nm corresponds to the $^6G_{11/2,\,9/2,\,5/2} \rightarrow {}^6P_{7/2,\,5/2}$ and $^6G_{7/2} \rightarrow {}^6P_{7/2}$ transitions. As can be observed in Figure 2, the undoped KGdP sample emits in the visible range mainly through the $^6P_{3/2,\,5/2,\,7/2} \rightarrow {}^8S_{7/2}$ transitions of Gd^{3+} after being excited under X-ray radiation.

In the RL spectra of the Ce^{3+}-doped type III KGdP samples (space group: $P2_1$), it can be observed an intense band that extends from 300 to 385 nm and that is formed by the overlapping of two bands corresponding to the $5d_1 \rightarrow {}^2F_{5/2}$ and $5d_1 \rightarrow {}^2F_{7/2}$ transitions of Ce^{3+} in KGdP, respectively. These two electronic transitions were already observed in a previous work[17] as a doublet band centred at 322 and 342 nm in the emission spectra of the same samples under VUV-UV excitation (direct $4f \rightarrow 5d$ excitation), confirming that these emissions of the RL spectra are originated from the active Ce^{3+} ions. This band is presented as a doublet because the $^2F_{5/2}$ and $^2F_{7/2}$ levels are separated by 2000 cm^{-1}.[18] In radioluminescence studies of compounds of the same family performed by Zhong *et al.* on Ce^{3+}-doped $MGdP_4O_{12}$ (M = Li, Na, K, Cs) under X-ray irradiation,[8] the doublet band corresponding to the $5d_1 \rightarrow {}^2F_{5/2}$ and $5d_1 \rightarrow {}^2F_{7/2}$ transitions of Ce^{3+} has been observed centred at 310 and 329 nm for Ce:$LiGdP_4O_{12}$ (space group: $C2/c$), 314 and 333 nm for Ce:$NaGdP_4O_{12}$ (space group: $P2_1/n$), 325 and 345 nm for Ce:$KGdP_4O_{12}$ (space group: $C2/c$, type B phase), 336 and 358 nm for Ce:$CsGdP_4O_{12}$ (space group: $P2_1/n$). As observed in the RL results of the two crystalline phases of $KGd(PO_3)_4$ mentioned (type III, studied in our work, and type B, in the ref.[8]), its polymorphism does not significantly affect the energy values of these $4f$ and $5d$ levels of Ce^{3+}.

Simultaneously, other bands with a lower intensity can also be observed in the visible region from 375 to 700 nm, and correspond to the $4f \rightarrow 4f$ transitions of Gd^{3+} mentioned in the RL spectra of the undoped KGdP samples.

It is interesting to note that the band corresponding to the $^6P_{3/2,5/2,7/2} \rightarrow {}^8S_{7/2}$ transitions of Gd^{3+} (around 312 nm) is not observed when Ce^{3+} is present in the crystal, even at low Ce^{3+} concentrations (0.25 at. %).

The radioluminescence under X-ray excitation has been studied for different doping levels to observe the effect of the Ce^{3+} concentration. In Figure 2, it can be seen that the intensity of the band corresponding to the $5d_1 \rightarrow {}^2F_{5/2}$ and $5d_1 \rightarrow {}^2F_{7/2}$ transitions of Ce^{3+} varies depending on the Ce^{3+} concentration, while the most intense Gd^{3+} band around 660 nm is maintained around the same intensity value at a specific excitation energy, whatever the doping level of Ce^{3+}. The decrease of the Ce^{3+} emission in the case of 1 at. % Ce:KGdP crystal with respect to the crystal of 0.5 at. % Ce:KGdP could be due to the reabsorption of the emission of a Ce^{3+} ion by its neighbouring Ce^{3+} ions.

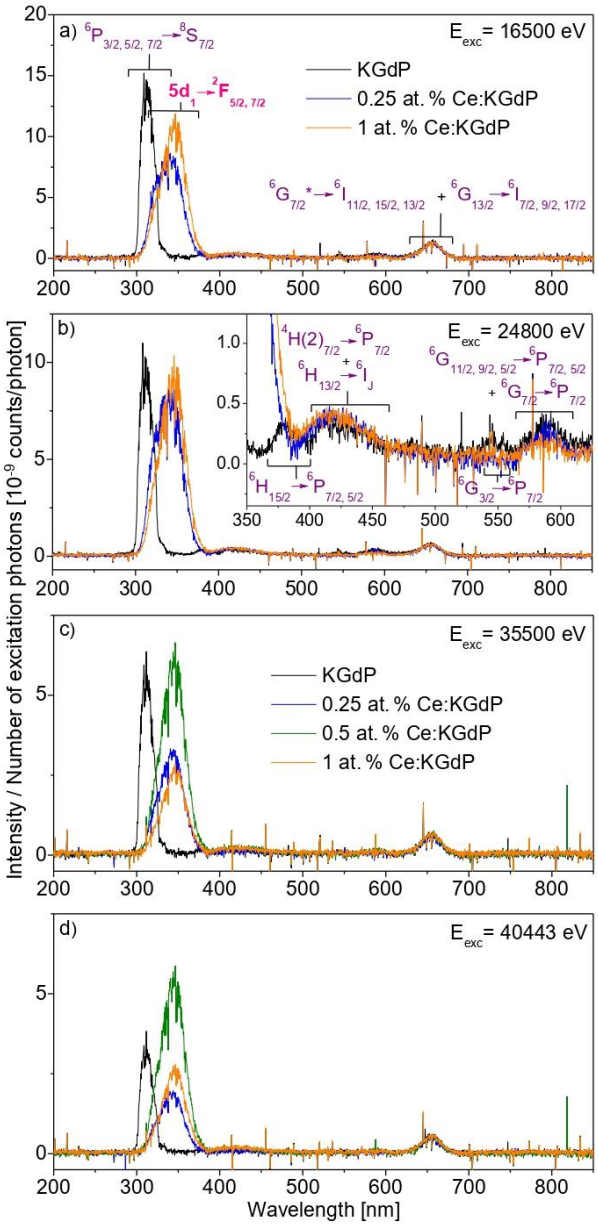
a) $^6P_{3/2, 5/2, 7/2} \rightarrow {}^8S_{7/2}$
E_{exc} = 16500 eV
KGdP
0.25 at. % Ce:KGdP
1 at. % Ce:KGdP
$5d_1 \rightarrow {}^2F_{5/2, 7/2}$
$^6G_{7/2}{}^* \rightarrow {}^6I_{11/2, 15/2, 13/2}$ + $^6G_{13/2} \rightarrow {}^6I_{7/2, 9/2, 17/2}$
b)
E_{exc} = 24800 eV
$^4H(2)_{7/2} \rightarrow {}^6P_{7/2}$
$^6H_{13/2} + {}^6I_J$
$^6G_{11/2, 9/2, 5/2} \rightarrow {}^6P_{7/2, 5/2}$
+ $^6G_{7/2} \rightarrow {}^6P_{7/2}$
$^6H_{15/2} \rightarrow {}^6P_{7/2, 5/2}$
$^6G_{3/2} \rightarrow {}^6P_{7/2}$
c)
E_{exc} = 35500 eV
KGdP
0.25 at. % Ce:KGdP
0.5 at. % Ce:KGdP
1 at. % Ce:KGdP
d)
E_{exc} = 40443 eV
Intensity / Number of excitation photons [10^{-9} counts/photon]
Wavelength [nm]

Figure 2. X-ray excited radioluminescence spectra of KGdP and Ce:KGdP at different Ce^{3+} concentrations under excitation at a) 16500 eV, b) 24800 eV, c) 35500 eV and d) 40443 eV. Labels in purple and italics indicate the electronic transitions of Gd^{3+} and labels in pink and bold those of Ce^{3+}.

3.2.2. Ce^{3+}:$KGd(PO_3)_4$ single crystals: Proposed mechanism

In cerium-doped scintillation materials, most of the energy absorbed by the material after its excitation with X-ray radiation is used for the formation of electron–hole pairs.[22] Consequently, in such materials, most of the localized excitations are electron–hole pairs and, therefore, the energy transfer process to Ce^{3+} ions is based on the sequential capture of charge carriers by Ce centres.[22,23,24,25,26] Since Ce^{3+} is a good hole trap,[25,27,28] in Ce^{3+}-doped crystals, the energy transfer process usually begins with the capture of a hole by Ce^{3+} and then of an electron by Ce^{4+}. The hole trap cross section of Ce^{3+} strongly depends on the energy difference between the 4*f* ground state of Ce^{3+} in the forbidden bandgap and the top of the valence band of the crystal, i.e. the lower the energy difference, the higher the efficiency of the capture of a hole by Ce^{3+}.[22,24,25,28,29,30] A high scintillation efficiency is connected with a high probability of hole capture.[22,29] It is worth mentioning that the initial coexistence of Ce^{4+} and Ce^{3+} ions in the scintillation crystal is harmful because Ce^{4+} is an efficient electron trap and, therefore, can compete with Ce^{3+} for the capture of charge carriers and induce severe limitations in scintillation efficiency.[24, 27]

So given the above information, after exciting the type III Ce:KGdP single crystals with X-ray radiation, most of the electronic excitations created in the crystal are electron–hole pairs and the energy transfer process to the Ce^{3+} ions is through a sequential capture of charge carriers. In these crystals, the presence of Ce^{4+} is not expected because this ion is not present in the initial reagents and because the crystalline network resulting from the partial substitution of Gd^{3+} by Ce^{3+} is

electrically neutral, with a higher stability than the resulting from the partial substitution by Ce^{4+}. Therefore, there would be no competition between the Ce^{4+} and Ce^{3+} ions in Ce:KGdP. In addition to this, it is interesting to mention that Gd^{3+} ion is very unlikely to introduce both hole and electron traps in materials and, for this reason, it is one of the two best candidates (together with Lu) to act as a neutral constituent in scintillation materials.[25] Thus, the energy transfer from the correlated electron–hole pairs to the emitting centres is expected to be more effective for Ce^{3+} ions than for Gd^{3+} ions, although it should be noted that the concentration of Gd^{3+} is considerably higher than that of Ce^{3+}. Once the emitting centres are excited, radioluminescence can be produced by these centres. Probably because of the above-mentioned facts, the emission band corresponding to the $5d_1 \rightarrow {}^2F_J$ transitions of Ce^{3+} is very intense, and simultaneously, weak emission bands corresponding to some transitions between the $4f$ high energy levels of Gd^{3+} can be observed.

The localization of the $5d$ and $4f$ levels of Ce^{3+} and Gd^{3+} with respect to conduction and valence bands in type III KGdP is shown in Figure 3.a. The energy difference between the $5d_1$ level of Ce^{3+} in KGdP and the bottom of the conduction band is expected to be similar to the one of Ce^{3+} doped $LiYP_4O_{12}$, determined in the work of Dorenbos *et al.*,[31] due to the high similarity with our host. The other $5d$ levels and all $4f$ levels of Ce^{3+} have been located with respect to the $5d_1$ level of Ce^{3+} in KGdP taking into account the spectroscopic studies performed in our previous work[17]. Since the energy difference between the $5d_1$ level of Ce^{3+} and that of Gd^{3+} is maintained independently of the host,[31] the $5d_1$ level of Gd^{3+} in KGdP has also been located with respect to the conduction and valence bands. The $4f$ levels of Gd^{3+} have been located with respect to its $5d_1$ level in KGdP taking into account the spectroscopic studies performed in our previous work[6], the extended Dieke's diagram[19] and the references[20,21].

Below, several works related to radioluminescence studies of Gd^{3+}-containing hosts doped with Ce^{3+} are summarized, focusing on the Ce^{3+} emissions corresponding to the $5d_1 \rightarrow {}^2F_J$ transitions, the Gd^{3+} emission at 312 nm and the possible energy transfer between Ce^{3+} and Gd^{3+} ions.[8,32,33,34]

In the work done by Zhong *et al.* previously mentioned about the radioluminescence properties of Ce^{3+}-doped $MGdP_4O_{12}$ (M = Li, Na, K, Cs),[8] it can be seen that the peak of Gd^{3+} at 312 nm clearly stands out from the band corresponding to the $5d_1 \rightarrow {}^2F_{5/2}$ transition of Ce^{3+} for $Ce:LiGdP_4O_{12}$, while it becomes weaker for $Ce:NaGdP_4O_{12}$. By contrast, the peak disappears completely for $Ce:KGdP_4O_{12}$ and $Ce:CsGdP_4O_{12}$. Therefore, as mentioned in their work, the energy transfer from Gd^{3+} to Ce^{3+} becomes more efficient as the M^+ radius increases.

The condition for $Gd \rightarrow Ce$ energy transfer from the ${}^6P_J$ levels of Gd^{3+} to the $5d_1$ level of Ce^{3+} is satisfied when there is no energy difference between the energy levels of ${}^6P_J$ and the absorption edge of the $4f \rightarrow 5d$ transitions of Ce^{3+}. The efficiency of this energy transfer becomes higher as the degree of overlap between the ${}^6P_J$ levels of Gd^{3+} and the Ce^{3+} absorption spectrum increases. These affirmations were confirmed in the work done by Shalapska *et al.* on the luminescence properties of $LiGd_{0.9}Ce_{0.1}P_4O_{12}$, $LiY_{0.9}Ce_{0.1}P_4O_{12}$ (both, space group: $C2/c$) and $NaGd_{0.9}Ce_{0.1}P_4O_{12}$ (space group: $P2_1/n$) upon vacuum-ultraviolet and X-ray excitation.[35] The doublet band corresponding to the $5d_1 \rightarrow {}^2F_{5/2}$ and $5d_1 \rightarrow {}^2F_{7/2}$ transitions of Ce^{3+} is observed in the X-ray excited emission spectra of the three compounds, while the peak of Gd^{3+} at 312 nm is present in the spectra of the two Gd^{3+}-containing phosphates.

In the research carried out by Liang *et al.* into the photoluminescence and radioluminescence of undoped and Ce^{3+}-activated $Na_3Gd(PO_4)_2$,[32] the X-ray excited radioluminescence spectrum of $Na_3Gd_{0.99}Ce_{0.01}(PO_4)_2$ shows an intense band that is formed by the overlapping of two bands

centred at 341 and 365 nm that corresponds to the $5d_1 \rightarrow {}^2F_{5/2}$ and $5d_1 \rightarrow {}^2F_{7/2}$ transitions of Ce^{3+} in this host, respectively. The peak centred at 312 nm corresponding to the ${}^6P_J \rightarrow {}^8S_{7/2}$ transitions of Gd^{3+} is not present in the spectrum mentioned above, which according to the authors implies that the energy transfer from the ${}^6P_J$ states to Ce^{3+} is efficient.

The X-ray excited radioluminescence of Ce^{3+}-doped multicomponent garnets with formula unit $(Ce_xGd_yR_{1-x-y})_3(Ga_zAl_{1-z})_5O_{12}$ (R = Y or Lu) have been studied by Kucera *et al.* at different Gd^{3+} doping concentrations.[33] In all Gd^{3+} concentrations studied, the emission band corresponding to the $5d_1 \rightarrow {}^2F_{5/2,7/2}$ transitions of Ce^{3+} is shown as a single broad band centred at approximately 510 nm. The authors concluded that for Gd^{3+} concentrations below 5 at. %, the total emission of the sample originates from two emission centres, Ce^{3+} and Gd^{3+}, with the $5d_1 \rightarrow {}^2F_J$ emission of Ce^{3+} and the ${}^6P_J \rightarrow {}^8S_{7/2}$ emission of Gd^{3+} (maximum near 312 nm). At higher Gd^{3+} concentrations (<50 at. %), the Ce^{3+} emission increases gradually while the Gd^{3+} emission decreases and the total integrated emission of the sample is significantly higher than the previous case, so that the Gd^{3+} receives the energy and contributes to increase the intensity of the Ce^{3+} emission through an energy transfer to Ce^{3+} ions. The Gd^{3+} emission peak disappears completely at Gd^{3+} concentrations ~50 at. % and higher caused by the energy migration across the Gd^{3+} ions and an efficient energy transfer from Gd^{3+} to Ce^{3+} that is favoured due to the downwards shift of the 5*d* levels of Ce^{3+}, since the increase of gadolinium content in the sample increases the crystal field.

In our case, in the X-ray excited radioluminescence spectra of type III Ce:KGdP single crystals, the band corresponding to the ${}^6P_J \rightarrow {}^8S_{7/2}$ transitions of Gd^{3+} (~312 nm) is not present, so it can be attributed to a very efficient non-radiative energy transfer process from the ${}^6P_J$ levels of Gd^{3+} to the $5d_1$ level of Ce^{3+}, as happened in other Gd^{3+}-containing hosts doped with Ce^{3+}.[8,32,33,34] Also, a bidirectional energy transfer between the $5d_5$ level of Ce^{3+} and the ${}^6F_J$ and ${}^6G_J$ levels of Gd^{3+} might

take place, which was also observed in photoluminescence studies in our previous work[17], since some emission bands corresponding to the electronic transitions from the ^6G_J levels to the ^6I_J and ^6P_J levels of Gd^{3+} have been observed. Therefore, different bidirectional energy transfer processes between Ce^{3+} and Gd^{3+} ions are expected. Although, it is clear that Gd^{3+} receives energy directly from the localized excitations because some of the Gd^{3+} emission bands that appear in the radioluminescence spectra correspond to electronic transitions starting from the ^6H_J and $^4H(2)_{7/2}$ levels of Gd^{3+}, which have higher energy than the $5d_5$ level of Ce^{3+} in type III KGdP. The different energy transfer processes can be observed in Figure 3.b.

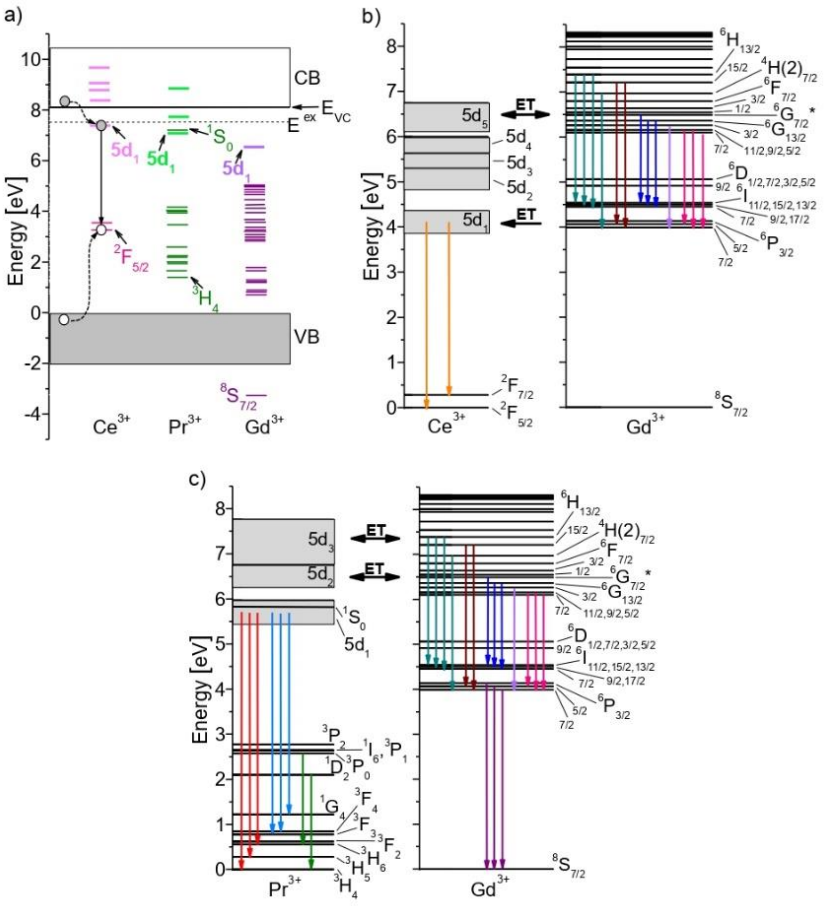

Figure 3. a) Energy levels scheme for Ce^{3+}, Pr^{3+} and Gd^{3+} with respect to conduction (CB) and valence bands (VB) of type III $KGd(PO_3)_4$, which schematically illustrates the energy transfer process corresponding to a fast decay rate for the Ce^{3+} case.[36] The references[6,17,31] have been used to place the energy levels in this host. b) Energy level diagram of Ce^{3+} and Gd^{3+} in $Ce:KGd(PO_3)_4$ and emissions observed under X-ray excitation. The arrows of the same colour appear as a single

band in the radioluminescence spectra. c) Energy level diagram of Pr^{3+} and Gd^{3+} in Pr:KGd$(PO_3)_4$ and emissions observed under X-ray excitation.

3.2.3. Pr^{3+}:KGd$(PO_3)_4$ single crystals: Emission labelling

A similar study to that performed with the previous Ce:KGdP samples, has been carried out with Pr:KGdP single crystals. Figure 4 shows the X-ray excited radioluminescence (RL) spectra of undoped and Pr^{3+}-doped type III KGdP (space group: $P2_1$) with different doping concentrations under 12000 eV, 16500 eV, 31000 eV and 46000 eV excitation. The emission intensities have been corrected by dividing them by the corresponding number of excitation photons per second for each excitation energy. The RL spectra of undoped KGdP have been used to correctly label the emission bands that appear in the spectra of Pr:KGdP. As mentioned in the previous study, the assignation of each emission band have been made by taking into account the Dieke's diagram[18], the extended Dieke's diagram[19] and the references[6,20,37].

Unlike Ce^{3+}-doped samples, the most intense emission band in all RL spectra of undoped and Pr^{3+}-doped KGdP samples is centred at 312 nm corresponding to the $^6P_{3/2,5/2,7/2} \rightarrow {}^8S_{7/2}$ transitions of Gd^{3+}. In the RL spectra of Pr:KGdP, two bands centred around 236 and 259 nm can be observed. They belong to $5d \rightarrow 4f$ transitions of Pr^{3+} in KGdP, which correspond more specifically to the $5d_1 \rightarrow {}^3H_{4,5,6}, {}^3F_2$ and $5d_1 \rightarrow {}^3F_{3,4}, {}^1G_4$ transitions, respectively. It is reaffirmed that these two emissions are originated from the active Pr^{3+} ions, since in our previous work regarding the luminescence properties of the same samples under VUV-UV excitation (direct $4f \rightarrow 5d$ excitation)[6], these and others bands corresponding to $5d \rightarrow 4f$ transitions of Pr^{3+} were also observed, such as the emission bands centred at 229, 239, 256, 265 nm, 358 and 435 nm labelled as the $5d_1 \rightarrow {}^3H_5$, $5d_1 \rightarrow {}^3H_6, {}^3F_2$ $5d_1 \rightarrow {}^3F_{3,4}$, $5d_1 \rightarrow {}^1G_4$, $5d_1 \rightarrow {}^1D_2$ and $5d_1 \rightarrow {}^3P_2$ transitions of Pr^{3+} in KGdP, respectively.

As regards to the spectral range from 350 to 850 nm, the broad band that extends from 560 to 700 nm when the crystals are excited at 12000 eV (Figure 4.a) could be attributed to the $^1D_2 \rightarrow {}^3H_4$ and $^3P_0 \rightarrow {}^3H_6$ transitions of Pr^{3+} since this band does not appear in the RL spectrum of undoped KGdP nor in that of the crystal with low Pr^{3+} content. This emission band has also been observed in the X-ray excited radioluminescence spectra of 0.3 at. % Pr:$(Gd,Lu)_3Ga_3Al_2O_{12}$,[38] 1 at. % Pr:$K_3(Lu,Y)(PO_4)_2$,[39] Pr:$Lu_2Si_2O_7$,[40] 0.2 at. % Pr:$Lu_3Al_5O_{12}$,[41] 0.2 and 2 at. % Pr:$Ca_3Sc_2Si_3O_{12}$.[42] When the excitation energies are 16500 eV (Figure 4.b), 31000 eV (Figure 4.c) and 46000 eV (Figure 4.d), all the emission bands that appear in the wavelength range from 360 to 725 nm belong to $4f \rightarrow 4f$ transitions of Gd^{3+} since these bands also appear in the RL spectra of undoped KGdP. The labelling of Gd^{3+} electronic transitions is the same as in the RL spectra of the Ce:KGdP samples.

The effect of the Pr^{3+} concentration has been studied for three different doping levels at several excitation energies. In the spectra obtained under 12000 eV excitation (Figure 4.a), it can be observed that in Ce:KGdP there is an increase of the photon conversion in the range from 200 to 350 nm in comparison with the undoped crystal, that is, there is a higher intensity of the overall emission in this range when Pr^{3+} is present in the crystal. When the crystal is doped with 5 at. % Pr^{3+}, the intensity of the $5d_1 \rightarrow 4f$ bands of Pr^{3+} is even higher than that observed in the crystal with 1 at. % Pr^{3+}, so there is no concentration quenching effect by Pr^{3+} concentration up to the value studied. In addition to this, it can also be observed that the intensity of the Gd^{3+} band decreases gradually. Since the bands belonging to Pr^{3+} increase and the Gd^{3+} band decreases in intensity when the Pr^{3+} content increases, it seems that there is an increase in efficiency in the energy transfer from Gd^{3+} to Pr^{3+}. This energy transfer could be from the Gd^{3+} $4f$ levels of higher energy to the

Pr^{3+} $5d_{2,3}$ levels, followed by a non-radiative relaxation to the $5d_1$ level. The different energy transfer processes are depicted in Figure 3.c.

Under 16500 eV (Figure 4.b) and 31000 eV (Figure 4.c) excitations, it can be seen that the Gd^{3+} band centred at 312 nm clearly varies depending on the Pr^{3+} concentration, while the Pr^{3+} bands (236 and 259 nm) and the other Gd^{3+} bands practically remain with the same intensity value. Since the intensity of the Gd^{3+} band centred at 312 nm is higher when the doping level is 0.25 and 1 at. % of Pr^{3+} with respect to the undoped KGdP and, at the same time, the $5d_1 \rightarrow 4f$ bands of Pr^{3+} have a similar intensity in the two concentrations, this could mean that there is an energy transfer from the Pr^{3+} $5d_{2,3}$ levels to the ^6G_J levels and other $4f$ levels of higher energy of Gd^{3+}, followed by the $^6G_J \rightarrow {}^6I_J$, ^6P_J radiative transitions of Gd^{3+} and then the $^6P_J \rightarrow {}^8S_{7/2}$ more intense transitions. So, there are bidirectional energy transfer processes between Pr^{3+} doping ions and Gd^{3+} ions constitutive of the host.

When the studied crystals are excited with energies from 35500 to 62500 eV (Figure 4.d), a clearly different behaviour can be observed according to the Pr^{3+} concentration in comparison with the spectra explained above. In this energy range, the 1 at. % Pr:KGdP crystal shows a higher emission intensity than the other Pr^{3+}-doped samples.

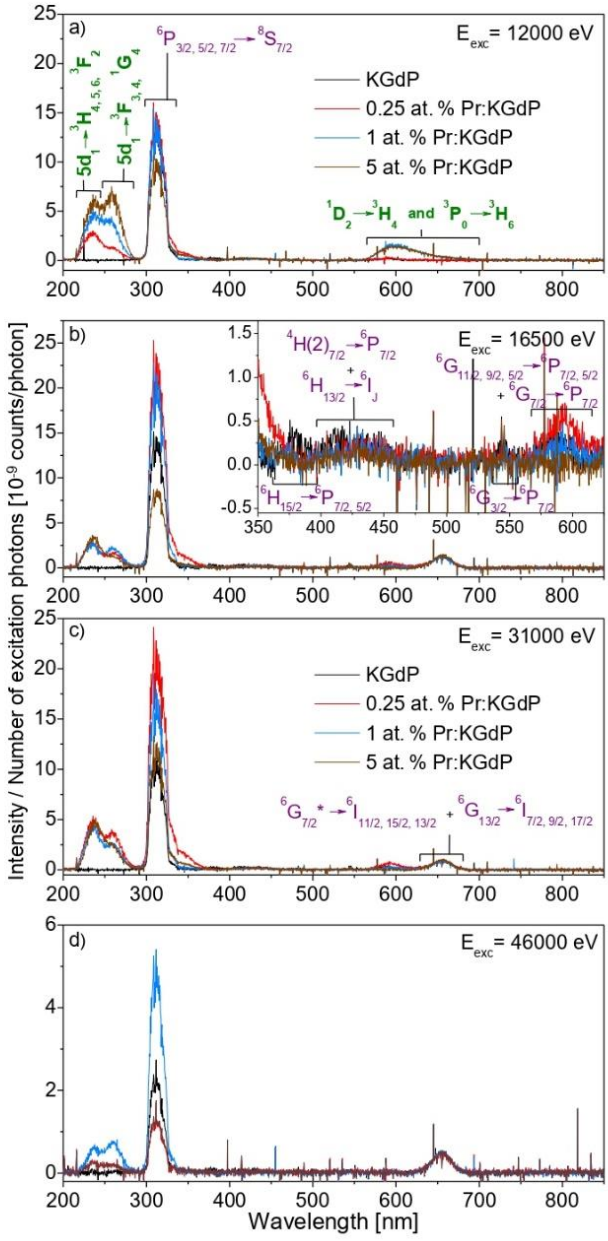
a)
E_exc = 12000 eV
KGdP
0.25 at. % Pr:KGdP
1 at. % Pr:KGdP
5 at. % Pr:KGdP
b)
E_exc = 16500 eV
c)
E_exc = 31000 eV
d)
E_exc = 46000 eV
Intensity / Number of excitation photons [10^-9 counts/photon]
Wavelength [nm]

Figure 4. X-ray excited radioluminescence spectra of KGdP and Pr:KGdP at different Pr^{3+} concentrations under excitation at a) 12000 eV, b) 16500 eV, c) 31000 eV and d) 46000 eV. Labels in purple and italics indicate the electronic transitions of Gd^{3+} and labels in green and bold those of Pr^{3+}.

3.2.4. Pr^{3+}:$KGd(PO_3)_4$ single crystals: Proposed mechanism

In praseodymium-doped scintillation materials, the energy transfer process based on the sequential capture of charge carriers by Pr centres usually begins with the capture of a hole because Pr^{3+} is a good candidate for hole trap.[25,28] Analogous to the explanation of the Ce^{3+}-doped crystals (see section 3.2.2), the efficiency of hole capture by Pr^{3+} ions strongly depends on the energy difference between the top of the valence band of the crystal and the 4*f* ground state of Pr^{3+} in the forbidden bandgap.[28] The smaller the energy difference mentioned, the higher the efficiency of hole capture, which is connected with a higher scintillation efficiency. Moreover, it is worth mentioning that in gadolinium-containing scintillation materials, Gd^{3+} ion acts as a neutral constituent because it is very unlikely to introduce both hole and electron traps.[25]

Therefore, in our case, after the creation of electronic excitations in the crystal lattice of the type III Pr:$KGd(PO_3)_4$ single crystals caused by X-ray irradiation, energy transfer processes from the localized excitations to the Pr^{3+} and Gd^{3+} ions take place.[23,24] When the localized excitations are electron–hole pairs, the energy transfer process from them to the emitting centres is expected to be more effective for Pr^{3+} ions than for Gd^{3+} ions, although it has to be taken into account that the concentration of Pr^{3+} is significantly smaller than that of Gd^{3+} in Pr:$KGd(PO_3)_4$.

The 5*d* and 4*f* levels of Pr^{3+} and Gd^{3+} have been located with respect to the conduction and valence bands in type III KGdP, as shown Figure 3.a. First, the $5d_1$ level of Ce^{3+} has been located

with respect to the bottom of the conduction band of type III KGdP assuming the same energy difference observed in the energy levels scheme for polyphosphate $LiYP_4O_{12}$ in the reference[31] due to the high similarity between these hosts. Then, since the energy difference between the $5d_1$ level of Ce^{3+} and the $5d_1$ levels of the other lanthanides (Ln^{3+}) is maintained independently of the host,[31] the $5d_1$ level of Pr^{3+} and that of Gd^{3+} have been located with respect to the conduction band. Finally, the other $5d$ levels and the $4f$ levels of Pr^{3+} have been located with respect to the $5d_1$ level of Pr^{3+} taking into account the spectroscopic studies performed in our previous work[6], and the $4f$ levels of Gd^{3+} have been located with respect to its $5d_1$ level considering the mentioned work[6], the extended Dieke's diagram[19] and the references[20,21].

As shown in Figure 4, once the Pr^{3+} and Gd^{3+} ions are excited, these centres emit light. Since the bands corresponding to the $5d_1 \rightarrow 4f$ transitions of Pr^{3+} and to the $^6P_J \rightarrow {}^8S_{7/2}$ transitions of Gd^{3+} are clearly present, the presence of this Gd^{3+} emission may be ascribed to an inefficient energy transfer process from the ^6D_J, ^6I_J and ^6P_J levels of Gd^{3+} to the $5d_1$ level of Pr^{3+}. This is due to the relatively high energy difference between the mentioned levels of the two ions in Pr:KGdP, and also the fact that the $5d_1$ is slightly higher in energy than the Gd^{3+} mentioned levels. The coexistence of these bands has also been observed in the X-ray excited radioluminescence spectra of some stoichiometries of the following Gd-based multicomponent aluminate garnets: 0.3 at. % $Pr:(Gd,Lu)_3Ga_3Al_2O_{12}$,[38] 0.2 and 1 at. % $Pr:(Gd,Lu)_3(Ga,Al)_5O_{12}$.[43] In the work done by Wu and Ren,[38] radioluminescence spectra of the multicomponent garnet 0.3 at. % $Pr:(Gd,Lu)_3Ga_3Al_2O_{12}$ were obtained at different Gd/Lu ratios and then compared. For $Gd_{0.025}Lu_{2.975}$, $Gd_{0.05}Lu_{2.95}$ and $Gd_{0.1}Lu_{2.9}$ samples, their spectra show the Gd^{3+} emission belonging to the $^6P_{7/2} \rightarrow {}^8S_{7/2}$ transition at about 311 nm, the Pr^{3+} bands corresponding to the $5d_1 \rightarrow {}^3H_4$, $5d_1 \rightarrow {}^3H_5$, $5d_1 \rightarrow {}^3H_6$,$^3F_2$ and $5d_1 \rightarrow {}^3F_{3,4}$ transitions around 295, 305, 320 and 330 nm, respectively, and the Pr^{3+} bands that belong

to several $4f \rightarrow 4f$ transitions in the spectral range from 450 to 650 nm. Whereas the spectra of $Gd_{0.2}Lu_{2.8}$, $Gd_{0.4}Lu_{2.6}$ and $Gd_{0.6}Lu_{2.4}$ samples show that, the bands corresponding to the $5d_1 \rightarrow 4f$ transitions of Pr^{3+} become irrelevant. A reduction in the intensity of the $5d_1 \rightarrow 4f$ bands of Pr^{3+} can be observed accompanied with a significant enhancement of the Gd^{3+} emission as the Gd^{3+} content increases. The authors attribute this behaviour to an energy transfer from the $5d$ levels of Pr^{3+} to the $4f$ levels of Gd^{3+}. In the second work, done by Kamada *et al.*,[44] the spectrum of 0.2 at. % $Pr:Gd_{0.5}Lu_{2.5}Ga_2Al_3O_{12}$ shows, in the range from 200 to 450 nm, clearly a broad band that extends from 290 to 420 nm, which corresponds to the $5d_1 \rightarrow 4f$ transitions of Pr^{3+}, and a hump with the maximum of intensity at 312 nm, which belongs to the $^6P_{7/2} \rightarrow {}^8S_{7/2}$ transition of Gd^{3+}. After increasing the Gd/Lu ratio to 0.5, it can be observed in the spectrum of the resulting sample that the Gd^{3+} band is narrow and intense and that the Pr^{3+} bands are practically non-existent.

In our case, the emission bands corresponding to the Pr^{3+} $5d_1 \rightarrow 4f$ transitions are present, despite the high atomic concentration of Gd^{3+} in the crystal. Besides, in contrast to the aforementioned inefficient energy transfer between the ^6D_J, ^6I_J and ^6P_J levels of Gd^{3+} and the $5d_1$ level of Pr^{3+}, bidirectional energy transfer processes between the Pr^{3+} $5d_{2,3}$ levels and the Gd^{3+} $4f$ levels of higher energy are expected (Figure 3.c) taking into account the discussion on the effect of the Pr^{3+} concentration (section 3.2.3).

3.3. Radiation damage in $KGd(PO_3)_4$ samples

As it is known, crystalline scintillators may suffer from radiation damage under continued X-ray and γ-ray irradiation. The most common damage is the appearance of radiation-induced absorption bands, which are caused by the formation of colour centres. The colour centres may be electrons located in anion vacancies (F centre) of the crystalline lattice, or holes located in cation

vacancies (V centre), or others. In oxides, the radiation damage usually consists of defects related to stoichiometry, such as oxygen vacancies. The missing of oxygen in the crystalline lattice leads to the existence of anion vacancies that act as traps for electrons. The colour centres can disappear at room temperature, although the recovery speed depends on the depth of the traps.[44]

During the radioluminescence measurements (section 3.2), some KGdP samples changed their colour in the region where they were being excited under prolonged X-ray irradiation. A dark brownish region was observed in the undoped sample and a brown-yellowish region in the Pr-doped KGdP samples, as shown in Figure 5. This behaviour was not observed in the Ce-doped samples. The coloured regions disappeared with time (in a few hours), indicating an apparent recovery of the samples. This change in coloration has been reported for other crystals after being excited with ionizing radiation, such as $Pr:Ca_3Sc_2Si_3O_{12}$ under X-ray irradiation,[42] $Gd:PbWO_4$ irradiated with neutrons,[45] and $Mn:Bi_4Ge_3O_{12}$ under γ-ray irradiation.[44,46] Regarding $Pr:Ca_3Sc_2Si_3O_{12}$, apart from the colour change, the authors observed a deviation of X-ray excited decay curves from exponential behaviour and faster decay components compared to those observed under VUV excitation. This behaviour was assigned to the creation of radiation defects which act as quenching centres in the scintillator activity.[42] In the case of $Gd:PbWO_4$ crystals, the authors attributed the change in colour from colourless to violet to the absorption of the inherent clusters of WO_{3-x} in the regular lattice of $PbWO_4$ that, after irradiation, change the valence of tungsten gradually (from W^{6+} via W^{5+} to W^{4+}) depending on the radiation dose applied, resulting in different optical absorption spectra and, consequently, different colours of the crystal.[45] For $Mn:Bi_4Ge_3O_{12}$, the authors noted that the crystal turned pinkish immediately after γ-ray irradiation and observed some radiation-induced absorption bands that extend from the absorption edge of BGO (306 nm) to approximately 750 nm and are centred at 326, 413 and 539 nm. The same

radiation-induced absorption bands were found in a series of 24-doped BGO samples and in all cases, they were assigned to colour centres related to defects of the crystal lattice, such as oxygen vacancies.[46]

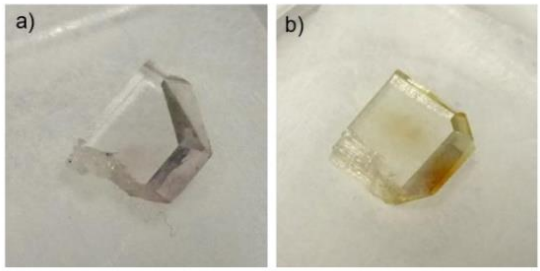

Figure 5. a) Undoped KGdP and b) 1 at. % Pr:KGdP single crystals just after continued X-ray irradiation.

In order to study these phenomena, the optical absorption of several KGdP samples was measured, comparing the spectrum obtained before the X-ray irradiation with that performed after several days of recovering (5-7 days). Figure 6 shows the optical absorption spectra of the three different types of samples studied in this work, undoped, Ce-doped and Pr-doped KGdP, together with the spectra resulting from the subtraction of the first data (before irradiation) from the second one (after irradiation). The absorption peaks present in the optical absorption spectra of the undoped KGdP sample (Figure 6.a) in the spectral range from 190 to 320 nm correspond to $4f \rightarrow 4f$ transitions of Gd^{3+}. As can be seen in the subtraction spectrum, there is an increase in absorbance from 190 to 600 nm after X-ray irradiation. In relation to the Ce-doped KGdP sample (Figure 6.b), the broad and intense band observed in the optical absorption spectra corresponds to the $^2F_{5/2} \rightarrow 5d_x$ transitions of Ce^{3+} along with the same $4f \rightarrow 4f$ transitions of Gd^{3+} present in the undoped sample, as clearly shown in our previous work[17]. In the corresponding subtraction spectrum, it can

be seen that the broad radiation-induced absorption band present in the previous sample is not present in the case of Ce-doped KGdP. About the optical absorption spectra of the Pr-doped KGdP sample (Figure 6.c), the broad and intense band centred around 218 nm corresponds to the $^3H_4 \rightarrow 5d_1$ transition of Pr^{3+}, while the absorption peaks within the spectral range from 425 to 625 nm correspond to some $4f \rightarrow 4f$ transitions of Pr^{3+} (as shown in our previous work[6]) and the other peaks correspond to Gd^{3+} $4f \rightarrow 4f$ transitions. In the subtraction spectrum, it can be seen that there is an increase in absorbance from 190 to 600 nm after X-ray irradiation with a maximum intensity centred at around 400 nm. The subtraction spectra are in agreement with the coloration of the samples, since the broad absorption band with uniform intensity present in the spectrum of the undoped KGdP results in the dark region (Figure 5.a), the non-existence of such band in the spectrum of the Ce-doped sample results in a colourless sample. The broad absorption band with higher absorbance in the blue region results in the brown-yellowish region in the Pr-doped KGdP samples (Figure 5.b). The difference in absorbance between the spectra before and after the X-ray irradiation is very low in all cases; although it should be taken into account that, the spectra obtained after the irradiation were measured after 5-7 days of recovering, so it is clear that the absorbance was higher just after irradiating the samples and this caused the coloration of the samples. The no appearance of radiation-induced absorption bands after several days of recovery and the no colour change visible to the naked eye in the Ce-doped KGdP samples could indicate that these samples might not suffer from radiation damage.

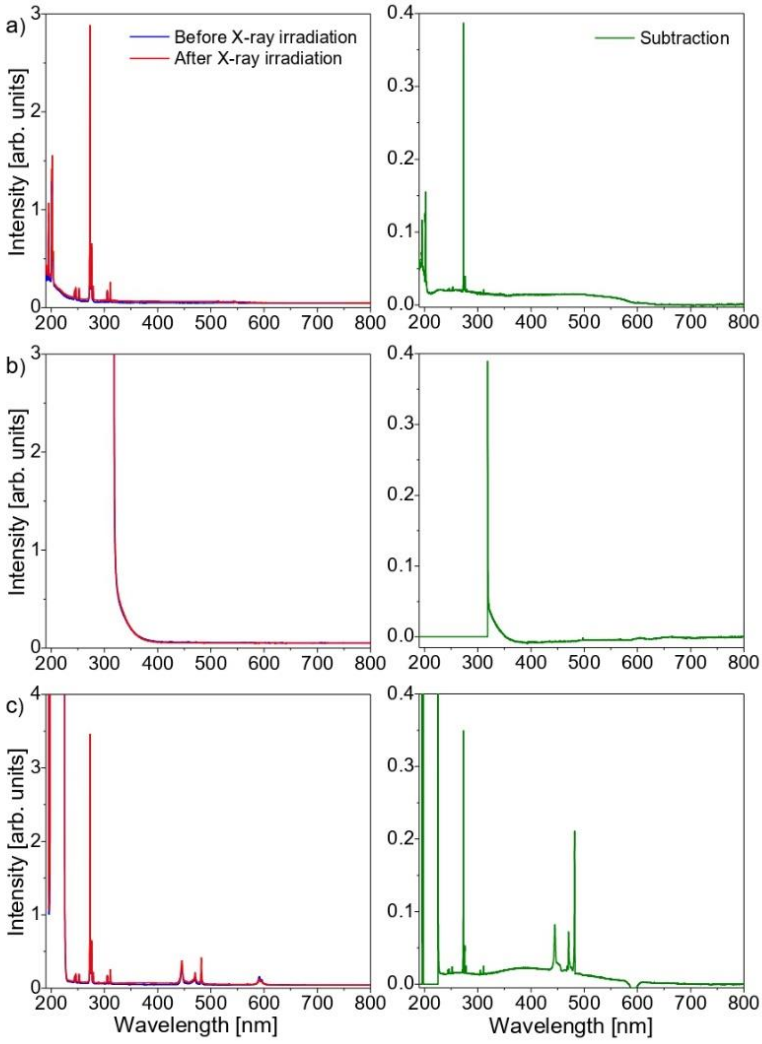
a)
b)
c)
Before X-ray irradiation
After X-ray irradiation
Subtraction
Intensity [arb. units]
Wavelength [nm]

Figure 6. Optical absorption spectra before and 5-7 days after continued X-ray irradiation (left) and the spectra resulting from the subtraction of the first data from the second one (right) for a) undoped KGdP, b) 1 at. % Ce:KGdP and c) 1 at. % Pr:KGdP single crystals.

As can be seen, the broad radiation-induced absorption band observed in the subtraction spectrum of the undoped KGdP sample is similar to that observed in the Pr-doped KGdP sample. Since this band is present in the undoped sample and only in one of the two doping ions used in this work, this behaviour has been attributed to the formation of colour centres related to defects in the crystal lattice, in particular due to the existence of oxygen vacancies that probably appeared in the crystal growth process. Therefore, according to the observed change in colour, the undoped and Pr-doped KGdP samples should have more oxygen vacancies after the crystal growth than the Ce-doped KGdP samples.

Due to the capture of electrons by oxygen vacancies and the sequential capture of charge carriers by the Ce^{3+}, Pr^{3+} and Gd^{3+} ions (see sections 3.2.2 and 3.2.4), there could be competition between these two processes and this would affect to the scintillation mechanism. In addition to this, the fact that the emission bands corresponding to the $5d_1 \rightarrow 4f$ transitions of Pr^{3+} overlap with the radiation-induced absorption band could also affect.

4. CONCLUSIONS

In the present paper, X-ray excited radioluminescence (RL) studies of type III $KGd(PO_3)_4$ bulk single crystals doped with Ce^{3+} and Pr^{3+} ions at different concentrations have been reported for the first time up to now. The RL spectra of the Ce:KGdP samples obtained after exciting them with different X-ray energies show an intense band extending from 300 to 385 nm, which has been

ascribed to the $5d_1 \rightarrow {}^2F_{5/2}$ and $5d_1 \rightarrow {}^2F_{7/2}$ transitions of Ce^{3+} in KGdP, and other bands with lower intensity in the visible region that belong to $4f \rightarrow 4f$ transitions of Gd^{3+}. Since the band corresponding to the ${}^6P_{3/2,5/2,7/2} \rightarrow {}^8S_{7/2}$ transitions of Gd^{3+} (around 312 nm) is not present when KGdP is doped with Ce^{3+}, this behaviour has been attributed to a very efficient energy transfer from the ${}^6P_J$ levels of Gd^{3+} to the $5d_1$ level of Ce^{3+}. In addition, bidirectional energy transfer processes between the $5d_5$ level of Ce^{3+} and the ${}^6F_J$ and ${}^6G_J$ levels of Gd^{3+} might take place. Among the concentrations studied, the doping level of Ce^{3+} in KGdP that provides the highest intensity of the emission band corresponding to the $5d_1 \rightarrow {}^2F_{5/2,7/2}$ transitions is 0.5 at. % of Ce^{3+} substituting Gd^{3+}. In contrast, the RL spectra of the Pr:KGdP samples obtained reveal the presence of the Gd^{3+} emission band centred at 312 nm belonging to the ${}^6P_{3/2,5/2,7/2} \rightarrow {}^8S_{7/2}$ transitions, this being the most intense band. These spectra also show two bands centred around 236 and 259 nm, corresponding to the $5d_1 \rightarrow {}^3H_{4,5,6}, {}^3F_2$ and $5d_1 \rightarrow {}^3F_{3,4}, {}^1G_4$ transitions of Pr^{3+} in KGdP, respectively. Additionally, other bands with lower intensity in the visible region, which have been attributed to $4f \rightarrow 4f$ transitions of Gd^{3+} or the ${}^1D_2 \rightarrow {}^3H_4$ and ${}^3P_0 \rightarrow {}^3H_6$ transitions of Pr^{3+} depending on the excitation energy have also been observed. In the Pr:KGdP samples, bidirectional energy transfer processes are also expected, in this case, between the $5d_{2,3}$ levels of Pr^{3+} and the Gd^{3+} $4f$ levels of higher energy. After exciting the samples under prolonged X-ray radiation, change in coloration in the region irradiated was observed in the undoped and Pr-doped KGdP samples, but not in the Ce-doped KGdP samples. A radiation-induced absorption band extending from 190 to 600 nm has been observed in the optical absorption spectra of the undoped and Pr-doped KGdP samples after X-ray irradiation, which could be related to the existence of colour centres due to the presence of oxygen vacancies in the crystalline lattice. There is evidence that allow us to conclude that the Ce-doped KGdP samples do not suffer from radiation damage under continued X-ray irradiation, so

they seem to be good candidates for scintillation applications. Nevertheless, in future works, it would be interesting to perform decay time measurements under X-ray radiation to know the scintillation mechanism in these samples, as well as X-ray photoelectron spectroscopy (XPS) measurements of type III $KCe(PO_3)_4$ and $KPr(PO_3)_4$ single crystals in order to estimate the energy differences between the top of the valence band and the $4f$ ground state of Ce^{3+} and of Pr^{3+}, respectively.

AUTHOR INFORMATION

Corresponding Authors

* E-mail address: mariacinta.pujol@urv.cat; Phone number: +34 977558628

* E-mail address: rosam.sole@urv.cat; Phone number: +34 977558787

Author Contributions

The manuscript was written through contributions of all authors. All authors have given approval to the final version of the manuscript.

Notes

The authors declare no competing financial interest.

ACKNOWLEDGMENTS

The authors are grateful for the financial support provided by the Spanish Government under Projects MAT2016-75716-C2-1-R (AEI/ FEDER,UE), and from the Catalan Government under Project 2017 SGR 755. I. Adell gratefully acknowledges the financial support of the Catalan Government with the grants 2015 FI_B 00711, 2016 FI_B1 00113 and 2017 FI_B2 00017. The authors thank ALBA Synchrotron for allocating beamtime at BL22-CLAESS beamline under the

project with proposal number 2016091932, and Carlo Marini for his help and technical support during the radioluminescence measurements.

REFERENCES

(1) T. Yanagida, Inorganic Scintillating materials and scintillation detectors, Proc. Jpn. Acad. Ser. B 94 (2018) 75-97.

(2) M. Khoshakhlgh, J.P. Islamian, S. M. Abedi, B. Mahmoudian, development of Scintillators in nuclear Medicine, World J. Nucl. Med. 14 (2015) 156-159.

(3) S. Heller, P. Zanzonico, Nuclear probes and intraoperative gamma cameras, Semin. Nucl. Med. 41 (2011) 166-181.

(4) M. Nikl, Scintillation detectors for x-rays, Meas. Sci. technol. 17 (2006) R37-R54.

(5) P. Lecoq, A. Annenkov, A. Gektin, M. Korzhik, C. Pedrini. Introduction: How to answer high light yield, short decay time, and good energy resolution. In Inorganic scintillators for detector systems: Physical principles and crystal engineering. Springer Berlin Heidelberg: The Netherlands, 2006; pp 81-82.

(6) I. Adell, M. C. Pujol, R. M. Solé, M. Lancry, N. Ollier, M. Aguiló, F. Díaz, Single crystal growth, optical absorption and luminescence properties under VUV-UV synchrotron excitation of type III Pr^{3+}:$KGd(PO_3)_4$, Submitted to Sci. Rep. (2019)

(7) T. Shalapska, G. Stryganyuk, P. Demchenko, A. Voloshinovskii, P. Dorenbos, Luminescence properties of Ce^{3+}-doped $LiGdP_4O_{12}$ upon vacuum-ultraviolet and x-ray excitation, J. Phys.: Condens. Matter 21 (2009) 445901 (8pp).

(8) J. Zhong, H. Liang, Q. Su, J. Zhou, I. V. Khodyuk, P. Dorenbos, Radioluminescence properties of Ce^{3+}-activated $MGd(PO_3)_4$ (M = Li, Na, K, Cs), Opt. Mater. 32 (2009) 378-381.

(9) A. Lukowiak, L. marciniak, I. Vasilchenko, C. Armellini, A. Chiasera, A. Vaccari, M. Ferrari, D. Dorosz, W. Strek, Phsophate-based Glasses and nanostructures, ICTOn, We.C6.2.

(10) Z. Mazurka, E. Lukowiak, B. Jesowska-Trzebiatowska, Growth and spectroscopic properties of the Pr^{3+} ions in the $LiPrP_4O_{12}$ single crystals, J. Mol. Struct. 115 (1984) 31-35.

(11) K. Horchani, J.C. Gâcon, C. Dujardin. Scintillation properties of $CsPrP_4O_{12}$ and $RbPr\ P_4O_{12}$, Nucl. Instrum. Method. A, 486 (2001) 283-287.

(12) I. Parreu, R. Solé, J. Massons, F. Díaz, M. Aguiló, Crystal growth and characterization of type III Ytterbium-doped $KGd(PO_3)_4$: A new nonlinear laser host, Chem. Mater. 19 (2007) 2868-2876.

(13) R. Solé, X. Ruiz, M. C. Pujol, X. Mateos, J. J. Carvajal, M. Aguiló, F. Díaz, Physical properties of self-flux and WO_3-containing solutions useful for growing type III $KGd(PO_3)_4$ single crystals, J. Cryst. Growth 311 (2009) 3656–3660.

(14) J. A. Bearden, A. F. Burr, Reevaluation of X-Ray Atomic Energy Levels, Rev. Mod. Phys. 1967, 39 (1967) 125-142.

(15) P. Luger, Generation of X-rays. In Modern X-ray analysis on single crystals. Walter de Gruyter: Berlin, Germany, 1980; pp 80.

(16) C. Suryanarayana and M. Grant Norton. X-rays and diffraction. In X-ray diffraction: A practical approach. Plenum Press: New York, NY, 1998; pp 12.

(17) I. Adell, R. M. Solé, M. C. Pujol, M. Lancry, N. Ollier, M. Aguiló, F. Díaz, Single crystal growth, optical absorption and luminescence properties under VUV-UV synchrotron excitation of type III Ce^{3+}:$KGd(PO_3)_4$, a promising scintillator material, Sci. Rep. 8 (2018) 11002 (11p)

(18) G. H. Dieke, H. M. Crosswhite, The Spectra of the Doubly and Triply Ionized Rare Earths, Appl. Opt. 2 (1963) 675-686.

(19) R. T. Wegh, A. Meijerink, R. J. Lamminmaki, J. Hölsa, Extending Dieke's Diagram, J. Lumin. 87-9 (2000) 1002-1004.

(20) R. T. Wegh, H. Donker,; A. Meijerink, R. Lamminmäki, J. Hölsä, Vacuum-Ultraviolet Spectroscopy and Quantum Cutting for Gd^{3+} in $LiYF_4$, Phys. Rev. B 56 (1997) 13841-13848.

(21) Z. Yang, J. H. Lin, M. Z. Su, Y. Tao, W. Wang, Photon Cascade Luminescence of Gd^{3+} in $GdBaB_9O_{16}$, J. Alloys Compd. 308 (2000) 94-97.

(22) C. Pédrini, D. Bouttet, C. Dujardin, A. Belsky, A. Vasil'ev, Energy transfer and quenching processes in cerium-doped scintillators. In: P. Dorenbos and C. W. E. van Eijk (Eds) Proceedings of the International Conference on Inorganic Scintillators and Their Applications, SCINT. Delft University Press, The Netherlands, 1995, pp 103-110.

(23) P. Lecoq, A. Annenkov, A. Gektin, M. Korzhik, C. Pedrini, Scintillation mechanisms in inorganic scintillators. In Inorganic scintillators for detector systems: Physical principles and crystal engineering. Springer Berlin Heidelberg: The Netherlands, 2006; pp 81-95.

(24) C. Pédrini, Scintillation mechanisms and limiting factors on each step of relaxation of electronic excitations, Phys. Solid State 47 (2005) 1406-1411.

(25) A. J. Wojtowicz, Scintillation mechanism: the significance of variable valence and electron-lattice coupling in R.E.-activated scintillators. In: P. Dorenbos and C. W. E. van Eijk (Eds) Proceedings of the International Conference on Inorganic Scintillators and Their Applications, SCINT. Delft University Press, The Netherlands, 1995, pp 95-102.

(26) P. A. Rodnyi, Cerium-activated compounds. In Physical processes in Inorganic scintillators. M. J. Weber, Ed.; CRC Press LLC: Boca Raton, FL, 1997; pp 152-154.

(27) P. Lecoq, A. Annenkov, A. Gektin, M. Korzhik and C. Pedrini. Specific killer ions. In Inorganic scintillators for detector systems: Physical principles and crystal engineering. Springer Berlin Heidelberg: The Netherlands, 2006; pp 88-89.

(28) C. Dujardin, C. Pedrini, J. C. Gâcon, A. G. Petrosyan, A. N. Belsky, A. N. Vasil'ev, Luminescence properties and scintillation mechanisms of cerium- and praseodymium-doped lutetium orthoaluminate, J. Phys.: Condens. Matter 9 (1997) 5229-5243.

(29) A. Canning, A. Chaudhry, R. Boutchko, N. Grønbech-Jensen, First-principles study of luminescence in Ce-doped inorganic scintillators, Phys. Rev. B 83 (2011) 125115 (12 pp).

(30) P. Lecoq, A. Annenkov, A. Gektin, M. Korzhik, C. Pedrini. Limitation in charge carriers capture probability. In Inorganic scintillators for detector systems: Physical principles and crystal engineering. Springer Berlin Heidelberg: The Netherlands, 2006; pp 88.

(31) P. Dorenbos, T. Shalapska, G. Stryganyuk, A. Gektin, A. Voloshinovskii, Spectroscopy and energy level location of the trivalent lanthanides in $LiYP_4O_{12}$, J. Lumin. 131 (2011) 633-639.

(32) H. Liang, Z. Tian, H. Lin, M. Xie, G. Zhang, P. Dorenbos, Q. Su, Photoluminescence and radioluminescence of pure and Ce^{3+} activated $Na_3Gd(PO_4)_2$, Opt. Mater. 33 (2011) 618-622.

(33) M. Kucera, M. Hanus, Z. Onderisinova, P. Prusa, A. Beitlerova, M. Nikl, Energy transfer and scintillation properties of Ce^{3+} doped $(LuYGd)_3(AlGa)_5O_{12}$ multicomponent garnets, IEEE Trans. Nucl. Sci. 61 (2014) 282-289.

(34) M. Rathaiah, M. Kucera, J. Pejchal, A. Beitlerova, R. Kucerkova, M. Nikl, Epitaxial growth, photoluminescence and scintillation properties of Gd^{3+} co-doped $YAlO_3:Ce^{3+}$ films, Radiat. Meas. 121 (2019) 86-90.

(35) T. Shalapska, G. Stryganyuk, P. Demchenko, A. Voloshinovskii, P. Dorenbos, Luminescence properties of Ce^{3+}-doped $LiGdP_4O_{12}$ upon vacuum-ultraviolet and x-ray excitation, J. Phys.: Condens. Matter 21 (2009) 445901 (8pp).

(36) X. Qin, X. Liu, W. Huang, M Bettinelli, X. Liu, Lanthanide-activated phosphors based on 4f-5d optical transitions: theoretical and experimental aspects, Chem. Rev. 117 (2017) 4488-4527.

(37) Z. Yang, J. H. Lin, M. Z. Su, Y. Tao, W. Wang, Photon Cascade Luminescence of Gd^{3+} in $GdBaB_9O_{16}$, J. Alloys Compd. 308 (2000) 94-97.

(38) Y. Wu, G. Ren, Energy transfer and radiative recombination processes in $(Gd,Lu)_3Ga_3Al_2O_{12}:Pr^{3+}$ scintillators, Opt. Mater. 35 (2013) 2146-2154.

(39) I. Carrasco, K. Bartosiewicz, F. Piccinelli, M. Nikl, M. Bettinelli, Structural effects and 5d→4f emission transition shifts induced by Y co-doping in Pr-doped $K_3Lu_{1-x}Y_x(PO_4)_2$, J. Lumin. 189 (2017) 113-119.

(40) M. Nikl, A. M. Begnamini, V. Jary, D. Niznansky, E. Mihokova, Pr^{3+} luminescence center in $Lu_2Si_2O_7$ host, Phys. Status Solidi RRL 3 (2009) 293-295.

(41) J. Pejchal, M. Buryi, V. Babin, P. Prusa, A. Beitlerova, J. Barta, L. Havlak, K. Kamada, A. Yoshikawa, V. Laguta, M. Nikl, Luminescence and scintillation properties of Mg-codoped LuAG:Pr single crystals annealed in air, J. Lumin. 181 (2017) 277-285.

(42) K. V. Ivanovskikh, A. Meijerink, F. Piccinelli, A. Speghini, E. I. Zinin, C. Ronda, M. Bettinelli. Optical spectroscopy of $Ca_3Sc_2Si_3O_{12}$, $Ca_3Y_2Si_3O_{12}$ and $Ca_3Lu_2Si_3O_{12}$ doped with Pr^{3+}, J. Lumin. 130 (2010) 893-901.

(43) K. Kamada, M. Nikl, S. Kurosawa, Y. Shoji, J. Pejchal, Y. Ohashi, Y. Yokota, A. Yoshikawa, Growth and scintillation properties of praseodymium doped $(Lu,Gd)_3(Ga,Al)_5O_{12}$ single crystals, J. Lumin. 169 (2016) 811-815.

(44) R. Y. Zhu, Radiation damage in scintillating crystals, Nucl. Instr. Meth. Phys. Res. A 413 (1998) 297-311.

(45) S. Burachas, Yu. Saveliev, M. Ippolitov, V. Manko, V. Lomonosov, A. Vasiliev, A. Apanasenko, A. Vasiliev, A. Uzunian, G. Tamulaitis, Physical origin of coloration and radiation hardness of lead tungstate scintillation crystals, J. Cryst. Growth 293 (2006) 62-67.

(46) R. Y. Zhu, H. Stone, H. Newman, T. Q. Zhou, H. R. Tan, C. F. He, A study on radiation damage in doped BGO crystals, Nucl. Instr. Meth. Phys. Res. A 302 (1991) 69-75.

For Table of Contents Only

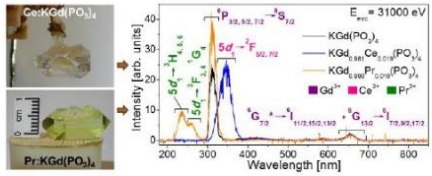

UNIVERSITAT ROVIRA I VIRGILI
CE OR PR-DOPED TYPE III KGD(PO3)4 CRYSTALLINE MATERIALS. GROWTH AND CHARACTERIZATION AS SCINTILLATORS
Irina Adell Barbarà

UNIVERSITAT
ROVIRA i VIRGILI